Engineering Earth-Abundant Metal Catalysts using Metal-Organic Frameworks (MOFs) for Selective Oxidation of Methane and other Hydrocarbons

Poorvi Gupta



Department of Chemistry

INDIAN INSTITUTE OF TECHNOLOGY DELHI

NEW DELHI–110016, INDIA

April, 2026

© Indian Institute of Technology Delhi (IITD), New Delhi, 2026

Engineering Earth-Abundant Metal Catalysts using Metal-Organic Frameworks (MOFs) for Selective Oxidation of Methane and other Hydrocarbons

by

Poorvi Gupta

Department of Chemistry

Submitted

In fulfillment of the requirements of the degree of

Doctor of Philosophy

to the



INDIAN INSTITUTE OF TECHNOLOGY DELHI

HAUZ KHAS, NEW DELHI-110016 INDIA

April, 2026

Dedicated to my parents

Your endless support, strength, and encouragement
have been the foundation of everything I have achieved.
I dedicate this work to you with all my love and gratitude.



CERTIFICATE

This is to certify that the thesis entitled **"Engineering Earth-Abundant Metal Catalysts using Metal-Organic Frameworks (MOFs) for Selective Oxidation of Methane and other Hydrocarbons"** being submitted by **Poorvi Gupta** (Entry No.: 2021CYZ8378) to Indian Institute of Technology Delhi, for the award of the degree of Doctor of Philosophy, is a record of bonafide research work carried out by her. Poorvi Gupta has worked under my supervision and has fulfilled all the requirements for the submission of her PhD thesis, which to my knowledge has reached the requisite standard and is worthy of consideration for the **award of PhD degree**. The work embodied in this thesis has not been submitted, in part or full, to other University or Institute for the award of any degree or diploma.

Dr. Kuntal Manna
Thesis Supervisor
Department of Chemistry
Indian Institute of Technology Delhi
Hauz Khas, New Delhi, 110016, India

New Delhi
April, 2026

ACKNOWLEDGEMENTS

Though I struggled and felt like quitting many times, I now stand close to completing my Ph.D. This journey of nearly five years would not have been possible without the constant support of numerous people around me.

I would like to express my deepest and heartfelt gratitude to my supervisor, ***Prof. Kuntal Manna****, whose mentorship has been the cornerstone of this PhD. He has been far more than an advisor—he has been a role model who shaped the way I think, work, and approach science. His unwavering support, clarity of thought, and exceptional problem-solving skills have guided me through every difficult phase of this journey. What truly set him apart was his ability to create a warm, stress-free research atmosphere, where learning felt natural and growth felt continuous. His encouraging words, his appreciation for even my smallest achievements, and his genuine belief in my abilities kept me motivated throughout these years. I feel profoundly fortunate to have worked under his supervision. The values, scientific discipline, and confidence I gained from him will stay with me long after my PhD. I will truly miss working with him and remain deeply grateful for everything he has taught me.*

I extend my heartfelt thanks to my parents, ***Mr. Subhash Gupta*** *and* ***Mrs. Sangeeta Gupta****, for their unconditional love and support. My father,* ***Mr. Subhash Gupta****, has made countless sacrifices to give me the best life. His silent yet unwavering love, financial support, and protective nature relieved me from every burden during this degree. His life lessons will stay with me forever. My mother,* ***Mrs. Sangeeta Gupta****, has always believed in me and been my emotional anchor. Her trust, affection, and heart-to-heart conversations have given me the strength to face every challenge. I am truly blessed to have her by my side.*

I am deeply thankful to my siblings, Saloni and Dhruv Gupta, who have filled my life with joy, laughter, and steady support. Their enthusiasm for every small milestone and the fun

memories we created helped me stay balanced through the toughest moments. I am equally grateful to my cousin, Dr. Priya Gupta, whose comforting words and uplifting presence always brought me strength during difficult times.

My sincere thanks to my SRC members: Prof. S. Nagendran, Prof. Subrata Kundu, and Prof. Arya V. for taking the time to attend my presentations and for their helpful feedback and guidance. I would also like to thank my external examiner: Prof. Partha Sarathi Mukherjee and Prof. Kaushik Ghosh for their valuable feedback and insightful comments, which helped improve the quality of this thesis.

I am thankful to the instrumentation facility staff, including Mr. Narugopal Kuily, Ms. Shubra Gupta, and Mr. Sandeep, for their assistance throughout my research work. I also appreciate the support from the Chemistry Department office staff—Mrs. Dimple Hindwani, Mr. Vinod Kumar, Mr. Shiv and Mr. Ashish—for their help with administrative procedures. My gratitude extends to Mr. Manoj Kumar and Ms. Poornima Kamboj for their assistance with NMR operations, and to the Central Research Facility (CRF) at IIT Delhi and Dr. Atul Kumar Singh for their support with various characterization techniques.

I would like to thank my friends, Rahul and Bharti, for being my constant help and emotional support throughout this PhD journey. I am also grateful to my PhD mentor, Dr. Naved, for his guidance and encouragement. Special thanks to my seniors: Dr. Rajashree, Dr. Neha, Dr. Wahida, and Dr. Manav for their advice and support. I appreciate the help and friendship of my juniors, especially Swapnaneel and Tanmay, as well as Chhaya, Rishabh, Akanksha, Aditya, Astha, and Shivangi. I also acknowledge the postdoctoral researchers Dr. Ajay Kumar and Dr. Bitan Sardar, along with my MSc and MTech colleagues, past and present, who made this journey memorable.

Finally, I am grateful to my dear friends Diksha and Tanisha, who were always there to listen, support, and make this distant place feel like home. Outside the lab, life becomes richer with the people who share their warmth and time. I am deeply grateful to my friends: Jyoti, Surya, Sagar, Nidhi, Teena, Vishal, Aarti, Archita, and many others whose support and companionship sustained me throughout my PhD journey.

I gratefully acknowledge the financial support received from the Council of Scientific and Industrial Research (CSIR). I also appreciate the research funding provided by the Science

and Engineering Research Board (SERB), the Anusandhan National Research Foundation (ANRF), and the Gas Authority of India Ltd. (GAIL), which greatly supported the progress of this work. I further thank the leadership of IIT Delhi, including former and current directors Prof. Ram Gopal Rao and Prof. Rangan Banerjee, whose continuous efforts have strengthened the institute's research environment.

Above all, I thank God for granting me the wisdom to make the right decisions, the strength to overcome challenges, and the good health that sustained me during the demanding years of my PhD.

Poorvi Gupta

ABSTRACT

The selective oxidation of methane into liquid oxygenates such as methanol and acetic acid represents one of the most compelling challenges in modern catalysis. Methane is abundant yet extremely inert because of its strong C–H bond, and under oxidative conditions it rapidly overoxidizes to CO_2. Developing catalysts that can activate methane at moderate temperatures while controlling product selectivity is therefore of great importance for both energy and chemical industries. This thesis addresses this challenge through the design of molecularly well-defined, single-site metal catalysts immobilized within metal-organic frameworks (MOFs), which provide a unique platform to isolate active centers, tune their coordination environments, and stabilize reactive intermediates that are difficult to control in conventional heterogeneous systems.

MOFs offer high porosity, structural modularity, and the ability to anchor active sites with near-molecular precision. By integrating monomeric Cu or mono- and dinuclear Fe hydroxyl units into tailored MOF architectures such as MIL-53(Al), MOF-253(Al), and bipyridyl-functionalized UiO frameworks, this research demonstrates how active-site nuclearity, ligand environment, and pore confinement collectively govern oxygen activation pathways and reaction selectivity. Across the thesis, these catalysts enable the conversion of methane selectively into acetic acid or methanol using O_2 as the sole oxidant, operating under significantly milder conditions than traditional systems. Beyond methane, the work extends to the oxidation of benzene and styrene, where shape-selective pores and isolated Fe hydroxyl centers allow highly selective formation of phenol, benzaldehyde, or benzoic acid.

Each chapter combines advanced synthetic strategies, comprehensive spectroscopic characterization (XPS, XAS, EPR, PXRD, BET), and DFT calculations to establish detailed structure-activity relationships. The findings demonstrate how the precise engineering of mono- versus dinuclear active sites inside MOFs enables control over radical and non-radical pathways, suppresses overoxidation, and enhances both activity and selectivity. Overall, this thesis highlights MOFs as powerful platforms for developing earth-abundant, recyclable, and

selective oxidation catalysts, providing molecular-level insights that can guide future catalyst design for hydrocarbon functionalization.

Chapter 1: Introduction to Metal-Organic Frameworks and Single-Site Catalysts.

This chapter provides an overview of metal–organic frameworks (MOFs) as crystalline, modular platforms for designing catalytically active sites with molecular precision. The tunable connectivity between metal nodes and organic linkers enables the construction of well-defined coordination environments that emulate enzymatic pockets while maintaining heterogeneous stability. Emphasis is placed on the role of linker functionality and post-synthetic metalation in tailoring the electronic and geometric structure of the active centers. The discussion traces the evolution of MOFs from inert porous hosts to redox-active catalytic materials, particularly those incorporating Fe and Cu sites capable of facilitating small-molecule activation and selective oxidation chemistry. By highlighting advances in framework engineering, site isolation, and cooperative multinuclear design, this chapter establishes the conceptual foundation for the Fe- and Cu-based catalytic systems discussed in the subsequent chapters.

Chapter 2: Materials and Methods.

This chapter summarizes the experimental procedures and characterization methods used throughout this work. All starting materials, reagents, and solvents were obtained from reliable commercial suppliers, with purification and drying performed when required. Glassware and reactors were cleaned using standardized solvent rinses and specialized treatments to ensure contamination-free synthesis. High-pressure methane and oxygen reactions were carried out in reinforced reactors under strict safety protocols, while air- and moisture-sensitive steps were conducted using Schlenk techniques or in an inert-atmosphere glovebox. A comprehensive suite of analytical tools was employed to characterize the structural, textural, and electronic properties of the MOF-based catalysts. PXRD, BET, FT-IR, TGA, SEM-EDX, ICP-OES, XPS, EPR, and XAS provided detailed insight into crystallinity, porosity, functional groups, metal loading, oxidation states, and local coordination environments. Reaction mixtures were analyzed using NMR, GC, and HPLC for accurate product identification and quantification. Complementary density functional theory (DFT) calculations were performed to probe active-site structures, reaction energetics, and mechanistic path-

ways. Together, these methods establish a rigorous and reproducible foundation for the catalytic studies presented in this thesis.

Chapter 3: Copper Catalyzed Selective Methane Oxidation into Acetic Acid using O_2.

The direct transformation of methane into C_2 oxygenates such as acetic acid selectively using molecular oxygen (O_2) is a significant challenge due to the chemical inertness of methane, the difficulty of methane C-H bond activation/C-C bond coupling and the thermodynamically favored over-oxidation. In this study, we have successfully developed a porous aluminium metal–organic framework (MOF)-supported single-site mono-copper(II) hydroxyl catalyst [MIL-53(Al)-Cu(OH)], which is efficient in directly oxidizing methane to acetic acid in water at 175 °C with a remarkable selectivity using only O_2. This heterogeneous catalyst achieved an exceptional acetic acid productivity of 11796 $mmol_{CH3CO2H}$ mol_{Cu}^{-1} h^{-1} in 9.3% methane conversion with 95% selectivity in the liquid phase and can be reused at least 6 times. Our experiments, along with computational studies and spectroscopic analyses, suggest a catalytic cycle involving the formation of a methyl radical ($^{\cdot}CH_3$). The confinement of Cu-active sites within the porous MIL-53(Al) MOF facilitates C-C bond coupling, resulting in the efficient formation of acetic acid with excellent selectivity due to the internal mass transfer limitations. This work advances the development of efficient and chemoselective earth-abundant metal catalysts using MOFs for the direct transformation of methane into value-added products under mild and eco-friendly conditions.

Chapter 4: Dinuclear Iron(II)-Hydroxyl Active Sites for Selective Methane Oxidation to Acetic Acid Using O_2

The selective oxidation of methane to liquid oxygenates using molecular oxygen under mild conditions remains a major challenge due to the inertness of methane and the competing overoxidation reactions. This chapter describes the development of a dinuclear bipyridyl Fe(II) hydroxyl catalyst confined within the porous MOF-253(Al) framework, denoted as MOF-253-Fe_2, featuring a $[(bpy)Fe^{II}(\mu_2\text{-}OH)(OH)]_2$ active site. The catalyst exhibits 100% liquid selectivity toward acetic acid with a productivity of 2,757 $mmol_{CH_3CO_2H}$ mol_{Fe}^{-1} h^{-1} at 160 °C. Detailed spectroscopic studies reveal that the confinement of the dinuclear Fe centers within the MOF facilitates redox cooperativity and multi-electron transfer, enabling efficient O_2 activation and methane C-H bond activation followed by C-C coupling with

in situ generated CO to yield acetic acid. The formation of a $[(bpy)Fe^{III}(\mu_2\text{-}OH)(OH)_2]_2$ intermediate is proposed as the key step in the catalytic cycle. These findings highlight the crucial role of binuclear site design in achieving selective methane-to-acetic acid conversion.

Chapter 5: Mononuclear Iron(II)-Hydroxyl Active Sites for Selective Methane Oxidation to Methanol Using O_2

Direct oxidation of methane to methanol using O_2 under mild conditions is highly desirable yet challenging due to methane's chemical inertness and the tendency of methanol to overoxidize. This chapter presents a mononuclear bipyridyl Fe(II) hydroxyl catalyst supported on MOF-253(Al), designated as MOF-253-Fe, containing a $(bpy)Fe^{II}(OH)_2$ active site. The catalyst achieves a methanol productivity of 6,060 $mmol_{CH_3OH}$ mol_{Fe}^{-1} h^{-1} with 96% selectivity in the aqueous phase at 95 °C. Spectroscopic investigations suggest that the isolated Fe(II)-OH centers promote selective C-H hydroxylation through a radical-mediated pathway, efficiently activating O_2 and methane without further oxidation of methanol. In contrast to the dinuclear analogue, MOF-253-Fe operates via single-site redox chemistry, emphasizing the importance of active site nuclearity in dictating product selectivity. This work provides mechanistic insight into the design of MOF-supported Fe catalysts for selective methane-to-methanol conversion.

Chapter 6: Bipyridyl based Metal-Organic Framework for Selective Hydroxylation of Benzene into Phenol

Direct hydroxylation of benzene to phenol is more appealing in the industry for the economic and environmentally friendly phenol synthesis than the conventional cumene process. We have developed a UiO-metal–organic framework (MOF)-supported mono bipyridyl-Iron(II) hydroxyl catalyst [bpy-UiO-$Fe(OH)_2$] for the selective benzene hydroxylation into phenol using H_2O_2 as the oxidant. The heterogeneous bpy-UiO-$Fe(OH)_2$ catalyst showed high activity and remarkable phenol selectivity of 99%, giving the phenol mass-specific activity up to 1261 $mmol_{PhOH}$ g_{Fe}^{-1} h^{-1} at 60 °C. Bpy-UiO-$Fe(OH)_2$ is significantly more active and selective than its homogeneous counterpart, bipyridine-$Fe(OH)_2$. This enhanced catalytic activity of bpy-UiO-$Fe(OH)_2$ over its homogeneous control is attributed to the active site isolation of the bpy-$Fe(OH)_2$ moiety by the solid MOF that prevents intermolecular decomposition. Moreover, the exceptional selectivity of bpy-UiO-$Fe(OH)_2$ in benzene to phenol conversion is originated via shape-selective catalysis, where the confined reaction

space within the porous UiO-MOF prevents the formation of larger overoxidized products such as hydroquinone or benzoquinone, leading to the formation of only smaller-sized phenol after monohydroxylation of benzene. Spectroscopic and controlled experiments and theoretical calculations elucidated the reaction pathway, in which the in situ generated $^{\cdot}OH$ radical mediated by bpy-UiO-$Fe^{II}(OH)_2$ is the key species for benzene hydroxylation. This work underscores the significance of MOF-supported earth-abundant metal catalysts for sustainable production of fine chemicals.

chapter 7: Mononuclear Bipyridyl-Iron(III) Hydroxide in Metal-Organic Framework for Selective Alkene Oxidation

The selective oxidation of styrene to value-added products such as benzaldehyde and benzoic acid is of significant industrial importance. We report the design of a single-site iron catalyst supported on a bipyridine-functionalized metal–organic framework, bpy-UiO-$Fe(OH)_3$, which enables selective oxidation of styrene into benzaldehyde or benzoic acid using H_2O_2 as the oxidant. Systematic optimization of solvent composition, temperature, and reaction time revealed that benzaldehyde can be obtained with 100% selectivity at 80 °C in 8 h, while prolonged reactions furnish benzoic acid in high yields. Control experiments confirmed the heterogeneous, single-site nature of the catalyst, which remained structurally robust and can be recycled at least three times with negligible Fe leaching. Mechanistic studies suggest a non-radical pathway involving epoxide and diol intermediates prior to carbon–carbon bond cleavage. This work demonstrates the potential of MOF-supported abundant-metal catalysts for sustainable oxidation of alkenes under environmentally benign conditions.

सारांश

मीथेन का चयनात्मक ऑक्सीकरण करके उसे मेथनॉल और एसीटिक अम्ल जैसे तरल ऑक्सीजनयुक्त उत्पादों में रूपांतरित करना आधुनिक उत्प्रेरक विज्ञान की सबसे चुनौतीपूर्ण समस्याओं में से एक है। यद्यपि मीथेन प्रचुर मात्रा में उपलब्ध है, इसकी C-H बंध ऊर्जा अत्यधिक होने के कारण यह अत्यंत निष्क्रिय रहता है, और ऑक्सीकरण परिस्थितियों में शीघ्र ही CO_2 तक अधिक-ऑक्सीकरण हो जाता है। अतः ऐसे उत्प्रेरकों का विकास अत्यंत महत्वपूर्ण है जो मध्यम तापमान पर मीथेन को सक्रिय कर सकें और साथ ही उत्पाद चयनात्मकता को नियंत्रित रखें। यह शोध-प्रबंध इसी चुनौती का समाधान प्रस्तुत करता है, जिसमें आणविक स्तर पर परिभाषित, एकल-स्थल धातु सक्रिय केंद्रों को धातु–कार्बनिक फ्रेमवर्क्स (MOFs) के भीतर स्थिरित करके अत्यधिक चयनात्मक उत्प्रेरकों का निर्माण किया गया है। MOFs इन सक्रिय केंद्रों को पृथक रखने, उनके समन्वय परिवेश को सटीक रूप से नियंत्रित करने, और पारंपरिक ठोस उत्प्रेरकों में अस्थिर रहने वाले मध्यवर्तियों को स्थिर करने की अद्वितीय क्षमता प्रदान करते हैं।

MOFs अत्यधिक छिद्रता, संरचनात्मक मॉड्यूलैरिटी, तथा लगभग आणविक-स्तर की सटीकता के साथ सक्रिय स्थलों को एंकर करने की क्षमता रखते हैं। MIL-53(Al), MOF-253(Al), और बाइपिरिडिल-संशोधित UiO फ्रेमवर्क्स में एकल-नाभिकीय Cu तथा एकल और द्वि-नाभिकीय Fe-हाइड्रॉक्सिल इकाइयों के समावेशन के माध्यम से यह शोध दर्शाता है कि सक्रिय स्थल की नाभिकीयता, लिगैंड परिवेश, और फ्रेमवर्क का सीमित स्थान (pore confinement), सभी मिलकर O_2 सक्रियण मार्गों और उत्पाद चयनात्मकता को नियंत्रित करते हैं। इस शोध-प्रबंध में वर्णित उत्प्रेरक O_2 को एकमात्र ऑक्सिडेंट के रूप में उपयोग करके मीथेन को अत्यधिक चयनात्मकता के साथ मेथनॉल या एसीटिक अम्ल में परिवर्तित करने में सक्षम हैं, और वह भी पारंपरिक उत्प्रेरकों की तुलना में कहीं अधिक सौम्य परिस्थितियों में। मीथेन के अतिरिक्त, यह कार्य बेंजीन और स्टाइरीन के चयनात्मक ऑक्सीकरण तक विस्तारित है, जहाँ छिद्र-चयनात्मकता तथा पृथक Fe-हाइड्रॉक्सिल केंद्र फिनॉल, बेंज़ाल्डिहाइड तथा बेंज़ोइक अम्ल जैसे उत्पादों की उच्च चयनात्मकता प्रदान करते हैं।

प्रत्येक अध्याय में उन्नत संश्लेषण रणनीतियों, व्यापक स्पेक्ट्रोस्कोपिक तकनीकों (XPS, XAS, EPR, PXRD, BET), तथा DFT गणनाओं का संयोजन करके विस्तृत संरचना–गतिविधि संबंध (structure–activity relationships) स्थापित किए गए हैं। निष्कर्ष यह दर्शाते हैं कि MOFs के भीतर मोनो- और डाइन्यूक्लियर सक्रिय स्थलों की सटीक अभियांत्रिकीकरण करने से रेडिकल तथा गैर-रेडिकल मार्गों पर नियंत्रण प्राप्त किया जा सकता है, अधिक-ऑक्सीकरण को दबाया जा सकता है, और समग्र सक्रियता व चयनात्मकता को बढ़ाया जा सकता है। संक्षेप में, यह शोध MOFs को पृथ्वी-प्रचुर धातुओं पर आधारित, पुनर्चक्रणीय, और अत्यधिक चयनात्मक ऑक्सीकरण उत्प्रेरकों के विकास के लिए एक शक्तिशाली मंच के रूप में स्थापित करता है, और हाइड्रोकार्बन सक्रियण हेतु भविष्य के उत्प्रेरक डिज़ाइन को दिशा देने वाली महत्वपूर्ण आणविक-स्तरीय अंतर्दृष्टि प्रदान करता है।

अध्याय 1: मेटल–ऑर्गेनिक फ्रेमवर्क्स और सिंगल-साइट उत्प्रेरकों का परिचय

यह अध्याय MOFs को क्रिस्टलीय, मॉड्यूलर प्लेटफ़ॉर्म के रूप में परिचित कराता है, जिनकी सहायता से आणविक-स्तर की सटीकता के साथ कैटलिटिक सक्रिय स्थलों का निर्माण संभव होता है। धातु नोड्स और ऑर्गेनिक लिंकर्स की समायोज्य संयोजकता सुव्यवस्थित समन्वय वातावरण उपलब्ध कराती है जो एंजाइम-समान सक्रिय स्थल बनाते हुए भी ठोस उत्प्रेरकों की स्थिरता बनाए रखते हैं। विशेष ध्यान लिंकर्स की रासायनिक कार्यक्षमता तथा पोस्ट-सिंथेटिक मेटलेशन पर दिया गया है, जो सक्रिय केंद्रों की

इलेक्ट्रॉनिक तथा ज्यामितीय संरचना नियंत्रित करते हैं। अध्याय यह भी बताता है कि किस प्रकार MOFs निष्क्रिय छिद्रदार पदार्थों से उन्नत रेडॉक्स-सक्रिय उत्प्रेरकों में विकसित हुए हैं, विशेषकर वे जो Fe और Cu केंद्रों के माध्यम से चयनात्मक ऑक्सीकरण सक्षम कर सकते हैं।

अध्याय 2: सामग्री और विधियाँ

इस अध्याय में सभी प्रायोगिक प्रक्रियाओं और चरित्रण तकनीकों का संक्षिप्त विवरण दिया गया है। सभी रसायन विश्वसनीय आपूर्तिकर्ताओं से प्राप्त किए गए, तथा आवश्यकता अनुसार शुद्धिकरण और सुखाने की प्रक्रियाएँ अपनाई गईं। काँच के बर्तन तथा रिएक्टरों को मानकीकृत विधियों से साफ़ किया गया। उच्च-दाब मीथेन/ऑक्सीजन प्रतिक्रियाएँ सुरक्षित, प्रबलित रिएक्टरों में संचालित की गईं, जबकि वायु-संवेदनशील चरण ग्लवबॉक्स या श्लेंक तकनीकों द्वारा किए गए। MOF उत्प्रेरकों की संरचनात्मक, बनावट-संबंधी और इलेक्ट्रॉनिक विशेषताओं को PXRD, BET, FT-IR, TGA, SEM-EDX, ICP-OES, XPS, EPR और XAS जैसी तकनीकों से विश्लेषित किया गया। प्रतिक्रिया उत्पादों के विश्लेषण हेतु NMR, GC, और HPLC का उपयोग किया गया। साथ ही, DFT गणनाओं का प्रयोग सक्रिय स्थलों की संरचना, ऊर्जा प्रोफ़ाइल, और तंत्र को समझने हेतु किया गया।

अध्याय 3: O_2 के उपयोग से तांबा-उत्प्रेरित मीथेन का चयनात्मक ऑक्सीकरण

इस अध्याय में porous MIL-53(Al) फ्रेमवर्क में समाविष्ट एकल-साइट Cu(II)-OH उत्प्रेरक [MIL-53(Al)-Cu(OH)] का वर्णन किया गया है, जो केवल O_2 का उपयोग करके जल माध्यम में 175 °C पर मीथेन को अत्यधिक चयनात्मकता के साथ एसीटिक अम्ल में परिवर्तित करता है। यह उत्प्रेरक 95% तरल-चयनात्मकता एवं उच्च उत्पादकता प्रदर्शित करता है और कम से कम 6 बार पुनः उपयोग किया जा सकता है। प्रयोगों और संगणकीय अध्ययनों से ज्ञात होता है कि उत्प्रेरक मेथिल रेडिकल मार्ग से कार्य करता है, और MOF की सीमितता C–C बन्ध निर्माण को बढ़ावा देती है।

अध्याय 4: डाइन्यूक्लियर Fe(II)-हाइड्रॉक्सिल सक्रिय स्थल द्वारा मीथेन का चयनात्मक एसीटिक अम्ल में ऑक्सीकरण

यह अध्याय MOF-253(Al) में समाविष्ट द्वि-नाभिकीय बाइपिरिडिल Fe(II)-हाइड्रॉक्सिल सक्रिय स्थल वाले उत्प्रेरक (MOF-253-Fe_2) पर आधारित है। यह 160 °C पर 100% तरल-चयनात्मकता के साथ एसीटिक अम्ल बनाता है और साइट-आइसोलेशन तथा रेडॉक्स सहयोगिता (cooperativity) के कारण अत्यधिक प्रभावी सिद्ध होता है। तंत्र दर्शाता है कि इन-situ CO के साथ C-C कपलिंग करके एसीटिक अम्ल बनता है।

अध्याय 5: मोनोन्यूक्लियर Fe(II)-हाइड्रॉक्सिल द्वारा मीथेन का चयनात्मक मेथनॉल में ऑक्सीकरण

इस अध्याय में MOF-253(Al)-आधारित एकल-स्थल Fe(II)-OH उत्प्रेरक (MOF-253-Fe) की चर्चा की गई है, जो 95 °C पर 96% चयनात्मकता के साथ मेथनॉल बनाता है। यह प्रणाली एक रेडिकल-सहायतित मार्ग द्वारा O_2 और मीथेन को सक्रिय करती है, और मेथनॉल के अधिक-ऑक्सीकरण को रोकती है। तुलना के माध्यम से यह स्पष्ट होता है कि सक्रिय स्थल की नाभिकीयता उत्पाद चयनात्मकता निर्धारित करने में एक केंद्रीय भूमिका निभाती है।

अध्याय 6: बाइपिरिडिल-आधारित MOF द्वारा बेंजीन का चयनात्मक हाइड्रॉक्सीलेशन

UiO-आधारित MOF में समाविष्ट bpy-$Fe(OH)_2$ उत्प्रेरक अत्यधिक चयनात्मकता (99%) के साथ बेंजीन को फिनॉल में परिवर्तित करता है। इसकी सक्रियता समान homogeneous उत्प्रेरक से कहीं अधिक है, जिसका कारण MOF द्वारा सक्रिय स्थल का पृथक्करण तथा आकार-चयनात्मकता है, जो बड़े ओवरऑक्सीकृत उप-उत्पादों (जैसे क्विनोन) के निर्माण को रोकता है। तंत्र $^{\cdot}OH$ रैडिकल की भूमिका को स्पष्ट करता है।

अध्याय 7: मोनोन्यूक्लियर Fe(III)-हाइड्रॉक्साइड द्वारा स्टाइरीन का चयनात्मक ऑक्सीकरण

इस अध्याय में bpy-UiO-$Fe(OH)_3$ उत्प्रेरक का वर्णन है, जो H_2O_2 का उपयोग करके स्टाइरीन को चयनात्मक रूप से बेंज़ाल्डिहाइड या बेंज़ोइक अम्ल में बदलता है। हल्की परिस्थितियों में 100% चयनात्मकता प्राप्त की जा सकती है। उत्प्रेरक संरचनात्मक रूप से स्थिर है और कई चक्रों तक पुनः उपयोग योग्य है। तंत्र दर्शाता है कि ऑक्सीकरण एक गैर-रैडिकल मार्ग से एपॉक्साइड/डायोल इंटरमीडिएटों के माध्यम से होता है।

Contents

CERTIFICATE ii

ACKNOWLEDGEMENTS iii

ABSTRACT vi

List of figures xx

List of tables xxxii

1 Introduction to Reticular Chemistry and Metal-Organic Frameworks 1

1.1 Introduction to Reticular Chemistry 2

1.2 Early Coordination Complex and the Origins of Framework Design 3

1.3 Metal-Organic Frameworks 5

1.3.1 Introduction to Metal-Organic Frameworks. 5

1.3.2 Orgnaic Linkers. 6

1.3.3 Metal Nodes and Secondary Building Units (SBUs). 8

1.4 Nomenclature of Metal–Organic Frameworks (MOFs) 9

1.5 Introduction to MOF synthesis 11

1.5.1 Importance of synthesis methods for catalytic and structural properties. 11

1.5.2 Synthetic Strategies. 12

1.5.3 Fundamental Chemistry Considerations for Reaction Parameters. . 16

1.6 Properties of MOFs. 21

1.6.1 Permanent Porosity and High Surface Area. 21

1.6.2 Themral and Chemical Stability. 22

1.6.3 Framework Flexibility - "Breathing". 22

1.6.4 Structural Diversity and Tunability. 22
1.6.5 Chemical Functionality and Tailored Reactivity. 23
1.7 Isoreticularity in MOFs. 23
1.8 Post-Sythetic Modification (PSM) in MOFs. 26
1.8.1 PSM Over Organic Linkers 26
1.8.2 PSM at Metal Nodes 27
1.8.3 Metal-Ion Exchange 28
1.8.4 Advantages and Challenges of PSM Advantages. 28
1.9 Applications of MOFs. 29
1.9.1 Magnetic Separation using MOFs. 30
1.9.2 Ion Exchange. 31
1.9.3 Drug Delivery. 31
1.9.4 Chemical Sensing. 32
1.9.5 Gas Storage and Separation. 33
1.10 MOFs as Heterogeneous Catalysts. 34
1.10.1 MOFs as Single-Site Catalysts. 35
1.10.2 Catalysis at MOF Nodes. 35
1.10.3 Catalysis at Organic Linkers. 36
1.10.4 Examples of Biomimetic MOF catalysts. 38
1.10.5 MOFs for C-H Activation. 39
1.10.6 MOFs for Oxidation Reactions. 40
1.11 Outline of Thesis. 41

2 Materials and Methods 62

2.1 Chemicals, Reagents, and Solvents Used 63
2.2 Cleaning of Glassware 63
2.3 High-Pressure Reactions 64
2.4 Air-Sesitive Reactions 65
2.5 Instrumental Methods 65
2.5.1 Powder X-ray Diffraction (PXRD). 66
2.5.2 Brunauer–Emmett–Teller (BET) Surface Area Analysis. 66
2.5.3 Thermogravimetric Analysis (TGA). 66

2.5.4 Fourier Transform Infrared Spectroscopy (FT-IR). 67
2.5.5 Scanning Electron Microscopy–Energy Dispersive X-ray Spectroscopy (SEM-EDS). 67
2.5.6 Inductively Coupled Plasma Optical Emission Spectroscopy (ICP-OES). 68
2.5.7 Electron Paramagnetic Resonance (EPR). 68
2.5.8 X-Ray Photoelectron Spectroscopy (XPS). 68
2.5.9 X-Ray Absorption Spectroscopy (XAS). 69
2.6 Analytical Technique 69
2.6.1 Nuclear Magnetic Resonance (NMR). 69
2.6.2 Gas Chromatography (GC). 69
2.6.3 High-Performance Liquid Chromatography (HPLC). 70
2.7 Calculations for conversion and selectivity 70
2.8 Metal Incorporation Analysis 71
2.9 Theoretical Studies 71

3 Copper Catalyzed Selective Methane Oxidation to Acetic Acid using O_2 73

3.1 Introduction 74
3.2 Results and Discussions 76
3.2.1 Synthesis and Characterization of MIL-53-Cu(OH) MOF 76
3.2.2 Catalytic performance for methane oxidation to acetic acid 79
3.2.3 Control experiments 82
3.2.4 Mechanistic exploration of MIL-53(Al)-Cu(OH) catalyzed oxidation of methane to acetic acid 85
3.3 Experimental Section 89
3.3.1 Synthesis of MIL-53(Al) and MIL-53(Al)-Cu(OH) 89
3.3.2 MIL-53(Al) catalysed oxidation of methane. 94
3.3.3 DFT Calculations. 109
3.3.4 X-ray absorption spectroscopic analysis. 126
3.4 Conclusions 137

4 Dinuclear Iron(II)-Hydroxyl Active Sites for Selective Methane Oxidation to Acetic Acid Using O_2 146

4.1 Introduction 147
4.2 Results and Discussion 149
4.2.1 Synthesis and Characterization of MOF-253-Fe_2 149
4.2.2 Catalytic Performance of MOF-253-Fe_2 in Selective Methane Oxidation using O_2. 152
4.2.3 Control Experiments 156
4.2.4 Identification of Reaction Intermediates 158
4.2.5 Mechanism Exploration of MOF-253-Fe_2 Catalyzed Methane to Acetic Acid Conversion. 160
4.2.6 Origin of High Selectivity in Partial Methane Oxidation. 163
4.3 Experimental Section 164
4.3.1 Synthesis and Characterization of MOF-253(Al) and MOF-253-Fe^2. 164
4.3.2 Binuclear MOF-253-Fe_2 catalysed oxidation of methane to acetic acid using O_2 166
4.3.3 DFT structure Optimization 184
4.3.4 X-ray absorption spectroscopic analysis. 187
4.4 Conclusion 199

5 Mononuclear Iron(II)-Hydroxyl Active Sites for Selective Methane Oxidation to Methanol Using O_2 206

5.1 Introduction 207
5.2 Results and Discussion 208
5.2.1 Synthesis and Characterization of MOF-253-Fe. 208
5.2.2 Catalytic Methane Oxidation using MOF-253-Fe. 210
5.2.3 Proposed Mechanism of MOF-253-Fe Catalyzed Methane Oxidation to Methanol. 211
5.3 Experimental Section 213
5.3.1 Synthesis and Characterization of MOF-253(Al) and MOF-253-Fe. . 213
5.3.2 Mononuclear MOF-253-Fe catalyzed methane oxidation. 214
5.3.3 DFT Structure Optimization. 217
5.3.4 X-ray Absorption Spectroscopic Analysis 219

6 Bipyridyl Based Metal-Organic Framework for Selective Hydroxylation of Benzene into Phenol 229

6.1 Introduction 230
6.2 Results and Discussions 231
6.2.1 Synthesis and Characterization of bpy-UiO-Fe(OH)$_2$ 231
6.2.2 Catalytic Performance for Benzene Hydroxylation 233
6.2.3 Control Experiments 237
6.2.4 Mechanism Exploration of Bpy-UiO-Fe(OH)$_2$-Catalyzed Oxidation of Benzene 238
6.3 Experimental Section 240
6.3.1 Synthesis and Characterization of Bpy-UiO-Fe MOF 240
6.3.2 Bpy-UiO-Fe catalyzed hydroxylation of benzene 243
6.3.3 Catalytic testing of Fe nanoparticles. 245
6.3.4 Test for "heterogeneity of bpy-UiO-Fe(OH)$_2$ in benzene hydroxylation to phenol. 246
6.3.5 Radical Scavenging Experiment. 247
6.3.6 DFT Calculations 249
6.3.7 X-ray absorption spectroscopic analysis (XAS) 252
6.3.8 XPS analysis of bpy-UiO-FeCl$_2$, bpy-UiO-Fe(OH)$_2$, bpy-UiO-Fe after catalysis. 257
6.3.9 GC-FID Spectra 258
6.4 Conclusions 260

7 Mononuclear Bipyridyl-Iron(III) Hydroxide in Metal-Organic Framework for Selective Alkene Oxidation 271

7.1 Introduction 272
7.2 Results and Discussion 274
7.2.1 Synthesis and Characterization of bpy-UiO-Fe(OH)$_3$ 274
7.2.2 Bpy-UiO-Fe(OH)$_3$ Catalyzed Oxidation of Styrene Derivatives. . . . 276
7.2.3 Control Experiments. 278
7.2.4 Mechanistic Insights into bpy-UiO-Fe(OH)$_3$-Catalyzed Oxidation of Styrene. 280
7.3 Experimental Section 281
7.3.1 Synthesis and Characterization of bpy-UiO-Fe(OH)$_3$. 281
7.3.2 Bpy-UiO-Fe(OH)$_3$ catalyzed oxidation of styrene substrates. 284

7.3.3 XPS analysis of bpy-UiO-Fe(OH)$_3$. 291
7.3.4 Characterization of the products. 293

Author's Profile **307**

Brief biodata and publications **308**

List of Figures

1.1 Design of nanoparticles (0D), chains (1D), sheets (2D), and networks (3D).[5] 3

1.2 Prussian Blue: the first synthetic coordination compound. 4

1.3 Design of Metal-Organic Framework. 6

1.4 Examples of different organic linkers used in the synthesis of Metal-Organic Framework. 7

1.5 Examples of secondary-building units along with the MOF structure (MOF-5 and HKUST-1) 8

1.6 Illustration of modulator effects during MOF synthesis, including linker equilibrium, coordination and Brønsted acid modulation, and final linker binding to metal nodes.[75] 18

1.7 An example of isoreticular MOF: Zr-based UiO MOFs 24

1.8 Postsynthetic modification at organic linkers and SBUs. 27

1.9 Applications of metal-organic frameworks (MOFs). 30

1.10 General design strategies to create biomimetic MOF catalyst 38

3.1 Development of the porous aluminium-MOF confined mono-Cu(II) hydroxyl catalyst for the direct and selective oxidation of methane to acetic acid utilizing only O_2 as the oxidant. 75

3.2 (a) PXRD patterns of the simulated MIL-53(Al) MOF (black), pristine MIL-53(Al) MOF (red), MIL-53(Al)-CuCl MOF (blue), MIL-53(Al)-CuOH MOF (green), MIL-53(Al)-Cu after run-2 (wine) and run-5 of catalysis (magenta). (b) N_2 sorption isotherms of MIL-53(Al) (black) and MIL-53(Al)-Cu(OH) (red) measured at 77 K. (c) Cu 2p XPS spectra of MIL-53(Al)-Cu(OH) (top) and MIL-53(Al)-Cu after catalysis (bottom). (d) Al 2p XPS spectra of MIL-53(Al)-Cu(OH) (top) and MIL-53(Al)-Cu after catalysis (bottom). (e) Cu K-edge XANES spectra of Cu-foil (grey), $CuCl_2$ (green), MIL-53(Al)-Cu(OH) (blue) and MIL-53(Al)-Cu after catalysis (red). (f) X-band EPR spectra of MIL-53(Al)-Cu(OH) at 298 K. (g) EXAFS spectra and fits in R-space at the Cu K-edge of MIL-53(Al)-Cu(OH) with the magnitude and real component of the Fourier transformation shown as solid and hollow triangles in blue color, respectively. The fitting range in R-space is 1.1–3.8 Å (within the grey line); (h) k^2-weighted Cu-EXAFS (R) spectra of MIL-53(Al)-Cu(OH) (black), CuO (pink), $Cu(OH)_2$ (blue), and Cu foil (red). (i) DFT optimized structure of MIL-53(Al)-Cu(OH)(OH_2). 77

3.3 (a) Effect of temperature on oxygenated product yields and selectivity of acetic acid. Reaction conditions: MIL-53(Al)-Cu(OH) (3.8 mg, 4.0 μmol), 30 bar CH_4, 10 bar O_2, 7 mL water and 32 h. (b) Effect of O_2 pressure on the oxygenated product yields and selectivity of acetic acid. Reaction conditions: MIL-53(Al)-Cu(OH) (3.8 mg, 4.0 mol), 30 bar CH_4, 175 °C, 7 mL water and 32 h, balanced with N_2 to maintain a total pressure of 40 bar. (c) Effect of CH_4 pressure on the oxygenated product yields and selectivity of acetic acid. Reaction conditions: MIL-53(Al)-Cu(OH) (3.8 mg, 4.0 μmol), 10 bar O_2, 175 °C, 7 mL water and 32 h, balanced with N_2 to maintain a total pressure of 40 bar. (d) Effect of time on the oxygenated product yields and selectivity of acetic acid. Conditions: MIL-53(Al)-Cu(OH) (3.8 mg, 4.0 μmol), 30 bar CH_4, 10 bar O_2, 7 mL water and 175 °C. 80

3.4 (a) EXAFS spectra and fits in R-space at the Cu K-edge of MIL-53(Al)-Cu after catalysis with the magnitude and real component of the Fourier transformation shown as solid and hollow triangles in green color, respectively. The fitting range in R-space is 1.1-3.8 Å (within the grey line). (b) Plot of productivity of acetic acid in various runs during recycling and reuse of the MIL-53(Al)-Cu(OH) catalyst for the methane oxidation reaction. (c) X-band (9.85 GHz) EPR spectroscopic spin-trapping experiments. EPR spectrum from the DMPO spin-trapping experiment of uncatalyzed methane oxidation by O_2 at 175 °C (black), MIL-53(Al)-Cu(OH)-catalyzed oxidation of methane by O_2 at room temperature (blue), MIL-53(Al)-Cu(OH) catalyzed methane oxidation in the absence of O_2 at 175 °C (green), MIL-53(Al)-Cu(OH) catalyzed oxidation of CH_4 (30 bar) by O_2 (10 bar) at 175 °C for 32 h (magenta), and simulated DMPO-CH_3 (red). 83

3.5 Comparison of the catalytic efficiency of MIL-53(Al)-Cu(OH) with other materials in direct methane oxidation to acetic acid under identical reaction conditions. Conditions: 30 bar CH_4, 10 bar O_2, 175 °C and 32 h. 83

3.6 The proposed catalytic cycle for MIL-53(Al)-Cu(OH) catalyzed direct oxidation of methane to acetic acid using O_2. 85

3.7 DFT calculated free energy diagram at 448 K for MIL-53(Al)-Cu(OH) catalyzed methane to acetaldehyde conversion. 88

3.8 PXRD patterns of (a) simulated MIL-53(Al) MOF (black), pristine MIL-53(Al) (red), MIL-53(Al)-CuOH (blue), recovered MIL-53(Al)-Cu after methane oxidation for 32 h at 175 °C (run 1) (green), and 200 °C (magenta). (b) freshly prepared MIL-53(Al)-Cu(OH) (black), recovered MIL-53(Al)-Cu after 32 h of catalysis (red), 40 h of catalysis (blue), 50 h of catalysis (green); reaction conditions: 30 bar CH_4, 10 bar O_2, 175 °C and 7 mL water. The PXRD patterns indicate that the crystallinity and the framework of MIL-53(Al) MOF remained intact even after 50 h reaction. 90

3.9 (a) TGA curve of freshly prepared MIL-53(Al) (black) and MIL-53(Al)-Cu(OH) (red). A solvent weight loss of 43.9% in MIL-53(Al) (black) and 28.7% in MIL-53(Al)-Cu(OH) (red) was observed from 40 °C to 200 °C. (b) TGA curve of freshly prepared MIL-53(Al) (black) and MIL-53(Al)-Cu(OH) (red) from 200-700 °C. The increased weight of MIL-53(Al)-Cu(OH) is due to the presence of Cu within the MOF. 91

3.10 IR spectra of freshly prepared MIL-53(Al) (blue), MIL-53(Al)-CuCl (red), and MIL-53(Al)-CuOH (black). In the IR spectra, μ_2-OH stretching frequency peak of MIL-53(Al) at 3706 cm^{-1} disappeared upon metalation, however, a small peak of μ_2-OH reappeared for MIL-53(Al)-Cu(OH) due to protonation of unreacted μ_3-OLi with water. The peak intensity of μ_2-OH stretching frequency of MIL-53(Al)-CuOH at 3706 cm^{-1} was smaller compared to that of pristine MIL-53(Al) MOF due to the partial metalation of the μ_2-OH of the SBUs. 93

3.11 (a) N_2 sorption isotherms of MIL-53(Al) (black) and MIL-53(Al)-Cu(OH) (red) measured at 77 K. (b) NLDFT pore size distribution curve of MIL-53(Al) (black) and MIL-53(Al)-CuOH (red). BET surface for MIL-53(Al) and MIL-53(Al)-Cu(OH) are 1386 m^2/g and 1263 m^2/g and the average pore size for MIL-53(Al) and MIL-53(Al)-CuOH was determined to be 0.62 nm and 0.6 nm, respectively. 93

3.12 SEM image and EDX mapping for MIL-53(Al)-Cu(OH).The uniform distribution of Al and Cu suggests Al and Cu are homogeneously distributed throughout the MOF. 94

3.13 Heterogeneity test of MIL-53(Al)-Cu(OH) in the oxidation of methane. . . 103

3.14 PXRD pattern of simulated DUT-5(Al) (black), synthesized DUT-5(Al) (red), DUT-5(Al)-Cu(OH) (blue), DUT-5(Al)-Cu MOF recovered after catalysis (green). 107

3.15 Proposed catalytic cycle of MIL-53(Al)-Cu(OH) catalyzed oxidation of methane to acetaldehyde. 109

3.16 DFT-calculated free energy diagram of methane oxidation to acetaldehyde over MIL-53(Al)-Cu(OH) at 448 K. 110

3.16 DFT-optimized structures of intermediates and transition states for MIL-53(Al)-Cu(OH) catalyzed oxidation of methane to acetaldehyde. 112

3.17 μ(E) XAS spectra of metallic Cu(0) (grey), $CuCl_2$ (green), MIL-53(Al)-Cu(OH) (blue), MIL-53(Al)-Cu after catalysis (red) 127

3.18 (a) EXAFS spectrum and fit of MIL-53(Al)-Cu(OH). (b) DFT-optimized structure of MIL-53(Al)-Cu(OH). 127

3.19 (a) EXAFS spectrum and fit of MIL-53(Al)-Cu after catalysis. (b) DFT-optimized structure of MIL-53(Al)-Cu after catalysis. 129

3.20 (a) EXAFS spectrum of MIL-53(Al)-Cu(OH) fitted with 5% CuO and 95% MIL-53(Al)-Cu(OH) (red); 25% CuO and 75% MIL-53(Al)-Cu(OH) (blue); 50% CuO and 50% MIL-53(Al)-Cu(OH) (green); 80% CuO and 20% MIL-53(Al)-Cu(OH) (magenta). (b) EXAFS spectrum of MIL-53(Al)-Cu(OH) fitted with 5% Cu (0) and 95% MIL-53(Al)-Cu(OH) (red); 25% Cu (0) and 75% MIL-53(Al)-Cu(OH) (blue); 50% Cu (0) and 50% MIL-53(Al)-Cu(OH) (green) and 80% Cu (0) and 20% MIL-53(Al)-Cu(OH) (magenta). The significant misfits indicate that MIL-53(Al)-Cu(OH) does not contain any Cu dimers/oligomers or Cu-nanoparticles. 129

3.21 (a) EXAFS spectrum of MIL-53(Al)-Cu after catalysis fitted with 5% CuO and 95% MIL-53(Al)-Cu(OH) (red); 25% CuO and 75% MIL-53(Al)-Cu(OH) (blue); 50% CuO and 50% MIL-53(Al)-Cu(OH) (green); 80% CuO and 20% MIL-53(Al)-Cu(OH) (magenta). (b) EXAFS spectrum of MIL-53(Al)-Cu after catalysis fitted with 5% Cu (0) and 95% MIL-53(Al)-Cu(OH) (red); 25% Cu (0) and 75% MIL-53(Al)-Cu(OH) (blue); 50% Cu (0) and 50% MIL-53(Al)-Cu(OH) (green) and 80% Cu (0) and 20% MIL-53(Al)-Cu(OH) (magenta). The significant misfits indicate that MIL-53(Al)-Cu(OH) does not contain any Cu dimers/oligomers or Cu-nanoparticles. 131

3.22 (a) Raw XPS data of MIL-53(Al)-Cu(OH). (b) XPS fitting of copper in MIL-53(Al)-Cu(OH). (c) XPS fitting of aluminium in MIL-53(Al)-Cu(OH). . . . 132

3.23 (a) Raw XPS data of MIL-53(Al)-Cu after catalysis. (b) XPS fitting of copper in MIL-53(Al)-Cu after catalysis. (c) XPS fitting of aluminium in MIL-53(Al)-Cu after catalysis. 133

3.24 XPS fitting of copper in Cu@MIL-53(Al). 133

3.25 (a) ^{13}C NMR (400 MHz, D_2O) spectrum of the reaction mixture obtained after $^{13}CH_4$ oxidation by O_2 using MIL-53(Al)-Cu(OH) as the catalyst. Reaction conditions: 3.8 mg MIL-53(Al)-Cu(OH) (4.0 μmol Cu), 30 bar $^{13}CH_4$, 10 bar O_2, 32 h, 175 °C. Signal centered at 21.2 ppm, corresponding to the sp^3 hybridized carbon and signal centred at 178 ppm corresponds to sp^2 hybridized carbon in $^{13}CH_3{}^{13}CO_2H$, confirms the involvement of CH_4-derived carbon atoms in the formation of acetic acid. (b) Mass spectra of the obtained $^{13}CH_3{}^{13}CO_2H$ after $^{13}CH_4$ oxidation using O_2. (c) Mass spectra of the obtained CH_3CO_2H after CH_4 oxidation using O_2 under identical reaction conditions. 135

4.1 Structural Analogy between Methane Monooxygenase and MOF-253(Al)-Fe_2 Catalysts. 148

4.2 (a) Synthesis of MOF-253-Fe_2. (b) PXRD patterns of simulated MOF-253(Al) (black), pristine MOF-253(Al) (red), MOF-253-$FeCl_2$ (blue), MOF-253-Fe_2 (green), and MOF-253-Fe_2 recovered after the first (wine) and fifth (magenta) run of methane oxidation. (c) Fe 2p XPS spectrum of MOF-253-Fe_2. (d) XANES spectra of Fe(0) foil (black), $FeCl_2$ (brown), $Fe(OH)_3$ (purple), MOF-253-Fe_2 (blue), and MOF-253-Fe_2 after catalysis (red). (e) EXAFS spectra (blue and black hollow squares) and fits (black and blue solid lines) of 90% dimeric MOF-253-Fe_2 and 10% monomeric Fe species in R-space at the Fe K-edge (1.0–3.25 Å). (f) DFT-optimized structure of the diiron(II) core $[(bpy)Fe^{II}(\mu_2\text{-OH})(OH)(OH_2)]_2$ of MOF-253-Fe_2; bond distances in Å. (g) k^2-weighted Fe-EXAFS χ(R) spectra of MOF-253-Fe_2 (black), MOF-253-Fe after catalysis (magenta), MOF-253-Fe (wine), $Fe(OH)_3$ (blue), Fe_2O_3 (green), and Fe foil (red); k range: 3–13 Å. Optimized reaction conditions: MOF-253-Fe_2 (4.7 mg, 10.5 μmol Fe), 20 bar CH_4, 8 bar O_2, 160 °C, 8 mL water, 38 h. . 150

4.3 SEM image of MOF-253-Fe_2 and the FE-SEM-energy dispersive X-ray (EDX) mapping of the respective particles. Scanning electron microscopy (SEM) images of the MOF-253-Fe_2 displayed spherical-shaped particles with diameters ranging from 160-190 nm. SEM-EDX mapping showed a homogeneous distribution of Fe and Al throughout the MOF particles. 151

4.4 N_2 sorption isotherms of MOF-253(Al) (black) and MOF-253-Fe_2 (red) measured at 77 K. BET surface for MOF-253(Al) and MOF-253-Fe_2 are 1586 m^2/g and 540 m_2/g, respectively. 151

4.5 (a) Effect of temperature on oxygenated product yields and selectivity of acetic acid. Reaction conditions: MOF-253-Fe_2 (10.5 μmol Fe), 20 bar CH_4, 8 bar O_2, 8 mL water and 38 h. (b) Effect of O_2 pressure on oxygenated product yields and selectivity of acetic acid. Reaction conditions: MOF-253-Fe_2 (10.5 μmol Fe), 20 bar CH_4, 160 °C, 8 mL water and 38 h, balanced with N_2 to maintain a total pressure of 28 bar. (c) Effect of CH_4 pressure on oxygenated product yields and selectivity of acetic acid. Reaction conditions: MOF-253-Fe_2 (10.5 μmol Fe), 8 bar O_2, 160 °C, 8 mL water and 38 h, balanced with N_2 to maintain a total pressure of 28 bar. (d) Effect of time on oxygenated product yields and selectivity of acetic acid. Reaction conditions: MOF-253-Fe_2 (10.5 μmol Fe), 20 bar CH_4, 8 bar O_2, 8 mL water and 160 °C. (e) ^{13}C NMR (400MHz) spectrum (top) and mass spectrum (bottom)of the reaction mixture obtained after $^{13}CH_4$ oxidation. (f) Comparison of catalytic activity for the oxidation of CH_4 over MOF-253-Fe_2 with other catalysts under identical reaction conditions. 155

4.6 Recyclability test for MOF-253-Fe_2 catalyzed oxidation of CH_4 into CH_3CO_2H under optimized reaction conditions. 156

4.7 (a) Control reactions for the production of CH_3CO_2H at 160 °C. (b) Fe 2p XPS spectra of MOF-253-Fe_2 recovered after catalysis. (c) DFT-optimized structure of the diiron(III) core of MOF-253-Fe_2 (INT-4) [(bpy)Fe^{III}(μ_2-OH)$(OH)_2$]$_2$. The bond distances are in Å. (d) EXAFS spectra (black and blue hollow squares) and fits (blue and black solid lines) of MOF-253-Fe_2 after catalytic methane oxidation to acetic acid in the R space at the Fe K-edge. The fitting range in the R space is 1.0–3.25 Å. (e) Productivity of acetic acid in the presence of different radical scavengers. (f) X-band (9.85 GHz) EPR spectroscopic spin-trapping experiments. EPR spectrum from DMPO spin-trapping experiment of MOF-253-Fe_2-catalyzed methane oxidation by O_2 at room temperature (wine), uncatalyzed oxidation of methane by O_2 at 160 °C for 38 h (mustard), MOF-253-Fe_2-catalyzed methane oxidation by O_2 at 160 °C for 38 h (black), simulated DMPO–CH_3 (red), simulated DMPO degraded during catalysis (green), simulated DMPO–$COCH_3$ (magenta), and simulated DMPO–OH (blue). Optimized conditions: MOF-253-Fe_2 (4.7 mg, 10.5 μmol Fe), 20 bar CH_4, 8 bar O_2, 160 °C, 8 mL H_2O, and 38 h. 158

4.8 (a) IR spectra of freshly prepared MOF-253(Al) (grey), MOF-253-Fe_2 (red), and MOF-253-Fe_2 recovered after catalysis (blue). (b) The peak at 3620 cm^{-1} in MOF-253-Fe_2 and MOF-253-Fe_2 recovered after methane oxidation corresponds to the stretching vibration of terminal Fe–OH, the peak at 3428 cm^{-1} represents the stretching mode of vibration for bridging μ_2-(OH)Fe–OH–Fe, and the peak at 3676 cm^{-1} corresponds to μ_2-$(OH)_{Al–OH–Al}$ within the SBU of the MOFs.[40] 160

4.9 Proposed catalytic cycle of MOF-253-Fe_2-catalyzed selective methane oxidation to acetic acid using O_2. 162

4.10 (a) TGA curve of freshly prepared MOF-253(Al) (black) and MOF-253-Fe_2 (red). A solvent weight loss of 22.1% in MOF-253(Al) (black) and 20.2% in MOF-253-Fe_2 (red) was observed from 30 °C to 200 °C. (b) TGA curve of freshly prepared MOF-253(Al) (black) and MOF-253-Fe_2 (red) from 200-700 °C. The increased weight of MOF-253-Fe_2 is due to the presence of Fe within the MOF. 165

4.11 Time-dependent formation of CO (black) and acetic acid (red) under identical reaction conditions. Reaction conditions: 4.7 mg of MOF-253-Fe_2 (10.5 μmol Fe), 20 bar CH_4, 8 bar O_2, 8 mL H_2O, 160 °C. 174

4.12 Hot filtration test of MOF-253-Fe_2 in methane oxidation to acetic acid. . . 174

4.13 (A) Synthesis of MOF-253-Fe_2 via postsynthetic modification of MOF-253(Al). (B) Attempt to synthesize analogous homogeneous (bpy)$Fe(OH)_2$ species by a similar method. 179

4.14 Comparison of structural features of MOF-253(Al) (rhombic) and bpy-UiO (octahedral). 181

4.15 (a) X-band (9.85 GHz) EPR spectroscopic spin-trapping experiments. EPR spectrum from DMPO spin-trapping experiment of MOF-253-Fe_2 catalyzed methane oxidation by water at 160 °C for 38 h (black). Reaction conditions: MOF-253-Fe_2 (4.7 mg, 10.5 µmol Fe), 20 bar CH_4, 8 bar N_2, 160 °C, 8 mL water, 38 h. (b) X-band (9.85 GHz) EPR spectroscopic spin-trapping experiments. EPR spectrum from DMPO spin-trapping experiment of MOF-253-Fe_2 catalyzed methane oxidation by O_2 at 160 °C for 38 h in toluene (red), in hexane (blue), in THF (black). 183

4.16 DFT-optimized structures of MOF-253-Fe_2, INT-4 [MOF-253-$(Fe_2(OH)_6)_{0.5}$] 184

4.17 $\mu(E)$ XAS spectra of metallic Fe(0) (black), $Fe(OH)_3$ (green), $FeCl_2$ (purple), and MOF-253-Fe_2 (red). The oxidation states of the Fe species within MOF-253-Fe_2 was determined by comparing the energy of their pre-edge positions to those of $Fe(OH)_3$ and $FeCl_2$. The positions of the Fe pre-edge of MOF-253-Fe_2 (7111.7 eV) aligned well with that of $FeCl_2$ (7111.0 eV), and are approximately 2 eV lower than that of $Fe(OH)_3$ (7113.0 eV). Therefore, we conclude that the Fe ions in MOF-253-Fe_2 is in the +2 oxidation state. . . 188

4.18 (a) EXAFS spectrum and fit of a combination of (90%) dimeric MOF-253-Fe_2 and (10%) monomeric Fe sites in the R space at the Fe K-edge. The fitting range in the R space is 1.0–3.25 Å. EXAFS fitting indicates that MOF-253-Fe_2 contains ∼90% dimeric $[(bpy)Fe^{II}(\mu_2\text{-}OH)(OH)(OH_2)]_2$ species and ∼10% monomeric $(bpy)Fe^{II}(OH)$ species. (b) DFT-optimized structure of MOF-253-Fe_2. 189

4.19 (a) EXAFS spectra of MOF-253-Fe_2 fitted with combined models of Fe(0) and MOF-253-Fe_2. (b) EXAFS spectra of MOF-253-Fe_2 fitted with combined models of Fe_2O_3 and MOF-253-Fe_2. The significant misfits indicate that MOF-253-Fe_2 does not contain any Fe nanoparticles or Fe_2O_3. 189

4.20 (a) EXAFS spectrum and fit of MOF-253(Al)-Fe_2 recovered after catalysis. EXAFS fitting indicates that MOF-253-Fe_2 after catalysis contains ∼90% dimeric $[(bpy)Fe^{III}(\mu_2\text{-}OH)(OH)_2]_2$ species and ∼10% monomeric $(bpy)Fe^{III}(OH)_3$ species. (b) DFT-optimized structure of MOF-253(Al)-Fe_2 after catalysis (INT-4). 190

4.21 (a) EXAFS spectra of MOF-253-Fe_2 recovered after catalysis fitted with combined models of Fe(0) and INT-4. (b) EXAFS spectra of MOF-253-Fe_2 after catalysis fitted with combined models of Fe_2O_3 and INT-4. The significant misfits indicate that MOF-253-Fe_2 recovered after methane oxidation does not contain any Fe nanoparticles or Fe_2O_3. 190

4.22 (a) EXAFS spectra of MOF-253-Fe_2 fitted with combined models of Fe supported on SBUs and linker of MOF-253-Fe_2. DFT-optimized structure of (b) MOF-253-Fe_2 $[(bpy)Fe^{II}(\mu_2\text{-}OH)(OH)(OH_2)]_2$. (c) $Fe^{II}(OH)$ species on SBU of MOF-253(Al). The significant misfits and higher R values indicate that MOF-253-Fe_2 does not contain any Fe supported on SBU. 191

4.23 (a) Raw XPS data of MOF-253-Fe_2. (b) XPS fitting of Fe in MOF-253-Fe_2. (c) XPS fitting of aluminium in MOF-253-Fe_2. 192

4.24 (a) Raw XPS data of MOF-253-Fe_2 recovered after catalysis. (b) XPS fitting of Fe in MOF-253-Fe_2 recovered after catalysis. (c) XPS fitting of aluminium in MOF-253-Fe_2 recovered after catalysis. 193

4.25 XPS analysis of Fe in MOF-253-Fe_2 sampled during the reaction. It reveals the presence of a mixed-valent state, with Fe existing as both Fe^{2+} and Fe^{3+}. 194

4.26 XPS fitting of Fe in MOF-253-Fe_2 recovered from the reaction of MOF-253-Fe_2 with O_2. Reaction conditions: MOF-253-Fe_2, 8 bar of O_2, 20 bar N_2, 8 mL water, 160 °C, 38 h. 195

4.27 GC-FID spectrum of the gas-phase sample collected after MOF-253-Fe_2-catalyzed methane oxidation to acetic acid (top). GC-FID spectrum of a standard gaseous mixture used for peak identification and retention time comparison (bottom). No detectable ethane or other hydrocarbon by-products were observed in the gas-phase sample (top). 196

5.1 Proposed mononuclear MOF-253(Al)-Fe Catalyst for Methane Oxidation. . 208

5.2 (a) Synthesis of MOF-253-Fe. (b) PXRD patterns of simulated MOF-253(Al) (black), MOF-253(Al)-$(bpy)_{0.1}$ (red), MOF-253-$(bpy)_{0.1}$-$FeCl_2$ (blue), MOF-253-Fe (green), and MOF-253-Fe recovered after catalysis (magenta). (c) Fe 2p XPS spectra of MOF-253-Fe. (d) EXAFS spectra (blue and black hollow squares) and fits (black and blue solid lines) of MOF-253-Fe in the R space at the Fe K-edge. The fitting range in the R space is 1.0–3.25 Å. (e) Comparison of catalytic activities between MOF-253-Fe_2 (10.5 μmol Fe) and MOF-253-Fe (10.5 μmol Fe) in the oxidation of methane to acetic acid and methanol at 160 °C and 95 °C, respectively. (f) GC-MS spectrum of the reaction mixture obtained after $^{13}CH_4$ oxidation. Reaction conditions: MOF-253-Fe (20.8 mg, 5.25 μmol Fe), 20 bar $^{13}CH_4$, 8 bar O_2, 22 h, and 95 °C. (g) Evaluation of the catalytic performance of MOF-253-Fe in the oxidation of CH_4 to CH_3OH using O_2, compared to previously documented base-metal catalysts. Reports marked with an asterisk do not specify selectivity. (h) Comparison of catalytic activity for the oxidation of CH_4 over MOF-253-Fe_2 and MOF-253-Fe with other catalysts at 95 °C (22 h) and 160 °C (38 h) under identical reaction conditions. Reaction conditions: catalyst (10.5 μmol Fe), CH_4 (20 bar), O_2 (8 bar), 8 mL water. 209

5.3 X-band (9.85 GHz) EPR spectroscopic spin-trapping experiments. EPR spectrum from DMPO spin-trapping experiment of MOF-253-Fe catalyzed methane oxidation by O_2 at 95 °C for 22 h (black), simulated DMPO–OH (red), simulated DMPO–CH_3 (blue), simulated DMPO–degraded during the reaction (green). Optimized reaction conditions: MOF-253-Fe (20.85 mg, 5.25 µmol Fe), 20 bar CH_4, 8 bar O_2, 95 °C, 8 mL water, and 22 h. 211

5.4 Proposed catalytic cycle of MOF-253-Fe-catalyzed selective methane oxidation to methanol using O_2. 212

5.5 ^{1}H NMR (400 MHz, DMSO-d_6) spectrum of digested MOF-253(Al)-$(bpy)_{0.1}$. 213

5.6 FT-IR spectra of MOF-253-Fe_2 (red), MOF-253-Fe_2 prepared in D_2O (black), MOF-253-Fe (blue), and MOF-253-Fe prepared in D_2O (green) in the wavenumber range of (a) 4000-500 cm^{-1}, (b) 3650-3400 cm^{-1}, and (c) 2700-2420 cm^{-1}. The peak at 3620 cm^{-1} in MOF-253-Fe_2 and MOF-253-Fe shifted to 2596 cm^{-1} in MOF-253-Fe_2(D_2O) and MOF-253-Fe(D_2O), corresponding to the stretching vibration of terminal Fe-OH. The peak at 3428 cm^{-1} in MOF-253-Fe_2 (absent in MOF-253-Fe) shifted to 2419 cm^{-1} in MOF-253-Fe_2(D_2O), representing the stretching mode of bridging μ_2-$(OH)_{Fe\text{-}OH\text{-}Fe}$.[4] Notably, the absence of a peak at 3428 cm^{-1} in MOF-253-Fe confirms the absence of dinuclear Fe species, indicating that Fe is present solely in monomeric form. 214

5.7 DFT-optimized structures of MOF-253-Fe. 218

5.8 $\mu(E)$ XAS spectra of metallic Fe(0) (black), $Fe(OH)_3$ (purple), $FeCl_2$ (brown), MOF-253-Fe (red), and MOF-253-Fe_2 (blue). The oxidation states of the Fe species within MOF-253-Fe_2 and MOF-253-Fe were determined by comparing the energies of their pre-edge positions to those of $Fe(OH)_3$ and $FeCl_2$. The pre-edge positions of MOF-253-Fe_2 (7111.7 eV) and MOF-253-Fe (7111.5 eV) aligned well with that of $FeCl_2$ (7111.0 eV) and are approximately 2 eV lower than that of $Fe(OH)_3$ (7113.0 eV). Therefore, we conclude that the Fe ions in MOF-253-Fe_2 and MOF-253-Fe possess a +2 oxidation state. 220

5.9 (a) EXAFS spectrum and fit of MOF-253-Fe. (b) DFT-optimized structure of MOF-253-Fe. (c) EXAFS spectra (blue and black hollow squares) and fits (black and blue solid lines) of a combination of 95% monomeric MOF-253-Fe and 5% dimeric Fe sites in R-space at the Fe K-edge. The fitting range in R-space is 1.0–3.25 Å. The significant misfits and high R-values observed even with 5% di-Fe further confirm that MOF-253-Fe does not contain any dinuclear MOF-253-Fe_2 species. 221

5.10 (a) Raw XPS data of MOF-253-Fe. (b) XPS fitting of Fe in MOF-253-Fe. (c) XPS fitting of aluminium in MOF-253-Fe. 221

6.1 (a) Postsynthetic metalation of bpy-UiO to form bpy-UiO-$Fe(OH)_2$ (b) PXRD patterns of the simulated UiO-67 MOF (black), pristine bpy-UiO (red), bpy-UiO-$FeCl_2$ (blue),bpy-$Fe(OH)_2$ (green), and bpy-UiO-Fe recovered after benzene hydroxylation (purple). (c) N_2 sorption isotherms of bpy-UiO (gray/black) and bpy-UiO-$Fe(OH)_2$ (red/orange) measured at 77 K. (d) SEM image of bpy-UiO-$Fe(OH)_2$ particles. (e) Fe 2p XPS spectra of bpy-UiO-$Fe(OH)_2$ and bpy-UiO-Fe after catalysis. (f) Zr 3d XPS spectra of bpy-UiO-$Fe(OH)_2$ and bpy-UiO-Fe after catalysis. (g) EPR spectra of solid bpy-UiO-$Fe(OH)_2$ (black) and bpy-UiO-Fe after catalysis (red). 233

6.2 (a) XANES spectra of metallic Fe(0) foil (black), bpy-UiO-Fe$(OH)_2$ (green), and bpy-UiO-Fe after catalysis of benzene oxidation to phenol (blue), Fe$(OH)_3$ (magenta), and $FeCl_2$ (red). (b) EXAFS spectra (blue solid and hollow triangles) and fits (black solid and dashed lines) of bpy-UiO-Fe$(OH)_2$ in R space at the Fe K-edge. The fitting range in the R space is 1.2–3.5 Å (c) DFT-optimized structure of the bpy-Fe$(OH)_2(H_2O)_2$ moiety within bpy-UiO-Fe$(OH)_2$ MOFs. The bond distances are given in Å. (d) EXAFS spectra (black solid and hollow triangles) and fits (gray solid and dashed lines) of bpy-UiO-Fe after catalytic benzene hydroxylation to phenol in the R space at the Fe K-edge. The fitting range in the R space is 1.2–3.5 Å. (e) DFT-optimized structure of the bpy-Fe$(OH)_3(H_2O)$ moiety within bpy-UiO-Fe MOFs. The bond distances are in Å. (f) k^2-weighted Fe-EXAFS (R) spectra of bpy-UiO-Fe$(OH)_2$ (black), Fe foil (red), Fe_2O_3 (green), and $FeCl_2$ (blue). 234

6.3 (a) Effect of temperature on % GC yield of PhOH and PhOH selectivity for bpy-UiO-Fe$(OH)_2$-catalyzed hydroxylation of benzene. Reaction conditions: benzene (0.3 mL, 3.37 mmol), bpy-UiO-Fe$(OH)_2$ (0.31 mol % Fe), mole ratio of benzene/H_2O_2 (1:5), water/CH_3CN [1:1, v/v, 4 mL], 4 h. (b) % GC yield of phenol and phenol selectivity with time plot for benzene hydroxylation. Reaction conditions: benzene (0.3 mL, 3.37 mmol), bpy-UiO-Fe$(OH)_2$ (0.31 mol %), mole ratio of benzene/H_2O_2 (1:5), water/CH_3CN [1:1, v/v, 4 mL], 60 °C. (c) Dependence of benzene conversion and phenol selectivity on the mole ratio of benzene/H_2O_2 catalyzed by bpy-UiO-Fe$(OH)_2$. Reaction conditions: benzene (0.3 mL, 3.37 mmol), bpy-UiO-Fe$(OH)_2$ (0.31 mol % Fe loading), water/CH_3CN [1:1, v/v, 4 mL], 60 °C, 4 h. (d) Comparison plot for catalytic activity and selectivity of bpy-UiO-Fe$(OH)_2$ and its homogeneous counterpart bpy-Fe$(OH)_2$. 236

6.4 X-band (9.85 GHz) EPR spectroscopic spin-trapping experiments. The EPR spectrum from DMPO spin-trapping experiment of uncatalyzed benzene hydroxylation by H_2O_2 at 60 °C (wine), bpy-UiO-Fe$(OH)_2$-catalyzed oxidation of benzene by H_2O_2 at 60 °C for 4 h (black), simulated DMPO-OH (red), and simulated DMPO-degraded adducts during the reaction (blue). 239

6.5 (a) Proposed catalytic cycle of bpy-UiO-Fe-catalyzed selective benzene oxidation to phenol. (b) DFT-calculated free energy diagram at 333.15 K for bpy-UiO-Fe-catalyzed benzene to phenol conversion. 240

6.6 (a) TGA curve of freshly prepared bpy-UiO and bpy-UiO-Fe$(OH)_2$. A solvent weight loss, attributed to THF within the pores, of 48.8% in bpy-UiO (black) and 40.4% in bpy-UiO-Fe$(OH)_2$ (red) was observed from 40 °C to 200 °C. (b) TGA curve of freshly prepared bpy-UiO (black) and bpy-UiO-Fe (red) from 200-600 °C. The increased weight of metalated MOF is due to the presence of iron within the MOF. 242

6.7 IR spectra (KBr) of freshly prepared bpy-UiO (black), bpy-UiO-$FeCl_2$ (red), and bpy-UiO-Fe$(OH)_2$ (blue). 244

6.8 SEM image of bpy-UiO-Fe$(OH)_2$ particles, and the SEM-EDX mapping of Fe and Zr of the respective particles. The uniform distribution of Fe and Zr suggests Fe and Zr are homogeneously distributed throughout the MOF. . 244

6.9 Test for "heterogeneity of bpy-UiO-Fe(OH)$_2$ in benzene hydroxylation to phenol. 246

6.10 Radical scavenger tests. Reaction conditions: bpy-UiO-Fe(OH)$_2$ (0.31 mol% Fe), benzene (3.372 mmol), 60 °C, $H_2 2O_2$ (30%) (5 eq.), 4 mL water:CH_3CN (1:1), trapping agent (10 mmol). 248

6.11 Proposed catalytic cycle of bpy-UiO-Fe-catalyzed selective benzene oxidation to phenol. 249

6.12 DFT-calculated free energy diagram of benzene oxidation to phenol over bpy-UiO-Fe(OH)$_2$ at 333 K. 250

6.13 DFT-optimized structures of intermediates for bpy-UiO-Fe(OH)$_2$ catalyzed oxidation of benzene to phenol. 251

6.14 μ(E) XAS spectra of metallic Fe(0) foil (black), bpy-UiO-Fe(OH)$_2$ (green), bpy-UiO-Fe after catalysis of benzene oxidation to phenol (dark blue), Fe_2O_3 (magenta), $Fe(OH)_3$ (light blue) and $FeCl_2$ (red). 253

6.15 (a) EXAFS spectra (red and blue hollow triangles) and fits (red solid and blue dashed line) of bpy-UiO-Fe(OH)$_2$(H_2O)$_2$ in the R space from 1.2 to 3.5 Å. (b) DFT optimized structure of bpy-UiO-Fe(OH)$_2$(H_2O)$_2$ 254

6.16 (a) EXAFS spectra (green and brown hollow triangles) and fits (green solid and brown dashed line) of bpy-UiO-Fe(OH)$_3$(H_2O) in the R space from 1.2 to 3.5 Å. (b) DFT optimized structure of bpy-UiO-Fe(OH)$_3$(H_2O). 254

6.17 EXAFS spectrum of bpy-UiO-Fe(OH)$_2$ fitted with; 5% Fe (0) and 95% bpy-UiO-Fe(OH)$_2$; 25% Fe (0) and 75% bpy-UiO-Fe(OH)$_2$; 50% Fe (0) and 50% bpy-UiO-Fe(OH)$_2$; and 80% Fe(0) and 20% bpy-UiO-Fe(OH)$_2$. The significant misfits indicates that bpy-UiO-Fe(OH)$_2$ does not contain any Fe-nanoparticles. 256

6.18 Wavelet transform for the k^2-weighted EXAFS signal at the Fe K-edge. . . 256

6.19 (a) Raw XPS data of bpy-UiO-$FeCl_2$. (b) XPS fitting of iron in bpy-UiO-$FeCl_2$. (c) XPS fitting of zirconium in bpy-UiO-$FeCl_2$. 257

6.20 (a) Raw XPS data of bpy-UiO-Fe(OH)$_2$. (b) XPS fitting of iron in bpy-UiO-Fe(OH)$_2$. (c) XPS fitting of zirconium in bpy-UiO-Fe(OH)$_2$. 257

6.21 (a) Raw XPS data of bpy-UiO-Fe after catalysis. (b) XPS fitting of iron in bpy-UiO-Fe after catalysis (c) XPS fitting of zirconium in bpy-UiO-Fe after catalysis. 258

6.22 Raw GC-FID spectra of bpy-UiO-Fe(OH)$_2$ (0.31 mol% Fe) catalysed hydroxylation of benzene for 4 h at 60 °C. Reaction conditions: benzene (0.3 mL, 3.37 mmol), 30% H_2O_2 (5 eq.), CH_3CN:water [(1:1), 4 mL]. 258

7.1 Postsynthetic metalation of bpy-UiO to form porous Zr-MOF-confined Fe(III) hydroxyl species for selective oxidation of styrene to benzaldehyde. 273

7.2 (a) PXRD patterns of simulated UiO-67 (black), pristine bpy-UiO (red), bpy-UiO-$FeCl_3$ (blue), bpy-UiO-$Fe(OH)_3$ (green), and bpy-UiO-Fe recovered after run-1 (pink) and run-4 (wine) of styrene oxidation. (b) N_2 sorption isotherms of bpy-UiO (blue/green) and bpy-UiO-$Fe(OH)_3$ (red/orange) measured at 77 K. (c) SEM-EDX mapping of bpy-UiO-$Fe(OH)_3$ particles. (d) Fe 2p XPS spectra of bpy-UiO-$Fe(OH)_3$. (e) Zr 3d XPS spectra of bpy-UiO-$Fe(OH)_3$. (f) EPR spectra of solid bpy-UiO-$Fe(OH)_3$. 275

7.3 (a) Effect of solvent on the conversion of styrene and benzaldehyde selectivity for bpy-UiO-$Fe(OH)_3$-catalyzed oxidation of styrene. Reaction conditions: bpy-UiO-$Fe(OH)_3$ (0.4 mol% Fe), styrene (1.5 mmol), H_2O_2 (30% w/v, 2.5 eq.), 80 °C, 8 h. (b) Effect of temperature on the conversion of styrene and benzaldehyde selectivity for bpy-UiO-$Fe(OH)_3$-catalyzed oxidation of styrene. Reaction conditions: bpy-UiO-$Fe(OH)_3$ (0.4 mol% Fe), styrene (1.5 mmol), H_2O_2 (30% w/v, 2.5 eq.), H_2O/CH_3CN (1:1, 4 mL), 8 h. (c) Effect of reaction time on styrene conversion and benzaldehyde selectivity for bpy-UiO-$Fe(OH)_3$-catalyzed oxidation of styrene. Reaction conditions: bpy-UiO-$Fe(OH)_3$ (0.4 mol% Fe), styrene (1.5 mmol), H_2O_2 (30% w/v, 2.5 eq.), H_2O/CH_3CN (1:1, 4 mL), 80 °C. Reaction products were analyzed by GC–MS. 276

7.4 Bpy-UiO-$Fe(OH)_3$ catalyzed oxidation of styrene derivatives.[a] 278

7.5 (a) Comparison of catalytic activity of bpy-UiO-$Fe(OH)_3$ with other catalysts at 80 °C (8 h). (b) Recycling test for bpy-UiO-$Fe(OH)_3$-catalyzed styrene oxidation to benzaldehyde under optimized reaction conditions in 6 h. . . . 279

7.6 Plausible reaction pathway illustrating the bpy-UiO-$Fe(OH)_3$ catalyzed styrene oxidation to benzaldehyde. 280

7.7 (a) TGA curves of freshly prepared bpy-UiO and bpy-UiO-$Fe(OH)_3$. A solvent weight loss of 42% in bpy-UiO (black) and 39% in bpy-UiO-$Fe(OH)_3$ (red) was observed from 40 °C to 200 °C. (b) TGA curves of freshly prepared bpy-UiO (black) and bpy-UiO-$Fe(OH)_3$ (red) from 200–700 °C. The increased weight of the metalated MOF is due to the presence of iron within the framework. 282

7.8 FT-IR (KBr) spectrum of freshly prepared bpy-UiO (black), bpy-UiO-$FeCl_3$ (red) and bpy-UiO-$Fe(OH)_3$ (blue). 283

7.9 Hot filtration test of bpy-UiO-$Fe(OH)_3$ catalyzed styrene oxidation. 289

7.10 Recyclability and reusability of bpy-UiO-$Fe(OH)_3$ for styrene oxidation. . . 290

7.11 (a) Raw XPS data of bpy-UiO-$Fe(OH)_3$. (b) XPS fitting of Zr 3d in bpy-UiO-$Fe(OH)_3$. (c) XPS fitting of Fe 2p in bpy-UiO-$Fe(OH)_3$. 291

List of Tables

3.1 Determination of defect sites in MIL-53(Al) and MIL-53(Al)-Cu(OH)$_2$ MOF by TGA analysis. 91

3.2 Optimization of catalytic conditions for MIL-53(Al)-Cu(OH) catalyzed oxidation of methane using O_2.[a] 98

3.3 Control experiments for MIL-53(Al)-Cu(OH) catalyzed oxidation of methane to acetic acid. 99

3.4 mmol of acetic acid formed and the leaching of Cu in various runs of the recycling of MIL-53(Al)-Cu(OH) for the oxidation of methane. 104

3.5 Summary of EXAFS fitting parameters of MIL-53(Al)-Cu(OH). 128

3.6 Summary of EXAFS fitting parameters of MIL-53(Al)-Cu after catalysis. . 130

3.7 XPS fitting parameters for Cu(II) in MIL-53(Al)-Cu(OH) MOF. 132

3.8 XPS fitting parameters for Cu(II) in MIL-53(Al)-Cu MOF recovered after catalysis. 133

3.9 XPS fitting parameters for Cu(0) in Cu@MIL-53(Al). 134

3.10 Simulated parameters of EPR spectroscopic spin-trapping experiments for MIL-53(Al)-Cu(OH) catalysed oxidation of methane.[a] 134

4.1 Determination of defect sites in MOF-253(Al) and MOF-253-Fe_2 MOF by TGA analysis. 165

4.2 Optimization of catalytic conditions for MOF-253-Fe_2 catalyzed oxidation of methane using O_2.[a] 168

4.3 Control experiments for MOF-253-Fe_2 catalyzed oxidation of methane to acetic acid.[a] 170

4.4 Carbon balance for methane oxidation reaction. 172

4.5 Productivity of acetic acid ($mmol_{CH_3CO_2H}$ $mol_{Fe}{}^{-1}$ h^{-1}) and the leaching of Fe and Al in various runs of the recycling of MOF-253-Fe_2 for the oxidation of methane. 176

4.6 Simulated parameters of EPR spectroscopic spin-trapping experiments for MOF-253-Fe_2 catalysed oxidation of methane.[a] 183

4.7 XPS fitting parameters for Fe(II) in MOF-253-Fe_2 MOF. 192

4.8 XPS fitting parameters for Fe(III) in MOF-253-Fe_2 MOF. 193

4.9 XPS fitting parameters for Fe(II) and Fe(III) in MOF-253-Fe_2 sampled during the reaction. 194

4.10 XPS fitting parameters for Fe(III) in MOF-253-Fe_2 MOF recovered after reaction with O_2. 195

4.11 Comparison of catalytic activity of MOF-253-Fe_2 catalysed oxidation of CH_4 to CH_3CO_2H using O_2 with other reported catalysts. 197

5.1 Control experiments for MOF-253-Fe catalyzed oxidation of methane.[a] . . 215

5.2 Comparison of catalytic activity and selectivity of MOF-253-Fe_2 and MOF-253-Fe at 160 °C and 95 °C.[a] 215

5.3 Carbon balance in MOF-253-Fe catalyzed oxidation of CH_4 using O_2. . . . 216

5.4 Simulated parameters of EPR spectroscopic spin-trapping experiments for MOF-253-Fe catalyzed oxidation of methane.[a] 216

5.5 XPS fitting parameters for Fe(II) in MOF-253-Fe. 222

5.6 Comparison of the catalytic activity of MOF-253-Fe for CH_4 oxidation to CH_3OH using O_2 with other reported catalysts containing only earth-abundant metals. 223

6.1 Hydroxylation of Benzene into Phenol Using H_2O_2 as the Oxidant[a] 235

6.2 Determination of defect sites in bpy-UiO and bpy-UiO-Fe$(OH)_2$ MOF by TGA analysis. 243

6.3 Simulated parameters of EPR spectroscopic spin-trapping experiments for bpy-UiO-Fe$(OH)_2$ catalysed oxidation of benzene.[24;25;83] 248

6.4 Relative energies of the structures in different spin states. All structures are geometry optimized. 250

6.5 Summary of EXAFS parameters of bpy-UiO-Fe$(OH)_2(H_2O)_2$. 255

6.6 Summary of EXAFS parameters of bpy-UiO-Fe$(OH)_3(H_2O)$. 255

7.1 Determination of defects in bpy-UiO and bpy-UiO-Fe$(OH)_3$ by TGA analysis. 283

7.2 Optimization of reaction conditions for the oxidation of styrene.[a]. 286

7.3 % GC yield of benzaldehyde and the leaching of Fe and Zr in various runs of the recycling of bpy-UiO-Fe$(OH)_3$ for the oxidation of styrene. 290

7.4 Fe 2p XPS fitting parameters for bpy-UiO-Fe$(OH)_3$. 292

Chapter 1

Introduction to Reticular Chemistry and Metal-Organic Frameworks

Abstract

This chapter provides an overview of metal–organic frameworks (MOFs) as crystalline, modular platforms for designing catalytically active sites with molecular precision. The tunable connectivity between metal nodes and organic linkers enables the construction of well-defined coordination environments that emulate enzymatic pockets while maintaining heterogeneous stability. Emphasis is placed on the role of linker functionality and post-synthetic metalation in tailoring the electronic and geometric structure of the active centers. The discussion traces the evolution of MOFs from inert porous hosts to redox-active catalytic materials, particularly those incorporating Fe and Cu sites capable of facilitating small-molecule activation and selective oxidation chemistry. By highlighting advances in framework engineering, site isolation, and cooperative multinuclear design, this chapter establishes the conceptual foundation for the Fe- and Cu-based catalytic systems discussed in the subsequent chapters.

1.1 Introduction to Reticular Chemistry

The concept of reticular chemistry was first articulated by Omar M. Yaghi in the late 1990s as a new way of thinking about the deliberate construction of extended crystalline materials from molecular precursors. The term reticular derives from the Latin reticulum, meaning "net-like," and aptly captures the essence of this chemistry, the linking of well-defined molecular building units through strong bonds to form predetermined, periodic networks.[1–3] Unlike traditional solid-state synthesis, which often produces extended structures through unpredictable reactions, reticular chemistry enables the design and realization of targeted architectures with atomic precision.

At its core, reticular chemistry involves the stitching together of molecules by strong bonds typically coordination or covalent bonds to generate robust frameworks that retain the integrity of their molecular components. This conceptual advance marked a paradigm shift: for the first time, chemists could conceive a desired three-dimensional structure and subsequently assemble it in the laboratory from discrete building blocks. Through the identification of secondary building units (SBUs), such as metal–carboxylate clusters, and organic linkers with defined geometries, it became possible to translate molecular connectivity into extended crystalline materials with predictable topologies.

The design logic of reticular chemistry rests on understanding joints and links as the fundamental structural elements of a network analogous to vertices and edges in a geometric net. Each building unit serves as a node with a defined coordination geometry, while the organic linkers act as struts determining the angle and distance between nodes. By judiciously selecting metal clusters and linker geometries, a vast landscape of network topologies can be realized, ranging from one-dimensional chains and two-dimensional sheets to highly porous three-dimensional frameworks (Figure 1.1).[4]

An illustrative example comes from the transformation of simple molecular clusters, such as copper acetate dimers, into extended frameworks by replacing terminal ligands with ditopic linkers like carboxylates. This design converts discrete molecular motifs into periodic networks that preserve the coordination geometry of the metal centers. By controlling the angular and torsional parameters of the linkers such as those in benzene dicarboxylates, one can direct the assembly toward specific nets (e.g., square, cubic, diamond, or NbO-type

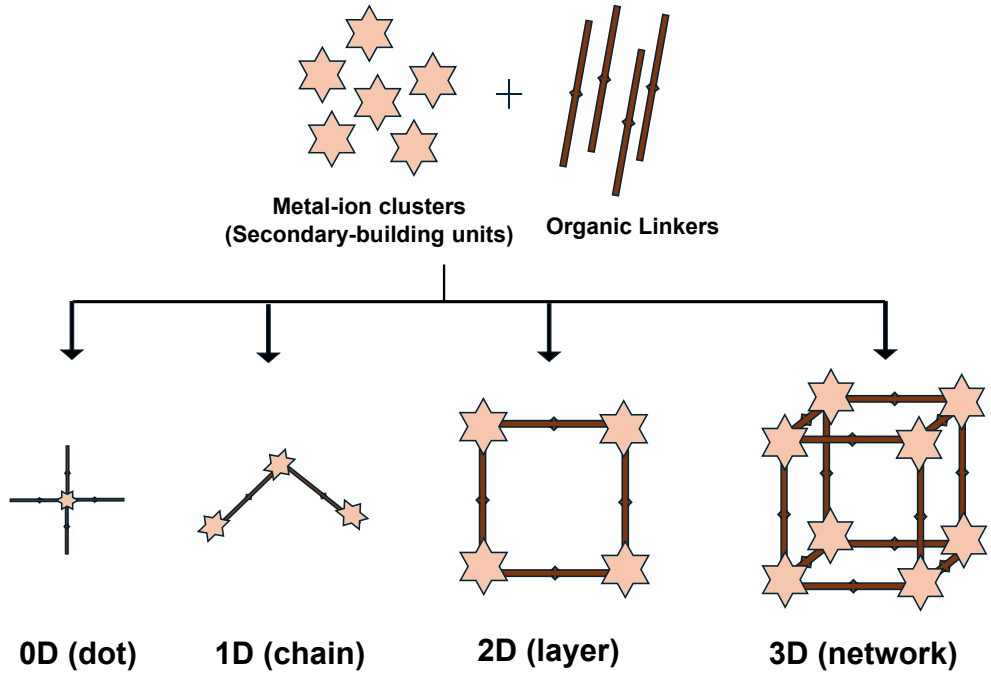


Figure 1.1: Design of nanoparticles (0D), chains (1D), sheets (2D), and networks (3D).[5]

frameworks).[5–7] Such geometrical control lies at the heart of framework design and is central to understanding why certain topologies are favored in MOF synthesis.[3]

The success of reticular chemistry has extended far beyond MOFs, influencing the creation of related classes of materials such as covalent organic frameworks (COFs)[8] and zeolitic imidazolate frameworks (ZIFs).[9] Collectively, these systems represent a new region of structure space in chemistry, characterized by modularity, structural predictability, and exceptional tunability. Reticular chemistry thus provides not only the conceptual foundation for MOF synthesis but also a unifying framework for the rational design of crystalline materials across molecular and solid-state boundaries.

1.2 Early Coordination Complex and the Origins of Framework Design

The conceptual roots of metal-organic frameworks trace back to the foundations of coordination chemistry, established by Alfred Werner in the early 20th century. Werner's pioneering work on the structure of coordination compounds laid the groundwork for understanding how metal centers can coordinate to multiple ligands through defined geometries, giving rise to predictable molecular architectures. His ideas introduced the notion of primary and secondary valence and clarified the spatial arrangement of ligands around a central metal

ion, principles that continue to underpin the structural logic of MOFs.

In the decades that followed, coordination chemistry evolved to include polymeric and supramolecular assemblies, where metal ions were linked through bridging ligands into extended one-, two-, or three-dimensional structures. Many early coordination polymers, such as copper and silver carboxylates, demonstrated that metal-ligand linkages could propagate indefinitely, forming crystalline solids with repeating coordination motifs. However, these early materials were often synthesized serendipitously rather than through a design-based approach, and their structures lacked the robustness and tunability characteristic of modern frameworks.

Building upon Werner's pioneering coordination theory, the 20th century witnessed the emergence of more structurally sophisticated coordination frameworks. A notable example was Prussian Blue ($Fe_4[Fe(CN)_6]_3$), in which transition metals are interconnected through cyanide bridges to form an extended cubic lattice (Figure 1.2). This structure demonstrated how coordination chemistry could transcend discrete molecular complexes to yield periodic, three-dimensional networks. Another significant milestone was the discovery of Hofmann-type clathrates such as $[Ni(CN)_2(L)](C_6H_6)$, which were capable of encapsulating guest molecules within their frameworks, a precursor to the concept of permanent porosity that later became central to reticular chemistry.[10;11] The subsequent development of macrocyclic and chelating ligands, including porphyrins and phthalocyanines, further refined the control over coordination geometry by introducing preorganized ligand scaffolds around metal centers.[12–14]

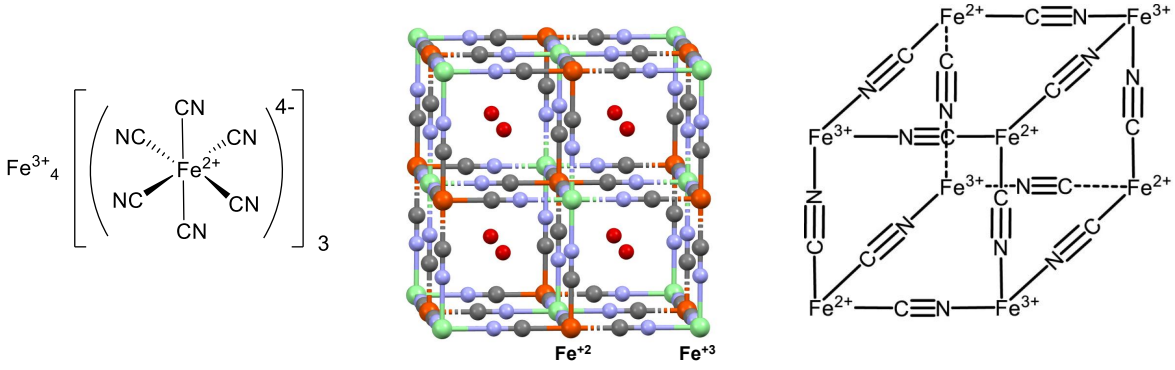


Figure 1.2: Prussian Blue: the first synthetic coordination compound.

The transformation from coordination complexes to extended frameworks was driven

by the realization that metal-ligand coordination could serve as a structural blueprint for constructing periodic materials. Advances in X-ray crystallography provided the ability to resolve atomic-level structures, allowing chemists to correlate metal coordination geometry with the resulting framework topology. This era also saw the emergence of crystal engineering, which sought to control molecular packing and intermolecular interactions in solids.

By the late 20th century, a new design paradigm began to take shape: the idea that extended frameworks could be rationally constructed by connecting predesigned molecular building blocks with predictable connectivity. This vision was realized through the concept of reticular chemistry, where the strength and directionality of coordination bonds could be harnessed to stitch together rigid inorganic and organic units into stable, porous frameworks. Early examples of such materials, including MOF-2 and MOF-5, demonstrated for the first time that modular assembly could yield crystalline networks with controllable topology, porosity, and chemical functionality, marking the true convergence of coordination chemistry and materials design.

Thus, the development of metal-organic frameworks represents a natural evolution of coordination chemistry, transforming the principles that once described discrete molecules into a systematic approach for constructing extended, functional materials.

1.3 Metal-Organic Frameworks

1.3.1 Introduction to Metal-Organic Frameworks.

The concept of reticular chemistry reached a major milestone with the advent of metal-organic frameworks (MOFs), a class of crystalline porous materials constructed by linking metal ions or clusters (secondary building units, SBUs) with multitopic organic linkers through strong coordination bonds (Figure 1.3).[15–17] This approach, pioneered in the late 1990s, enabled chemists to design frameworks with predetermined topology, tunable pore environments, and exceptional structural diversity.

MOFs combine the robustness of inorganic metal nodes with the flexibility of organic ligands, resulting in materials that exhibit high surface areas, adjustable pore sizes, and well-defined active sites.[15] These attributes distinguish them from traditional porous solids such

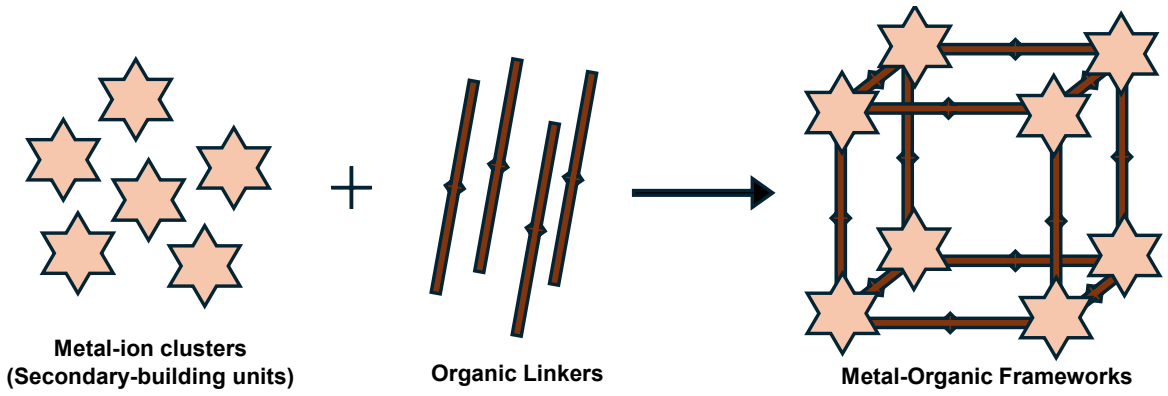


Figure 1.3: Design of Metal-Organic Framework.

as zeolites or activated carbons, which offer limited tunability. The reticular design principle allows the modular construction of MOFs by selecting suitable metal-ligand combinations, giving rise to a vast structural landscape encompassing frameworks such as MOF-5, HKUST-1, and MIL-53.

Over the past two decades, MOFs have emerged as one of the most versatile platforms in materials science, with applications spanning gas storage and separation, catalysis, drug delivery, sensing, and energy storage.[18;19] Their ability to host single atoms, clusters, or functional groups within well-defined cavities has also made them valuable model systems for studying heterogeneous catalysis at the molecular level.

In recognition of the profound impact of this field, the 2025 Nobel Prize in Chemistry was jointly awarded to Omar M. Yaghi, Susumu Kitagawa, and Richard Robson for the development of metal-organic frameworks (MOFs), a landmark achievement that established reticular chemistry as a cornerstone of modern materials design. Their pioneering contributions transformed the vision of atomically precise framework assembly into a practical and widely applicable reality.

1.3.2 Orgnaic Linkers.

Organic linkers serve as the structural and functional backbones of metal-organic frameworks, connecting the metal nodes or secondary building units (SBUs) into extended three-dimensional architectures. The choice of linker determines not only the topology and pore size of a MOF but also its chemical stability, flexibility, and reactivity.[20;21]

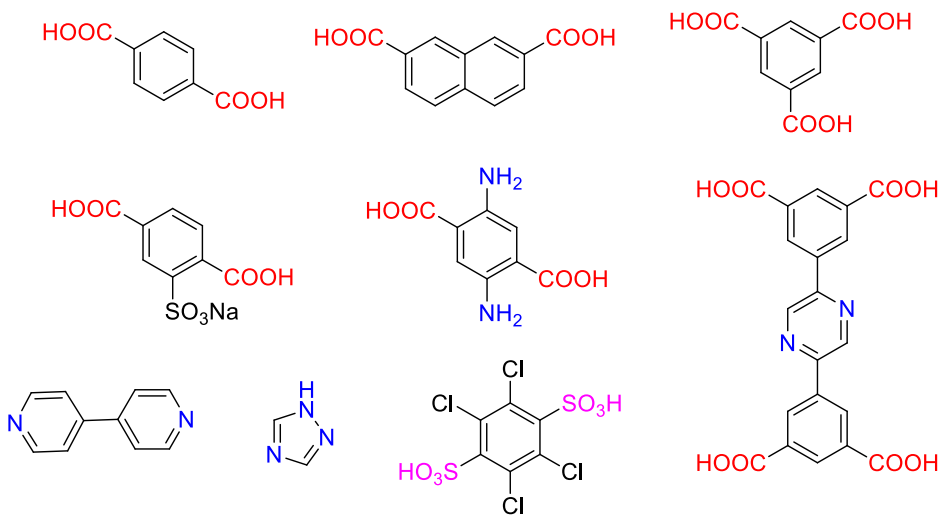


Figure 1.4: Examples of different organic linkers used in the synthesis of Metal-Organic Framework.

Typically, linkers are multidentate ligands bearing functional groups such as carboxylates, azolates, phosphonates, or pyridyl moieties capable of coordinating to metal centers (Figure 1.4). Among these, carboxylate-based linkers such as terephthalic acid (H_2BDC) and trimesic acid (H_3BTC) are the most widely used due to their predictable coordination geometries and robustness.[22] These linkers form strong metal–oxygen bonds, yielding thermally and chemically stable frameworks like MOF-5,[23] HKUST-1,[24;25] and MIL families.[26;27]

Beyond structural roles, linkers can also impart chemical functionality to the framework.[28;29] The incorporation of substituents such as -NH_2, -OH, -NO_2, or -SO_3H enables post-synthetic modification, enhances adsorption selectivity, or provides coordination sites for further metalation. For example, bipyridyl linkers in MOF-253 or MIL-101 derivatives create nitrogen donor environments ideal for anchoring transition metal ions, facilitating catalytic and redox-active sites within otherwise inert frameworks.[30;31]

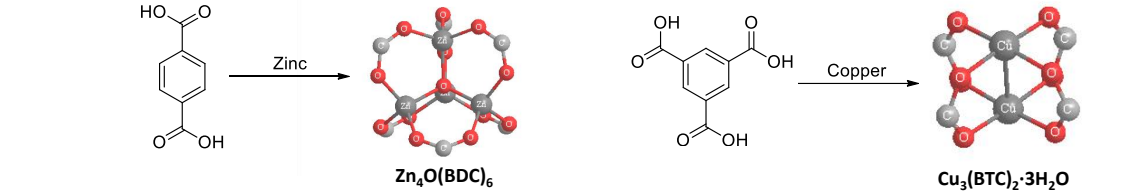
Recent developments have focused on heteroatom-containing linkers, flexible backbones, and π-conjugated systems to enable electronic conductivity and photoresponsiveness. Computational studies combined with topological analysis now allow predictive design of linkers that yield desired pore architectures and functionalities.

Thus, the organic linker is not merely a spacer but a tunable molecular component that dictates the framework's geometry, chemical environment, and ultimately its application

potential.

1.3.3 Metal Nodes and Secondary Building Units (SBUs).

The metal nodes, also known as secondary building units (SBUs), form the inorganic vertices of metal-organic frameworks and are central to defining their geometry, connectivity, and functionality. SBUs are typically composed of one or more metal ions coordinated to inorganic or organic ligands (e.g., hydroxide, oxide, carboxylate), serving as rigid, directional coordination motifs that dictate the overall topology of the framework (Figure 1.5). [1;15]



Secondary Building Units (SBUs): Poly-nuclear clusters / Metal-carboxylate nodes

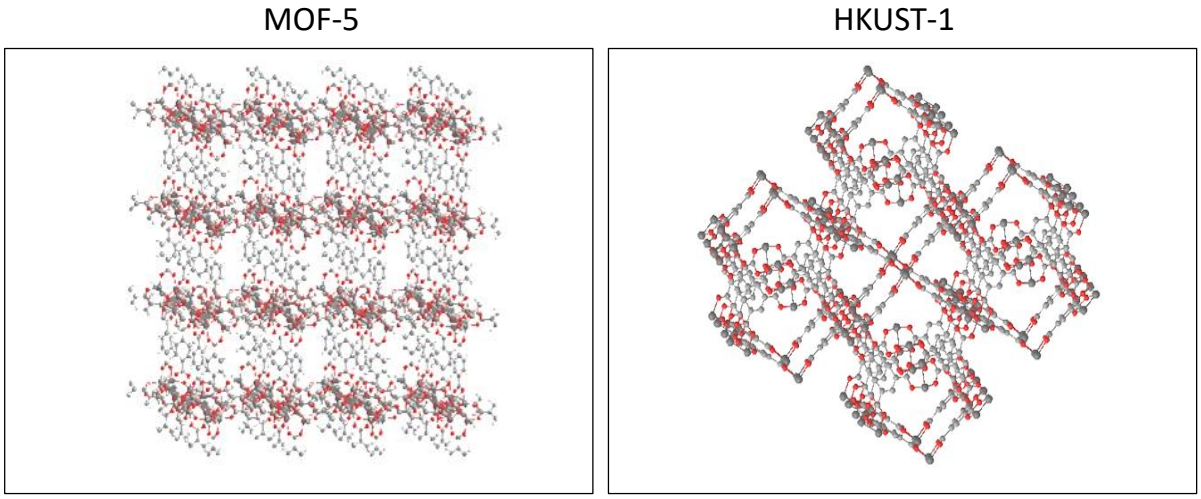


Figure 1.5: Examples of secondary-building units along with the MOF structure (MOF-5 and HKUST-1)

The concept of using SBUs as modular building blocks is one of the defining advances introduced by Yaghi and co-workers, [1;4] allowing predictable assembly of complex frameworks from known coordination geometries. Depending on the metal's coordination preferences, SBUs can exhibit diverse architectures, paddle-wheel, trimeric, chain-like, or cluster-based each imparting characteristic pore dimensions and framework stability. [32;33]

For instance, the $Cu_2(COO)_4$ paddle-wheel cluster found in HKUST-1 ($Cu_3(BTC)_2$) serves as a canonical SBU, where two Cu(II) centers are bridged by four carboxylates, forming a robust and open coordination site that can interact with guest molecules.[34;35] Similarly, the $Zr_6O_4(OH)_4$ cluster in the UiO series provides exceptional thermal and chemical stability due to its strong Zr-O bonds and high connectivity.[36–38] The Fe_3O and Al-OH chains in MIL-type frameworks illustrate how one-dimensional SBUs can also propagate into extended networks with tunable flexibility.[39–41]

The SBU's chemical composition strongly influences the framework's electronic structure and catalytic potential. Transition metal-based SBUs (e.g., Fe, Cu, Ni, Co) often exhibit redox activity and can participate directly in small-molecule activation, whereas main-group or rare-earth nodes (e.g., Al, Zr, Ce) provide structural rigidity and resistance to hydrolysis.[42–45] Mixed-metal SBUs, incorporating two or more distinct metal ions, have emerged as powerful platforms to introduce cooperative or synergistic effects for catalysis and electronic tuning.

In recent years, the integration of oxo- and hydroxo-bridged metal clusters has gained prominence due to their resemblance to enzymatic active sites, particularly in oxidation and reduction reactions. The modular nature of SBUs allows deliberate incorporation of such motifs through post-synthetic metal exchange or direct solvothermal synthesis, bridging the gap between biomimetic and heterogeneous catalysis.

Thus, SBUs function as the inorganic scaffolds that, in conjunction with organic linkers, define the geometry, functionality, and reactivity of MOFs. The ability to rationally design and modify these metal clusters represents a cornerstone of modern reticular chemistry and underpins the exceptional tunability that distinguishes MOFs from other porous solids.

1.4 Nomenclature of Metal–Organic Frameworks (MOFs)

Currently, no unified or standardized system exists for the nomenclature of metal-organic frameworks (MOFs). This is largely due to the vast structural diversity and rapid expansion of reported frameworks, which makes it difficult to define a universal convention. As a result, researchers in the field generally follow descriptive and laboratory-specific naming practices, using short acronyms combined with numerical identifiers that typically denote the order in

which the materials were synthesized.

Several approaches are commonly adopted in the literature:

(a) Composition-based nomenclature: Frameworks are often named according to their general class or elemental composition. Examples include MOF-x,[46] RPF-x (rare-earth polymeric framework),[47] and COF-x (covalent organic framework).[8] These names emphasize the chemical family or bonding nature of the framework rather than its structural features.

(b) Structure-based nomenclature: Some designations describe the topology or structural analogy to known materials. Examples include ZMOF-x (zeolite-like MOF),[48] ZIF-x (zeolitic imidazolate framework),[9] and mesoMOF-x (mesoporous MOF).[49] This approach highlights the framework's geometry or pore characteristics, often comparing it to familiar inorganic architectures such as zeolites.

(c) Laboratory-based nomenclature: Another widely used system links the name to the research group or institution where the material originated. Notable examples include MIL-n (Matériaux de l'Institut Lavoisier),[50] HKUST-x (Hong Kong University of Science and Technology), UiO-x (University of Oslo), and CPO-x (Coordination Polymer of Oslo). Such acronyms have become internationally recognized identifiers of specific MOF families.[51;52]

In addition to these empirical and descriptive approaches, MOFs may also be named based on their empirical formulas, representing the stoichiometry of metals and ligands in the repeating unit. For instance, $[Cu(2\text{-pymo})_2]$ and $[Zn_4O(bdc)_3]$ denote copper and zinc frameworks containing 2-hydroxypyrimidinolate (2-pymo) and 1,4-benzenedicarboxylate (bdc) ligands, respectively.[4;5]

A more systematic nomenclature based on topological representation has also been proposed, wherein frameworks are classified by their network connectivity (e.g., pcu, bcu, rho, sod, gis). Although this method allows for structural comparison across different materials, it does not convey information about chemical composition, metal identity, or functional groups.

1.5 Introduction to MOF synthesis

1.5.1 Importance of synthesis methods for catalytic and structural properties.

The way a metal-organic framework is synthesized plays a decisive role in determining its structure, crystallinity, porosity, and ultimately its catalytic performance. MOFs are most commonly prepared through solvothermal or hydrothermal crystallization, where metal precursors and organic linkers react in a heated solvent over several hours to days.[53] Under these conditions, the organic ligands remain chemically intact, allowing their functional groups to be precisely incorporated into the final framework architecture.

One advantage of MOF chemistry is the ability to combine more than one type of organic linker in a single material, enabling the creation of mixed-linker frameworks with multiple functionalities distributed throughout the pores.[54;55] This synthetic flexibility allows researchers to tailor the chemical environment for specific catalytic or adsorption applications.

MOF synthesis is typically designed with the intended application in mind. For instance, materials developed for gas storage or separation are often synthesized in coordinating solvents such as DMF, DEF, or water. These solvents can bind temporarily to metal nodes during crystal growth. Upon activation, where the solvent is removed, the coordinated solvent molecules vacate the metal sites, generating open metal sites that strongly interact with guest molecules such as CO_2, CH_4, or H_2.[56;57]

A key feature of MOF assembly is the reversible nature of metal-ligand coordination. Because these bonds can break and reform under synthesis conditions, the growing crystals have the capacity to correct structural imperfections. This dynamic error-correction mechanism helps the framework approach a low-defect, thermodynamically favored structure.[57] As a result, solvothermally synthesized MOFs often exhibit high uniformity in pore structure and composition, which is crucial for consistent catalytic behavior and reproducible adsorption properties.

1.5.2 Synthetic Strategies.

Solvothermal Synthesis of MOFs.

Solvothermal synthesis is one of the most established and versatile routes for preparing metal-organic frameworks. In this method, a mixture of metal salts and organic linkers is dispersed in a suitable solvent, commonly high-boiling aprotic or protic media such as DMF, DEF, DMSO, or alcohols.[58] These solvent systems, particularly those containing formamide functionalities, provide excellent solubility for both components and facilitate controlled coordination between the metal nodes and organic ligands.

The reaction mixture is typically sealed in a Teflon-lined autoclave and heated to temperatures above the boiling point of the solvent. Under these conditions, elevated temperature and autogenous pressure promote slow, directed nucleation and crystal growth, allowing MOFs to form with high crystallinity and well-defined pore architectures. The reversible nature of metal-ligand coordination at these temperatures enables the framework to self-correct, minimizing structural defects and producing materials close to thermodynamic equilibrium.

Advantages

1. One-step synthesis of highly crystalline MOFs.
2. Ability to obtain single crystals suitable for structural analysis.
3. Moderate operating temperatures and broad solvent compatibility.

Disadvantages

1. Longer reaction times compared to alternative techniques.
2. Increased susceptibility to by-product formation.
3. Requires post-synthetic solvent removal from pores or metal coordination sites.

Microwave-assisted Synthesis of MOFs.

Microwave-assisted synthesis has emerged as an efficient alternative to conventional solvothermal routes for producing metal-organic frameworks. Microwaves interact directly with mobile charges such as polar solvent molecules, ions, or electrons and convert electromagnetic energy into thermal energy within the reaction mixture. As a result, heating is rapid, volumetric, and highly energy-efficient, often leading to accelerated nucleation and the formation of smaller, more uniform crystals.[59]

Principle of Microwave Heating: When an oscillating electromagnetic field is applied, polar molecules continuously attempt to realign with the changing field direction. This repeated reorientation causes molecular friction and collisions, which increases the kinetic energy of the system and thus raises the temperature. In solids, microwaves induce localized currents, and resistive losses generate heat internally. Because the radiation couples directly with the material, microwave heating is significantly faster and more homogeneous compared to conventional external heating.

Microwave irradiation has been widely applied to many MOF families, enabling much faster crystallization than conventional solvothermal methods. Metal carboxylates such as Cr-MIL-100 and Fe-MIL-101 can form within minutes to under an hour, often without mineralizers like HF, and typically yield nanocrystals.[60;61] Isoreticular frameworks (MIL-47, MIL-53, CAU-1) and IRMOF series also crystallize rapidly, sometimes with enhanced surface areas and gas uptake.[62–64] HKUST-1 is a benchmark example, where high-purity crystals with excellent microporosity form in less than an hour.[65] Azolate MOFs (e.g., ZIF-7, ZIF-8) and mixed-linker or membrane-type materials have also been produced efficiently.[61;66] Overall, microwave heating provides accelerated kinetics, smaller and more uniform particle sizes, and reliable crystallization across diverse MOF systems.

Advantages

1. Extremely rapid crystallization and reduced synthesis times.
2. Often produces high-purity and phase-selective products.
3. Enables smaller, more uniform crystal sizes, beneficial for catalysis and membranes.
4. Efficient, uniform internal heating improves reaction control.

5. Potential for direct growth of films and membrane layers.

Disadvantages

1. Reproducibility can be limited due to non-uniform heating in some solvents.

2. Scaling up microwave processes remains challenging for industrial production.

3. Differences in microwave reactor design make method transfer between systems non-trivial.

Mechanochemical Synthesis of MOFs.

Mechanochemical synthesis represents a solvent-free or near solvent-free strategy for assembling metal-organic frameworks using mechanical energy as the driving force for bond formation. In this method, metal salts and organic ligands are ground together, either manually in a mortar and pestle or more commonly in a ball mill, where repeated impact, shear, and friction events promote the cleavage and reorganization of bonds, ultimately yielding crystalline coordination frameworks.

The first demonstration of MOF formation via mechanochemistry was reported in 2006, marking the beginning of a rapidly growing area within green materials synthesis.[67] Since then, mechanochemical approaches have been widely applied to prepare a broad range of MOFs, including carboxylate-based frameworks (e.g., HKUST-1), pillared-layered structures, and imidazolate frameworks such as ZIF-4 and ZIF-8.[68–70]

Principles of the Mechanochemical Process: Under mechanical force, reactants undergo localized bond breakage and activation, enabling metal-ligand coordination without the need for bulk solvents or elevated temperatures. This makes mechanochemical reactions fundamentally different from solution-based synthesis, where solubility and diffusion govern assembly. Reactivity can be significantly enhanced by:

1. Liquid-assisted grinding (LAG): The addition of microliter quantities of a liquid, such as DMF, methanol, or water, improves mobility at the molecular level and often leads to faster and more selective framework formation.[68]

2. Ion- and liquid-assisted grinding (ILAG): The combination of small liquid amounts

with inorganic salts (e.g., ammonium or alkali nitrates) can exert structure-directing effects, enabling selective synthesis of specific phases or topologies.[70;71]

Advantages

1. Performed at ambient temperature with short reaction times (10-60 min).
2. Solvent-free or uses only microliter amounts of benign liquids.
3. Environmentally friendly; often produces less hazardous by-products.
4. Allows use of insoluble metal oxides, broadening precursor options.

Disadvantages

1. Products may exhibit lower crystallinity compared to solvothermal methods.
2. Resulting frameworks often have reduced pore size or surface area.

Electrochemical Synthesis of MOFs.

Electrochemical synthesis is an alternative route for producing MOFs in which metal ions are generated in situ by anodic dissolution instead of using conventional metal salts. This strategy was first demonstrated in 2005 and was motivated by the need to avoid undesirable counter-anions (e.g., nitrate, chloride, perchlorate) that complicate large-scale production.

In a typical setup, the metal anode gradually releases metal ions into a solution containing the organic linker and a supporting electrolyte. These ions immediately coordinate with the linker molecules, forming the MOF either as a powder or as a film deposited near the electrode surface.[72] Using protic solvents or sacrificial reducible species can prevent unwanted metal deposition on the cathode.

Electrochemical synthesis has been successfully applied to several Cu- and Zn-based frameworks, including HKUST-1, Zn-BDC systems, and later azolate-based MOFs such as ZIF-8 and related structures. In some cases, the method enables continuous production and higher solid content than traditional batch solvothermal processes. Electrochemical routes have also allowed controlled growth of MOF films and patterned coatings on conductive surfaces by tuning the applied potential and reaction time.

However, comparative studies show that although the crystal structure of electrochemically synthesized MOFs is generally correct, the product quality such as porosity, purity, or thermal stability may be lower due to incorporation of electrolyte or unreacted linkers during crystallization.

Advantages

1. Real-time control of MOF growth through applied voltage.
2. Mild reaction conditions.
3. Rapid synthesis compared to solvothermal routes.
4. Ability to form thin films and patterned coatings.

Disadvantages

1. Often poor or inconsistent crystallinity.
2. Lower yield compared to solution-phase routes.
3. Possible contamination from supporting electrolytes.

1.5.3 Fundamental Chemistry Considerations for Reaction Parameters.

The successful synthesis of a MOF is governed not only by the choice of metal nodes and organic linkers but also by the fundamental chemical principles that dictate how these components assemble under given reaction conditions. While solvothermal synthesis remains the most widely used method, the rationale behind parameters such as reagent ratios, solvent composition, temperature, and reaction time lies in basic coordination chemistry and nucleation-growth theory. This section discusses how these considerations influence MOF formation and guide rational optimization.

Linker and Node Chemistry.

The geometry and connectivity of the metal center and linker determine the topology of the final MOF, making their selection the first critical step. Their assembly is guided by simple stoichiometric relationships and coordination preferences. Varying the metal-to-ligand ratio

can shift the reaction toward different SBUs or entirely different frameworks, as the limiting reagent dictates which coordination motifs dominate during nucleation. For example, using a larger excess of metal ions favored the formation of PCN-13, whereas progressively lowering the metal-to-ligand ratio shifted the reaction toward other frameworks, ultimately yielding PCN-132 and PCN-131.[73]

Hard-soft acid-base (HSAB) compatibility also plays a role: hard carboxylate linkers pair more effectively with hard metal ions (e.g., Zr^{4+}, Al^{3+}), while softer N-donor linkers tend to coordinate better with transition metals such as Zn^{2+} or Cu^{2+}. These considerations help identify combinations that will assemble efficiently under the selected reaction conditions.

Modulator.

While the metal nodes and organic linkers dictate the framework's ultimate structure, using only these two components often leads to rapid precipitation and poorly ordered solids. To overcome this, MOF syntheses commonly incorporate modulators, small molecules that slow down assembly, guide crystallization, and tune particle size, phase purity, and defect density. Their behavior can be understood through basic principles such as HSAB interactions, stoichiometry, acid-base equilibria, and pK_a matching.[74]

Coordinating modulators: These are typically monotopic acids whose binding chemistry resembles that of the linker (e.g., carboxylates for carboxylate linkers, phosphonates for phosphonate linkers). Upon deprotonation, both the linker and the modulator form conjugate bases that compete for coordination to the metal centers (Figure 1.6). Because modulators are monotopic, they can bind to a metal ion but cannot bridge between two metals, which slows down network formation. Elevated temperature later promotes modulator displacement by the multitopic linker, allowing the extended framework to assemble in a controlled manner.

Successful competition requires the modulator to deprotonate under similar conditions as the linker. Therefore, matching pK_a values is essential. A classic example is the synthesis of UiO-66, where acetic acid is used because its acidity closely aligns with that of terephthalic acid, ensuring both species are present in their reactive, deprotonated forms during crystallization.[76]

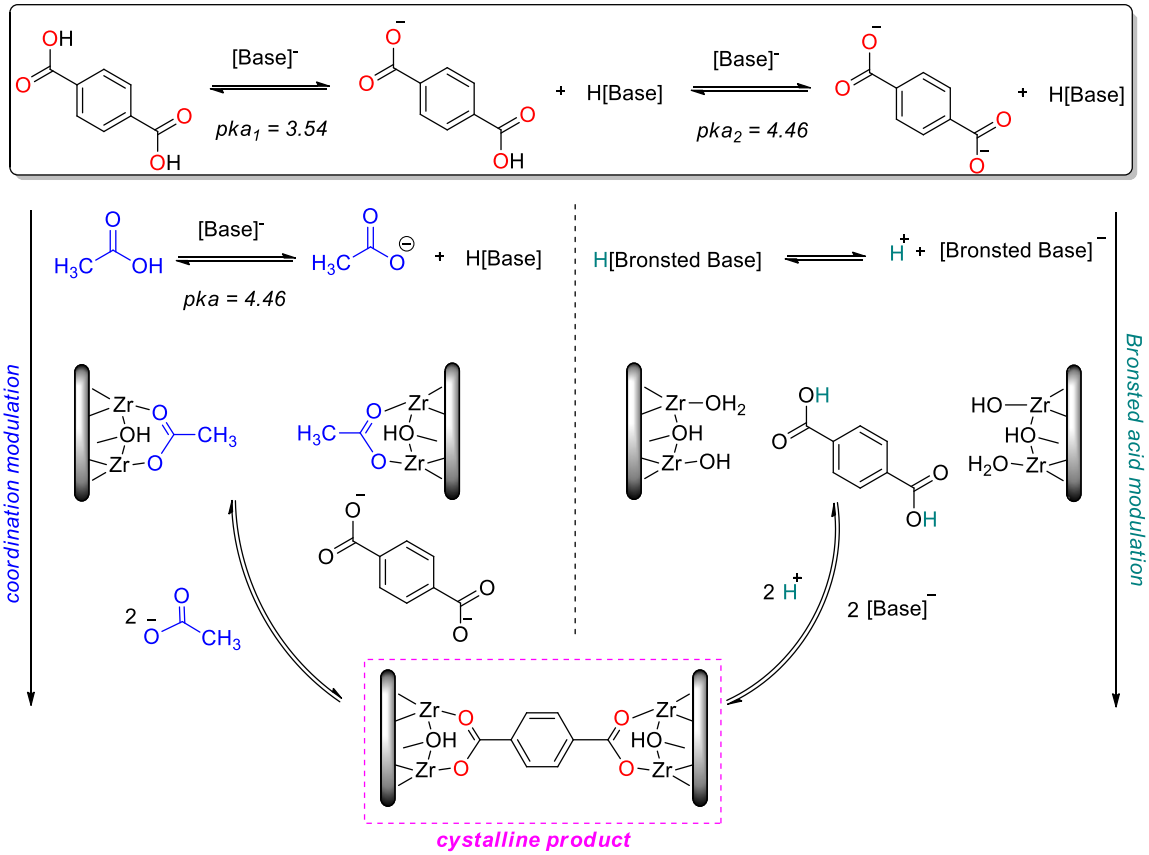


Figure 1.6: Illustration of modulator effects during MOF synthesis, including linker equilibrium, coordination and Brønsted acid modulation, and final linker binding to metal nodes.[75]

Brønsted acid modulators: Strong acids such as HCl or HBF_4 regulate crystallization by a different mechanism.[77] Instead of competing for coordination sites, they shift the acid-base equilibrium toward the protonated form of the linker, reducing the concentration of its conjugate base and slowing nucleation (Figure 1.6). Stronger acids whose conjugate bases are weakly coordinating are especially effective because they maintain high proton activity without interfering with metal-ligand bonding (Figure 1.6).

Overall, modulators provide a powerful handle to tune nucleation and growth, enabling MOF crystals with higher order, controlled defect levels, and enhanced reproducibility.

Solvent.

In typical MOF synthesis, the solvent primarily serves as the medium that dissolves the metal source, linker, modulator, and other additives. Because reactions are often conducted

at elevated temperatures, solvents with sufficiently high boiling points are required. This is why formamide-based solvents such as DMF and DEF are frequently chosen, they provide good solubility and remain stable under solvothermal conditions.

Beyond acting as a medium, the solvent can directly influence reaction pathways through factors such as basicity and steric bulk. At high temperatures, DMF and DEF gradually decompose to form dimethylamine or diethylamine, which help drive assembly by deprotonating the linker and interacting with modulators.[74] Their slow decomposition is also beneficial, as it avoids rapid precipitation and promotes controlled crystal growth. Additionally, the steric size of the solvent can act as a template, steering the structure toward different frameworks. For instance, Ma and co-workers found that DMF yielded an interpenetrated MOF with smaller pores, whereas the bulkier DEF favored the formation of a non interpenetrated structure with larger channels.[78]

Enthalpy of Formation and Reaction Temperature.

The successful assembly of a MOF relies not only on choosing suitable linkers, metal nodes, modulators, and solvents, but also on selecting reaction conditions that support framework formation. Concepts such as HSAB theory, reaction enthalpy, and kinetic energy help rationalize why many MOF syntheses require elevated temperatures.

Calorimetric studies from the Navrotsky group have shown that different MOFs exhibit either endothermic or exothermic formation energies when compared to their corresponding dense precursor phases. Frameworks like MOF-5,[79] Mg-MOF-74, and Ni-MOF-74 form endothermically,[80] whereas systems such as Zn-HKUST synthesized in DMF or Cu-HKUST made in water show exothermic formation due to stabilizing interactions between the solvent and the framework.[81] In ZIFs, formation becomes exothermic as the metal center transitions from less favorable Zn-O interactions in the precursors to more favorable Zn-N coordination within the MOF, consistent with HSAB preferences for borderline-soft matching.[82]

Regardless of whether formation is endothermic or exothermic, higher temperatures play a critical role. Increasing temperature boosts the kinetic energy of the reactants, enabling them to overcome activation barriers, collide more frequently, and reach the thermodynamically preferred product more quickly. Elevated temperatures also enhance the lability of

modulators, promoting competitive coordination, and influence solubility and supersaturation, key factors that drive nucleation and subsequent crystal growth.[83]

Reaction Time and Concentration.

Along with temperature, both reaction duration and concentration strongly influence the type and quality of the MOF obtained.[84] Products that are kinetically favored often form at shorter reaction times, while longer durations typically allow the system to reorganize toward more stable, thermodynamically preferred structures.

Concentration also plays a central role. According to collision theory, increasing the concentration of reactants raises the frequency of molecular encounters, accelerating reaction rates and promoting faster nucleation. Highly concentrated mixtures can lead to rapid particle formation, whereas dilute conditions tend to slow nucleation and may yield larger, better-defined crystals.

MOF Nucleation and Growth.

MOF crystallization typically unfolds through two interconnected stages, nucleation followed by crystal growth, although the two can overlap in time. Both stages are strongly influenced by fundamental chemical principles such as supersaturation, temperature, concentration, and the coordination behavior of the building units.

MOF Nucleation. According to classical nucleation concepts, small clusters of metal-linker units continuously form and dissolve until they reach a critical size that becomes stable enough to grow. This process is driven by supersaturation, which itself depends on reaction concentration and temperature.[85]

Because MOFs assemble from metal ions, linkers, and sometimes pre-formed SBU fragments, several alternative nucleation pathways have been proposed. Some studies point to monomers or partial SBUs as the earliest building units, while others report non classical pathways involving intermediate amorphous or liquid-like phases before crystallization. Regardless of the exact mechanism, nucleation always decreases supersaturation and transitions the system into the growth phase.

MOF Growth. Once nuclei form, crystal growth proceeds through the addition of solvated species to the crystal surface. Supersaturation makes this process thermodynamically favorable, while diffusion and adsorption control the kinetics. Growth may occur through multiple mechanisms, including stepwise rearrangements described by Ostwald's Rule of Stages.

Recent kinetic studies show that increasing temperature accelerates growth and that the influence of metal nodes and linkers on growth does not always correspond directly to their stoichiometry in the final framework. Evidence also suggests the presence of a dynamic interfacial layer where ordering occurs before incorporation into the bulk crystal.[86]

Beyond temperature and concentration, factors such as modulators, capping agents, and solvent identity can tune crystal size, shape, and polymorph selection during growth.

1.6 Properties of MOFs.

Metal-organic frameworks (MOFs) exhibit a unique combination of structural and chemical features that distinguish them from traditional porous materials such as zeolites, activated carbons, or mesoporous silica. Their hybrid nature, metal nodes connected by organic linkers, allows unprecedented tunability in porosity, functionality, and reactivity. Below, we summarize the key properties that define MOFs and underpin their diverse applications.

1.6.1 Permanent Porosity and High Surface Area.

MOFs are known for their extremely high porosities:

1. Surface areas often exceed 1000–6000 m^2 g^{-1}.[87]

2. Pores can range from microporous (<2 nm) to mesoporous (>2 nm), depending on the framework design.[88;89]

3. Uniform pore environments and modular voids support selective adsorption and high uptake capacities.

The periodic arrangement of pores enhances diffusion and host-guest interactions, making MOFs excellent candidates for gas storage, separation, and catalysis.

1.6.2 Themral and Chemical Stability.

Stability varies widely across MOF families:

1. High stability: Zr-, Ti-, Al-, and Cr-based MOFs (e.g., UiO-66, MIL-101, MOF-74) exhibit strong metal-oxygen bonds and can withstand high temperatures and water exposure.[53;90]

2. Moderate stability: Cu(II) paddlewheel MOFs such as HKUST-1 may degrade in humid environments.[91]

3. Lower stability: Zn(II)-imidazolate frameworks generally show good thermal stability but may be sensitive to acids or bases depending on topology.[92]

Stability depends on bond strength, node connectivity, framework topology, and guest-framework interactions.

1.6.3 Framework Flexibility - "Breathing".

Some MOFs exhibit dynamic behavior in response to external stimuli such as pressure, temperature, or guest molecules:

1. Breathing and swelling: Frameworks like MIL-53 and DUT-49 undergo large, reversible structural transitions.[93]

2. Gate-opening effects: Adsorption of certain gases induces changes in pore aperture size.[94]

3. Stimuli-responsive behavior: Changes can be triggered by light, electric fields, or solvent exchange.[95;96]

Such flexibility allows unusual sorption isotherms, high selectivity, and switchable properties.

1.6.4 Structural Diversity and Tunability.

A defining property of MOFs is the ability to precisely design and control their structure through linker and metal node selection.

1. Topology control: Varying linker rigidity, length, and functional groups enables access to a wide range of network geometries.[97;98]

2. Isoreticular design: Linker elongation can preserve topology while expanding pore sizes, allowing systematic tuning of physical properties.[99]

3. Functionalization: Linkers can incorporate chemical groups (-NH_2, -OH, -SO_3H, halogens, etc.) that modulate chemical activity or enable post-synthetic modification.[100]

This structural programmability is a major advantage over purely inorganic porous solids.

1.6.5 Chemical Functionality and Tailored Reactivity.

Because organic linkers and metal clusters can be engineered independently, MOFs allow fine control over their chemical environment:

1. Active sites on linkers: Functional groups can directly participate in catalysis, hydrogen bonding, or acid-base interactions.[101;102]

2. Open metal sites: Removal of coordinated ligands upon activation generates Lewis-acidic sites that enhance catalytic activity or adsorption selectivity.[103;104]

3. Post-synthetic modification (PSM): MOFs can undergo covalent, coordination, or ionic modifications without compromising their structure, allowing tailored reactivity for specific applications.[28;29]

This chemical flexibility is usually rare in other crystalline solids.

1.7 Isoreticularity in MOFs.

A central design strategy in MOF chemistry is isoreticularity, which refers to constructing a family of frameworks that retain the same underlying topology while systematically varying their internal dimensions or functionality.[105] This is typically achieved by modifying the length or structure of the organic linker without altering the connectivity of the metal-based secondary building unit (SBU). As long as the SBU preserves its geometry and coordination environment, the overall network remains topologically identical, allowing predictable changes in porosity and chemical functionality.

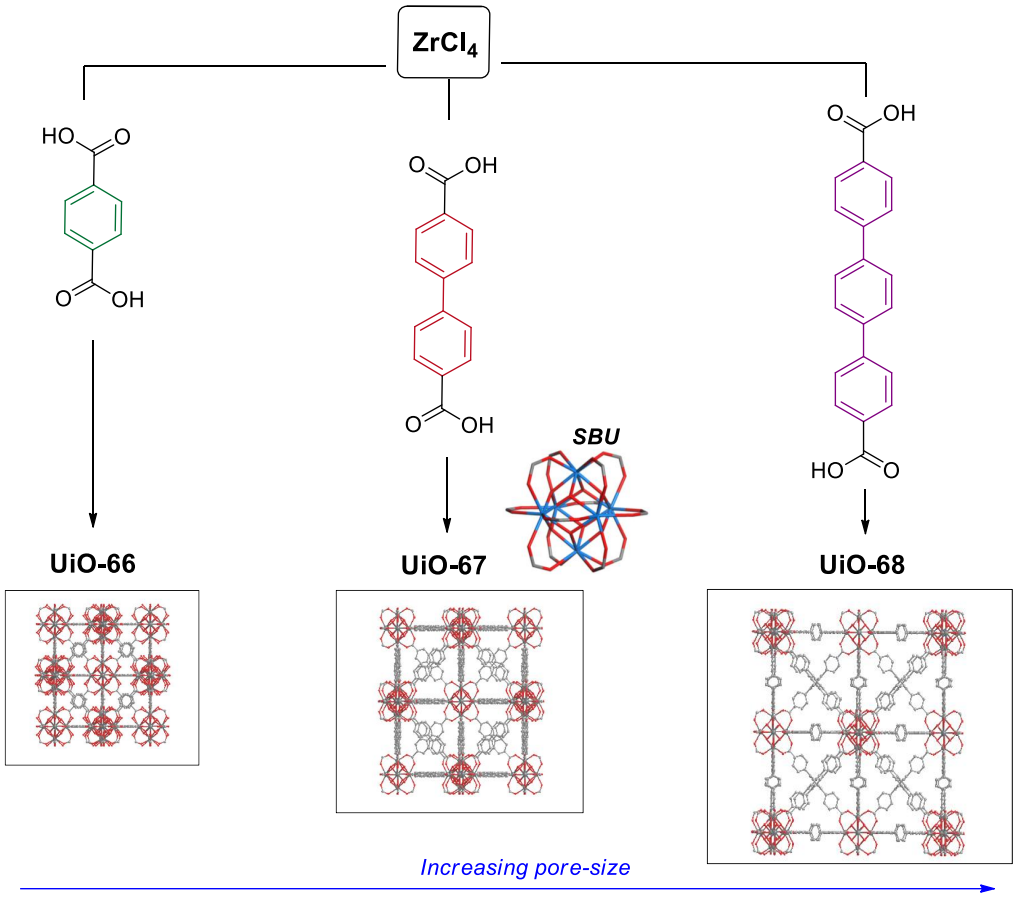


Figure 1.7: An example of isoreticular MOF: Zr-based UiO MOFs

Principle of Isoreticular Design: In an isoreticular series, the parent MOF serves as the structural template. Expansion is carried out by using a set of linkers that are chemically similar but differ in length or substituents. Because the SBU connectivity controls the framework topology, maintaining the same metal cluster ensures the same structural arrangement, even as the pore sizes or window apertures increase. This modular approach enables: controlled pore enlargement, tuning of internal functional groups, and systematic adjustment of surface area and pore volume.

Although most isoreticular series rely on identical SBUs, in some cases different metals have been used to generate analogous topologies. For example, the well-known HKUST-1 network has been replicated using Zn^{2+}, Fe^{2+}, and Cr^{2+} in place of Cu^{2+} while preserving the same connectivity.[106]

Limitations of Isoreticular Expansion: Increasing linker length is an effective route to expand pore dimensions; however, structural stability tends to decrease as the framework

becomes more open. Larger pores may collapse upon solvent removal or thermal activation. A well-documented example is the UiO series, where UiO-67, with a biphenyl linker, shows higher surface area but reduced robustness compared to UiO-66.[107;108] This trade-off underscores the challenge of designing large-pore MOFs that remain mechanically and chemically stable.

Representative Examples

1. MOF-5 Series One of the earliest demonstrations of isoreticular expansion used the MOF-5 topology.[109;110] By progressively elongating the benzene dicarboxylate linker (BDC → BPDC → HPDC → TPDC), the pore diameters increased from ∼13 Å to nearly 29 Å while preserving the cubic Zn_4O node connectivity.

2. Zr-based Isoreticular MOFs (UiO Series) The UiO family is a benchmark example of isoreticularity in high-stability frameworks.[111;112] All members are constructed from $Zr_6O_4(OH)_4$ clusters connected by linear dicarboxylates: UiO-66: BDC; UiO-67: BPDC; UiO-68: TPDC (Figure 1.7).

Increasing linker length progressively enlarges the pore system yet maintains the same face-centered cubic topology.

3. NU-1100 Series A series of Zr_6-based MOFs (NU-1101 to NU-1104) demonstrated that even extremely long π-conjugated linkers can be incorporated while preserving topology.[113;114]These frameworks achieved geometric surface areas exceeding 5000 m^2 g^{-1} using systematically extended tetratopic ligands.

Importance of SBU Reproducibility: For an isoreticular series to form correctly, synthesis conditions must reliably generate the same metal cluster in each reaction. Changes to the cluster's size, shape, oxidation state, ligand environment, or number of open coordination sites can redirect assembly toward different topologies. Thus, controlling reaction conditions (solvent, temperature, acidity, modulators) is essential to preserving the connectivity of the parent MOF.

Thus, isoreticular synthesis provides a powerful platform for: tailoring pore size without altering the framework arrangement, tuning internal surfaces for catalysis or adsorption, studying structure-property relationships across a controlled series, and developing MOFs for gas storage, separations, sensing, and drug delivery.

By enabling rational expansion of a known structure, isoreticularity has been instrumental in transforming MOF chemistry into a predictable and modular design field.

1.8 Post-Sythetic Modification (PSM) in MOFs.

Metal-organic frameworks are exceptionally modular materials, and one of the most powerful expressions of this modularity is post-synthetic modification (PSM), the collection of chemical strategies applied after MOF assembly to introduce new functionalities, tune chemical environments, or install catalytically active sites without disrupting the crystalline framework.

Over the past decade, PSM has grown into a central tool for tailoring MOFs for catalysis, adsorption, sensing, and biomedical applications.

1. Principles and Motivation Behind PSM

PSM is enabled by two intrinsic properties of MOFs:

(i) Chemically addressable organic linkers. Linkers often contain pendant functional groups (-NH_2, -OH, -CHO, -CN, etc.) that can undergo selective organic reactions without collapsing the framework (Figure 1.8).[115;116]

(ii) Labile or partially saturated metal clusters (SBUs) Coordinated solvent molecules, terminal -OH/-OH_2 groups, and structural defects create accessible metal sites for post-synthetic binding or exchange (Figure 1.8).

Together, these features allow MOFs to undergo chemical transformations while maintaining the original topology.

PSM strategies fall into three broad categories: (i) Modifying the organic linker (ii) Modifying the metal node (iii) Metal ion exchange within SBUs

1.8.1 PSM Over Organic Linkers

Many MOFs are deliberately synthesized with reactive functional groups (e.g., -NH_2 in IRMOF-3, UiO-66-NH_2) that serve as handles for covalent transformations.[115]

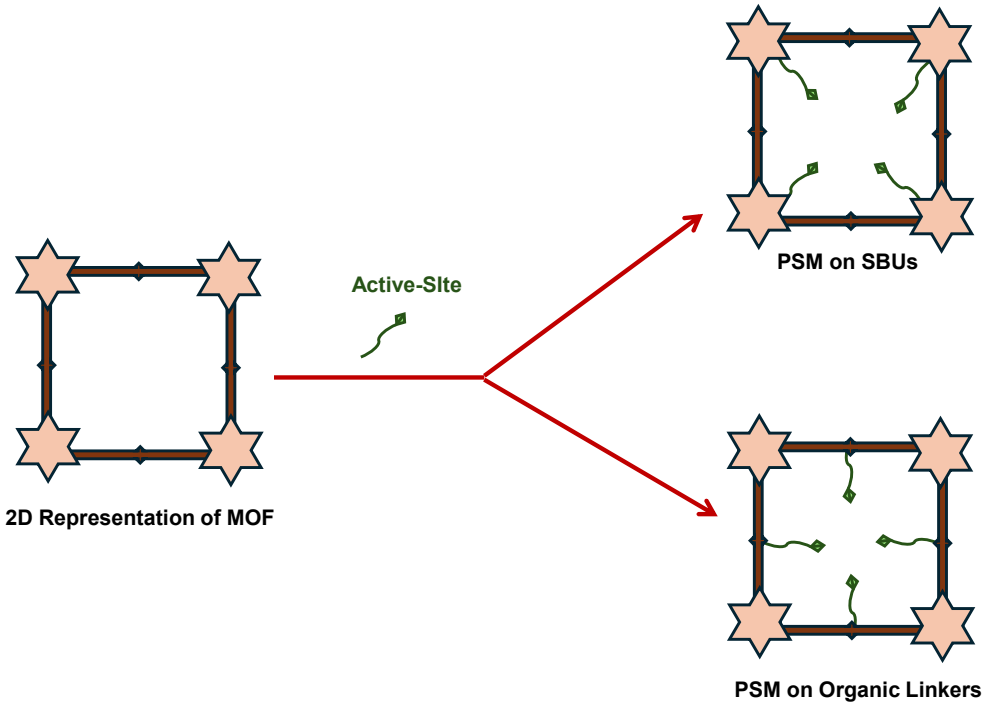


Figure 1.8: Postsynthetic modification at organic linkers and SBUs.

Covalent Linker Modification

Common reactions include: Imine formation (amine + aldehyde);[117] Amide coupling; Urea and thiourea formation; Click chemistry (azide-alkyne cycloaddition); Halogenation, reduction, or oxidation. These reactions enable precise molecular editing inside the pores.

Example: IRMOF-3 undergoes imine condensation with salicylaldehyde to generate a chelating site, which can then be metalated.[118] This two-step sequence allows installation of Au(III), Pd(II), or other catalytic centers directly onto the linker environment.

It retains the parent topology. Allows introduction of catalytic groups without altering the metal cluster. Enables spatially isolated catalysts resembling molecular catalysts but within a porous solid.

1.8.2 PSM at Metal Nodes

Metal clusters often contain terminal ligands (H_2O, OH^-, formate, etc.) that can be displaced, offering a direct avenue to functionalize the inorganic node.

Direct Grafting on Open Metal Sites

Upon thermal activation, coordinated solvent molecules are removed, generating unsaturated metal sites.

Example: In HKUST-1 ($Cu_3(BTC)_2$), each Cu center can shed a coordinated water molecule to expose a vacant site, enabling ligand grafting or substrate binding.[51]

Anchoring Organic Molecules

Amine-bearing ligands (e.g., ethylenediamine) have been grafted onto Cr sites in MIL-101 to introduce Brønsted or Lewis basic functionality.[119] Similar strategies allow coordination of amino acids (e.g., proline), converting MOFs into chiral or bifunctional catalysts.

1.8.3 Metal-Ion Exchange

In many MOFs, the metal cluster tolerates replacement of one metal with another without altering the overall topology. Researchers first demonstrated that amine-containing molecules can be directly attached to the open metal sites of MIL-101; for example, Hwang and co-workers grafted ethylenediamine onto the chromium clusters. Building on this strategy, Banerjee's group later introduced proline onto the Cr nodes of MIL-101, converting the framework into an efficient organocatalyst.[120] A related approach was reported by Long and collaborators, who coordinated ethylenediamine to the open Cu(II) sites in a MOF, enabling enhanced CO_2 adsorption performance.[121]

1.8.4 Advantages and Challenges of PSM Advantages.

Advantages: Precise control over chemical functionality, ability to introduce catalytic centers not compatible with solvothermal synthesis, retention of crystallinity and porosity, tunable active-site environment (coordination number, geometry, electronic properties).

Challenges: Ensuring complete diffusion of reagents throughout the MOF, avoiding framework collapse under reactive conditions, achieving uniform functionalization at high loadings, maintaining phase purity and single-site dispersion.

1.9 Applications of MOFs.

Metal-organic frameworks have emerged as one of the most impactful classes of reticular materials, owing to the breadth of applications they can address across chemistry, materials science, and engineering. Their exceptional versatility arises from a combination of structural and chemical attributes that can be systematically tuned.

Highly designable architectures: Because MOFs are built from modular organic linkers and metal-based secondary building units (SBUs), the geometry, connectivity, and overall topology of the framework can be precisely tailored. This structural control allows researchers to engineer materials suited for targeted functions.

Extraordinary porosity with adjustable pore dimensions: MOFs can exhibit extremely high surface areas, and the internal pore size can be systematically modulated by linker length, SBU geometry, or by incorporating hierarchical pores. This tunability directly translates to selective uptake, diffusion, and confinement properties.

Ease of post-synthetic modification (PSM): Chemical modification after framework assembly enables fine-tuning of catalytic sites, pore environments, hydrophilicity/hydrophobicity, or electronic features. PSM expands the scope of accessible functionalities far beyond what is achievable through direct synthesis alone.

Well-ordered structures that facilitate characterization: Unlike many traditional heterogeneous materials, MOFs possess crystalline long-range order, enabling detailed structural analysis by techniques such as X-ray diffraction. Their predictable and periodic arrangement of metal nodes and linkers makes it easier to correlate structure with function.

Presence of Single-Site Catalytic Centers:: Many MOFs can host isolated, well-defined active sites, either as part of the metal nodes or introduced through post-synthetic modification. These single-site centers mimic the uniformity of homogeneous catalysts while remaining embedded in a solid framework. As a result, they enable precise mechanistic studies, offer high selectivity in catalytic reactions, and minimize complications arising from particle aggregation or heterogeneous site distributions. The ability to engineer and stabilize such atomically dispersed sites is a key advantage that distinguishes MOFs from traditional porous materials.

These features have accelerated the translation of MOFs from research to commercial use. Several companies are now scaling up MOF production, with early applications including controlled release of 1-methylcyclopropane for fruit ripening,[122] and safe storage of reactive industrial gases. MOFs have also made significant progress in biomedicine; notably, the Hf-based RiMO-301 became the first MOF to enter human clinical trials for radio-immunotherapy.[123]

The following sections highlight major application areas including gas storage and separation, catalysis, sensing, drug delivery, ion exchange, and magnetic separation, demonstrating how MOF tunability enables diverse technological functions.



Figure 1.9: Applications of metal-organic frameworks (MOFs).

1.9.1 Magnetic Separation using MOFs.

MOFs can be integrated with magnetic nanoparticles to produce magnetically responsive composites that maintain the high surface area, tunable porosity, and chemical versatility of the parent framework while gaining the benefit of rapid, magnet-assisted recovery. These magnetic-MOFs act as efficient adsorbents for dyes, pollutants, and metal ions, and can be removed from solution simply by applying an external magnet avoiding energy-intensive steps such as filtration or centrifugation. Their recyclability, structural stability, and ability to be functionalized for selective adsorption make them particularly attractive for wastew-

ater remediation and industrial separation processes.[124;125] A representative example is the La-MOF-NH_2@Fe_3O_4 material, which shows ultrafast and selective uptake of Congo Red, removing more than 90% of the dye within two minutes.[126] The composite can be magnetically isolated and reused over multiple cycles with minimal performance loss, underscoring the promise of magnetic-MOFs as practical, selective, and highly recyclable separation platforms.

1.9.2 Ion Exchange.

Metal-organic frameworks have emerged as promising next-generation ion-exchange materials owing to their exceptionally high surface areas, ordered porosity, and the presence of diverse functional groups that can interact selectively with ionic species. Unlike conventional organic resins or inorganic exchangers, MOFs offer well-defined pore channels and tunable binding environments, enabling fast ion uptake and high selectivity toward targeted cations or anions. Many frameworks such as UiO-66, MIL-101, ZIF-8, and IRMOF-3 have been shown to efficiently remove heavy metal ions like Pb^{2+}, Cr^{6+}, and Cu^{2+} from aqueous solutions through mechanisms involving coordination, electrostatic attraction, or direct ion exchange at the metal clusters or functionalized linkers.[127;128] In some zinc-based MOFs, for example, Pb^{2+} removal has been attributed to a combination of Zn-Pb ion exchange and strong coordination with linker-based functional groups such as -NH_2. The high crystallinity of MOFs further allows structure-property relationships to be probed at the atomic level, aiding in the rational design of improved ion-exchange materials. With advances in stability and green synthesis methods, MOFs and their composites are increasingly being explored for practical wastewater treatment, offering rapid sorption, excellent selectivity, and good regeneration potential for industrial applications.[129;130]

1.9.3 Drug Delivery.

Metal-organic frameworks have emerged as highly adaptable carriers for drug delivery because of their large surface areas, tunable pore networks, and easily modifiable chemical environments. These properties enable MOFs to load and release a wide range of therapeutics, from small molecules to complex biomacromolecules. Early studies demonstrated

controlled release of small drugs such as ibuprofen,[131;132] doxorubicin, and curcumin, with MOFs achieving far higher loading capacities than many traditional carriers.[133–136] More recent breakthroughs involve biomimetic mineralization, where proteins and nucleic acids are encapsulated during MOF formation allowing sensitive cargos like gelonin, Cas9–sgRNA complexes, siRNAs, and plasmid DNA to be protected from degradation and delivered intracellularly.[137–139] Gasotransmitter-loaded MOFs (e.g., nitric oxide and carbon monoxide releasing frameworks) have also been explored for anti-inflammatory and antimicrobial therapies.[140] In another notable example, ZIF-8 nanoparticles have been used to deliver insulin and protect it from enzymatic breakdown, significantly improving its stability in biological environments.[141] These examples highlight how MOFs can be engineered to combine high loading, targeted release, and molecular protection, making them powerful platforms for next-generation drug delivery systems.

1.9.4 Chemical Sensing.

Metal-organic frameworks have emerged as powerful sensing materials because their highly ordered pores, tunable chemical environments, and modular structures enable selective interactions with a wide range of analytes. Their ability to concentrate guest molecules within well-defined channels significantly enhances detection sensitivity, while the presence of functional linkers and metal nodes allows diverse signal-transduction pathways,[33] including fluorescence modulation, electrochemical responses, and changes in impedance or mass. A fundamental origin of selectivity in MOF-based sensing arises from simple size discrimination: only molecules small enough to pass through the framework apertures can diffuse into the pores, while bulkier species are sterically blocked.[142] Many MOFs exhibit intrinsic luminescence, and guest binding can lead to characteristic "turn-on" or "turn-off" optical signals through mechanisms such as ligand-to-metal charge transfer or quenching by redox-active species. Similarly, frameworks with open metal sites can respond selectively to gases like NO, CO_2, or volatile organics through reversible coordination interactions. Because MOF structures can be engineered through linker design, pore-size control, and post-synthetic functionalization, sensors can be tailored for specific targets including toxic gases, humidity, pH, metal ions, explosives, and even biomolecules. These features, combined with their thermal robustness and compatibility with thin-film device fabrication, make MOFs promising

candidates for next-generation chemical sensing technologies.

Some examples:

• Detection of Nitroaromatic Explosives (Fluorescence Quenching): A classic example involves luminescent Zn-based MOFs, such as $Zn_2(BDC)_2(DABCO)$,[143;144] whose fluorescence is strongly quenched upon exposure to nitroaromatics like TNT (2,4,6-trinitrotoluene). The high electron affinity of nitro groups induces photoinduced electron transfer, enabling rapid and selective detection even at trace levels.

• Humidity Sensing Using HKUST-1: MOFs can also function as highly responsive humidity sensors due to their strong affinity for water. For instance, HKUST-1 is known to take up nearly 40 wt% water, making it suitable for humidity detection in various sensing platforms.[51;145]

• VOC Detection with ZIF-8 Thin Films (Mass-Sensitive Sensing):[146] ZIF-8 coated on quartz crystal microbalance (QCM) sensors can selectively detect volatile organic compounds (e.g., ethanol, toluene). VOC adsorption alters the film's mass, producing measurable frequency shifts, with pore-size selectivity governed by the sodalite cages.

• Biomolecule Sensing (Post-Synthetically Modified MOFs): Amino-functionalized MOFs (e.g., NH_2-MIL-53(Al)) can be modified with fluorescent dyes or aptamers to detect biomolecules like glucose or dopamine.[147;148] Binding of the analyte to the functional group changes the fluorescence lifetime or intensity, allowing sensitive quantification.

1.9.5 Gas Storage and Separation.

Metal–organic frameworks have emerged as exceptional materials for gas storage and separation because of their ultrahigh surface areas, precisely tunable pore dimensions, and chemically functionalizable internal surfaces. These features allow MOFs to pack large quantities of gases within their pores, making them attractive for storing energy-relevant gases such as H_2, CH_4, and CO_2 under moderate pressures. Their uniform and adjustable pore apertures also enable molecular sieving, where gases are separated based on subtle differences in size, shape, or adsorption strength. Beyond size exclusion, the presence of open metal sites and tailored functional groups enhances specific host-guest interactions, providing highly selec-

tive uptake of targeted molecules. Together, these designable attributes make MOFs one of the most versatile platforms for achieving efficient gas storage and energy-saving separations.

Some examples:

• MOF-5 (IRMOF-1): Hydrogen Storage Benchmark

One of the earliest and most iconic MOFs, MOF-5, demonstrated that frameworks with very high porosity (BET $>$ 3000 m^2/g) could store significant amounts of hydrogen at cryogenic temperatures.[149] Its discovery triggered the global pursuit of MOFs for H_2 storage.

• MOF-210: Record H_2 Uptake

MOF-210 possesses one of the highest surface areas reported ($>$ 6000 m^2/g).[150] It holds 17.6 wt% H_2 at 77 K, representing one of the highest gravimetric hydrogen storage capacities ever measured in a porous material.

• HKUST-1: Exceptional Volumetric Methane Storage

Despite its moderate surface area (1850 m^2/g), HKUST-1 exhibits one of the highest volumetric CH_4 storage capacities ($\sim$267 cm^3 STP cm^{-3} at 65 bar).[51;151] Its multiple cage types and open Cu^{2+} sites create strong interactions with methane, making it a model MOF for natural-gas storage.

• SIFSIX-3-Zn: Ultra-Selective CO_2 Capture[152]

This MOF, with its ultra-narrow 3.84 Å channels, shows outstanding CO_2/N_2 and CO_2/CH_4 selectivity. Its pore size and strong quadrupole interactions make it one of the most selective adsorbents for low-pressure CO_2 capture (e.g., flue gas or natural-gas purification).

1.10 MOFs as Heterogeneous Catalysts.

MOFs have become an important class of heterogeneous catalysts because their well-defined, crystalline architectures allow catalytic sites to be incorporated with exceptional spatial precision. Instead of being randomly dispersed as is common in conventional solid catalysts, active centers in MOFs can be positioned uniformly within the framework, enabling clearer structure-activity correlations. Moreover, the modular nature of MOFs allows catalytic

functionality to be introduced directly at the metal nodes, embedded in the organic linkers, or installed post-synthetically as isolated molecular species. This level of control has enabled MOFs to catalyze reactions ranging from oxidation, hydrogenation, and C-C coupling to biomimetic and enzyme-like transformations, often with enhanced selectivity and stability compared to traditional supports. Because their catalytic environments can be engineered at the molecular level, MOFs serve as highly adaptable platforms for designing next-generation heterogeneous catalysts.

1.10.1 MOFs as Single-Site Catalysts.

Single-site heterogeneous catalysis has gained significant attention because isolated metal centers offer uniform coordination environments, high atom efficiency, and well-defined electronic structures, advantages often lost in nanoparticle-based catalysts. Metal-organic frameworks provide an ideal scaffold for installing such isolated active sites due to their crystalline order, modular construction, and predictable anchoring positions within nodes, linkers, or pore surfaces. The regularity of their structure allows catalytic species to be immobilized without bulky stabilizing ligands, minimizing site aggregation while maintaining unhindered substrate access.[153;154] Moreover, the confined pore environment can further tune reactivity and selectivity, enabling MOF-supported single sites to bridge the precision of homogeneous catalysts with the robustness and recyclability of heterogeneous systems. Within this context, single-site catalysis in MOFs can arise from intrinsic open metal nodes or engineered active sites on organic linkers, each offering distinct opportunities for controlling activity, selectivity, and mechanism.

1.10.2 Catalysis at MOF Nodes.

Metal nodes in MOFs often contain open or weakly coordinated metal centers that can directly participate in bond activation and redox processes. Several landmark studies have demonstrated how these intrinsically accessible nodes function as highly active and structurally well-defined catalytic sites:

- Vanadium-based MIL-47 and MOF-48 Yaghi and co-workers showed that the VO_6 units in MIL-47 and MOF-48 behave like molecular vanadium oxidation catalysts, enabling

direct methane oxidation to acetic acid with impressive yields using $K_2S_2O_8$ as the terminal oxidant. These frameworks preserve the geometry of homogeneous VO catalysts while providing the advantages of a stable heterogeneous support.[155]

• Iron nodes in Fe-MOF-74 ($Fe_{0.1}Mg_{1.9}$(dobdc)) Long and co-workers demonstrated that site-isolated Fe(II) centers embedded in MOF-74 can react with N_2O to form a non-heme Fe(IV)=O intermediate, capable of cleaving strong C-H bonds.[156] This system performs ethane oxidation to ethanol and acetaldehyde, showing how MOF nodes can stabilize otherwise fleeting high-valent metal-oxo species.

• Fe-cluster nodes in MIL-100(Fe) and MIL-68(Fe) The trinuclear FeO_6 cluster in these frameworks activates H_2O_2 under visible light to generate ·OH radicals, achieving photocatalytic hydroxylation of benzene to phenol.[157] The rigid Fe-oxo cluster environment prevents overoxidation and supports efficient regeneration of the catalytic cycle.

• Open metal sites in MOF-74 series (Co-, Ni-, Mg-, Zn-MOF-74) The 1D channels lined with coordinatively unsaturated metal sites make MOF-74 variants effective for olefin isomerization, Lewis acid catalysis, and adsorption-driven activation due to their dense packing of exposed metal centers.[158]

These examples demonstrate the versatility of MOF nodes as built-in catalytic sites capable of mediating oxidation, C-H activation, and acid-base transformations with molecular-level precision.

1.10.3 Catalysis at Organic Linkers.

Beyond metal nodes, MOFs offer a powerful route to heterogeneous catalysis by incorporating catalytic functionality directly into the organic linkers. Because linkers are molecularly well-defined and uniformly distributed throughout the framework, they allow high loadings of active sites while preserving the structural order essential for mechanistic analysis. Catalytic motifs including organometallic complexes, organocatalysts, Lewis/Brønsted acids, and redox-active ligands can be embedded either through de novo synthesis using pre-functionalized linkers or via post-synthetic modification. This strategy enables MOFs to mimic homogeneous catalysts while providing the robustness, recyclability, and confinement effects of a solid support.[159]

Representative examples:

• Metalloporphyrin-based MOFs (e.g., PCN-222/PCN-224) Porphyrins, which naturally mediate oxygen transport and redox chemistry, can be directly built into the framework. Fe-TCPP–based MOFs such as PCN-222(Fe) show exceptional peroxidase-like activity, outperforming natural enzymes like horseradish peroxidase.[160] Variants containing Co-porphyrins (e.g., PCN-224(Co)) catalyze CO_2 cycloaddition to cyclic carbonates, combining high stability with excellent reusability.

• Tunable porphyrin linkers for selective oxidation: Modifying substituents (e.g., halogens, alkyl groups) on porphyrin rings within the PCN-224 family allows fine control over the electronic environment of the metal center.[160;161] These subtle changes can switch catalytic selectivity, for instance, enabling highly selective oxidation of branched alkanes, where Br-substituted porphyrin MOFs achieve turnover numbers >7000 and 99% selectivity for tertiary alcohols.

• N-heterocyclic carbene (NHC) metal complexes on linkers Embedding NHC–metal complexes into UiO-type frameworks creates robust single-site catalysts that retain the tunability of homogeneous NHC systems.[162] Ir–NHC functionalized UiO-68 shows efficient isomerization of allylic alcohols, aided by hydrogen-bonding interactions from pendant hydroxyl groups. Similarly, Pd–NHC linkers integrated into UiO-67 catalyze Heck coupling reactions and benzyne–alkene insertions, demonstrating how linker design can expand reaction scope.[163]

• Pincer-type organometallic linkers Zr-MOFs incorporating Pd-POCOP (aryl diphosphinite) pincer linkers exhibit transfer hydrogenation activity that surpasses the performance of the analogous homogeneous complex.[164] The rigid MOF environment stabilizes reactive Pd species and enhances turnover, especially in acidic media where many catalysts fail.

These examples illustrate how MOF linkers can host single, well-defined catalytic centers with tunable electronic and steric environments. By positioning these sites within ordered and accessible pores, linker-based MOFs bridge the gap between molecular catalysis and solid-state stability, enabling reactions that are challenging for conventional supports.

1.10.4 Examples of Biomimetic MOF catalysts.

Nature's enzymes achieve remarkable rates and selectivities under mild conditions, but their fragile structures, narrow operating windows, and complex architectures often limit large-scale use. Biomimetic catalysis aims to capture enzyme-like activity in robust synthetic platforms. Metal-organic frameworks have emerged as exceptional candidates for this purpose: their ordered pores, modular chemistry, and accessibility of active sites allow precise replication and sometimes enhancement of enzymatic functions in a heterogeneous material.[165]

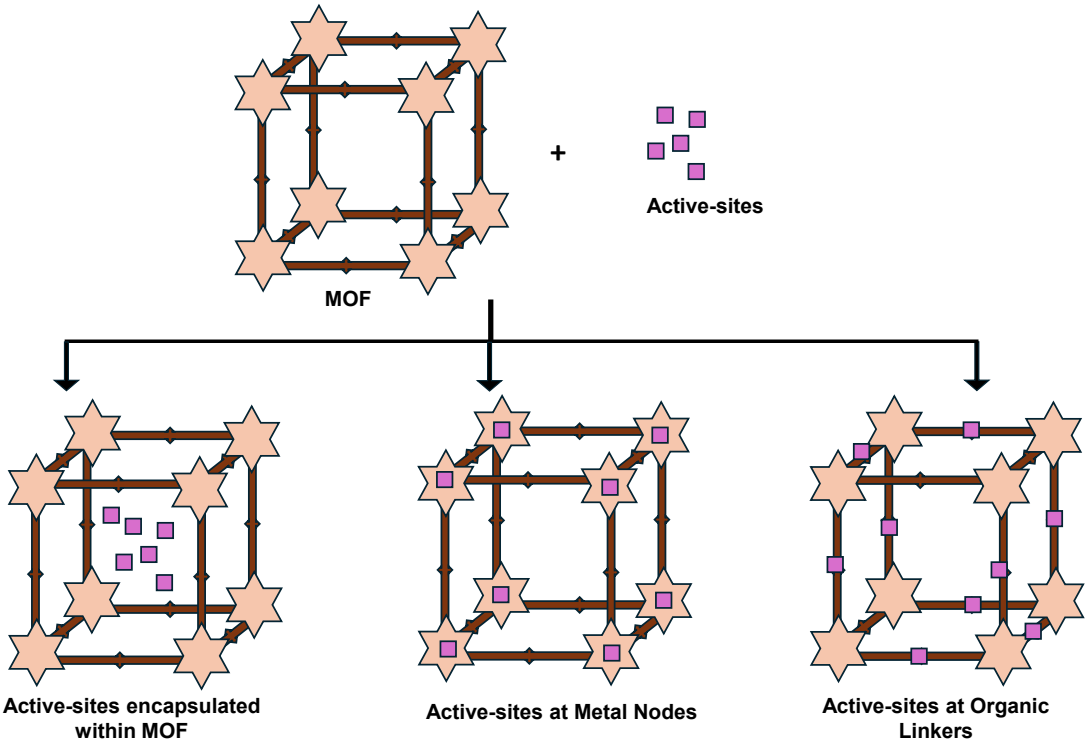


Figure 1.10: General design strategies to create biomimetic MOF catalyst

Two general design strategies are used to create biomimetic MOF catalysts (Figure 1.10):

1. Enzyme Immobilization within MOFs.[166]

Enzymes can be embedded in MOFs either during synthesis (one-pot encapsulation) or post-synthetically through adsorption, pore entrapment, or covalent attachment. The rigid crystalline environment protects the enzyme from denaturation, broadens its operational stability, and often improves recyclability.

Example: Horseradish peroxidase (HRP) encapsulated in ZIF-8 retains activity in or-

ganic solvents and elevated temperatures, far exceeding the stability of the free enzyme.[167]

2. Installation of Enzyme-Like Active Sites within MOFs.

Instead of loading whole enzymes, MOFs can be built to structurally resemble enzyme active sites. Their metal nodes,[168] ligand environments,[169;170] and pore microenvironments can be engineered to reproduce the coordination geometry and secondary-sphere effects found in natural metalloenzymes.

Representative examples include Cytochrome P450 mimics: Fe-porphyrin-based MOFs (e.g., PCN-222(Fe)) replicate the heme pocket and catalyze oxidation of inert C-H bonds, showing higher stability and turnover than the native enzyme.[171]

Why MOFs Excel as Biomimetic Catalysts.[172–175]

• Confinement: Pores recreate enzyme-like cavities, stabilizing transition states and controlling selectivity.

• Secondary-sphere control: Hydrogen bonding, hydrophobic pockets, and electrostatic tuning can be rationally introduced through linker functionalization.

• Stability: Unlike fragile enzymes, MOFs tolerate heat, organic solvents, and oxidative conditions.

• Modular design: Active sites can be installed with atomic precision either as metalloligands, doped metal nodes, or site-isolated single atoms, allowing direct structure-function correlations.

Altogether, biomimetic MOFs offer a powerful platform that merges the sophistication of enzymatic catalysis with the durability and tunability of porous solids. Their ability to integrate enzyme mimics, stabilize real enzymes, and participate in cascade transformations positions them as a versatile class of catalysts bridging biology and synthetic chemistry.

1.10.5 MOFs for C-H Activation.

MOFs have emerged as powerful platforms for selective C-H bond activation, particularly because their well-defined metal nodes and confined pore environments mimic the precision of molecular catalysts while offering the advantages of a heterogeneous support. Their crys-

talline structures allow the installation of open metal sites or metal-oxo/hydroxo species that can activate strong C-H bonds including methane, aromatics, and alkanes under relatively mild conditions. The spatial confinement within MOFs helps stabilize high-valent metal-oxo intermediates and control the approach of substrates, thereby enhancing selectivity for specific C-H positions.

Several MOF systems have demonstrated remarkable activity in C-H functionalization. Fe-MIL-53, Fe-MOF-74, and MOF-253-Fe generate Fe-oxo or Fe-hydroxo species capable of activating aromatic C-H bonds for hydroxylation or halogenation.[45;156] These examples illustrate how MOFs combine site isolation, tunable coordination environments, and pore confinement to achieve controlled C-H activation that is difficult to realize using traditional heterogeneous catalysts.

1.10.6 MOFs for Oxidation Reactions.

Metal nodes in MOFs provide isolated, well-defined environments that make them excellent platforms for oxidation catalysis. Transition-metal centers such as Fe, Cu, Mn, V, and Ti can function either as Lewis acids that activate hydroperoxides or as redox-active sites that cycle between oxidation states to mediate oxygen transfer. Because these sites are embedded within uniform, porous frameworks, MOFs often show higher selectivity than conventional heterogeneous catalysts and can operate with greener oxidants such as tert-butyl hydroperoxide or molecular oxygen.[176;177] Their tunable pore environments further allow control over substrate diffusion and confinement, enabling selective oxidation of alkenes, alkanes, and alcohols under relatively mild conditions.

Several examples illustrate the advantages of MOF-based oxidation catalysts. Fe_2(dobdc) and its Mg-diluted analogue $Fe_{0.1}Mg_{1.9}$(dobdc) can oxidize ethane to ethanol and acetaldehyde using N_2O, with studies indicating the formation of a high-valent Fe(IV)=O species as the active oxidant.[156] These cases highlight how MOFs combine isolated metal sites, redox flexibility, and tailored pore microenvironments to deliver efficient and selective oxidation reactions.

1.11 Outline of Thesis.

This thesis investigates the rational design of MOF-supported single-site catalysts through both linker-centered and SBU-centered engineering, and demonstrates how these structural strategies influence C-H activation and selective oxidation reactivity. Chapter 1 introduces the foundational concepts of reticular chemistry and MOFs, highlighting how their modularity enables precise control over active-site environments. Chapter 2 outlines the experimental and computational methods used throughout the work. Chapters 3-5 focus on methane oxidation, beginning with a mononuclear Cu(II)-hydroxyl site in MIL-53(Al) for selective methane-to-acetic-acid conversion, followed by the development of dinuclear Fe(II)-hydroxyl sites in MOF-253 that mimic *methane monooxygenase* (MMO)-like O_2 activation to produce acetic acid, and finally a mononuclear Fe(II)-hydroxyl analogue that steers selectivity toward methanol, thereby elucidating how active-site nuclearity governs mechanistic pathways. Chapters 6 and 7 extend the linker-functionalization approach to aromatic and alkene oxidation, presenting UiO-based bipyridyl-Fe catalysts that achieve highly selective benzene hydroxylation to phenol and tunable styrene oxidation using H_2O_2. Together, these studies establish a coherent framework connecting MOF architecture, metal coordination environment, and catalytic behavior, offering design principles for next-generation MOF-based catalysts for sustainable oxidative transformations.

References

[1] Yaghi, O. M.; Li, Q. Reticular Chemistry and Metal-Organic Frameworks for Clean Energy. *MRS Bulletin* **2009**, *34*, 682–690.

[2] Hoskins, B. F.; Robson, R. Infinite Polymeric Frameworks Consisting of Three Dimensionally Linked Rod-like Segments. *Journal of the American Chemical Society* **1989**, *111*, 5962–5964.

[3] Yaghi, O. M.; Li, G.; Li, H. Selective Binding and Removal of Guests in a Microporous Metal–Organic Framework. *Nature* **1995**, *378*, 703–706.

[4] O'Keeffe, M.; Peskov, M. A.; Ramsden, S. J.; Yaghi, O. M. The Reticular Chemistry

Structure Resource (RCSR) Database of, and Symbols for, Crystal Nets. *Accounts of Chemical Research* **2008**, *41*, 1782–1789.

[5] Ockwig, N. W.; Delgado-Friedrichs, O.; O'Keeffe, M.; Yaghi, O. M. Reticular Chemistry: Occurrence and Taxonomy of Nets and Grammar for the Design of Frameworks. *Accounts of Chemical Research* **2005**, *38*, 176–182.

[6] Delgado Friedrichs, O.; O'Keeffe, M.; Yaghi, O. M. Three-Periodic Nets and Tilings: Semiregular Nets. *Acta crystallographica Section A, Foundations of crystallography* **2003**, *59*, 515–525.

[7] Delgado-Friedrichs, O.; O'Keeffe, M.; Yaghi, O. M. Three-Periodic Nets and Tilings: Edge-Transitive Binodal Structures. *Acta Crystallographica Section A: Foundations of Crystallography* **2006**, *62*, 350–355.

[8] Côté, A. P.; Benin, A. I.; Ockwig, N. W.; O'Keeffe, M.; Matzger, A. J.; Yaghi, O. M. Porous, Crystalline, Covalent Organic Frameworks. *Science* **2005**, *310*, 1166–1170.

[9] Park, K. S.; Ni, Z.; Côté, A. P.; Choi, J. Y.; Huang, R.; Uribe-Romo, F. J.; Chae, H. K.; O'Keeffe, M.; Yaghi, O. M. Exceptional Chemical and Thermal Stability of Zeolitic Imidazolate Frameworks. *Proceedings of the National Academy of Sciences* **2006**, *103*, 10186–10191.

[10] Diercks, C. S.; Kalmutzki, M. J.; Diercks, N. J.; Yaghi, O. M. Conceptual Advances from Werner Complexes to Metal–Organic Frameworks. *ACS Central Science* **2018**, *4*, 1457–1464.

[11] Lindsey, J. S.; Schreiman, I. C.; Hsu, H. C.; Kearney, P. C.; Marguerettaz, A. M. Rothemund and Adler-Longo Reactions Revisited: Synthesis of Tetraphenylporphyrins under Equilibrium Conditions. *The Journal of Organic Chemistry* **1987**, *52*, 827–836.

[12] Linstead, R. P. 212. Phthalocyanines. Part I . A New Type of Synthetic Coburing Matters. **1934**, 1017.

[13] Rothemund, P. A New Porphyrin Synthesis. The Synthesis of Porphin[1]. *Journal of the American Chemical Society* **1936**, *58*, 625–627.

[14] Adler, A. D.; Longo, F. R.; Finarelli, J. D.; Goldmacher, J.; Assour, J.; Korsakoff, L. A Simplified Synthesis for Meso-Tetraphenylporphine. *The Journal of Organic Chemistry* **1967**, *32*, 476–476.

[15] Introduction to Metal–Organic Frameworks. *Chemical Reviews* **2012**, *112*, 673–674.

[16] Furukawa, H.; Cordova, K. E.; O'Keeffe, M.; Yaghi, O. M. The Chemistry and Applications of Metal-Organic Frameworks. *Science* **2013**, *341*, 1230444.

[17] Zhou, H.-C. J.; Kitagawa, S. Metal–Organic Frameworks (MOFs). *Chemical Society Reviews* **2014**, *43*, 5415–5418.

[18] Cui, Y.; Li, B.; He, H.; Zhou, W.; Chen, B.; Qian, G. Metal–Organic Frameworks as Platforms for Functional Materials. *Accounts of Chemical Research* **2016**, *49*, 483–493.

[19] Pettinari, C.; Marchetti, F.; Mosca, N.; Tosi, G.; Drozdov, A. Application of Metal Organic Frameworks. *Polymer International* **2017**, *66*, 731–744.

[20] Ali Akbar Razavi, S.; Morsali, A. Linker Functionalized Metal-Organic Frameworks. *Coordination Chemistry Reviews* **2019**, *399*, 213023.

[21] Lu, W.; Wei, Z.; Gu, Z.-Y.; Liu, T.-F.; Park, J.; Park, J.; Tian, J.; Zhang, M.; Zhang, Q.; Iii, T. G.; Bosch, M.; Zhou, H.-C. Tuning the Structure and Function of Metal–Organic Frameworks via Linker Design. *Chemical Society Reviews* **2014**, *43*, 5561–5593.

[22] Kim, M.; Lee, Y.; Moon, H. R. Carboxylate-Based Metal–Organic Framework and Coordination Polymer Glasses: Progress and Perspectives. *Accounts of Chemical Research* **2024**, *57*, 2347–2357.

[23] Choi, J.-S.; Son, W.-J.; Kim, J.; Ahn, W.-S. Metal–Organic Framework MOF-5 Prepared by Microwave Heating: Factors to Be Considered. *Microporous and Mesoporous Materials* **2008**, *116*, 727–731.

[24] Chong, K. C.; Lai, S. O.; Mah, S. K.; Thiam, H. S.; Chong, W. C.; Shuit, S. H.; Lee, S. S.; Chong, W. E. A Review of HKUST-1 Metal-Organic Frameworks in Gas Adsorption. *IOP Conference Series: Earth and Environmental Science* **2023**, *1135*, 012030.

[25] H. Hendon, C.; Walsh, A. Chemical Principles Underpinning the Performance of the Metal–Organic Framework HKUST-1. *Chemical Science* **2015**, *6*, 3674–3683.

[26] Zou, M.; Dong, M.; Zhao, T. Advances in Metal-Organic Frameworks MIL-101(Cr). *International Journal of Molecular Sciences* **2022**, *23*, 9396.

[27] Millange, F.; Walton, R. I. MIL-53 and Its Isoreticular Analogues: A Review of the Chemistry and Structure of a Prototypical Flexible Metal-Organic Framework. *Israel Journal of Chemistry* **2018**, *58*, 1019–1035.

[28] Mandal, S.; Natarajan, S.; Mani, P.; Pankajakshan, A. Post-Synthetic Modification of Metal–Organic Frameworks Toward Applications. *Advanced Functional Materials* **2021**, *31*, 2006291.

[29] Cohen, S. M. Postsynthetic Methods for the Functionalization of Metal-Organic Frameworks. *Chemical Reviews* **2012**, *112*, 970–1000.

[30] Guo, Q.; Wang, Z.; Feng, X.; Fan, Y.; Lin, W. Generation and Stabilization of a Dinickel Catalyst in a Metal-Organic Framework for Selective Hydrogenation Reactions. *Angewandte Chemie International Edition* **2023-08-28**, *62*, e202306905.

[31] Wang, Z.; Yeary, P.; Feng, X.; Lin, W. Self-Adaptive Metal–Organic Framework Assembles Di-iron Active Sites to Mimic Monooxygenases. *Journal of the American Chemical Society* **2023**, *145*, 8647–8655.

[32] Kim, J.; Chen, B.; Reineke, T. M.; Li, H.; Eddaoudi, M.; Moler, D. B.; O'Keeffe, M.; Yaghi, O. M. Assembly of MetalOrganic Frameworks from Large Organic and Inorganic Secondary Building Units: New Examples and Simplifying Principles for Complex Structures. *Journal of the American Chemical Society* **2001**, *123*, 8239–8247.

[33] Tranchemontagne, D. J.; Mendoza-Cortés, J. L.; O'Keeffe, M.; Yaghi, O. M. Secondary Building Units, Nets and Bonding in the Chemistry of Metal–Organic Frameworks. *Chemical Society Reviews* **2009**, *38*, 1257.

[34] Prestipino, C.; Regli, L.; Vitillo, J. G.; Bonino, F.; Damin, A.; Lamberti, C.; Zecchina, A.; Solari, P. L.; Kongshaug, K. O.; Bordiga, S. Local Structure of Framework Cu(II) in HKUST-1 Metallorganic Framework: Spectroscopic Characterization

upon Activation and Interaction with Adsorbates. *Chemistry of Materials* **2006**, *18*, 1337–1346.

[35] Liu, Y.; Liu, B.; Zhou, Q.; Zhang, T.; Wu, W. Morphology Effect of Metal-Organic Framework HKUST-1 as a Catalyst on Benzene Oxidation. *Chemical Research in Chinese Universities* **2017**, *33*, 971–978.

[36] Biswas, S.; Van Der Voort, P. A General Strategy for the Synthesis of Functionalised UiO-66 Frameworks: Characterisation, Stability and CO2 Adsorption Properties. *European Journal of Inorganic Chemistry* **2013**, *2013*, 2154–2160.

[37] Stawowy, M.; Ciesielski, R.; Maniecki, T.; Matus, K.; Łużny, R.; Trawczynski, J.; Silvestre-Albero, J.; Łamacz, A. CO2 Hydrogenation to Methanol over Ce and Zr Containing UiO-66 and Cu/UiO-66. *Catalysts* **2019**, *10*, 39.

[38] Shearer, G. C.; Chavan, S.; Bordiga, S.; Svelle, S.; Olsbye, U.; Lillerud, K. P. Defect Engineering: Tuning the Porosity and Composition of the Metal–Organic Framework UiO-66 via Modulated Synthesis. *Chemistry of Materials* **2016**, *28*, 3749–3761.

[39] Simons, M. C.; Vitillo, J. G.; Babucci, M.; Hoffman, A. S.; Boubnov, A.; Beauvais, M. L.; Chen, Z.; Cramer, C. J.; Chapman, K. W.; Bare, S. R.; Gates, B. C.; Lu, C. C.; Gagliardi, L.; Bhan, A. Structure, Dynamics, and Reactivity for Light Alkane Oxidation of Fe(II) Sites Situated in the Nodes of a Metal–Organic Framework. *Journal of the American Chemical Society* **2019**, *141*, 18142–18151.

[40] Vitillo, J. G.; Lu, C. C.; Cramer, C. J.; Bhan, A.; Gagliardi, L. Influence of First and Second Coordination Environment on Structural Fe(II) Sites in MIL-101 for C–H Bond Activation in Methane. *ACS Catalysis* **2021**, *11*, 579–589.

[41] Embrechts, H.; Kriesten, M.; Ermer, M.; Peukert, W.; Hartmann, M.; Distaso, M. In Situ Raman and FTIR Spectroscopic Study on the Formation of the Isomers MIL-68(Al) and MIL-53(Al). *RSC Advances* **2020**, *10*, 7336–7348.

[42] Antil, N.; Chauhan, M.; Akhtar, N.; Newar, R.; Begum, W.; Malik, J.; Manna, K. Metal–Organic Framework-Encaged Monomeric Cobalt(III) Hydroperoxides Enable Chemoselective Methane Oxidation to Methanol. *ACS Catalysis* **2022**, *12*, 11159–11168.

[43] Chauhan, M.; Rana, B.; Gupta, P.; Kalita, R.; Choudhary, A.; Manna, K. Architecting Molecularly Dispersed Cu(I)-Active Sites at UiO-MOF Nodes for Thermocatalytic Oxidation of Methane to Ethanol Using O2. *Applied Catalysis B: Environment and Energy* **2025**, *377*, 125474.

[44] Zhao, W.; Shi, Y.; Jiang, Y.; Zhang, X.; Long, C.; An, P.; Zhu, Y.; Shao, S.; Yan, Z.; Li, G.; Tang, Z. Fe-O Clusters Anchored on Nodes of Metal–Organic Frameworks for Direct Methane Oxidation. *Angewandte Chemie* **2021**, *133*, 5875–5879.

[45] Osadchii, D. Y.; Olivos-Suarez, A. I.; Szécsényi, ; Li, G.; Nasalevich, M. A.; Dugulan, I. A.; Crespo, P. S.; Hensen, E. J. M.; Veber, S. L.; Fedin, M. V.; Sankar, G.; Pidko, E. A.; Gascon, J. Isolated Fe Sites in Metal Organic Frameworks Catalyze the Direct Conversion of Methane to Methanol. *ACS Catalysis* **2018**, *8*, 5542–5548.

[46] Eddaoudi, M.; Li, H.; Yaghi, O. M. Highly Porous and Stable MetalOrganic Frameworks: Structure Design and Sorption Properties. *Journal of the American Chemical Society* **2000**, *122*, 1391–1397.

[47] Gándara, F.; Andrés, A. D.; Gómez-Lor, B.; Gutiérrez-Puebla, E.; Iglesias, M.; Monge, M. A.; Proserpio, D. M.; Snejko, N. A Rare-Earth MOF Series: Fascinating Structure, Efficient Light Emitters, and Promising Catalysts. *Crystal Growth & Design* **2008**, *8*, 378–380.

[48] Liu, Y.; Kravtsov, V. C.; Larsen, R.; Eddaoudi, M. Molecular Building Blocks Approach to the Assembly of Zeolite-like Metal–Organic Frameworks (ZMOFs) with Extra-Large Cavities. *Chemical Communications* **2006**, 1488–1490.

[49] Wang, X.-S.; Ma, S.; Sun, D.; Parkin, S.; Zhou, H.-C. A Mesoporous MetalOrganic Framework with Permanent Porosity. *Journal of the American Chemical Society* **2006**, *128*, 16474–16475.

[50] Férey, G.; Mellot-Draznieks, C.; Serre, C.; Millange, F.; Dutour, J.; Surblé, S.; Margiolaki, I. A Chromium Terephthalate-Based Solid with Unusually Large Pore Volumes and Surface Area. *Science* **2005**, *309*, 2040–2042.

[51] Chui, S. S.-Y.; Lo, S. M.-F.; Charmant, J. P. H.; Orpen, A. G.; Williams, I. D. A

Chemically Functionalizable Nanoporous Material [Cu_3 (TMA)$_2$ (H_2 O)$_3$]$_n$. *Science* **1999**, *283*, 1148–1150.

[52] Kongshaug, K. O.; Fjellvåg, H. Synthesis and Characterization of CPO-1; Three-Dimensional Coordination Polymers with 2,6-Naphthalenedicarboxylate (Ndc) Ligands [M(Ndc)(H2O)], M=Mn(II), Zn(II) or Cd(II). *Solid State Sciences* **2002**, *4*, 443–447.

[53] Yuan, S. et al. Stable Metal–Organic Frameworks: Design, Synthesis, and Applications. *Advanced Materials* **2018**, *30*, 1704303.

[54] Kleist, W.; Jutz, F.; Maciejewski, M.; Baiker, A. Mixed-Linker Metal-Organic Frameworks as Catalysts for the Synthesis of Propylene Carbonate from Propylene Oxide and CO2. *European Journal of Inorganic Chemistry* **2009**, *2009*, 3552–3561.

[55] Dhakshinamoorthy, A.; M. Asiri, A.; Garcia, H. Mixed-Metal or Mixed-Linker Metal Organic Frameworks as Heterogeneous Catalysts. **2016**,

[56] Dincă, M.; Long, J. R. Hydrogen Storage in Microporous Metal–Organic Frameworks with Exposed Metal Sites. *Angewandte Chemie International Edition* **2008**, *47*, 6766–6779.

[57] Dincă, M.; Dailly, A.; Long, J. R. Structure and Charge Control in Metal–Organic Frameworks Based on the Tetrahedral Ligand Tetrakis(4-Tetrazolylphenyl)Methane. *Chemistry – A European Journal* **2008**, *14*, 10280–10285.

[58] Pachfule, P.; Das, R.; Poddar, P.; Banerjee, R. Solvothermal Synthesis, Structure, and Properties of Metal Organic Framework Isomers Derived from a Partially Fluorinated Link. *Crystal Growth & Design* **2011**, *11*, 1215–1222.

[59] Rehman, A.; Farrukh, S.; Hussain, A.; Pervaiz, E. Synthesis and Effect of Metal–Organic Frame Works on CO2 Adsorption Capacity at Various Pressures: A Contemplating Review. *Energy & Environment* **2020**, *31*, 367–388.

[60] Taylor-Pashow, K. M. L.; Della Rocca, J.; Xie, Z.; Tran, S.; Lin, W. Postsynthetic Modifications of Iron-Carboxylate Nanoscale MetalOrganic Frameworks for Imaging and Drug Delivery. *Journal of the American Chemical Society* **2009**, *131*, 14261–14263.

[61] Jhung, S. H.; Lee, J.-H.; Yoon, J. W.; Serre, C.; Férey, G.; Chang, J.-S. Microwave Synthesis of Chromium Terephthalate MIL-101 and Its Benzene Sorption Ability. *Advanced Materials* **2007**, *19*, 121–124.

[62] Haque, E.; Khan, N. A.; Park, J. H.; Jhung, S. H. Synthesis of a Metal–Organic Framework Material, Iron Terephthalate, by Ultrasound, Microwave, and Conventional Electric Heating: A Kinetic Study. *Chemistry – A European Journal* **2010**, *16*, 1046–1052.

[63] Ahnfeldt, T.; Moellmer, J.; Guillerm, V.; Staudt, R.; Serre, C.; Stock, N. High-Throughput and Time-Resolved Energy-Dispersive X-Ray Diffraction (EDXRD) Study of the Formation of CAU-1-(OH)2: Microwave and Conventional Heating. *Chemistry – A European Journal* **2011**, *17*, 6462–6468.

[64] Centrone, A.; Yang, Y.; Speakman, S.; Bromberg, L.; Rutledge, G. C.; Hatton, T. A. Growth of MetalOrganic Frameworks on Polymer Surfaces. *Journal of the American Chemical Society* **2010**, *132*, 15687–15691.

[65] Khan, N. A.; Haque, E.; Jhung, S. H. Rapid Syntheses of a Metal–Organic Framework Material Cu3(BTC)2(H2O)3 under Microwave: A Quantitative Analysis of Accelerated Syntheses. *Physical Chemistry Chemical Physics* **2010**, *12*, 2625–2631.

[66] Bux, H.; Liang, F.; Li, Y.; Cravillon, J.; Wiebcke, M.; Caro, J. Zeolitic Imidazolate Framework Membrane with Molecular Sieving Properties by Microwave-Assisted Solvothermal Synthesis. *Journal of the American Chemical Society* **2009**, *131*, 16000–16001.

[67] Pichon, A.; Lazuen-Garay, A.; L. James, S. Solvent -Free Synthesis of a Microporous Metal–Organic Framework. *CrystEngComm* **2006**, *8*, 211–214.

[68] Friščić, T.; Fábián, L. Mechanochemical Conversion of a Metal Oxide into Coordination Polymers and Porous Frameworks Using Liquid-Assisted Grinding (LAG). *CrystEngComm* **2009**, *11*, 743–745.

[69] Yuan, W.; Friščić, T.; Apperley, D.; James, S. L. High Reactivity of Metal–Organic Frameworks under Grinding Conditions: Parallels with Organic Molecular Materials. *Angewandte Chemie International Edition* **2010**, *49*, 3916–3919.

[70] Friščić, T.; Reid, D. G.; Halasz, I.; Stein, R. S.; Dinnebier, R. E.; Duer, M. J. Ion- and Liquid-Assisted Grinding: Improved Mechanochemical Synthesis of Metal–Organic Frameworks Reveals Salt Inclusion and Anion Templating. *Angewandte Chemie International Edition* **2010**, *49*, 712–715.

[71] Beldon, P. J.; Fábián, L.; Stein, R. S.; Thirumurugan, A.; Cheetham, A. K.; Friščić, T. Rapid Room-Temperature Synthesis of Zeolitic Imidazolate Frameworks by Using Mechanochemistry. *Angewandte Chemie International Edition* **2010**, *49*, 9640–9643.

[72] *Metal-Organic Frameworks for Biomedical Applications*; Woodhead Publishing, 2020; pp 177–195.

[73] Gao, Q.; Xie, Y.-B.; Li, J.-R.; Yuan, D.-Q.; Yakovenko, A. A.; Sun, J.-H.; Zhou, H.-C. Tuning the Formations of Metal–Organic Frameworks by Modification of Ratio of Reactant, Acidity of Reaction System, and Use of a Secondary Ligand. *Crystal Growth & Design* **2012**, *12*, 281–288.

[74] Forgan, R. S. Modulated Self-Assembly of Metal–Organic Frameworks. *Chemical Science* **2020**, *11*, 4546–4562.

[75] Kirlikovali, K. O.; Hanna, S. L.; Son, F. A.; Farha, O. K. Back to the Basics: Developing Advanced Metal–Organic Frameworks Using Fundamental Chemistry Concepts. *ACS Nanoscience Au* **2023**, *3*, 37–45.

[76] Islamoglu, T.; Ray, D.; Li, P.; Majewski, M. B.; Akpinar, I.; Zhang, X.; Cramer, C. J.; Gagliardi, L.; Farha, O. K. From Transition Metals to Lanthanides to Actinides: Metal-Mediated Tuning of Electronic Properties of Isostructural Metal–Organic Frameworks. *Inorganic Chemistry* **2018**, *57*, 13246–13251.

[77] Farha, O. K.; Özgür Yazaydın, A.; Eryazici, I.; Malliakas, C. D.; Hauser, B. G.; Kanatzidis, M. G.; Nguyen, S. T.; Snurr, R. Q.; Hupp, J. T. De Novo Synthesis of a Metal–Organic Framework Material Featuring Ultrahigh Surface Area and Gas Storage Capacities. *Nature Chemistry* **2010**, *2*, 944–948.

[78] Ma, L.; Lin, W. Chirality-Controlled and Solvent-Templated Catenation Isomerism in MetalOrganic Frameworks. *Journal of the American Chemical Society* **2008**, *130*, 13834–13835.

[79] Hughes, J. T.; Navrotsky, A. MOF-5: Enthalpy of Formation and Energy Landscape of Porous Materials. *Journal of the American Chemical Society* **2011**, *133*, 9184–9187.

[80] Voskanyan, A. A.; Goncharov, V. G.; Novendra, N.; Guo, X.; Navrotsky, A. Thermodynamics Drives the Stability of the MOF-74 Family in Water. *ACS Omega* **2020**, *5*, 13158–13163.

[81] Bhunia, M. K.; Hughes, J. T.; Fettinger, J. C.; Navrotsky, A. Thermochemistry of Paddle Wheel MOFs: Cu-HKUST-1 and Zn-HKUST-1. *Langmuir* **2013**, *29*, 8140–8145.

[82] Novendra, N.; Marrett, J. M.; Katsenis, A. D.; Titi, H. M.; Arhangelskis, M.; Friščić, T.; Navrotsky, A. Linker Substituents Control the Thermodynamic Stability in Metal–Organic Frameworks. *Journal of the American Chemical Society* **2020**, *142*, 21720–21729.

[83] Van Vleet, M. J.; Weng, T.; Li, X.; Schmidt, J. In Situ, Time-Resolved, and Mechanistic Studies of Metal–Organic Framework Nucleation and Growth. *Chemical Reviews* **2018**, *118*, 3681–3721.

[84] Cheetham, A. K.; Kieslich, G.; Yeung, H. H.-M. Thermodynamic and Kinetic Effects in the Crystallization of Metal–Organic Frameworks. *Accounts of Chemical Research* **2018**, *51*, 659–667.

[85] Bruckner, E. P.; Stupp, S. I. Designing Supramolecular Polymers with Nucleation and Growth Processes. *Polymer International* **2022**, *71*, 590–595.

[86] Han, J.; He, X.; Liu, J.; Ming, R.; Lin, M.; Li, H.; Zhou, X.; Deng, H. Determining Factors in the Growth of MOF Single Crystals Unveiled by in Situ Interface Imaging. *Chem* **2022**, *8*, 1637–1657.

[87] Grünker, R.; Bon, V.; Müller, P.; Stoeck, U.; Krause, S.; Mueller, U.; Senkovska, I.; Kaskel, S. A New Metal–Organic Framework with Ultra-High Surface Area. *Chemical Communications* **2014**, *50*, 3450–3452.

[88] Kim, Y.; Yang, T.; Yun, G.; Ghasemian, M. B.; Koo, J.; Lee, E.; Cho, S. J.; Kim, K. Hydrolytic Transformation of Microporous Metal–Organic Frameworks to Hierarchical

Micro- and Mesoporous MOFs. *Angewandte Chemie International Edition* **2015**, *54*, 13273–13278.

[89] Liu, D.; Zou, D.; Zhu, H.; Zhang, J. Mesoporous Metal–Organic Frameworks: Synthetic Strategies and Emerging Applications. *Small* **2018**, *14*, 1801454.

[90] Kandiah, M.; Nilsen, M. H.; Usseglio, S.; Jakobsen, S.; Olsbye, U.; Tilset, M.; Larabi, C.; Quadrelli, E. A.; Bonino, F.; Lillerud, K. P. Synthesis and Stability of Tagged UiO-66 Zr-MOFs. *Chemistry of Materials* **2010**, *22*, 6632–6640.

[91] family=Silva Montani, p. u., given=Samara; family=Lima, p. u., given=Juliana Fonseca; Zanon Zotin, F. M.; Palacio, L. A. Thermal Stability of Copper-Based MOF under Different Atmospheres. *Journal of Thermal Analysis and Calorimetry* **2023**, *148*, 119–131.

[92] Ye, X.; Bai, C.; Zhang, P.; Han, F.; Xia, J.; Gao, X.; Xu, W.; Guo, L.; Li, J. Engineering the Activity and Stability of the Zn-MOF Catalyst via the Interaction of Doped Zr with Zn. *Inorganic Chemistry* **2024**, *63*, 10346–10357.

[93] Krause, S.; Evans, J. D.; Bon, V.; Senkovska, I.; Ehrling, S.; Stoeck, U.; Yot, P. G.; Iacomi, P.; Llewellyn, P.; Maurin, G.; Coudert, F.-X.; Kaskel, S. Adsorption Contraction Mechanics: Understanding Breathing Energetics in Isoreticular Metal–Organic Frameworks. *The Journal of Physical Chemistry C* **2018**, *122*, 19171–19179.

[94] Wang, X.; Krishna, R.; Li, L.; Wang, B.; He, T.; Zhang, Y.-Z.; Li, J.-R.; Li, J. Guest-Dependent Pressure Induced Gate-Opening Effect Enables Effective Separation of Propene and Propane in a Flexible MOF. *Chemical Engineering Journal* **2018**, *346*, 489–496.

[95] Nagarkar, S. S.; Desai, A. V.; Ghosh, S. K. Stimulus-Responsive Metal–Organic Frameworks. *Chemistry – An Asian Journal* **2014**, *9*, 2358–2376.

[96] Cai, W.; Wang, J.; Chu, C.; Chen, W.; Wu, C.; Liu, G. Metal–Organic Framework-Based Stimuli-Responsive Systems for Drug Delivery. *Advanced Science* **2019**, *6*, 1801526.

[97] Zhao, D.; Timmons, D. J.; Yuan, D.; Zhou, H.-C. Tuning the Topology and Functionality of MetalOrganic Frameworks by Ligand Design. *Accounts of Chemical Research* **2011**, *44*, 123–133.

[98] Li, X.; Liu, J.; Zhou, K.; Ullah, S.; Wang, H.; Zou, J.; Thonhauser, T.; Li, J. Tuning Metal–Organic Framework (MOF) Topology by Regulating Ligand and Secondary Building Unit (SBU) Geometry: Structures Built on 8-Connected M6 (M = Zr, Y) Clusters and a Flexible Tetracarboxylate for Propane-Selective Propane/Propylene Separation. *Journal of the American Chemical Society* **2022**, *144*, 21702–21709.

[99] Aulakh, D.; Islamoglu, T.; Bagundes, V. F.; Varghese, J. R.; Duell, K.; Joy, M.; Teat, S. J.; Farha, O. K.; Wriedt, M. Rational Design of Pore Size and Functionality in a Series of Isoreticular Zwitterionic Metal–Organic Frameworks. *Chemistry of Materials* **2018**, *30*, 8332–8342.

[100] Lee, G.; Ahmed, I.; Hossain, M. A.; Lee, H. J.; Jhung, S. H. Preparation and Functionalization of Metal-Organic Frameworks, MOF-808s, and Their Application in Adsorption. *Coordination Chemistry Reviews* **2025**, *524*, 216325.

[101] Liu, M.; Wu, J.; Hou, H. Metal–Organic Framework (MOF)-Based Materials as Heterogeneous Catalysts for CH Bond Activation. *Chemistry – A European Journal* **2019**, *25*, 2935–2948.

[102] Gupta, P.; Chauhan, M.; Rana, B.; Kalita, R.; Maurya, R.; Manna, K. Engineering Mono- vs Dinuclear Iron(II)-Active Sites to Steer Liquid Oxygenate Selectivity in Methane Oxidation Pathways Using O2. *Journal of the American Chemical Society* **2025**, *147*, 25372–25384.

[103] Montoro, C.; García, E.; Calero, S.; A. Pérez-Fernández, M.; L. López, A.; Barea, E.; R. Navarro, J. A. Functionalisation of MOF Open Metal Sites with Pendant Amines for CO 2 Capture. *Journal of Materials Chemistry* **2012**, *22*, 10155–10158.

[104] Kökçam-Demir, ; Goldman, A.; Esrafili, L.; Gharib, M.; Morsali, A.; Weingart, O.; Janiak, C. Coordinatively Unsaturated Metal Sites (Open Metal Sites) in Metal–Organic Frameworks: Design and Applications. *Chemical Society Reviews* **2020**, *49*, 2751–2798.

[105] Kirchon, A.; Feng, L.; F. Drake, H.; A. Joseph, E.; Zhou, H.-C. From Fundamentals to Applications: A Toolbox for Robust and Multifunctional MOF Materials. *Chemical Society Reviews* **2018**, *47*, 8611–8638.

[106] Mancuso, J. L.; Mroz, A. M.; Le, K. N.; Hendon, C. H. Electronic Structure Modeling of Metal–Organic Frameworks. *Chemical Reviews* **2020**, *120*, 8641–8715.

[107] Kaposi, M.; Cokoja, M.; H. Hutterer, C.; A. Hauser, S.; Kaposi, T.; Klappenberger, F.; Pöthig, A.; V. Barth, J.; A. Herrmann, W.; E. Kühn, F. Immobilisation of a Molecular Epoxidation Catalyst on UiO-66 and -67: The Effect of Pore Size on Catalyst Activity and Recycling. *Dalton Transactions* **2015**, *44*, 15976–15983.

[108] Chavan, S.; G. Vitillo, J.; Gianolio, D.; Zavorotynska, O.; Civalleri, B.; Jakobsen, S.; H. Nilsen, M.; Valenzano, L.; Lamberti, C.; Petter Lillerud, K.; Bordiga, S. H 2 Storage in Isostructural UiO-67 and UiO-66 MOFs. *Physical Chemistry Chemical Physics* **2012**, *14*, 1614–1626.

[109] Martin, R. L.; Lin, L.-C.; Jariwala, K.; Smit, B.; Haranczyk, M. Mail-Order Metal–Organic Frameworks (MOFs): Designing Isoreticular MOF-5 Analogues Comprising Commercially Available Organic Molecules. *The Journal of Physical Chemistry C* **2013**, *117*, 12159–12167.

[110] Tranchemontagne, D. J.; Hunt, J. R.; Yaghi, O. M. Room Temperature Synthesis of Metal-Organic Frameworks: MOF-5, MOF-74, MOF-177, MOF-199, and IRMOF-0. *Tetrahedron* **2008**, *64*, 8553–8557.

[111] Guillerm, V.; Ragon, F.; Dan-Hardi, M.; Devic, T.; Vishnuvarthan, M.; Campo, B.; Vimont, A.; Clet, G.; Yang, Q.; Maurin, G.; Férey, G.; Vittadini, A.; Gross, S.; Serre, C. A Series of Isoreticular, Highly Stable, Porous Zirconium Oxide Based Metal–Organic Frameworks. *Angewandte Chemie International Edition* **2012**, *51*, 9267–9271.

[112] Lu, F.-F.; Gu, X.-W.; Wu, E.; Li, B.; Qian, G. Systematic Evaluation of Water Adsorption in Isoreticular UiO-type Metal–Organic Frameworks. *Journal of Materials Chemistry A* **2023**, *11*, 1246–1255.

[113] Islamoglu, T.; Otake, K.-i.; Li, P.; T. Buru, C.; W. Peters, A.; Akpinar, I.;

J. Garibay, S.; K. Farha, O. Revisiting the Structural Homogeneity of NU-1000, a Zr-based Metal–Organic Framework. *CrystEngComm* **2018**, *20*, 5913–5918.

[114] Chen, Z.; Kirlikovali, K. O.; Li, P.; Farha, O. K. Reticular Chemistry for Highly Porous Metal–Organic Frameworks: The Chemistry and Applications. *Accounts of Chemical Research* **2022**, *55*, 579–591.

[115] Manna, K.; Zhang, T.; Greene, F. X.; Lin, W. Bipyridine- and Phenanthroline-Based Metal–Organic Frameworks for Highly Efficient and Tandem Catalytic Organic Transformations via Directed C–H Activation. *Journal of the American Chemical Society* **2015**, *137*, 2665–2673.

[116] Gupta, P.; Akhtar, N.; Begum, W.; Rana, B.; Kalita, R.; Chauhan, M.; Thadhani, C.; Manna, K. Metal–Organic Framework-Supported Mono Bipyridyl–Iron Hydroxyl Catalyst for Selective Benzene Hydroxylation into Phenol. *Inorganic Chemistry* **2024**, *63*, 11907–11916.

[117] Akhtar, N.; Chauhan, M.; Gupta, P.; Antil, N.; Manna, K. A Supported Pyridylimine–Cobalt Catalyst for N-formylation of Amines Using CO2. *Dalton Transactions* **2023**, *52*, 15384–15393.

[118] Ingleson, M. J.; Barrio, J. P.; Guilbaud, J.-B.; Khimyak, Y. Z.; Rosseinsky, M. J. Framework Functionalisation Triggers Metal Complex Binding. *Chemical Communications* **2008**, 2680–2682.

[119] Hwang, Y. K.; Hong, D.-Y.; Chang, J.-S.; Jhung, S. H.; Seo, Y.-K.; Kim, J.; Vimont, A.; Daturi, M.; Serre, C.; Férey, G. Amine Grafting on Coordinatively Unsaturated Metal Centers of MOFs: Consequences for Catalysis and Metal Encapsulation. *Angewandte Chemie* **2008**, *120*, 4212–4216.

[120] Banerjee, M.; Das, S.; Yoon, M.; Choi, H. J.; Hyun, M. H.; Park, S. M.; Seo, G.; Kim, K. Postsynthetic Modification Switches an Achiral Framework to Catalytically Active Homochiral MetalOrganic Porous Materials. *Journal of the American Chemical Society* **2009**, *131*, 7524–7525.

[121] Demessence, A.; D'Alessandro, D. M.; Foo, M. L.; Long, J. R. Strong CO2 Binding

in a Water-Stable, Triazolate-Bridged MetalOrganic Framework Functionalized with Ethylenediamine. *Journal of the American Chemical Society* **2009**, *131*, 8784–8786.

[122] Alonso-Salinas, R.; López-Miranda, S.; Pérez-López, A. J.; Acosta-Motos, J. R. Strategies to Delay Ethylene-Mediated Ripening in Climacteric Fruits: Implications for Shelf Life Extension and Postharvest Quality. *Horticulturae* **2024**, *10*, 840.

[123] Tibbetts, I.; Kostakis, G. E. Recent Bio-Advances in Metal-Organic Frameworks. *Molecules* **2020**, *25*, 1291.

[124] Zhao, G.; Qin, N.; Pan, A.; Wu, X.; Peng, C.; Ke, F.; Iqbal, M.; Ramachandraiah, K.; Zhu, J. Magnetic Nanoparticles@Metal-Organic Framework Composites as Sustainable Environment Adsorbents. *Journal of Nanomaterials* **2019**, *2019*, 1454358.

[125] Zhang, H.-j.; Qi, S.-d.; Niu, X.-y.; Hu, J.; Ren, C.-l.; Chen, H.-l.; Chen, X.-g. Metallic Nanoparticles Immobilized in Magnetic Metal–Organic Frameworks: Preparation and Application as Highly Active, Magnetically Isolable and Reusable Catalysts. *Catalysis Science & Technology* **2014**, *4*, 3013–3024.

[126] Valadi, F. M.; Ekramipooya, A.; Gholami, M. R. Selective Separation of Congo Red from a Mixture of Anionic and Cationic Dyes Using Magnetic-MOF: Experimental and DFT Study. *Journal of Molecular Liquids* **2020**, *318*, 114051.

[127] Chen, D.; Shen, W.; Wu, S.; Chen, C.; Luo, X.; Guo, L. Ion Exchange Induced Removal of Pb(Ii) by MOF-derived Magnetic Inorganic Sorbents. *Nanoscale* **2016**, *8*, 7172–7179.

[128] Wang, L.; Zhao, X.; Zhang, J.; Xiong, Z. Selective Adsorption of Pb (II) over the Zinc-Based MOFs in Aqueous Solution-Kinetics, Isotherms, and the Ion Exchange Mechanism. *Environmental Science and Pollution Research* **2017**, *24*, 14198–14206.

[129] Rapti, S.; Pournara, A.; Sarma, D.; T. Papadas, I.; S. Armatas, G.; S. Hassan, Y.; H. Alkordi, M.; G. Kanatzidis, M.; J. Manos, M. Rapid, Green and Inexpensive Synthesis of High Quality UiO-66 Amino-Functionalized Materials with Exceptional Capability for Removal of Hexavalent Chromium from Industrial Waste. *Inorganic Chemistry Frontiers* **2016**, *3*, 635–644.

[130] Selective Capture of Hexavalent Chromium from an Anion-Exchange Column of Metal Organic Resin–Alginic Acid Composite. *Chemical Science* **2016**, *7*, 2427–2436.

[131] Horcajada, P.; Serre, C.; Vallet-Regí, M.; Sebban, M.; Taulelle, F.; Férey, G. Metal–Organic Frameworks as Efficient Materials for Drug Delivery. *Angewandte Chemie International Edition* **2006**, *45*, 5974–5978.

[132] Wang, L.; Zheng, M.; Xie, Z. Nanoscale Metal–Organic Frameworks for Drug Delivery: A Conventional Platform with New Promise. *Journal of Materials Chemistry B* **2018**, *6*, 707–717.

[133] Zheng, H.; Zhang, Y.; Liu, L.; Wan, W.; Guo, P.; Nyström, A. M.; Zou, X. One-Pot Synthesis of Metal–Organic Frameworks with Encapsulated Target Molecules and Their Applications for Controlled Drug Delivery. *Journal of the American Chemical Society* **2016**, *138*, 962–968.

[134] Vasconcelos, I. B.; family=Silva, p. u., given=Teresinha G.; Militão, G. C. G.; Soares, T. A.; Rodrigues, N. M.; Rodrigues, M. O.; family=Costa, p. u., given=Nivan B.; Freire, R. O.; Junior, S. A. Cytotoxicity and Slow Release of the Anti-Cancer Drug Doxorubicin from ZIF-8. *RSC Advances* **2012**, *2*, 9437–9442.

[135] Wang, L.; Wang, W.; Xie, Z. Tetraphenylethylene-Based Fluorescent Coordination Polymers for Drug Delivery. *Journal of Materials Chemistry B* **2016**, *4*, 4263–4266.

[136] Li, Y.; Zheng, Y.; Lai, X.; Chu, Y.; Chen, Y. Biocompatible Surface Modification of Nano-Scale Zeolitic Imidazolate Frameworks for Enhanced Drug Delivery. *RSC Advances* **2018**, *8*, 23623–23628.

[137] Cheng, G.; Li, W.; Ha, L.; Han, X.; Hao, S.; Wan, Y.; Wang, Z.; Dong, F.; Zou, X.; Mao, Y.; Zheng, S.-Y. Self-Assembly of Extracellular Vesicle-like Metal–Organic Framework Nanoparticles for Protection and Intracellular Delivery of Biofunctional Proteins. *Journal of the American Chemical Society* **2018**, *140*, 7282–7291.

[138] Zhou, Y.; Liu, L.; Cao, Y.; Yu, S.; He, C.; Chen, X. A Nanocomposite Vehicle Based on Metal–Organic Framework Nanoparticle Incorporated Biodegradable Microspheres

for Enhanced Oral Insulin Delivery. *ACS Applied Materials & Interfaces* **2020**, *12*, 22581–22592.

[139] Alsaiari, S. K.; Patil, S.; Alyami, M.; Alamoudi, K. O.; Aleisa, F. A.; Merzaban, J. S.; Li, M.; Khashab, N. M. Endosomal Escape and Delivery of CRISPR/Cas9 Genome Editing Machinery Enabled by Nanoscale Zeolitic Imidazolate Framework. *Journal of the American Chemical Society* **2018**, *140*, 143–146.

[140] Zhang, P.; Li, Y.; Tang, Y.; Shen, H.; Li, J.; Yi, Z.; Ke, Q.; Xu, H. Copper-Based Metal–Organic Framework as a Controllable Nitric Oxide-Releasing Vehicle for Enhanced Diabetic Wound Healing. *ACS Applied Materials & Interfaces* **2020**, *12*, 18319–18331.

[141] Luzuriaga, M. A.; Welch, R. P.; Dharmarwardana, M.; Benjamin, C. E.; Li, S.; Shahrivarkevishahi, A.; Popal, S.; Tuong, L. H.; Creswell, C. T.; Gassensmith, J. J. Enhanced Stability and Controlled Delivery of MOF-Encapsulated Vaccines and Their Immunogenic Response In Vivo. *ACS Applied Materials & Interfaces* **2019**, *11*, 9740–9746.

[142] Dincă, M.; Long, J. R. Strong H2 Binding and Selective Gas Adsorption within the Microporous Coordination Solid Mg3(O2C-C10H6-CO2)3. *Journal of the American Chemical Society* **2005**, *127*, 9376–9377.

[143] Lan, A.; Li, K.; Wu, H.; Olson, D. H.; Emge, T. J.; Ki, W.; Hong, M.; Li, J. A Luminescent Microporous Metal–Organic Framework for the Fast and Reversible Detection of High Explosives. *Angewandte Chemie International Edition* **2009**, *48*, 2334–2338.

[144] Pramanik, S.; Zheng, C.; Zhang, X.; Emge, T. J.; Li, J. New Microporous MetalOrganic Framework Demonstrating Unique Selectivity for Detection of High Explosives and Aromatic Compounds. *Journal of the American Chemical Society* **2011**, *133*, 4153–4155.

[145] Min Wang, Q.; Shen, D.; Bülow, M.; Ling Lau, M.; Deng, S.; Fitch, F. R.; Lemcoff, N. O.; Semanscin, J. Metallo-Organic Molecular Sieve for Gas Separation and Purification. *Microporous and Mesoporous Materials* **2002**, *55*, 217–230.

[146] Yuan, H.; Li, N.; Fan, W.; Cai, H.; Zhao, D. Metal-Organic Framework Based Gas Sensors. *Advanced Science* **2022**, *9*, 2104374.

[147] Hameed, Y. A. S.; Alkhathami, N.; Snari, R. M.; Munshi, A. M.; Alaysuy, O.; Hadi, M.; Alsharif, M. A.; Khalil, M. A.; El-Metwaly, N. M. Novel Amino-Functionalized MOF-based Sensor for Zinc Ion Detection in Water and Blood Serum Samples. *Spectrochimica Acta Part A: Molecular and Biomolecular Spectroscopy* **2025**, *327*, 125432.

[148] Yi, X.; Dong, W.; Zhang, X.; Xie, J.; Huang, Y. MIL-53(Fe) MOF-mediated Catalytic Chemiluminescence for Sensitive Detection of Glucose. *Analytical and Bioanalytical Chemistry* **2016**, *408*, 8805–8812.

[149] Kepert, C. J.; Rosseinsky, M. J. Zeolite-like Crystal Structure of an Empty Microporous Molecular Framework. *Chemical Communications* **1999**, 375–376.

[150] Kong, G.-Q.; Han, Z.-D.; He, Y.; Ou, S.; Zhou, W.; Yildirim, T.; Krishna, R.; Zou, C.; Chen, B.; Wu, C.-D. Expanded Organic Building Units for the Construction of Highly Porous Metal–Organic Frameworks. *Chemistry – A European Journal* **2013**, *19*, 14886–14894.

[151] Peng, Y.; Krungleviciute, V.; Eryazici, I.; Hupp, J. T.; Farha, O. K.; Yildirim, T. Methane Storage in Metal–Organic Frameworks: Current Records, Surprise Findings, and Challenges. *Journal of the American Chemical Society* **2013**, *135*, 11887–11894.

[152] Nugent, P.; Belmabkhout, Y.; Burd, S. D.; Cairns, A. J.; Luebke, R.; Forrest, K.; Pham, T.; Ma, S.; Space, B.; Wojtas, L.; Eddaoudi, M.; Zaworotko, M. J. Porous Materials with Optimal Adsorption Thermodynamics and Kinetics for CO2 Separation. *Nature* **2013**, *495*, 80–84.

[153] Drake, T.; Ji, P.; Lin, W. Site Isolation in Metal–Organic Frameworks Enables Novel Transition Metal Catalysis. *Accounts of Chemical Research* **2018**, *51*, 2129–2138.

[154] Otake, K.-i.; Cui, Y.; Buru, C. T.; Li, Z.; Hupp, J. T.; Farha, O. K. Single-Atom-Based Vanadium Oxide Catalysts Supported on Metal–Organic Frameworks: Selective Alcohol Oxidation and Structure–Activity Relationship. *Journal of the American Chemical Society* **2018**, *140*, 8652–8656.

[155] Phan, A.; Czaja, A. U.; Gándara, F.; Knobler, C. B.; Yaghi, O. M. Metal–Organic Frameworks of Vanadium as Catalysts for Conversion of Methane to Acetic Acid. *Inorganic Chemistry* **2011**, *50*, 7388–7390.

[156] Xiao, D. J. et al. Oxidation of Ethane to Ethanol by N2O in a Metal–Organic Framework with Coordinatively Unsaturated Iron(II) Sites. *Nature Chemistry* **2014**, *6*, 590–595.

[157] Wang, D.; Wang, M.; Li, Z. Fe-Based Metal–Organic Frameworks for Highly Selective Photocatalytic Benzene Hydroxylation to Phenol. *ACS Catalysis* **2015**, *5*, 6852–6857.

[158] Liu, H.; Liu, W.; Xue, G.; Tan, T.; Yang, C.; An, P.; Chen, W.; Zhao, W.; Fan, T.; Cui, C.; Tang, Z.; Li, G. Modulating Charges of Dual Sites in Multivariate Metal–Organic Frameworks for Boosting Selective Aerobic Epoxidation of Alkenes. *Journal of the American Chemical Society* **2023**, *145*, 11085–11096.

[159] Shieh, F.-K.; Wang, S.-C.; Yen, C.-I.; Wu, C.-C.; Dutta, S.; Chou, L.-Y.; Morabito, J. V.; Hu, P.; Hsu, M.-H.; Wu, K. C.-W.; Tsung, C.-K. Imparting Functionality to Biocatalysts via Embedding Enzymes into Nanoporous Materials by a de Novo Approach: Size-Selective Sheltering of Catalase in Metal–Organic Framework Microcrystals. *Journal of the American Chemical Society* **2015**, *137*, 4276–4279.

[160] Feng, D.; Chung, W.-C.; Wei, Z.; Gu, Z.-Y.; Jiang, H.-L.; Chen, Y.-P.; Darensbourg, D. J.; Zhou, H.-C. Construction of Ultrastable Porphyrin Zr Metal–Organic Frameworks through Linker Elimination. *Journal of the American Chemical Society* **2013**, *135*, 17105–17110.

[161] Huang, N.; Yuan, S.; Drake, H.; Yang, X.; Pang, J.; Qin, J.; Li, J.; Zhang, Y.; Wang, Q.; Jiang, D.; Zhou, H.-C. Systematic Engineering of Single Substitution in Zirconium Metal–Organic Frameworks toward High-Performance Catalysis. *Journal of the American Chemical Society* **2017**, *139*, 18590–18597.

[162] Carson, F.; Martínez-Castro, E.; Marcos, R.; González Miera, G.; Jansson, K.; Zou, X.; Martín-Matute, B. Effect of the Functionalisation Route on a Zr-MOF with an Ir–NHC Complex for Catalysis. *Chemical Communications* **2015**, *51*, 10864–10867.

[163] Bartoszewicz, A.; Marcos, R.; Sahoo, S.; Inge, A. K.; Zou, X.; Martín-Matute, B. A Highly Active Bifunctional Iridium Complex with an Alcohol/Alkoxide-Tethered N-Heterocyclic Carbene for Alkylation of Amines with Alcohols. *Chemistry – A European Journal* **2012**, *18*, 14510–14519.

[164] Burgess, S. A.; Kassie, A.; Baranowski, S. A.; Fritzsching, K. J.; Schmidt-Rohr, K.; Brown, C. M.; Wade, C. R. Improved Catalytic Activity and Stability of a Palladium Pincer Complex by Incorporation into a Metal–Organic Framework. *Journal of the American Chemical Society* **2016**, *138*, 1780–1783.

[165] Pascanu, V.; González Miera, G.; Inge, A. K.; Martín-Matute, B. Metal–Organic Frameworks as Catalysts for Organic Synthesis: A Critical Perspective. *Journal of the American Chemical Society* **2019**, *141*, 7223–7234.

[166] Luo, F.; Lin, Y.; Zheng, L.; Lin, X.; Chi, Y. Encapsulation of Hemin in Metal–Organic Frameworks for Catalyzing the Chemiluminescence Reaction of the H2O2–Luminol System and Detecting Glucose in the Neutral Condition. *ACS Applied Materials & Interfaces* **2015**, *7*, 11322–11329.

[167] Liang, K.; Ricco, R.; Doherty, C. M.; Styles, M. J.; Bell, S.; Kirby, N.; Mudie, S.; Haylock, D.; Hill, A. J.; Doonan, C. J.; Falcaro, P. Biomimetic Mineralization of Metal-Organic Frameworks as Protective Coatings for Biomacromolecules. *Nature Communications* **2015**, *6*, 7240.

[168] Chen, K.; Wu, C.-D. Designed Fabrication of Biomimetic Metal–Organic Frameworks for Catalytic Applications. *Coordination Chemistry Reviews* **2019**, *378*, 445–465.

[169] Yuan, S.; Chen, Y.-P.; Qin, J.; Lu, W.; Wang, X.; Zhang, Q.; Bosch, M.; Liu, T.-F.; Lian, X.; Zhou, H.-C. Cooperative Cluster Metalation and Ligand Migration in Zirconium Metal–Organic Frameworks. *Angewandte Chemie International Edition* **2015**, *54*, 14696–14700.

[170] Yuan, S.; Chen, Y.-P.; Qin, J.-S.; Lu, W.; Zou, L.; Zhang, Q.; Wang, X.; Sun, X.; Zhou, H.-C. Linker Installation: Engineering Pore Environment with Precisely Placed Functionalities in Zirconium MOFs. *Journal of the American Chemical Society* **2016**, *138*, 8912–8919.

[171] Feng, D.; Gu, Z.-Y.; Li, J.-R.; Jiang, H.-L.; Wei, Z.; Zhou, H.-C. Zirconium-Metalloporphyrin PCN-222: Mesoporous Metal–Organic Frameworks with Ultrahigh Stability as Biomimetic Catalysts. *Angewandte Chemie International Edition* **2012**, *51*, 10307–10310.

[172] Cui, J.; Cui, L.; Jia, S.; Su, Z.; Zhang, S. Hybrid Cross-Linked Lipase Aggregates with Magnetic Nanoparticles: A Robust and Recyclable Biocatalysis for the Epoxidation of Oleic Acid. *Journal of Agricultural and Food Chemistry* **2016**, *64*, 7179–7187.

[173] Cui, J.; Feng, Y.; Jia, S. Silica Encapsulated Catalase@metal-Organic Framework Composite: A Highly Stable and Recyclable Biocatalyst. *Chemical Engineering Journal* **2018**, *351*, 506–514.

[174] Cui, J.; Ren, S.; Lin, T.; Feng, Y.; Jia, S. Shielding Effects of Fe3+-Tannic Acid Nanocoatings for Immobilized Enzyme on Magnetic Fe3O4@silica Core Shell Nanosphere. *Chemical Engineering Journal* **2018**, *343*, 629–637.

[175] Cui, J. D.; Jia, S. R. Optimization Protocols and Improved Strategies of Cross-Linked Enzyme Aggregates Technology: Current Development and Future Challenges. *Critical Reviews in Biotechnology* **2015**, *35*, 15–28.

[176] Corma, A.; García, H. Lewis Acids as Catalysts in Oxidation Reactions: From Homogeneous to Heterogeneous Systems. *Chemical Reviews* **2002**, *102*, 3837–3892.

[177] Corma, A.; García, H. Lewis Acids: From Conventional Homogeneous to Green Homogeneous and Heterogeneous Catalysis. *Chemical Reviews* **2003**, *103*, 4307–4366.

Chapter 2

Materials and Methods

Abstract

This chapter summarizes the experimental procedures and characterization methods used throughout this work. All starting materials, reagents, and solvents were obtained from reliable commercial suppliers, with purification and drying performed when required. Glassware and reactors were cleaned using standardized solvent rinses and specialized treatments to ensure contamination-free synthesis. High-pressure methane and oxygen reactions were carried out in reinforced reactors under strict safety protocols, while air- and moisture-sensitive steps were conducted using Schlenk techniques or in an inert-atmosphere glovebox. A comprehensive suite of analytical tools was employed to characterize the structural, textural, and electronic properties of the MOF-based catalysts. PXRD, BET, FT-IR, TGA, SEM-EDX, ICP-OES, XPS, EPR, and XAS provided detailed insight into crystallinity, porosity, functional groups, metal loading, oxidation states, and local coordination environments. Reaction mixtures were analyzed using NMR, GC, and HPLC for accurate product identification and quantification. Complementary density functional theory (DFT) calculations were performed to probe active-site structures, reaction energetics, and mechanistic pathways. Together, these methods establish a rigorous and reproducible foundation for the catalytic studies presented in this thesis.

2.1 Chemicals, Reagents, and Solvents Used

All chemicals, precursors, and solvents employed in the studies presented in subsequent chapters were acquired from reliable commercial suppliers to ensure reproducibility and consistency. Most linker molecules and metal salts required for MOF syntheses were obtained directly, including terephthalic acid and biphenyldicarboxylic acid from Alfa Aesar. Transition-metal precursors such as Fe(II)/Fe(III) chlorides, aluminium chloride, sodium borohydride, and sodium triethylborohydride were sourced from Sigma-Aldrich. Additional materials, including $ZrCl_4$ (GLR Innovations), $CuCl_2$, sodium sulfite, DMPO, and TEMPO derivatives (CDH Chemicals), were procured as needed. Isotopically enriched substrates used for tracer and mechanistic experiments, including $^{13}CH_4$ were obtained from Sigma-Aldrich. When certain intermediates or reagents were not commercially available, they were synthesized in-house following established literature procedures, as detailed in the corresponding experimental sections. This combined procurement–preparation strategy ensured high reliability and precise control over all materials used throughout the thesis.Benzene, styrene, and other substituted styrene derivatives used in oxidation studies were similarly procured from commercial chemical suppliers in high-purity grades.

Solvents were purchased in high-purity analytical grades from suppliers such as CDH Chemicals (DMF, THF, acetonitrile, ethylene glycol) and Avra Synthesis (toluene, anisole, 2-butanone). Ultrapure deionized water was generated using a Milli-Q EQ-7000 purification system. Where required, moisture-sensitive solvents were dried prior to use, for example, THF was purified by initial treatment with calcium hydride followed by distillation over a sodium/benzophenone mixture to ensure rigorous anhydrous conditions.

2.2 Cleaning of Glassware

All glassware used in synthesis or catalytic reactions was cleaned following a strict multistep protocol to eliminate any trace impurities that could interfere with sensitive experiments. Initially, each piece was rinsed with a nonpolar solvent such as hexane to remove grease or residual organic films, followed by sequential washes with acetone and a laboratory detergent solution. After an extensive rinse with tap water, the glassware was submerged in a strongly alkaline cleaning bath for several hours to dissolve stubborn residues and surface-bound

contaminants.

Once removed from the base bath, the items were thoroughly washed with running water to remove alkaline residues and briefly treated with a dilute hydrochloric acid rinse to neutralize any remaining basic species. This was followed by washing with soap solution, successive rinsing with tap water, deionized water, and finally acetone to ensure complete removal of moisture. Cleaned glassware was dried in an oven maintained at 110 °C and cooled either under vacuum or in the glovebox antechamber whenever air-sensitive work was anticipated.

The alkaline bath used for deep cleaning was prepared by dissolving potassium hydroxide flakes in a mixture of isopropanol and water, stored in a sealed plastic container to minimize evaporation. Fresh isopropanol was added periodically to maintain the bath's effectiveness, and the solution was replaced once a dark coloration indicated saturation with contaminants.

2.3 High-Pressure Reactions

Reactions involving compressed gases were carried out in dedicated high-pressure reactors (Amar PP-100-6624-00), equipped with calibrated gauges capable of reading up to 3000 psi. Because most of the catalytic systems in this work require methane-oxygen mixtures, all experiments were performed under strict safety controls to mitigate the inherent risk of combustion or explosion. The reactors were placed inside a reinforced polycarbonate fume hood, allowing continuous visual inspection while providing an additional containment barrier.

A meticulous operational procedure was followed for every run. Before loading reagents, the reactor body, head assembly, valves, and sealing components were examined for damage, corrosion, or loose fittings. O-rings, gaskets, and rupture discs were replaced whenever signs of wear were detected. To eliminate residual air, the assembled reactor was repeatedly purged with dry nitrogen until an oxygen-free atmosphere was assured.

For methane oxidation experiments, methane was always introduced first, followed by oxygen, ensuring controlled and safe pressurization. During the reaction, pressure and temperature were monitored continuously through external displays. After completion, the reactor was cooled to room temperature and depressurized slowly according to standard

safety procedures to avoid sudden pressure release.

Cleaning was performed immediately after venting: the interior chamber, dip tubes, and valves were rinsed with acetone and then washed with deionized water using non-abrasive methods to prevent scratching the metal surface. The reactor was subsequently dried under vacuum or under a stream of inert gas. Before storage, a final leak test was done to confirm system integrity, ensuring that the reactor was fully prepared for the next high-pressure experiment.

2.4 Air-Sesitive Reactions

Reactions involving moisture- or oxygen-sensitive reagents were carried out exclusively in a Vigor SG1200/750TS-F glovebox maintained under a high-purity nitrogen atmosphere. Before starting any experiment, the glovebox environment was stabilized by ensuring that both O_2 and H_2O levels remained below 3 ppm, and all work surfaces were cleaned to avoid cross-contamination. Chemicals, consumables, and reaction vessels were transferred through the antechamber using repeated evacuation–refill cycles to prevent air ingress. Throughout each experiment, the glovebox atmosphere was continuously monitored and maintained to ensure inert conditions. Solvent removal and sample drying inside the glovebox were performed using an integrated high-vacuum line fitted with a liquid-nitrogen cold trap, preventing volatile contaminants from re-entering the working environment. This controlled setup ensured the safe and reliable handling of all air-sensitive materials used in subsequent chapters.

2.5 Instrumental Methods

A comprehensive suite of analytical and spectroscopic tools was utilized to examine the structural, compositional, and electronic features of the synthesized MOF-based catalysts. The techniques outlined in the following subsections detail the instruments used, the key operating conditions, and the specific type of information each method provided. Together, these methods ensured an in-depth and reliable characterization of the materials discussed in this thesis.

2.5.1 Powder X-ray Diffraction (PXRD).

Air-dried MOF samples were analyzed by powder X-ray diffraction to verify their crystalline structure and confirm phase purity. PXRD patterns were recorded at ambient temperature on a Bruker Advance diffractometer using Ni-filtered Cu Kα radiation (λ = 1.5406 Å). Diffraction data were collected over a 2θ range of 4–70 °C, with a step size of 0.05°and a counting time of 1 s per step. The obtained patterns were compared with simulated diffractograms generated from crystallographic models to ensure that the materials were monophasic and structurally consistent with the expected framework. Any discrepancies in peak positions or relative intensities were further examined to assess possible impurities, structural distortions, or secondary phases.

2.5.2 Brunauer–Emmett–Teller (BET) Surface Area Analysis.

Surface area and porosity measurements were carried out after carefully preparing the MOF samples to preserve their structural integrity. Initially, each material was dried under vacuum at room temperature to remove loosely bound moisture. To avoid framework collapse during solvent removal, a freeze-drying protocol was employed: the MOFs were exchanged into benzene, cooled to 10 °C, and gradually evacuated under low temperature conditions. This step ensured gentle solvent extraction while maintaining pore architecture. The samples were then subjected to a final activation at 80 °C under dynamic vacuum for 24 h to fully eliminate residual solvents.

BET measurements were performed using a Microtrac BELLSORP MAX II system operating under ultra-high vacuum. Nitrogen adsorption–desorption isotherms were collected, and the linear region of the BET plot was used to calculate surface areas. The resulting isotherms were examined to confirm the characteristic microporous behavior of the frameworks and to extract reliable textural parameters such as surface area and pore volume.

2.5.3 Thermogravimetric Analysis (TGA).

Thermal behaviour and framework stability were examined using a *PerkinElmer* TGA7 instrument. Samples were finely powdered before loading and analysed under a steady ni-

trogen stream to maintain an inert environment. Each sample was heated from 40 °C to 800 °C at a uniform ramp rate of 10 °C min^{-1}, allowing clear identification of mass-loss events associated with solvent removal, guest desorption, and eventual framework decomposition. In selected cases, MOF samples dispersed in THF were analysed without prior drying to observe the influence of retained solvent on their thermal response. The combined measurements provided detailed insight into both activation-related mass losses and intrinsic thermal robustness of the materials.

2.5.4 Fourier Transform Infrared Spectroscopy (FT-IR).

FT-IR measurements were carried out to probe functional groups and verify the coordination environment within the synthesized MOFs. Prior to analysis, samples were dried overnight under dynamic vacuum at 90 °C and transferred into the glovebox to avoid exposure to ambient moisture. Inside the inert atmosphere, a small quantity of the activated solid was finely ground with anhydrous KBr and pressed into a transparent pellet to ensure uniform dispersion of the material. Spectra were recorded on a *Nicolet Protege* 460 (Bruker) operating in transmission mode. Before collecting data, the instrument compartment was purged with dry nitrogen for approximately 20 minutes to remove atmospheric CO_2 and water vapour, ensuring a clean baseline and reliable spectral features.

2.5.5 Scanning Electron Microscopy–Energy Dispersive X-ray Spectroscopy (SEM-EDS).

Surface morphology and elemental distribution were examined using a Zeiss FE-SEM Ultra Plus 55 operated at an accelerating voltage of 20 kV. Before analysis, the MOF samples were thoroughly dried under vacuum, and a small portion of the powder (approximately 1–2 mg) was gently spread onto conductive carbon tape to ensure good adhesion and charge dissipation. High-resolution SEM imaging was used to visualize particle size, shape, and surface texture, while the integrated EDS detector provided complementary compositional information by identifying and mapping the elements present within the sample.

2.5.6 Inductively Coupled Plasma Optical Emission Spectroscopy (ICP-OES).

Quantitative metal analysis was performed using an *Agilent* 5110 ICP-OES instrument. Prior to measurement, the MOF samples were thoroughly dried under vacuum and digested in a mixture of HF and HNO_3 to ensure complete breakdown of the framework. The digested solutions were then diluted with 5% HNO_3 and analyzed against a six-point external calibration curve (0.1–20 ppm), which consistently showed correlation coefficients above 0.999. Certified reference standards and repeated measurements were used to validate both accuracy and reproducibility.

2.5.7 Electron Paramagnetic Resonance (EPR).

EPR measurements were carried out in the X-band using a Bruker A300-9.5/12/S/W spectrometer. Solid-state samples were first dried under vacuum and sealed in quartz tubes before data acquisition at ambient temperature. For liquid-phase measurements, an aliquot of the reaction mixture was mixed with 5,5-dimethyl-1-pyrroline N-oxide (DMPO) to trap short-lived radical species, and the solution was immediately transferred to an EPR tube. Spectra were analyzed and simulated using Bruker *Simfonia* software, allowing resolution of overlapping features and identification of radical intermediates generated during catalysis.

2.5.8 X-Ray Photoelectron Spectroscopy (XPS).

Surface elemental composition and oxidation states were examined using a Physical Electronics 5000 VersaProbe III system equipped with an Al-Kα radiation source (1486.6 eV). All spectra were referenced to the adventitious carbon C 1s peak at 284.8 eV to ensure accurate energy calibration. Peak fitting and deconvolution were carried out using CasaXPS, allowing reliable distinction of closely spaced or overlapping features. This analysis provided detailed information on the chemical environment and electronic state of the metal centers within the MOF samples.

2.5.9 X-Ray Absorption Spectroscopy (XAS).

X-ray absorption measurements, encompassing both XANES and EXAFS regions, were carried out at the Energy Scanning EXAFS beamline (BL-9) at the *Indus*-2 Synchrotron Radiation Facility, Indore. Experiments were performed at room temperature across an energy window of approximately 4–25 keV. The beamline configuration included a Rh/Pt-coated collimating mirror, a Si(111) double-crystal monochromator for precise energy selection, and a downstream Rh/Pt-coated focusing mirror to maintain beam stability. Data were collected in transmission geometry using a pair of ionization chambers, with metal foil standards measured simultaneously to ensure accurate energy calibration. For analysis, finely ground MOF powders were blended with cellulose and pressed into 15-mm pellets to achieve appropriate absorption edge step heights. Spectral processing and fitting of XANES and EXAFS features were performed using the Demeter software suite, enabling detailed insight into local coordination environments around the metal centers.

2.6 Analytical Technique

2.6.1 Nuclear Magnetic Resonance (NMR).

After each catalytic reaction, the liquid phase was mixed with D_2O in a 1:1 ratio and sonicated to ensure complete dissolution of all analytes. The solution was then transferred to an NMR tube for analysis. ^{1}H and ^{13}C NMR spectra were recorded on a *Bruker* DRX instrument operating between 300–500 MHz. These measurements were used to identify and quantify reaction products based on well-resolved chemical shifts and integrals. Routine data processing such as phase correction, baseline adjustment, and signal integration was performed to ensure reliable evaluation of product distribution and reaction conversion.

2.6.2 Gas Chromatography (GC).

Once the reactor returned to room temperature, gases were withdrawn using a Tedlar bag and analyzed on an Agilent 8890 GC equipped with a thermal conductivity detector (TCD). The system was fitted with a PoraPlot Q column coupled to a molecular-sieve column, enabling separation of light hydrocarbons and permanent gases.

For liquid-phase analysis, 1 mL of the reaction mixture was collected while still cold, briefly centrifuged to remove solids, and the clear supernatant was transferred to a GC vial. Ethylene glycol (5 μL) was added as an internal standard to ensure accurate quantification. Liquid products were examined using two complementary instruments: an Agilent 8890 GC with an FID and a DB-WAX column for routine quantification, and an Agilent 7890B GC coupled to a mass spectrometer for product identification. Instrumental parameters, calibration details, and compound response factors are described in the relevant experimental chapters.

2.6.3 High-Performance Liquid Chromatography (HPLC).

For HPLC analysis, 1 mL of the chilled reaction mixture was collected and briefly centrifuged to remove any suspended solids. The clear supernatant was transferred to an HPLC vial and spiked with 10 μL of 2-butanone, which served as the internal standard. A 100 μL portion of this solution was injected into an *Agilent* 1260 Infinity II system equipped with a refractive index detector and a Hi-Plex H column. Product concentrations were determined using external calibration curves generated from authentic standards, enabling accurate quantification of liquid-phase components and calculation of their yields.

2.7 Calculations for conversion and selectivity

The catalytic performance across all reactions was evaluated in terms of substrate conversion, product selectivity, and carbon balance. The extent of conversion was determined from the difference between the initial and post-reaction amounts of the substrate, as quantified using gas chromatography (GC) and/or other appropriate analytical techniques depending on the system.

The **substrate conversion (%)** was calculated using the following expression:

$$\text{Conversion (\%)} = \frac{\text{moles of substrate consumed}}{\text{initial moles of substrate}} \times 100 \tag{2.1}$$

The **product selectivity (%)** toward a specific product was calculated as:

$$\text{Selectivity (\%)} = \frac{\text{moles of desired product formed}}{\text{moles of substrate consumed}} \times 100 \tag{2.2}$$

For reactions involving multiple carbon-containing products, a **carbon balance analysis** was performed by accounting for all products in both liquid and gas phases. The carbon balance (%) was calculated as:

$$\text{Carbon balance (\%)} = \frac{\text{total carbon in all products}}{\text{total carbon consumed from substrate}} \times 100 \tag{2.3}$$

2.8 Metal Incorporation Analysis

The extent of metal incorporation into the MOF frameworks was determined using **Inductively Coupled Plasma Optical Emission Spectroscopy (ICP-OES)**. The experimentally measured metal content was compared with the theoretical metal loading based on the number of available coordination sites within the framework.

The **metal site incorporation (%)** was calculated as:

$$\text{Metal incorporation (\%)} = \frac{\text{experimental metal loading}}{\text{theoretical metal loading}} \times 100 \tag{2.4}$$

The results indicate that metal incorporation is not necessarily complete and varies depending on factors such as the metal precursor, synthesis conditions, and accessibility of coordination sites within the porous framework. These values are discussed in the respective chapters for each catalyst system.

2.9 Theoretical Studies

Computational investigations were performed using density functional theory (DFT) as implemented in the Gaussian software package. Geometry optimizations were carried out at the unrestricted level with hybrid functionals such as B3LYP, and appropriate basis sets were chosen for main-group elements and transition metals to achieve a balance between accuracy and computational cost. Solvent effects were modeled using the IEFPCM variant

of the polarizable continuum model, with parameters tailored to match the reaction medium used experimentally. Each optimized structure underwent vibrational frequency analysis to verify that intermediates corresponded to true minima and transition states displayed a single imaginary frequency. Thermochemical corrections were derived from these calculations to obtain Gibbs free energies.

For metal-containing species, multiple spin states were examined to identify the energetically preferred configuration, and alternative coordination environments were evaluated when relevant. Corrections were applied for coordinated solvent molecules when necessary to ensure realistic energetic comparisons. All key intermediates and transition states were validated through relative energy analysis, and system-specific computational details are provided in the relevant results chapters.

Chapter 3

Copper Catalyzed Selective Methane Oxidation to Acetic Acid using O_2

Title of Paper: "Copper Catalyzed Selective Methane Oxidation to Acetic Acid using O_2"

Citation: Chemical Science, **2025**, *16*, 2785-2795.
(doi.org/10.1039/d4sc06281g)

Author: Poorvi Gupta, Bharti Rana, Rishabh Maurya, Rahul Kalita, Manav Chauhan, and Kuntal Manna*

Abstract

The direct transformation of methane into C_2 oxygenates such as acetic acid selectively using molecular oxygen (O_2) is a significant challenge due to the chemical inertness of methane, the difficulty of methane C-H bond activation/C-C bond coupling and the thermodynamically favored over-oxidation. In this study, we have successfully developed a porous aluminum metal-organic framework (MOF)-supported single-site mono-copper(II) hydroxyl catalyst [MIL-53(Al)-Cu(OH)], which is efficient in directly oxidizing methane to acetic acid in water at 175 °C with a remarkable selectivity using only O_2. This heterogeneous catalyst achieved an exceptional acetic acid productivity of 11796 $mmol_{CH3CO2H}$ mol_{Cu}^{-1} h^{-1} in 9.3% methane conversion with 95% selectivity in the liquid phase and can be reused at least 6 times. Our experiments, along with computational studies and spectroscopic analyses, suggest a catalytic cycle involving the formation of a methyl radical ($^{\cdot}CH_3$). The confinement of Cu-active sites within the porous MIL-53(Al) MOF facilitates C-C bond coupling, resulting in the efficient formation of acetic acid with excellent selectivity due to the internal mass transfer limitations. This work advances the development of efficient and chemoselective earth-abundant metal catalysts using MOFs for the direct transformation of methane into value-added products under mild and eco-friendly conditions.

3.1 Introduction

Acetic acid is a crucial commodity chemical in the industrial sector, with a global market volume exceeding 19 million metric tons.[1] It is used extensively as vinegar, an antiseptic, and a solvent and also serves as a precursor in the production of acetate esters, vinyl acetate monomers, and acetic anhydride.[2–4] The industrial synthesis of acetic acid involves a three-step process that is capital- and energy-intensive: (1) conversion of coal or methane into synthesis gas (syngas) through steam reforming of methane or coal gasification at high temperatures; (2) catalytic conversion of syngas to methanol at elevated temperatures; (3) subsequent rhodium or iridium catalyzed carbonylation of methanol by the Monsanto or Cativa process to yield acetic acid.[5–10] Direct conversion of methane to acetic acid utilizing only O_2 would be both environmentally friendly and economically advantageous. However, this process is extremely challenging due to methane's chemical inertness caused by its high

C-H bond energy (104 kcal mol^{-1}), low polarizability, low acidity (pKa $\sim$ 50), and large HOMO-LUMO gap.[11;12] Direct oxidation of methane to acetic acid also suffers from poor productivity and selectivity due to the challenges associated with simultaneous methane C-H bond activation/C-C bond coupling and the over-oxidation of the acetic acid to produce CO and CO_2.

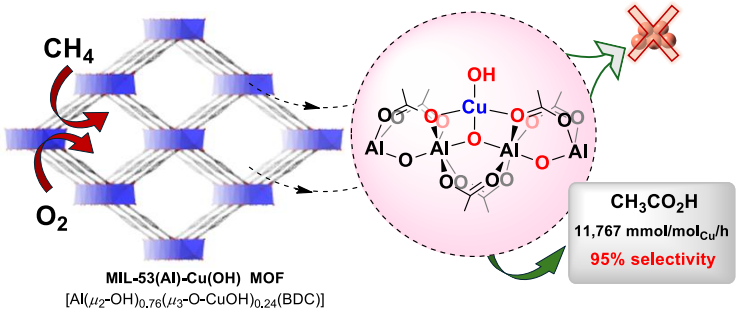


Figure 3.1: Development of the porous aluminium-MOF confined mono-Cu(II) hydroxyl catalyst for the direct and selective oxidation of methane to acetic acid utilizing only O_2 as the oxidant.

Several late-transition metal catalysts, such as Au/H-MOR (Au nanoparticles dispersed on mordenite),[13] Rh_1/pMOF,[14] and ZSM-5-supported-Rh,[15] Ru,[16] and Ir[17] have been developed, which utilize toxic CO along with O_2 for the conversion of methane to acetic acid. However, the use of toxic CO and precious metals, along with poor selectivity and low productivity of acetic acid, highlights the need for further advancements in designing and synthesizing catalysts for the cost-effective and environmentally sustainable production of acetic acid. Examples of catalysts enabling the conversion of methane to acetic acid using only O_2 are rare.[18–22] Recent interest has focused on metal-organic frameworks (MOFs) to develop catalysts for direct methane oxidation to valuable products.[23–36] MOFs, built from metal-oxo cluster nodes interconnected by organic linkers, have been used to develop well-defined earth-abundant metal catalysts for chemoselective reactions owing to their crystalline structure, tunable pore size, reticular synthesis, ease of post-synthetic modification and active-site isolation.[28;37–49] Notably, the post-synthetic metalation of MOFs' nodes allows the development of highly electrophilic base-metal catalysts, enabling methane activation via σ-bond metathesis.[22;27;28] In addition, the high surface area of MOFs prevents overoxidation by adsorbing the reactive intermediates formed during the catalysis. Moreover, the confined space within the MOF's micropores enhances the local concentration of methane around the active site and facilitates C-C coupling within the pores (Figure 3.1).

We recently reported a cerium UiO-MOF's node-supported electrophilic copper(II) hydroxide catalyst, which activates methane via σ-bond metathesis and subsequently converts it to acetic acid using only O_2 as the oxidant.[22] We envisioned that developing MIL-53(Al) node supported Cu(II) hydroxyl species would be more efficient in activating methane in a similar manner due to the increased charge density of Al^{3+} ions and two additional oxygen atoms in the coordination sphere of the Cu^{2+} ion. Moreover, the less sterically hindered Al-oxo nodes in MIL-53(Al) would provide more accessible active copper centres compared to the UiO-MOF analogues. Herein, we report the development of a mono-copper(II) hydroxyl species confined within the porous aluminium MOF, enabling direct methane oxidation to acetic acid using O_2 at 175 °C. This process achieves a productivity of 11796 $mmol_{CH3CO2H}$ mol_{Cu}^{-1} h^{-1}, with a methane conversion of 9.3% and a selectivity of 95% in the liquid phase.

3.2 Results and Discussions

3.2.1 Synthesis and Characterization of MIL-53-Cu(OH) MOF

MIL-53-Cu(OH) was synthesized through a post-synthetic modification of the aluminium hydroxyl nodes of the MIL-53(Al) MOF, which has the chemical formula of [Al(OH)(BDC)] (H_2BDC = 1,4-benzenedicarboxylic acid). The synthesis involved a solvothermal reaction of 1,4-benzenedicarboxylic acid (H_2BDC) and $AlCl_3.6H_2O$ in dimethylformamide (DMF) at 120 °C for 2 days, resulting in the formation of MIL-53(Al) as a white crystalline solid. In MIL-53(Al) MOF, Al^{3+} ions are coordinated in an octahedral manner with μ_2-hydroxide and 1,4-benzenedicarboxylate (bdc^{2-}) bridging linkers forming a three-dimensional porous topology with rhombic channels.[50;51] The μ_2-OH of the SBUs was deprotonated using *n*-BuLi, followed by a salt metathesis reaction of $CuCl_2$ in tetrahydrofuran (THF) to yield MIL-53(Al)-CuCl as a yellowish-green solid. Further treatment of MIL-53(Al)-CuCl with $NaEt_3BH$ in THF at room temperature facilitated halide–hydride exchange at the Cu ion, resulting in MIL-53(Al)-CuH. This material, upon subsequent treatment with water transformed into MIL-53(Al)-Cu(OH). Analysis by inductively coupled plasma optical emission spectroscopy (ICP-OES) showed that MIL-53(Al)-Cu(OH) has 24% copper loading with respect to μ_2-OH, resulting in the chemical formula of $AlO_{5.24}C_8H_5Cu_{0.24}$. The similarity in the powder X-ray diffraction (PXRD) patterns of MIL-53(Al)-CuCl, MIL-53(Al)-Cu(OH) and

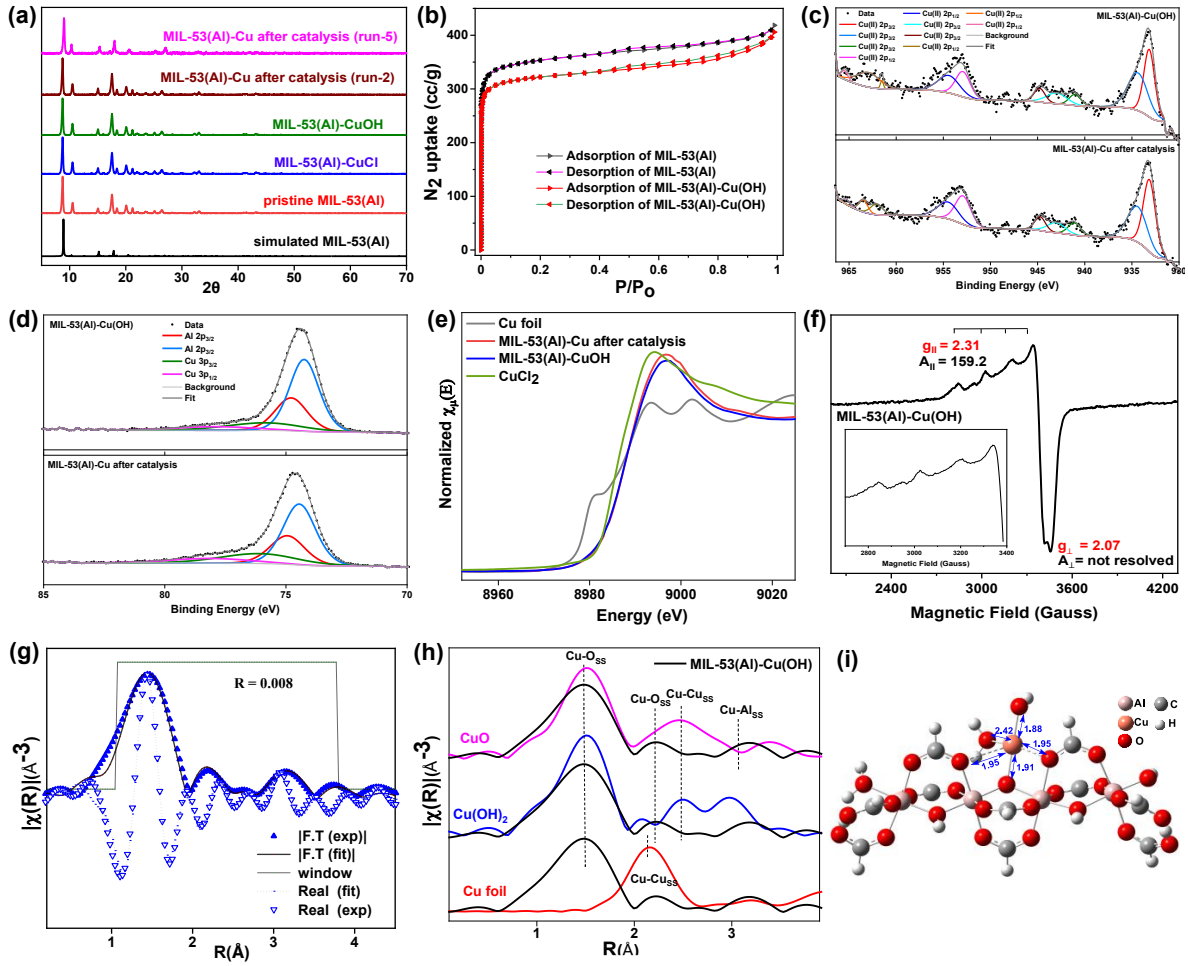


Figure 3.2: (a) PXRD patterns of the simulated MIL-53(Al) MOF (black), pristine MIL-53(Al) MOF (red), MIL-53(Al)-CuCl MOF (blue), MIL-53(Al)-CuOH MOF (green), MIL-53(Al)-Cu after run-2 (wine) and run-5 of catalysis (magenta). (b) N_2 sorption isotherms of MIL-53(Al) (black) and MIL-53(Al)-Cu(OH) (red) measured at 77 K. (c) Cu 2p XPS spectra of MIL-53(Al)-Cu(OH) (top) and MIL-53(Al)-Cu after catalysis (bottom). (d) Al 2p XPS spectra of MIL-53(Al)-Cu(OH) (top) and MIL-53(Al)-Cu after catalysis (bottom). (e) Cu K-edge XANES spectra of Cu-foil (grey), $CuCl_2$ (green), MIL-53(Al)-Cu(OH) (blue) and MIL-53(Al)-Cu after catalysis (red). (f) X-band EPR spectra of MIL-53(Al)-Cu(OH) at 298 K. (g) EXAFS spectra and fits in R-space at the Cu K-edge of MIL-53(Al)-Cu(OH) with the magnitude and real component of the Fourier transformation shown as solid and hollow triangles in blue color, respectively. The fitting range in R-space is 1.1–3.8 Å (within the grey line); (h) k^2-weighted Cu-EXAFS (R) spectra of MIL-53(Al)-Cu(OH) (black), CuO (pink), $Cu(OH)_2$ (blue), and Cu foil (red). (i) DFT optimized structure of MIL-53(Al)-Cu(OH)(OH_2).

MIL-53(Al) reveals that the crystallinity and structure of the MIL-53(Al) MOF remained intact even after post-synthetic metalation (Figure 3.2a). MIL-53(Al)-Cu(OH) has a BET

surface area of 1263 m^2 g^{-1} and a pore diameter of 0.60 nm (Figure 3.2b). The slightly reduced surface area of MIL-53(Al)-Cu(OH) compared to that of MIL-53(Al) (1386 m^2 g^{-1}) is ascribed to the presence of Cu(OH) species within the MOF pores (Figure 3.2b). The structure and stability of the MOF were further examined by infrared spectroscopy (IR) and thermogravimetric analysis (TGA), respectively (Figure 3.10 and 3.9). Scanning electron microscopy (SEM) images showed that MIL-53(Al)-Cu(OH) particles are nearly spherical, with an average size of 200 nm (Figure 3.12). In the scanning electron microscopy (SEM) energy-dispersive X-ray (EDX) mapping of MIL-53(Al)-Cu(OH), it was observed that Al and Cu are uniformly distributed throughout the MOF particles (Figure 3.12).

The X-ray photoemission spectroscopy (XPS) spectrum of MIL-53(Al)-Cu(OH) showed Cu $2p_{3/2}$ binding energies at 933.13 eV and 934.37 eV with satellite peaks at 941.05 eV, 943 eV, and 944.79 eV, indicating a +2-oxidation state of the copper ion. In this XPS spectrum, the Cu $2p_{1/2}$ binding energies are centered at 952.92 eV and 954.41 eV, with satellite features at 961.52 eV, 962.96 eV and 965.49 eV, which is consistent with the presence of Cu^{2+} ions (Figure 3.2c).[52] The fitted Al 2p spectrum displays four peaks at binding energies of 74.44 eV, 74.9 eV, 76.09 eV, and 78.1 eV (Figure 3.2d). The peaks at 74.44 eV and 74.9 eV are assigned to the spin-orbit coupled components Al^{3+} $2p_{3/2}$ and Al^{3+} $2p_{1/2}$, respectively. Additionally, the peaks at 76.09 eV and 78.1 eV are attributed to the Cu(II) ($3p_{3/2}$-$3p_{1/2}$) doublet.[53] The existence of Cu^{2+} ions was further supported by X-ray absorption near edge structure (XANES) analysis, which demonstrated the alignment of the K-edge energy of Cu ions in MIL-53(Al)-Cu(OH) (8984.9 eV) with that of penta-coordinated Cu^{2+} (Figure 3.2e).[54] The X-band electron paramagnetic resonance (EPR) spectrum of MIL-53(Al)-Cu(OH) recorded at 298 K displayed $g_{\|}$ = 2.31, $A_{\|}$ = 159.2 and $g_{\perp}$ = 2.07 with a poorly resolved perpendicular component, corresponding to the square pyramidal geometry of Cu^{2+} ions (Figure 3.2f).[55–57] Furthermore, fitting the extended X-ray absorption fine structure (EXAFS) data with the density functional theory (DFT) optimized structure of MIL-53(Al)-Cu(OH)(OH_2) (Figure 3.2g) revealed that the Cu^{2+} ion has a distorted square pyramidal geometry, coordinating with one μ_3-O^- (Cu-$O^-_{\mu_3\text{-O}}$-: 1.91 Å), one hydroxide (Cu-O_{OH}: 1.88 Å), two neutral carboxylate oxygen atoms (Cu-$O_{carboxylate}$: 1.95 Å) and one water molecule (Cu-O_{H_2O}: 2.42 Å) (Figure 3.2i). The phase uncorrected k^2-weighted Cu-EXAFS (R) spectrum of MIL-53(Al)-Cu(OH) lacked the Cu-Cu scattering feature at 2.14 Å of Cu foil, further con-

firming the absence of Cu nanoparticles in the MIL-53(Al)-Cu(OH) MOF (Figure 3.2h). The distinctive scattering feature at 1.47 Å in the same spectrum corresponds to Cu-O scattering, similar to that observed in CuO and $Cu(OH)_2$ (Figure 3.2h). In addition, the EXAFS data of MIL-53(Al)-Cu(OH) were also fitted to its DFT model with 5-80% metallic Cu or 5-80% CuO (Figure 3.20). Significant discrepancies and elevated *R*-factors indicated that no metallic Cu nanoparticles or CuO were present in MIL-53(Al)-Cu(OH). The EXAFS analysis revealed that MIL-53(Al)-Cu(OH) contains node-supported single-site monomeric $Cu^{II}(OH)$ species, which have no Cu neighbours.

3.2.2 Catalytic performance for methane oxidation to acetic acid

MIL-53(Al)-Cu(OH) was tested as a heterogeneous catalyst for methane conversion to acetic acid using O_2 as the oxidant. The methane oxidation reactions were performed in a high--pressure batch reactor by varying the temperature, ratio of methane to O_2 in the feed, solvents, and reaction time. The liquid products were analyzed using a gas-chromatograph equipped with a mass spectrometry (MS) detector and a flame-ionization detector (GC-FID), while the gas analysis was performed using a GC-thermal conductivity detector (GC-TCD). The quantification of liquid oxygenates was further confirmed using a high performance liquid chromatograph (HPLC) equipped with a refractive index detector. The reaction of methane (30 bar) and O_2 (10 bar) in an aqueous suspension of MIL-53(Al)-Cu(OH) (3.8 mg, 4.0 mol Cu) at 150 °C in 32 h produced 1.15 mmol of CH_3CO_2H as the primary product along with minor quantities (9.5%) of methanol and ethanol in the liquid phase. In this reaction, no formic acid or any other oxygenated products were observed. Additionally, 0.032 mmol of CO_2 were detected as a side product in the gas phase. The reaction conditions were further optimized to get the highest yield and selectivity of acetic acid.

***Effect of Solvent*:**

Various polar and non-polar solvents were tested to optimize the yield of acetic acid for MIL-53(Al)-Cu(OH) catalyzed methane oxidation. Acetic acid was only formed in water and the catalyst was inactive in other solvents such as heptane, toluene, and THF (entries 22-24, Table 3.2). This result may be attributed to the role of water as one of the reactants

in the synthesis of acetic acid. Subsequently, we conducted experiments to optimize the amount of water solvent for maximizing the yield of acetic acid. 1.15 mmol of acetic acid was achieved using 7 mL of water under the same reaction conditions (150 °C, 30 bar CH_4, 10 bar O_2, and 32 h).

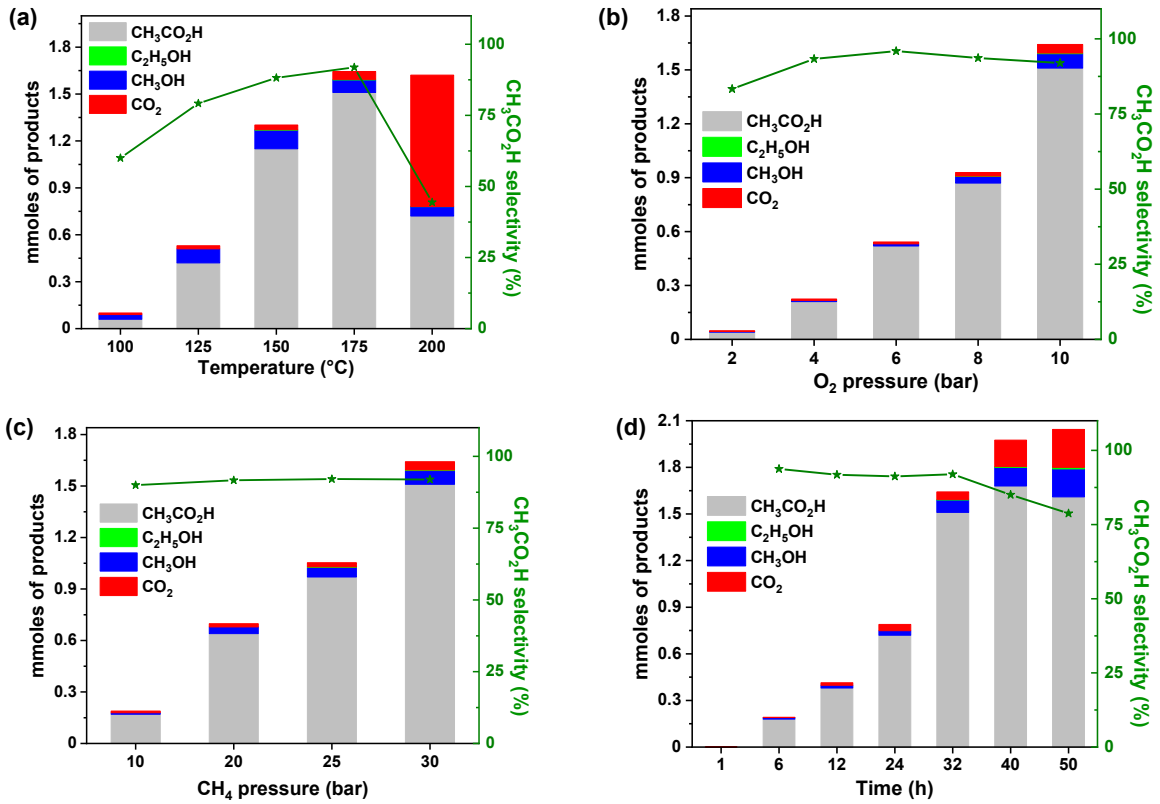


Figure 3.3: (a) Effect of temperature on oxygenated product yields and selectivity of acetic acid. Reaction conditions: MIL-53(Al)-Cu(OH) (3.8 mg, 4.0 μmol), 30 bar CH_4, 10 bar O_2, 7 mL water and 32 h. (b) Effect of O_2 pressure on the oxygenated product yields and selectivity of acetic acid. Reaction conditions: MIL-53(Al)-Cu(OH) (3.8 mg, 4.0 mol), 30 bar CH_4, 175 °C, 7 mL water and 32 h, balanced with N_2 to maintain a total pressure of 40 bar. (c) Effect of CH_4 pressure on the oxygenated product yields and selectivity of acetic acid. Reaction conditions: MIL-53(Al)-Cu(OH) (3.8 mg, 4.0 μmol), 10 bar O_2, 175 °C, 7 mL water and 32 h, balanced with N_2 to maintain a total pressure of 40 bar. (d) Effect of time on the oxygenated product yields and selectivity of acetic acid. Conditions: MIL-53(Al)-Cu(OH) (3.8 mg, 4.0 μmol), 30 bar CH_4, 10 bar O_2, 7 mL water and 175 °C.

***Effect of reaction temperature*:**

To determine the minimum temperature required to achieve maximum acetic acid yield in methane oxidation using O_2, the influence of temperature was examined within the range

of 100–200 °C with methane (30 bar) and O_2 (10 bar) over 32 h (Figure 3.3a). The yields of liquid products increased as the temperature was raised from 100 to 175 °C reaching a peak of 1.51 mmol of acetic acid at 175 °C. However, when the temperature was further increased beyond 175 °C, the yield of acetic acid decreased significantly, with CO_2 as the major product. This decline in the yield of acetic acid beyond 175 °C is primarily attributed to the over-oxidation of methane (Figure 3.3a).

***Effect of partial pressure of O_2 and methane*:**

To optimize the partial pressures of O_2 and methane, the total reaction vessel pressure was maintained at a constant 40 bar, balanced with nitrogen, to ensure accurate comparisons as different pressures can influence methane solubility. The effect of O_2 partial pressure on methane oxidation was investigated at 175 °C under a mixture of CH_4 (30 bar) and varying partial pressures of O_2 (2–10 bar) for 32 h. As illustrated in Figure 3.3b, the optimal productivity of CH_3CO_2H (acetic acid) with MIL-53(Al)-Cu(OH) was achieved at a P_{O_2} of 10 bar. The oxidation of methane to acetic acid increased with higher partial pressures of O_2, peaking at 10 bar of O_2 pressure (entries 8-11, Table 3.2). At an elevated O_2 pressure of 15 bar (entry 24, Table 3.3), acetic acid selectivity dropped to 38.3%, with CO_2 becoming the major product. This suggests that higher O_2 pressures favor C-O bond formation due to the increased reactivity of carbon-centered radicals with molecular oxygen. Additionally, the methane oxidation reactions were conducted at 175 °C for 32 h in a mixture of 10 bar of O_2 and variable methane pressures to examine the correlation between the pressure of methane and the yield of acetic acid (Figure 3.3c). It was observed that the yield of acetic acid increased from 0.17 to 0.97 mmol as the methane pressure was raised from 10 to 25 bar (entries 12-14, Table 3.2). The highest yield of 1.51 mmol of acetic acid was achieved at a methane pressure of 30 bar (Figure 3.3c).

***Effect of reaction time*:**

The impact of reaction time on methane oxidation was evaluated over a period of 1-50 h using CH_4 (30 bar) and O_2 (10 bar) at 175 °C (Figure 3.3d). The findings indicated a direct relationship between the acetic acid yield and reaction time within the 1-40 h range. Initially, no acetic acid was detected within the first hour, but as the reaction time increased,

0.18, 0.38, and 0.72 mmol of acetic acid were obtained in 6, 12 and 24 h, respectively. The highest yield of 1.51 mmol of acetic acid was achieved at 32 h, with an impressive 92% selectivity. Extending the reaction time to 40 h resulted in a slight increase in acetic acid yield to 1.68 mmol, although with reduced selectivity (84%). Further continuing the reaction to 50 h resulted in a decrease in acetic acid yield to 1.61 mmol, along with an increase in CO_2, which are thermodynamically more favorable. This decline in product selectivity can be attributed to the over-oxidation of liquid products due to the prolonged reaction time. As a result, MIL-53(Al)-Cu(OH) (3.8 mg, 4.0 μmol Cu) exhibited an exceptionally high acetic acid productivity of 3,77,472 $mmol_{CH_3CO_2H}$ mol_{Cu}^{-1} under 30 bar of methane and 10 bar of O_2 in 7 mL water at 175 °C for 32 h achieving 95% liquid selectivity and 92% overall carbon selectivity with a methane conversion of 9.3%. In the reaction, 3.2 mmol of methane is oxidized by O_2 to yield 1.51 mmol of acetic acid, 0.048 mmol of CO_2 and 1.4 mmol of H_2. The total amount of carbon-containing products obtained was 3.16 mmol, based on the consumption of 3.2 mmol of methane, leading to a carbon balance of 98.75%. MIL-53(Al)-Cu(OH) is recyclable for at least six consecutive cycles with consistent activity, giving a cumulative TON of 2204 (Figure 3.4b). The percentages of leached Cu and Al after run-1 were 0.06 and 0.05, respectively, and after run-5 they were 0.05 and 0.08, respectively (Table 3.4). The robustness of the MOF was confirmed by PXRD, XPS, and X-ray absorption studies (XAS) and ICP-analysis of the used catalyst for selective methane oxidation to acetic acid. MIL-53(Al)-Cu(OH) with a maximum productivity of 4,20,000 $mmol_{CH_3CO_2H}$ mol_{Cu}^{-1} exceeds the performance of all previously reported catalysts composed solely of abundant metals for methane oxidation to CH_3CO_2H (Table 3.11).

3.2.3 Control experiments

Several controlled experiments were conducted to identify the actual catalytic species responsible for MIL-53(Al)-Cu(OH) catalyzed oxidation of methane to acetic acid. No acetic acid was detected when the reaction was conducted without a catalyst or without O_2 (entries 2 and 3, Table 3.2). In addition, the catalytic reaction under N_2 instead of CH_4 did not produce any carbon-containing products, confirming CH_4 as the exclusive carbon source for acetic acid formation (entry 11, Table 3.3). The production of CH_3CO_2H at 175 °C via CH_4 oxidation using O_2 was further confirmed using isotopically labeled $^{13}CH_4$. The reaction

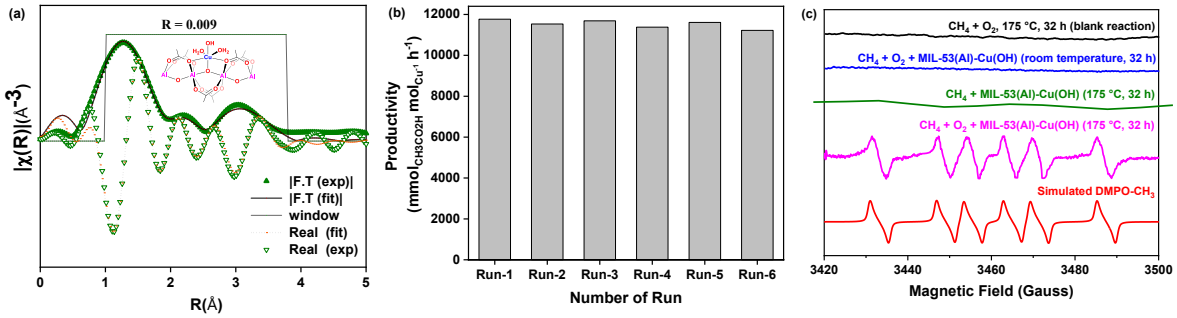


Figure 3.4: (a) EXAFS spectra and fits in R-space at the Cu K-edge of MIL-53(Al)-Cu after catalysis with the magnitude and real component of the Fourier transformation shown as solid and hollow triangles in green color, respectively. The fitting range in R-space is 1.1-3.8 Å (within the grey line). (b) Plot of productivity of acetic acid in various runs during recycling and reuse of the MIL-53(Al)-Cu(OH) catalyst for the methane oxidation reaction. (c) X-band (9.85 GHz) EPR spectroscopic spin-trapping experiments. EPR spectrum from the DMPO spin-trapping experiment of uncatalyzed methane oxidation by O_2 at 175 °C (black), MIL-53(Al)-Cu(OH)-catalyzed oxidation of methane by O_2 at room temperature (blue), MIL-53(Al)-Cu(OH) catalyzed methane oxidation in the absence of O_2 at 175 °C (green), MIL-53(Al)-Cu(OH) catalyzed oxidation of CH_4 (30 bar) by O_2 (10 bar) at 175 °C for 32 h (magenta), and simulated DMPO-CH_3 (red).

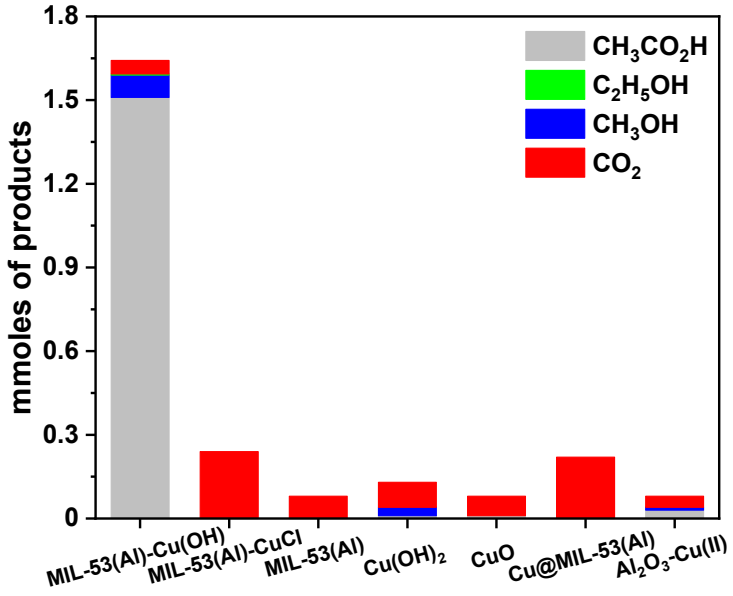


Figure 3.5: Comparison of the catalytic efficiency of MIL-53(Al)-Cu(OH) with other materials in direct methane oxidation to acetic acid under identical reaction conditions. Conditions: 30 bar CH_4, 10 bar O_2, 175 °C and 32 h.

catalyzed by MIL-53(Al)-Cu(OH) generated $^{13}CH_3{}^{13}CO_2H$, as verified by carbon-13 nuclear magnetic resonance (13C NMR) spectroscopy and gas chromatography-mass spectrometry (GC-MS) (Figure 3.25). It is noteworthy that the methane oxidation reaction ceased upon removal of the solid MIL-53(Al)-Cu(OH) MOF from the reaction mixture, confirming the embedding of the active catalytic species within the MOF (Figure S6, ESI†). Importantly, $Cu(OH)_2$ and CuO proved to be inactive for methane oxidation under identical reaction conditions (entries 8 and 14, Table 3.3 or Figure 3.5). Similarly, the pristine MIL-53(Al) MOF, MIL-53(Al)-CuCl, MIL-53(Al) encapsulated Cu(0) nanoparticles [Cu@MIL-53(Al)], or alumina-supported Cu(II) also failed to yield acetic acid under identical reaction conditions and Cu-loading, underscoring that Cu(OH) confined within the MIL-53(Al) MOF pores is the genuine catalytic species for methane oxidation (entries 2, 4, 15, and 7, Table 3.3 or Figure 3.5). Moreover, the PXRD patterns of the MOF recovered after catalysis showed no characteristic peak of Cu nanoparticles at higher 2θ angles (Figure 3.2a).

To investigate the impact of pore sizes of the MIL-53(Al) MOF on acetic acid selectivity, we synthesized isoreticular DUT-5(Al)-Cu(OH), which has a larger pore size (0.78 nm) than MIL-53(Al)-Cu(OH) (0.6 nm). Under identical reaction conditions and equivalent Cu loading, DUT-5(Al)-Cu(OH) exhibited lower acetic acid selectivity, producing only 0.08 mmol of acetic acid, 0.04 mmol of methanol, and a higher amount of CO_2 (0.9 mmol). These experiments suggest that the increased selectivity for acetic acid associated with smaller pore sizes of MIL-53(Al)-Cu(OH) is likely due to internal mass transfer limitation of the product. The larger channels of DUT-5(Al) allow acetic acid molecules to diffuse more easily, which can lead to their over-oxidation. In contrast, the smaller pore size of MIL-53(Al)-Cu(OH) restricts the diffusion of larger acetic acid molecules (5.9 Å), allowing only smaller molecules like methane (3.8 Å) to access the catalytic copper sites within the pores. This internal mass transfer limitation effectively enhances the production of acetic acid with excellent selectivity by preventing its over-oxidation within the pores of MIL-53(Al)-Cu(OH). Thus, under identical conditions with equivalent copper loading, MIL-53(Al)-Cu(OH) demonstrates greater reactivity and selectivity for acetic acid production compared to MIL-53(Al)-CuCl, $Cu(OH)_2$, CuO, Al_2O_3-supported Cu(II), and DUT-5(Al)-Cu(OH). This emphasizes the critical role of the MOF's node-supported single-site mono-Cu^{II}(OH) species confined within the uniform pores in chemoselective oxidation of methane.

3.2.4 Mechanistic exploration of MIL-53(Al)-Cu(OH) catalyzed oxidation of methane to acetic acid

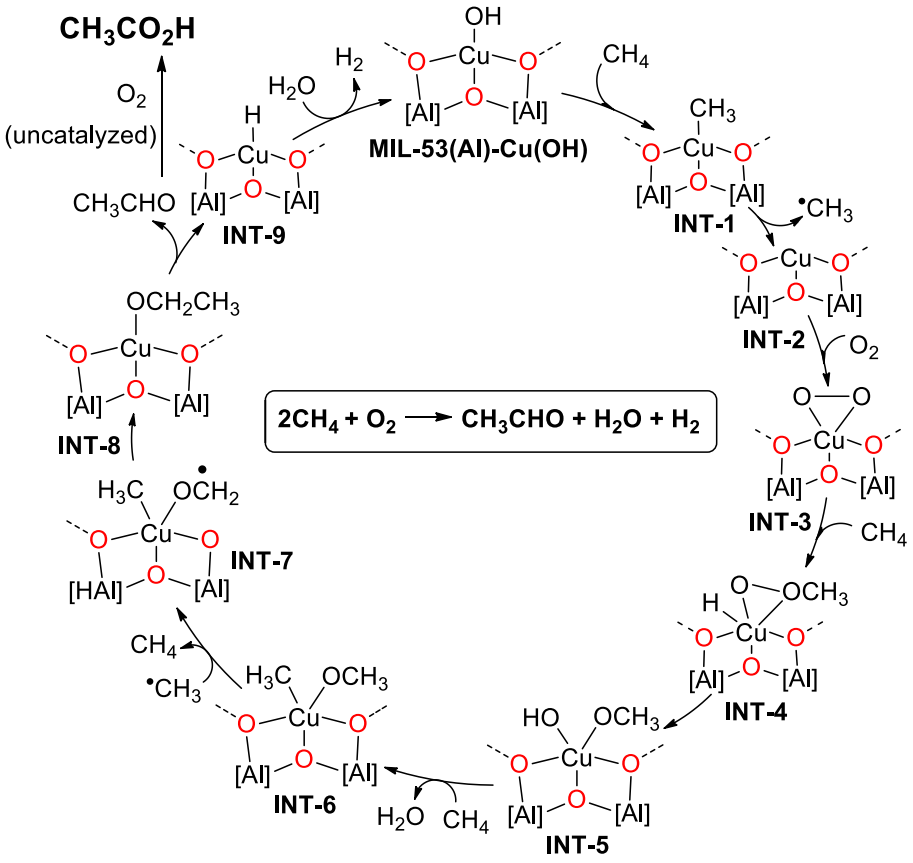


Figure 3.6: The proposed catalytic cycle for MIL-53(Al)-Cu(OH) catalyzed direct oxidation of methane to acetic acid using O_2.

To investigate the mechanism for MIL-53(Al)-Cu(OH)-catalyzed oxidation of methane to acetic acid, the oxidation state and coordination environment of the MOF recovered after catalysis were analyzed. The XPS of recovered MIL-53(Al)-Cu confirmed the +2 oxidation state of Cu ion in the MOF after catalysis (Figure 3.2c). The K-edge energy of 8985.6 eV for the recovered MOF also showed that Cu is in a +2 oxidation state, having an octahedral geometry. (Figure 3.2e).[58] The prediction of the geometries can be further established by the white line intensity. The K edge energy is attributed to the transition from 1s - $4p_{xy}$, while the transition from 1s - $4p_x$ is associated with white line intensity. The increase in axial co-ordination led to the increased in white line intensity of the recovered MOF. The EXAFS data of the MOF recovered after catalysis fitted well with the DFT-optimized model of MIL-53(Al)-Cu(OH)$(OH_2)_2$, which suggests that Cu in the MOF recovered after catalysis adopted a distorted octahedral geometry (Figure 3.19). Additionally, fitting the

EXAFS spectra with the DFT model of MIL-53(Al)-Cu(OH) containing 5-80% CuO or 5-80% metallic Cu showed significant deviations and elevated R factors, indicating the absence of any Cu nanoparticles or CuO within the MOF post catalysis (Figure 3.21). These findings demonstrate that Cu nanoparticles or CuO do not serve as the active catalytic species in the oxidation of methane. Instead, they highlight the pivotal role of single-site Cu(OH) species supported on the MOF nodes in driving the chemoselective oxidation of methane.

Radical trap experiments were conducted to explore the involvement of $^{\cdot}OH$ or $^{\cdot}CH_3$ radical in MIL-53(Al)-Cu(OH) catalyzed oxidation of methane using O_2. The rate of acetic acid production remained unchanged in the presence of $^{\cdot}OH$ scavengers such as Na_2SO_3 or tert-butanol (entry 5 and 20, Table 3.3), eliminating the role of $^{\cdot}OH$ in conversion of methane to acetic acid using O_2. However, radical trapping experiments conducted with a $^{\cdot}CH_3$ scavenger, such as TEMPO (2,2,6,6-tetramethylpiperidine 1-oxyl), showed a reduction in acetic acid formation to 0.34 mmol (entry 22, Table 3.3) under the identical reaction conditions, which indicates the involvement of $^{\cdot}CH_3$ radicals in the reaction mechanism. The potential free radicals generated during the reaction were captured using the spin-trapping agent 5,5-dimethyl-1-pyrroline N-oxide (DMPO). The EPR spectrum of MIL-53(Al)-Cu(OH)-catalyzed methane oxidation in the presence of O_2 and DMPO at ambient temperature did not show any $^{\cdot}CH_3$ radicals (Figure 3.4c). However, the supernatant after catalysis by MIL-53(Al)-Cu(OH) at 175 °C with DMPO revealed a six-line signal characteristic of the DMPO-CH_3 radical adduct, closely matching the simulated model (Figure 3.4c and Table 3.10). In both cases there were no $^{\cdot}OH$ and $H_2O^{\cdot}$ radicals detected, aligning with the observation that acetic acid formation cannot be suppressed by $^{\cdot}OH$ scavengers such as Na_2SO_3 or *t*-butanol. These experiments suggest that the $^{\cdot}CH_3$ is involved in the CH_4 oxidation to acetic acid. No radical adduct was observed in the absence of MIL-53(Al)-Cu(OH) (Figure 3.4c), indicating that CH_4 activation requires Cu-active sites. Importantly, no $^{\cdot}CH_3$ signal was observed when the reaction was done in the absence of O_2 at 175 °C, suggesting methyl radical is only generated by the CH_4-loaded MIL-53(Al)-Cu(OH) MOF in presence of O_2 at 175 °C. Based on the above spectroscopic and experimental observations, we propose that MIL-53(Al)-Cu(OH) initially reacts with CH_4 to form MIL-53(Al)-$Cu^{II}(CH_3)$ (INT-1) and H_2O via σ-bond metathesis between Cu-OH and C-H bonds (Figure 3.6). Since the direct insertion of triplet O_2 into Cu-CH_3 bond of INT-1 is spin-forbidden,[59;60] we propose that

INT-1 undergoes homolytic cleavage at 175 °C, forming a Cu(I) species (INT-2) and a $^{\cdot}CH_3$ radical. INT-2 then reacts with O_2 to give a Cu-$OO^{\cdot}$ species, which undergoes spin crossover to generate Cu(III)-η^2-peroxy species (INT-3).[61;62] In the next step, INT-3 participates in σ-bond metathesis with CH_4, resulting in the formation of INT-4. INT-4 rearranges to form INT-5, which undergoes σ-bond metathesis with CH_4, producing INT-6. Subsequently, a previously generated $^{\cdot}CH_3$ radical abstracts a hydrogen from the methoxy group of INT-6, yielding INT-7 and CH_4. INT-7 then rearranges to form INT-8, which undergoes β-hydride elimination, producing acetaldehyde and MIL-53(Al)-Cu-H (INT-9). Hydrolysis of INT-9 regenerates MIL-53(Al)-Cu(OH), and thus completing the catalytic cycle (Figure 3.6).

The acetaldehyde is subsequently oxidized by O_2 to give acetic acid. In order to confirm the role of MIL-53(Al)-Cu(OH) in the transformation of acetaldehyde to acetic acid, we conducted an experiment where we oxidized acetaldehyde under 10 bar of O_2 and 30 bar of N_2 at 175 °C in the presence or absence of the MOF catalyst. The results of these reactions revealed that the rate of oxidation of acetaldehyde to acetic acid remained unchanged in both cases, ruling out the involvement of MIL-53(Al)-Cu(OH) in the oxidation of acetaldehyde (entry 18-19, Table 3.3). In addition, small quantity of acetaldehyde was detected in the GC-FID spectrum, when the reaction was conducted for a shorter duration (18 h), which suggests that acetaldehyde might be a potential reaction intermediate in the methane to acetic acid conversion. Furthermore, the formation of the stoichiometric amount of H_2 with respect to acetic acid further supports the balanced chemical equation depicted in Figure 3.6. According to this equation, MIL-53(Al)-Cu(OH) catalyzed reaction between methane and O_2 first produces acetaldehyde, water and H_2. Then, the *in situ* generated acetaldehyde is oxidized by O_2 to furnish acetic acid.

We then attempted to synthesize potential intermediates to further support our proposed catalytic cycle. We synthesised MIL-53(Al)-Cu(OC_2H_5) (INT-8), by treating MIL-53(Al)-CuH with ethanol and tested its catalytic activity. Notably, MIL-53(Al)-Cu(OH) and MIL-53(Al)-Cu(OC_2H_5) shows similar catalytic activities in the oxidation of methane to acetic acid under identical reaction conditions, indicating MIL-53(Al)-Cu(OC_2H_5) as a potential intermediate, and supporting our proposed catalytic cycle (Entry 21, Table 3.3). Furthermore, reaction of ethanol and O_2 also gives 0.35 mmol CH_3CO_2H under identical reaction conditions in the presence of MIL-53(Al)-Cu(OH) (entry 12, Table 3.3), suggesting

that the small amount of ethanol generated during the reaction is oxidized to acetic acid.

Several controlled experiments were carried out to assess the involvement of *in situ* generated CO, CO_2, methanol as potential intermediates in the formation of CH_3CO_2H. The reaction between CH_4 and CO or CH_4 and CO_2 did not result in the formation of CH_3CO_2H (entry 9 and 13, Table 3.3), ruling out acetic acid production via methane carbonylation or the reaction of methane with CO_2. Additionally, the reaction between methanol and CO also failed to produce any significant amount of CH_3CO_2H (entry 17, Table 3.3), excluding the possibility of acetic acid formation through methanol carbonylation.

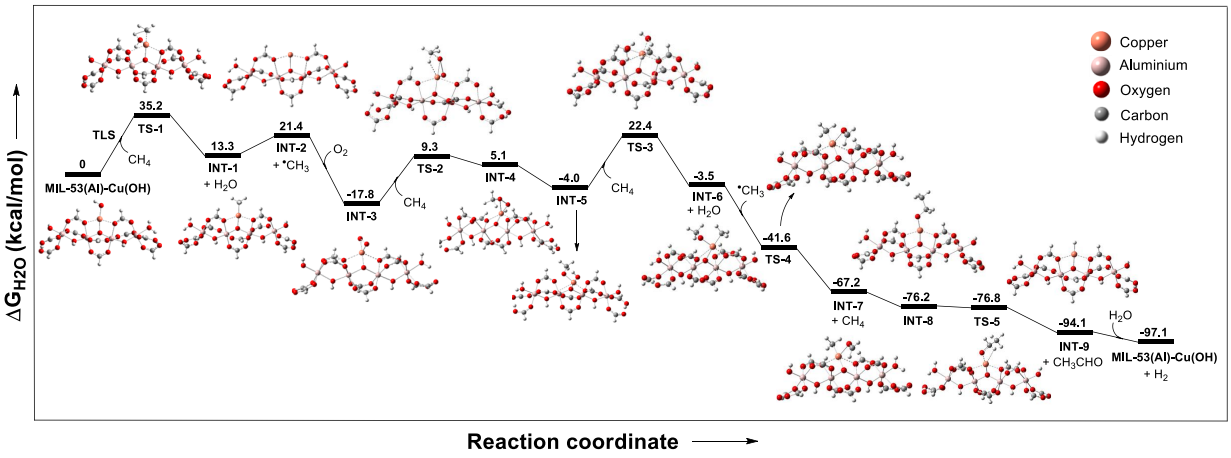


Figure 3.7: DFT calculated free energy diagram at 448 K for MIL-53(Al)-Cu(OH) catalyzed methane to acetaldehyde conversion.

Based on the above observations, we proposed CH_4 is oxidised to CH_3CO_2H in presence of O_2 via $^{\cdot}CH_3$ radical pathway with ethanol and acetaldehyde as the key intermediates. To further explore the reaction mechanism and identify the turnover-limiting step (TLS), the complete catalytic cycle was examined through DFT calculations (Figure 3.7). The DFT-calculated energy profile diagram indicates that methane C-H bond activation through σ-bond metathesis has an energy barrier of 35 kcal/mol, while the formation of INT-1 from MIL-53(Al)-Cu(OH) is endergonic by 13.3 kcal/mol. The subsequent homolytic cleavage of INT-1 to form INT-2 (Cu^+ species) and a methyl radical is endergonic by 8.1 kcal/mol. INT-2 reacts with O_2 to form a Cu-$OO^{\cdot}$ species which is exergonic by 35.6 kcal/mol, and this process is followed by a spin crossover to form INT-3 (Cu(III)-η^2-peroxy species), with a barrier of 6.8 kcal/mol. INT-3 undergoes σ-bond metathesis with CH_4 through TS-2, leading to the formation of INT-4 with an energy barrier of 27.1 kcal/mol. INT-4 rearranges to form

INT-5, which is exergonic by 4.2 kcal/mol, and INT-5 undergoes another -bond metathesis via TS-3 to generate INT-6 with a barrier of 26.4 kcal/mol. The $^{\cdot}CH_3$ abstracts a hydrogen atom from the methoxy group of INT-6, generating INT-7, which is exergonic by 63.7 kcal/mol. INT-7 then rearranges to form INT-8, which is exergonic by 9 kcal/mol. Finally, INT-8 undergoes beta hydride elimination via TS-4, which is exergonic by 17.9 kcal/mol to yield acetaldehyde and MIL-53(Al)-CuH species (INT-9). The MIL-53(Al)-CuH is then hydrolysed to regenerate the catalyst MIL-53(Al)-Cu(OH), an exergonic process by 3 kcal/-mol. The energy profile diagram reveals that methane C-H bond activation through σ-bond metathesis presents the highest energy barrier in the catalytic cycle, identifying it as the turnover-limiting step. As mentioned earlier that no methyl radical was detected in the EPR spectrum of DMPO-loaded reaction mixture of methane (30 bar) and MIL-53(Al)-Cu(OH) catalyst in the absence of O_2, despite the fact that $^{\cdot}CH_3$ is likely forming prior to the addition of O_2 as shown in the catalytic cycle. The DFT calculated energy profile diagram showed that the conversion of INT-1 to INT-2 is thermodynamically uphill by 8.1 kcal/mol. Therefore, the concentration of $^{\cdot}CH_3$ remains very low in the absence of O_2. However, during the methane oxidation in presence of O_2, INT-2 rapidly reacts with O_2 to give INT-3, which is highly exergonic nature of this step (downhill by 39.2 kcal/mol). This mechanistic insight, supported by DFT and experimental evidence, underscores the critical role of O_2 in driving the reaction forward and aligns with the observed catalytic behavior of the system.

3.3 Experimental Section

3.3.1 Synthesis of MIL-53(Al) and MIL-53(Al)-Cu(OH)

Synthesis of MIL-53(Al).[51]

MIL-53(Al) was synthesized via a solvothermal reaction of 1,4-benzenedicarboxylic acid and $AlCl_3.6H_2O$ in DMF. 1,4-Benzenedicarboxylic acid (0.050 g, 0.301 mmol) and $AlCl_3.6H_2O$ (0.048 g, 0.198 mmol) were dissolved in 3 mL DMF in a glass vial and the resultant mixture was stirred for 2 h. The solution was transferred to a hydrothermal bomb with a Teflon liner and kept it in a preheated oven at 120 °C for 48 h. After cooling to room temperature, the white solid was collected via centrifugation, which was washed several times with DMF. Finally, the resultant white crystalline solid of MIL-53(Al) was washed and stored in THF.

Synthesis of MIL-53(Al)-CuCl.

n-BuLi (50 μL, 1.65 M in cyclohexane) was added to the slurry of MIL-53(Al) (0.015 g, 0.072 mmol) in 1 ml THF in a vial, and the mixture was stirred for 1.5 h at room temperature inside the glovebox. The solid was washed with THF several times to remove the excess *n*-BuLi. A THF solution of $CuCl_2$ (0.042 g, 0.312 mmol) was added to the brown solid of MIL-53(Al)-Li, and the mixture was stirred overnight at room temperature. The MIL-53(Al)-CuCl was obtained as crystalline green solid and washed with THF several times.

Synthesis of MIL-53(Al)-Cu(OH).

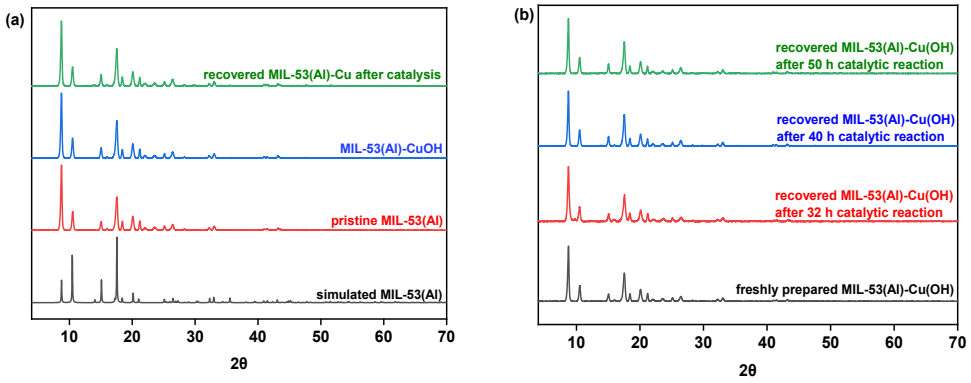


Figure 3.8: PXRD patterns of (a) simulated MIL-53(Al) MOF (black), pristine MIL-53(Al) (red), MIL-53(Al)-CuOH (blue), recovered MIL-53(Al)-Cu after methane oxidation for 32 h at 175 °C (run 1) (green), and 200 °C (magenta). (b) freshly prepared MIL-53(Al)-Cu(OH) (black), recovered MIL-53(Al)-Cu after 32 h of catalysis (red), 40 h of catalysis (blue), 50 h of catalysis (green); reaction conditions: 30 bar CH_4, 10 bar O_2, 175 °C and 7 mL water. The PXRD patterns indicate that the crystallinity and the framework of MIL-53(Al) MOF remained intact even after 50 h reaction.

Inside the glovebox, $NaEt_3BH$ (40 μL, 1 M in THF) was added dropwise to the vial containing slurry of MIL-53(Al)-CuCl (0.016 g) in 3 mL THF and was kept at room temperature for 1 h. The resultant dark purple solid of MIL-53(Al)-CuH was separated via centrifugation and washed several times with THF to remove excess $NaEt_3BH$. MIL-53(Al)-CuH was taken out of the glovebox and was kept in water for 30 minutes to afford MIL-53(Al)-Cu(OH).

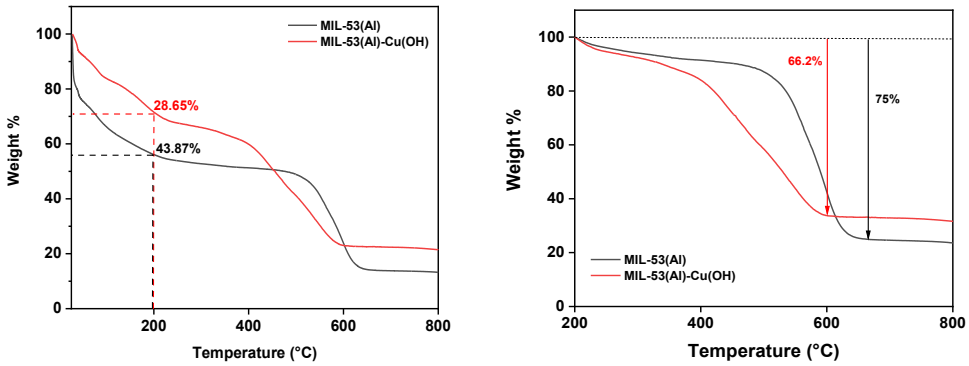


Figure 3.9: (a) TGA curve of freshly prepared MIL-53(Al) (black) and MIL-53(Al)-Cu(OH) (red). A solvent weight loss of 43.9% in MIL-53(Al) (black) and 28.7% in MIL-53(Al)-Cu(OH) (red) was observed from 40 °C to 200 °C. (b) TGA curve of freshly prepared MIL-53(Al) (black) and MIL-53(Al)-Cu(OH) (red) from 200-700 °C. The increased weight of MIL-53(Al)-Cu(OH) is due to the presence of Cu within the MOF.

Table 3.1: Determination of defect sites in MIL-53(Al) and MIL-53(Al)-$Cu(OH)_2$ MOF by TGA analysis.

Sample	**Condition**	**% Solvent**	**% Linker**	**% Residue**
	Calculated	–	75.5	24.5
MIL-53(Al)	TGA	44	42	14
	Corrected	–	75	25
	Calculated	–	69.2	30.8
MIL-53(Al)-$Cu(OH)_2$	TGA	29	47	24
(24% Cu-loading)	Corrected	–	66	34

The MIL-53(Al)-Cu(OH) has 24% copper loading with respect to μ_2-OH as analyzed by ICP-OES. This corresponds to the formula $AlO_{5.24}C_8H_5Cu_{0.24}$. TGA analysis showed that MIL-53(Al)-CuOH had 29% solvent weight (Figure 3.9).

Theoretical Calculation

(a) For MIL-53(Al) with formula AlOH)(BDC):

$$1 \text{ mole of Al(OH)(BDC)} = 0.5 \text{ moles } Al_2O_3$$

$$208.1 \text{ g of AlOH(BDC)} = 50.98 \text{ g } Al_2O_3$$

$$\% \text{ Linker} = \left(\frac{50.98}{208.1}\right) \times 100 = 24.5\%$$

$$\% \text{ Residue} = 100 - 24.5 = 75.5\%$$

(b) For MIL-53(Al)-Cu(OH) with formula $[AlOH_{0.71}BDC[OCu(OH)]_{0.24}]$:

$$1 \text{ mole of } Al(OH)_{0.71}BDC[OCu(OH)]_{0.24} = 0.5 \text{ moles } Al_2O_3 \text{ and } 0.24 \text{ moles CuO}$$

$$227.19 \text{ g of } AlOH_0.71(BDC)([OCu(OH)])_{0.24} = 50.98 \text{ g } Al_2O_3 \text{ and } 19.09 \text{ g CuO}$$

$$\% \text{ Residue} = \left(\frac{50.98 + 19.09}{227.19}\right) \times 100 = 30.8\%$$

$$\% \text{ Linker} = 100 - 30.8 = 69.2\%$$

The wt% ligand calculated theoretically matches closely with that of wt% ligand observed experimentally for MIL-53(Al) and MIL-53(Al)-Cu(OH) MOFs. This indicates the absence of any missing-linker defects within MIL-53(Al) and MIL-53(Al)-Cu(OH) MOFs.

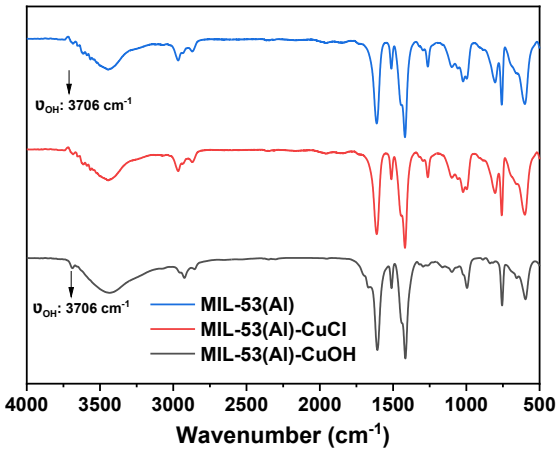


Figure 3.10: IR spectra of freshly prepared MIL-53(Al) (blue), MIL-53(Al)-CuCl (red), and MIL-53(Al)-CuOH (black). In the IR spectra, μ_2-OH stretching frequency peak of MIL-53(Al) at 3706 cm^{-1} disappeared upon metalation, however, a small peak of μ_2-OH reappeared for MIL-53(Al)-Cu(OH) due to protonation of unreacted μ_3-OLi with water. The peak intensity of μ_2-OH stretching frequency of MIL-53(Al)-CuOH at 3706 cm^{-1} was smaller compared to that of pristine MIL-53(Al) MOF due to the partial metalation of the μ_2-OH of the SBUs.

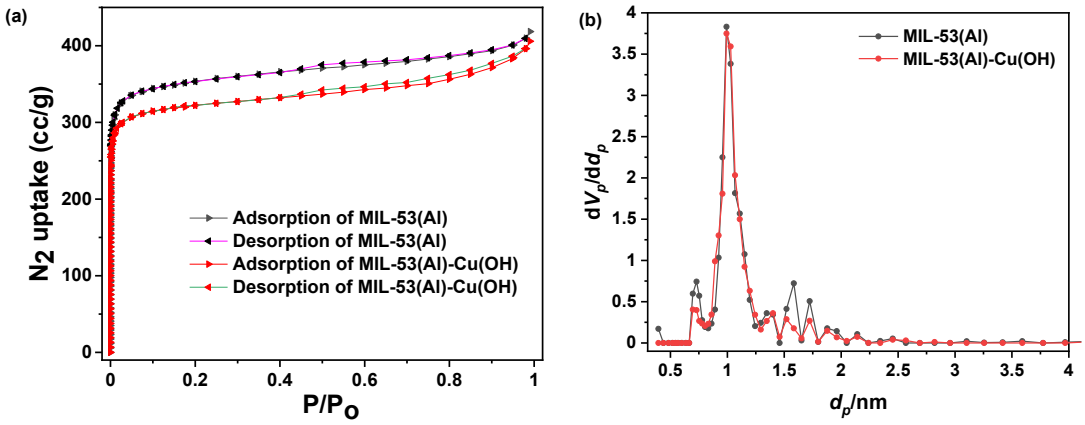


Figure 3.11: (a) N_2 sorption isotherms of MIL-53(Al) (black) and MIL-53(Al)-Cu(OH) (red) measured at 77 K. (b) NLDFT pore size distribution curve of MIL-53(Al) (black) and MIL-53(Al)-CuOH (red). BET surface for MIL-53(Al) and MIL-53(Al)-Cu(OH) are 1386 m^2/g and 1263 m^2/g and the average pore size for MIL-53(Al) and MIL-53(Al)-CuOH was determined to be 0.62 nm and 0.6 nm, respectively.

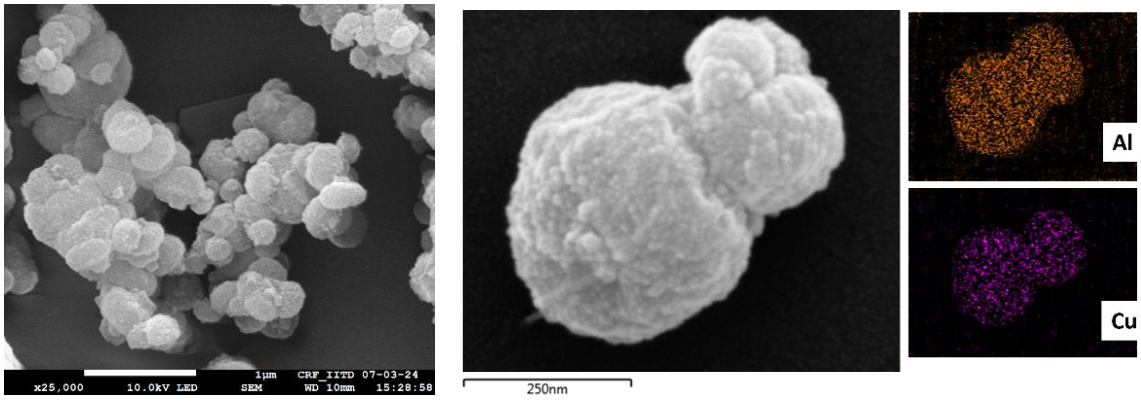
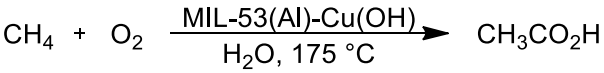


Figure 3.12: SEM image and EDX mapping for MIL-53(Al)-Cu(OH).The uniform distribution of Al and Cu suggests Al and Cu are homogeneously distributed throughout the MOF.

3.3.2 MIL-53(Al) catalysed oxidation of methane.

Standard procedure for MIL-53(Al) catalysed oxidation of methane to acetic acid using O_2.



A 1 mL slurry of MIL-53(Al)-Cu(OH) (3.8 mg, 4.0 μmol Cu) in water was transferred to a glass liner containing 6 mL of water. Then the glass liner was fitted into a high-pressure reactor. The high-pressure reactor was sealed and then purged with methane two times. The reactor was pressurized with 30 bar methane followed by 10 bar oxygen and then heated at 175 °C for 32 h without any mechanical stirring. After the reaction, the reactor was cooled to room temperature, and the gas was analysed directly by GC-TCD. A 1 mL of the aqueous solution was transferred to a centrifuge tube, which was centrifuged for 1 min. Then, 1 mL of the clear solution was quickly transferred to a GC vial and 5 μL of ethylene glycol (internal standard) was added. The sample was then analysed by GC-FID/MS to identify the products and their yields in the liquid phase. 1 μL sample was injected in GC and standard calibration curves were used for the quantification of acetic acid. MIL-53(Al)-Cu(OH) (3.8 mg, 4.0 μmol Cu) under 30 bar of CH_4 and 10 bar of O_2 for 32 h, at 175 °C yielded 1.51 mmol of acetic acid (Entry 1, Table 3.2). The GC-MS analysis detected minor quantities

of methanol (0.08 mmol) and ethanol (0.004 mmol), with no traces of formic acid or other oxygenated products.

Detection and quantification of liquid oxygenates.

GC-MS conditions: The column used was the Agilent DB-WAX column with 30 m length, 0.320 mm internal diameter, and 0.25 μm film. The chromatographic conditions were: flow rate of helium at 1 mL min^{-1}, injection volume: 1 μL, column oven temperature was initially 45.0 °C and then increased up to 230 °C with the rate of 5 °C per minute, and detector temperature was 250 °C.

GC-FID conditions: The column used was the Agilent DB-WAX column with 30 m length, 0.320 mm internal diameter, and 0.25 μm film. The chromatographic conditions were: flow rate of nitrogen at 1 mL min^{-1}, injection volume of 1 μL, column oven temperature at 40.0 °C for 4 minutes followed by 5 °C/min ramp to 70 °C and then followed by 35 °C/min ramp to 200 °C and finally a hold time of 5 minutes, and 19 min for total run time. The detector temperature was 250 °C. Products were quantified using a calibration plot of ethylene glycol as the internal standard.

Detection and quantification of methane and gaseous oxygenates.

GC-TCD conditions: The gas after catalysis was analysed by an Agilent GC (8890) equipped with a PoraPlot Q column in sequence with a molecular sieves column and a Thermal conductivity detector (TCD). The chromatographic conditions are as follows; Carrier gas: helium, Column: 45 °C, TCD: 250 °C, and Injection temperature: 100 °C. Retention time for CO_2, CH_4 and CO were 4 minutes, 9.3 minutes and 10.75 minutes, respectively. The methane conversion was calculated by determining the mmol of methane before and after the catalysis using a GC-TCD response factor-based calculation. For this calculation, a high-pressure reactor containing a glass liner was filled with 7 mL mixture of water and MIL-53(Al)-Cu(OH) catalyst, and then purged it with methane two times. Then pressurized it with 30 bar methane followed by 10 bar oxygen. The gas was analysed with GC-TCD at room temperature (35 °C) before catalysis to quantify the amount of methane in the

feed. The gas of the same high-pressure reactor was analysed after the reaction at room temperature (35 °C) to quantify the amount of unreacted methane after the catalysis and the other gaseous products. At the optimized reaction condition (entry 1, Table 3.2), the amount of methane was calculated as 34 mmol before catalysis and 30.8 mmol after catalysis. Therefore, the loss of methane during the reaction is 3.16 mmol and a methane conversion of 9.3%.

Procedure for taking gas sample.

First, the gas from the Parr reactor was filled in an evacuated Tedlar bag via making an air-tight fitting connection of Parr reactor outlet with the bag using a hose pipe. Then 2.5 mL from the bag was taken in an air-tight syringe and injected into GC for analysis. Then, the mmol of methane, CO and CO_2 was calculated. Separately, 2.5 mL of a known sample of a standard gas containing a specific composition of CO, CO_2 and CH_4 was also injected, which was used to calculate the individual gas (x) response factor (R_f) following the given formula. The detailed calculation to quantify the initial methane amount in the feed is as follows:

Step 1:

$$R_f(\text{methane}) = \frac{\text{Fraction of methane (g)}}{\text{Area of peak of methane in chromatogram (GC–TCD)}}$$

$$\text{Fraction of methane} = (\text{Volume injected (mL)}) \times (\text{Composition of methane in standard})$$

$$R_f(\text{methane}) = \frac{2.5 \times 10^{-4}\,\text{g}}{62,000}$$

$$R_f(\text{methane}) = 4.03 \times 10^{-9}\,\text{g}$$

Step 2: The volume of CH_4 in the unknown sample taken from the high-pressure reactor was measured. The injected volume of the unknown sample was also the same as that of the standard (2.5 mL).

$$\begin{aligned}\text{Amount of } CH_4 \text{ in unknown sample} &= R_f(CH_4) \times \text{Area of the peak of } CH_4 \text{ in chromatogram} \\ &= \left(4.03 \times 10^{-9}\,\text{g}\right) \times 178{,}000 \\ &= 7.18 \times 10^{-4}\,\text{g}\end{aligned}$$

Step 3:

$$\begin{aligned}\text{Molar mass of } CH_4 &= 16.04\,\text{g/mol} \\ \text{Moles of } CH_4 &= \frac{7.18 \times 10^{-4}}{16.04}\,\text{mol} \\ &= 44.75\,\mu\text{mol}\end{aligned}$$

So, the initial moles of CH_4 in 2.5 mL of the unknown gas sample were measured. This measurement is at atmospheric pressure and 308 K.

Subsequently, the initial amount of methane in the reactor before catalysis was calculated to be 34 mmol.

Using the similar method described above, the methane and other gaseous products were quantified after the catalysis.

Table 3.2: Optimization of catalytic conditions for MIL-53(Al)-Cu(OH) catalyzed oxidation of methane using O_2.[a]

Entry No.	**Temp.** (°C)	**P[CH_4] (bar), Initial mmol CH_4**	**P[O_2]** (bar)	**CH_3CO_2H** (mmol)[b]	**CH_3OH** (mmol)[b]	**C_2H_5OH** (mmol)[b]	**CO_2**[c] (mmol)
1	175	30, 34	10	1.51	0.08	0.004	0.048
2[d]	175	30, 34	10	0	0	0	0.04
3	175	30, 34	0	0	0	0	nd
4	100	30, 34	10	0.06	0.03	0	0.01
5	125	30, 34	10	0.42	0.09	0	0.019
6	150	30, 34	10	1.15	0.12	0.002	0.032
7	200	30, 34	10	0.72	0.06	0.001	0.84
8	175	30, 34	2	0.04	0.004	0	0.004
9	175	30, 34	4	0.21	0.007	0	0.008
10	175	30, 34	6	0.52	0.012	0	0.01
11	175	30, 34	8	0.87	0.038	0.001	0.02
12	175	10, 11	10	0.17	0.0089	0	0.01
13	175	20, 23	10	0.64	0.039	0	0.019
14	175	25, 29	10	0.97	0.056	0.003	0.024
15[e]	175	30, 34	10	0	0	0	0.001
16[f]	175	30, 34	10	0.18	0.01	0	0.002
17[g]	175	30, 34	10	0.38	0.018	0	0.016
18[h]	175	30, 34	10	0.72	0.29	0	0.04
19[i]	175	30, 34	10	1.68	0.12	0.005	0.17
20[j]	175	30, 34	10	1.61	0.18	0.01	0.244
22[k]	175	30, 34	10	0	0	0	0.45
23[l]	175	30, 34	10	0	0	0	nd
24[m]	175	30, 34	10	0	0	0	nd

[a] Standard conditions: 3.8 mg of MIL-53(Al)-Cu(OH) (4.0 μmol Cu), 7 mL H_2O, 32 h; N_2 balance was applied to optimize partial pressures of O_2 and CH_4 (entries 8–14), maintaining total reaction pressure at 40 bar; nd: not determined.
[b] Analysed by GC-FID using ethylene glycol as the internal standard.
[c] Analysed by GC-TCD.
[d] No catalyst was used.
[e] Reaction time was 1 h.
[f] Reaction time was 6 h.
[g] Reaction time was 12 h.
[h] Reaction time was 24 h.
[i] Reaction time was 40 h.
[j] Reaction time was 50 h.
[k] Toluene was used as the solvent.
[l] THF was used as the solvent.
[m] Heptane was used as the solvent.

Table 3.3: Control experiments for MIL-53(Al)-Cu(OH) catalyzed oxidation of methane to acetic acid.

Entry No.	**Temp.** (°C)	**P[CH_4] (bar), Initial mmol CH_4**	**P[O_2]** (bar)	**CH_3CO_2H** (mmol)[b]	**CH_3OH** (mmol)[b]	**C_2H_5OH** (mmol)[b]	**CO_2**[c] (mmol)
1	175	30	10	1.51	0.08	0.004	0.048
2[d]	175	30	10	0	0	0	0.08
3	175	30	0	0	0	0	0.02
4[e]	175	30	10	0	0	0	0.24
5[f]	175	30	10	1.51	0.078	0.003	0.061
6[g]	175	30	10	1.56	0.09	0.002	0.10
7[h]	175	30	10	0.03	0.01	0	0.04
8[i]	175	30	10	0.01	0.03	0	0.09
9[j]	175	30	0	0	0	0	nd
10[k]	175	30	10	1.61	0.07	-	0.052
11[l]	175	0	10	0	0	0	nd
12[m]	175	0	10	0.35	-	-	nd
13[n]	175	30	0	0.08	0	0	nd
14[o]	175	30	10	0.01	-	0	0.07
15[p]	175	30	10	0		0	0.22
16[q]	175	0	10	0.01	-	0.002	nd
17[r]	175	0	0	0.05	-	-	nd
18[s]	175	0	10	0.42	-	-	nd
19[t]	175	0	10	0.41	-	-	nd
20[u]	175	30	10	1.49	0.074	0.003	0.049
21[v]	175	30	10	1.61	0.02	NA	nd
22[w]	175	30	10	0.34	-	-	nd
23[x]	175	30	10	0.08	0.04	-	0.9
24	175	30	15	0.46	0.02	-	0.72

a Standard conditions: 3.8 mg of MIL-53(Al)-Cu(OH) (4.0 μmol Cu), 7 mL H_2O, 32 h; N_2 balance applied to keep constant pressure of 40 bar; nd: not determined; NA: not applicable.

b Analysed by GC-FID using ethylene glycol as the internal standard.

c Analysed by GC-TCD.

d MIL-53(Al) was used.

e MIL-53(Al)-CuCl was used.

f Na_2SO_3 was used as an $^{\cdot}OH$ scavenger.

g 7.6 mg of MIL-53(Al)-Cu(OH) was used (8.0 µmol Cu).

h 6.0 mg Al_2O_3 supported Cu(II) (4.0 µmol Cu).

i 1 mg $Cu(OH)_2$ (10.24 µmol Cu).

j 10 bar CO was used as the oxidant.

k 0.5 mmol ethanol was added to the reaction mixture.

l Nitrogen was used instead of methane.

m Oxidation of 1.5 mmol ethanol using 10 bar O_2.

n 10 bar CO_2 used as oxidant.

o CuO (1 mg, 12.6 µmol Cu).

p Cu@MIL-53(Al) (4.0 µmol Cu).

q Oxidation of 0.5 mmol methanol.

r Oxidation of 1.5 mmol methanol using 1 bar CO.

s Oxidation of 0.5 mmol acetaldehyde (5 h); reaction time: 5 h.

t Same as above, no catalyst.

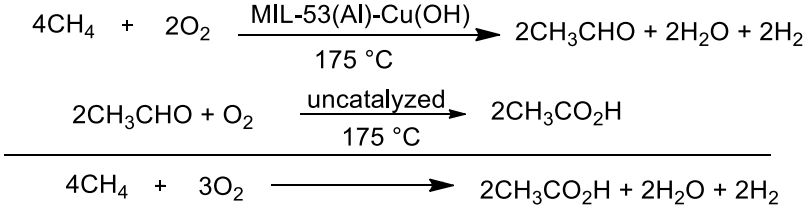
u *t*-Butanol used as $^{\cdot}OH$ scavenger.

v MIL-53(Al)-Cu(OC_2H_5) (4.0 µmol Cu) was used as the catalyst. .

w TEMPO used as a radical scavenger.

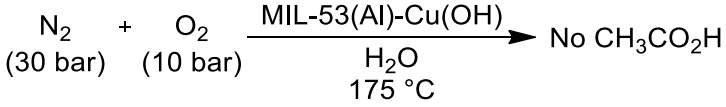
x DUT-5(Al)-Cu(OH) (4.0 µmol Cu) was used as the catalyst.

Under optimized reaction conditions (30 bar CH_4, 10 bar O_2, 175 °C, 32 h), 1.51 mmol of acetic acid, 0.08 mmol of methanol, 0.004 mmol of ethanol, and 0.048 mmol of CO_2 were formed. The total carbon balance was confirmed, as 3.2 mmol of methane was consumed, yielding 3.16 mmol of carbon-containing products (carbon balance of 98.75%). Additionally, 1.4 mmol of H_2 was generated as a side product, further supporting our proposed mechanism. Initially, methane reacts with O_2 to produce acetaldehyde, water, and hydrogen. The acetaldehyde is then converted into acetic acid in the presence of O_2.



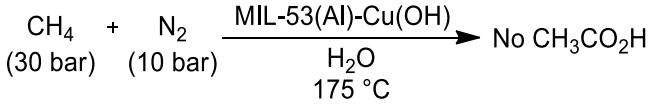
Proposed experiments for MIL-53(Al)-Cu(OH) catalyzed oxidation of methane.

Blank reaction with O_2 under N_2 without methane.



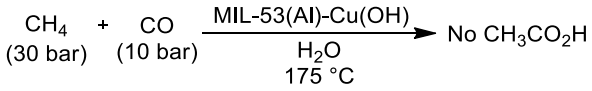
Reaction conditions: 3.8 mg of MIL-53(Al)-Cu(OH) (4.0 μmol Cu), 7 mL H_2O, 30 bar N_2, 10 bar O_2, 32 h. General procedure mentioned in Section 3.3.2. was followed replacing methane with nitrogen. No liquid products were detected (Entry 11, Table 3.3, suggesting CH_4 as the sole carbon source for CH_3CO_2H production in the MIL-53(Al)-Cu(OH) catalyzed methane oxidation.

Blank reaction without O_2 under N_2.



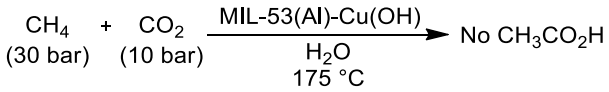
Reaction conditions: 3.8 mg of MIL-53(Al)-Cu(OH) (4.0 μmol Cu), 7 mL H_2O, 30 bar CH_4, 10 bar N_2, 32 h. General procedure mentioned in Section 3.3.2 was followed replacing oxygen with nitrogen. No liquid products were detected (Entry 3, Table 3.2, suggesting O_2 as the only oxidant for CH_3CO_2H production in the MIL-53(Al)-Cu(OH) catalyzed methane oxidation.

Reaction of methane in presence of CO using MIL-53(Al)-Cu(OH).



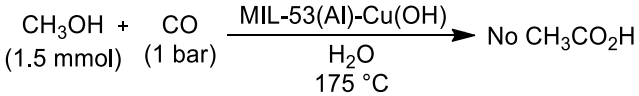
Reaction conditions: 3.8 mg of MIL-53(Al)-Cu(OH) (4.0 μmol Cu), 7 mL H_2O, 30 bar CH_4, 10 bar CO, 32 h. General procedure mentioned in Section 3.3.2 was followed replacing oxygen with carbon monoxide. In this reaction, no acetic acid (Entry 9, Table 3.3) was formed which rules out the formation of acetic acid via reaction of methane carbonylation with CO at 175 °C.

Reaction of methane in presence of CO_2 using MIL-53(Al)-Cu(OH).



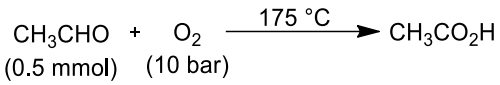
Reaction conditions: 3.8 mg of MIL-53(Al)-Cu(OH) (4.0 μmol Cu), 7 mL H_2O, 30 bar CH_4, 10 bar CO_2, 32 h. General procedure mentioned in Section 3.3.2 was followed replacing oxygen with carbon dioxide. In this reaction, negligible acetic acid (Entry 13, Table 3.3) was formed, which rules out the formation of acetic acid via methane carboxylation with CO_2 at 175 °C.

Reaction of methanol in presence of CO using MIL-53(Al)-Cu(OH).



Reaction conditions: 3.8 mg of MIL-53(Al)-Cu(OH) (4.0 μmol Cu), 7 mL H_2O, 1.5 mmol methanol, 1 bar CO, 32 h. General procedure mentioned in Section 3.3.2 was followed replacing oxygen with carbon monoxide and methane with methanol. In this reaction, no significant amount of acetic acid (Entry 18, Table 3.3) was formed. We thus conclude that MIL-53(Al)-Cu(OH) catalyzed methane oxidation does not occur via the reaction of insitu generated methanol and CO.

Reaction of acetaldehyde in presence of O_2 in the absence of MIL-53(Al)-Cu(OH).



Reaction conditions: 7 mL H_2O, 0.5 mmol acetaldehyde, 10 bar O_2, 32 h. General procedure mentioned in Section 3.3.2 was followed replacing methane with acetaldehyde and the reaction was done in the absence of the catalyst. In this reaction, 0.41 mmol of acetic acid (Entry 19, Table 3.3) was formed. We thus conclude that acetaldehyde formed gets oxidized to acetic acid without the aid of MOF catalyst.

Test for "heterogeneity of MIL-53(Al)-Cu(OH) in methane oxidation to acetic acid.

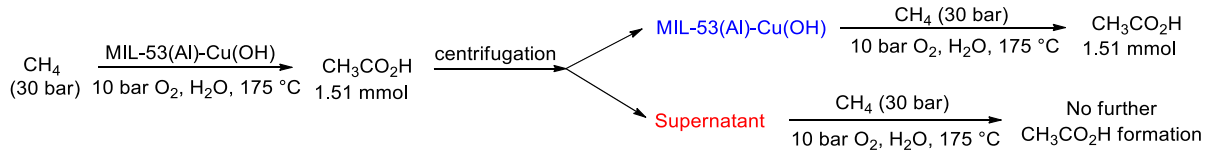
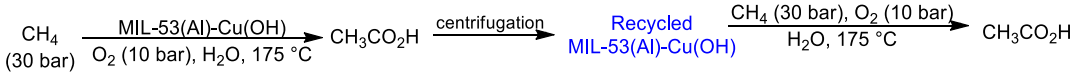


Figure 3.13: Heterogeneity test of MIL-53(Al)-Cu(OH) in the oxidation of methane.

General procedure mentioned in Section 3.3.2 was followed. After 32 h of reaction, the solid was centrifuged out of suspension. Two reactions were set up separately in two different high-pressure reactors with solid and supernatant. The extracted solid and supernatant were added into two separate glass liners. Then added 7 mL of water to the glass liner containing solid MOF. Then both the glass liners were fitted into two separate reactors. The reactors were sealed and purged them with methane. The reactors were pressurized with 30 bar methane and 10 bar oxygen and then heated at 175 °C for 32 h without any mechanical stirring. The reactor was cooled to room temperature, and gas was analysed directly with GC-TCD. The liquid phase of reactions was analysed with GC. No further acetic acid was produced in the reaction involving just the supernatant. While the other reaction containing the solid MOF yielded 1.51 mmol of acetic acid. This experiment excludes the potential of any leached Cu-species responsible for catalysis and confirms that solid MIL-53(Al)-Cu(OH) was the actual catalyst for the oxidation of methane.

Recycling of MIL-53(Al)-Cu(OH) for oxidation of methane.



The recycle and reuse experiment was conducted to check the stability of the MOF-catalyst. General procedure mentioned in Section 3.3.2 was followed, except the recovered MOF-catalyst was washed several times with water. It was added to the glass liner along with 7 mL H_2O. The glass liner was fitted into a high-pressure reactor which was then sealed and purged with CH_4 twice. The reactor was pressurized with 30 bar CH_4 followed by 10 bar O_2 and then heated at 175 °C. The procedure was repeated 6 times with very minimal % leaching of copper and aluminium (Table 3.4). The MOF retains its crystallinity and stability as can be seen by the PXRD patterns of the recycling experiments (Figure 3.8). The MOF could be recycled and reused at least 5 times without drop of activity giving a cumulative TON of 2204.

Table 3.4: mmol of acetic acid formed and the leaching of Cu in various runs of the recycling of MIL-53(Al)-Cu(OH) for the oxidation of methane.

No. of Run	Time (h)	Productivity ($mmol_{CH_3CO_2H}$ mol_{Cu}^{-1} h^{-1})	% Leaching (Al, Cu)
Run-1	32	11,767	0.05, 0.06
Run-2	32	11,533	0.03, 0.04
Run-3	32	11,689	0.03, 0.026
Run-4	32	11,377	–
Run-5	32	11,611	0.08, 0.05
Run-6	32	11,221	–

Comparison of catalytical activity between MIL-53(Al)-Cu(OH) and other materials for oxidation of methane with oxygen.

Cu(II)/Al_2O_3 catalyzed oxidation of methane. Al_2O_3 was activated at 150 °C under vacuum for 24 h. Then inside the glove box, *n*-BuLi (130 μL, 1.65 M in cyclohexane) was

added to activated alumina (30.0 mg) in 1 mL THF in a 5 mL glass vial and kept for stirring at room temperature for overnight. The solid was washed with the THF several times. The lithiated Al_2O_3 was treated with $CuCl_2$ (108 mg, 0.808 mmol) and stirred overnight. The excess of $CuCl_2$ was washed away with the multiple washing using THF. The metalated Al_2O_3 was dried, and the content of copper in Cu(II)/Al_2O_3 was determined to be 3.8 wt % via ICP-OES. $NaEt_3BH$ (36 μL, 1 M in toluene) was added dropwise into the vial containing Al_2O_3-CuCl (30.0 mg, 0.018 mmol Cu) as a slurry in 3 mL THF and the mixture was stirred gently at room temperature for 1 h. The light grey solid was washed with THF several times and then it was taken outside from the glovebox and added water to afford alumina-supported Cu(II) [Al_2O_3-Cu(II)], which was directly used for catalysis. General procedure mentioned in Section 3.3.2 was followed, using Cu(II)/Al_2O_3 (6.7 mg, 4.0 μmol Cu) instead of MIL-53(Al)-Cu(OH). Reaction conditions: Cu(II)/Al_2O_3 (6.7 mg, 4.0 μmol Cu), 7 mL water, 30 bar CH_4, 10 bar O_2, 175 °C, 32 h. Results are summarized in entry 7, Table 3.3, the major product was CO and CO_2 with CH_3CO_2H productivity of 233.8 $mmol_{product} \cdot mol_{Cu}^{-1} \cdot h^{-1}$ in case of Cu(II)/Al_2O_3 while 11,767.45 $mmol_{product} \cdot mol_{Cu}^{-1} \cdot h^{-1}$ using MIL-53(Al)-Cu(OH) (entry 1, Table 3.2). Al_2O_3-Cu(OH) is less active than MIL-53(Al)-Cu(OH).

CuO catalyzed methane oxidation. CuO nanoparticles were prepared according to the reported procedure.[63] $CuCl_2.2H_2O$ (1.70 g, 0.01 mole) was dissolved in 100 mL deionised water. 0.1 M NaOH solution was slowly added under vigorous stirring until the colour of the solution changed from blue to deep black and pH reached 14. Black precipitate of CuO nanoparticles was thus obtained and washed with water and ethanol. General procedure mentioned in Section 3.3.2 was followed, using CuO (1 mg, 12.6 μmol Cu) instead of MIL-53(Al)-Cu(OH). Reaction conditions: CuO (1 mg, 12.6 μmol Cu), 7 mL water, 30 bar CH_4, 10 bar O_2, 175 °C, 32 h. Results are summarized in entry 7, Table 3.3. No acetic acid was observed (Entry 14, Table 3.3).

Cu@MIL-53(Al) catalyzed methane oxidation. In a 5 mL round bottom flask, $CuCl_2 \cdot 2H_2O$ (50 mg, 0.18 mmol) was dissolved in ethyl acetate (2 mL), followed by the addition of the MIL-53(Al) (100 mg). The mixture was heated for 48 h at a temperature of 50 °C. After which the solid was collected after centrifugation and washed thoroughly and dried to give MIL-53(Al)-$CuCl_2$. $NaBH_4$ (10 mg) was added to 6 mL of deionized water

in a round-bottom flask, after which 80 mg of MIL-53(Al)-$CuCl_2$ was added. The pH was proposedled in the range of 6-8 throughout the addition of $NaBH_4$. The obtained mixture was stirred for 30 min, then was subject to filtration. The collected solid was washed thoroughly with deionized water to give black powder of Cu@MIL-53(Al).[64] The content of Cu in Cu@MIL-53(Al) is 4.2 wt%. General procedure mentioned in Section 3.3.2 was followed, using 6.1 mg Cu@MIL-53(Al) (4.0 μmol of Cu) instead of MIL-53(Al)-Cu(OH). Reaction conditions: 6.1 mg Cu@MIL-53(Al) (4.0 μmol of Cu), 7 mL water, 30 bar CH_4, 10 bar O_2, 175 °C, 32 h. CO and CO_2 were observed as significant products (Entry 15, Table 3.3) with no acetic acid observed in the liquid phase.

MIL-53(Al)-Cu(OC_2H_5) catalyzed methane oxidation. MIL-53(Al)-CuH was synthesised as per the method mentioned in Section 3.3.1, and was taken out of the glovebox and was kept in ethanol for 30 minutes to afford MIL-53(Al)-Cu(OC_2H_5). General procedure mentioned in Section 3.3.2 was followed, using MIL-53(Al)-Cu(OC_2H_5) (4.0 μmol of Cu) instead of MIL-53(Al)-Cu(OH). Reaction conditions: MIL-53(Al)-Cu(OC_2H_5) (4.0 μmol of Cu), 7 mL water, 30 bar CH_4, 10 bar O_2, 175 °C, 32 h. 1.61 mmol of acetic acid was observed (Entry 21, Table 3.3) in the liquid phase, confirming MIL-53(Al)-Cu(OC_2H_5) as one of the intermediate in the reaction pathway.

DUT-5(Al)-Cu(OH) catalyzed methane oxidation.

Synthesis of DUT-5(Al)-Cu(OH): DUT-5(Al) was synthesized via modifying the reported procedure.[65] A solution of 4,4'-bipenyldicarboxylic acid (0.100 g, 0.412 mmol) in 3 mL DMF was transferred to a vial containing a solution of aluminium chloride hexahydrate (0.064 g, 0.270 mmol) in 3 mL DMF and kept on stirring for 2 h. The solution was kept in a preheated oven at 120 °C in a Teflon lined hydrothermal autoclave for 48 h. After cooling to room temperature, the white solid was collected via centrifugation, which was washed with DMF several times. The PXRD pattern of DUT-5(Al) MOF matches well with the simulated PXRD of DUT-5(Al) (Figure 3.14). The resulting solid was stored in THF at room temperature to give DUT-5(Al) as a white solid with 58% yield. *n*-BuLi (0.235 mL, 1.65 M in cyclohexane) was added to the slurry of DUT-5(Al) (0.050 g, 0.17 mmol) in 1.5 mL THF in a vial, and the mixture was stirred for 1.5 h at room temperature inside the glovebox. The light brown solid was washed with THF several times to remove the excess *n*-BuLi. A THF solution of $CuCl_2.2H_2O$ (0.06 g, 0.34 mmol) was added, and the mixture

was stirred overnight at room temperature. The DUT-5(Al)-CuCl was centrifuged out of the suspension, and the resultant yellowish-green solid was washed with THF several times. Inside the glovebox, $NaEt_3BH$ (300 μL, 1 M in toluene) was added dropwise into a vial containing DUT-5(Al)-CuCl (0.080 g) as a slurry in 3 mL THF, and the mixture was kept at room temperature for 1 h. The resultant black solid of DUT-5(Al)-CuH was separated via centrifugation followed by washing with THF several times. DUT-5(Al)-CuH was taken outside of the glovebox and kept in water for 30 minutes to afford DUT-5(Al)-Cu(OH). 25% iron-loading with respect to the μ_2-OH moiety was analyzed by ICP-OES, giving an empirical formula of $C_{14}H_9O_{5.25}AlCu_{0.25}$.

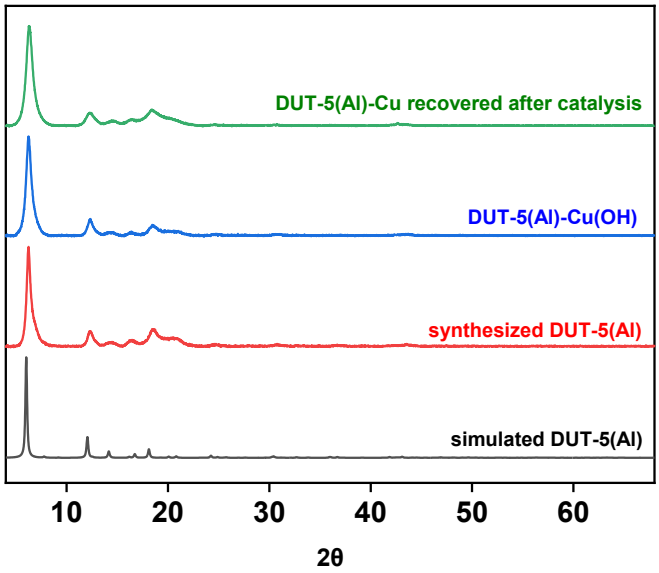


Figure 3.14: PXRD pattern of simulated DUT-5(Al) (black), synthesized DUT-5(Al) (red), DUT-5(Al)-Cu(OH) (blue), DUT-5(Al)-Cu MOF recovered after catalysis (green).

General procedure for methane oxidation mentioned in Section 3.3.2 was followed, using DUT-5(Al)-Cu(OH) (4.0 μmol of Cu) instead of MIL-53(Al)-Cu(OH). Reaction conditions: DUT-5(Al)-Cu(OH) (4.0 μmol of Cu), 7 mL water, 30 bar CH_4, 10 bar O_2, 175 °C, 32 h. 0.08 mmol of acetic acid along with 0.04 mmol of methanol was observed (Entry 21, Table 3.3) in the liquid phase, and 0.9 mmol of CO_2 in the gaseous phase. This reduction in selectivity can be attributed to increased diffusion of acetic acid into the larger pores of DUT-5(Al)-Cu(OH), where it undergoes further oxidation to CO_2. In contrast, MIL-53(Al) exhibits a unique diffusion profile that selectively facilitates the entry of methane (3.8 Å in diameter) to the catalytic sites while restricting the diffusion of larger products like acetic

acid (5.9 Å in diameter). Thus, the mass transfer limitations and pore size play a critical role in proposedling the reaction selectivity. By tuning the pore size, we can effectively control the diffusion of reactants and products, which is a key factor in maintaining high selectivity for acetic acid in methane oxidation reactions.

Radical scavenging experiment with MIL-53(Al)-Cu(OH) catalyst.

Radical scavenging experiment with Na_2SO_3. To investigate any role of $^{\cdot}OH$ in MIL-53(Al)-Cu(OH) catalysed methane to acetic acid conversion, we had performed the catalysis in presence of a known $^{\cdot}OH$ radical scavenger such as Na_2SO_3, and then catalytic activity and selectivity were compared to those of reactions done in absence of Na_2SO_3.

Reaction conditions: 3.8 mg of MIL-53(Al)-Cu(OH) (4.0 μmol Cu), 7 mL H_2O, 30 bar CH_4, 10 bar O_2, 32 h, Na_2SO_3 (250 mg, 1.98 mmol). General procedure mentioned in Section 3.3.2 was followed, and Na_2SO_3 (250 mg, 1.98 mmol) was added to study its effect on the catalytic reaction. The yield of acetic acid as determined by GC using ethylene glycol as the internal standard was 1.48 mmol, which is similar to that obtained without scavenger under identical reaction conditions (Entry 5, Table 3.2). We conclude that the presence of the $^{\cdot}OH$ radical scavenger (Na_2SO_3) does not affect the rate of the oxidation of methane to acetic acid catalysed by MIL-53(Al)-Cu(OH), which illustrates that $^{\cdot}OH$ radicals do not participate in the mechanism.

Radical scavenging experiment with TEMPO. To investigate any role of $\cdot CH_3$ in MIL-53(Al)-Cu(OH) catalysed methane to acetic acid conversion, we had performed the catalysis in presence of a known $^{\cdot}CH_3$ and $^{\cdot}OH$ radical scavenger such as TEMPO and then catalytic activity and selectivity were compared to those of reactions done in absence of $^{\cdot}OH$ radical scavengers.

General procedure mentioned in Section 3.3.2. was followed, and TEMPO (249.8 mg, 1.6 mmol) was added to study its effect on the catalytic reaction. Reaction conditions: 3.8 mg of MIL-53(Al)-Cu(OH) (4.0 μmol Cu), 7 mL H_2O, 30 bar CH_4, 10 bar O_2, 32 h, TEMPO (249.8 mg, 1.6 mmol). The yield of acetic acid as determined by GC using ethylene glycol as the internal standard was 0.34 mmol, which is significantly lower to that obtained without scavenger under identical reaction conditions (Entry 22, Table 3.3), which illustrates that $^{\cdot}CH_3$ radicals are involved in the reaction mechanism.

3.3.3 DFT Calculations.

All quantum chemical calculations were done using the density functional theory (DFT) functional B3LYP/def2TZVP augmented with the D3 version of Grimme's empirical dispersion correction[66–68] as implemented in the Gaussian 16 software suite.[69–73] Electronic structure complexes were optimized at the unrestricted level. All calculations were performed in the solvated state and at 448.15 K. We used the Polarizable Continuum Model (PCM) using the integral equation formalism variant (IEFPCM) as the default SCRF method by using water as the solvent in this DFT calculation at 175 °C. Each structure was first optimized, and then frequency calculation was performed to confirm its geometry, to obtain the thermochemical data, and to provide the thermal corrections to Gibbs free energy. MIL-53(Al)-Cu(OH) was calculated with zero, one, and two H_2O molecule coordinated to Cu. Internal energies were compared directly after accounting for the difference in the number of coordinated H_2O molecules. Optimized structures were visualized by GaussView 5.0 software.

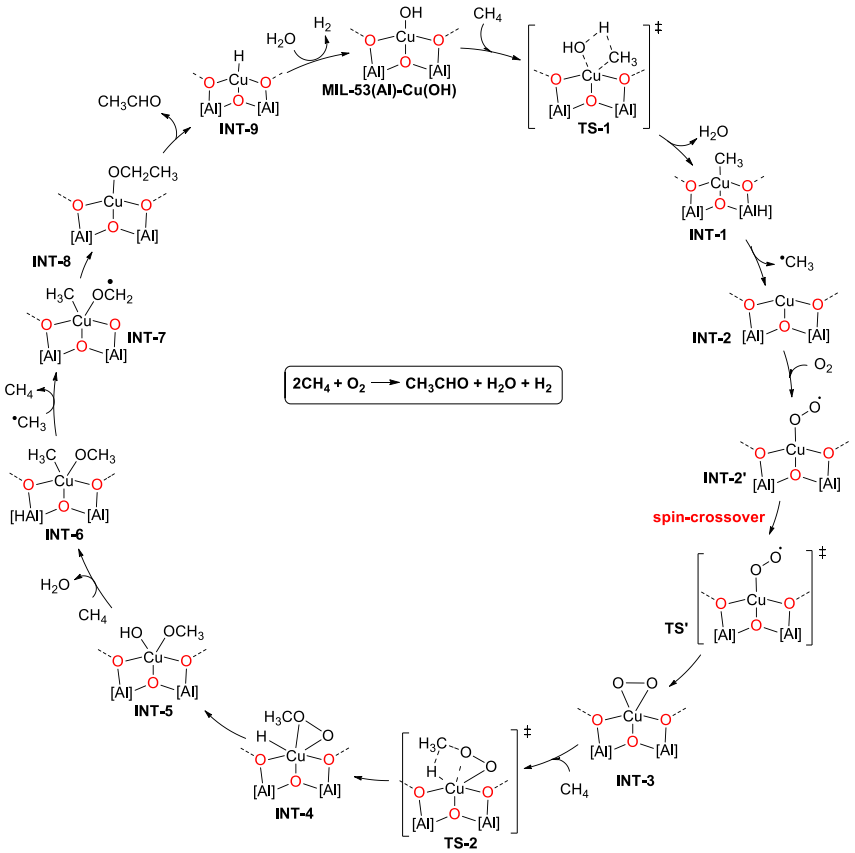


Figure 3.15: Proposed catalytic cycle of MIL-53(Al)-Cu(OH) catalyzed oxidation of methane to acetaldehyde.

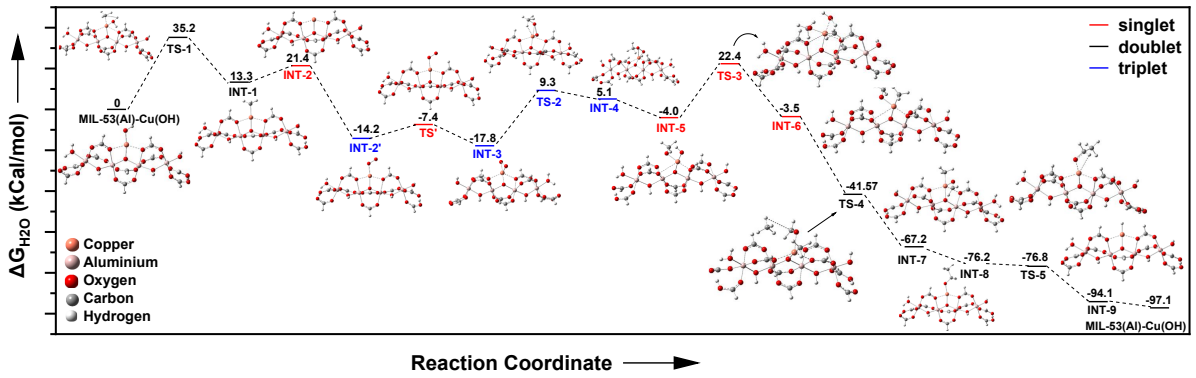
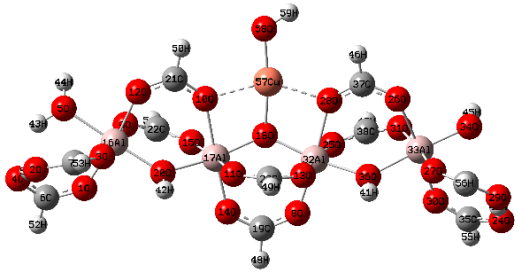
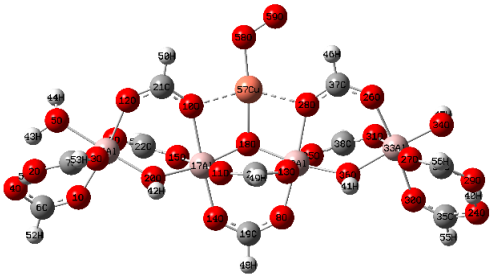


Figure 3.16: DFT-calculated free energy diagram of methane oxidation to acetaldehyde over MIL-53(Al)-Cu(OH) at 448 K.

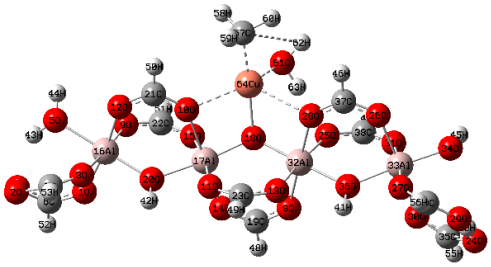
To explore the reaction mechanism and determine the turnover-limiting step (TLS), the entire catalytic cycle was examined through DFT calculations (Figure 3.16). The DFT-calculated energy profile reveals that methane C–H bond activation via σ-bond metathesis has an energy barrier of 35 kcal/mol. The formation of INT-1 (MIL-53(Al)-$Cu^{II}(CH_3)$) from MIL-53(Al)-Cu(OH) is endergonic by 13.3 kcal/mol. Subsequently, the homolytic cleavage of INT-1 to generate INT-2 (Cu^+ species) and a $\cdot CH_3$ radical is slightly endergonic by 8.1 kcal/mol. INT-2 reacts with O_2 to form a Cu-OO$\cdot$ (triplet) species [INT-2'], an exergonic process by 35.6 kcal/mol. This is followed by a spin crossover to a Cu-OO$\cdot$ (singlet) species [TS'], with an associated barrier of 6.8 kcal/mol, leading to the formation of INT-3 (Cu^{III}-η^2-peroxy). INT-3 undergoes -bond metathesis with CH_4 via TS-2, resulting in the formation of INT-4, with an energy barrier of 27.1 kcal/mol. INT-4 rearranges to form INT-5, an exergonic step by 4.2 kcal/mol. INT-5 undergoes a second σ-bond metathesis via TS-3 to generate INT-6, with a barrier of 26.4 kcal/mol. The $\cdot CH_3$ radical abstracts a hydrogen atom from the methoxy group of INT-6 to form INT-7, a highly exergonic step by 63.7 kcal/mol. INT-7 then rearranges to form INT-8, an exergonic step by 9 kcal/mol. Finally, INT-8 undergoes β-hydride elimination via TS-4, which is exergonic by 17.9 kcal/mol, yielding acetaldehyde and MIL-53(Al)-CuH (INT-9). The hydrolysis of INT-9 regenerates MIL-53(Al)-Cu(OH), completing the catalytic cycle, an exergonic process by 3 kcal/mol. The energy profile showed that methane activation through σ-bond metathesis has the highest activation barrier and thus it is the turnover-limiting step.



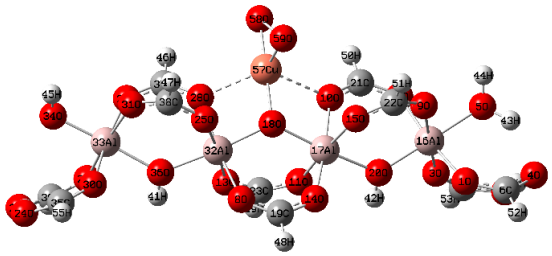
MIL-53(Al)-Cu(OH)



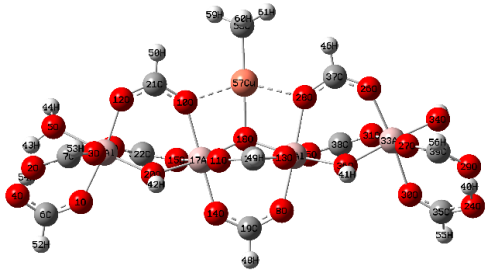
TS'



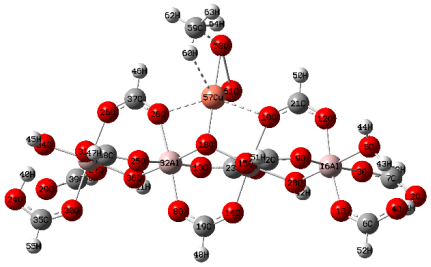
TS-1



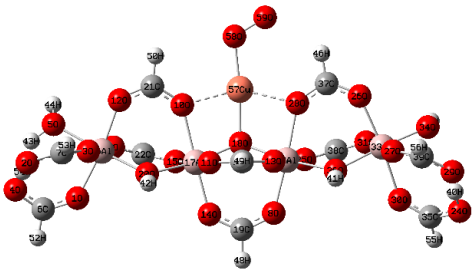
INT-3



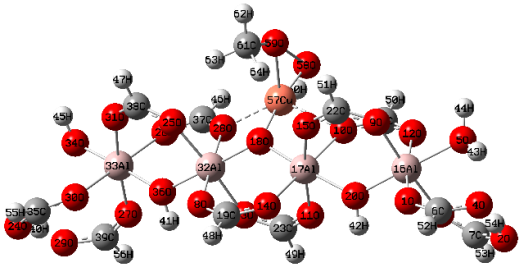
INT-1



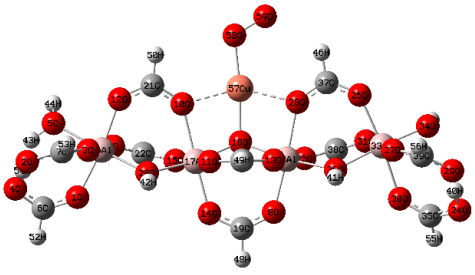
TS-2



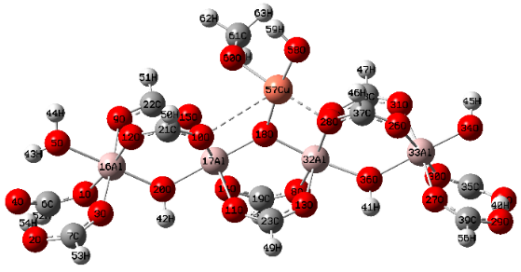
INT-2



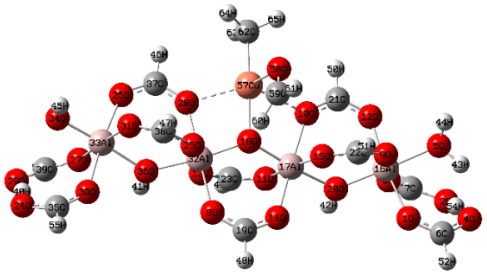
INT-4



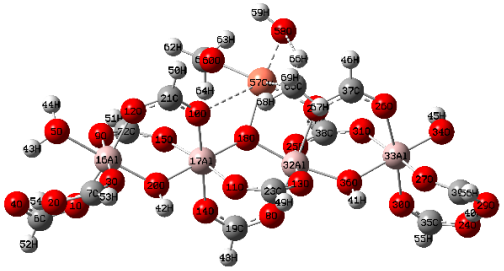
INT-2'



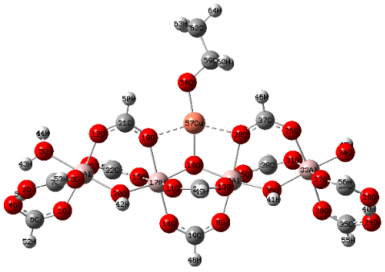
INT-5



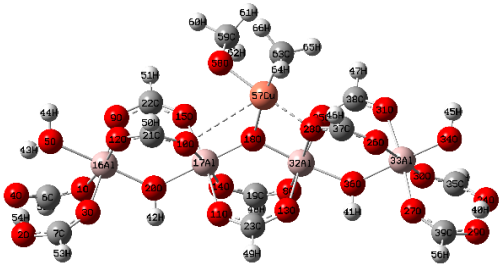
INT-7



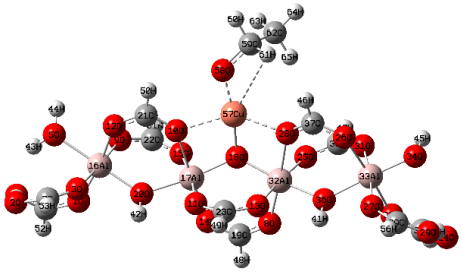
TS-3



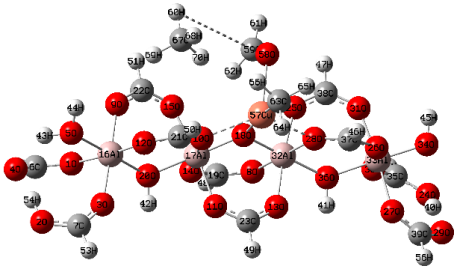
INT-8



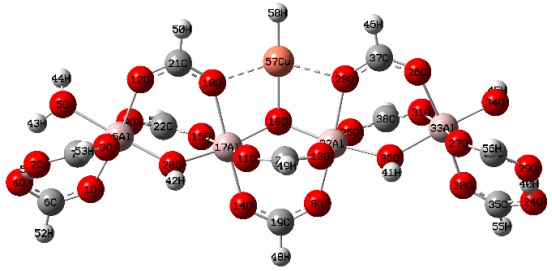
INT-6



TS-5



TS-4



INT-9

Figure 3.16: DFT-optimized structures of intermediates and transition states for MIL-53(Al)-Cu(OH) catalyzed oxidation of methane to acetaldehyde.

Cartesian coordinates of the DFT-optimized structures.

MIL-53(Al)-Cu(OH)

Coordinates (Angstroms)

S.No.	Atom	X	Y	Z
1	O	23.007351	12.375311	17.036534
2	O	20.565758	10.863509	19.156597
3	O	21.136450	13.042531	18.999734
4	O	21.799933	10.492970	16.876532
5	O	20.380511	12.700922	16.394554
6	C	22.878394	11.128020	16.828877
7	C	20.654206	12.073897	19.595291
8	O	26.009986	18.490461	18.681110
9	O	22.244916	14.510990	15.608678
10	O	21.359912	16.987642	17.685584
11	O	23.155932	16.730612	19.912611
12	O	20.290436	15.040724	17.443303
13	O	23.880670	18.802624	20.435702
14	O	25.278202	16.416406	18.157504
15	O	23.551670	16.287708	16.060288
16	Al	21.752589	13.780943	17.283833
17	Al	23.384502	16.637533	17.957673
18	O	23.402361	18.416715	17.777891
19	C	26.169313	17.269178	18.425628
20	O	22.967845	14.820628	18.219611
21	C	20.310711	16.286389	17.580486
22	C	23.024909	15.453973	15.288584
23	C	23.404546	17.672976	20.714805
24	O	27.932037	24.416017	20.924055
25	O	25.049844	20.497871	17.107854
26	O	22.984887	22.664556	19.493031
27	O	24.785965	22.755590	21.538106
28	O	22.660952	20.640933	18.594368
29	O	26.074185	24.283137	22.585896
30	O	27.034640	22.813347	19.612523
31	O	25.126640	22.673825	17.689886
32	Al	24.419452	19.594898	18.682669
33	Al	24.990800	22.825084	19.636795
34	O	24.936204	24.604483	19.554230
35	C	27.949173	23.567573	19.956075
36	O	25.141139	20.936536	19.746302
37	C	22.254542	21.766848	19.046093
38	C	25.230091	21.722604	16.876453
39	C	25.145887	23.459236	22.534847
40	H	27.069105	24.364040	21.513977
41	H	25.160096	20.674925	20.673187
42	H	23.040717	14.594298	19.153690
43	H	20.616470	11.766359	16.224040
44	H	19.847720	13.058320	15.674110
45	H	25.083562	24.937686	18.666235
46	H	21.169873	21.917334	19.014642
47	H	25.500334	21.984605	15.845595
48	H	27.200723	16.898056	18.442802
49	H	23.180235	17.481338	21.771677
50	H	19.360399	16.827279	17.606510
51	H	23.253575	15.548635	14.221657

TS-1

Coordinates (Angstroms)

S.No.	Atom	X	Y	Z
1	O	22.683704	12.948666	17.113356
2	O	20.802492	11.037637	19.400491
3	O	21.121815	13.268895	19.388866
4	O	21.697177	10.945216	16.966110
5	O	19.962285	13.006051	16.938075
6	C	22.666640	11.721292	16.804853
7	C	20.835506	12.206347	19.942729
8	O	25.394008	19.097663	18.524493
9	O	21.456223	15.039625	16.005770
10	O	20.745694	17.285971	18.434326
11	O	22.874781	17.104881	20.240046
12	O	19.854917	15.248551	18.177134
13	O	23.704251	19.134638	20.748651
14	O	24.661787	17.005176	18.115286
15	O	22.580381	16.951311	16.370707
16	Al	21.362371	14.180928	17.676761
17	Al	22.765243	17.153612	18.292848
18	O	22.695287	18.926074	18.203294
19	C	25.544625	17.900470	18.185596
20	O	22.604851	15.280228	18.453256
21	C	19.781369	16.478063	18.413747
22	C	22.032937	16.101912	15.638206
23	C	23.262849	17.996815	21.037068

24	O	27.945133	24.539426	21.019646
25	O	23.942070	21.162372	17.398984
26	O	22.881568	23.185784	19.933581
27	O	24.806585	23.050432	21.845966
28	O	22.173199	21.091998	19.518736
29	O	26.228900	24.494043	22.824064
30	O	26.873609	23.002888	19.768585
31	O	24.849450	23.136427	17.983358
32	Al	23.789741	20.075068	19.025906
33	Al	24.851579	23.178737	19.942755
34	O	24.956967	24.955400	19.953873
35	C	27.849349	23.698638	20.051724
36	O	24.860184	21.303203	19.925012
37	C	22.002247	22.307324	19.813161
38	C	24.435004	22.300502	17.155540
39	C	25.259860	23.714664	22.823359
40	H	27.120516	24.535195	21.676105
41	H	25.142624	20.954139	20.775691
42	H	22.918453	14.985303	19.314276
43	H	20.284638	12.133050	16.635101
44	H	19.354878	13.377065	16.285380
45	H	24.997696	25.339833	19.075659
46	H	20.961420	22.618584	19.970774
47	H	24.490638	22.582013	16.096269
48	H	26.564935	17.590535	17.926149
49	H	23.213214	17.747277	22.104886
50	H	18.787681	16.890369	18.615688
51	H	22.042533	16.292304	14.559169
52	H	23.589421	11.327482	16.360063
53	H	20.579811	12.199771	21.003494
54	H	21.097869	11.025777	18.427361
55	H	28.760285	23.623406	19.448854
56	H	24.731127	23.562537	23.777293
57	C	18.955275	20.016145	18.350119
58	H	18.375156	19.615429	17.513405
59	H	18.556250	19.610888	19.285514
60	H	18.855206	21.105330	18.361580
61	O	21.327651	20.676454	16.387703
62	H	20.912718	21.548001	16.380591
63	H	22.284050	20.827358	16.522566
64	Cu	20.835359	19.510230	18.163099

INT-1

Coordinates (Angstroms)

S.No.	Atom	X	Y	Z
1	O	23.087255	12.424929	17.076709
2	O	20.728249	10.789805	19.109902
3	O	21.192061	12.994030	19.024765
4	O	21.999311	10.480676	16.866968
5	O	20.445717	12.637790	16.429084
6	C	23.034881	11.183433	16.834260
7	C	20.751811	11.987887	19.583528
8	O	25.908182	18.499712	18.715912
9	O	22.217783	14.507369	15.659210
10	O	21.259195	16.953943	17.761528
11	O	23.027491	16.773212	19.936140
12	O	20.287036	14.957724	17.506487
13	O	23.771248	18.833245	20.458171
14	O	25.160682	16.436645	18.197087
15	O	23.429333	16.346925	16.103190
16	Al	21.781105	13.767651	17.332086
17	Al	23.279186	16.677875	17.999459
18	O	23.313863	18.443247	17.801872
19	C	26.057183	17.280540	18.459129
20	O	22.948634	14.843824	18.250366
21	C	20.254133	16.201034	17.651792
22	C	22.941548	15.490477	15.336273
23	C	23.260675	17.720894	20.730856
24	O	28.024666	24.307517	20.828854
25	O	24.936429	20.495064	17.137860
26	O	23.054566	22.698000	19.597232
27	O	24.905424	22.725100	21.573167
28	O	22.615925	20.698896	18.692983
29	O	26.230187	24.253414	22.557733
30	O	27.067405	22.697072	19.578183
31	O	25.098577	22.658797	17.730225
32	Al	24.327140	19.598785	18.716374
33	Al	25.041715	22.782537	19.671349
34	O	25.056218	24.560716	19.620930
35	C	28.002877	23.437925	19.882139
36	O	25.131573	20.903196	19.760455
37	C	22.279437	21.833792	19.158882
38	C	25.146027	21.712007	16.909585
39	C	25.290761	23.439599	22.544793
40	H	27.173152	24.291204	21.448541
41	H	25.182625	20.627593	20.681287
42	H	23.067656	14.602239	19.174929
43	H	20.750034	11.729425	16.229073
44	H	19.979278	13.004255	15.666955

45	H	25.117950	24.912767	18.730364
46	H	21.205149	22.049740	19.158227
47	H	25.390476	21.975309	15.872462
48	H	27.086625	16.902299	18.469727
49	H	22.986673	17.550931	21.780001
50	H	19.271029	16.680391	17.680795
51	H	23.153419	15.599665	14.267023
52	H	23.988978	10.706538	16.576218
53	H	20.330275	12.066204	20.586823
54	H	21.172222	10.695813	18.199788
55	H	28.940890	23.382071	19.320420
56	H	24.725498	23.301307	23.479498
57	Cu	21.498267	19.120572	17.812324
58	C	19.672576	19.802512	17.698759
59	H	19.102144	19.235399	16.957368
60	H	19.186470	19.698622	18.673828
61	H	19.673935	20.858602	17.415517

INT-2

Coordinates (Angstroms)

S.No.	Atom	X	Y	Z
1	O	23.039916	12.402129	17.068797
2	O	20.594906	10.849339	19.072432
3	O	21.137335	13.035490	18.994359
4	O	21.902761	10.485998	16.862631
5	O	20.415722	12.690787	16.390651
6	C	22.956189	11.160750	16.832192
7	C	20.649690	12.046170	19.544881
8	O	25.960295	18.474481	18.738984
9	O	22.255059	14.513200	15.646154
10	O	21.344129	16.969763	17.706403
11	O	23.059427	16.761734	19.918522
12	O	20.303721	15.013903	17.456407
13	O	23.798397	18.823655	20.437373
14	O	25.215342	16.408449	18.228146
15	O	23.531644	16.303624	16.106580
16	Al	21.772358	13.779719	17.309259
17	Al	23.343727	16.640038	17.991712
18	O	23.390220	18.415839	17.780923
19	C	26.110105	17.251127	18.500010
20	O	22.963826	14.821490	18.244553
21	C	20.308183	16.257773	17.583594
22	C	23.022519	15.464931	15.332594
23	C	23.284297	17.712770	20.711564
24	O	27.935045	24.407551	20.793519
25	O	25.014360	20.463406	17.138727
26	O	23.022955	22.641755	19.568256
27	O	24.867192	22.738717	21.543933
28	O	22.642389	20.654000	18.622463
29	O	26.131530	24.327392	22.511440
30	O	27.034825	22.747745	19.565360
31	O	25.082167	22.637673	17.707355
32	Al	24.395149	19.578455	18.710729
33	Al	25.017137	22.783651	19.645793
34	O	24.973426	24.558817	19.574630
35	C	27.946836	23.520585	19.863876
36	O	25.144262	20.903729	19.756686
37	C	22.269346	21.770415	19.116807
38	C	25.180047	21.685525	16.898177
39	C	25.221868	23.480905	22.507179
40	H	27.079292	24.378103	21.407375
41	H	25.174116	20.643327	20.683196
42	H	23.052935	14.579210	19.172552
43	H	20.688163	11.775005	16.183807
44	H	19.942591	13.073266	15.640693
45	H	25.020074	24.904667	18.680747
46	H	21.189078	21.951825	19.128471
47	H	25.430411	21.945510	15.861999
48	H	27.137022	16.869404	18.537322
49	H	22.998718	17.549077	21.758108
50	H	19.350053	16.784506	17.583774
51	H	23.256685	15.563484	14.267219
52	H	23.898974	10.658257	16.581456
53	H	20.209633	12.142061	20.538610
54	H	21.056962	10.737070	18.172393
55	H	28.890856	23.479554	19.311385
56	H	24.657040	23.335948	23.440914
57	Cu	21.612440	19.073428	17.776007

INT-2'

Coordinates (Angstroms)

S.No.	Atom	X	Y	Z
1	O	23.065145	12.415609	17.069404
2	O	20.662739	10.824426	19.091538
3	O	21.164300	13.020020	19.003730
4	O	21.956360	10.482290	16.868865
5	O	20.430923	12.660041	16.405888
6	C	22.999422	11.172999	16.833973
7	C	20.700067	12.023293	19.560883
8	O	25.933222	18.487056	18.727677

9	O	22.233990	14.505655	15.642932
10	O	21.279113	16.973240	17.720046
11	O	23.039244	16.772532	19.909894
12	O	20.293264	14.985122	17.469664
13	O	23.771319	18.836093	20.430661
14	O	25.194780	16.420624	18.205793
15	O	23.478605	16.320749	16.093822
16	Al	21.775949	13.773094	17.312757
17	Al	23.321839	16.658548	17.981981
18	O	23.367271	18.424902	17.767103
19	C	26.086937	17.266921	18.478473
20	O	22.950900	14.838578	18.238624
21	C	20.266036	16.227837	17.604401
22	C	22.978930	15.473255	15.323637
23	C	23.262094	17.723463	20.704046
24	O	27.971507	24.344895	20.850738
25	O	24.983175	20.477342	17.125135
26	O	23.049000	22.691151	19.510621
27	O	24.848837	22.743040	21.533478
28	O	22.622276	20.676364	18.636259
29	O	26.131883	24.297252	22.532397
30	O	27.058732	22.712429	19.595428
31	O	25.138480	22.646365	17.698619
32	Al	24.358412	19.591995	18.698501
33	Al	25.033143	22.787872	19.636440
34	O	25.037728	24.565102	19.571203
35	C	27.980861	23.463754	19.914724
36	O	25.130838	20.907714	19.744697
37	C	22.278737	21.824635	19.069708
38	C	25.199510	21.692026	16.888465
39	C	25.202587	23.472557	22.506369
40	H	27.103840	24.330329	21.446900
41	H	25.158916	20.644193	20.670208
42	H	23.042195	14.604406	19.168558
43	H	20.719779	11.747954	16.203205
44	H	19.956476	13.031909	15.651392
45	H	25.109190	24.910709	18.678836
46	H	21.206659	22.043503	19.028680
47	H	25.463778	21.943783	15.853506
48	H	27.115876	16.889043	18.506591
49	H	22.978542	17.556674	21.750821
50	H	19.286767	16.716093	17.618496
51	H	23.200514	15.577987	14.256107
52	H	23.948756	10.684565	16.580203
53	H	20.267655	12.113208	20.558518
54	H	21.117601	10.718867	18.187351
55	H	28.933700	23.407556	19.378690
56	H	24.616597	23.337380	23.428636
57	Cu	21.565705	19.082824	17.764676
58	O	19.765433	19.602629	17.587805
59	O	19.578871	20.872636	17.538256

TS'

Coordinates (Angstroms)

S.No.	Atom	X	Y	Z
1	O	23.064937	12.415582	17.069379
2	O	20.663092	10.824609	19.091926
3	O	21.164258	13.020263	19.003866
4	O	21.955875	10.482492	16.868402
5	O	20.430761	12.659974	16.406063
6	C	22.999070	11.173018	16.833785
7	C	20.700290	12.023500	19.561185
8	O	25.933504	18.487012	18.727415
9	O	22.233875	14.505647	15.642998
10	O	21.279160	16.973182	17.719917
11	O	23.039373	16.772551	19.909799
12	O	20.293103	14.985147	17.469705
13	O	23.771681	18.836031	20.430591
14	O	25.194850	16.420655	18.205551
15	O	23.478579	16.320714	16.093709
16	Al	21.775803	13.773151	17.312788
17	Al	23.321888	16.658578	17.981855
18	O	23.367457	18.424907	17.767030
19	C	26.087096	17.266860	18.478153
20	O	22.950914	14.838621	18.238531
21	C	20.266019	16.227887	17.604453
22	C	22.978898	15.473150	15.323607
23	C	23.262466	17.723391	20.703982
24	O	27.971555	24.344259	20.851614
25	O	24.983407	20.477322	17.125044
26	O	23.049111	22.691159	19.510350
27	O	24.848661	22.743144	21.533230
28	O	22.622410	20.676304	18.636171
29	O	26.130898	24.297620	22.532774
30	O	27.058814	22.712618	19.595161
31	O	25.138762	22.646349	17.698492
32	Al	24.358720	19.591929	18.698365
33	Al	25.033159	22.787932	19.636280
34	O	25.037768	24.565148	19.571152

35	C	27.980922	23.463718	19.915052
36	O	25.131069	20.907714	19.744529
37	C	22.278856	21.824579	19.069517
38	C	25.199689	21.692014	16.888339
39	C	25.201756	23.472733	22.506280
40	H	27.104012	24.329456	21.447963
41	H	25.159236	20.644182	20.670034
42	H	23.042353	14.604308	19.168413
43	H	20.719663	11.747868	16.203515
44	H	19.956337	13.031702	15.651484
45	H	25.109108	24.910905	18.678835
46	H	21.206790	22.043474	19.028376
47	H	25.463868	21.943759	15.853355
48	H	27.116012	16.888915	18.506155
49	H	22.979233	17.556493	21.750828
50	H	19.286752	16.716154	17.618717
51	H	23.200545	15.577723	14.256075
52	H	23.948344	10.684473	16.579998
53	H	20.268007	12.113431	20.558874
54	H	21.117824	10.719102	18.187680
55	H	28.933762	23.407915	19.378979
56	H	24.615291	23.337548	23.428229
57	Cu	21.565805	19.082871	17.764651
58	O	19.765048	19.602633	17.588371
59	O	19.578611	20.872790	17.538517

INT-3

Coordinates (Angstroms)

S.No.	Atom	X	Y	Z
1	O	23.007351	12.375311	17.036534
2	O	20.565758	10.863509	19.156597
3	O	21.136450	13.042531	18.999734
4	O	21.799933	10.492970	16.876532
5	O	20.380511	12.700922	16.394554
6	C	22.878394	11.128020	16.828877
7	C	20.654206	12.073897	19.595291
8	O	26.009986	18.490461	18.681110
9	O	22.244916	14.510990	15.608678
10	O	21.359912	16.987642	17.685584
11	O	23.155932	16.730612	19.912611
12	O	20.290436	15.040724	17.443303
13	O	23.880670	18.802624	20.435702
14	O	25.278202	16.416406	18.157504
15	O	23.551670	16.287708	16.060288
16	Al	21.752589	13.780943	17.283833
17	Al	23.384502	16.637533	17.957673
18	O	23.402361	18.416715	17.777891
19	C	26.169313	17.269178	18.425628
20	O	22.967845	14.820628	18.219611
21	C	20.310711	16.286389	17.580486
22	C	23.024909	15.453973	15.288584
23	C	23.404546	17.672976	20.714805
24	O	27.932037	24.416017	20.924055
25	O	25.049844	20.497871	17.107854
26	O	22.984887	22.664556	19.493031
27	O	24.785965	22.755590	21.538106
28	O	22.660952	20.640933	18.594368
29	O	26.074185	24.283137	22.585896
30	O	27.034640	22.813347	19.612523
31	O	25.126640	22.673825	17.689886
32	Al	24.419452	19.594898	18.682669
33	Al	24.990800	22.825084	19.636795
34	O	24.936204	24.604483	19.554230
35	C	27.949173	23.567573	19.956075
36	O	25.141139	20.936536	19.746302
37	C	22.254542	21.766848	19.046093
38	C	25.230091	21.722604	16.876453
39	C	25.145887	23.459236	22.534847
40	H	27.069105	24.364040	21.513977
41	H	25.160096	20.674925	20.673187
42	H	23.040717	14.594298	19.153690
43	H	20.616470	11.766359	16.224040
44	H	19.847720	13.058320	15.674110
45	H	25.083562	24.937686	18.666235
46	H	21.169873	21.917334	19.014642
47	H	25.500334	21.984605	15.845595
48	H	27.200723	16.898056	18.442802
49	H	23.180235	17.481338	21.771677
50	H	19.360399	16.827279	17.606510
51	H	23.253575	15.548635	14.221657
52	H	23.803711	10.588551	16.589897
53	H	20.251312	12.199192	20.601260
54	H	20.984549	10.735234	18.246087
55	H	28.901310	23.545030	19.416245
56	H	24.559504	23.295002	23.452510
57	Cu	21.617433	19.043682	17.875396
58	O	20.283805	19.292515	18.801035
59	O	20.790674	19.663560	16.598874

TS-2

Coordinates (Angstroms)

S.No.	Atom	X	Y	Z
1	O	22.460309	12.597699	17.566406
2	O	19.968907	11.009199	19.791186
3	O	20.526150	13.189529	19.538079
4	O	21.432176	10.627830	17.259523
5	O	19.814316	12.800523	16.920352
6	C	22.446946	11.357064	17.309839
7	C	20.061262	12.237290	20.168502
8	O	25.252080	18.675547	19.254274
9	O	21.597667	14.684372	16.168553
10	O	20.629709	17.100213	18.231637
11	O	22.395767	16.936581	20.449498
12	O	19.635120	15.119143	17.975385
13	O	23.125931	19.001014	20.977255
14	O	24.515028	16.614063	18.726790
15	O	22.831198	16.502475	16.636367
16	Al	21.133563	13.923860	17.825062
17	Al	22.642832	16.820280	18.515877
18	O	22.657205	18.617264	18.330208
19	C	25.407423	17.457476	19.000577
20	O	22.290155	14.999663	18.768145
21	C	19.612879	16.360169	18.114086
22	C	22.335809	15.658798	15.858256
23	C	22.633318	17.879851	21.249394
24	O	27.396722	24.448469	21.421761
25	O	24.327803	20.653805	17.681111
26	O	22.404060	22.902471	20.070661
27	O	24.206683	22.937267	22.083883
28	O	21.996079	20.893960	19.181772
29	O	25.536736	24.450307	23.082328
30	O	26.426549	22.874773	20.137546
31	O	24.494896	22.821686	18.253987
32	Al	23.696517	19.790653	19.253296
33	Al	24.399955	22.977581	20.192999
34	O	24.418728	24.750267	20.116803
35	C	27.371861	23.593120	20.461405
36	O	24.473511	21.094254	20.304256
37	C	21.640743	22.033799	19.632410
38	C	24.546184	21.868804	17.442947
39	C	24.592925	23.644056	23.062357
40	H	26.539550	24.432802	22.026526
41	H	24.493043	20.832871	21.230869
42	H	22.363531	14.768308	19.700614
43	H	20.092841	11.880082	16.741273
44	H	19.278366	13.144828	16.195445
45	H	24.566484	25.086400	19.229953
46	H	20.565491	22.242872	19.606891
47	H	24.807980	22.118293	16.407400
48	H	26.436244	17.080941	19.024010
49	H	22.384438	17.695843	22.301257
50	H	18.636070	16.852450	18.123999
51	H	22.562150	15.772095	14.792986
52	H	23.426385	10.908702	17.101564
53	H	19.665249	12.405467	21.170971
54	H	20.377761	10.820764	18.879668
55	H	28.315162	23.528094	19.910389
56	H	24.018043	23.505902	23.990852
57	Cu	20.869805	19.262736	18.381652
58	O	19.338113	19.618370	19.168077
59	C	18.900477	20.146678	17.959166
60	H	19.795938	19.976465	17.398739
61	O	20.496665	19.125380	20.139066
62	H	19.081334	21.193188	17.828751
63	H	18.421825	19.448262	17.304944
64	H	17.938830	20.389655	18.360535

INT-4

Coordinates (Angstroms)

S.No.	Atom	X	Y	Z
1	O	22.912907	12.423347	16.826359
2	O	20.471314	10.911545	18.946422
3	O	21.042006	13.090567	18.789559
4	O	21.705489	10.541007	16.666357
5	O	20.286068	12.748958	16.184379
6	C	22.783950	11.176057	16.618702
7	C	20.559762	12.121933	19.385116
8	O	25.915542	18.538497	18.470935
9	O	22.150472	14.559026	15.398503
10	O	21.265468	17.035678	17.475409
11	O	23.061489	16.778648	19.702435
12	O	20.195992	15.088760	17.233127
13	O	23.786227	18.850660	20.225527
14	O	25.183758	16.464442	17.947329
15	O	23.457227	16.335745	15.850113
16	Al	21.658146	13.828979	17.073658
17	Al	23.290058	16.685569	17.747498
18	O	23.307917	18.464752	17.567716
19	C	26.074869	17.317214	18.215452

20	O	22.873401	14.868664	18.009436
21	C	20.216267	16.334425	17.370311
22	C	22.930465	15.502010	15.078408
23	C	23.310102	17.721012	20.504630
24	O	27.837593	24.464053	20.713880
25	O	24.955400	20.545907	16.897679
26	O	22.890443	22.712592	19.282856
27	O	24.691521	22.803626	21.327931
28	O	22.566508	20.688969	18.384193
29	O	25.979741	24.331173	22.375721
30	O	26.940196	22.861383	19.402348
31	O	25.032197	22.721861	17.479710
32	Al	24.325008	19.642934	18.472494
33	Al	24.896356	22.873120	19.426619
34	O	24.841760	24.652519	19.344055
35	C	27.854729	23.615609	19.745900
36	O	25.046695	20.984573	19.536127
37	C	22.160098	21.814884	18.835918
38	C	25.135647	21.770640	16.666278
39	C	25.051443	23.507272	22.324672
40	H	26.974661	24.412076	21.303801
41	H	25.065652	20.722961	20.463012
42	H	22.946273	14.642335	18.943515
43	H	20.522026	11.814395	16.013865
44	H	19.753277	13.106356	15.463935
45	H	24.989119	24.985722	18.456060
46	H	21.075429	21.965371	18.804467
47	H	25.405891	22.032641	15.635420
48	H	27.106279	16.946092	18.232626
49	H	23.085791	17.529374	21.561502
50	H	19.265955	16.875315	17.396334
51	H	23.159132	15.596671	14.011481
52	H	23.709267	10.636587	16.379722
53	H	20.156869	12.247229	20.391084
54	H	20.890105	10.783270	18.035912
55	H	28.806867	23.593066	19.206070
56	H	24.465060	23.343038	23.242334
57	Cu	21.522989	19.091719	17.665221
58	O	20.019054	19.553393	17.896226
59	O	21.342904	19.286521	16.046820
60	H	21.732905	19.510413	15.198663
61	C	21.151019	18.905942	19.560142
62	H	20.215307	19.372542	19.787360
63	H	21.102754	17.867618	19.814023
64	H	21.929836	19.375201	20.124180

INT-5

Coordinates (Angstroms)

S.No.	Atom	X	Y	Z
1	O	23.131809	12.474023	17.071917
2	O	20.820032	10.789909	19.110798
3	O	21.243924	13.003432	19.033291
4	O	22.081888	10.509405	16.854985
5	O	20.479879	12.632342	16.442917
6	C	23.103437	11.233075	16.825681
7	C	20.826140	11.987764	19.589565
8	O	25.863969	18.503877	18.785417
9	O	22.214084	14.522266	15.636638
10	O	21.187797	16.940276	18.105030
11	O	23.107007	16.816539	19.964810
12	O	20.309355	14.959886	17.504920
13	O	23.756135	18.891894	20.524079
14	O	25.042706	16.545468	18.043785
15	O	23.168485	16.498121	16.119560
16	Al	21.801207	13.799280	17.327746
17	Al	23.117711	16.776487	18.016644
18	O	23.264987	18.584394	17.832348
19	C	25.969649	17.314968	18.382943
20	O	22.956943	14.897351	18.226342
21	C	20.237689	16.166388	17.868209
22	C	22.794652	15.602354	15.336312
23	C	23.307276	17.747391	20.780670
24	O	28.048046	24.313985	21.069979
25	O	24.990912	20.563136	17.274880
26	O	23.075542	22.737746	19.747306
27	O	24.925008	22.723848	21.739053
28	O	22.685953	20.778642	18.765572
29	O	26.224354	24.246652	22.763915
30	O	27.104607	22.734331	19.770767
31	O	25.146142	22.715286	17.906038
32	Al	24.362015	19.649657	18.839959
33	Al	25.102070	22.814787	19.848892
34	O	25.084166	24.589838	19.820432
35	C	28.039216	23.464704	20.107004
36	O	25.169942	20.932853	19.902366
37	C	22.319419	21.934283	19.200526
38	C	25.204727	21.784173	17.068683
39	C	25.287632	23.431200	22.725757
40	H	27.185713	24.293218	21.677472

41	H	25.205201	20.645338	20.820763
42	H	23.200534	14.611840	19.111892
43	H	20.805766	11.733077	16.235678
44	H	20.002329	12.992800	15.684957
45	H	25.131165	24.959019	18.935955
46	H	21.264910	22.175735	19.049282
47	H	25.461434	22.064155	16.039555
48	H	26.988105	16.911991	18.332103
49	H	23.070623	17.539295	21.831360
50	H	19.226787	16.573599	17.983839
51	H	22.982615	15.765995	14.269241
52	H	24.066953	10.774950	16.567579
53	H	20.410078	12.052054	20.596373
54	H	21.257772	10.707984	18.197613
55	H	28.985521	23.413000	19.559772
56	H	24.703437	23.282893	23.646632
57	Cu	21.855175	19.720078	17.361403
58	O	20.574299	20.950732	17.067732
59	H	20.043934	20.614177	16.333156
60	O	21.294219	18.799925	15.909141
61	C	22.101890	19.097774	14.797296
62	H	21.728353	18.476090	13.973175
63	H	22.021986	20.147338	14.490232
64	H	23.149582	18.837173	14.969420

TS-3

Coordinates (Angstroms)

S.No.	Atom	X	Y	Z
1	O	23.225460	12.475400	17.001341
2	O	20.979989	10.718724	19.058803
3	O	21.360674	12.940657	19.000039
4	O	22.206814	10.495279	16.775816
5	O	20.561311	12.591231	16.417133
6	C	23.215262	11.237127	16.741059
7	C	20.971840	11.911120	19.551470
8	O	25.920176	18.484317	18.742078
9	O	22.243755	14.525372	15.608832
10	O	21.237373	16.892898	18.080100
11	O	23.158613	16.800859	19.938196
12	O	20.363445	14.900330	17.517788
13	O	23.831018	18.868581	20.501223
14	O	25.087817	16.532603	17.999150
15	O	23.202009	16.500378	16.088948
16	Al	21.873790	13.771611	17.296871
17	Al	23.163830	16.761725	17.989243
18	O	23.297114	18.574061	17.824940
19	C	26.020037	17.297209	18.334589
20	O	23.023193	14.879067	18.190293
21	C	20.289328	16.107500	17.877889
22	C	22.815611	15.609498	15.306087
23	C	23.368625	17.728961	20.755086
24	O	28.179170	24.255390	21.003111
25	O	25.041131	20.537835	17.242258
26	O	23.176259	22.733060	19.742091
27	O	25.048263	22.700676	21.711071
28	O	22.763441	20.783004	18.752431
29	O	26.376812	24.209081	22.719606
30	O	27.203205	22.685329	19.716300
31	O	25.221611	22.687731	17.874619
32	Al	24.420310	19.631486	18.815322
33	Al	25.203241	22.788188	19.818708
34	O	25.204882	24.563409	19.788766
35	C	28.149544	23.405955	20.040796
36	O	25.249131	20.906333	19.872022
37	C	22.409328	21.937987	19.198207
38	C	25.262512	21.757370	17.035272
39	C	25.430647	23.403996	22.693077
40	H	27.324236	24.244424	21.621757
41	H	25.294238	20.616863	20.789312
42	H	23.302330	14.582916	19.061530
43	H	20.902791	11.699802	16.199457
44	H	20.073154	12.949444	15.664878
45	H	25.244563	24.931318	18.903406
46	H	21.355371	22.187432	19.059464
47	H	25.509374	22.036814	16.003580
48	H	27.036717	16.891054	18.274628
49	H	23.127191	17.522786	21.804876
50	H	19.278544	16.504697	18.025180
51	H	22.982713	15.781849	14.236922
52	H	24.182872	10.798862	16.464461
53	H	20.572159	11.955847	20.565952
54	H	21.403179	10.656589	18.137656
55	H	29.088505	23.343876	19.482105
56	H	24.856117	23.262423	23.621054
57	Cu	21.892673	19.726011	17.374288
58	O	20.632712	20.980273	17.087426
59	H	20.069570	20.637574	16.380702
60	O	21.287967	18.801806	15.943036
61	C	22.060422	19.098767	14.805996

62	H	21.658968	18.478923	13.993751
63	H	21.973225	20.148675	14.502389
64	H	23.112505	18.835338	14.943934
65	C	20.204632	19.378619	20.332024
66	H	19.891729	20.107287	19.584789
67	H	20.929072	19.834524	21.005401
68	H	20.663255	18.531323	19.825175
69	H	19.338468	19.039728	20.899398

INT-6

Coordinates (Angstroms)

S.No.	Atom	X	Y	Z
1	O	23.172870	12.505830	17.090497
2	O	20.831568	10.782720	19.066541
3	O	21.247098	12.998935	19.026161
4	O	22.149545	10.530825	16.837080
5	O	20.528239	12.646374	16.421251
6	C	23.162452	11.267333	16.832567
7	C	20.822776	11.975180	19.560719
8	O	25.874969	18.497428	18.870032
9	O	22.258032	14.554883	15.653715
10	O	21.189064	16.940430	18.128909
11	O	23.088671	16.820492	20.031860
12	O	20.322804	14.963427	17.497451
13	O	23.708832	18.913608	20.573860
14	O	25.069478	16.520857	18.148108
15	O	23.210063	16.526840	16.159032
16	Al	21.827969	13.823754	17.334518
17	Al	23.138890	16.802062	18.070130
18	O	23.276218	18.572985	17.897499
19	C	25.987716	17.302745	18.485826
20	O	22.960451	14.915563	18.262864
21	C	20.245941	16.169202	17.871522
22	C	22.840793	15.639337	15.367116
23	C	23.262977	17.768160	20.835148
24	O	28.112398	24.243280	21.032511
25	O	24.994851	20.545693	17.297919
26	O	23.100218	22.745507	19.790295
27	O	24.967038	22.722397	21.754844
28	O	22.629033	20.837544	18.729908
29	O	26.309458	24.228385	22.751892
30	O	27.114029	22.678907	19.755823
31	O	25.140264	22.703284	17.914242
32	Al	24.342243	19.626827	18.859411
33	Al	25.106946	22.798502	19.856859
34	O	25.132347	24.575902	19.828269
35	C	28.069950	23.387053	20.074158
36	O	25.135860	20.921785	19.919923
37	C	22.310574	21.966662	19.249204
38	C	25.202919	21.764651	17.083846
39	C	25.358029	23.429370	22.730928
40	H	27.262223	24.245020	21.652088
41	H	25.155722	20.635350	20.839038
42	H	23.190140	14.628276	19.151414
43	H	20.867991	11.754026	16.206922
44	H	20.062337	13.013301	15.659191
45	H	25.179195	24.938851	18.941071
46	H	21.254463	22.244249	19.198750
47	H	25.461401	22.039850	16.053397
48	H	27.009168	16.902969	18.452774
49	H	23.004381	17.574126	21.884343
50	H	19.231056	16.570804	17.976140
51	H	23.033685	15.810457	14.301720
52	H	24.135754	10.822201	16.588025
53	H	20.386581	12.023656	20.559988
54	H	21.288446	10.715071	18.162423
55	H	29.009504	23.307601	19.518581
56	H	24.784562	23.297613	23.661243
57	Cu	21.799020	19.733999	17.325906
58	O	21.190197	18.803028	15.897557
59	C	21.910799	19.115133	14.730766
60	H	21.623170	18.380211	13.968552
61	H	21.669294	20.113336	14.342479
62	H	22.994970	19.039477	14.871811
63	C	20.425231	21.036385	16.881510
64	H	19.903070	21.178182	17.827349
65	H	20.983200	21.918221	16.568133
66	H	19.777884	20.647634	16.105524

TS-4

Coordinates (Angstroms)

S.No.	Atom	X	Y	Z
1	O	23.109064	12.478888	17.046703
2	O	20.570367	10.860388	18.867948
3	O	21.073304	13.057615	18.846891
4	O	22.035012	10.537485	16.753513
5	O	20.525217	12.709778	16.201155
6	C	23.071225	11.237922	16.798630
7	C	20.567999	12.054093	19.352888
8	O	25.849870	18.499118	18.907267

9	O	22.371623	14.563482	15.568189
10	O	21.272960	17.015808	17.610626
11	O	22.847721	16.843274	19.898795
12	O	20.306884	15.027998	17.258777
13	O	23.578285	18.895294	20.470021
14	O	25.103818	16.451353	18.330103
15	O	23.537276	16.407811	16.102306
16	Al	21.798114	13.831347	17.204856
17	Al	23.243939	16.739423	17.992623
18	O	23.352695	18.497172	17.777691
19	C	25.994162	17.278631	18.657806
20	O	22.896236	14.898683	18.210678
21	C	20.278473	16.273272	17.410425
22	C	23.112131	15.550173	15.300556
23	C	23.021935	17.796294	20.702047
24	O	28.035309	24.167640	21.252239
25	O	25.067266	20.513617	17.245317
26	O	23.153124	22.806104	19.515471
27	O	24.783065	22.738572	21.682132
28	O	22.669570	20.800232	18.635879
29	O	26.069884	24.217093	22.786767
30	O	27.136326	22.583143	19.927314
31	O	25.378813	22.650775	17.876113
32	Al	24.290784	19.639579	18.780879
33	Al	25.109908	22.779801	19.802467
34	O	25.236721	24.554929	19.759125
35	C	28.069877	23.283623	20.318486
36	O	25.092267	20.902226	19.887776
37	C	22.372784	21.966949	19.028645
38	C	25.405522	21.708283	17.051440
39	C	25.100697	23.445613	22.683172
40	H	27.124051	24.199933	21.777174
41	H	25.073593	20.616410	20.806386
42	H	22.958581	14.648416	19.138192
43	H	20.833042	11.804058	16.001190
44	H	20.086152	13.088607	15.429050
45	H	25.399873	24.899060	18.878320
46	H	21.320179	22.254152	18.916339
47	H	25.755481	21.953286	16.040195
48	H	27.013447	16.880880	18.740652
49	H	22.646371	17.642722	21.722148
50	H	19.300108	16.760558	17.355170
51	H	23.400255	15.663478	14.249802
52	H	24.040742	10.759312	16.610211
53	H	20.057283	12.131022	20.314121
54	H	21.098511	10.765384	18.002791
55	H	29.057891	23.174956	19.859307
56	H	24.438310	23.342388	23.556872
57	Cu	21.590006	19.252729	17.402515
58	O	22.364640	20.062519	15.389653
59	C	23.440357	19.651778	15.004898
60	H	20.773148	17.428861	13.195352
61	H	23.941345	20.128747	14.148936
62	H	23.928515	18.805699	15.496688
63	C	19.759778	19.919471	17.237472
64	H	19.219052	19.751690	18.174274
65	H	19.771612	20.990326	17.016346
66	H	19.245801	19.393998	16.427686
67	C	20.374073	17.288154	14.199095
68	H	19.376189	17.720513	14.259853
69	H	20.323383	16.223243	14.422448
70	H	21.021833	17.785110	14.917951

INT-7

Coordinates (Angstroms)

S.No.	Atom	X	Y	Z
1	O	23.111269	12.517630	17.113181
2	O	20.669086	10.870576	19.046235
3	O	21.142471	13.073997	18.991046
4	O	22.064917	10.552667	16.882959
5	O	20.489513	12.689603	16.374458
6	C	23.088159	11.273345	16.880715
7	C	20.669938	12.068154	19.522768
8	O	25.849207	18.572633	18.753393
9	O	22.269449	14.570119	15.641526
10	O	21.184862	17.022898	17.837866
11	O	22.962056	16.857537	19.976736
12	O	20.276513	15.016938	17.418059
13	O	23.735654	18.899076	20.530576
14	O	25.067239	16.535046	18.190348
15	O	23.309612	16.506050	16.114546
16	Al	21.781435	13.847735	17.311246
17	Al	23.172698	16.801006	18.035345
18	O	23.246332	18.566039	17.864290
19	C	25.978071	17.360143	18.456544
20	O	22.903115	14.945332	18.252030
21	C	20.214703	16.253680	17.633294
22	C	22.914689	15.610883	15.337438
23	C	23.208580	17.789784	20.784564

24	O	28.154197	24.277309	20.878224
25	O	24.874171	20.599481	17.215887
26	O	23.121990	22.800170	19.773414
27	O	25.030202	22.746028	21.700126
28	O	22.619181	20.828122	18.837256
29	O	26.417492	24.231027	22.665480
30	O	27.128085	22.700031	19.639678
31	O	25.105625	22.745815	17.846360
32	Al	24.275292	19.686149	18.800985
33	Al	25.103225	22.831699	19.794163
34	O	25.166284	24.610617	19.772587
35	C	28.086137	23.419757	19.922356
36	O	25.150639	20.951755	19.845595
37	C	22.321847	21.960971	19.323881
38	C	25.103401	21.815843	17.005423
39	C	25.462013	23.435606	22.669898
40	H	27.322941	24.268314	21.524638
41	H	25.236858	20.652634	20.756115
42	H	23.063668	14.680182	19.163163
43	H	20.808794	11.789232	16.168554
44	H	20.016623	13.054410	15.615656
45	H	25.202889	24.974697	18.885475
46	H	21.253977	22.209063	19.335360
47	H	25.318174	22.095573	15.965780
48	H	27.003891	16.971256	18.432845
49	H	22.933721	17.607354	21.831734
50	H	19.216563	16.704301	17.636755
51	H	23.142424	15.739709	14.273340
52	H	24.058955	10.810966	16.660645
53	H	20.195272	12.145076	20.502343
54	H	21.166059	10.776383	18.163140
55	H	29.005054	23.354162	19.330709
56	H	24.925712	23.291907	23.620871
57	Cu	21.465800	19.359379	17.699039
58	O	21.635207	19.301396	15.420911
59	C	22.749812	19.171125	14.956902
60	H	23.631912	19.169810	15.603885
61	H	22.885409	19.050804	13.871428
62	C	19.653103	20.092342	17.767706
63	H	19.306706	20.135459	18.805057
64	H	19.644417	21.102384	17.347457
65	H	18.974601	19.460325	17.187446

INT-8

Coordinates (Angstroms)

S.No.	Atom	X	Y	Z
1	O	23.033923	12.437204	17.080433
2	O	20.562217	10.899712	19.065253
3	O	21.121806	13.081770	18.992992
4	O	21.893009	10.523340	16.872672
5	O	20.415094	12.733410	16.385115
6	C	22.948242	11.195416	16.847029
7	C	20.620832	12.096232	19.538189
8	O	25.973025	18.490653	18.750095
9	O	22.266716	14.546898	15.646535
10	O	21.356723	17.008463	17.706696
11	O	23.053551	16.804205	19.922300
12	O	20.305663	15.059142	17.442996
13	O	23.802464	18.862533	20.441485
14	O	25.212505	16.430922	18.238123
15	O	23.538662	16.340300	16.109516
16	Al	21.770343	13.821200	17.309617
17	Al	23.342247	16.680647	17.995691
18	O	23.406146	18.455997	17.783523
19	C	26.113483	17.266351	18.511120
20	O	22.960664	14.859703	18.248413
21	C	20.318760	16.303857	17.572607
22	C	23.035052	15.498843	15.335215
23	C	23.278818	17.755733	20.714265
24	O	28.061732	24.328015	20.854622
25	O	25.045583	20.488199	17.144619
26	O	23.117715	22.698751	19.552416
27	O	24.934772	22.752266	21.554125
28	O	22.669973	20.710596	18.629022
29	O	26.233305	24.297489	22.546402
30	O	27.124611	22.710791	19.597601
31	O	25.191862	22.657453	17.717925
32	Al	24.414262	19.607560	18.715827
33	Al	25.106280	22.797471	19.656057
34	O	25.109073	24.574004	19.591956
35	C	28.056605	23.451112	19.915225
36	O	25.186430	20.916804	19.764231
37	C	22.337017	21.846416	19.107735
38	C	25.255113	21.703998	16.906974
39	C	25.297856	23.479516	22.525200
40	H	27.197613	24.320930	21.457744
41	H	25.207358	20.653771	20.690182
42	H	23.050679	14.615814	19.175759
43	H	20.684976	11.817405	16.177377

44	H	19.942838	13.118076	15.635778
45	H	25.175554	24.921321	18.699873
46	H	21.266192	22.070188	19.113105
47	H	25.514560	21.957127	15.871252
48	H	27.137412	16.876409	18.549823
49	H	22.984255	17.596784	21.759178
50	H	19.365165	16.839137	17.563917
51	H	23.275432	15.594400	14.270846
52	H	23.891256	10.689691	16.603559
53	H	20.170889	12.195410	20.527204
54	H	21.034582	10.783588	18.170778
55	H	29.005452	23.386585	19.373254
56	H	24.715242	23.349091	23.450162
57	Cu	21.631701	19.135668	17.741825
58	O	19.882277	19.531918	17.434742
59	C	19.371910	20.835346	17.509159
60	H	19.250507	21.149486	18.558693
61	H	20.053381	21.560113	17.036597
62	C	18.017103	20.907651	16.815091
63	H	17.316143	20.211981	17.281505
64	H	17.600749	21.915978	16.880909
65	H	18.116072	20.640108	15.760932

TS-5

Coordinates (Angstroms)

S.No.	Atom	X	Y	Z
1	O	23.016930	12.480505	17.112615
2	O	20.583149	10.947676	19.138096
3	O	21.136943	13.130912	19.054241
4	O	21.866028	10.571451	16.916437
5	O	20.389512	12.785360	16.457122
6	C	22.923238	11.239871	16.876425
7	C	20.649204	12.144452	19.609553
8	O	26.002542	18.526568	18.728722
9	O	22.236399	14.592827	15.690736
10	O	21.358924	17.058389	17.783075
11	O	23.097049	16.844757	19.960736
12	O	20.303481	15.111342	17.514326
13	O	23.871302	18.896406	20.469290
14	O	25.221832	16.469974	18.234477
15	O	23.507009	16.391171	16.137975
16	Al	21.761464	13.868982	17.360910
17	Al	23.346242	16.725271	18.029145
18	O	23.414854	18.500587	17.819310
19	C	26.132149	17.301326	18.486929
20	O	22.968858	14.903452	18.282348
21	C	20.320055	16.355538	17.650697
22	C	22.996368	15.548291	15.369884
23	C	23.344888	17.792851	20.749959
24	O	28.137000	24.380781	20.754992
25	O	25.040179	20.533372	17.151493
26	O	23.153837	22.722806	19.646196
27	O	25.049352	22.780351	21.574061
28	O	22.702953	20.752329	18.688870
29	O	26.384940	24.320586	22.524203
30	O	27.160332	22.760857	19.532308
31	O	25.154391	22.702746	17.730612
32	Al	24.447042	19.645438	18.733862
33	Al	25.147813	22.833827	19.671847
34	O	25.134086	24.610242	19.614229
35	C	28.098893	23.508245	19.812589
36	O	25.241774	20.952744	19.768234
37	C	22.371044	21.874407	19.199873
38	C	25.215154	21.754469	16.913213
39	C	25.450862	23.500764	22.535012
40	H	27.300484	24.361544	21.396249
41	H	25.289048	20.685581	20.692056
42	H	23.076519	14.655506	19.206706
43	H	20.653974	11.868273	16.246451
44	H	19.907636	13.170968	15.714450
45	H	25.164857	24.961654	18.721817
46	H	21.298056	22.088810	19.231093
47	H	25.438221	22.017740	15.871608
48	H	27.155110	16.907271	18.502867
49	H	23.070164	17.633681	21.800224
50	H	19.366601	16.891247	17.649881
51	H	23.221657	15.645886	14.302393
52	H	23.860527	10.731517	16.616855
53	H	20.219302	12.242819	20.607512
54	H	21.035305	10.832230	18.233337
55	H	29.023636	23.454397	19.229435
56	H	24.907103	23.361961	23.482085
57	Cu	21.647254	19.196258	17.800518
58	O	19.889041	19.598657	17.531667
59	C	19.432154	20.907710	17.329167
60	H	18.363269	20.858633	17.076634
61	H	19.491559	21.496040	18.259258
62	C	20.173738	21.641672	16.216285
63	H	20.076644	21.096406	15.275099

64	H	19.781199	22.652308	16.077826
65	H	21.238962	21.720509	16.450749

INT-9

Coordinates (Angstroms)

S.No.	Atom	X	Y	Z
1	O	23.057589	12.422511	17.066548
2	O	20.651281	10.831565	19.083347
3	O	21.156339	13.026584	19.000195
4	O	21.942262	10.493898	16.857500
5	O	20.424338	12.676578	16.400738
6	C	22.987939	11.181073	16.826702
7	C	20.690621	12.029455	19.555225
8	O	25.934142	18.489831	18.721832
9	O	22.232895	14.518446	15.644137
10	O	21.288000	16.980817	17.734043
11	O	23.049214	16.769250	19.925151
12	O	20.292669	14.999740	17.471978
13	O	23.790747	18.829955	20.446808
14	O	25.188714	16.426097	18.202214
15	O	23.472161	16.336140	16.099707
16	Al	21.771596	13.783482	17.311941
17	Al	23.313017	16.666219	17.991509
18	O	23.346777	18.433366	17.791926
19	C	26.084246	17.269498	18.470497
20	O	22.948908	14.843045	18.240798
21	C	20.270846	16.241760	17.614617
22	C	22.976019	15.488709	15.327592
23	C	23.280947	17.717252	20.720212
24	O	27.974019	24.353450	20.838115
25	O	24.976002	20.477127	17.131115
26	O	23.044335	22.688075	19.532111
27	O	24.860289	22.744722	21.539892
28	O	22.627796	20.675006	18.653903
29	O	26.145277	24.302223	22.530937
30	O	27.058081	22.719014	19.587593
31	O	25.124004	22.646582	17.704822
32	Al	24.359422	19.591123	18.708589
33	Al	25.035153	22.789085	19.642333
34	O	25.031019	24.565882	19.576385
35	C	27.980444	23.472245	19.902485
36	O	25.135011	20.909158	19.750739
37	C	22.277357	21.817792	19.096907
38	C	25.185145	21.692680	16.893733
39	C	25.217206	23.475956	22.510307
40	H	27.109797	24.337158	21.440125
41	H	25.170565	20.644962	20.675813
42	H	23.049163	14.601444	19.167803
43	H	20.711939	11.763565	16.199346
44	H	19.957835	13.050618	15.642352
45	H	25.101958	24.911894	18.684139
46	H	21.202204	22.026985	19.075592
47	H	25.442333	21.946525	15.857506
48	H	27.112679	16.889860	18.492376
49	H	23.005765	17.547781	21.768887
50	H	19.295244	16.736002	17.633081
51	H	23.198814	15.595345	14.260451
52	H	23.935896	10.690019	16.572823
53	H	20.258594	12.117809	20.553171
54	H	21.105226	10.727438	18.178691
55	H	28.930578	23.417441	19.361591
56	H	24.635809	23.340970	23.435445
57	Cu	21.538121	19.099901	17.816653
58	H	20.119710	19.636007	17.722699

3.3.4 X-ray absorption spectroscopic analysis.

X-ray Near-Edge Structure (XANES) and Extended X-ray Absorption Fine Structure (EXAFS) measurements have been carried out at the Energy-Scanning EXAFS beamline (BL-9) at the Indus-2 Synchrotron Source at Raja Ramanna Centre for Advanced Technology (RRCAT), Indore, India.[74] All the measurements were performed at room temperature. This beamline operates in the energy range of 4 keV to 25 keV. The beamline optics consist of a Rh/Pt coated collimating meridional cylindrical mirror and the collimated beam reflected by the mirror is monochromatized by a Si (111) based double crystal monochromator (DCM). The second crystal of the DCM is a sagittal cylindrical crystal which is used for horizontal focusing of the beam while another Rh/Pt coated bendable post mirror facing downward is used for vertical focusing of the beam at the sample position. Two ionization chambers (300 mm length each) have been used for data collection in the transmission mode; one ionization chamber for measuring incident flux, the second one for measuring transmitted flux. For energy calibration, standard metal foils were used. Appropriate gas pressure and gas mixture have been chosen to achieve 10-20% absorption in the first ionization chamber and 70-90% absorption in the second ionization chamber to obtain a better signal-to-noise ratio. Pellets were made from powder samples for recording absorption spectra. Sample powder was mixed homogeneously with cellulose powder in appropriate proportion and pressed (2 Ton) into a 15 mm diameter disc. The amount of the sample was estimated such that to get a reasonable edge jump at a particular absorption edge of the element to be probed. Spectra were collected at the copper K-edge in transmission mode and were calibrated against the reference spectrum of metallic copper (8978.9 eV). Data were processed using Demeter software.[75] A metallic copper foil standard was used as a reference for energy calibration and was measured simultaneously with experimental samples.

XANES analysis. The oxidation states of the Cu species within MIL-53(Al)-Cu(OH) and MIL-53(Al)-Cu after oxidation of methane were determined by the comparison of the energy of its K-edge positions to that of $CuCl_2$. The positions of the Cu K-edge of MIL-53(Al)-CuCl, MIL-53(Al)-Cu(OH), MIL-53(Al)-Cu after oxidation of methane aligned well with that of $CuCl_2$ (8985.3 eV). We, therefore, concluded that Cu ion in MIL-53(Al)-Cu(OH) and MIL-53(Al)-Cu after oxidation of methane has +2 oxidation state.

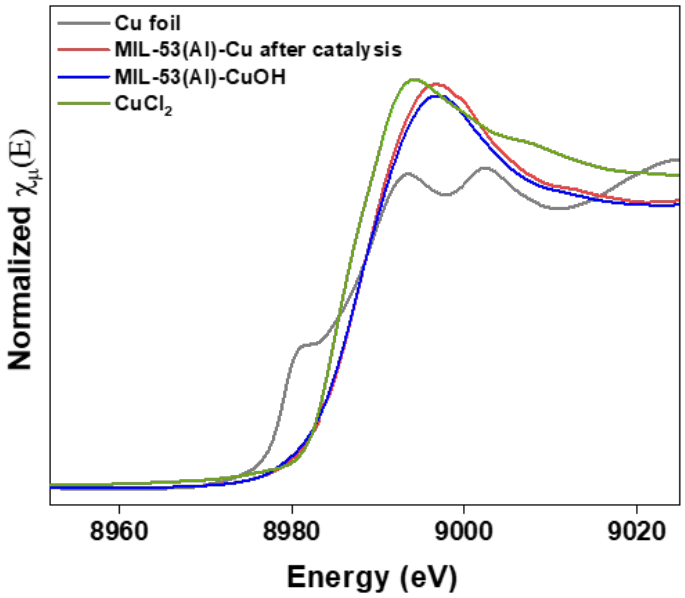


Figure 3.17: μ(E) XAS spectra of metallic Cu(0) (grey), $CuCl_2$ (green), MIL-53(Al)-Cu(OH) (blue), MIL-53(Al)-Cu after catalysis (red)

EXAFS fitting using DFT optimized structures. The spectra were calibrated against the reference spectra and aligned to the first peak in the smoothed first derivative of the absorption spectrum, the background noise was removed, and the spectra were processed to obtain a normalized unit edge step. The fitting parameters of MIL-53(Al)-Cu(OH) and MIL-53(Al)-Cu after oxidation of methane are summarized in Table 3.5 and Table3.6, respectively.

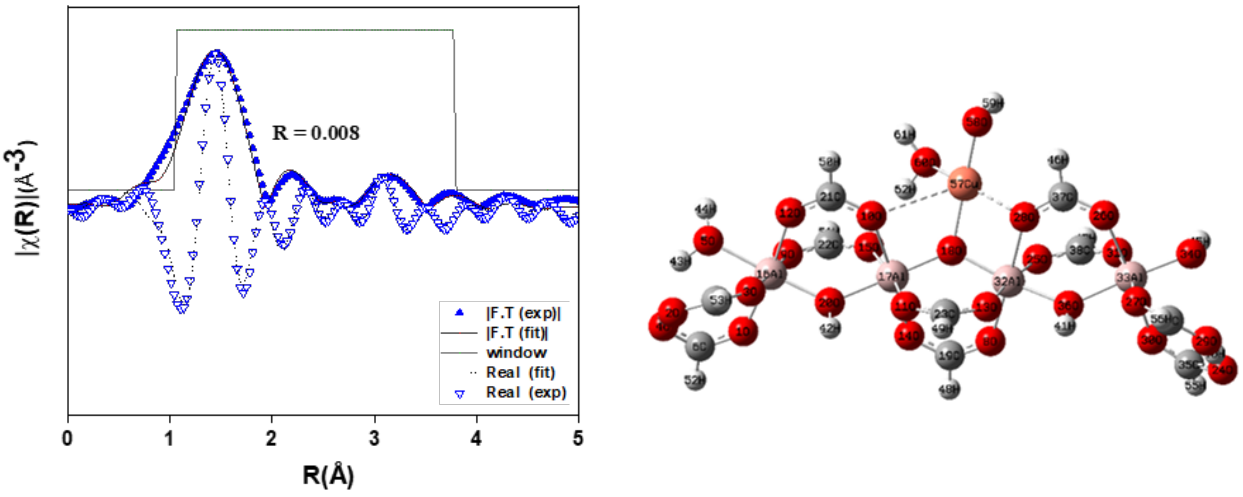


Figure 3.18: (a) EXAFS spectrum and fit of MIL-53(Al)-Cu(OH). (b) DFT-optimized structure of MIL-53(Al)-Cu(OH).

Table 3.5: Summary of EXAFS fitting parameters of MIL-53(Al)-Cu(OH).

Sample	**MIL(Al)-Cu(OH)**	**Fitting range**	***k*** **(2-10 Å^{-1}), R (1.0-3.8 Å)**
Independent points	10	**R-factor**	0.008
Variables	6	$\mathbf{S_0^2}$	0.71
Reduced chi-square	179	ΔE_0 **(eV)**	3.11
R(Cu-O58) (Å)	1.88±0.07	σ^2**(Cu-O58) (Å^2)**	0.004±0.003
R(Cu-O18) (Å)	1.91±0.07	σ^2**(Cu-O18) (Å^2)**	0.004±0.003
R(Cu-O10) (Å)	1.95±0.07	σ^2**(Cu-O10) (Å^2)**	0.004±0.003
R(Cu-O28) (Å)	1.95±0.07	σ^2**(Cu-O28) (Å^2)**	0.004±0.003
R(Cu-O60) (Å)	2.42±0.09	σ^2**(Cu-O60) (Å^2)**	0.002±0.001
R(Cu-H59) (Å)	2.32±0.09	σ^2**(Cu-H59) (Å^2)**	0.002±0.001
R(Cu-H60) (Å)	2.66±0.09	σ^2**(Cu-H60) (Å^2)**	0.002±0.001
R(Cu-H61) (Å)	2.66±0.09	σ^2**(Cu-H61) (Å^2)**	0.002±0.001
R(Cu-Al17) (Å)	3.1±0.04	σ^2**(Cu-Al17) (Å^2)**	0.01±0.001
R(Cu-Al32) (Å)	3.1±0.04	σ^2**(Cu-Al32) (Å^2)**	0.01±0.001
R(Cu-C21) (Å)	3.31±0.04	σ^2**(Cu-C21) (Å^2)**	0.01±0.001
R(Cu-C37) (Å)	3.31±0.04	σ^2**(Cu-C37) (Å^2)**	0.01±0.001
R(Cu-O11) (Å)	3.42±0.04	σ^2**(Cu-O11) (Å^2)**	0.01±0.001
R(Cu-O13) (Å)	3.42±0.04	σ^2**(Cu-O13) (Å^2)**	0.01±0.001
R(Cu-C23) (Å)	3.66±0.04	σ^2**(Cu-C23) (Å^2)**	0.01±0.001

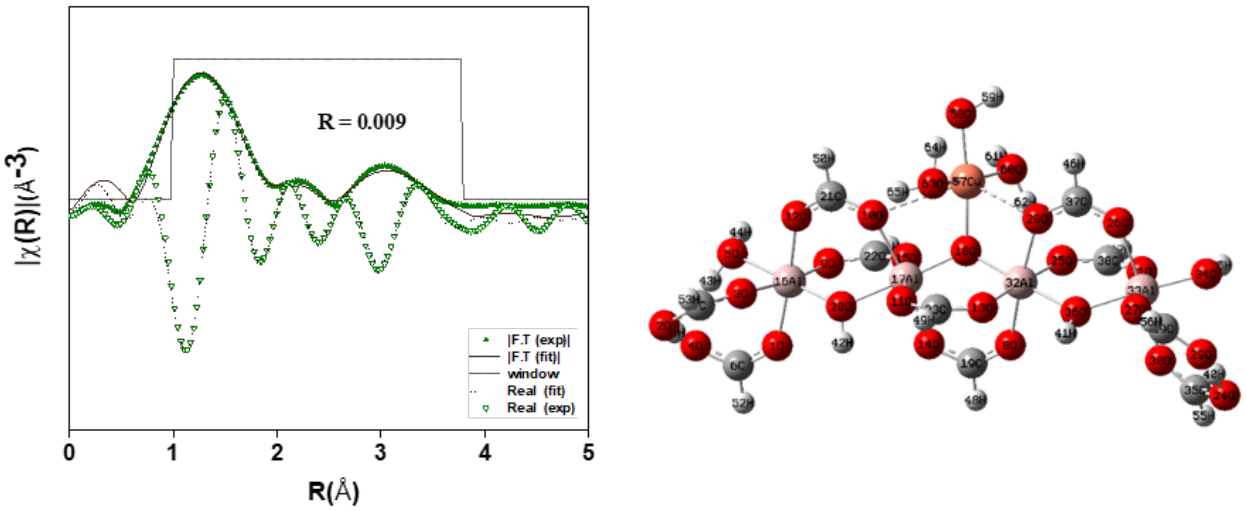


Figure 3.19: (a) EXAFS spectrum and fit of MIL-53(Al)-Cu after catalysis. (b) DFT-optimized structure of MIL-53(Al)-Cu after catalysis.

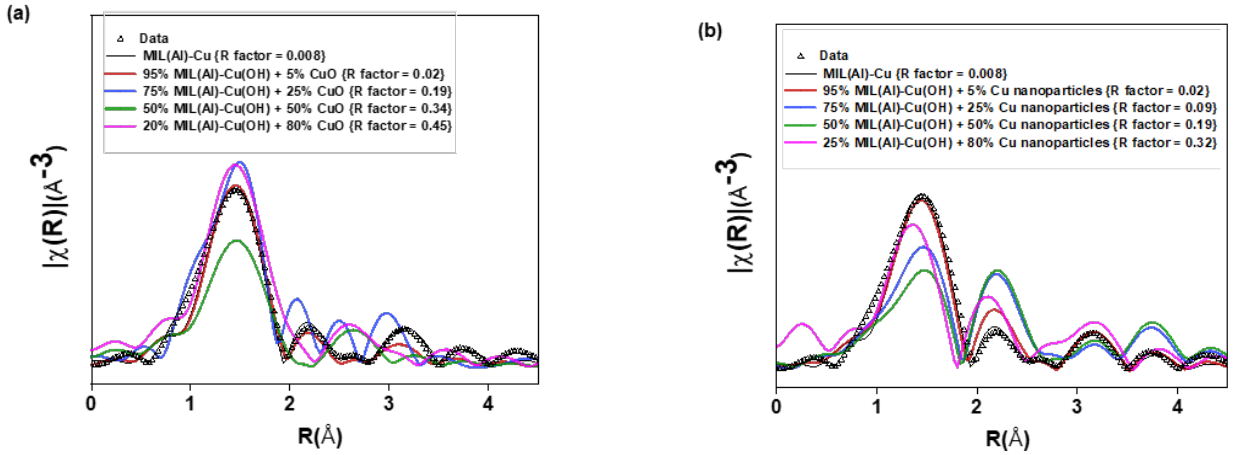


Figure 3.20: (a) EXAFS spectrum of MIL-53(Al)-Cu(OH) fitted with 5% CuO and 95% MIL-53(Al)-Cu(OH) (red); 25% CuO and 75% MIL-53(Al)-Cu(OH) (blue); 50% CuO and 50% MIL-53(Al)-Cu(OH) (green); 80% CuO and 20% MIL-53(Al)-Cu(OH) (magenta). (b) EXAFS spectrum of MIL-53(Al)-Cu(OH) fitted with 5% Cu (0) and 95% MIL-53(Al)-Cu(OH) (red); 25% Cu (0) and 75% MIL-53(Al)-Cu(OH) (blue); 50% Cu (0) and 50% MIL-53(Al)-Cu(OH) (green) and 80% Cu (0) and 20% MIL-53(Al)-Cu(OH) (magenta). The significant misfits indicate that MIL-53(Al)-Cu(OH) does not contain any Cu dimers/oligomers or Cu-nanoparticles.

Table 3.6: Summary of EXAFS fitting parameters of MIL-53(Al)-Cu after catalysis.

Sample	**MIL(Al)Cu-OH**	**Fitting range**	***k* (2-10 Å^{-1}), R (1.0-3.8 Å)**
Independent points	10	**R-factor**	0.009
Variables	6	$\mathbf{S_0^2}$	0.74
Reduced chi-square	168	ΔE_0 **(eV)**	1.11
R(Cu-O58) (Å)	1.88±0.003	σ^2**(Cu-O58) (Å^2)**	0.003±0.001
R(Cu-O18) (Å)	1.91±0.003	σ^2**(Cu-O18) (Å^2)**	0.003±0.001
R(Cu-O10) (Å)	1.95±0.003	σ^2**(Cu-O10) (Å^2)**	0.003±0.001
R(Cu-O28) (Å)	1.95±0.003	σ^2**(Cu-O28) (Å^2)**	0.003±0.001
R(Cu-O60) (Å)	2.42±0.09	σ^2**(Cu-O60) (Å^2)**	0.002±0.001
R(Cu-O63) (Å)	2.42±0.09	σ^2**(Cu-O63) (Å^2)**	0.002±0.001
R(Cu-H59) (Å)	2.32±0.09	σ^2**(Cu-H59) (Å^2)**	0.002±0.001
R(Cu-H61) (Å)	2.66±0.09	σ^2**(Cu-H61) (Å^2)**	0.002±0.001
R(Cu-H65) (Å)	2.66±0.09	σ^2**(Cu-H65) (Å^2)**	0.002±0.001
R(Cu-H64) (Å)	2.66±0.09	σ^2**(Cu-H64) (Å^2)**	0.002±0.001
R(Cu-Al17) (Å)	3.27±0.06	σ^2**(Cu-Al17) (Å^2)**	0.01±0.004
R(Cu-Al32) (Å)	3.27±0.06	σ^2**(Cu-Al32) (Å^2)**	0.01±0.004
R(Cu-C21) (Å)	3.36±0.06	σ^2**(Cu-C21) (Å^2)**	0.01±0.004
R(Cu-C37) (Å)	3.36±0.06	σ^2**(Cu-C37) (Å^2)**	0.01±0.004
R(Cu-O11) (Å)	3.44±0.06	σ^2**(Cu-O11) (Å^2)**	0.01±0.004
R(Cu-O13) (Å)	3.44±0.06	σ^2**(Cu-O13) (Å^2)**	0.01±0.004
R(Cu-C23) (Å)	3.7±0.04	σ^2**(Cu-C23) (Å^2)**	0.01±0.004

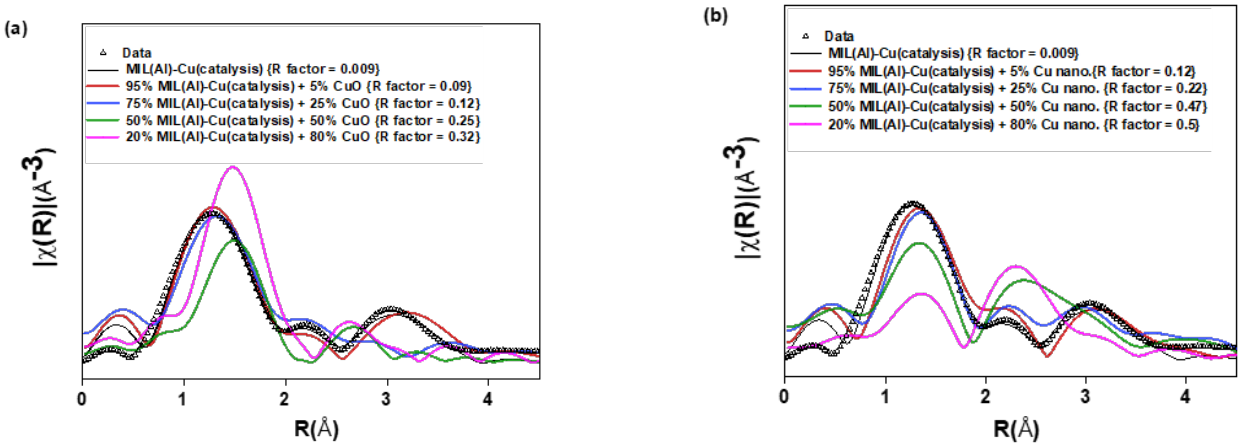


Figure 3.21: (a) EXAFS spectrum of MIL-53(Al)-Cu after catalysis fitted with 5% CuO and 95% MIL-53(Al)-Cu(OH) (red); 25% CuO and 75% MIL-53(Al)-Cu(OH) (blue); 50% CuO and 50% MIL-53(Al)-Cu(OH) (green); 80% CuO and 20% MIL-53(Al)-Cu(OH) (magenta). (b) EXAFS spectrum of MIL-53(Al)-Cu after catalysis fitted with 5% Cu (0) and 95% MIL-53(Al)-Cu(OH) (red); 25% Cu (0) and 75% MIL-53(Al)-Cu(OH) (blue); 50% Cu (0) and 50% MIL-53(Al)-Cu(OH) (green) and 80% Cu (0) and 20% MIL-53(Al)-Cu(OH) (magenta). The significant misfits indicate that MIL-53(Al)-Cu(OH) does not contain any Cu dimers/oligomers or Cu-nanoparticles.

XPS analaysis of MIL-53(Al)-Cu(OH).

All the binding energies were corrected with reference to the C1s peak at 284.8 eV. MULTIPAK software was used for peak analysis and de-convolution studies.

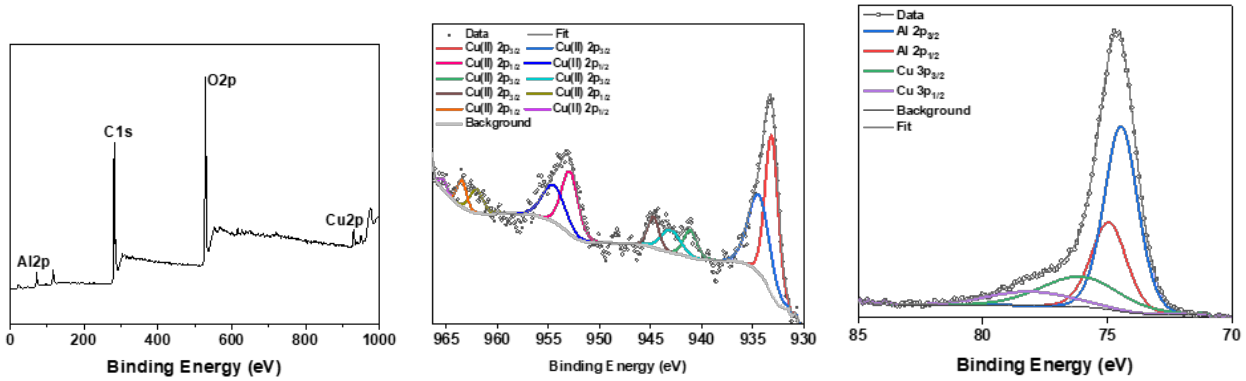


Figure 3.22: (a) Raw XPS data of MIL-53(Al)-Cu(OH). (b) XPS fitting of copper in MIL-53(Al)-Cu(OH). (c) XPS fitting of aluminium in MIL-53(Al)-Cu(OH).

Table 3.7: XPS fitting parameters for Cu(II) in MIL-53(Al)-Cu(OH) MOF.

Component	**Position (eV)**	**FWHM (eV)**	**Area**	**Area%**
Cu(II) 2p	933.13	1.35	745.08	23.46
Cu(II) 2p	934.37	2.48	761.72	23.97
Cu(II) 2p	941.05	1.44	129.14	4.05
Cu(II) 2p	943.00	2.50	255.04	7.05
Cu(II) 2p	944.79	1.35	151.00	4.73
Cu(II) 2p	952.92	1.80	372.54	11.63
Cu(II) 2p	954.41	2.64	380.86	11.88
Cu(II) 2p	961.52	0.35	24.88	0.77
Cu(II) 2p	962.96	2.88	344.03	10.69
Cu(II) 2p	965.49	0.8	56.86	1.76

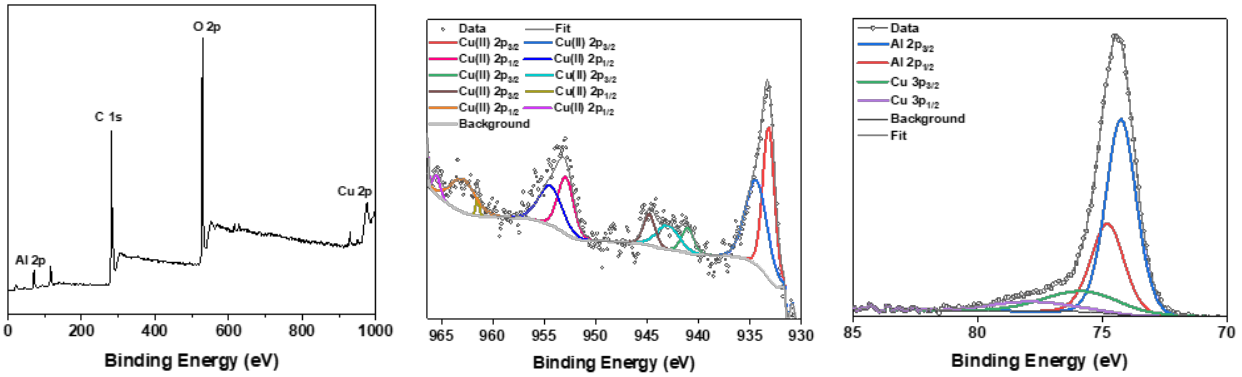


Figure 3.23: (a) Raw XPS data of MIL-53(Al)-Cu after catalysis. (b) XPS fitting of copper in MIL-53(Al)-Cu after catalysis. (c) XPS fitting of aluminium in MIL-53(Al)-Cu after catalysis.

Table 3.8: XPS fitting parameters for Cu(II) in MIL-53(Al)-Cu MOF recovered after catalysis.

Component	**Position (eV)**	**FWHM (eV)**	**Area**	**Area%**
Cu(II) 2p	933.13	1.35	745.08	23.46
Cu(II) 2p	934.37	2.48	761.72	23.97
Cu(II) 2p	941.05	1.44	129.14	4.05
Cu(II) 2p	943.00	2.50	255.04	7.05
Cu(II) 2p	944.79	1.35	151.00	4.73
Cu(II) 2p	952.92	1.80	372.54	11.63
Cu(II) 2p	954.41	2.64	380.86	11.88
Cu(II) 2p	961.52	0.35	24.88	0.77
Cu(II) 2p	962.96	2.88	344.03	10.69
Cu(II) 2p	965.49	0.8	56.86	1.76

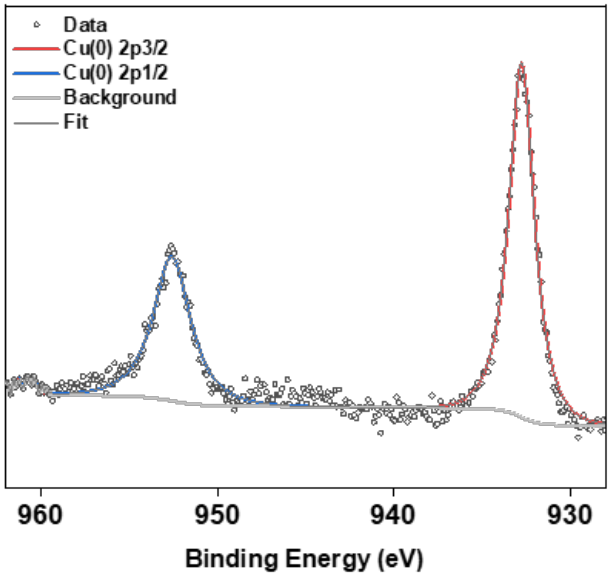


Figure 3.24: XPS fitting of copper in Cu@MIL-53(Al).

Table 3.9: XPS fitting parameters for Cu(0) in Cu@MIL-53(Al).

Component	**Position (eV)**	**FWHM (eV)**	**Area**	**Area%**
Cu(0) 2p	932.68	0.7	1263.1	62.74
Cu(0) 2p	952.52	1.6	757	37.26

Table 3.10: Simulated parameters of EPR spectroscopic spin-trapping experiments for MIL-53(Al)-Cu(OH) catalysed oxidation of methane.[a]

Adducts	**g-factor**	**A^{14}N (G)**	$A_{\alpha H}$ **(G)**	**lw (mT)[b]**
DMPO-CH_3	2.01	22.4	15.9	0.8

[a]Reaction conditions: 3.8 mg MIL-53(Al)-Cu(OH) (4.0 μmol Cu), 30 bar CH_4, 10 bar O_2, 50 μL DMPO, 32 h, 175 °C.
[b]The linewidth (lw, in mT) defines the FWHM (full width at half height) of the absorption Gaussian (first number).

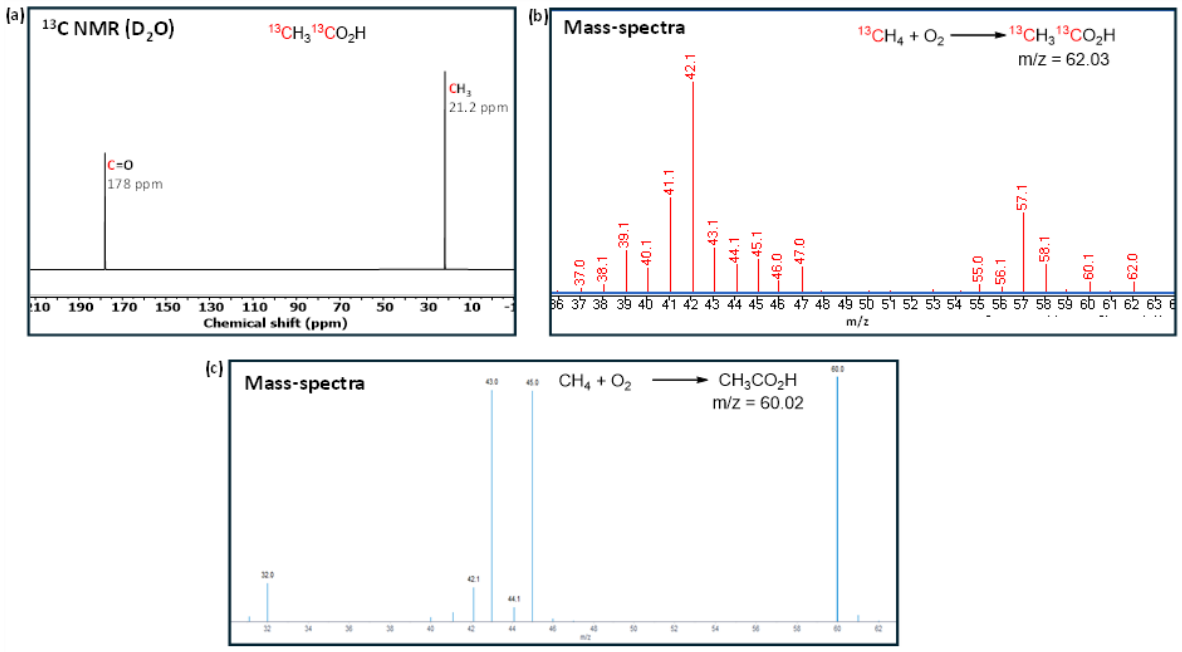


Figure 3.25: (a) ^{13}C NMR (400 MHz, D_2O) spectrum of the reaction mixture obtained after $^{13}CH_4$ oxidation by O_2 using MIL-53(Al)-Cu(OH) as the catalyst. Reaction conditions: 3.8 mg MIL-53(Al)-Cu(OH) (4.0 μmol Cu), 30 bar $^{13}CH_4$, 10 bar O_2, 32 h, 175 °C. Signal centered at 21.2 ppm, corresponding to the sp^3 hybridized carbon and signal centred at 178 ppm corresponds to sp^2 hybridized carbon in $^{13}CH_3{}^{13}CO_2H$, confirms the involvement of CH_4-derived carbon atoms in the formation of acetic acid. (b) Mass spectra of the obtained $^{13}CH_3{}^{13}CO_2H$ after $^{13}CH_4$ oxidation using O_2. (c) Mass spectra of the obtained CH_3CO_2H after CH_4 oxidation using O_2 under identical reaction conditions.

Comparison of catalytic activity of MIL-53(Al)-Cu(OH) catalysed oxidation of CH_4 to CH_3CO_2H using O_2 with other reported catalysts.

Reference	**Catalyst**	**Oxidant (Flow/Total pressure)**	**Condition**	**Temp (°C)**	**CH_3CO_2H Selectivity**	**CH_3CO_2H Productivity**			
						μmol g^{-1}_{cat} h^{-1}	mmol mol^{-1}_{metal} h^{-1}	mmol mol^{-1}_{metal}	μmol g^{-1}_{cat}
This Work	MIL-53(Al)-Cu(OH)	CH_4 (30 bar), O_2 (10 bar)	Batch	175	92	**12,418**	**11,796**	**3,77,472**	**3,97,368**
ACS Catal. 14, 1797–1807 (2024)	Au/24h-ZSM5(DR-24)	CH_4 (20.7 bar), O_2 (3.5 bar)	Batch	240	21				12.1
Nat. Commun. 14, 3047 (2023)	PdO/Pd–WO_3-2	CH_4 + H_2O	Flow/Light	r.t	91.6	90.7			
		CH_4 (10 bar) + H_2O	Batch/Light	r.t	60.2	62.5			
Appl. Catal. B 337, 122983 (2023)	Ag/AgCl-WO_x	0.1 bar CH_4:N_2 (1:9), 0.1 bar O_2	Light	25	62.7	188.5			
ACS Catal. 13, 7199–7209 (2023)	Au/ZSM-5+XC72R	CH_4 (20.7 bar), O_2 (3.5 bar)	Batch	240	2.5				31.4
J. Am. Chem. Soc. 145, 6156–6165 (2023)	Ce-UiO-Cu(OH)	CH_4 (30 bar), O_2 (6 bar)	Batch	115	96				3,24,324
Nat. Catal. 5, 45–54 (2022)	Au-ZSM-5	CH_4 (20.7 bar), O_2 (3.5 bar)	Batch	240	41	45.48			3.79

3.4 Conclusions

In conclusion, we have developed a highly active single-site and heterogeneous earth-abundant metal catalyst for direct methane oxidation to acetic acid using only O_2. The catalyst displayed outstanding productivity of 3,77,472 $mmol_{CH_3CO_2H} \cdot mol_{Cu}^{-1}$ and maintained 95% liquid selectivity over six consecutive runs without any loss in activity. The catalytic pathway of MIL-53(Al)-Cu(OH) catalyst differs from that of our previously reported cerium-UiO MOF node-supported copper(II)-hydroxyl catalysts, [Ce-UiO-66-Cu(OH)].[76] In the case of Ce-UiO-66-Cu(OH) catalyst, the conversion of methane to acetic acid occurs 115 °C through a non-radical pathway, where the carbonylation of methane with CO forms acetic acid. This difference in mechanism can be attributed to the distinct reaction temperatures. For the MIL-53(Al)-Cu(OH) catalyzed transformation of methane to acetic acid, the homolytic cleavage of the "Cu-CH_3" species is likely favored at 175 °C; however, this process does not occur under the operating conditions of 115 °C used for the Ce-UiO-66-Cu(OH) catalyst. Spectroscopic analyses and controlled experiments suggested that the direct oxidation of methane to acetic acid occurs via a catalytic cycle, where methane is first oxidized to acetaldehyde mediated by MIL-53(Al)-Cu(OH), followed by the further thermal oxidation of acetaldehyde to acetic acid by O_2. This research provides valuable insights for the development of environmentally friendly heterogeneous catalysts using abundant metals, enabling the efficient activation and partial C-H methane oxidation into acetic acid under mild and eco-friendly reaction conditions.

References

[1] Acetic Acid Global Market Volume 2015-2030. https://www.statista.com/statistics/1245203/acetic-acid-market-volume-worldwide/.

[2] Harris, F. Applications of Acetic Acid to Well Completion, Stimulation and Reconditioning. *Journal of Petroleum Technology* **1961**, *13*, 637–639.

[3] Le Berre, C.; Serp, P.; Kalck, P.; Torrence, G. P. *Ullmann's Encyclopedia of Industrial Chemistry*; John Wiley Sons, Ltd, 2014; pp 1–34.

[4] Micciche, A. C.; Barabote, R. D.; Dittoe, D. K.; Ricke, S. C. In silico genome analysis

of an acid mine drainage species, Acidiphilium multivorum, for potential commercial acetic acid production and biomining. *Journal of Environmental Science and Health, Part B* **2020**, *55*, 447–454.

[5] Singh, A. D.; Krase, N. W. Synthesis of Acetic Acid from Methanol and Carbon Monoxide. *Industrial & Engineering Chemistry* **1935**, *27*, 909–914.

[6] Knifton, J. F. Syngas Reactions: IX. Acetic Acid from Synthesis Gas. *Journal of Catalysis* **1985**, *96*, 439–453.

[7] Sunley, G. J.; Watson, D. J. High Productivity Methanol Carbonylation Catalysis Using Iridium: The Cativa™ Process for the Manufacture of Acetic Acid. *Catalysis Today* **2000**, *58*, 293–307.

[8] Thomas, C. M.; Süss-Fink, G. Ligand Effects in the Rhodium-Catalyzed Carbonylation of Methanol. *Coordination Chemistry Reviews* **2003**, *243*, 125–142.

[9] Budiman, A. W.; Nam, J. S.; Park, J. H.; Mukti, R. I.; Chang, T. S.; Bae, J. W.; Choi, M. J. Review of Acetic Acid Synthesis from Various Feedstocks Through Different Catalytic Processes. *Catalysis Surveys from Asia* **2016**, *20*, 173–193.

[10] Pruett, R. L. Synthesis Gas: A Raw Material for Industrial Chemicals. *Science* **1981**, *211*, 11–16.

[11] Schwarz, H. Chemistry with Methane: Concepts Rather than Recipes. *Angewandte Chemie International Edition* **2011**, *50*, 10096–10115.

[12] Taifan, W.; Baltrusaitis, J. CH4 Conversion to Value Added Products: Potential, Limitations and Extensions of a Single Step Heterogeneous Catalysis. *Applied Catalysis B: Environmental* **2016**, *198*, 525–547.

[13] Wang, W.; Zhou, W.; Tang, Y.; Cao, W.; Docherty, S. R.; Wu, F.; Cheng, K.; Zhang, Q.; Copéret, C.; Wang, Y. Selective Oxidation of Methane to Methanol over Au/H-MOR. *Journal of the American Chemical Society* **2023**, *145*, 12928–12934.

[14] Li, H.; Xiong, C.; Fei, M.; Ma, L.; Zhang, H.; Yan, X.; Tieu, P.; Yuan, Y.; Zhang, Y.; Nyakuchena, J.; Huang, J.; Pan, X.; Waegele, M. M.; Jiang, D.-e.; Wang, D. Selective Formation of Acetic Acid and Methanol by Direct Methane Oxidation Using Rhodium

Single-Atom Catalysts. *Journal of the American Chemical Society* **2023**, *145*, 11415–11419.

[15] Shan, J.; Li, M.; Allard, L. F.; Lee, S.; Flytzani-Stephanopoulos, M. Mild Oxidation of Methane to Methanol or Acetic Acid on Supported Isolated Rhodium Catalysts. *Nature* **2017**, *551*, 605–608.

[16] Lanza, R.; Järås, S. G.; Canu, P. Partial Oxidation of Methane over Supported Ruthenium Catalysts. *Applied Catalysis A: General* **2007**, *325*, 57–67.

[17] Li, H.; Fei, M.; Troiano, J. L.; Ma, L.; Yan, X.; Tieu, P.; Yuan, Y.; Zhang, Y.; Liu, T.; Pan, X.; Brudvig, G. W.; Wang, D. Selective Methane Oxidation by Heterogenized Iridium Catalysts. *Journal of the American Chemical Society* **2023**, *145*, 769–773.

[18] Cao, J. et al. Methane Conversion to Methanol Using Au/ZSM-5 Is Promoted by Carbon. *ACS Catalysis* **2023**, *13*, 7199–7209.

[19] Zhang, W.; Xi, D.; Chen, Y.; Chen, A.; Jiang, Y.; Liu, H.; Zhou, Z.; Zhang, H.; Liu, Z.; Long, R.; Xiong, Y. Light-Driven Flow Synthesis of Acetic Acid from Methane with Chemical Looping. *Nature Communications* **2023**, *14*, 3047.

[20] Qi, G. et al. Au-ZSM-5 Catalyses the Selective Oxidation ofCH4 to CH3OH andCH3COOH Using O2. *Nature Catalysis* **2022**, *5*, 45–54.

[21] Wang, J.; Zhang, L.; Zeng, D.; Wang, W.; Li, R.; Jia, T.; Cui, B.; Chu, H.; Wang, W. Corrigendum to "Multi-radicals Mediated One-Step Conversion of Methane to Acetic Acid via Photocatalysis" [Appl. Catal. B Environ. 337 (2023) 122983]. *Applied Catalysis B: Environmental* **2023**, *338*, 123062.

[22] Antil, N.; Chauhan, M.; Akhtar, N.; Kalita, R.; Manna, K. Selective Methane Oxidation to Acetic Acid Using Molecular Oxygen over a Mono-Copper Hydroxyl Catalyst. *Journal of the American Chemical Society* **2023**, *145*, 6156–6165.

[23] Szécsényi, Á.; Li, G.; Gascon, J.; Pidko, E. A. Unraveling Reaction Networks behind the Catalytic Oxidation of Methane with H2O2 over a Mixed-Metal MIL-53(Al,Fe) MOF Catalyst. *Chemical Science* **2018**, *9*, 6765–6773.

[24] Begum, W.; Chauhan, M.; Kalita, R.; Gupta, P.; Akhtar, N.; Antil, N.; Newar, R.; Manna, K. Synergetic Ni–Ce Active Sites in Mixed Cerium/Zirconium Metal–Organic Framework Nodes for Selective Methane Oxidation into Ethanol. *ACS Catalysis* **2024**, *14*, 10427–10436.

[25] Rungtaweevoranit, B.; Abdel-Mageed, A. M.; Khemthong, P.; Eaimsumang, S.; Chakarawet, K.; Butburee, T.; Kunkel, B.; Wohlrab, S.; Chainok, K.; Phanthasri, J.; Wannapaiboon, S.; Youngjan, S.; Seehamongkol, T.; Impeng, S.; Faungnawakij, K. Structural Evolution of Iron-Loaded Metal–Organic Framework Catalysts for Continuous Gas-Phase Oxidation of Methane to Methanol. *ACS Applied Materials & Interfaces* **2023**, *15*, 26700–26709.

[26] Ikuno, T. et al. Methane Oxidation to Methanol Catalyzed by Cu-Oxo Clusters Stabilized in NU-1000 Metal–Organic Framework. *Journal of the American Chemical Society* **2017**, *139*, 10294–10301.

[27] Andrade, L. S.; Lima, H. H.; Silva, C. T.; Amorim, W. L.; Poço, J. G.; López-Castillo, A.; Kirillova, M. V.; Carvalho, W. A.; Kirillov, A. M.; Mandelli, D. Metal–Organic Frameworks as Catalysts and Biocatalysts for Methane Oxidation: The Current State of the Art. *Coordination Chemistry Reviews* **2023**, *481*, 215042.

[28] Antil, N.; Chauhan, M.; Akhtar, N.; Newar, R.; Begum, W.; Malik, J.; Manna, K. Metal–Organic Framework-Encaged Monomeric Cobalt(III) Hydroperoxides Enable Chemoselective Methane Oxidation to Methanol. *ACS Catalysis* **2022**, *12*, 11159–11168.

[29] Wu, M.; Miao, M.; Li, W.; Zhang, X.; Zhang, L.; Zhen, T.; Fu, Y.; Jin, J.; Yuan, L. Metal-Organic Framework-Derived One-Dimensional Pd@CeO2 Catalysts with Enhanced Activity for Methane Oxidation. *Fuel* **2023**, *331*, 125575.

[30] Hall, J. N.; Bollini, P. Low-Temperature, Ambient Pressure Oxidation of Methane to Methanol Over Every Tri-Iron Node in a Metal–Organic Framework Material. *Chemistry – A European Journal* **2020**, *26*, 16639–16643.

[31] Barona, M.; Snurr, R. Q. Exploring the Tunability of Trimetallic MOF Nodes for Partial Oxidation of Methane to Methanol. *ACS Applied Materials & Interfaces* **2020**, *12*, 28217–28231.

[32] Tavani, F.; Tofoni, A.; D'Angelo, P. Exploring the Methane to Methanol Oxidation over Iron and Copper Sites in Metal–Organic Frameworks. *Catalysts* **2023**, *13*, 1338.

[33] Sui, J.; Gao, M.-L.; Qian, B.; Liu, C.; Pan, Y.; Meng, Z.; Yuan, D.; Jiang, H.-L. Bioinspired Microenvironment Modulation of Metal–Organic Framework-Based Catalysts for Selective Methane Oxidation. *Science Bulletin* **2023**, *68*, 1886–1893.

[34] Baek, J.; Rungtaweevoranit, B.; Pei, X.; Park, M.; Fakra, S. C.; Liu, Y.-S.; Matheu, R.; Alshmimri, S. A.; Alshehri, S.; Trickett, C. A.; Somorjai, G. A.; Yaghi, O. M. Bioinspired Metal–Organic Framework Catalysts for Selective Methane Oxidation to Methanol. *Journal of the American Chemical Society* **2018**, *140*, 18208–18216.

[35] Simons, M. C.; Prinslow, S. D.; Babucci, M.; Hoffman, A. S.; Hong, J.; Vitillo, J. G.; Bare, S. R.; Gates, B. C.; Lu, C. C.; Gagliardi, L.; Bhan, A. Beyond Radical Rebound: Methane Oxidation to Methanol Catalyzed by Iron Species in Metal–Organic Framework Nodes. *Journal of the American Chemical Society* **2021**, *143*, 12165–12174.

[36] Zheng, J. et al. Selective Methane Oxidation to Methanol on Cu-Oxo Dimers Stabilized by Zirconia Nodes of an NU-1000 Metal–Organic Framework. *Journal of the American Chemical Society* **2019**, *141*, 9292–9304.

[37] Li, H.; Eddaoudi, M.; O'Keeffe, M.; Yaghi, O. M. Design and Synthesis of an Exceptionally Stable and Highly Porous Metal-Organic Framework. *Nature* **1999**, *402*, 276–279.

[38] Lee, J.; Farha, O. K.; Roberts, J.; Scheidt, K. A.; Nguyen, S. T.; Hupp, J. T. Metal–Organic Framework Materials as Catalysts. *Chemical Society Reviews* **2009**, *38*, 1450–1459.

[39] Cohen, S. M. Postsynthetic Methods for the Functionalization of Metal–Organic Frameworks. *Chemical Reviews* **2012**, *112*, 970–1000.

[40] Kutzscher, C.; Nickerl, G.; Senkovska, I.; Bon, V.; Kaskel, S. Proline Functionalized UiO-67 and UiO-68 Type Metal–Organic Frameworks Showing Reversed Diastereoselectivity in Aldol Addition Reactions. *Chemistry of Materials* **2016**, *28*, 2573–2580.

[41] Bai, Y.; Dou, Y.; Xie, L.-H.; Rutledge, W.; Li, J.-R.; Zhou, H.-C. Zr-Based Metal–Organic Frameworks: Design, Synthesis, Structure, and Applications. *Chemical Society Reviews* **2016**, *45*, 2327–2367.

[42] Metzger, E. D.; Comito, R. J.; Hendon, C. H.; Dincă, M. Mechanism of Single-Site Molecule-Like Catalytic Ethylene Dimerization in Ni-MFU-4l. *Journal of the American Chemical Society* **2017**, *139*, 757–762.

[43] Furukawa, H.; Cordova, K. E.; O'Keeffe, M.; Yaghi, O. M. The Chemistry and Applications of Metal-Organic Frameworks. *Science* **2013**, *341*, 1230444.

[44] Kalaj, M.; Cohen, S. M. Postsynthetic Modification: An Enabling Technology for the Advancement of Metal–Organic Frameworks. *ACS Central Science* **2020**, *6*, 1046–1057.

[45] Manna, K.; Zhang, T.; Carboni, M.; Abney, C. W.; Lin, W. Salicylaldimine-Based Metal–Organic Framework Enabling Highly Active Olefin Hydrogenation with Iron and Cobalt Catalysts. *Journal of the American Chemical Society* **2014**, *136*, 13182–13185.

[46] Newar, R.; Kalita, R.; Akhtar, N.; Antil, N.; Chauhan, M.; Manna, K. N-Formylation of Amines Utilizing CO2 by a Heterogeneous Metal–Organic Framework Supported Single-Site Cobalt Catalyst. *Catalysis Science & Technology* **2022**, *12*, 6795–6804.

[47] Zhang, T.; Manna, K.; Lin, W. Metal–Organic Frameworks Stabilize Solution-Inaccessible Cobalt Catalysts for Highly Efficient Broad-Scope Organic Transformations. *Journal of the American Chemical Society* **2016**, *138*, 3241–3249.

[48] Manna, K.; Ji, P.; Lin, Z.; Greene, F. X.; Urban, A.; Thacker, N. C.; Lin, W. Chemoselective Single-Site Earth-abundant Metal Catalysts at Metal–Organic Framework Nodes. *Nature Communications* **2016**, *7*, 12610.

[49] Newar, R.; Akhtar, N.; Antil, N.; Kumar, A.; Shukla, S.; Begum, W.; Manna, K. Amino Acid-Functionalized Metal-Organic Frameworks for Asymmetric Base–Metal Catalysis. *Angewandte Chemie International Edition* **2021**, *60*, 10964–10970.

[50] Feng, X.; Ji, P.; Li, Z.; Drake, T.; Oliveres, P.; Chen, E. Y.; Song, Y.; Wang, C.; Lin, W. Aluminum Hydroxide Secondary Building Units in a Metal–Organic Framework Support Earth-Abundant Metal Catalysts for Broad-Scope Organic Transformations. *ACS Catalysis* **2019**, *9*, 3327–3337.

[51] Shi, J.; Han, R.; Lu, S.; Liu, Q. A Metal-OH Group Modification Strategy to Prepare Highly-Hydrophobic MIL-53-Al for Efficient Acetone Capture under Humid Conditions. *Journal of Environmental Sciences* **2021**, *107*, 111–123.

[52] Torres-Ochoa, J. A.; Cabrera-German, D.; Cortazar-Martinez, O.; Bravo-Sanchez, M.; Gomez-Sosa, G.; Herrera-Gomez, A. Peak-Fitting of Cu 2p Photoemission Spectra in Cu0, Cu1+, and Cu2+ Oxides: A Method for Discriminating Cu0 from Cu1+. *Applied Surface Science* **2023**, *622*, 156960.

[53] Khalakhan, I.; Vorokhta, M.; Xie, X.; Piliai, L.; Matolínová, I. On the Interpretation of X-ray Photoelectron Spectra of Pt-Cu Bimetallic Alloys. *Journal of Electron Spectroscopy and Related Phenomena* **2021**, *246*, 147027.

[54] Gaur, A.; Klysubun, W.; Nitin Nair, N.; Shrivastava, B. D.; Prasad, J.; Srivastava, K. XAFS Study of Copper(II) Complexes with Square Planar and Square Pyramidal Coordination Geometries. *Journal of Molecular Structure* **2016**, *1118*, 212–218.

[55] Kucherov, A. V.; Slinkin, A. A.; Kondrat'ev, D. A.; Bondarenko, T. N.; Rubinstein, A. M.; Minachev, Kh. M. Cu2+-Cation Location and Reactivity in Mordenite and ZSM-5: E.s.r.-Study. *Zeolites* **1985**, *5*, 320–324.

[56] Tavernier, S. D.; Schoonheydt, R. A. Coordination of Cu2+ in Synthetic Mordenites. *Zeolites* **1991**, *11*, 155–163.

[57] Dedecek, J.; Sobalik, Z.; Tvaruazkova, Z.; Kaucky, D.; Wichterlova, B. Coordination of Cu Ions in High-Silica Zeolite Matrixes. Cu+ Photoluminescence, IR of NO Adsorbed on Cu2+, and Cu2+ ESR Study. *The Journal of Physical Chemistry* **1995**, *99*, 16327–16337.

[58] Gaur, A.; Shrivastava, B. D. Speciation Using X-ray Absorption Fine Structure (XAFS). *Review Journal of Chemistry* **2015**, *5*, 361–398.

[59] Petersen, A. R.; Taylor, R. A.; Vicente-Hernández, I.; Mallender, P. R.; Olley, H.; White, A. J. P.; Britovsek, G. J. P. Oxygen Insertion into Metal Carbon Bonds: Formation of Methylperoxo Pd(II) and Pt(II) Complexes via Photogenerated Dinuclear Intermediates. *Journal of the American Chemical Society* **2014**, *136*, 14089–14099.

[60] Fernández-Alvarez, V. M.; Ho, S. K. Y.; Britovsek, G. J. P.; Maseras, F. A DFT-based Mechanistic Proposal for the Light-Driven Insertion of Dioxygen into Pt(II)–C Bonds. *Chemical Science* **2018**, *9*, 5039–5046.

[61] Paria, S.; Morimoto, Y.; Ohta, T.; Okabe, S.; Sugimoto, H.; Ogura, T.; Itoh, S. Copper(I)–Dioxygen Reactivity in the Isolated Cavity of a Nanoscale Molecular Architecture. *European Journal of Inorganic Chemistry* **2018**, *2018*, 1976–1983.

[62] Paria, S.; Ohta, T.; Morimoto, Y.; Sugimoto, H.; Ogura, T.; Itoh, S. Structure and Reactivity of Copper Complexes Supported by a Bulky Tripodal N4 Ligand: Copper(I)/Dioxygen Reactivity and Formation of a Hydroperoxide Copper(II) Complex. *Zeitschrift für anorganische und allgemeine Chemie* **2018**, *644*, 780–789.

[63] Murinzi, T. W.; Clement, T. A.; Chitsa, V.; Mehlana, G. Copper Oxide Nanoparticles Encapsulated in HKUST-1 Metal-Organic Framework for Electrocatalytic Oxidation of Citric Acid. *Journal of Solid State Chemistry* **2018**, *268*, 198–206.

[64] Yang, Q.; Zhang, H.-Y.; Wang, L.; Zhang, Y.; Zhao, J. Ru/UiO-66 Catalyst for the Reduction of Nitroarenes and Tandem Reaction of Alcohol Oxidation/Knoevenagel Condensation. *ACS Omega* **2018**,

[65] Senkovska, I.; Hoffmann, F.; Fröba, M.; Getzschmann, J.; Böhlmann, W.; Kaskel, S. New Highly Porous Aluminium Based Metal-Organic Frameworks: Al(OH)(Ndc) (Ndc = 2,6-Naphthalene Dicarboxylate) and Al(OH)(Bpdc) (Bpdc = 4,4′-Biphenyl Dicarboxylate). *Microporous and Mesoporous Materials* **2009**, *122*, 93–98.

[66] Grimme, S.; Antony, J.; Ehrlich, S.; Krieg, H. A consistent and accurate ab initio parametrization of density functional dispersion correction (DFT-D) for the 94 elements H-Pu. *The Journal of chemical physics* **2010**, *132*.

[67] Ganji, M. D.; Hosseini-Khah, S.; Amini-Tabar, Z. Theoretical insight into hydrogen adsorption onto graphene: a first-principles B3LYP-D3 study. *Physical Chemistry Chemical Physics* **2015**, *17*, 2504–2511.

[68] Impeng, S.; Siwaipram, S.; Bureekaew, S.; Probst, M. Ethane C–H bond activation on the Fe (iv)–oxo species in a Zn-based cluster of metal–organic frameworks: a density functional theory study. *Physical Chemistry Chemical Physics* **2017**, *19*, 3782–3791.

[69] Araujo, M.; Lasorne, B.; Magalhães, A. L.; Worth, G. A.; Bearpark, M. J.; Robb, M. A. The molecular dissociation of formaldehyde at medium photoexcitation energies: A quantum chemistry and direct quantum dynamics study. *The Journal of chemical physics* **2009**, *131*.

[70] Yempally, V.; Kyran, S. J.; Raju, R. K.; Fan, W. Y.; Brothers, E. N.; Darensbourg, D. J.; Bengali, A. A. Thermal and photochemical reactivity of manganese tricarbonyl and tetracarbonyl complexes with a bulky diazabutadiene ligand. *Inorganic Chemistry* **2014**, *53*, 4081–4088.

[71] Canneaux, S.; Bohr, F.; Henon, E. KiSThelP: a program to predict thermodynamic properties and rate constants from quantum chemistry results. *Journal of computational chemistry* **2014**, *35*, 82–93.

[72] Park, H.; Brothers, E. N.; Merz, K. M. Hybrid QM/MM and DFT Investigations of the Catalytic Mechanism and Inhibition of the Dinuclear Zinc Metallo--Lactamase CcrA from Bacteroides fragilis. *Journal of the American Chemical Society* **2005**, *127*, 4232–4241, PMID: 15783205.

[73] Vreven, T.; Byun, K. S.; Komáromi, I.; Dapprich, S.; Montgomery, J. A. J.; Morokuma, K.; Frisch, M. J. Combining Quantum Mechanics Methods with Molecular Mechanics Methods in ONIOM. *Journal of Chemical Theory and Computation* **2006**, *2*, 815–826.

[74] Poswal, A.; Agrawal, A.; Yadav, A.; Nayak, C.; Basu, S.; Kane, S.; Garg, C.; Bhattachryya, D.; Jha, S.; Sahoo, N. Commissioning and first results of scanning type EXAFS beamline (BL-09) at INDUS-2 synchrotron source. AIP Conference Proceedings. 2014; pp 649–651.

[75] Ravel, B.; Newville, M. ATHENA, ARTEMIS, HEPHAESTUS: data analysis for X-ray absorption spectroscopy using IFEFFIT. *Journal of synchrotron radiation* **2005**, *12*, 537–541.

[76] Antil, N.; Chauhan, M.; Akhtar, N.; Kalita, R.; Manna, K. Selective methane oxidation to acetic acid using molecular oxygen over a mono-copper hydroxyl catalyst. *Journal of the American Chemical Society* **2023**, *145*, 6156–6165.

Chapter 4

Dinuclear Iron(II)-Hydroxyl Active Sites for Selective Methane Oxidation to Acetic Acid Using O_2

Title of Paper: " Engineering Mono- Vs Dinuclear Iron(II)-Active Sites to Steer Liquid Oxygenate Selectivity in Methane Oxidation Pathways using O_2"

Citation: Journal of the American Chemical Society, **2025**, *147* (29), 25372-25384. (doi.org/10.1021/jacs.5c04682)

Author: Poorvi Gupta, Manav Chauhan, Bharti Rana, Rahul Kalita, Rishabh Maurya, and Kuntal Manna*

Abstract

The selective oxidation of methane to liquid oxygenates using molecular oxygen under mild conditions remains a major challenge due to the inertness of methane and the competing overoxidation reactions. This chapter describes the development of a dinuclear bipyridyl Fe(II) hydroxyl catalyst confined within the porous MOF-253(Al) framework, denoted as MOF-253-Fe_2, featuring a $[(bpy)Fe^{II}(\mu_2\text{-}OH)(OH)]_2$ active site. The catalyst exhibits 100% liquid selectivity toward acetic acid with a productivity of 2,757 $mmol_{CH_3CO_2H}$ mol_{Fe}^{-1} h^{-1} at 160 °C. Detailed spectroscopic studies reveal that the confinement of the dinuclear Fe centers within the MOF facilitates redox cooperativity and multi-electron transfer, enabling efficient O_2 activation and methane C-H bond activation followed by C-C coupling with in situ generated CO to yield acetic acid. The formation of a $[(bpy)Fe^{III}(\mu_2\text{-}OH)(OH)_2]_2$ intermediate is proposed as the key step in the catalytic cycle. These findings highlight the crucial role of binuclear site design in achieving selective methane-to-acetic acid conversion.

4.1 Introduction

Methane, the primary component of natural gas, represents an abundant yet underutilized carbon feedstock. Its direct transformation into value-added oxygenates such as methanol, formaldehyde, or acetic acid under mild conditions remains a long-standing challenge in catalysis.[1–7] The high bond dissociation energy of the C-H bond in methane (104 kcal mol^{-1}) and the thermodynamic tendency toward overoxidation to CO_2 hinder selective activation.[8–11] Developing catalytic systems that can precisely mediate multielectron redox transformations and stabilize reaction intermediates is thus crucial for achieving selective methane functionalization.

In biological systems, diiron enzymes such as methane monooxygenase (MMO) accomplish the oxidation of methane under ambient conditions via cooperative redox behavior between two iron centers bridged by hydroxyl groups.[12] The development of bimetallic catalysts has brought significant advances in catalysis, harnessing the combined function of two metal active centers for the synergistic activation of substrates.[13–18] These interactions enhance redox cooperativity, promote multi-electron transfer processes, and impart improved sta-

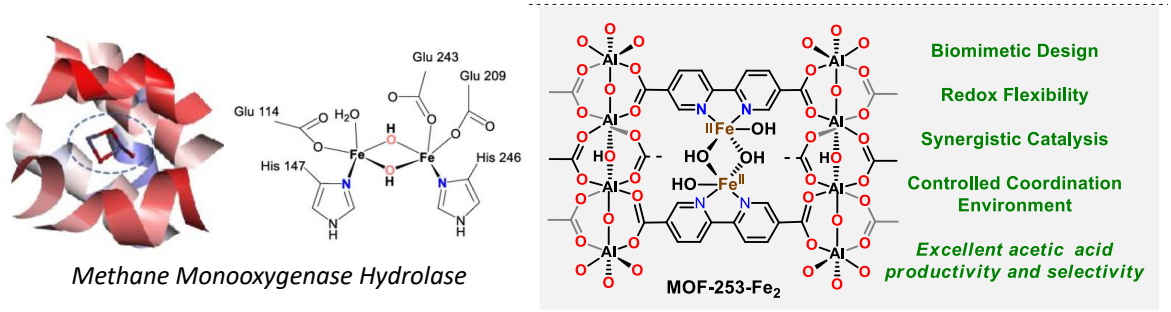


Figure 4.1: Structural Analogy between Methane Monooxygenase and MOF-253(Al)-Fe_2 Catalysts.

bility to the catalytic system, which makes bimetallic catalysts particularly appealing for challenging chemical transformations. Despite significant advances in synthesizing well-defined homogeneous bimetallic complexes,[16;19;20] overcoming the challenges associated with heterogeneous bimetallic species such as precise structural characterization, control over metal spatial arrangement, and comprehensive mechanistic understanding remains a significant hurdle. As porous and tunable molecular materials, MOFs offer a versatile platform to synthesize well-defined dinuclear earth-abundant metal species.[21–24] Composed of metal nodes or secondary building units (SBUs) and organic linkers, MOFs exhibit high porosity, crystallinity, and molecular tunability, enabling precise structural and functional customization.[25–28] The development of MOF-based artificial enzymes has garnered significant attention, particularly for applications such as CO_2 reduction and methane oxidation.[29] By integrating biomimetic design principles, MOFs can mimic enzymatic active sites, facilitating efficient catalytic processes. MOF-253(Al) is composed of aluminum hydroxide SBUs and a linear dicarboxylate bipyridyl bridging linker, exhibiting remarkable thermal and chemical stability.[30–32] Its unique architecture features parallel bipyridyl dicarboxylate linkers that form rhombic channels with an inter-linker distance of approximately 6.6 Å.

This structural arrangement is particularly well-suited for coordinating dinuclear active sites, enabling the adaptive coordination of two metal centers through μ_2-OH groups.[24] The bipyridine-coordinated dinuclear Fe(II) hydroxyl moiety, $[(bpy)Fe^{II}(\mu_2\text{-}OH)]_2$, confined within MOF-253, offers a promising strategy for methane oxidation by mimicking the enzymatic mechanisms found in the MMO system. We hypothesize that, similar to the MMO system, the $[(bpy)Fe^{II}(\mu_2\text{-}OH)]_2$ active site will react with O_2 to generate a reactive Fe^{III}-O-O-Fe^{III} intermediate, which will initiate methane oxidation by activating the

methane C-H bond through a radical-mediated pathway. In addition, the hierarchical structure of MOF-253, along with the confinement of active sites and radical intermediates, facilitates C-C coupling. Herein, we report the development of MOF-253-confined dinuclear Fe(II) hydroxyl active species, efficiently catalyzes the oxidation of methane to afford acetic acid in 100% liquid selectivity (Figure 5.1)

4.2 Results and Discussion

4.2.1 Synthesis and Characterization of MOF-253-Fe_2

The solvothermal reaction between $AlCl_3{\cdot}6H_2O$ and 2,2'-bipyridine-5,5'-dicarboxylic acid (H_2bpydc) in dimethyl-formamide (DMF) at 120 °C for 1 d, resulted in the formation of MOF-253(Al) as a white crystalline solid.[32–34] The powder X-ray diffraction (PXRD) pattern of the freshly prepared MOF is similar to the simulated pattern, confirming the successful synthesis of MOF-253(Al) (Figure 4.2b). Stirring a slurry of MOF-253(Al) in tetrahydrofuran (THF) solution of $FeCl_2$ afforded the corresponding iron-functionalized MOF (MOF-253-$FeCl_2$). Subsequently, the treatment of MOF-253-$FeCl_2$ with $NaEt_3BH$ followed by the reaction with water furnished MOF-253-Fe_2 (Figure 4.2a). Inductively coupled plasma-optical emission spectroscopy (ICP-OES) analysis of digested MOF-253-Fe_2 revealed an Fe:Al ratio of 0.8, which indicates that 80% of the bipyridine moieties in MOF-253(Al) are coordinated with Fe ions, leading to a chemical formula of $Al(OH)(bpy)(Fe_{0.8}(OH)_{1.6})$. The PXRD patterns of both MOF-253-$FeCl_2$ and MOF-253-Fe_2 closely match that of the pristine MOF-253(Al), confirming the retention of crystallinity and structure of the MOF during the post-synthetic modification (Figure 4.2b). Scanning electron microscopy (SEM)-energy-dispersive X-ray (EDX) mapping showed a homogeneous distribution of Fe and Al ions throughout the MOF particles (Figure 4.3). MOF-253(Al) and MOF-253-Fe_2 had a BET surface area of 1,586 and 540 m_2/g, respectively (Figure 4.4). The significant reduction in the surface area of MOF-253-Fe_2 compared to the pristine MOF-253(Al) is attributed to the incorporation of $Fe(OH)_2$ moieties within the pores of the MOF. The X-ray photoelectron spectroscopy (XPS) analysis of MOF-253-Fe_2 was fitted with Gaussian (70%)-Lorentzian (30%) profile with a Shirley background, revealing an Fe oxidation state of +2. The Fe $2p_{3/2}$ component was deconvoluted into a pre-peak, surface peak, satellite peak, and three

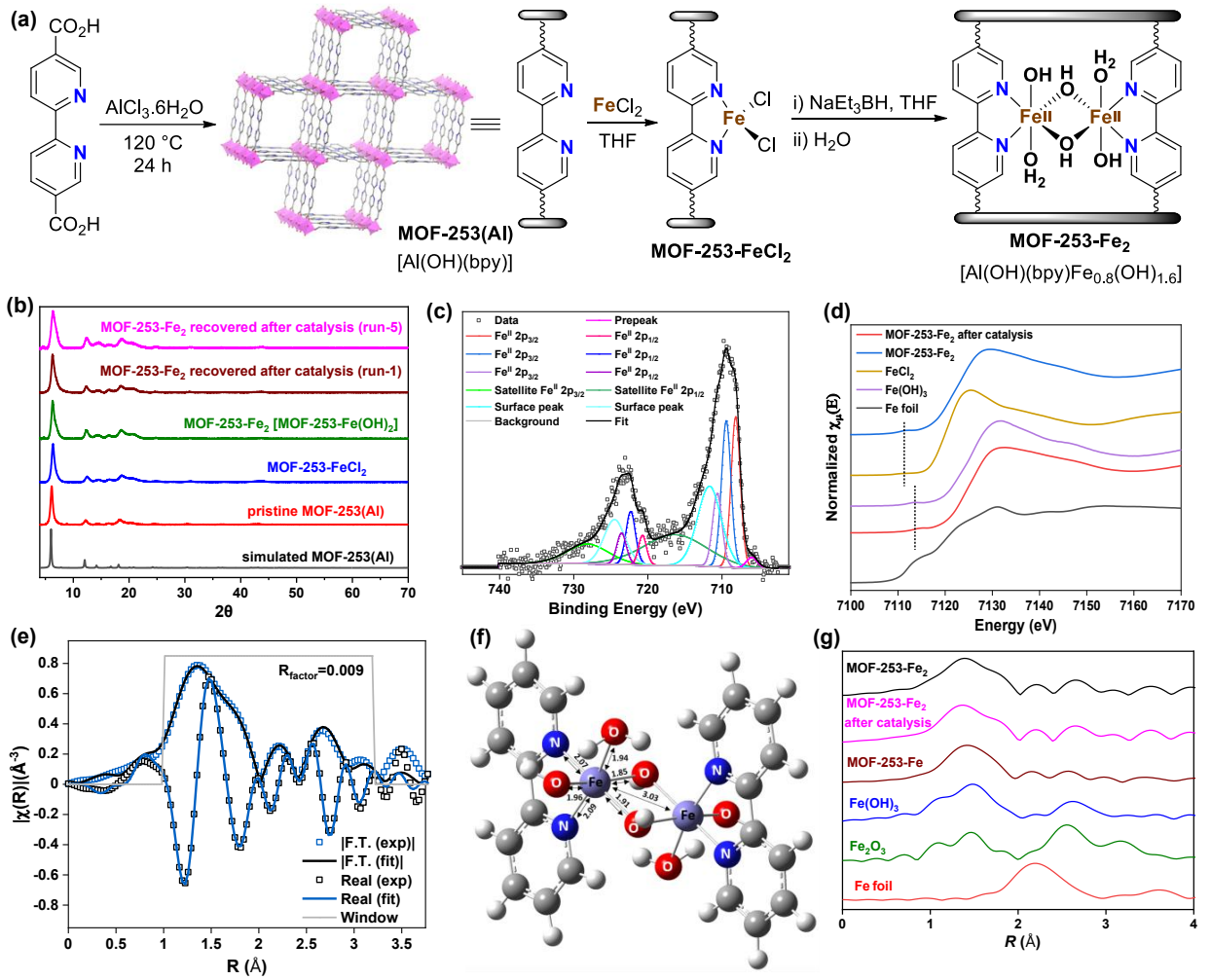


Figure 4.2: (a) Synthesis of MOF-253-Fe_2. (b) PXRD patterns of simulated MOF-253(Al) (black), pristine MOF-253(Al) (red), MOF-253-$FeCl_2$ (blue), MOF-253-Fe_2 (green), and MOF-253-Fe_2 recovered after the first (wine) and fifth (magenta) run of methane oxidation. (c) Fe 2p XPS spectrum of MOF-253-Fe_2. (d) XANES spectra of Fe(0) foil (black), $FeCl_2$ (brown), $Fe(OH)_3$ (purple), MOF-253-Fe_2 (blue), and MOF-253-Fe_2 after catalysis (red). (e) EXAFS spectra (blue and black hollow squares) and fits (black and blue solid lines) of 90% dimeric MOF-253-Fe_2 and 10% monomeric Fe species in R-space at the Fe K-edge (1.0–3.25 Å). (f) DFT-optimized structure of the diiron(II) core $[(bpy)Fe^{II}(\mu_2\text{-}OH)(OH)(OH_2)]_2$ of MOF-253-Fe_2; bond distances in Å. (g) k^2-weighted Fe-EXAFS χ(R) spectra of MOF-253-Fe_2 (black), MOF-253-Fe after catalysis (magenta), MOF-253-Fe (wine), $Fe(OH)_3$ (blue), Fe_2O_3 (green), and Fe foil (red); k range: 3–13 Å. Optimized reaction conditions: MOF-253-Fe_2 (4.7 mg, 10.5 μmol Fe), 20 bar CH_4, 8 bar O_2, 160 °C, 8 mL water, 38 h.

multiplet peaks (Figure 4.2c), which align with the characteristic features of Fe^{2+} oxidation state as reported in the literature (Table 4.7).[35]

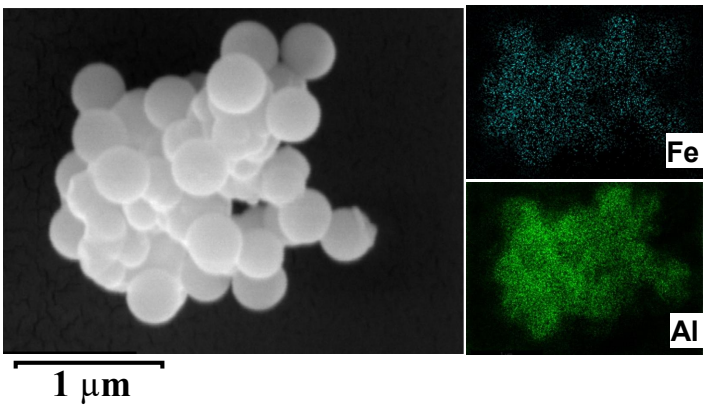


Figure 4.3: SEM image of MOF-253-Fe_2 and the FE-SEM-energy dispersive X-ray (EDX) mapping of the respective particles. Scanning electron microscopy (SEM) images of the MOF-253-Fe_2 displayed spherical-shaped particles with diameters ranging from 160-190 nm. SEM-EDX mapping showed a homogeneous distribution of Fe and Al throughout the MOF particles.

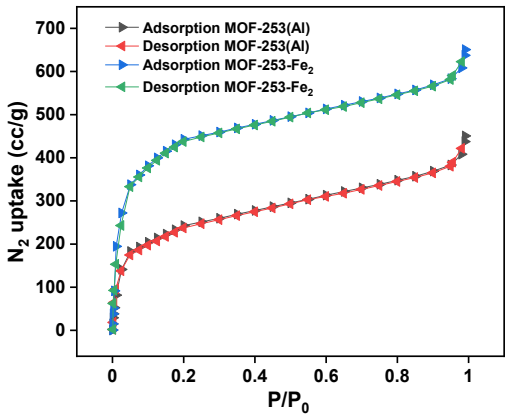


Figure 4.4: N_2 sorption isotherms of MOF-253(Al) (black) and MOF-253-Fe_2 (red) measured at 77 K. BET surface for MOF-253(Al) and MOF-253-Fe_2 are 1586 m^2/g and 540 m_2/g, respectively.

X-ray absorption near-edge structure (XANES) showed that the Fe pre-edge energy of MOF-253-Fe_2 appears at 7111.7 eV, which is close to that of $FeCl_2$ at 7111 eV and 2 eV lower than that of $Fe(OH)_3$ (Figure 4.2d), further supporting the +2-oxidation state of Fe ion in MOF-253-Fe_2 (Figure 4.2d). Fitting the Extended X-ray absorption fine structure (EXAFS) data of MOF-253-Fe_2 with a DFT-optimized struc-ture revealed that MOF-253-Fe_2 contains 90% dimeric $[(bpy)Fe^{II}(\mu_2\text{-}OH)(OH)(OH_2)]_2$ species and 10% mono-meric $(bpy)Fe^{II}(OH)_2$ species. In the Fe_2-dimer active-sites, each Fe^{2+} ion is octahedral coordinated by two nitrogen atoms of the bipyridine moiety (2.07 Å, 2.09 Å), one terminal hydroxyl group (1.96 Å), two bridged hydroxyl groups (1.85 Å, 1.91 Å) and one water molecule (1.94 Å) (Figures 4.2e-f). In the raw phase uncorrected k^2-weighted Fe-EXAFS χ(R) spectrum of

MOF-253-Fe_2, a distinctive scattering feature is evident at 1.43 Å, which can be attributed to Fe-O scattering, similar to what has been observed in Fe_2O_3 and $Fe(OH)_3$ (Figure 4.2g). The feature at 2.6 Å arises from the collective contributions from Fe-Fe and C-C scattering in the second shell (Figure 4.2e), and Figure 4.18).

The potential existence of Fe(0) nanoparticles or Fe_2O_3 secondary species within MOF was excluded by fitting the raw EXAFS data of MOF-253-Fe_2 with varying percentages (5-20%) of these species, which resulted in significant misfits (Figure 4.19). Furthermore, we fitted the raw EXAFS data of MOF-253-Fe_2 with varying percentages (10-20%) of Al-oxo SBU-coordinated Fe-hydroxyl species, which resulted in significant misfits, which excludes the existence of Fe species at MOF's SBUs (Figure 4.22).[36]

4.2.2 Catalytic Performance of MOF-253-Fe_2 in Selective Methane Oxidation using O_2.

The catalytic performance of MOF-253-Fe_2 for selective partial methane oxidation was investigated in a high-pressure batch reactor by varying reaction temperature, methane-to-oxygen ratio and the reaction time. After the reaction, liquid products were analyzed by gas chromatography equipped with a mass spectrometry (GC-MS) and a flame ionization detector (GC-FID) and also confirmed by a high-performance liquid chromatography (HPLC) equipped with a refractive index detector. Heating an aqueous suspension of MOF-253-Fe_2 (10.5 μmol of Fe) under a mixture of CH_4 (20 bar) and O_2 (8 bar) at 120 °C yielded 0.08 mmol of CH_3CO_2H, 0.06 mmol CO_2, and trace CO. Increasing the temperature to 140 °C raised the acetic acid yield to 0.22 mmol with 76% selectivity. Temperature optimization revealed that the highest selectivity for acetic acid was obtained at 160 °C.

Under these conditions, methane (20 bar) and oxygen (8 bar) were reacted with an aqueous suspension of MOF-253-Fe_2 (10.5 μmol Fe), producing acetic acid as the sole liquid-phase product (1.1 mmol) with a high selectivity of 93% along with minimal formation of CO_2 (0.08 mmol) and trace quantities of CO. However, increasing the reaction temperature beyond 160 °C, resulted in a significant decline in acetic acid selectivity. At 200 °C, acetic acid selectivity dropped sharply to 15%, with an acetic acid yield of 0.3 mmol, accompanied by a substantial

increase in CO_2 formation (1.7 mmol), due to overoxidation of methane (Figure 3a). Water was the only effective solvent for acetic acid production. No carbon-containing products were formed in liquid phase, when the reaction was performed in organic solvents, such as THF, toluene, heptane or perfluorohexane (Entry 18-21, Table 4.2), which indicates the crucial role of water in methane to acetic acid transformation. The effect of methane-to-oxygen ratio was also explored, ranging from 10:1 to 1:1.6, while keeping the total pressure constant at 28 bar. The optimal ratio of methane to oxygen for acetic acid formation was determined to be 2.5:1, with methane at a pressure of 20 bar and oxygen at 8 bar, as illustrated in Figures 3b and 3c. Time evaluation studies conducted at 160 °C under a mixture of 20 bar methane and 8 bar O_2 showed negligible formation of acetic acid during the initial 6 h of the reaction. Then, a steady increase in acetic acid concentration was observed between 6 and 38 h, reaching ∼1.1 mmol by 38 h. However, prolonged reaction time of more than 38 h led to a decline in acetic acid yield and CO_2 becoming the dominant product, due to the thermodynamically favored overoxidation (Figure 4.5d). However, there was no sign of catalyst decomposition and linker modification was observed even after 50 h of reaction, as shown by PXRD, ICP-OES, and NMR analysis of the recovered MOF -253-Fe_2. The optimum conditions for methane-to-acetic-acid transformation involved MOF-253-Fe_2 (10.5 μmol Fe), 20 bar methane, 8 bar O_2 and 8 mL of water at 160 °C for 38 h, yielding 1.1 mmol of acetic acid (Entry 1, Table 4.2). Under these conditions, MOF-253-Fe_2 gave an acetic acid productivity of 2,757 $mmol_{CH_3CO_2H}$ mol_{Fe}^{-1} h^{-1} (equivalent to 6,159 $\mu mol_{CH_3CO_2H}$ g_{cat}^{-1} h^{-1}) with 100% selectivity in the aqueous phase and an overall selectivity of 93%. The methane conversion reached 5.8%, and the theoretical methane consumption was calculated to be 2.28 mmol, compared to the experimental methane consumption of 2.29 mmol, resulting in a carbon balance of 99.5%, indicating no undetected carbon products (Table 4.4).

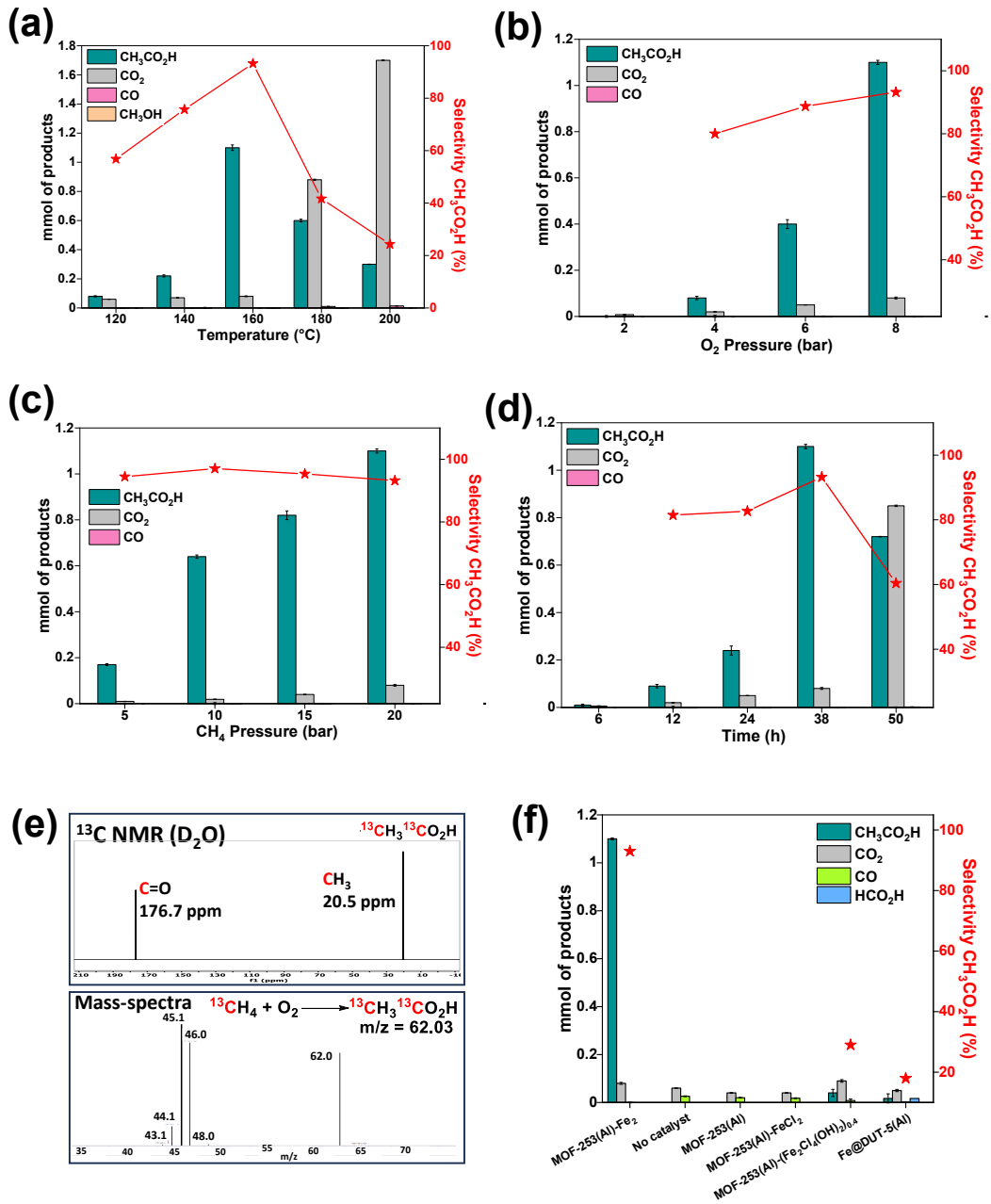


Figure 4.5: (a) Effect of temperature on oxygenated product yields and selectivity of acetic acid. Reaction conditions: MOF-253-Fe_2 (10.5 μmol Fe), 20 bar CH_4, 8 bar O_2, 8 mL water and 38 h. (b) Effect of O_2 pressure on oxygenated product yields and selectivity of acetic acid. Reaction conditions: MOF-253-Fe_2 (10.5 μmol Fe), 20 bar CH_4, 160 °C, 8 mL water and 38 h, balanced with N_2 to maintain a total pressure of 28 bar. (c) Effect of CH_4 pressure on oxygenated product yields and selectivity of acetic acid. Reaction conditions: MOF-253-Fe_2 (10.5 μmol Fe), 8 bar O_2, 160 °C, 8 mL water and 38 h, balanced with N_2 to maintain a total pressure of 28 bar. (d) Effect of time on oxygenated product yields and selectivity of acetic acid. Reaction conditions: MOF-253-Fe_2 (10.5 μmol Fe), 20 bar CH_4, 8 bar O_2, 8 mL water and 160 °C. (e) ^{13}C NMR (400MHz) spectrum (top) and mass spectrum (bottom)of the reaction mixture obtained after $^{13}CH_4$ oxidation. (f) Comparison of catalytic activity for the oxidation of CH_4 over MOF-253-Fe_2 with other catalysts under identical reaction conditions.

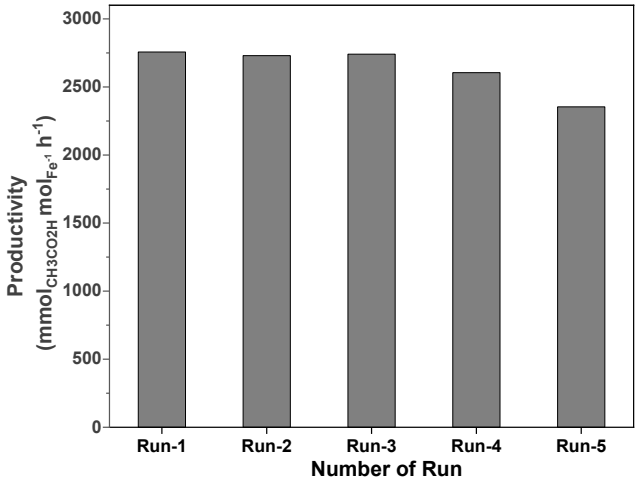


Figure 4.6: Recyclability test for MOF-253-Fe_2 catalyzed oxidation of CH_4 into CH_3CO_2H under optimized reaction conditions.

Importantly, the MOF-253-Fe_2 catalyst could be reused and recycled for at least four cycles without any decline in catalytic activity (Figure 4.6). PXRD (Figure 4.5b), and NMR of the digested MOF recovered after methane oxidation confirmed that the MOF-253-Fe_2 framework remain structurally and chemically robust during catalysis, with no evidence of linker functionalization or degradation. ICP-OES analysis after catalysis showed a minimal leaching of Fe (0.06%) and Al (0.04%) into the supernatant (Table 4.5).

4.2.3 Control Experiments

Several control experiments were carried out to confirm the heterogeneity and single-site nature of MOF-253-Fe_2 catalyst in the methane-to-acetic-acid transformation. In the absence of the MOF catalyst, no acetic acid was detected in the liquid phase during methane oxidation (Figure 4.5f). Additionally, the production of CH_3CO_2H stopped once the MOF was removed from the reaction mixture through hot filtration (Figure 4.12). These findings indicate that the active catalytic species are embedded within the MOF. In a separate control reaction, using 8 bar O_2 and 20 bar N_2 instead of CH_4, conducted at 160 °C in water for 38 h, no carbon-containing products were formed (Entry 4, Table 4.3). Furthermore, MOF-253-Fe_2 catalyzed methane oxidation using isotopically labeled $^{13}CH_4$ produced only $^{13}CH_3{}^{13}CO_2H$, as verified by ^{13}C NMR spectroscopy and GC-MS analysis (Figure 4.5e). This result further substantiates that CH_4 is the sole carbon source for CH_3CO_2H production. Similarly, replacing O_2 with N_2 under the identical reaction conditions did not produce

CH_3CO_2H, verifying that O_2 acts as the sole oxidant, and that water itself is not an oxidizing agent, in MOF-253-Fe_2 catalyzed oxidation of methane to acetic acid conversion (Entry 3, Table 4.2). Interestingly, when air (40 bar) was used instead of pure O_2 under identical conditions, CH_3CO_2H was still formed, albeit at a lower yield of ∼0.1 mmol (Entry 27, Table 4.3). This result demonstrates the potential practical application of the MOF-253-Fe_2 catalyst for upcycling methane. Pristine MOF-253(Al) without post-synthetic modification with $Fe(OH)_2$, also failed to produce acetic acid (Figure 4.5f) No acetic acid was formed when MOF-253-$FeCl_2$ or MOF-253-$(Fe_2Cl_4(OH)_2)_{0.5}$,[35] were used as catalysts for methane oxidation (Figure 4.5f). In addition, we prepared Fe nanoparticles encapsulated within the DUT-5 MOF; Fe@DUT-5 (Section 4.3.2).[36] Methane oxidation using Fe@DUT-5 MOF or Fe(0) nanoparticles under similar conditions resulted in negligible acetic acid formation, with formic acid and CO_2 being the major product, ruling out the possibility of in situ generated Fe nanoparticles being the active species (Figures 4.5f). Attempts to synthesize the homogeneous monomeric or dimeric 2,2'-bipyridyl-$Fe(OH)_2$ complex were unsuccessful. The reaction between (bpy)$FeCl_2$[37] and $NaEt_3BH$ in 1:2.2 molar ratio in THF at room temperature instantaneously produced sparingly soluble Fe(0) nano-particles, along with unidentified homogeneous bipyridyl-iron species and H_2 (section 4.3.2, Figure 4.13), likely due to the intermolecular decomposition of the putative (bpy)FeH_2 intermediate.[38] The resultant reaction mixture was inactive in methane oxidation in water. In contrast, the facile synthesis of the robust $[(bpy)Fe^{II}(\mu_2\text{-}OH)(OH)(OH_2)]_2$ species through post-synthetic modification of the pristine MOF-253 underscores the significance of the active site isolation within the porous MOF, which prevents intermolecular decomposition pathway.[39] Furthermore, testing $Fe(OH)_3$, Fe_2O_3, and Fe_3O_4 for methane oxidation under the same reaction conditions at 160 °C, showed negligible CH_3CO_2H formation, highlighting the importance of the site-isolated dimeric Fe-hydroxyl species spatially confined within the MOF's pores for methane C-H activation.

Under the optimized reaction conditions of MOF-253-Fe_2 catalyzed methane-to-acetic acid transformation, the mononuclear catalyst MOF-253-Fe produced only 0.14 mmol of acetic acid and 0.09 mmol of methanol, with CO_2 (1.21 mmol) as the predominant product (Entry 16, Table 4.3). This represents an eightfold reduction in catalytic activity for methane oxidation to acetic acid with MOF-253-Fe compared to the dinuclear catalyst MOF-253-Fe_2,

with acetic acid selectivity dropping from 93% to 10%. These results highlight the critical role of dinuclear active sites in enabling cooperative O_2 activation and C-C coupling during the transformation of methane into acetic acid.

4.2.4 Identification of Reaction Intermediates

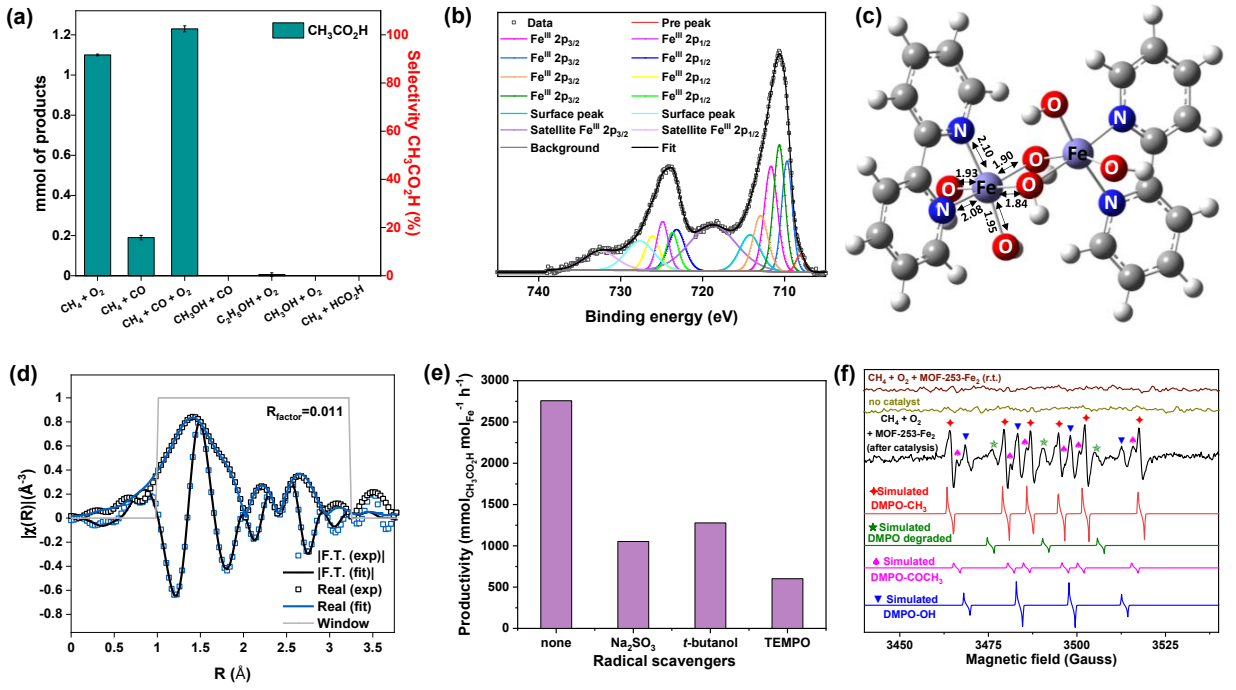


Figure 4.7: (a) Control reactions for the production of CH_3CO_2H at 160 °C. (b) Fe 2p XPS spectra of MOF-253-Fe_2 recovered after catalysis. (c) DFT-optimized structure of the diiron(III) core of MOF-253-Fe_2 (INT-4) $[(bpy)Fe^{III}(\mu_2\text{-OH})(OH)_2]_2$. The bond distances are in Å. (d) EXAFS spectra (black and blue hollow squares) and fits (blue and black solid lines) of MOF-253-Fe_2 after catalytic methane oxidation to acetic acid in the R space at the Fe K-edge. The fitting range in the R space is 1.0–3.25 Å. (e) Productivity of acetic acid in the presence of different radical scavengers. (f) X-band (9.85 GHz) EPR spectroscopic spin-trapping experiments. EPR spectrum from DMPO spin-trapping experiment of MOF-253-Fe_2-catalyzed methane oxidation by O_2 at room temperature (wine), uncatalyzed oxidation of methane by O_2 at 160 °C for 38 h (mustard), MOF-253-Fe_2-catalyzed methane oxidation by O_2 at 160 °C for 38 h (black), simulated DMPO–CH_3 (red), simulated DMPO degraded during catalysis (green), simulated DMPO–$COCH_3$ (magenta), and simulated DMPO–OH (blue). Optimized conditions: MOF-253-Fe_2 (4.7 mg, 10.5 μmol Fe), 20 bar CH_4, 8 bar O_2, 160 °C, 8 mL H_2O, and 38 h.

To assess the role of any *in situ*-generated methanol, ethanol, formic acid, CO, or CO_2 in the MOF-253-Fe_2-catalyzed methane-to-acetic-acid transformation, several control experiments were conducted. The results showed that neither ethanol nor methanol produced CH_3CO_2H in the reaction with O_2 (Figure 5a), ruling out acetic acid formation via methanol or ethanol intermediates. In addition, the reaction of methane with formic acid at 160 °C did not yield CH_3CO_2H, ruling out its formation via the coupling of formic acid with methane (Figure 5a). No acetic acid was generated in the reaction between methanol and CO, further suggesting that the conversion of methane to acetic acid does not occur via methanol carbonylation (Figure 5a). The reaction between methane and CO_2 produced only trace amounts (0.005 mmol) of acetic acid (Entry 18, Table 4.3). However, the reaction between methane (20 bar) and CO (1 bar) in the presence of MOF-253-Fe_2 yielded 0.19 mmol of CH_3CO_2H at 160 °C (Figure 5a), but an undetectable amount of CH_3CO_2H at 95 °C (Entry 41, Table 4.3). Furthermore, the addition of CO to the reaction mixture of methane and O_2 at 160 °C increased the production of acetic acid to 1.23 mmol (Figure 5a). A control experiment involving heating methane (20 bar) and O_2 (8 bar) in the absence of MOF-253-Fe_2 at 160 and 95 °C produced 0.026 mmol and no detectable CO, respectively (Entries 2 and 22, Table 4.2). These experiments indicate that *in situ*-generated CO likely serves as a reaction intermediate for the formation of acetic acid at 160 °C. We also conducted time-resolved gas-phase analysis under the standard catalytic conditions in aqueous media, which revealed no detectable CO during the initial 6 h, despite the formation of 0.01 mmol of acetic acid. A control experiment using TEMPO as a $\cdot CH_3/\cdot OH$ radical scavenger under identical reaction conditions showed 0.008 mmol of CO at 6 h (Entry 8, Table 4.3), while no acetic acid was formed, supporting its transient formation and rapid consumption of CO in the acetic acid pathway (Section 4.3.2). In contrast, the mononuclear MOF-253-Fe, under identical catalytic conditions at 160 °C with 1 bar of CO, produced only $\sim 1/14^{\text{th}}$ the amount of acetic acid compared to the dinuclear MOF-253-Fe_2. This suggests that while the mononuclear system may have limited capability to promote C–C bond formation, the diiron system appears more effective in facilitating acetic acid production via the CO-mediated pathway.

4.2.5 Mechanism Exploration of MOF-253-Fe_2 Catalyzed Methane to Acetic Acid Conversion.

The radical-rebound mechanism is commonly proposed for the hydroxylation of methane by O_2 to methanol, catalyzed by the diiron active site of the MMO enzyme system, which functions under ambient conditions in the presence of sacrificial reductants such as NADH (NAD: nicotinamide adenine dinucleotide) within a finely tuned protein matrix.[39] In contrast, our MOF-253-Fe_2 catalyst, which features a $[(bpy)Fe^{II}(\mu_2\text{–}OH)(OH)(OH_2)]_2$ active site supported by the rigid MOF framework, oxidizes methane to acetic acid at elevated temperature and pressure without the need for any external reductants or cofactors, unlike the enzymatic system. These sharp contrasts between MMO and MOF-253-Fe_2 catalysts indicate that the underlying mechanisms in methane oxidation may fundamentally differ between these two systems.

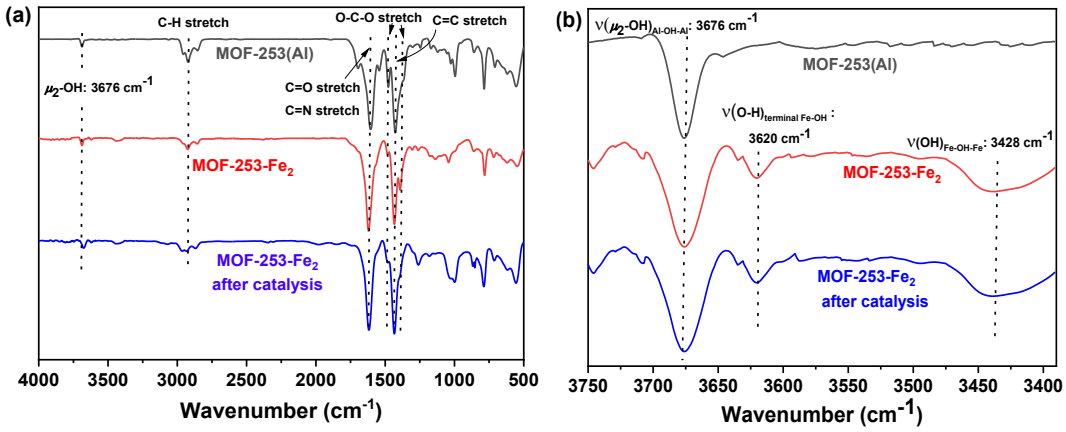


Figure 4.8: (a) IR spectra of freshly prepared MOF-253(Al) (grey), MOF-253-Fe_2 (red), and MOF-253-Fe_2 recovered after catalysis (blue). (b) The peak at 3620 cm^{-1} in MOF-253-Fe_2 and MOF-253-Fe_2 recovered after methane oxidation corresponds to the stretching vibration of terminal Fe–OH, the peak at 3428 cm^{-1} represents the stretching mode of vibration for bridging μ_2-(OH)Fe–OH–Fe, and the peak at 3676 cm^{-1} corresponds to μ_2-$(OH)_{Al–OH–Al}$ within the SBU of the MOFs.[40]

To explore the mechanism of MOF-253-Fe_2-catalyzed direct oxidation of methane to acetic acid, we first analyzed the oxidation state and coordination environment of the Fe center in the MOF recovered after catalysis at 160 °C. The XPS analysis of the MOF-253-Fe_2 recovered after catalysis revealed the existence of Fe^{3+} species (Figure 4.7b and Table S16). XANES analysis further confirmed the +3 oxidation state of Fe, with a pre-edge energy

of 7114 eV, closely aligned with the $Fe(OH)_3$ pre-edge at 7113 eV (Figure 4.2d). Post-catalysis EXAFS analysis was best fitted to the DFT-optimized models of ∼90% dimeric $[(bpy)Fe^{III}(\mu_2–OH)(OH)_2]_2$ species and ∼10% monomeric $(bpy)Fe^{III}(OH)_3$ species (Figure 4.7d). In the recovered MOF-253-Fe_2, each Fe^{3+} center adopts an octahedral geometry, coordinated by two bipyridine, two terminal hydroxyl groups, and two bridging μ_2–OH groups (Figure 4.7c). In the infrared spectra, the recovered MOF-253-Fe_2 exhibited two additional peaks at 3620 cm^{-1} and 3428 cm^{-1} compared to those of MOF-253(Al) (Figure 6.7), which are attributed to the stretching vibrations of the terminal Fe–OH and bridging μ_2-$(OH)_{Fe–OH–Fe}$ groups, respectively. Under identical reaction conditions, this postcatalytic MOF material exhibited a productivity of 2632 $mmol_{CH_3CO_2H}$ mol_{Fe}^{-1} h^{-1}, similar to that of MOF-253-Fe_2, which suggests that $[(bpy)Fe^{III}(\mu_2–OH)(OH)_2]_2$ species is likely a catalytic intermediate in the catalytic cycle of methane-to-acetic-acid transformation (Entry 9, Table 4.3). The PXRD of the recovered MOF showed no characteristic reflections of Fe nanoparticles at higher 2θ angles, ruling out their presence (Figure 4.2b). The potential existence of Fe(0) or Fe_2O_3 secondary species, which might form during the catalytic process, was further excluded by fitting the raw EXAFS data of MOF-253-Fe_2 recovered after catalysis with varying percentages (5–20%) of these species, which resulted in significant misfits (Figure 4.21), ruling out the formation of these nanoparticle-based secondary species during the catalytic reaction.

The acetic acid productivity of MOF-253-Fe_2 at 160 °C in water significantly decreased when Na_2SO_3 or *t*-butanol, a hydroxyl radical (·OH) scavenger,[41;42] or 2,2,6,6- tetramethyl-1-piperidinyloxy (TEMPO) as a $\cdot CH_3$ and ·OH radical scavenger, was introduced into the feed (Figure 4.7e).[43] To confirm the presence of potential radical intermediates involved in the reaction mechanism, 5,5-dimethyl-1-pyrroline *N*-oxide (DMPO) was employed as a radical trapping agent.[44] The EPR spectrum of the reaction mixture containing MOF-253-Fe_2, methane, oxygen, and DMPO at room temperature did not show signals corresponding to $\cdot CH_3$ or ·OH radicals (Figure 4.7f). However, the EPR spectrum of the DMPO-loaded reaction mixture after catalysis at 160 °C displayed signals corresponding to DMPO–OH, DMPO–CH_3, and DMPO–$COCH_3$ radical adducts (Figure 4.7f and Table 4.3.2).[44;45] These findings indicate that $\cdot CH_3$ and ·OH radicals play a role in the conversion of CH_4 to acetic acid. In contrast, no $\cdot CH_3$ or ·OH radicals were detected in the

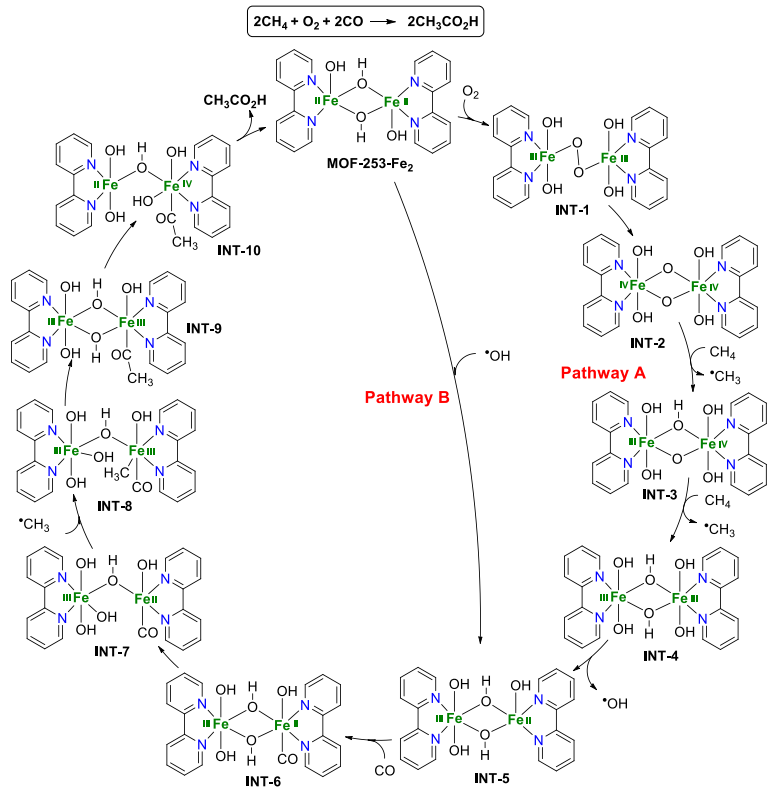


Figure 4.9: Proposed catalytic cycle of MOF-253-Fe_2-catalyzed selective methane oxidation to acetic acid using O_2.

reaction mixture without MOF-253-Fe_2 or in the presence of pristine MOF-253(Al), which confirms that methane activation occurs solely at the Fe active sites. Additionally, a control reaction conducted with MOF-253-Fe_2 and methane at 160 °C in water without O_2 did not produce any $\cdot CH_3$ radicals, emphasizing the importance of O_2 in the methane activation process.

Based on the above spectroscopic and control experiments, we propose a catalytic cycle in which MOF-253-Fe_2-catalyzed methane-to-acetic-acid conversion occurs via two interconnected radical-mediated pathways (pathway A and pathway B) (Figure 4.9). In pathway A, the two Fe(II) centers in MOF-253-Fe_2 activate O_2 to sequentially form $[Fe^{III}{}_2(\mu_2\text{-}O_2)]$ (INT-1) and $[Fe^{IV}(\mu_2\text{-}O)]_2$ (INT-2) species.[24] Then, hydrogen atom abstraction from two methane molecules liberates two $\cdot CH_3$ radicals and a $[Fe^{III}(\mu_2\text{–}OH)]_2$ species (INT-4). INT-4 is spectroscopically characterized as discussed above (Figure 4.7b-d). A control experiment was conducted by heating a mixture of INT-4, O_2, and DMPO at 160 °C, which exhibited EPR signals corresponding to $\cdot OH$ radicals (Figure S15). We propose that INT-4 is converted to a mixed-valent Fe^{2+}/Fe^{3+} center (INT-5) by the liberation of an $\cdot OH$ radical

(possibly due to the synergy of the two Fe centers), which combines with the in situ-generated CO, leading to the formation of INT-6 (Figure 4.9). XPS analysis of the catalyst recovered after an early stage of the reaction, conducted for a shorter duration (6 h), confirmed the presence of mixed-valent Fe^{2+}/Fe^{3+} species (Figure 4.25). The $\cdot CH_3$ radical then likely reacts with INT-6, leading to the formation of INT-8, which is converted to INT-9 via a migratory insertion. With the synergy of the two Fe centers in INT-9, a rearrangement of the bridging OH to terminal OH may generate a mixed-valent Fe^{2+}/Fe^{4+} species (INT-10), which undergoes reductive elimination of acetic acid, regenerating the Fe^{2+}/Fe^{2+} species. The remaining $\cdot OH$ radical in pathway A may enter pathway B by reacting directly with MOF-253-Fe_2, forming INT-5 and continuing the catalytic cycle, consuming an additional $\cdot CH_3$ radical, and leading to the formation of a second molecule of acetic acid (Figure 4.9). Although the transformation of methane to acetic acid involved short-lived methyl radicals, no ethane formation was detected by GC-FID (Figure 4.27), indicating that $\cdot CH_3$-$\cdot CH_3$ combination is negligible under the reaction conditions. Although some steps in the above catalytic cycle are conjectural and require further investigation, such reactions may be plausible under harsh reaction conditions.

4.2.6 Origin of High Selectivity in Partial Methane Oxidation.

The distinct methane oxidation pathways leading to acetic acid originate from the contrasting reactivity of mononuclear and dinuclear bipyridyl Fe(II) hydroxyl species confined within the MOF-253(Al) framework. The single-site nature of these Fe catalysts is crucial, as indicated by the lack of acetic acid production when using bulk Fe oxides or Fe nanoparticles. At $\sim$ 160 °C, no acetic acid formation is obseverved with the MOF-253-Fe containing mononuclear (bpy)$Fe^{II}(OH)_2$ catalyst. In contrast, the dinuclear Fe catalyst (MOF-253-Fe_2) benefits from synergistic effects that facilitate multi-electron transfer processes, which are likely essential for acetic acid production. The proximity of two Fe centers enables cooperative redox behavior, facilitating sequential O_2 activation, methane C-H activation, and subsequent C-C bond formation with the *in situ* generated CO. At higher temperatures, increased *in situ* CO generation activates the dinuclear Fe catalyst, driving C-C bond formation and facilitating the acetic acid pathway. However, externally introducing CO at 95 °C gave a negligible amount of acetic acid (Entry 34, Table 4.3), indicating that both high tempera-

ture and an active dinuclear Fe center in MOF-253-Fe_2 are required for efficient C-C bond formation. While CO is essential for acetic acid production, the dinuclear structure of the Fe species is crucial in lowering the overall activation energy, facilitating the sequential oxidation steps necessary for its formation. The dinuclear Fe species in MOF-253-Fe_2 catalyst stabilize the reactive $[(bpy)Fe^{IV}(\mu_2\text{-}O)(OH)_2]_2$ intermediates, enabling controlled methane C-H activation and C-C coupling within the MOF pores. Our spectroscopic, and experimental analyses thus reveal that the selectivity of acetic acid formation for MOF-253-Fe_2, respectively, stems from various factors such as structure–activity relationship of active sites and their single-site nature, active-site stabilization via site isolation, confinement of the active sites within the well-defined porous environment, MOF's unique 3D porous structure, optimum pore sizes, and radical stabilization.

4.3 Experimental Section

4.3.1 Synthesis and Characterization of MOF-253(Al) and MOF-253-Fe^2.

Synthesis of MOF-253(Al).

[2,2'-bipyridine]-5,5'-dicarboxylic acid (H_2bpydc) was synthesised following a reported procedure.[38] 28.2 mg (0.115 mmol) of $AlCl_3{\cdot}6H_2O$ and 26 mg (0.11 mmol) of H_2bpydc were added into 3 mL of N,N-dimethylformamide (DMF) and stirred for 30 minutes. The solution was transferred to a hydrothermal bomb with a Teflon liner and kept in a preheated oven at 120 °C for 24 h. After cooling to room temperature, the white solid was collected via centrifugation and washed several times with DMF. Finally, the resultant white crystalline solid of MOF-253(Al) was washed and stored in THF and characterized using PXRD.

Synthesis of MOF-253-Fe_2.

A 1 mL THF solution of $FeCl_2$ (0.01 g, 0.079 mmol) was added to MOF-253(Al) (0.009 g), and the mixture was stirred overnight at room temperature inside the glovebox. The MOF-253-$FeCl_2$ was obtained as a crystalline solid and washed with THF several times. Inside the glovebox, $NaEt_3BH$ (80 μL, 1 M in THF) was added dropwise to the vial containing a slurry of MOF-253-$FeCl_2$ (0.012 g, 0.031 mmol) in 3 mL THF and was kept at room

temperature for 1 h. The resultant black solid of MOF-253-FeH_2 was separated via centrifugation and washed several times with THF to remove excess $NaEt_3BH$. MOF-253-FeH_2 was taken out of the glovebox and was kept in water for 30 minutes to afford MOF-253-Fe_2 [MOF-253-$Fe(OH)_2$]. MOF-253-Fe_2 has 80% Fe-loading with respect to the bpy moiety as analyzed by ICP-OES, giving the formula $AlC_{12}H_{8.6}N_2O_{6.6}Fe_{0.8}$. TGA analysis showed that MOF-253-Fe_2 had 20.2% solvent weight.

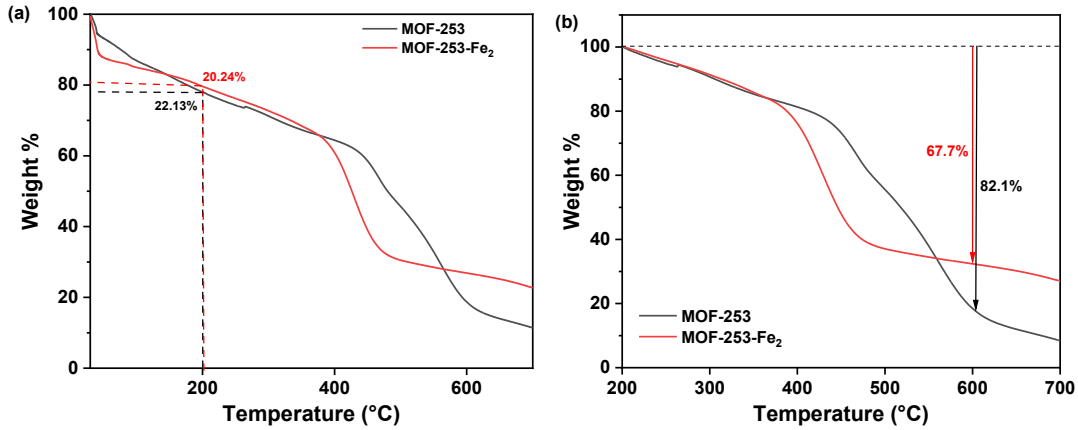


Figure 4.10: (a) TGA curve of freshly prepared MOF-253(Al) (black) and MOF-253-Fe_2 (red). A solvent weight loss of 22.1% in MOF-253(Al) (black) and 20.2% in MOF-253-Fe_2 (red) was observed from 30 °C to 200 °C. (b) TGA curve of freshly prepared MOF-253(Al) (black) and MOF-253-Fe_2 (red) from 200-700 °C. The increased weight of MOF-253-Fe_2 is due to the presence of Fe within the MOF.

Table 4.1: Determination of defect sites in MOF-253(Al) and MOF-253-Fe_2 MOF by TGA analysis.

Sample	**Condition**	**% Solvent**	**% Linker**	**% Residue**
	Calculated	–	82.2	17.8
MOF-253	TGA	22.1	63.9	14.0
	Corrected	–	82.1	17.9
	Calculated	–	67.6	32.4
MOF-253-Fe_2	TGA	20.2	53.9	25.8
(80% Fe-loading)	Corrected	–	67.7	32.3

Theoretical calculation:

(a) For MOF-253(Al):

1 mole of Al(OH)(bpydc) = 0.5 moles Al_2O_3

286.2 g of Al(OH)(bpydc) = 50.98 g Al_2O_3

% Residue = $\frac{50.98}{286.2} \times 100 = 17.8\%$

% Linker = 100 – 17.8 = 82.2%

(b) For MOF-253-Fe_2 (80% Fe-loading):

1 mole Al(OH)(bpydc)$[Fe(OH)_2]_{0.8}$ = 1 mole linker bpydc ($C_{12}H_6N_2O_4$)

358.06 g of Al(OH)(bpydc)$[Fe(OH)_2]_{0.8}$ = 242.18 g linker bpydc

% Linker = $\frac{242.18}{358.06} \times 100 = 67.6\%$

% Residue = 100 - 67.6 = 32.4%

The wt% ligand calculated theoretically matches closely with that of the wt% ligand observed experimentally for MOF-253(Al) and MOF-253-Fe_2. This indicates the absence of any missing-linker defects within MOF-253(Al) and MOF-253-Fe_2.

4.3.2 Binuclear MOF-253-Fe_2 catalysed oxidation of methane to acetic acid using O_2

Standard procedure for MOF-253-Fe_2 catalyzed oxidation of methane to acetic acid using O_2

$$CH_4 + O_2 \xrightarrow[H_2O,\ 160\ °C]{\text{MOF-253-Fe}_2} CH_3CO_2H$$

A 1 mL slurry of MOF-253-Fe_2 (4.7 mg, 10.5 μmol Fe) in water was transferred to a glass liner containing 7 mL of water. The glass liner was then fitted into a high-pressure reactor. The reactor was sealed and purged with methane twice. It was subsequently pressurized with 20 bar methane followed by 8 bar oxygen and heated at 160 °C for 38 h without any mechanical stirring. After the reaction, the reactor was cooled to room temperature, and the gas phase was analysed directly by GC-TCD. A 1 mL aliquot of the aqueous solution was transferred to a centrifuge tube and centrifuged for 1 min. Then, 1 mL of the clear solution was quickly transferred to a GC vial, and 5 μL of ethylene glycol (internal standard) was added. The sample was analysed by GC-FID/MS to identify the products and determine their yields in the liquid phase. A 1 μL sample was injected in GC, and standard calibration

curves were used for quantification of acetic acid. MOF-253-Fe_2 (4.7 mg, 10.5 μmol Fe) under 20 bar of CH_4 and 8 bar of O_2 for 38 h at 160 °C yielded 1.1 mmol of acetic acid (Entry 1, Table 4.2). GC-MS analysis of the reaction mixture confirmed the absence of any other carbon-containing products in the liquid phase.

Detection and quantification of liquid oxygenates.

GC-MS conditions: The column used was an Agilent DB-WAX column with 30 m length, 0.320 mm internal diameter, and 0.25 μm film. The chromatographic conditions were: flow rate of helium at 1 mL min^{-1}, injection volume: 1 μL, column oven temperature initially at 45.0 °C and then increased to 230.0 °C at a rate of 5 °C per minute, and detector temperature of 250 °C.

GC-FID conditions: The column used was an Agilent DB-WAX column with 30 m length, 0.320 mm internal diameter, and 0.25 μm film. The chromatographic conditions were: flow rate of nitrogen at 1 mL min^{-1}, injection volume of 1 μL, column oven temperature at 40.0 °C for 4 minutes, followed by a 5 °C/min ramp to 70 °C, then a 35 °C/min ramp to 200 °C, and a final hold time of 5 minutes (total run time: 19 min). The detector temperature was 250 °C. Products were quantified using a calibration plot of ethylene glycol as the internal standard.

Detection and quantification of methane and gaseous oxygenates.

GC-TCD conditions: The gas after catalysis was analysed using an Agilent GC (8890) equipped with a PoraPlot Q column in sequence with a molecular sieves column and a Thermal Conductivity Detector (TCD). The chromatographic conditions were as follows: carrier gas: helium, column temperature: 45 °C, TCD temperature: 250 °C, and injection temperature: 100 °C. Retention times for CO_2, CH_4, and CO were 4 min, 9.3 min, and 10.75 min, respectively. The methane conversion was calculated by determining the mmol of methane before and after catalysis using a GC-TCD response factor-based calculation. For this, a high-pressure reactor containing a glass liner was filled with 8 mL of a mixture of water and MOF-253-Fe_2 catalyst, and then purged with methane twice. The reactor was

pressurized with 20 bar methane followed by 8 bar oxygen. The gas was analysed with GC-TCD at room temperature (35 °C) before catalysis to quantify the amount of methane in the feed. After the reaction, the gas from the same reactor was analysed at 35 °C to quantify the amount of unreacted methane and other gaseous products. At the optimized reaction condition (Entry 1, Table 4.2), the amount of methane was calculated as 39 mmol before catalysis and 36.71 mmol after catalysis. Therefore, the loss of methane during the reaction was 2.29 mmol, corresponding to a methane conversion of approximately 5.8%.

Procedure to quantify methane and other gases within the high-pressure reactor before and after catalysis. The gas calculations were carried out using a GC-TCD response factor-based method. After the catalytic reaction, the high-pressure reactor was cooled to room temperature, and its contents were transferred into a Tedlar bag through an air-tight connection. A 2.5 mL sample was withdrawn from the bag using an air-tight syringe and injected into the GC-TCD for analysis, allowing for the calculation of the amounts of CO, CO_2, and CH_4. Additionally, 2.5 mL of a standard gas with a known composition of CO, CO_2, and CH_4 was injected separately to determine the response factor (R_f) of each gas.

Table 4.2: Optimization of catalytic conditions for MOF-253-Fe_2 catalyzed oxidation of methane using O_2.[a]

Entry No.	**Temp (°C)**	**P[CH_4] (bar), Initial mmol CH_4**	**P[O_2] (bar)**	**CH_3CO_2H (mmol)** [b]	**CO/CO_2 (mmol)** [c]
1	160	20, 39	8	1.1	0.00014/0.08
2[d]	160	20, 39	8	0	0.026/0.06
3	160	20, 39	0	0	nd
4	120	20, 39	8	0.08[m]	0.0008/0.06
5	140	20, 39	8	0.22	0.0006/0.07
6	180	20, 39	8	0.6	0.01/0.88
7	200	20, 39	8	0.3	0.014/1.7

Continued on next page

Table 4.2 – continued from previous page

Entry No.	Temp (°C)	P[CH_4] (bar), Initial mmol CH_4	P[O_2] (bar)	CH_3CO_2H (mmol) [b]	CO/CO_2 (mmol) [c]
8	160	20, 39	2	0	nd/0.008
9	160	20, 39	4	0.08	nd/0.02
10	160	20, 39	6	0.4	0.0008/0.05
11	160	5, 10	8	0.17	0/0.01
12	160	10, 21	8	0.64	0.0006/0.019
13	160	15, 30	8	0.82	0.0002/0.04
14[e]	160	20, 39	8	0.01	0/0.006
15[f]	160	20, 39	8	0.09	0.0005/0.02
16[g]	160	20, 39	8	0.24	0.0003/0.05
17[h]	160	20, 39	8	0.72	0.002/0.85
18[i]	160	20, 39	8	0	nd
19[j]	160	20, 39	8	0	nd
20[k]	160	20, 39	8	0	nd
21[l]	160	20, 39	8	0	nd

[a] Standard conditions: 4.7 mg of MOF-253-Fe_2 (10.5 μmol Fe), 8 mL H_2O, 38 h; N_2 balance was applied to optimize partial pressures of O_2 and CH_4 (Entry 8-13) maintaining total reaction pressure at 28 bar; nd: not determined.

[b] Analysed by GC-FID using ethylene glycol as the internal standard.

[c] Analysed by GC-TCD.

[d] No catalyst was used.

[e] Reaction time was 6 h.

[f] Reaction time was 12 h.

[g] Reaction time was 24 h.

[h] Reaction time was 50 h.

[i] Toluene was used as the solvent.

[j] THF was used as the solvent.

[k] Heptane was used as the solvent.

[l] Perfluoro hexane was used as the solvent.

[m] Reaction time was 22 h.

Table 4.3: Control experiments for MOF-253-Fe_2 catalyzed oxidation of methane to acetic acid.[a]

Entry No.	Temp (°C)	P[CH_4] (bar), Initial CH_4 mmol	P[O_2] (bar)	CH_3CO_2H (mmol) [b]	CO/CO_2 (mmol) [c]
1	160	20, 39	8	1.1	0.00014/0.08
2[d]	160	20, 39	8	0	0.02/0.04
3[e]	160	20, 39	8	0	0.018/0.04
4[f]	160	0	8	0	nd
5[g]	160	20, 39	0	0	nd
6[h]	160	20, 39	8	0.42	0.0002/0.06
7[i]	160	20, 39	8	0.51	0.0004/0.06
8[j]	160	20, 39	8	0	0.008/0.016
9[k]	160	20, 39	8	1.05	0.0021/0.07
10[l]	160	20, 39	8	0.03	0.001/0.09
11[m]	160	20, 39	8	0.017[aj]	0.0014/0.05
12[n]	160	20, 39	8	0.01[aj]	0.0017/0.03
13[o]	160	20, 39	8	0.014[aj]	0.001/0.05
14[p]	160	20, 39	8	0.019[aj]	0.0016/0.06
15[q]	160	20, 39	0	0	nd
16[r]	160	20, 39	8	0.14[ak]	0.0016/1.21
17[s]	160	20, 39	0	0.19	nd
18[t]	160	20, 39	0	0.005	nd
19[u]	160	0	8	0.006	nd
20[v,s]	160	0	0	0	nd
21[w]	160	0	8	0	nd
22[x]	160	20, 39	8	1.08	0.00018/0.07
23[y]	160	20, 39	8	1.12	0.0002/0.08
24[z]	160	20, 39	0	0	nd
25[aa]	160	20, 39	8	0.07	0.004/0.12
26[ab]	160	20, 39	8	0.04	0.008/0.09
27[ac]	160	20, 39	0	0.1	nd
28[ad]	160	20, 39	8	0.24	0.0018/0.05
29[s]	95	20, 39	8	0.07	nd
30[ai]	160	20, 39	8	0.23[al]	nd/0.28

Continued on next page

Table 4.3 – continued from previous page

Entry No.	Temp (°C)	P[CH_4] (bar), Initial CH_4 mmol	P[O_2] (bar)	CH_3CO_2H (mmol) [b]	CO/CO_2 (mmol) [c]
31[s,ae]	160	20, 39	8	0.086[am]	0/0.009
32[s]	95	20, 39	0	0	nd

[a] Standard conditions: 4.7 mg of MOF-253-Fe_2 (10.5 μmol Fe), 8 mL H_2O, 38 h; N_2 balance was applied to keep constant pressure of 28 bar if needed; nd: not determined.
[b] Analysed by GC-FID using ethylene glycol as the internal standard.
[c] Analysed by GC-TCD.
[d] MOF-253(Al) was used.
[e] MOF-253-$FeCl_2$ (10.5 μmol Fe) was used.
[f] N_2 was used instead of CH_4.
[g] N_2 was used instead of O_2.
[h] Na_2SO_3 was used as an ·OH scavenger.
[i] t-Butanol was used as an ·OH scavenger.
[j] Toluene was used as the solvent; reaction time was 6 h.
[k] MOF-253-$(Fe_2(III)(OH)_6)_{0.5}$ (10.5 μmol Fe) was used as the catalyst.
[l] $Fe(OH)_3$ (10.5 μmol Fe) was used as the catalyst.
[m] Fe@DUT-5(Al) (10.5 μmol Fe) was used as the catalyst.
[n] Fe(0) (10.5 μmol Fe) was used as the catalyst.
[o] Fe_2O_3 (10.5 μmol Fe) was used as the catalyst.
[p] Fe_3O_4 (10.5 μmol Fe) was used as the catalyst.
[q] 5 bar CO was used as the oxidant.
[r] MOF-253-Fe [$Al(OH)(bpdc)_{0.9}(bpydc)_{0.1}$-$Fe(OH)_2$] (10.5 μmol Fe) was used as the catalyst.
[s] 1 bar CO was used as the oxidant.
[t] CO_2 (8 bar) was used as an oxidant.
[u] Oxidation of 0.5 mmol of ethanol using 8 bar O_2.
[v] Oxidation of 0.5 mmol of methanol using 1 bar of CO.
[w] Oxidation of 0.5 mmol of methanol using 8 bar O_2.
[x] 0.5 mmol of methanol added to the reaction mixture.
[y] 0.5 mmol of ethanol added to the reaction mixture.
[z] 1.5 mmol of formic acid was added to the reaction mixture.
[aa] $Fe(OH)_3/Al_2O_3$ (10.5 μmol Fe) was used as the catalyst.
[ab] MOF-253-$(FeCl_2(OH)_2)_{0.4}$ (10.5 μmol Fe) was used as the catalyst.
[ac] 40 bar of air used for oxidation instead of pure O_2.
[ad] TEMPO was used as a $\cdot CH_3$ scavenger.
[ae] MOF-253-Fe [$Al(OH)(bpdc)_{0.9}(bpydc)_{0.1}$-$Fe(OH)_2$] (5.25 μmol Fe) was used as the catalyst.
[af] 0.38 mmol of methanol was formed.
[ah] 0.24 mmol of methanol was formed.
[ai] bpy-UiO-Fe (10.5 μmol Fe) was used as the catalyst.
[aj] Formic acid was formed as the major product.
[ak] 0.091 mmol of methanol was formed as the side product.
[al] 0.22 mmol of methanol was formed as the side product.
[am] 0.046 mmol of methanol was formed.

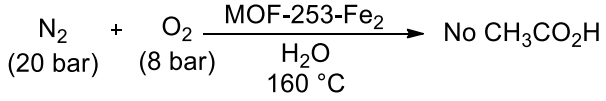
Control experiments for MOF-253-Fe_2 catalysed oxidation of methane.

Reaction conditions: 4.7 mg of MOF-253-Fe_2 (10.5 μmol Fe), 8 mL H_2O, 20 bar N_2, 8 bar O_2, 38 h. The general procedure mentioned in Section 4.3.2 was followed, replacing methane with nitrogen. No liquid products were detected (Entry 4, Table 4.3), suggesting CH_4 as

Blank reaction with O_2 under N_2 without methane.

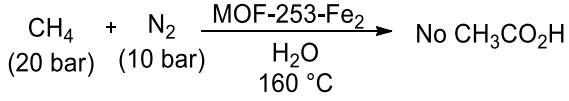
Table 4.4: Carbon balance for methane oxidation reaction.

Initial CH_4 (mmol)	**Post-reaction CH_4 (mmol)**	**CH_4 consumed (mmol)**	**CH_3CO_2H (mmol)**	**CO_2 (mmol)**	**CO (mmol)**	**Total C yield (mmol)**
39	36.71	2.29	1.1	0.08	0.00014	2.28



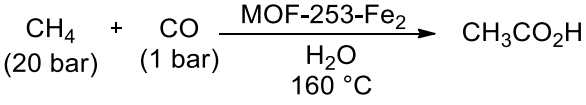
the sole carbon source for CH_3CO_2H production in the MOF-253-Fe_2-catalyzed methane oxidation.

Blank reaction without O_2 under N_2.



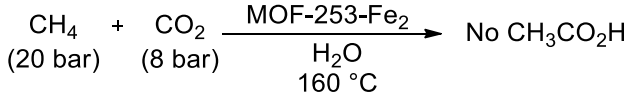
Reaction conditions: 4.7 mg of MOF-253-Fe_2 (10.5 μmol Fe), 8 mL H_2O, 20 bar N_2, 8 bar O_2, 38 h. The general procedure mentioned in Section 4.3.2 was followed, replacing methane with nitrogen. No liquid products were detected (Entry 4, Table 4.3), suggesting CH_4 as the sole carbon source for CH_3CO_2H production in the MOF-253-Fe_2-catalyzed methane oxidation.

Reaction of methane in presence of CO using MOF-253-Fe_2.



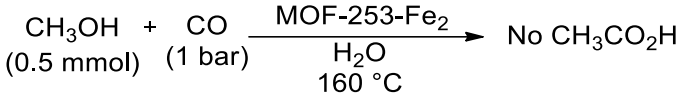
Reaction conditions: 4.7 mg of MOF-253-Fe_2 (10.5 μmol Fe), 8 mL H_2O, 20 bar CH_4, 1 bar CO, 38 h, balanced with N_2 to maintain a total pressure of 28 bar. The general procedure mentioned in Section 4.3.2 was followed, replacing oxygen with carbon monoxide. In this reaction, 0.19 mmol CH_3CO_2H (Entry 17, Table 4.3) was formed, which infers that CO is involved in the MOF-253-Fe_2-catalyzed methane oxidation to acetic acid.

Reaction of methane in presence of CO_2 using MOF-253-Fe_2.



Reaction conditions: 4.7 mg of MOF-253-Fe_2 (10.5 μmol Fe), 8 mL H_2O, 20 bar CH_4, 8 bar CO_2, 38 h. The general procedure mentioned in Section 4.3.2 was followed, replacing oxygen with carbon dioxide. In this reaction, negligible CH_3CO_2H (Entry 18, Table 4.3) was formed, which rules out the formation of acetic acid via methane carboxylation with CO_2 at 160 °C.

Reaction of methanol in presence of CO using MOF-253-Fe_2.



Reaction conditions: 4.7 mg of MOF-253-Fe_2 (10.5 μmol Fe), 8 mL H_2O, 0.5 mmol CH_3OH, 1 bar CO, 38 h, balanced with N_2 to maintain a total pressure of 28 bar. The general procedure mentioned in Section 4.3.2 was followed, replacing oxygen with carbon monoxide and methane with methanol. In this reaction, no CH_3CO_2H (Entry 20, Table 4.3) was formed. We thus conclude that MOF-253-Fe_2-catalyzed methane oxidation does not occur via the reaction of *in situ* generated methanol and CO.

Time-Resolved CO Evolution Studies To understand the role of CO as a possible intermediate in acetic acid formation, time-resolved gas-phase CO quantification was performed under standard reaction conditions (4.7 mg of MOF-253-Fe_2 (10.5 µmol Fe), 20 bar CH_4, 8 bar O_2, 8 mL H_2O, 160 °C). In the presence of MOF-253-Fe_2, no detectable CO was observed at 6 h, although 0.01 mmol of acetic acid had already formed. This initially raised questions regarding the carbon source for acetic acid in the apparent absence of CO.

To further probe this, we conducted a control experiment in toluene as the solvent under identical conditions. In this case, 0.008 mmol of CO was detected at 6 h, suggesting that CO can be thermally generated. These findings indicate that under aqueous conditions, CO

is likely formed transiently and rapidly consumed for acetic acid formation, preventing its accumulation in the gas phase during the early stages of the reaction.

We therefore propose that CO serves as a reactive intermediate that is continuously generated and incorporated into the C–C bond formation step, particularly through carbonylation of a methyl intermediate. A comparative time-resolved plot (Figure 4.11) shows the evolution of both CO and acetic acid. At extended time points, CO accumulation is observed, suggesting a decline in its consumption, possibly due to plateauing acetic acid formation and subsequent overoxidation.

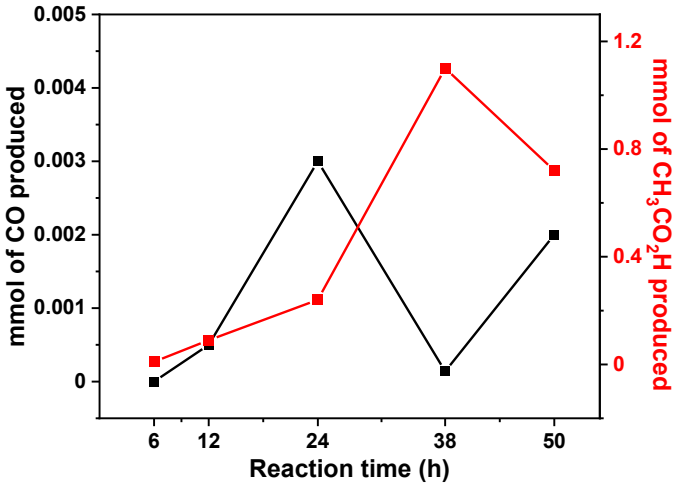


Figure 4.11: Time-dependent formation of CO (black) and acetic acid (red) under identical reaction conditions. Reaction conditions: 4.7 mg of MOF-253-Fe_2 (10.5 μmol Fe), 20 bar CH_4, 8 bar O_2, 8 mL H_2O, 160 °C.

Together, these findings support the hypothesis that CO acts as a transient, *in situ* intermediate. Its rapid consumption during the early stages of the reaction accounts for the low gas-phase concentration, while its accumulation at later times reflects a shift in the reaction dynamics, likely due to the overoxidation of acetic acid into CO and CO_2.

Test for "heterogeneity of MOF-253-Fe_2 in methane oxidation to acetic acid.

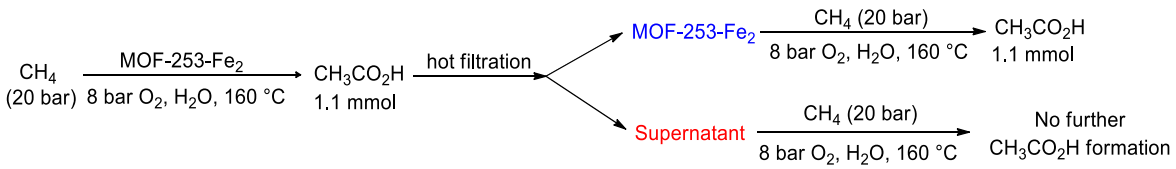
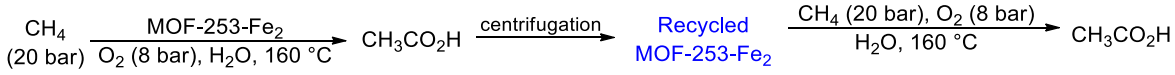


Figure 4.12: Hot filtration test of MOF-253-Fe_2 in methane oxidation to acetic acid.

The general procedure mentioned in Section 4.3.2 was followed. After 38 h of reaction, the solid MOF catalyst was removed from the hot reaction mixture by filtration and thoroughly washed with water. Two reactions were set up separately in two different high-pressure reactors: one with the extracted solid and the other with the supernatant. The solid and supernatant were transferred into separate glass liners. Then, 8 mL of water was added to the glass liner containing the solid MOF. Both glass liners were fitted into two separate reactors, which were sealed and purged with methane. The reactors were pressurized with 20 bar CH_4 and 8 bar O_2, and then heated at 160 °C for 38 h without any mechanical stirring. After the reaction was completed, the solid MOF catalyst was again removed from the hot reaction mixture by filtration and thoroughly washed with water. The gas phase was analysed directly using GC-TCD, and the liquid phase of the reactions was analysed with GC. No further CH_3CO_2H was produced in the reaction involving just the supernatant, whereas the reaction containing the solid MOF yielded 1.1 mmol of CH_3CO_2H. This experiment excludes the potential contribution of any leached Fe species to the catalysis and confirms that solid MOF-253-Fe_2 is the actual catalyst for the oxidation of methane.

Recycling of MOF-253-Fe_2 for oxidation of methane..



The recycle and reuse experiment was conducted to assess the stability of the MOF catalyst. The general procedure mentioned in Section 4.3.2 was followed, except that the recovered MOF catalyst was washed several times with water. It was added to the glass liner along with 8 mL of H_2O. The glass liner was fitted into a high-pressure reactor, which was then sealed and purged with CH_4 twice. The reactor was pressurized with 20 bar CH_4 followed by 8 bar O_2, and then heated at 160 °C. This procedure was repeated four times, with very minimal leaching of iron and aluminium (Table 4.5). The MOF retained its crystallinity and stability, as evidenced by the PXRD patterns from the recycling experiments (Figure 4.2b). The MOF could be recycled and reused at least four times without a drop in activity, giving a cumulative TON of 448.

Table 4.5: Productivity of acetic acid ($mmol_{CH_3CO_2H}$ mol_{Fe}^{-1} h^{-1}) and the leaching of Fe and Al in various runs of the recycling of MOF-253-Fe_2 for the oxidation of methane.

No. of Run	**Time (h)**	**Productivity ($mmol_{CH_3CO_2H}$ mol_{Fe}^{-1} h^{-1})**	**% Leaching (Al, Fe)**
Run-1	38	2,757	0.04, 0.06
Run-2	38	2,730	0.03, 0.05
Run-3	38	2,741	0.04, 0.03
Run-4	38	2,605	–
Run-5	38	2,354	0.04, 0.05

Comparison of catalytical activity between MOF-253-Fe_2 and other materials for oxidation of methane with oxygen.

$Fe(OH)_3/Al_2O_3$ catalyzed oxidation of methane.[46] A 2 M NaOH solution in 50 mL of water was added gradually into a 0.01 M $Fe(NO_3)_3{\cdot}9H_2O$ solution containing Al_2O_3, with constant stirring for 8 h at room temperature, to obtain $Fe(OH)_3/Al_2O_3$. The $Fe(OH)_3/Al_2O_3$ powder was calcined in air at 240 °C and 400 °C, respectively, for 2 h to yield clusters made of Fe and Al oxides. The loading amount of Fe was 12 wt%. Fe/Al_2O_3 (4.9 mg, 10.5 μmol of Fe) was transferred into a glass liner containing 8 mL of water. The glass liner was fitted into a high-pressure reactor, which was then sealed and purged with CH_4 twice. The reactor was pressurized with 20 bar CH_4 followed by 8 bar O_2, and then heated at 160 °C. The results are summarized in Entry 25, Table 4.3; the major product was CO_2 with a negligible quantity of CH_3CO_2H.

Fe@DUT-5 catalyzed methane oxidation.[47] In a 5 mL round-bottom flask, $FeCl_3{\cdot}6H_2O$ (50 mg, 0.18 mmol) was dissolved in ethyl acetate (2 mL), followed by the addition of DUT-5 (100 mg). The mixture was heated at 50 °C for 48 h. The solid was then collected by centrifugation, washed thoroughly, and dried to give DUT-5-$FeCl_3$. $NaBH_4$ (10 mg) was added to 6 mL of deionized water in a round-bottom flask, after which 80 mg of DUT-5-$FeCl_3$ was added. The pH was maintained in the range of 6–8 throughout the addition of $NaBH_4$. The resulting mixture was stirred for 30 min and then filtered. The collected solid was washed

thoroughly with deionized water to give a black powder of Fe@DUT-5. Finally, Fe@DUT-5 was activated at 150 °C for 12 h under high vacuum. The Fe content in Fe@DUT-5 was 3.2 wt%. Fe@DUT-5 (18.3 mg, 10.5 μmol of Fe) was transferred into a glass liner containing 8 mL of water. The glass liner was fitted into a high-pressure reactor, which was then sealed and purged with CH_4 twice. The reactor was pressurized with 20 bar CH_4 followed by 8 bar O_2 and then heated at 160 °C. Negligible CH_3CO_2H was observed (Entry 11, Table 4.3).

Fe(0) catalyzed methane oxidation.[48] An aqueous solution of 1.6 M $NaBH_4$ was added slowly into a 1.0 M aqueous solution of $FeCl_3{\cdot}3H_2O$ with constant stirring at room temperature to obtain black-coloured Fe(0) nanoparticles. The black solid was then washed several times with THF and dried. 0.58 mg of Fe nanoparticles (10.5 μmol of Fe) was then transferred into a glass liner containing 8 mL of water. The glass liner was fitted into a high-pressure reactor, which was then sealed and purged with CH_4 twice. The reactor was pressurized with 20 bar CH_4 followed by 8 bar O_2 and then heated at 160 °C for 38 h. Negligible quantities of CH_3CO_2H were observed, whereas HCO_2H was observed as the dominant product (Entry 12, Table 4.3).

Synthesis of MOF-253-$(Fe_2Cl_4(OH)_2)_{0.4}$[24] In a 20 mL vial, MOF-253-$FeCl_2$ was dispersed in 5 mL of methanol with vigorous stirring. With an oxygen-inflated balloon, MOF-253-$FeCl_2$ was oxidized to form di-Fe^{III} centers with μ_2-OH groups. The mixture was heated at 50 °C for 24 h, and the color of the MOF changed from dark grey to yellow, suggesting the oxidation of Fe^{II} to Fe^{III} and a change in the coordinating environment. The solid was collected by centrifugation and washed with methanol three times. The obtained MOF-253-$(Fe_2Cl_4(OH)_2)_{0.4}$ was dried under vacuum and stored in THF. The general procedure mentioned in Section 4.3.2 was followed, using MOF-253-$(Fe_2Cl_4(OH)_2)_{0.4}$ (10.5 μmol of Fe). Reaction conditions: MOF-253- $(Fe_2Cl_4(OH)_2)_{0.4}$ (10.5 μmol of Fe), 8 mL H_2O, 20 bar CH_4, 8 bar O_2, 160 °C, 38 h. Negligible CH_3CO_2H (0.04 mmol) was observed (Entry 26, Table 4.3).

Synthesis of MOF-253-Fe $[Al(OH)(bpdc)_{0.9}(bpy)_{0.1}$-$Fe(OH)_2]$[24] Similar to the synthesis of MOF-253(Al), 2,2′-bipyridine-5,5′-dicarboxylic acid (H_2bpydc, 2.6 mg, 0.0106 mmol, 0.1 eq.), biphenyl-4,4′-dicarboxylic acid (H_2bpdc, 23.1 mg, 0.0954 mmol, 0.9 eq.), and $AlCl_3$ (26 mg, 0.11 mmol, 1 eq.) were added into 3 mL of N,N-dimethylformamide (DMF) and stirred for 30 min. The solution was transferred to a hydrothermal bomb with a Teflon liner

and kept in a preheated oven at 120 ℃ for 24 h. After cooling to room temperature, the white solid was collected via centrifugation and washed several times with DMF. Finally, the resultant white crystalline solid of MOF-253(Al)-$(bpy)_{0.1}$ was washed and stored in THF. MOF-253(Al)-$(bpy)_{0.1}$ showed the same PXRD pattern as MOF-253(Al). The detailed characterization of the mononuclear MOF-253-Fe is given in next chapter.

The general procedure mentioned in Section 4.3.2 was followed, using MOF-253-Fe (10.5 μmol of Fe). Reaction conditions: MOF-253-Fe (41.7 mg, 10.5 μmol of Fe), 8 mL H_2O, 20 bar CH_4, 8 bar O_2, 160 ℃, 38 h. The methane oxidation reaction with the mononuclear catalyst MOF-253-Fe gave 0.12 mmol of CH_3CO_2H and 0.08 mmol of CH_3OH under the same conditions (Entry 16, Table 4.3), resulting in a 9-fold decrease in the catalytic activity of MOF-253(Al)-Fe compared to MOF-253-Fe_2, along with a decline in liquid selectivity from 100% to 60%. The di-iron system showed much enhanced activity and selectivity over the mononuclear system under the same catalytic conditions.

Investigation of Fe adsorption at the SBU of MOF-253(Al) using DUT-5(Al) with biphenyl linkers as a control. To confirm there is no coordination of Fe at the SBUs, this control experiment was performed.

We conducted a control experiment in which 1 mL of a THF solution of $FeCl_2$ (0.01 g, 0.079 mmol) was added to DUT-5 MOF (0.009 g), which contained biphenyl linkers instead of bipyridyl linkers. The mixture was stirred overnight at room temperature inside a glovebox. The resulting MOF was washed several times with THF. ICP-OES analysis of the resulting MOF indicated 2% Fe loading with respect to the μ_2-OH moiety.

Inside the glovebox, $NaEt_3BH$ (80 µL, 1 M in THF) was added dropwise to the vial containing the resulting MOF in 3 mL THF, and the mixture was left at room temperature for 1 h. The MOF was then separated by centrifugation and washed multiple times with THF to remove any excess $NaEt_3BH$. The MOF was then removed from the glovebox and immersed in water for 30 minutes to yield Fe-adsorbed DUT-5.

A controlled reaction was then performed using the DUT-5 MOF (20 mg) having adsorbed Fe under identical reaction conditions (20 bar CH_4, 8 bar O_2, 8 mL H_2O, 160 °C, 38 h). No carbon-containing products were formed, further supporting the conclusion that Fe binds to the bipyridyl (bpy) linkers rather than to the alumina SBUs, thereby confirming

the critical role of Fe-bpy species in catalysis.

Attempt to make homogeneous bpyFe(OH)$_2$.

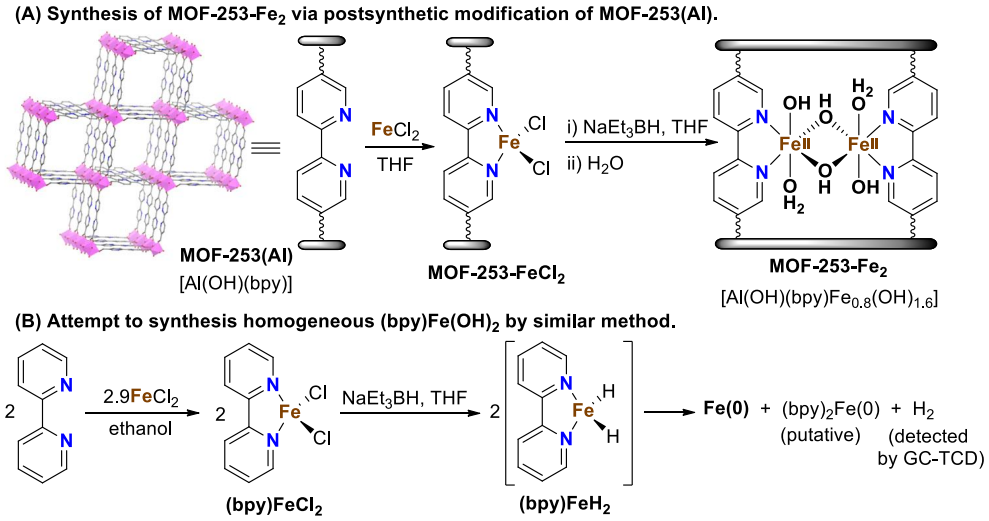


Figure 4.13: (A) Synthesis of MOF-253-Fe$_2$ via postsynthetic modification of MOF-253(Al). (B) Attempt to synthesize analogous homogeneous (bpy)Fe(OH)$_2$ species by a similar method. .

Initially, we synthesized the (bpy)FeCl$_2$ precursor following a reported procedure.[35] Subsequent attempts to generate the corresponding (bpy)Fe(OH)$_2$ species by reacting (bpy)FeCl$_2$ with NaEt$_3$BH in THF (1:2.2 molar ratio) resulted in instantaneous formation of sparingly soluble Fe(0) nanoparticles (confirmed by XANES analysis, Figure 4.17), along with unidentified bipyridyl-iron species, and H$_2$ gas (detected by GC-TCD) (Figure 4.13B). These observations suggest that the putative (bpy)FeH$_2$ intermediate undergoes rapid intermolecular decomposition, thereby preventing formation of the desired (bpy)Fe(OH)$_2$ complex in water.[49] The resultant mixture showed no catalytic activity in methane oxidation in water. In contrast, the facile synthesis of the robust [(bpy)Fe^{II}(μ_2-OH)(OH)(OH$_2$)]$_2$ species through post-synthetic modification of the pristine MOF-253 underscores the significance of the active site isolation within the porous MOF, which prevents intermolecular decomposition pathways (Figure 4.13A).

Additionally, the synthesis of mono bipyridyl-Fe(II) complexes in solution requires a carefully controlled molar ratio of bpy to FeCl$_2$ to favor formation of the mono-ligated species over bis- or tris-substituted complexes such as [Fe(bpy)$_2$Cl$_2$] or [Fe(bpy)$_3$]Cl$_2$. To avoid such uncontrolled ligand coordination, or intermolecular deactivation into oligomeric

species or metal/metal oxide nanoparticles, sterically demanding chelating ligands are often employed.[50;51] While steric protection around the metal center can enhance the stability of the complex and suppress undesirable side reactions, it may also impose limitations on catalytic activity.

Immobilization of homogeneous catalysts in structurally regular porous solid supports can provide catalytic site isolation without relying on bulky ligands, thus offering an alternative route to obtaining highly active base metal catalysts.[52] These challenges underline a fundamental advantage of using MOFs: active-site isolation within a rigid, porous framework prevents undesired intermolecular interactions, stabilizes reactive intermediates, and mimics the spatial confinement observed in enzymatic systems. In our system, incorporation of the Fe site into the MOF backbone avoids oligomerization and bimolecular decomposition to Fe nanoparticles, thereby enabling stable and selective methane oxidation.

Furthermore, it is well documented that homogeneous bipyridyl–Fe complexes are thermally unstable and tend to decompose under elevated temperatures,[53] which further limits their viability in high-temperature catalytic systems such as ours.

Synthesis of bpy-UiO-Fe[38] [2,2′-bipyridine]-5,5′-dicarboxylic acid (0.027 g, 0.111 mmol) and $ZrCl_4$ (0.026 g, 0.112 mmol) were dissolved in 13 mL DMF. After sonication for 30 min, TFA (0.040 mL, 0.523 mmol) was added, and the resultant mixture was heated in a sealed 15 mL glass vial at 100 °C for 4 days in an oven.[54] The reaction mixture was allowed to cool to room temperature, and the white crystalline solid was isolated via centrifugation. The MOF was washed with DMF multiple times, followed by THF, and stored in THF at room temperature.

A solution of $FeCl_2$ (0.003 g, 0.024 mmol) in THF was added to the bpy-UiO MOF and kept overnight with periodic shaking at room temperature inside a glovebox. The purple solid was centrifuged out of solution and washed 8–10 times with THF to give bpy-UiO-$FeCl_2$ MOF. Bpy-UiO-$FeCl_2$ ($Zr_6C_{72}H_{40}N_{12}O_{32}Fe_{2.4}Cl_{4.8}$) has 40 % Fe-loading with respect to the bpy moiety as determined by ICP-OES.

$NaEt_3BH$ (35 μL, 1 M in toluene) was added dropwise to the vial containing a slurry of bpy-UiO-$FeCl_2$ (0.016 g, 0.006 mmol) in 3 mL THF inside the glovebox and kept at room temperature for 1 h. The resultant dark green solid bpy-UiO-FeH_2 was separated via

centrifugation and washed several times with THF to remove excess $NaEt_3BH$. Bpy-UiO-FeH_2 was then taken out of the glovebox and kept in water for 30 min to afford bpy-UiO-$Fe(OH)_2$ [bpy-UiO-Fe].

PXRD characterization confirmed the MOF structure, and other characterization details for this MOF are given in Chapter 6.

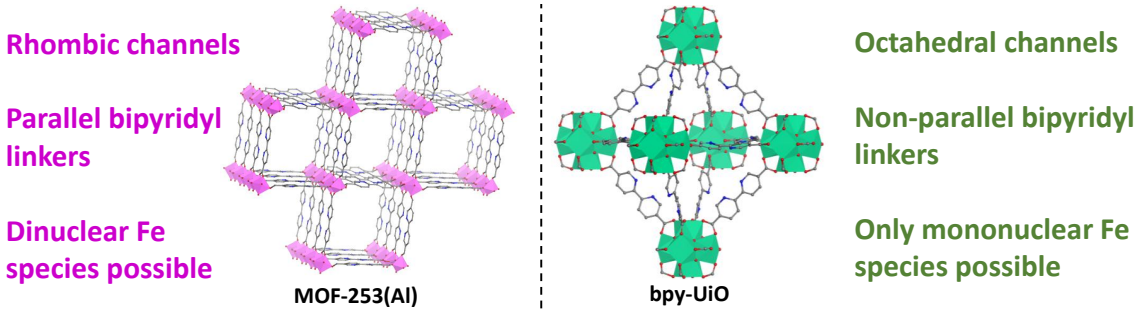


Figure 4.14: Comparison of structural features of MOF-253(Al) (rhombic) and bpy-UiO (octahedral).

To validate the presence of mononuclear Fe species in MOF-253-Fe, we compared its catalytic activity with bpy-UiO-Fe, which is known to contain 100% monomeric species due to its non-parallel linkers in the UiO topology. Both catalysts were tested under identical conditions for methane oxidation. At 160 °C, both mononuclear catalysts, MOF-253-Fe and bpy-UiO-Fe, exhibited low selectivity for acetic acid, of 10% and 32%, respectively. In contrast, the dinuclear MOF-253-Fe_2 achieved a significantly higher acetic acid selectivity of 93%, with a corresponding yield of 1.1 mmol (Table 4.3.2).

Catalyst	**mmol of products**			**% Overall Selectivity**	
	CH_3OH	**CH_3CO_2H**	**CO/CO_2**	**CH_3OH**	**CH_3CO_2H**
MOF-253-Fe_2	-	1.1	0.00014/0.08	-	93
MOF-253-Fe	0.091	0.14	0.0016/1.21	6	10
bpy-UiO-Fe	0.22	0.23	0.0007/0.28	30	32

[a] Reaction conditions: catalyst (10.5 μmol Fe), 20 bar CH_4, 8 bar O_2, 160 °C, 8 mL water, 38 h.

These observations confirm that MOF-253-Fe contains mononuclear Fe sites, as the selectivity of MOF-253-Fe for acetic acid at 160 °C is similar to that of bpy-UiO-Fe, but

markedly different from the dinuclear MOF-253-Fe_2. This further supports the conclusion that both catalysts (MOF-253-Fe and bpy-UiO-Fe) possess similar monomeric Fe sites, reinforcing that the differences in catalytic activity and selectivity arise from distinct active site structures rather than differences in active site density.

Radical Scavenging experiment with MOF-253-Fe_2 catalyst.

Radical scavenging experiment with Na_2SO_3. To investigate any role of ·OH in MOF-253-Fe_2 catalysed methane-to-acetic acid conversion, the catalysis was performed in the presence of known ·OH radical scavengers such as Na_2SO_3 or t-butanol, and the catalytic activity and selectivity were compared to reactions conducted in the absence of radical scavengers.

Reaction conditions: 4.7 mg of MOF-253-Fe_2 (10.5 μmol Fe), 8 mL H_2O, 20 bar CH_4, 8 bar O_2, 38 h, Na_2SO_3 (250 mg, 1.98 mmol). The general procedure mentioned in Section 4.3.2 was followed, with Na_2SO_3 added to study its effect on the catalytic reaction. The yield of acetic acid, determined by GC using ethylene glycol as the internal standard, was 0.42 mmol, significantly lower than that obtained without scavenger under identical reaction conditions (Entry 6, Table 4.3), illustrating that ·OH radicals are involved in the reaction mechanism. Similarly, the use of t-butanol as a scavenger resulted in an acetic acid yield of 0.51 mmol (Entry 7, Table 4.3), further supporting the role of ·OH radicals in the catalytic cycle.

Radical scavenging experiment with TEMPO. To investigate any role of $\cdot CH_3$ in MOF-253-Fe_2 catalysed methane-to-acetic acid conversion, the catalysis was performed in the presence of a known $\cdot CH_3$ and ·OH radical scavenger such as TEMPO, and the catalytic activity and selectivity were compared to reactions conducted in the absence of radical scavengers.

Reaction conditions: 4.7 mg of MOF-253-Fe_2 (10.5 μmol Fe), 8 mL H_2O, 20 bar CH_4, 8 bar O_2, 38 h, TEMPO (179.7 mg, 1.15 mmol). The general procedure mentioned in Section 4.3.2 was followed, with TEMPO added to study its effect on the catalytic reaction. The yield of acetic acid, determined by GC using ethylene glycol as the internal standard, was 0.24 mmol, significantly lower than that obtained without scavenger under identical reaction

conditions (Entry 28, Table 4.3), illustrating that ·CH_3 and ·OH radicals are involved in the reaction mechanism.

Table 4.6: Simulated parameters of EPR spectroscopic spin-trapping experiments for MOF-253-Fe_2 catalysed oxidation of methane.[a]

Adducts	**g-factor**	**A_{14N} (G)**	**$A_\alpha H$ (G)**	**lw (mT)[b]**
DMPO-CH_3	2.01	15.7	22.5	0.12
DMPO-OH	2.01	15.2	14.7	0.08
DMPO-$COCH_3$	2.01	15.28	19.7	0.27
DMPO-degraded	2.01	15.55	–	0.13

[a] Reaction conditions: 4.7 mg MOF-253-Fe_2 (10.5 μmol Fe), 20 bar CH_4, 8 bar O_2, 50 μL DMPO, 38 h, 160 °C.

[b] The linewidth (lw, in mT) defines the FWHM (full width at half height) of the absorption Gaussian.

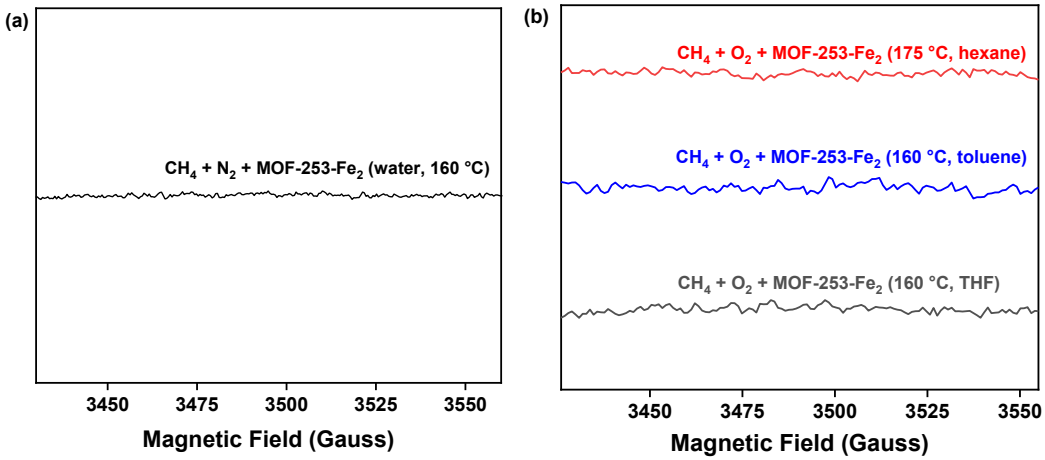


Figure 4.15: (a) X-band (9.85 GHz) EPR spectroscopic spin-trapping experiments. EPR spectrum from DMPO spin-trapping experiment of MOF-253-Fe_2 catalyzed methane oxidation by water at 160 °C for 38 h (black). Reaction conditions: MOF-253-Fe_2 (4.7 mg, 10.5 µmol Fe), 20 bar CH_4, 8 bar N_2, 160 °C, 8 mL water, 38 h. (b) X-band (9.85 GHz) EPR spectroscopic spin-trapping experiments. EPR spectrum from DMPO spin-trapping experiment of MOF-253-Fe_2 catalyzed methane oxidation by O_2 at 160 °C for 38 h in toluene (red), in hexane (blue), in THF (black).

4.3.3 DFT structure Optimization

All density functional theory (DFT) calculations were carried out using Gaussian 16.[55] Geometry optimizations were performed using the hybrid B3LYP functional,[56;57] in combination with the def2-SVP basis set[58] and Grimme's D3 dispersion correction.[59] Solvent effects were included using the polarizable continuum model (PCM) with the integral equation formalism variant (IEFPCM), employing water as the solvent at 303.15 K. All optimized structures were visualized using GaussView 5.0.

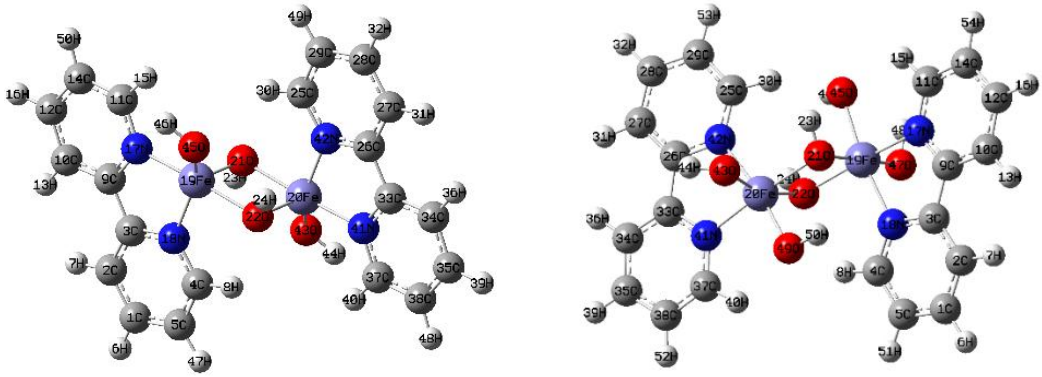


Figure 4.16: DFT-optimized structures of MOF-253-Fe_2, INT-4 [MOF-253-$(Fe_2(OH)_6)_{0.5}$]

Cartesian coordinates of the DFT-optimized structures.

MOF-253-Fe$_2$

Coordinates (Å)

S.No.	Atom	X	Y	Z
1	C	-3.689446	-0.719905	0.452731
2	C	-2.313288	-0.928480	0.405737
3	C	-1.461285	0.165428	0.199090
4	C	-3.287226	1.627130	0.091283
5	C	-4.182421	0.584350	0.295358
6	H	-4.369717	-1.558670	0.613473
7	H	-1.900341	-1.930008	0.530074
8	H	-3.594164	2.666294	-0.032364
9	C	0.002382	0.106323	0.127220
10	C	0.782593	-1.048635	0.276803
11	C	1.918527	1.412066	-0.167237
12	C	2.170159	-0.950004	0.198397
13	H	0.306973	-2.012887	0.458231
14	C	2.750244	0.307169	-0.023068
15	H	2.312041	2.417409	-0.332441
16	H	2.793363	-1.838903	0.314800
17	N	0.577190	1.320460	-0.107102
18	H	-1.955054	1.426606	0.032672
19	Fe	-0.644945	2.810771	-0.218373
20	Fe	-2.006585	4.605981	1.656219
21	O	-0.651133	3.162206	1.707154
22	O	-2.000740	4.254163	-0.269167
23	H	-1.065063	2.462164	2.234781
24	H	-1.588296	4.954673	-0.797312
25	C	0.635635	5.789244	1.346466
26	C	-1.190035	7.251392	1.239851
27	C	-0.337833	8.345278	1.033880
28	C	1.038270	8.136466	0.986567
29	C	1.530990	6.831980	1.142960
30	H	0.942460	4.749972	1.469430
31	H	-0.750615	9.346971	0.910305
32	H	1.718707	8.975193	0.826340
33	C	-2.653690	7.310677	1.311749
34	C	-3.433749	8.465838	1.162878
35	C	-4.821335	8.367294	1.241037
36	H	-2.958004	9.430168	0.982197
37	C	-4.570022	6.004957	1.605113
38	C	-5.401608	7.110039	1.461553
39	H	-5.444431	9.256341	1.125178
40	H	-4.963661	4.999551	1.769661
41	N	-3.228688	6.096477	1.545207
42	N	-0.696517	5.989997	1.405393
43	O	-2.960290	3.603963	2.886742
44	H	-3.784184	3.987141	3.219101
45	O	0.308823	3.812915	-1.448712
46	H	1.132612	3.429715	-1.781301
47	H	-5.253247	0.792344	0.336484
48	H	-6.484397	6.986124	1.518125
49	H	2.601770	6.623808	1.101516
50	H	3.833011	0.431182	-0.079885

INT-4

Coordinates (Angstroms)

S.No.	Atom	X	Y	Z
1	C	-3.903633	-0.595409	-0.077361
2	C	-2.561118	-0.892009	0.159193
3	C	-1.619836	0.144910	0.110025
4	C	-3.281830	1.707600	-0.367280
5	C	-4.271045	0.724453	-0.356299
6	H	-4.653501	-1.388978	-0.050378
7	H	-2.250175	-1.916214	0.364843

8	H	-3.492220	2.762295	-0.541970
9	C	-0.162701	-0.035604	0.279583
10	C	0.463190	-1.248267	0.594535
11	C	1.900720	1.056215	0.166318
12	C	1.854757	-1.287387	0.693778
13	H	-0.126325	-2.149886	0.760507
14	C	2.588449	-0.117667	0.471820
15	H	2.374186	2.022452	-0.028968
16	H	2.359997	-2.223929	0.939391
17	N	0.566256	1.087143	0.080178
18	N	-1.996603	1.420406	-0.135789
19	Fe	-0.488656	2.721004	-0.254358
20	Fe	-1.855994	4.556631	1.681308
21	O	-0.560153	3.064200	1.680543
22	O	-1.672495	4.220256	-0.219111
23	H	0.304881	3.384991	1.971004
24	H	-1.383083	4.987604	-0.733082
25	C	0.656913	6.204963	1.189718
26	C	-1.342271	7.394265	1.351189
27	C	-0.663281	8.617750	1.316421
28	C	0.729450	8.610574	1.225939
29	C	1.399374	7.387588	1.151809
30	H	1.106193	5.216340	1.034330
31	H	-1.209018	9.559856	1.362426
32	H	1.281608	9.552565	1.204252
33	C	-2.811074	7.250018	1.427501
34	C	-3.722146	8.311295	1.369498
35	C	-5.088432	8.033625	1.415741
36	C	-3.371000	9.339041	1.280239
37	C	-4.547529	5.698555	1.577313
38	C	-5.510012	6.705174	1.518329
39	H	-5.815189	8.847224	1.368960
40	H	-4.790310	4.638469	1.671377
41	N	-3.236901	5.970633	1.534122
42	N	-0.675384	6.220273	1.302074
43	O	-1.405945	4.882164	3.423963
44	H	-1.502655	5.825325	3.624061
45	O	1.141778	3.752610	-0.375570
46	H	1.039928	4.421770	-1.067193
47	O	-0.461862	2.473691	-2.092471
48	H	0.451799	2.705692	-2.320887
49	O	-3.116064	3.281113	2.005647
50	H	-2.606370	2.467161	2.132640
51	H	-5.309691	0.994702	-0.554150
52	H	-6.569325	6.446204	1.554713
53	H	2.485830	7.342146	1.057786
54	H	3.677969	-0.110783	0.535186

4.3.4 X-ray absorption spectroscopic analysis.

X-ray Near-Edge Structure (XANES) and Extended X-ray Absorption Fine Structure (EXAFS) measurements were carried out at the Energy-Scanning EXAFS beamline (BL-9) at the Indus-2 Synchrotron Source, Raja Ramanna Centre for Advanced Technology (RRCAT), Indore, India.[60] All measurements were performed at room temperature. This beamline operates in the energy range of 4 keV to 25 keV. The beamline optics consist of a Rh/Pt-coated collimating meridional cylindrical mirror, and the collimated beam reflected by the mirror is monochromatized by a Si(111)-based double crystal monochromator (DCM). The second crystal of the DCM is a sagittal cylindrical crystal used for horizontal focusing of the beam, while another Rh/Pt-coated bendable post mirror facing downward is employed for vertical focusing of the beam at the sample position. Two ionization chambers (300 mm length each) were used for data collection in transmission mode; one ionization chamber measured the incident flux, and the second measured the transmitted flux. For energy calibration, standard metal foils were used. Appropriate gas pressure and gas mixture were selected to achieve 10–20% absorption in the first ionization chamber and 70–90% absorption in the second ionization chamber to obtain a better signal-to-noise ratio. Pellets were prepared from powder samples for recording absorption spectra. The sample powder was homogeneously mixed with cellulose powder in appropriate proportions and pressed (2 Ton) into a 15 mm diameter disc. The sample amount was optimized to achieve a reasonable edge jump at the specific absorption edge of the element being probed. Spectra were collected at the Fe K-edge in transmission mode and calibrated against the reference spectrum of metallic Fe (7112 eV). Data were processed using DEMETER software.[61] A metallic Fe foil standard was used as a reference for energy calibration and was measured simultaneously with experimental samples.

XANES Analysis

The oxidation states of the Fe species within MOF-253-Fe_2, and MOF-253-Fe_2 recovered after the oxidation of methane were determined by comparing the energies of their pre-edge positions to those of $FeCl_2$ and $Fe(OH)_3$.

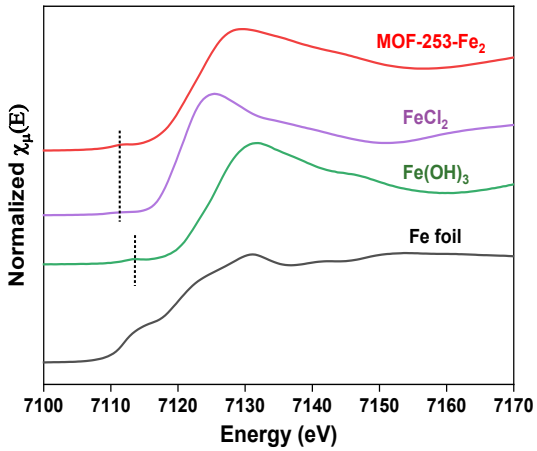


Figure 4.17: $\mu(E)$ XAS spectra of metallic Fe(0) (black), $Fe(OH)_3$ (green), $FeCl_2$ (purple), and MOF-253-Fe_2 (red). The oxidation states of the Fe species within MOF-253-Fe_2 was determined by comparing the energy of their pre-edge positions to those of $Fe(OH)_3$ and $FeCl_2$. The positions of the Fe pre-edge of MOF-253-Fe_2 (7111.7 eV) aligned well with that of $FeCl_2$ (7111.0 eV), and are approximately 2 eV lower than that of $Fe(OH)_3$ (7113.0 eV). Therefore, we conclude that the Fe ions in MOF-253-Fe_2 is in the +2 oxidation state.

EXAFS fitting using DFT optimized structures.

The spectra were calibrated against the reference spectra and aligned to the first peak in the smoothed first derivative of the absorption spectrum, the background noise was removed, and the spectra were processed to obtain a normalized unit edge step.

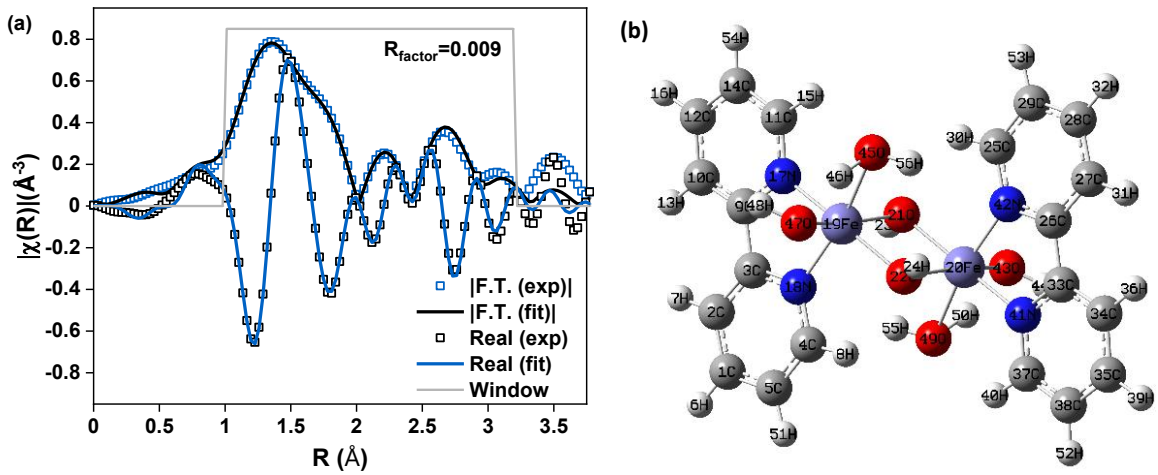


Figure 4.18: (a) EXAFS spectrum and fit of a combination of (90%) dimeric MOF-253-Fe_2 and (10%) monomeric Fe sites in the R space at the Fe K-edge. The fitting range in the R space is 1.0–3.25 Å. EXAFS fitting indicates that MOF-253-Fe_2 contains ∼90% dimeric $[(bpy)Fe^{II}(\mu_2\text{-}OH)(OH)(OH_2)]_2$ species and ∼10% monomeric $(bpy)Fe^{II}(OH)$ species. (b) DFT-optimized structure of MOF-253-Fe_2.

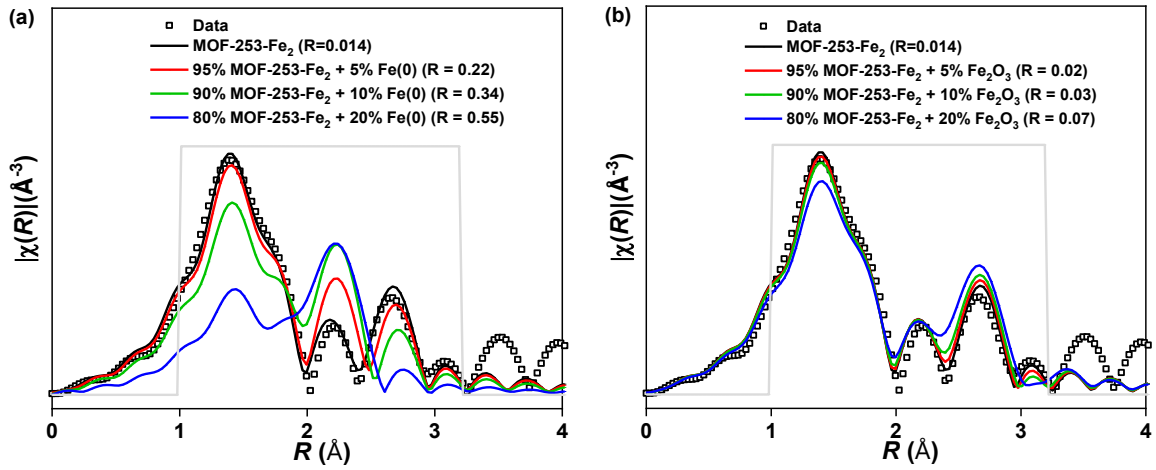


Figure 4.19: (a) EXAFS spectra of MOF-253-Fe_2 fitted with combined models of Fe(0) and MOF-253-Fe_2. (b) EXAFS spectra of MOF-253-Fe_2 fitted with combined models of Fe_2O_3 and MOF-253-Fe_2. The significant misfits indicate that MOF-253-Fe_2 does not contain any Fe nanoparticles or Fe_2O_3.

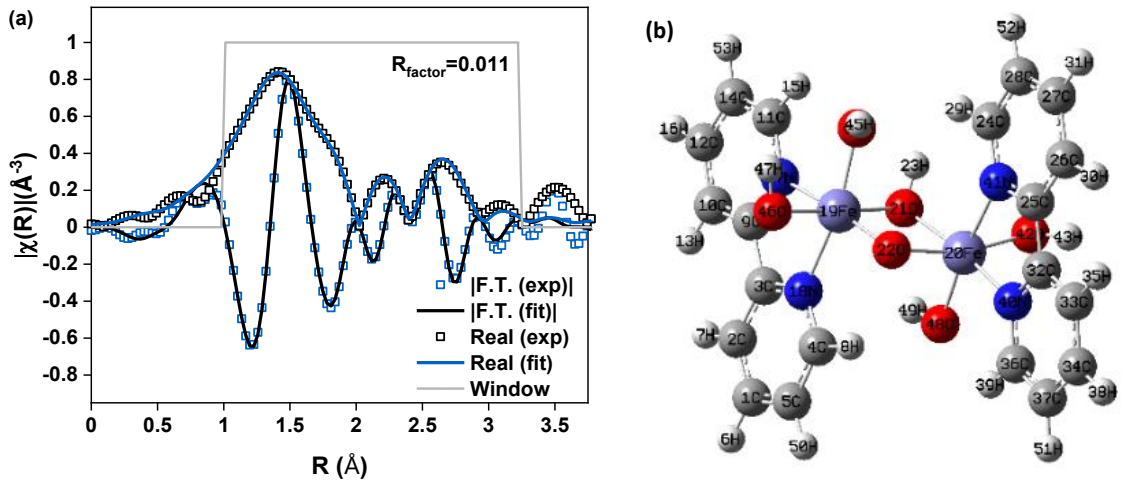


Figure 4.20: (a) EXAFS spectrum and fit of MOF-253(Al)-Fe_2 recovered after catalysis. EXAFS fitting indicates that MOF-253-Fe_2 after catalysis contains ∼90% dimeric $[(bpy)Fe^{III}(\mu_2\text{-}OH)(OH)_2]_2$ species and ∼10% monomeric $(bpy)Fe^{III}(OH)_3$ species. (b) DFT-optimized structure of MOF-253(Al)-Fe_2 after catalysis (INT-4).

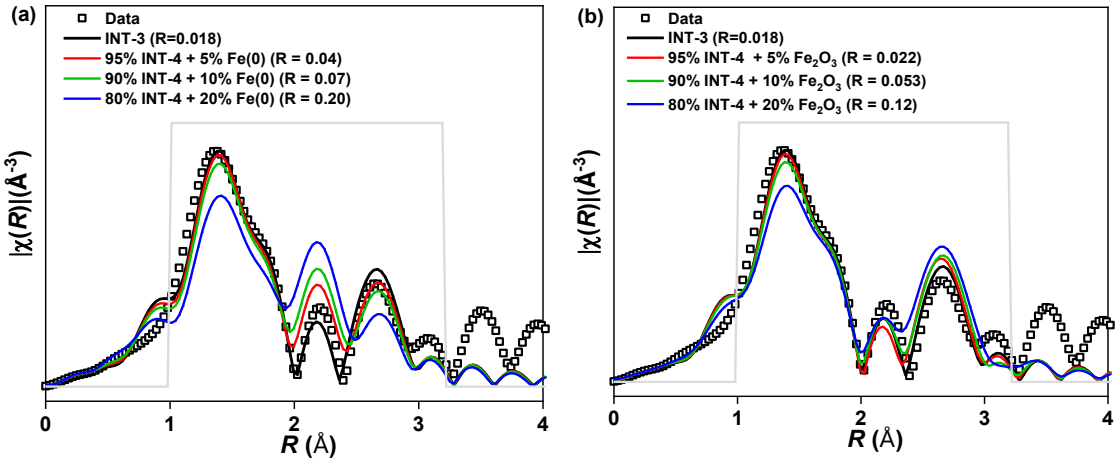


Figure 4.21: (a) EXAFS spectra of MOF-253-Fe_2 recovered after catalysis fitted with combined models of Fe(0) and INT-4. (b) EXAFS spectra of MOF-253-Fe_2 after catalysis fitted with combined models of Fe_2O_3 and INT-4. The significant misfits indicate that MOF-253-Fe_2 recovered after methane oxidation does not contain any Fe nanoparticles or Fe_2O_3.

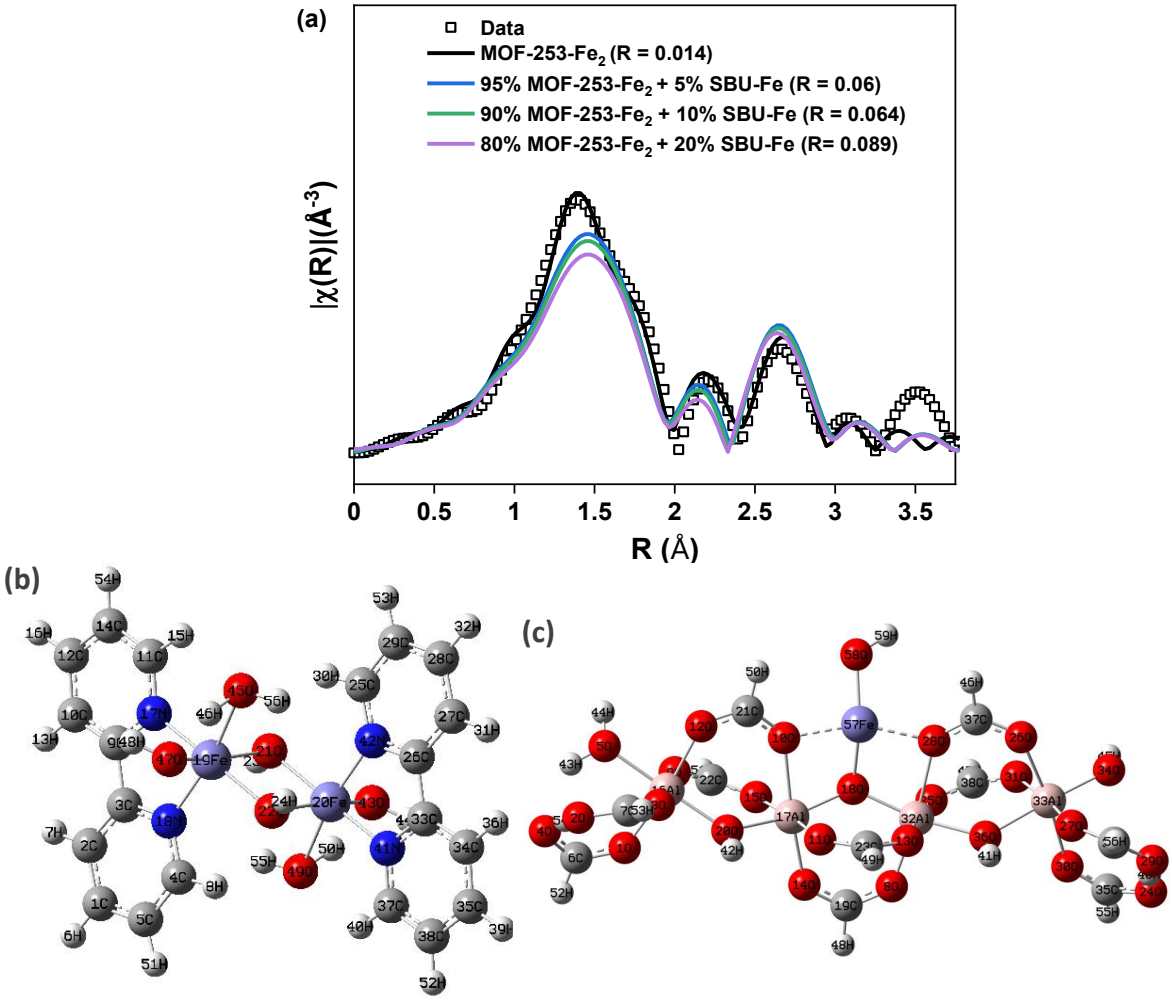


Figure 4.22: (a) EXAFS spectra of MOF-253-Fe_2 fitted with combined models of Fe supported on SBUs and linker of MOF-253-Fe_2. DFT-optimized structure of (b) MOF-253-Fe_2 $[(bpy)Fe^{II}(\mu_2\text{-}OH)(OH)(OH_2)]_2$. (c) $Fe^{II}(OH)$ species on SBU of MOF-253(Al). The significant misfits and higher R values indicate that MOF-253-Fe_2 does not contain any Fe supported on SBU.

XPS analysis.

All the binding energies were corrected with reference to the C1s peak at 284.8 eV. MULTIPAK software was used for peak analysis and de-convolution studies.

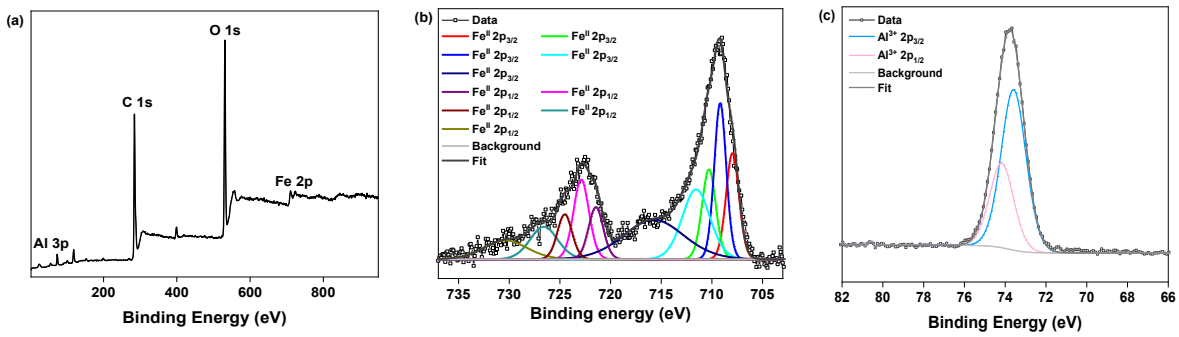


Figure 4.23: (a) Raw XPS data of MOF-253-Fe_2. (b) XPS fitting of Fe in MOF-253-Fe_2. (c) XPS fitting of aluminium in MOF-253-Fe_2.

Table 4.7: XPS fitting parameters for Fe(II) in MOF-253-Fe_2 MOF.

Component	**Position (eV)**	**FWHM (eV)**	**Area%**	**Lineshape**
Fe(II) 2p	708.39	1.5	10.46	GL(30)
Fe(II) 2p	709.54	1.2	16.73	GL(30)
Fe(II) 2p	710.60	1.6	9.44	GL(30)
Fe(II) 2p	711.88	2.7	12.17	GL(30)
Fe(II) 2p	715.67	5.3	18.07	GL(30)
Fe(II) 2p	721.93	1.7	5.80	GL(30)
Fe(II) 2p	722.93	1.8	9.38	GL(30)
Fe(II) 2p	724.73	1.7	5.00	GL(30)
Fe(II) 2p	727.08	2.85	6.82	GL(30)
Fe(II) 2p	730.33	5.00	6.15	GL(30)

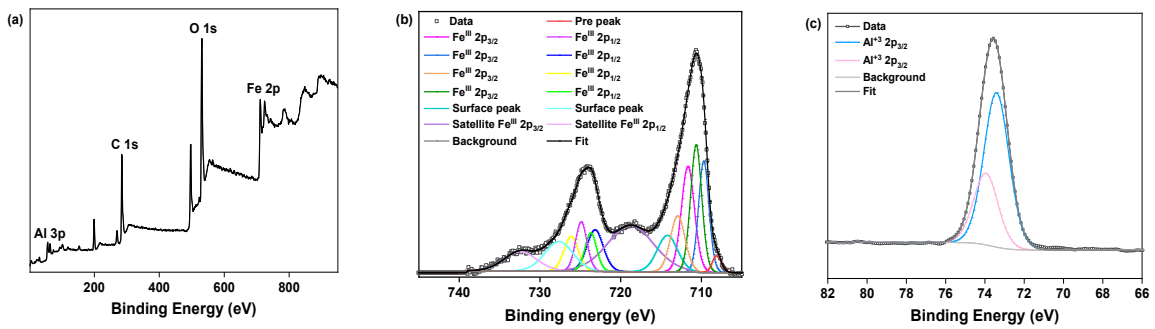


Figure 4.24: (a) Raw XPS data of MOF-253-Fe_2 recovered after catalysis. (b) XPS fitting of Fe in MOF-253-Fe_2 recovered after catalysis. (c) XPS fitting of aluminium in MOF-253-Fe_2 recovered after catalysis.

Table 4.8: XPS fitting parameters for Fe(III) in MOF-253-Fe_2 MOF.

Component	**Position (eV)**	**FWHM (eV)**	**Area%**	**Lineshape**
Fe(III) 2p	708.11	1.3	1.36	GL(30)
Fe(III) 2p	709.71	1.5	10.03	GL(30)
Fe(III) 2p	710.65	1.6	11.42	GL(30)
Fe(III) 2p	711.67	1.6	11.07	GL(30)
Fe(III) 2p	712.95	1.7	7.18	GL(30)
Fe(III) 2p	714.24	2.9	6.47	GL(30)
Fe(III) 2p	718.82	4.3	18.57	GL(30)
Fe(III) 2p	723.20	1.7	5.96	GL(30)
Fe(III) 2p	723.71	1.7	4.91	GL(30)
Fe(III) 2p	724.90	1.6	5.94	GL(30)
Fe(III) 2p	726.16	1.8	4.33	GL(30)
Fe(III) 2p	727.69	2.1	7.28	GL(30)
Fe(III) 2p	732.49	4.3	5.48	GL(30)

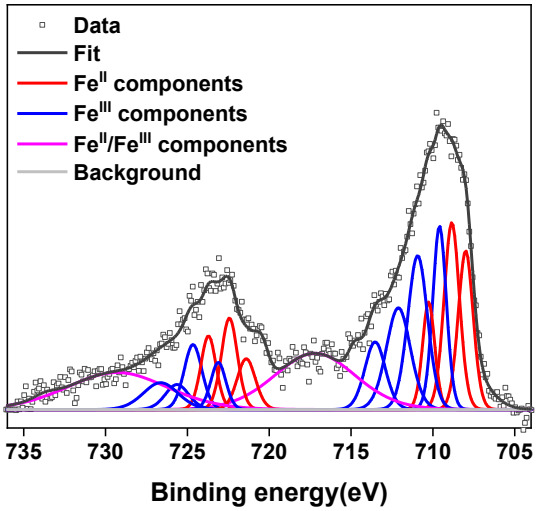


Figure 4.25: XPS analysis of Fe in MOF-253-Fe_2 sampled during the reaction. It reveals the presence of a mixed-valent state, with Fe existing as both Fe^{2+} and Fe^{3+}.

Table 4.9: XPS fitting parameters for Fe(II) and Fe(III) in MOF-253-Fe_2 sampled during the reaction.

Component	**Position (eV)**	**FWHM (eV)**	**Area%**	**Lineshape**
Fe(II) 2p	708.1	1.2	7.40	GL(30)
Fe(II) 2p	709.1	1.2	8.99	GL(30)
Fe(II) 2p	710.2	1.1	5.11	GL(30)
Fe(III) 2p	709.7	1.1	7.78	GL(30)
Fe(III) 2p	711.1	1.4	9.59	GL(30)
Fe(III) 2p	712.2	1.4	7.68	GL(30)
Fe(III) 2p	713.5	1.4	4.36	GL(30)
Fe(III)/Fe(II) 2p	717.8	4.3	14.25	GL(30)
Fe(II) 2p	721.40	1.3	2.91	GL(30)
Fe(II) 2p	722.43	1.2	4.58	GL(30)
Fe(III) 2p	723.71	1.2	3.54	GL(30)
Fe(III) 2p	723.11	1.2	3.22	GL(30)
Fe(III) 2p	724.66	1.3	3.64	GL(30)
Fe(III) 2p	725.64	1.4	2.42	GL(30)
Fe(III) 2p	726.63	1.7	2.95	GL(30)
Fe(III)/Fe(II) 2p	730.26	5.2	11.61	GL(30)

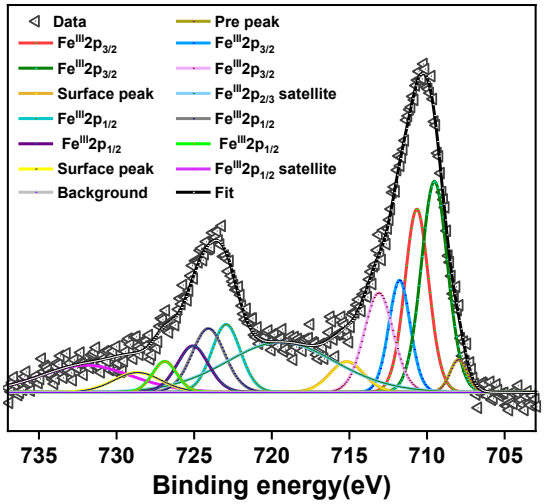


Figure 4.26: XPS fitting of Fe in MOF-253-Fe_2 recovered from the reaction of MOF-253-Fe_2 with O_2. Reaction conditions: MOF-253-Fe_2, 8 bar of O_2, 20 bar N_2, 8 mL water, 160 °C, 38 h.

Table 4.10: XPS fitting parameters for Fe(III) in MOF-253-Fe_2 MOF recovered after reaction with O_2.

Component	**Position (eV)**	**FWHM (eV)**	**Area%**	**Lineshape**
Fe(III) 2p3/2	708.23	2.5	1.75	GL(30)
Fe(III) 2p3/2	709.52	1.6	17.35	GL(30)
Fe(III) 2p3/2	710.65	1.6	13.66	GL(30)
Fe(III) 2p3/2	711.77	1.6	9.08	GL(30)
Fe(III) 2p3/2	713.12	1.7	7.07	GL(30)
Fe(III) 2p3/2	715.17	2.5	3.27	GL(30)
Fe(III) 2p3/2	719.43	6.2	17.35	GL(30)
Fe(III) 2p1/2	722.94	1.8	6.55	GL(30)
Fe(III) 2p1/2	724.09	1.9	6.13	GL(30)
Fe(III) 2p1/2	725.09	1.8	4.55	GL(30)
Fe(III) 2p1/2	726.89	1.8	2.35	GL(30)
Fe(III) 2p1/2	728.67	2.5	2.94	GL(30)
Fe(III) 2p1/2	731.99	4.8	3.27	GL(30)

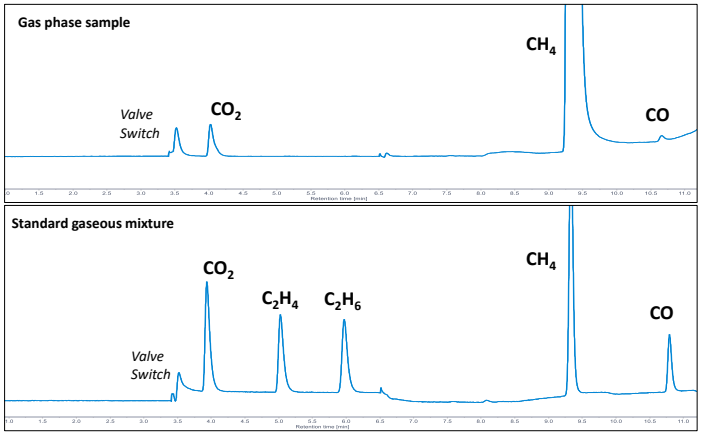


Figure 4.27: GC-FID spectrum of the gas-phase sample collected after MOF-253-Fe_2-catalyzed methane oxidation to acetic acid (top). GC-FID spectrum of a standard gaseous mixture used for peak identification and retention time comparison (bottom). No detectable ethane or other hydrocarbon by-products were observed in the gas-phase sample (top).

Table 4.11: Comparison of catalytic activity of MOF-253-Fe_2 catalysed oxidation of CH_4 to CH_3CO_2H using O_2 with other reported catalysts.

Reference	**Catalyst**	**Oxidant (Flow/-Total pressure)**	**Condition**	**Temp (°C)**	**CH_3CO_2H Selectivity (%)**	**μmol g_{cat}^{-1} h^{-1}**	**mmol mol_{metal}^{-1} h^{-1}**	**mmol mol_{metal}^{-1}**	**μmol g_{cat}^{-1}**
This work	MOF-253-Fe_2	CH_4 (20 bar), O_2 (8 bar)	Batch	160	93	6,159	2,757	1,04,766	2,34,043
Chem. Sci. **16**, 2785–2795 (2025)	MIL-53(Al)-Cu(OH)	CH_4 (30 bar), O_2 (10 bar)	Batch	175	92	12,418	11,767	3,76,559	3,97,376
Nat. Commun. **15**, 9798 (2024)	DUT-5-$Fe(OH)_2$	CH_4 (30 bar), O_2 (8 bar)	Batch	150	79	1,667	1,724	68,965	66,667
ACS Catal. **14**, 1797–1807 (2024)	Au/24h-ZSM5(DR-24)	CH_4 (20.7 bar), O_2 (3.5 bar)	Batch	240	21	–	–	–	12.1
Nat. Commun. **14**, 3047 (2023)	PdO/Pd–WO_3-2	CH_4 + H_2O	Flow/Light	r.t	91.6	–	90.7	–	–
		CH_4 (10 bar) + H_2O	Batch/Light	r.t	60.2	–	62.5	–	–
Appl. Catal. B **337**, 122983 (2023)	Ag/AgCl-WO_3-X	0.1 bar CH_4:N_2 (1:9), 0.1 bar O_2	Light	25	62.7	188.5	–	–	–

Continued on next page

Table 4.11 (continued)

Reference	**Catalyst**	**Oxidant (Flow/- Total pressure)**	**Condition**	**Temp (°C)**	**CH_3CO_2H Selectivity (%)**	**μmol g_{cat}^{-1} h^{-1}**	**mmol mol_{metal}^{-1} h^{-1}**	**mmol mol_{metal}^{-1}**	**μmol g_{cat}^{-1}**
ACS Catal. **13**, 7199–7209 (2023)	Au/ZSM-5+XC72R	CH_4 (20.7 bar), O_2 (3.5 bar)	Batch	240	2.5	–	–	–	31.4
J. Am. Chem. Soc. **145**, 6156–6165 (2023)	Ce-UiO-Cu(OH)	CH_4 (30 bar), O_2 (6 bar)	Batch	115	96	–	–	–	3,24,324
Nat. Catal. **5**, 45–54 (2022)	Au-ZSM-5	CH_4 (20.7 bar), O_2 (3.5 bar)	Batch	240	41	45.48	–	–	3.79

4.4 Conclusion

The selective oxidation of methane into acetic acid presents a significant challenge, requiring careful design and precise control over the structure of the active sites. This study demonstrates that the nature of the Fe active sites, specifically dimeric, plays a crucial role in determining product selectivity. The dimeric $[Fe^{II}(\mu_2\text{-OH})(OH)]_2$ site in MOF-253-Fe_2 gave acetic acid in 100% selectivity in the aqueous phase with a high productivity of 2757 $mmol_{CH_3CO_2H}$ $mol_{Fe}{}^{-1}$ h^{-1} at 160 °C. These findings establish an elegant strategy for directing methane oxidation towards C_2 products selectively by tailoring the nuclearity of the active site. This approach thus offers a rational method for designing chemoselective heterogeneous base-metal catalysts for alkane functionalization. Our proposed catalytic pathways for MOF-253-Fe_2-catalyzed methane oxidation at high temperature and pressure are still speculative and significantly different from those observed in enzymatic and homogeneous systems. While MOF-253 allows for the confinement of the active site within its pores and offers thermal stability, it lacks dynamic control, sacrificial reductants, or cofactors and precisely tuned protein scaffolding of MMO, resulting in a distinct coordination environment and catalytic pathway. Furthermore, the rigid framework of MOF-253 enforces a fixed Fe···Fe distance and a static coordination geometry of the diiron center, which prevents it from replicating the flexibility and unique microenvironment around the diiron center provided by the protein scaffolds in the MMO system. Therefore, further experimental and computational studies are necessary to elucidate the detailed mechanisms of methane functionalization using these MOF systems.

References

[1] Budiman, A. W.; Nam, J. S.; Park, J. H.; Mukti, R. I.; Chang, T. S.; Bae, J. W.; Choi, M. J. Review of Acetic Acid Synthesis from Various Feedstocks Through Different Catalytic Processes. *Catalysis Surveys from Asia* **2016**, *20*, 173–193.

[2] Dummer, N. F.; Willock, D. J.; He, Q.; Howard, M. J.; Lewis, R. J.; Qi, G.; Taylor, S. H.; Xu, J.; Bethell, D.; Kiely, C. J.; Hutchings, G. J. Methane Oxidation to Methanol. *Chemical Reviews* **2023**, *123*, 6359–6411.

[3] Pruett, R. L. Synthesis Gas: A Raw Material for Industrial Chemicals. *Science* **1981**, *211*, 11–16.

[4] Singh, A. D.; Krase, N. W. Synthesis of Acetic Acid from Methanol and Carbon Monoxide. *Industrial & Engineering Chemistry* **1935**, *27*, 909–914.

[5] Knifton, J. F. Syngas Reactions: IX. Acetic Acid from Synthesis Gas. *Journal of Catalysis* **1985**, *96*, 439–453.

[6] Sunley, G. J.; Watson, D. J. High Productivity Methanol Carbonylation Catalysis Using Iridium: The Cativa™ Process for the Manufacture of Acetic Acid. *Catalysis Today* **2000**, *58*, 293–307.

[7] Thomas, C. M.; Süss-Fink, G. Ligand Effects in the Rhodium-Catalyzed Carbonylation of Methanol. *Coordination Chemistry Reviews* **2003**, *243*, 125–142.

[8] Kishore, M. A.; Lee, S.; Yoo, J. S. Fundamental Limitation in Electrochemical Methane Oxidation to Alcohol: A Review and Theoretical Perspective on Overcoming It. *Advanced Science* **2023**, *10*, 2301912.

[9] Xu, W.; Wang, Z.; Huang, C.; Wang, X. Direct Methane Conversion to Acetic Acid: From Homogeneous Catalysis to Heterogeneous Catalysis. *ChemCatChem* **2024**, *16*, e202400692.

[10] Schwarz, H. Chemistry with Methane: Concepts Rather than Recipes. *Angewandte Chemie International Edition* **2011**, *50*, 10096–10115.

[11] Taifan, W.; Baltrusaitis, J. CH4 Conversion to Value Added Products: Potential, Limitations and Extensions of a Single Step Heterogeneous Catalysis. *Applied Catalysis B: Environmental* **2016**, *198*, 525–547.

[12] Tucci, F. J.; Rosenzweig, A. C. Direct Methane Oxidation by Copper- and Iron-Dependent Methane Monooxygenases. *Chemical Reviews* **2024**, *124*, 1288–1320.

[13] Wang, J.-W.; Zhong, D.-C.; Lu, T.-B. Artificial Photosynthesis: Catalytic Water Oxidation and CO2 Reduction by Dinuclear Non-Noble-Metal Molecular Catalysts. *Coordination Chemistry Reviews* **2018**, *377*, 225–236.

[14] Tsurugi, H.; Laskar, P.; Yamamoto, K.; Mashima, K. Bonding and Structural Features of Metal-Metal Bonded Homo- and Hetero-Dinuclear Complexes Supported by Unsaturated Hydrocarbon Ligands. *Journal of Organometallic Chemistry* **2018**, *869*, 251–263.

[15] Meyer, T. J.; Sheridan, M. V.; Sherman, B. D. Mechanisms of Molecular Water Oxidation in Solution and on Oxide Surfaces. *Chemical Society Reviews* **2017**, *46*, 6148–6169.

[16] Mankad, N. P. Selectivity Effects in Bimetallic Catalysis. *Chemistry – A European Journal* **2016**, *22*, 5822–5829.

[17] Cooper, B. G.; Napoline, J. W.; Thomas, C. M. Catalytic Applications of Early/Late Heterobimetallic Complexes. *Catalysis Reviews* **2012**, *54*, 1–40.

[18] Rüttinger, W.; Dismukes, G. C. Synthetic Water-Oxidation Catalysts for Artificial Photosynthetic Water Oxidation. *Chemical Reviews* **1997**, *97*, 1–24.

[19] Hu, Y.; Wang, C.; [1] 100190,[1] Beijing National Laboratory for Molecular Sciences, CAS Key Laboratory of Molecular Recognition and Function, CAS Research/Education Center for Excellence in Molecular Sciences, Institute of Chemistry, Chinese Academy of Sciences, Beijing 100190, P. R. China; [2] 100049,[2] University of Chinese Academy of Sciences, Beijing 100049, P. R. China Bimetallic C—H Activation in Homogeneous Catalysis. *Acta Physico-Chimica Sinica* **2019**, *35*, 913–922.

[20] Osadchii, D. Y.; Olivos-Suarez, A. I.; Szécsényi, ; Li, G.; Nasalevich, M. A.; Dugulan, I. A.; Crespo, P. S.; Hensen, E. J. M.; Veber, S. L.; Fedin, M. V.; Sankar, G.; Pidko, E. A.; Gascon, J. Isolated Fe Sites in Metal Organic Frameworks Catalyze the Direct Conversion of Methane to Methanol. *ACS Catalysis* **2018**, *8*, 5542–5548.

[21] Li, J.; Huang, H.; Xue, W.; Sun, K.; Song, X.; Wu, C.; Nie, L.; Li, Y.; Liu, C.; Pan, Y.; Jiang, H.-L.; Mei, D.; Zhong, C. Self-Adaptive Dual-Metal-Site Pairs in Metal-Organic Frameworks for Selective CO2 Photoreduction to CH4. *Nature Catalysis* **2021**, *4*, 719–729.

[22] Castner, A. T.; Johnson, B. A.; Cohen, S. M.; Ott, S. Mimicking the Electron Transport Chain and Active Site of [FeFe] Hydrogenases in One Metal–Organic Framework: Factors That Influence Charge Transport. *Journal of the American Chemical Society* **2021**, *143*, 7991–7999.

[23] Feng, X.; Song, Y.; Chen, J. S.; Xu, Z.; Dunn, S. J.; Lin, W. Rational Construction of an Artificial Binuclear Copper Monooxygenase in a Metal–Organic Framework. *Journal of the American Chemical Society* **2021**, *143*, 1107–1118.

[24] Wang, Z.; Yeary, P.; Feng, X.; Lin, W. Self-Adaptive Metal–Organic Framework Assembles Di-iron Active Sites to Mimic Monooxygenases. *Journal of the American Chemical Society* **2023**, *145*, 8647–8655.

[25] Kalita, R.; Chauhan, M.; Gupta, P.; Begum, W.; Manna, K. Selective Monoborylation of Methane by a Mono Bipyridyl-Nickel(II) Hydride Catalyst. *Angewandte Chemie* **2025**, *137*, e202413402.

[26] Chauhan, M.; Antil, N.; Rana, B.; Akhtar, N.; Thadhani, C.; Begum, W.; Manna, K. Isoreticular Metal–Organic Frameworks Confined Mononuclear Ru-Hydrides Enable Highly Efficient Shape-Selective Hydrogenolysis of Polyolefins. *JACS Au* **2023**, *3*, 3473–3484.

[27] Kalmutzki, M. J.; Hanikel, N.; Yaghi, O. M. Secondary Building Units as the Turning Point in the Development of the Reticular Chemistry of MOFs. *Science Advances* **2018**, *4*, eaat9180.

[28] Sahoo, R.; Mondal, S.; Chand, S.; Das, M. C. Highly Robust Metal–Organic Framework for Efficiently Catalyzing Knoevenagel Condensation and the Strecker Reaction under Solvent-Free Conditions. *Inorganic Chemistry* **2023**, *62*, 12989–13000.

[29] Lan, G.; Fan, Y.; Shi, W.; You, E.; Veroneau, S. S.; Lin, W. Biomimetic Active Sites on Monolayered Metal–Organic Frameworks for Artificial Photosynthesis. *Nature Catalysis* **2022**, *5*, 1006–1018.

[30] Gupta, P.; Rana, B.; Maurya, R.; Kalita, R.; Chauhan, M.; Manna, K. Copper Catalyzed Selective Methane Oxidation to Acetic Acid Using O2. *Chemical Science* **2025**, *16*, 2785–2795.

[31] Antil, N.; Kumar, A.; Akhtar, N.; Begum, W.; Chauhan, M.; Newar, R.; Rawat, M. S.; Manna, K. Chemoselective and Tandem Reduction of Arenes Using a Metal–Organic Framework-Supported Single-Site Cobalt Catalyst. *Inorganic Chemistry* **2022**, *61*, 1031–1040.

[32] Bloch, E. D.; Britt, D.; Lee, C.; Doonan, C. J.; Uribe-Romo, F. J.; Furukawa, H.; Long, J. R.; Yaghi, O. M. Metal Insertion in a Microporous MetalOrganic Framework Lined with 2,2-Bipyridine. *Journal of the American Chemical Society* **2010**, *132*, 14382–14384.

[33] Grosvenor, A. P.; Kobe, B. A.; Biesinger, M. C.; McIntyre, N. S. Investigation of Multiplet Splitting of Fe 2p XPS Spectra and Bonding in Iron Compounds. *Surface and Interface Analysis* **2004**, *36*, 1564–1574.

[34] Zhang, P.; Ma, S.; Zhang, Y.; He, C.; Hu, T. Enhancing CO 2 /N 2 and CH 4 /N 2 Separation Performance by Salt-Modified Aluminum-Based Metal–Organic Frameworks. *Dalton Transactions* **2024**, *53*, 2957–2963.

[35] Khrizanforov, M.; Strekalova, S.; Khrizanforova, V.; Grinenko, V.; Kholin, K.; Kadirov, M.; Burganov, T.; Gubaidullin, A.; Gryaznova, T.; Sinyashin, O.; Xu, L.; Vicic, D. A.; Budnikova, Y. Iron-Catalyzed Electrochemical C–H Perfluoroalkylation of Arenes. *Dalton Transactions* **2015**, *44*, 19674–19681.

[36] Chauhan, M.; Rana, B.; Gupta, P.; Kalita, R.; Thadhani, C.; Manna, K. Tailored Pore-Confined Single-Site Iron(III) Catalyst for Selective CH4 Oxidation to CH3OH or CH3CO2H Using O2. *Nature Communications* **2024**, *15*, 9798.

[37] Manna, K.; Zhang, T.; Carboni, M.; Abney, C. W.; Lin, W. Salicylaldimine-Based Metal–Organic Framework Enabling Highly Active Olefin Hydrogenation with Iron and Cobalt Catalysts. *Journal of the American Chemical Society* **2014**, *136*, 13182–13185.

[38] Gupta, P.; Akhtar, N.; Begum, W.; Rana, B.; Kalita, R.; Chauhan, M.; Thadhani, C.; Manna, K. Metal–Organic Framework-Supported Mono Bipyridyl–Iron Hydroxyl Catalyst for Selective Benzene Hydroxylation into Phenol. *Inorganic Chemistry* **2024**, *63*, 11907–11916.

[39] Zhang, S.; Karthikeyan, R.; Fernando, S. D. Low-Temperature Biological Activation of Methane: Structure, Function and Molecular Interactions of Soluble and Particulate Methane Monooxygenases. *Reviews in Environmental Science and Bio/Technology* **2017**, *16*, 611–623.

[40] Hadjiivanov, K. I.; Panayotov, D. A.; Mihaylov, M. Y.; Ivanova, E. Z.; Chakarova, K. K.; Andonova, S. M.; Drenchev, N. L. Power of Infrared and Raman Spectroscopies to Characterize Metal-Organic Frameworks and Investigate Their Interaction with Guest Molecules. *Chemical Reviews* **2021**, *121*, 1286–1424.

[41] Wang, L.; Li, B.; Dionysiou, D. D.; Chen, B.; Yang, J.; Li, J. Overlooked Formation of H2O2 during the Hydroxyl Radical-Scavenging Process When Using Alcohols as Scavengers. *Environmental Science & Technology* **2022**, *56*, 3386–3396.

[42] Hu, D.; Addad, A.; Ben Tayeb, K.; Ordomsky, V. V.; Khodakov, A. Y. Thermocatalysis Enables Photocatalytic Oxidation of Methane to Formic Acid at Room Temperature beyond the Selectivity Limits. *Cell Reports Physical Science* **2023**, *4*, 101277.

[43] Li, L.; Hao, C.; Zhai, R.; He, W.; Deng, C. Study on the Mechanism of Free Radical Scavenger TEMPO Blocking in Coal Oxidation Chain Reaction. *Fuel* **2023**, *331*, 125853.

[44] Ab Rahim, M. H.; Forde, M. M.; Jenkins, R. L.; Hammond, C.; He, Q.; Dimitratos, N.; Lopez-Sanchez, J. A.; Carley, A. F.; Taylor, S. H.; Willock, D. J.; Murphy, D. M.; Kiely, C. J.; Hutchings, G. J. Oxidation of Methane to Methanol with Hydrogen Peroxide Using Supported Gold–Palladium Alloy Nanoparticles. *Angewandte Chemie International Edition* **2013**, *52*, 1280–1284.

[45] Bonini, M. G.; Miyamoto, S.; Mascio, P. D.; Augusto, O. Production of the Carbonate Radical Anion during Xanthine Oxidase Turnover in the Presence of Bicarbonate. *Journal of Biological Chemistry* **2004**, *279*, 51836–51843.

[46] Li, H.; Zhao, N.; He, C.; Shi, C.; Du, X.; Li, J. Catalytic Synthesis of Carbon Nanostructures Using Fe(OH)3/Al as Catalyst Precursors. *Journal of Alloys and Compounds* **2009**, *468*, 64–68.

[47] Yang, Q.; Zhang, H.-Y.; Wang, L.; Zhang, Y.; Zhao, J. Ru/UiO-66 Catalyst for the Reduction of Nitroarenes and Tandem Reaction of Alcohol Oxidation/Knoevenagel Condensation. *ACS Omega* **2018**,

[48] Ma, X.; He, D.; Jones, A. M.; Collins, R. N.; Waite, T. D. Reductive Reactivity of Borohydride- and Dithionite-Synthesized Iron-Based Nanoparticles: A Comparative Study. *Journal of Hazardous Materials* **2016**, *303*, 101–110.

[49] Zhang, T.; Manna, K.; Lin, W. Metal–Organic Frameworks Stabilize Solution-Inaccessible Cobalt Catalysts for Highly Efficient Broad-Scope Organic Transformations. *Journal of the American Chemical Society* **2016**, *138*, 3241–3249.

[50] Chirik, P. J. Iron- and Cobalt-Catalyzed Alkene Hydrogenation: Catalysis with Both Redox-Active and Strong Field Ligands. *Accounts of Chemical Research* **2015**, *48*, 1687–1695.

[51] Matsubara, Y.; Yamaguchi, T.; Hashimoto, T.; Yamaguchi, Y. Iron(II) Bipyridine Complexes for the Cross-Coupling Reaction of Bromocyclohexane with Phenylmagnesium Bromide. *Polyhedron* **2017**, *128*, 198–202.

[52] Staples, O.; Ferrandon, M. S.; Laurent, G. P.; Kanbur, U.; Kropf, A. J.; Gau, M. R.; Carroll, P. J.; McCullough, K.; Sorsche, D.; Perras, F. A.; Delferro, M.; Kaphan, D. M.; Mindiola, D. J. Silica Supported Organometallic IrI Complexes Enable Efficient Catalytic Methane Borylation. *Journal of the American Chemical Society* **2023**, *145*, 7992–8000.

[53] Sato, H.; Tominaga, T. Mössbauer Studies of the Thermal Decomposition of Tris(2,2-Bipyridine)Iron(II) Chloride and the Structures of the Isomers of 2,2-Bipyridineiron(II) Chloride. *Bulletin of the Chemical Society of Japan* **1976**, *49*, 697–700.

[54] Zhao, Y.; Zhang, S.; Wang, M.; Han, J.; Wang, H.; Li, Z.; Liu, X. Engineering Iridium-Based Metal Organic Frameworks towards Electrocatalytic Water Oxidation. *Dalton Transactions* **2018**, *47*, 4646–4652.

[55] Citation | Gaussian.Com. https://gaussian.com/citation/.

[56] Lee, C.; Yang, W.; Parr, R. G. Development of the Colle-Salvetti Correlation-Energy Formula into a Functional of the Electron Density. *Physical Review B* **1988-01-15**, *37*, 785–789.

[57] Becke, A. D. Density-functional Thermochemistry. III. The Role of Exact Exchange. *The Journal of Chemical Physics* **1993-04-01**, *98*, 5648–5652.

[58] Weigend, F.; Ahlrichs, R. Balanced Basis Sets of Split Valence, Triple Zeta Valence and Quadruple Zeta Valence Quality for H to Rn: Design and Assessment of Accuracy. *Physical Chemistry Chemical Physics* **2005-08-30**, *7*, 3297–3305.

[59] Grimme, S. Semiempirical GGA-type density functional constructed with a long-range dispersion correction. *Journal of Computational Chemistry* **2006**, *27*, 1787–1799.

[60] Poswal, A.; Agrawal, A.; Yadav, A.; Nayak, C.; Basu, S.; Kane, S.; Garg, C.; Bhattachryya, D.; Jha, S.; Sahoo, N. Commissioning and first results of scanning type EXAFS beamline (BL-09) at INDUS-2 synchrotron source. AIP Conference Proceedings. 2014; pp 649–651.

[61] Ravel, B.; Newville, M. ATHENA, ARTEMIS, HEPHAESTUS: data analysis for X-ray absorption spectroscopy using IFEFFIT. *Journal of synchrotron radiation* **2005**, *12*, 537–541.

Chapter 5

Mononuclear Iron(II)-Hydroxyl Active Sites for Selective Methane Oxidation to Methanol Using O_2

Title of Paper: " Engineering Mono- Vs Dinuclear Iron(II)-Active Sites to Steer Liquid Oxygenate Selectivity in Methane Oxidation Pathways using O_2"

Citation: Journal of the American Chemical Society, **2025**, *147* (29), 25372-25384. (doi.org/10.1021/jacs.5c04682)

Author: Poorvi Gupta, Manav Chauhan, Bharti Rana, Rahul Kalita, Rishabh Maurya, and Kuntal Manna*

Abstract

Direct oxidation of methane to methanol using O_2 under mild conditions is highly desirable yet challenging due to methane's chemical inertness and the tendency of methanol to overoxidize. This chapter presents a mononuclear bipyridyl Fe(II)-hydroxyl catalyst supported on MOF-253(Al), designated as MOF-253-Fe, containing a (bpy)$Fe^{II}(OH)_2$ active site. The catalyst achieves a methanol productivity of 6,060 $mmol_{CH_3OH}$ mol_{Fe}^{-1} h^{-1} with 96% selectivity in the aqueous phase at 95 °C. Spectroscopic investigations suggest that the isolated Fe(II)-OH centers promote selective C-H hydroxylation through a radical-mediated pathway, efficiently activating O_2 and methane without further oxidation of methanol. In contrast to the dinuclear analogue, MOF-253-Fe operates via single-site redox chemistry, emphasizing the importance of active site nuclearity in dictating product selectivity. This work provides mechanistic insight into the design of MOF-supported Fe catalysts for selective methane-to-methanol conversion.

5.1 Introduction

Building upon the insights gained from dinuclear Fe(II) systems that facilitate C–C coupling to form acetic acid, the subsequent focus shifts toward steering the oxidation pathway to achieve methane hydroxylation. In this context, mononuclear Fe-based active sites offer a distinct reaction environment compared to their binuclear counterparts. The isolated Fe centers can potentially promote site-confined activation of O_2 and CH_4, allowing controlled C–H bond functionalization while minimizing undesired overoxidation. This approach provides an opportunity to understand how the nuclearity of Fe sites influences oxygen activation, reaction selectivity, and product distribution in methane oxidation.

Selective methane-to-methanol conversion remains a key goal in both academic and industrial catalysis due to the direct utility of methanol as a fuel and chemical feedstock. Traditional gas-phase oxidation routes suffer from poor selectivity and high energy requirements.[1–4] In recent years, MOF-supported transition-metal catalysts have emerged as promising candidates owing to their uniform site distribution and the ability to mimic enzyme-like environments within porous frameworks.[5–9]

In this chapter, we report a mononuclear Fe(II)-hydroxyl catalyst, (bpy)$Fe^{II}(OH)_2$, immobilized in MOF-253(Al), which exhibits remarkably high methanol productivity and selectivity under mild aqueous conditions (Figure 5.1). Spectroscopic studies suggest that the reaction proceeds via a

radical-mediated C-H activation pathway, where the Fe-OH species promotes partial oxidation of methane to methanol without further oxidation to CO_2. Comparison with the dinuclear analogue highlights how site isolation and single-site redox chemistry govern product selectivity. This work provides key insights into the role of metal nuclearity in determining methane oxidation pathways within MOF-based catalytic systems.

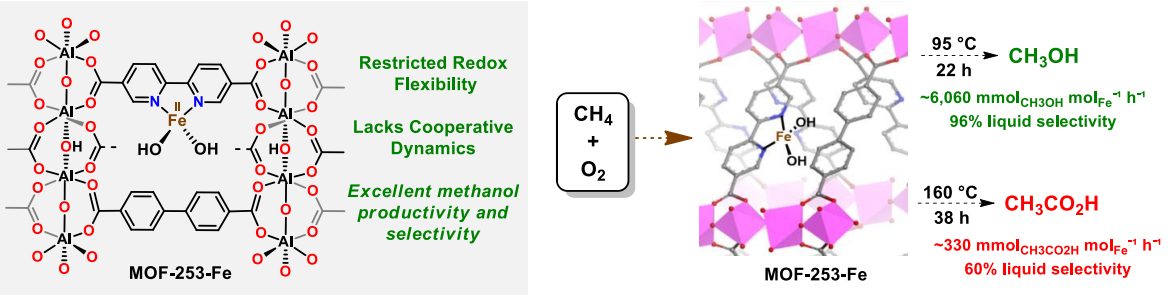


Figure 5.1: Proposed mononuclear MOF-253(Al)-Fe Catalyst for Methane Oxidation.

5.2 Results and Discussion

5.2.1 Synthesis and Characterization of MOF-253-Fe.

MOF-253-Fe was synthesized through post-synthetic metalation of the mixed-MOF-253(Al), containing bipyridyl and biphenyl linkers in a 1:9 ratio (Figure 5.2a).[10] ICP-OES analysis of the digested MOF-253-Fe revealed that all bipyridine moieties are coordinated by Fe^{2+}. We further characterized MOF-253-Fe using PXRD (Figure 5.2b), XPS (Figure 5.2c), and X-ray absorption spectroscopy (Figure 5.2d). XPS and XANES analysis (Figure 5.8) of MOF-253-Fe confirmed the presence of Fe^{2+} species. EXAFS analysis of MOF-253-Fe suggested the existence of a mononuclear tetrahedral (bpy)$Fe^{II}(OH)_2$ species, featuring two Fe-N_{bpy} bonds at 2.07 Å and two terminal hydroxyl groups at 1.89 Å (Figure 5.2d).

In the raw phase uncorrected k^2-weighted Fe-EXAFS $\chi(R)$ spectra, the signal intensity of MOF-253-Fe at 2.6 Å is visibly diminished in comparison to that of MOF-253-Fe_2, likely due to the absence of Fe-Fe scattering in MOF-253-Fe (Figure 5.2d). To further confirm the absence of dinuclear species in MOF-253-Fe, we fitted the EXAFS data at the Fe K-edge with varying percentages (5–20%) of a DFT-optimized model of $[(bpy)Fe^{II}(\mu_2\text{-}OH)(OH)(OH_2)]_2$; inclusion of even 5% dimer showed significant misfits and higher R-values (Figure 5.9).

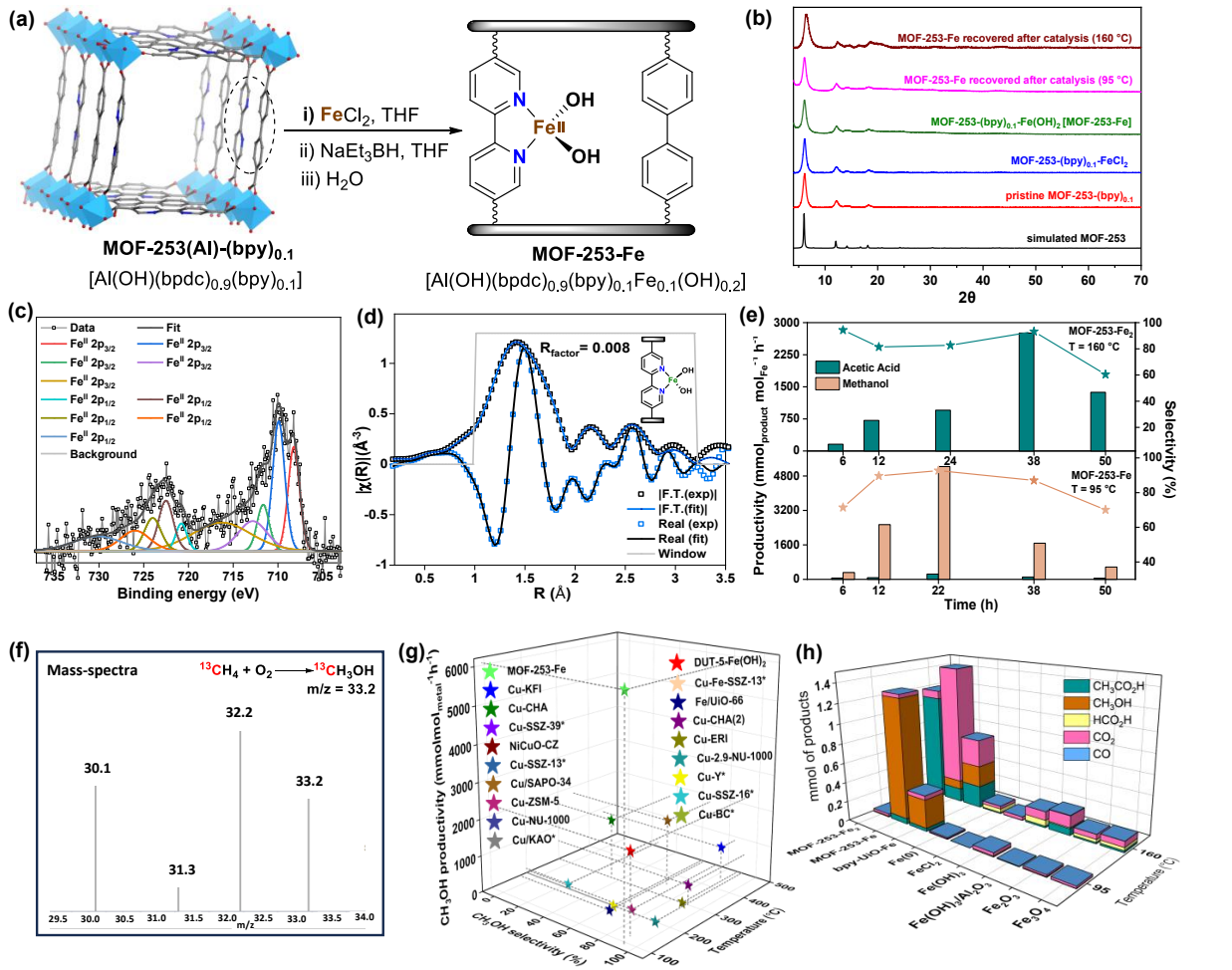


Figure 5.2: (a) Synthesis of MOF-253-Fe. (b) PXRD patterns of simulated MOF-253(Al) (black), MOF-253(Al)-$(bpy)_{0.1}$ (red), MOF-253-$(bpy)_{0.1}$-$FeCl_2$ (blue), MOF-253-Fe (green), and MOF-253-Fe recovered after catalysis (magenta). (c) Fe 2p XPS spectra of MOF-253-Fe. (d) EXAFS spectra (blue and black hollow squares) and fits (black and blue solid lines) of MOF-253-Fe in the R space at the Fe K-edge. The fitting range in the R space is 1.0–3.25 Å. (e) Comparison of catalytic activities between MOF-253-Fe_2 (10.5 μmol Fe) and MOF-253-Fe (10.5 μmol Fe) in the oxidation of methane to acetic acid and methanol at 160 °C and 95 °C, respectively. (f) GC-MS spectrum of the reaction mixture obtained after $^{13}CH_4$ oxidation. Reaction conditions: MOF-253-Fe (20.8 mg, 5.25 μmol Fe), 20 bar $^{13}CH_4$, 8 bar O_2, 22 h, and 95 °C. (g) Evaluation of the catalytic performance of MOF-253-Fe in the oxidation of CH_4 to CH_3OH using O_2, compared to previously documented base-metal catalysts. Reports marked with an asterisk do not specify selectivity. (h) Comparison of catalytic activity for the oxidation of CH_4 over MOF-253-Fe_2 and MOF-253-Fe with other catalysts at 95 °C (22 h) and 160 °C (38 h) under identical reaction conditions. Reaction conditions: catalyst (10.5 μmol Fe), CH_4 (20 bar), O_2 (8 bar), 8 mL water.

FT-IR spectra of MOF-253-Fe_2 showed both terminal OH (3620 cm^{-1}) and bridging OH (3428 cm^{-1}) peaks, while MOF-253-Fe only exhibited the terminal OH peak, further indicating the mononuclear nature of the Fe species in MOF-253-Fe (Figure 5.6).

5.2.2 Catalytic Methane Oxidation using MOF-253-Fe.

MOF-253-Fe (5.25 μmol Fe) gave a significant amount of methanol when a mixture of 20 bar CH_4 and 8 bar O_2 was heated at a low temperature ranging from 80–110 °C (entries 1–2, 6, Table 5.1).

We observed that the methane oxidation reaction with mononuclear MOF-253-Fe catalyst (20.8 mg, 5.25 μmol Fe) at 95 °C for 22 h yielded 0.7 mmol of methanol and 0.03 mmol of acetic acid (Figure 4e and Entry 1, Table 5.1). This corresponds to a methanol selectivity of 96% in the liquid phase with an exceptionally high productivity of 6,060 $mmol_{CH_3OH}$ mol_{Fe}^{-1} h^{-1}, the highest recorded among all base-metal catalysts reported to date (Figure 5.2g and Table 5.6). The formation of CH_3OH at 95 °C was also confirmed using isotopically labelled $^{13}CH_4$, which revealed the formation of only $^{13}CH_3OH$ as analyzed by GC-MS (Figure 5.2f).

The PXRD pattern of MOF-253-Fe recovered after methane oxidation showed the retention of its crystallinity and structure during catalysis (Figure 5.2b). Importantly, the MOF-253-Fe catalyst demonstrated excellent reusability, maintaining its catalytic activity over at least five consecutive cycles without any decline in productivity.

To confirm whether the mononuclear (bpy)$Fe^{II}(OH)_2$ species in MOF-253-Fe is primarily responsible for methanol production at 95 °C, we compared the reaction with bpy-UiO-$Fe^{II}(OH)_2$, which contains only mononuclear (bpy)$Fe^{II}(OH)_2$ moieties due to its non-parallel bipyridyl linkers and octahedral geometry.[11] The comparable methanol selectivity observed for bpy-UiO-Fe (80%) under identical reaction conditions further supports that the mononuclear Fe active sites in MOF-253-Fe are responsible for its high methanol selectivity (Figure 5.2h).

In contrast, the dinuclear MOF-253-Fe_2 exhibited significantly lower methanol selectivity (24%) at 95 °C (Table 5.2). This poor selectivity can be attributed to the fact that methanol is primarily formed by the mononuclear (bpy)$Fe^{II}(OH)_2$ site. While MOF-253-Fe_2 mostly contains dinuclear Fe species, some mononuclear Fe sites are still present, mostly at the surface of the MOF particles, contributing to the observed minimal quantity of methanol at 95 °C.

5.2.3 Proposed Mechanism of MOF-253-Fe Catalyzed Methane Oxidation to Methanol.

Methane oxidation at 95 °C using MOF-253(Al), MOF-253-Fe_2, or with Fe(0), and various Fe oxides (Fe_2O_3,Fe_3O_4, $Fe(OH)_3$, $Fe(OH)_3/Al_2O_3$) yielded negligible methanol (<0.04 mmol), underscoring the critical role of mononuclear Fe-hydroxyl active species embedded within the MOF framework (Figure 5.2h). The EPR spectrum of the DMPO-loaded reaction mixture at 95 °C showed signals for $\cdot CH_3$ and ·OH (Figure 5.3). Radical scavenging experiments using Na_2SO_3 and TEMPO further substantiated the involvement of both $\cdot CH_3$ and ·OH radicals in MOF-253-Fe catalyzed methanol production (Entry 4–5, Table 5.1).

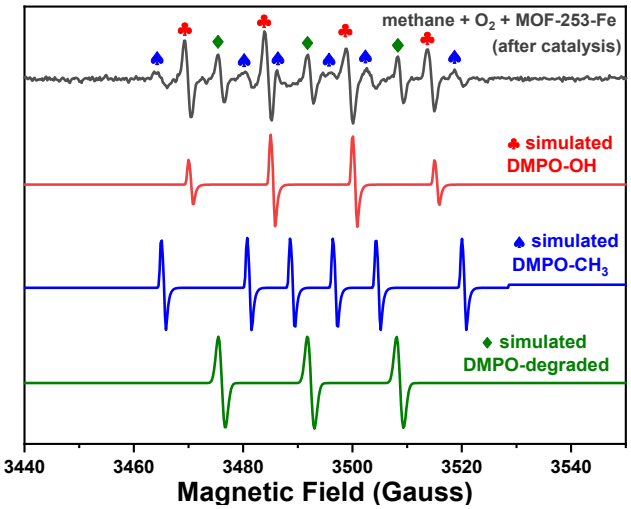


Figure 5.3: X-band (9.85 GHz) EPR spectroscopic spin-trapping experiments. EPR spectrum from DMPO spin-trapping experiment of MOF-253-Fe catalyzed methane oxidation by O_2 at 95 °C for 22 h (black), simulated DMPO–OH (red), simulated DMPO–CH_3 (blue), simulated DMPO–degraded during the reaction (green). Optimized reaction conditions: MOF-253-Fe (20.85 mg, 5.25 µmol Fe), 20 bar CH_4, 8 bar O_2, 95 °C, 8 mL water, and 22 h.

Based on these findings, we propose that the reaction between the Fe(II) site of MOF-253-Fe and O_2 may form a reactive Fe(III)-superoxo or Fe(IV)-peroxo species that initiates C–H activation of methane to generate INT-1 and a $\cdot CH_3$ radical (Figure 5.4).[12;13] Subsequently, INT-1 may undergo O–O bond cleavage to release a ·OH radical, resulting in the formation of an Fe(IV)=O species (INT-2).[14;15] The free ·OH combines with $\cdot CH_3$ to produce a molecule of CH_3OH. Besides, the Fe(IV)=O species in INT-2 then facilitates hydrogen atom transfer from a second methane molecule, generating another $\cdot CH_3$ and forming an Fe(III)-OH intermediate (INT-3).[16;17] The $\cdot CH_3$ then recombines with Fe–OH of INT-3 to form INT-4. Finally, the release of another methanol molecule regenerates MOF-253-Fe and completes the catalytic cycle (Figure 5.4).

Notably, water-assisted O–O bond cleavage of Fe^{III}–OOH species in INT-1 may also form a high-valent $Fe^{V}(O)(OH)$ species,[16] which could facilitate methane activation. However, controlled experiments involving MOF-253-Fe-catalyzed methane oxidation in water or a water–acetonitrile mixture at 95 °C, in the presence of an alkene such as cyclohexene or styrene, did not yield any vicinal diol products (Section 5.3.2), which suggests that the $Fe^{V}(O)(OH)$-mediated oxidation of methane is unlikely.[16;17] Future investigations are necessary to explore the O_2 activation process and to understand the species involved in the abstraction of hydrogen during the conversion of MOF-253-Fe to INT-1.

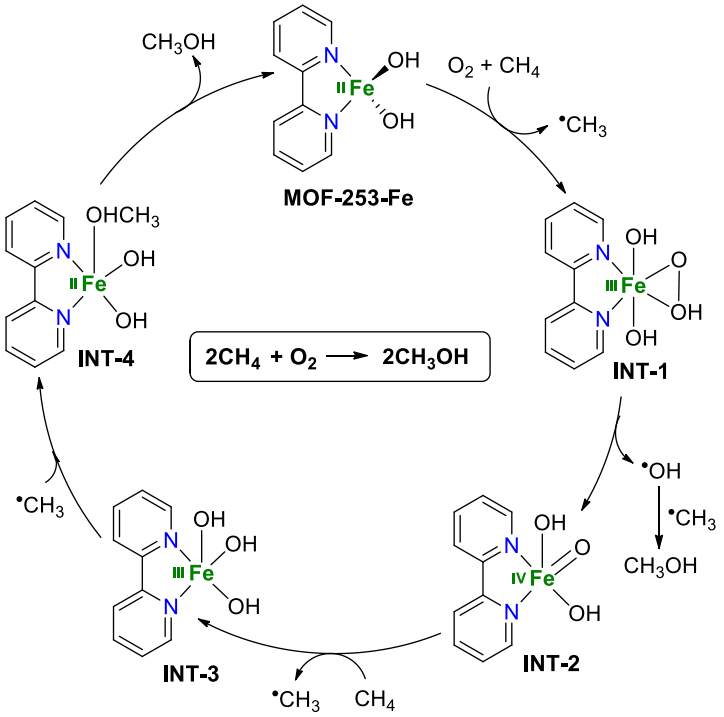


Figure 5.4: Proposed catalytic cycle of MOF-253-Fe-catalyzed selective methane oxidation to methanol using O_2.

Mechanistic divergence between mono- and dinuclear Fe sites.

The distinct methane oxidation pathways leading to methanol or acetic acid originate from the contrasting reactivity of mononuclear and dinuclear bipyridyl Fe(II) hydroxyl species confined within the MOF-253(Al) framework. The single-site nature of these Fe catalysts is crucial, as indicated by the lack of methanol or acetic acid production when using bulk Fe oxides or Fe nanoparticles (Figure 5.2h). At low temperature (∼95 °C), methanol formation is highly favored with the MOF-253-Fe containing mononuclear (bpy)$Fe^{II}(OH)_2$ catalyst. In contrast, the dinuclear Fe catalyst (MOF-253-Fe_2) benefits from synergistic effects that facilitate multi-electron transfer processes, which are likely essential for acetic acid production at 160 °C.

5.3 Experimental Section

5.3.1 Synthesis and Characterization of MOF-253(Al) and MOF-253-Fe.

Synthesis of MOF-253-Fe [$Al(OH)(bpdc)_{0.9}(bpy)_{0.1}$-$Fe(OH)_2$].

Similar to the synthesis of MOF-253(Al), 2,2-bipyridine-5,5-dicarboxylic acid (H_2bpydc, 2.6 mg, 0.0106 mmol, 0.1 eq.), biphenyl-4,4-dicarboxylic acid (H_2bpdc, 23.1 mg, 0.0954 mmol, 0.9 eq.), and $AlCl_3$ (26 mg, 0.11 mmol, 1 eq.) were added into 3 mL of *N,N*-dimethylformamide (DMF) and stirred for 30 minutes. The solution was then transferred into a Teflon-lined stainless-steel autoclave and heated at 120 °C for 24 h. After cooling to room temperature, the resulting white solid was collected by centrifugation and washed several times with DMF. Finally, the obtained white crystalline solid of MOF-253(Al)-$(bpy)_{0.1}$ was washed and stored in THF.

The PXRD pattern of MOF-253(Al)-$(bpy)_{0.1}$ was found to be identical to that of MOF-253(Al) (Figure 5.2b). To determine its chemical composition, 1 mg of MOF-253(Al)-$(bpy)_{0.1}$ was digested in 60 μL of D_3PO_4 and sonicated for 15 minutes. Subsequently, 600 μL of DMSO-d_6 and 60 μL of D_2O were added, and the mixture was analyzed using ^{1}H NMR spectroscopy (Figure 5.5). The bpydc to bpdc ratio was determined to be 1:9, corresponding to the formula $Al(OH)(bpdc)_{0.9}(bpydc)_{0.1}$.

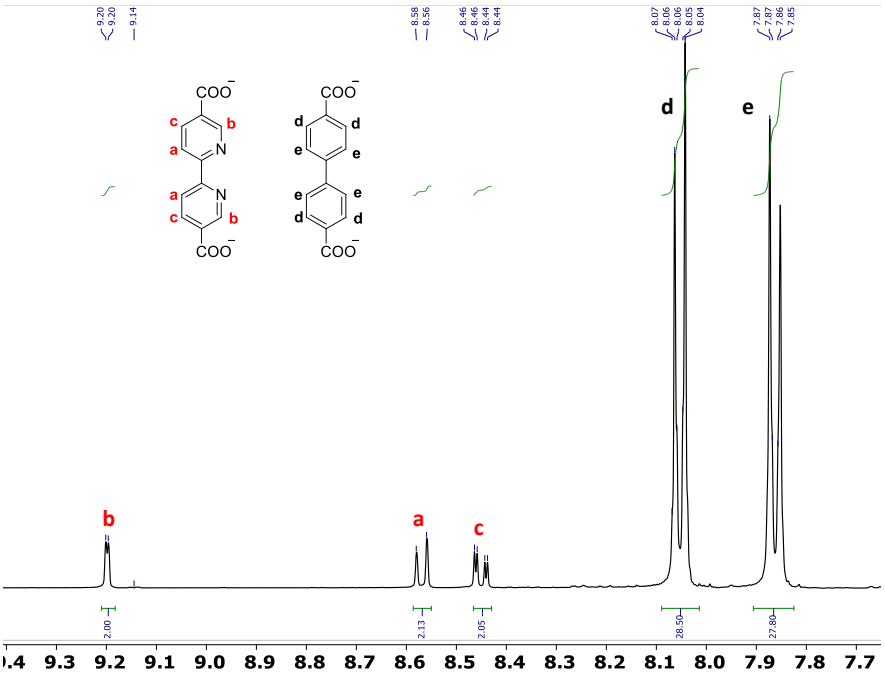


Figure 5.5: ^{1}H NMR (400 MHz, DMSO-d_6) spectrum of digested MOF-253(Al)-$(bpy)_{0.1}$.

Using the same post-synthetic modification for MOF-253(Al), MOF-253(Al)-$(bpy)_{0.1}$ was metalated to form the mononuclear Fe catalyst. ICP-OES showed a 98% Fe-loading with respect to bpy moiety for MOF-253-Fe.

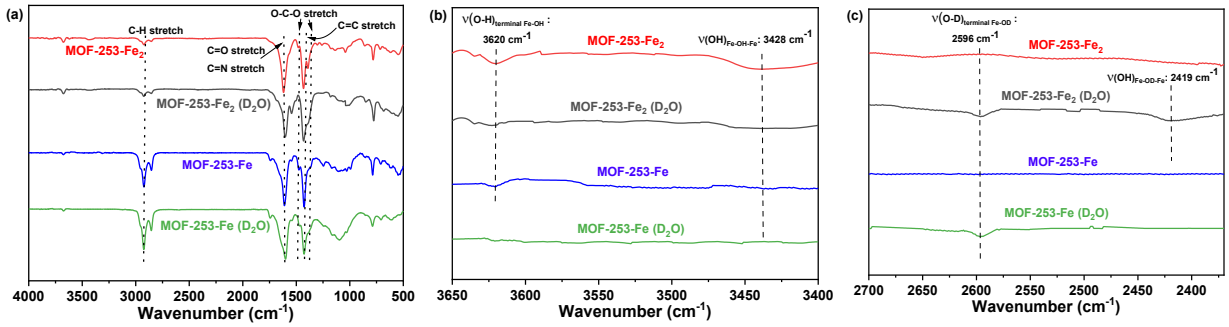


Figure 5.6: FT-IR spectra of MOF-253-Fe_2 (red), MOF-253-Fe_2 prepared in D_2O (black), MOF-253-Fe (blue), and MOF-253-Fe prepared in D_2O (green) in the wavenumber range of (a) 4000-500 cm^{-1}, (b) 3650-3400 cm^{-1}, and (c) 2700-2420 cm^{-1}. The peak at 3620 cm^{-1} in MOF-253-Fe_2 and MOF-253-Fe shifted to 2596 cm^{-1} in MOF-253-Fe_2(D_2O) and MOF-253-Fe(D_2O), corresponding to the stretching vibration of terminal Fe-OH. The peak at 3428 cm^{-1} in MOF-253-Fe_2 (absent in MOF-253-Fe) shifted to 2419 cm^{-1} in MOF-253-Fe_2(D_2O), representing the stretching mode of bridging μ_2-$(OH)_{Fe\text{-}OH\text{-}Fe}$.[4] Notably, the absence of a peak at 3428 cm^{-1} in MOF-253-Fe confirms the absence of dinuclear Fe species, indicating that Fe is present solely in monomeric form.

5.3.2 Mononuclear MOF-253-Fe catalyzed methane oxidation.

General procedure mentioned in Section 4.3.2 was followed, using MOF-253-Fe (5.25 μmol of Fe). Reaction conditions: MOF-253-Fe (20.85 mg, 5.25 μmol of Fe), 8 mL water, 20 bar CH_4, 8 bar O_2, 95 °C, 22 h. The methane oxidation reaction with the mononuclear catalyst MOF-253-Fe gave 0.7 mmol of methanol and 0.03 mmol of acetic acid (Entry 1, Table 5.1). Methane conversion of 2% and productivity of methanol 6,060 $mmol_{CH_3OH}$ $mol_{Fe}{}^{-1}$ h^{-1} were achieved. This pronounced shift in product distribution led to a methanol selectivity of 93%, distinctly contrasting with the exclusive acetic acid selectivity observed for MOF-253-Fe_2 (Figure 5.2e). These findings underscore the intrinsic preference of the mononuclear Fe catalyst for methanol formation under milder conditions, attributed to differences in active site configuration and the absence of cooperative redox interactions that drive C-C coupling in the dinuclear system (Table 5.2).

Table 5.1: Control experiments for MOF-253-Fe catalyzed oxidation of methane.[a]

Entry No.	Temp (°C)	P[CH_4] (bar), mmol CH_4	Initial P[O_2] (bar)	CH_3CO_2H (mmol)[b]	CO/CO_2 (mmol)[c]
1	95	20, 39	8	0.03[f]	0/0.019
2	110	20, 39	8	0.04[g]	0/0.14
3	95	20, 39	8	0.004[h]	0.0002/0.024
4[d]	95	20, 39	8	0[i]	nd
5[e]	95	20, 39	8	0[j]	nd
6	80	20, 39	8	0.01[k]	0/0.009

[a] Standard conditions: 20.8 5 mg of MOF-253-Fe (5.25 μmol Fe), 8 mL H_2O, 22 h; N_2 balance was applied to keep constant pressure of 28 bar if needed; nd: not determined.

[b] Analysed by GC-FID using ethylene glycol as the internal standard.

[c] Analysed by GC-TCD.

[d] Na_2SO_3 was used as an $^{\cdot}OH$ scavenger.

[e] TEMPO was used as a $^{\cdot}CH_3$ scavenger.

[f] 0.7 mmol of methanol was formed as the major product.

[g] 0.61 mmol of methanol was formed as the major product.

[h] 0.009 mmol of methanol was formed as the only product.

[i] 0.38 mmol of methanol was formed.

[j] 0.24 mmol of methanol was formed.

[k] 0.26 mmol of methanol was formed.

Table 5.2: Comparison of catalytic activity and selectivity of MOF-253-Fe_2 and MOF-253-Fe at 160 °C and 95 °C.[a]

Catalyst	T (°C)	CH_3OH (mmol)	CH_3CO_2H (mmol)	CO/CO_2 (mmol)	CH_3OH %	CH_3CO_2H %
MOF-253-Fe_2[b]	160	0	1.1	0.00014/0.08	–	93
MOF-253-Fe[b]	160	0.091	0.14	0.0016/1.21	6	10
MOF-253-Fe_2[c]	95	0.009	0.004	0.0002/0.024	24	11
MOF-253-Fe[c]	95	1.21	0.056	0/0.038	93	4

[a] Reaction conditions: catalyst (10.5 μmol Fe), CH_4 (20 bar), O_2 (8 bar), water (8 mL).

[b] Reaction time: 38 h.

[c] Reaction time: 22 h.

Table 5.3: Carbon balance in MOF-253-Fe catalyzed oxidation of CH_4 using O_2.

Initial CH_4 (mmol)	**Post-reaction CH_4 (mmol)**	**CH_4 consumed (mmol)**	**CH_3OH (mmol)**	**CH_3CO_2H (mmol)**	**CO_2 (mmol)**	**CO (mmol)**	**Total C yield (mmol)**
39	36.71	2.29	1.1	0.08	0.00014	2.28	2.28

Investigating $Fe^V(O)(OH)$ as a possible intermediate in MOF-253-Fe catalyzed methane oxidation.

$Fe^V(O)(OH)$ species are well known for catalyzing the oxidation of olefins.[17–19] To investigate whether such a species forms during MOF-253-Fe catalyzed methane oxidation to methanol, control experiments were conducted using olefins such as cyclohexene and styrene. Reactions were performed in either water or a 1:1 water-acetonitrile mixture at 95 °C. The general procedure described in Section 3.1 was followed, using MOF-253-Fe (5.25 μmol of Fe) and styrene (0.4 mmol). Reaction conditions: MOF-253-Fe (20.9 mg, 5.25 μmol of Fe), 8 mL water, 20 bar CH_4, 8 bar O_2, and 0.4 mmol styrene were reacted at 95 °C for 22 h. A similar setup was used for cyclohexene as the substrate. Each reaction was also repeated using the water-acetonitrile (1:1) solvent system. None of the four reactions yielded vicinal diol or epoxidation products from olefins, which suggests that the formation of $Fe^V(O)(OH)$ as a reactive intermediate under these conditions is unlikely.

Table 5.4: Simulated parameters of EPR spectroscopic spin-trapping experiments for MOF-253-Fe catalyzed oxidation of methane.[a]

Adducts	**g-factor**	**A_{14N} (G)**	**$A_\alpha H$ (G)**	**lw (mT)[b]**
DMPO-OH	2.01	15.0	15.0	0.31
DMPO-CH_3	2.01	15.7	23.58	1.1
DMPO-degraded	2.01	16.3	–	1.1

[a] Reaction conditions: 20.85 mg MOF-253-Fe (5.25 μmol Fe), 20 bar CH_4, 8 bar O_2, 50 μL DMPO, 22 h, 95 ℃.

[b] The linewidth (lw, in mT) defines the FWHM (full width at half height) of the absorption Gaussian (first number).

5.3.3 DFT Structure Optimization.

All density functional theory (DFT) calculations were performed using Gaussian 16.0.[18] The geometries of the structures were optimized using the B3LYP[19;20] hybrid density functional in combination with the def2-SVP[21] (split valence polarization) basis set, along with Grimme's D3[26] dispersion corrections. The Polarizable Continuum Model (PCM), using the integral equation formalism variant (IEFPCM), was employed as the default SCRF method with water as the solvent. All calculations were carried out at 303.15 K. Optimized structures were visualized using GaussView 5.0.

Cartesian coordinates of the DFT-optimized structures.

MOF-253-Fe

Coordinates (Å)

S.No.	Atom	X	Y	Z
1	C	-3.596452	-0.889699	0.134437
2	C	-2.201292	-0.889699	0.134437
3	C	-1.503754	0.318052	0.134437
4	C	-3.596233	1.526483	0.132759
5	C	-4.293834	0.318277	0.133755
6	H	-4.146211	-1.842016	0.134887
7	H	-1.651784	-1.842212	0.135752
8	H	-4.146355	2.478764	0.131806
9	C	0.036246	0.318164	0.135325
10	C	0.733839	-0.889690	0.136241
11	C	2.128391	1.526872	0.135558
12	C	2.128976	-0.889484	0.137470
13	H	0.184311	-1.842133	0.136421
14	C	2.826310	0.318516	0.136991
15	H	2.678186	2.479249	0.134924
16	H	2.678730	-1.841977	0.138607
17	N	0.733679	1.526493	0.135325
18	N	-2.201408	1.526561	0.133238
19	Fe	-0.676662	2.798773	0.003367
20	H	-5.363834	0.318306	0.133996
21	H	3.896310	0.318642	0.137722
22	O	-0.656135	4.052561	1.322456
23	H	-0.657429	4.929264	0.931317
24	O	-0.654104	3.757568	-1.543437
25	H	-0.675159	4.695413	-1.339468

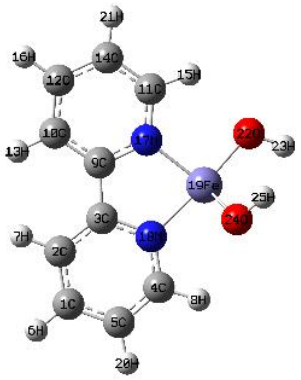


Figure 5.7: DFT-optimized structures of MOF-253-Fe.

5.3.4 X-ray Absorption Spectroscopic Analysis

X-ray Near-Edge Structure (XANES) and Extended X-ray Absorption Fine Structure (EXAFS) measurements were carried out at the Energy-Scanning EXAFS beamline (BL-9) at the Indus-2 Synchrotron Source at Raja Ramanna Centre for Advanced Technology (RRCAT), Indore, India.[22] All measurements were performed at room temperature. The beamline operates in the energy range of 4–25 keV.

The beamline optics consist of a Rh/Pt coated collimating meridional cylindrical mirror, and the collimated beam is monochromatized by a Si(111) based double crystal monochromator (DCM). The second crystal of the DCM is a sagittal cylindrical crystal used for horizontal focusing, while an additional Rh/Pt coated bendable post mirror facing downward is used for vertical focusing of the beam at the sample position.

Two ionization chambers (300 mm length each) were used for data collection in transmission mode: one for measuring the incident flux and the second for measuring the transmitted flux. For energy calibration, standard metal foils were used. Appropriate gas pressures and gas mixtures were chosen to achieve 10–20% absorption in the first ionization chamber and 70–90% absorption in the second ionization chamber to optimize the signal-to-noise ratio.

Pellets were prepared from powder samples for recording absorption spectra. Sample powder was mixed homogeneously with cellulose powder in an appropriate proportion and pressed (2 Ton) into 15 mm diameter discs. The amount of sample was optimized to achieve a reasonable edge jump at the particular absorption edge of the element being probed. Spectra were collected at the Fe K-edge in transmission mode and calibrated against the reference spectrum of metallic Fe (7112 eV). Data were processed using Demeter software.[23] A metallic Fe foil standard was used as a reference for energy calibration and was measured simultaneously with experimental samples.

XANES analysis

The oxidation states of the Fe species within MOF-253-Fe and MOF-253-Fe_2 were determined by comparing the energies of their pre-edge positions to those of $FeCl_2$ and $Fe(OH)_3$.

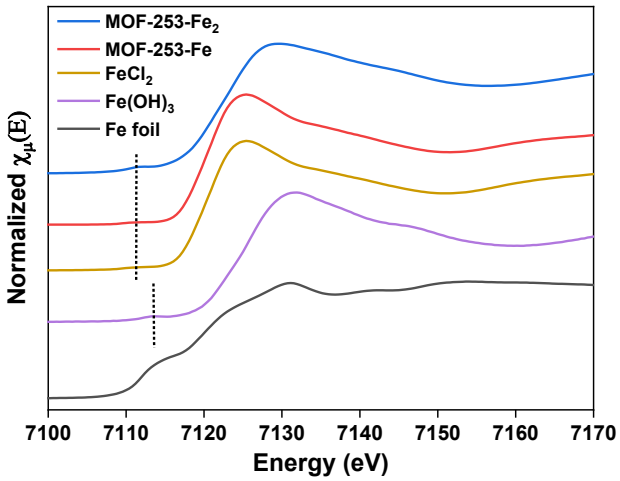


Figure 5.8: $\mu(E)$ XAS spectra of metallic Fe(0) (black), $Fe(OH)_3$ (purple), $FeCl_2$ (brown), MOF-253-Fe (red), and MOF-253-Fe_2 (blue). The oxidation states of the Fe species within MOF-253-Fe_2 and MOF-253-Fe were determined by comparing the energies of their pre-edge positions to those of $Fe(OH)_3$ and $FeCl_2$. The pre-edge positions of MOF-253-Fe_2 (7111.7 eV) and MOF-253-Fe (7111.5 eV) aligned well with that of $FeCl_2$ (7111.0 eV) and are approximately 2 eV lower than that of $Fe(OH)_3$ (7113.0 eV). Therefore, we conclude that the Fe ions in MOF-253-Fe_2 and MOF-253-Fe possess a +2 oxidation state.

EXAFS fitting using DFT-optimized structures

The spectra were calibrated against the reference spectra and aligned to the first peak in the smoothed first derivative of the absorption spectrum. Background noise was removed, and the spectra were processed to obtain a normalized unit edge step.

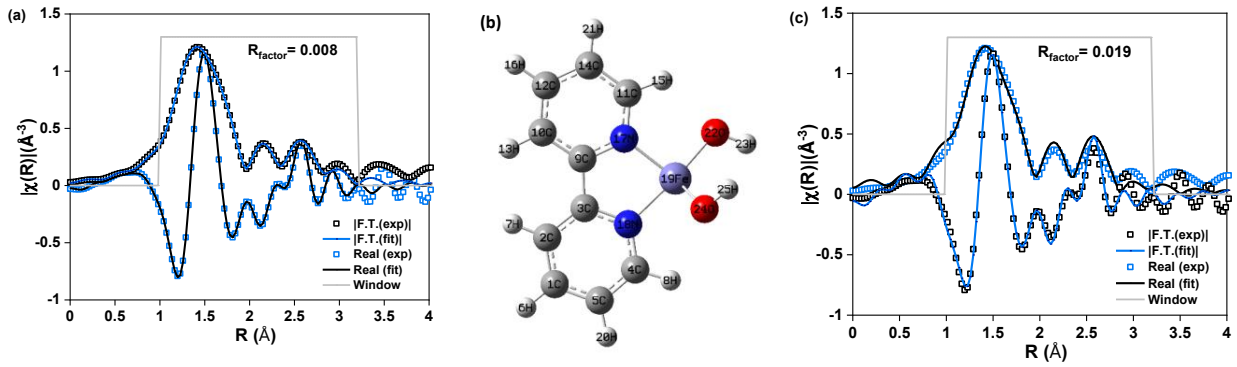


Figure 5.9: (a) EXAFS spectrum and fit of MOF-253-Fe. (b) DFT-optimized structure of MOF-253-Fe. (c) EXAFS spectra (blue and black hollow squares) and fits (black and blue solid lines) of a combination of 95% monomeric MOF-253-Fe and 5% dimeric Fe sites in R-space at the Fe K-edge. The fitting range in R-space is 1.0–3.25 Å. The significant misfits and high R-values observed even with 5% di-Fe further confirm that MOF-253-Fe does not contain any dinuclear MOF-253-Fe_2 species.

XPS Analysis

All binding energies were corrected with reference to the C1s peak at 284.8 eV. Casa-XPS software was used for peak analysis and deconvolution studies.

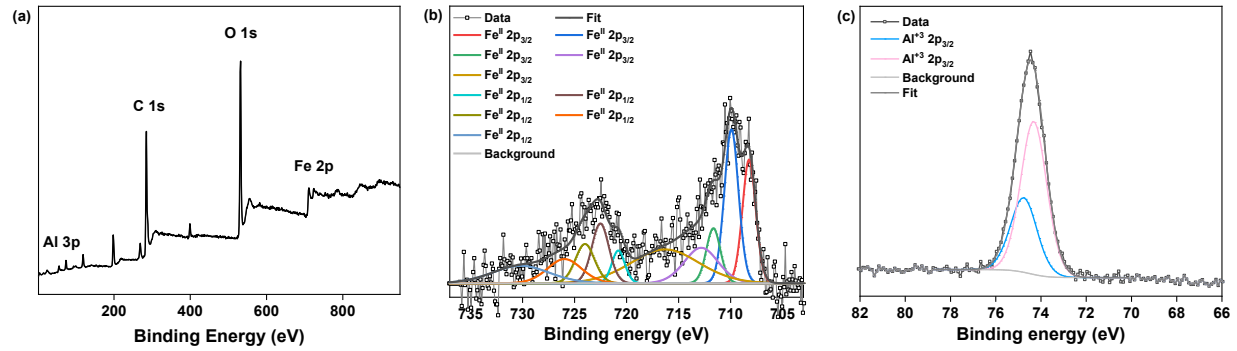


Figure 5.10: (a) Raw XPS data of MOF-253-Fe. (b) XPS fitting of Fe in MOF-253-Fe. (c) XPS fitting of aluminium in MOF-253-Fe.

Table 5.5: XPS fitting parameters for Fe(II) in MOF-253-Fe.

Component	**Position (eV)**	**FWHM (eV)**	**Area%**	**Lineshape**
Fe(II) 2p	708.23	1.5	13.52	GL(30)
Fe(II) 2p	710.09	1.5	17.90	GL(30)
Fe(II) 2p	710.90	1.6	6.40	GL(30)
Fe(II) 2p	712.11	2.6	9.93	GL(30)
Fe(II) 2p	715.87	5.4	17.02	GL(30)
Fe(II) 2p	721.34	1.4	5.51	GL(30)
Fe(II) 2p	722.53	1.7	8.42	GL(30)
Fe(II) 2p	724.42	1.7	6.24	GL(30)
Fe(II) 2p	726.53	2.8	6.82	GL(30)
Fe(II) 2p	730.19	4.7	8.24	GL(30)

Table 5.6: Comparison of the catalytic activity of MOF-253-Fe for CH_4 oxidation to CH_3OH using O_2 with other reported catalysts containing only earth-abundant metals.

Reference	**Catalyst**	**Oxidant (Flow/-Total pressure)**	**Condition**	**Temp (°C)**	**CH_3OH Selectivity (%)**	**μmol g_{cat}^{-1} h^{-1}**	**mmol mol_{metal}^{-1} h^{-1}**	**mmol mol_{metal}^{-1}**	**μmol g_{cat}^{-1}**
This Work	MOF-253-Fe	CH_4 (20 bar), O_2 (8 bar)	Batch	95	93	1,529.7	6,060	133,333	33,654
Chem. Eur. J. **e202404037**, 2025	Co-VT-1	CH_4:O_2 (2.05:0.35 MPa)	Batch	90	–	70	–	–	140
J. Anal. Appl. Pyrolysis **177**, 106359 (2024)	Cu/BC	21% O_2/N_2 (13.3 mL/min) + 28% CH_4 (20 mL/min)	Flow	280	–	20.61	–	–	–
Nat. Commun. **15**, 9798 (2024)	DUT-5-$Fe(OH)_2$	CH_4 (30 bar), O_2 (8 bar)	Batch	125	90	–	2,155	86,206	–
Chem. Commun. **60**, 228–231 (2024)	Cu-KFI	15 mL min^1 (96.8% CH_4, 3.2% H_2O), 100 ppm O_2	Flow	450	83	–	880.3	–	–

Continued on next page

Table 5.6 (continued)

Reference	Catalyst	Oxidant (Flow/-Total pressure)	Condition	Temp (°C)	CH_3OH Selectivity (%)	$\mu mol\ g_{cat}^{-1}\ h^{-1}$	$mmol\ mol_{metal}^{-1}\ h^{-1}$	$mmol\ mol_{metal}^{-1}$	$\mu mol\ g_{cat}^{-1}$
Int. J. Hydrogen Energy **81**, 535547 (2024)	Cu/KAO	28% CH_4 + 21% O_2 + H_2O	Flow	320	–	10.10	21.4	–	–
ACS Catal. **14**, 292–298 (2024)	Cu–Fe–SSZ-13	10% CH_4, 400 ppm O_2, Ar balance (total flow 60 mL/min)	Flow	200	–	188.3	–	–	–
Molecules **29**, 2273 (2024)	Cu/SAPO-34	CH_4 (60 mL/min), 2% H_2O, 400 ppm O_2	Flow	350	65	504	1,800	–	–
Energy Fuels **37**, 9411-9418 (2023)	Cu-CHA	$CH_4/O_2/H_2O$ (96.4/2/40 mL)	Flow	300	33.7	254.9	–	–	–
ACS Appl. Mater. Interfaces **15**, 2670–2679 (2023)	Fe/Uio-66	5 bar CH_4, 5% O_2 + 0.2% H_2O balance Ar	Flow	180	62	7.2	–	–	–

Continued on next page

Table 5.6 (continued)

Reference	**Catalyst**	**Oxidant (Flow/- Total pressure)**	**Condition**	**Temp (°C)**	**CH_3OH Selectivity (%)**	**μmol g_{cat}^{-1} h^{-1}**	**mmol mol_{metal}^{-1} h^{-1}**	**mmol mol_{metal}^{-1}**	**μmol g_{cat}^{-1}**
J. Catal. **421**, 300–308 (2023)	Cu–SSZ-39	WHSV 6000 mL h^{-1} g^{-1}, 50% CH_4, 2% water, 250 ppm O_2	Flow	225	–	9.82	–	–	–

Conclusion

The mononuclear Fe(II)-hydroxyl sites confined within the MOF-253 framework exhibit outstanding catalytic performance for the selective oxidation of methane to methanol under mild conditions. The single-site nature of MOF-253-Fe enables efficient C-H activation using O_2 as the sole oxidant, achieving 96% methanol selectivity and an impressive productivity of 6,060 $mmol_{CH_3OH}$ $mol_{Fe}{}^{-1}$ h^{-1} at 95 °C in aqueous medium. Radical trapping and isotopic labeling studies confirm that the reaction proceeds through radical-mediated pathways involving $\cdot CH_3$ and $\cdot OH$ intermediates. The structural confinement of the (bpy)Fe(II)$(OH)_2$ moiety within the MOF channels stabilizes reactive intermediates and suppresses overoxidation of methanol to acetic acid or CO_2. These findings highlight the critical role of isolated Fe(II)–hydroxyl centers in enabling selective partial oxidation of methane and provide a mechanistic basis for designing single-site heterogeneous catalysts capable of controlled alkane functionalization.

References

[1] Schwarz, H. Chemistry with Methane: Concepts Rather than Recipes. *Angewandte Chemie International Edition* **2011**, *50*, 10096–10115.

[2] Taifan, W.; Baltrusaitis, J. CH4 Conversion to Value Added Products: Potential, Limitations and Extensions of a Single Step Heterogeneous Catalysis. *Applied Catalysis B: Environmental* **2016**, *198*, 525–547.

[3] Kishore, M. A.; Lee, S.; Yoo, J. S. Fundamental Limitation in Electrochemical Methane Oxidation to Alcohol: A Review and Theoretical Perspective on Overcoming It. *Advanced Science* **2023**, *10*, 2301912.

[4] Xu, W.; Wang, Z.; Huang, C.; Wang, X. Direct Methane Conversion to Acetic Acid: From Homogeneous Catalysis to Heterogeneous Catalysis. *ChemCatChem* **2024**, *16*, e202400692.

[5] Liu, G.; Cui, H.; Wang, S.; Zhang, L.; Su, C.-Y. A Series of Highly Stable Porphyrinic Metal–Organic Frameworks Based on Iron–Oxo Chain Clusters: Design, Synthesis and Biomimetic Catalysis. *Journal of Materials Chemistry A* **2020**, *8*, 8376–8382.

[6] Lan, G.; Fan, Y.; Shi, W.; You, E.; Veroneau, S. S.; Lin, W. Biomimetic Active Sites on Monolayered Metal–Organic Frameworks for Artificial Photosynthesis. *Nature Catalysis* **2022**, *5*, 1006–1018.

[7] Osadchii, D. Y.; Olivos-Suarez, A. I.; Szécsényi, ; Li, G.; Nasalevich, M. A.; Dugulan, I. A.; Crespo, P. S.; Hensen, E. J. M.; Veber, S. L.; Fedin, M. V.; Sankar, G.; Pidko, E. A.; Gascon, J. Isolated Fe Sites in Metal Organic Frameworks Catalyze the Direct Conversion of Methane to Methanol. *ACS Catalysis* **2018**, *8*, 5542–5548.

[8] Castner, A. T.; Johnson, B. A.; Cohen, S. M.; Ott, S. Mimicking the Electron Transport Chain and Active Site of [FeFe] Hydrogenases in One Metal–Organic Framework: Factors That Influence Charge Transport. *Journal of the American Chemical Society* **2021**, *143*, 7991–7999.

[9] Wang, Z.; Yeary, P.; Feng, X.; Lin, W. Self-Adaptive Metal–Organic Framework Assembles Di-iron Active Sites to Mimic Monooxygenases. *Journal of the American Chemical Society* **2023**, *145*, 8647–8655.

[10] Li, J.; Huang, H.; Xue, W.; Sun, K.; Song, X.; Wu, C.; Nie, L.; Li, Y.; Liu, C.; Pan, Y.; Jiang, H.-L.; Mei, D.; Zhong, C. Self-Adaptive Dual-Metal-Site Pairs in Metal-Organic Frameworks for Selective CO2 Photoreduction to CH4. *Nature Catalysis* **2021**, *4*, 719–729.

[11] Wang, L.; Li, B.; Dionysiou, D. D.; Chen, B.; Yang, J.; Li, J. Overlooked Formation of H2O2 during the Hydroxyl Radical-Scavenging Process When Using Alcohols as Scavengers. *Environmental Science & Technology* **2022**, *56*, 3386–3396.

[12] Nam, W. Synthetic Mononuclear Nonheme Iron–Oxygen Intermediates. *Accounts of Chemical Research* **2015**, *48*, 2415–2423.

[13] Zhang, T.; Manna, K.; Lin, W. Metal–Organic Frameworks Stabilize Solution-Inaccessible Cobalt Catalysts for Highly Efficient Broad-Scope Organic Transformations. *Journal of the American Chemical Society* **2016**, *138*, 3241–3249.

[14] Krebs, C.; Galonić Fujimori, D.; Walsh, C. T.; Bollinger, J. M. J. Non-Heme Fe(IV)–Oxo Intermediates. *Accounts of Chemical Research* **2007**, *40*, 484–492.

[15] Simons, M. C.; Prinslow, S. D.; Babucci, M.; Hoffman, A. S.; Hong, J.; Vitillo, J. G.; Bare, S. R.; Gates, B. C.; Lu, C. C.; Gagliardi, L.; Bhan, A. Beyond Radical Rebound: Methane Oxidation to Methanol Catalyzed by Iron Species in Metal–Organic Framework Nodes. *Journal of the American Chemical Society* **2021**, *143*, 12165–12174.

[16] Borrell, M.; Costas, M. Mechanistically Driven Development of an Iron Catalyst for Selective Syn-Dihydroxylation of Alkenes with Aqueous Hydrogen Peroxide. *Journal of the American Chemical Society* **2017**, *139*, 12821–12829.

[17] Barry, S. M.; Challis, G. L. Mechanism and Catalytic Diversity of Rieske Non-Heme Iron-Dependent Oxygenases. *ACS Catalysis* **2013**, *3*, 2362–2370.

[18] Citation | Gaussian.Com. `https://gaussian.com/citation/`.

[19] Lee, C.; Yang, W.; Parr, R. G. Development of the Colle-Salvetti Correlation-Energy Formula into a Functional of the Electron Density. *Physical Review B* **1988**, *37*, 785–789.

[20] Becke, A. D. Density-functional Thermochemistry. III. The Role of Exact Exchange. *The Journal of Chemical Physics* **1993**, *98*, 5648–5652.

[21] Weigend, F.; Ahlrichs, R. Balanced Basis Sets of Split Valence, Triple Zeta Valence and Quadruple Zeta Valence Quality for H to Rn: Design and Assessment of Accuracy. *Physical Chemistry Chemical Physics* **2005**, *7*, 3297–3305.

[22] Poswal, A. K.; Agrawal, A.; Yadav, A. K.; Nayak, C.; Basu, S.; Kane, S. R.; Garg, C. K.; Bhattachryya, D.; Jha, S. N.; Sahoo, N. K. Commissioning and First Results of Scanning Type EXAFS Beamline (BL-09) at INDUS-2 Synchrotron Source. *AIP Conference Proceedings* **2014**, *1591*, 649–651.

[23] Ravel, B.; Newville, M. ATHENA, ARTEMIS, HEPHAESTUS: data analysis for X-ray absorption spectroscopy using IFEFFIT. *Journal of synchrotron radiation* **2005**, *12*, 537–541.

Chapter 6

Bipyridyl Based Metal-Organic Framework for Selective Hydroxylation of Benzene into Phenol

Title of Paper: "Metal-Organic Framework Supported Mono Bipyridyl-Iron Hydroxyl Catalyst for Selective Benzene Hydroxylation into Phenol"

Citation: Inorganic Chemistry, **2024**, *63* (25), 11907-11916.
(doi.org/10.1021/acs.inorgchem.4c01825)

Author: Poorvi Gupta, Naved Akhtar, Wahida Begum, Bharti Rana, Rahul Kalita, Manav Chauhan, Chhaya Thadhani, and Kuntal Manna*

Abstract

Direct hydroxylation of benzene to phenol is more appealing in the industry for the economic and environmentally friendly phenol synthesis than the conventional cumene process. We have developed a UiO-metal-organic framework (MOF)-supported mono bipyridyl-Iron(II) hydroxyl catalyst [bpy-UiO-Fe(OH)$_2$] for the selective benzene hydroxylation into phenol using H_2O_2 as the oxidant. The heterogeneous bpy-UiO-Fe(OH)$_2$ catalyst showed high activity and remarkable phenol selectivity of 99%, giving the phenol mass-specific activity up to 1261 $mmol_{PhOH}$ g_{Fe}^{-1} h^{-1} at 60 °C. Bpy-UiO-Fe(OH)$_2$ is significantly more active and selective than its homogeneous counterpart, bipyridine-Fe(OH)$_2$. This enhanced catalytic activity of bpy-UiO-Fe(OH)$_2$ over its homogeneous control is attributed to the active site isolation of the bpy-Fe(OH)$_2$ moiety by the solid MOF that prevents intermolecular decomposition. Moreover, the exceptional selectivity of bpy-UiO-Fe(OH)$_2$ in benzene to phenol conversion is originated via shape-selective catalysis, where the confined reaction space within the porous UiO-MOF prevents the formation of larger overoxidized products such as hydroquinone or benzoquinone, leading to the formation of only smaller-sized phenol after monohydroxylation of benzene. Spectroscopic and controlled experiments and theoretical calculations elucidated the reaction pathway, in which the in situ generated $^{\cdot}OH$ radical mediated by bpy-UiO-$Fe^{II}(OH)_2$ is the key species for benzene hydroxylation. This work underscores the significance of MOF-supported earth-abundant metal catalysts for sustainable production of fine chemicals.

6.1 Introduction

Phenol is a pivotal chemical in industries, which is extensively used in synthesizing caprolactam, phenolic resins, synthetic fragrances, dyes, adipic acid, and pharmaceuticals.[1–3] The industrial production of phenol is currently dominated by the cumene process, in which the gas-phase Friedel-Crafts alkylation of benzene by propene using a Lewis acid catalyst gives cumene, followed by oxidation of cumene by O_2 to form cumene hydroperoxide, and the subsequent transformation of cumene hydroperoxide into phenol and acetone via the Hock rearrangement.,[4–6] Single-step direct hydroxylation of benzene to phenol under mild conditions could be more economical, avoiding the energy-intensive and high-pressure reactions involved in the multistep cumene process.[7–9] Various homogeneous[10–13] and heterogeneous catalysts[14–25] have been developed recently for one-step hydroxylation of benzene to phenol using O_2 and hydrogen peroxide (H_2O_2) as the oxidant. Among the plethora of metal catalysts, heterogeneous catalysts based on iron have been extensively explored for benzene hydroxylation. These catalysts offer notable advantages, such as cost-effectiveness, easy separation, and environmental compatibility. ElMetwally et al. reported an iron oxychloride catalyst for selective hydroxylation of benzene.[14] Liu et al. produced metal single-atom catalysts for selective benzene hydroxylation.[17] Zeng et al. demonstrated the bimetallic FeCo nanoalloys for direct hydroxylation of benzene to phenol.[19] Chen et al. constructed Fe

clusters embedded in a porous carbon–nitride catalyst for benzene transformation.[23] Bu et al. studied the spin-state controlled nuclearity effect on iron sub-nanocatalysts for benzene oxidation.[22] All of these catalysts generated hydroxyl radical ($^{\cdot}OH$) from H_2O_2, which is the active species for the hydroxylation of benzene. Despite significant progress, all these catalyst systems suffer from poor activity and selectivity due to the catalyst decomposition and lack of control over the overoxidation of phenol. As porous and tunable molecular materials, metal–organic frameworks (MOFs) have garnered significant attention for developing robust single-site heterogeneous catalysts for diverse applications.[26–49] In particular, UiO-MOFs, constructed from $Zr_6(\mu_3-O)_4(\mu_3-OH)_4$ secondary building units (SBUs) or nodes and linear dicarboxylate bridging linkers, offer excellent thermally and chemically robust platforms.[46;50–52] The inherent capability of MOFs to sustain postsynthetic modification allows the functionalization of organic linkers of MOFs, which leads to the formation of single-site base-metal catalysts upon metalation.[27;53–65] Furthermore, MOF-supported single-site catalysts offer a blend of advantages from homogeneous catalysts, including uniform distribution of active sites, and heterogeneous counterparts, such as robustness and easy catalyst recycling.[54;66–68] Pan et al. recently reported nitrogen atom-ligated single-site Fe-catalysts, in which increasing the Fe-N coordination number enhanced the benzene oxidation activity.[16] We surmised that bipyridyl iron species confined within a porous MOF could be highly robust and selective heterogeneous catalysts for hydroxylation of benzene via active-site isolation. Herein, we report an efficient single-step hydroxylation of benzene into phenol using H_2O_2 over a MOF-supported mono 2,2′-bipyridine-iron catalyst in excellent yield and selectivity.

6.2 Results and Discussions

6.2.1 Synthesis and Characterization of bpy-UiO-Fe(OH)$_2$

Bpy-UiO-Fe(OH)$_2$ was synthesized via postsynthetic metalation of the bipyridyl linkers of the freshly prepared bpy-UiO-67 MOF. The solvothermal reaction between $ZrCl_4$ and 2,2′-bipyridine-5,5′-dicarboxylic acid with CF_3CO_2H as the modulator in the presence of DMF at 100 °C for 4 days gave the bpy-UiO MOF in 69% yield.[35] The pristine bpy-UiO MOFs,[69] featuring three-dimensional porous UiO-topology,[50;51;70] are constructed from $Zr_6O_4(OH)_4$ nodes interconnected with 2,2′-bipyridine-5,5′-dicarboxylate (bpy) bridging linkers. Stirring a THF solution of $FeCl_2$ with a slurry of bpy-UiO afforded bpy-UiO-$FeCl_2$, bearing bipyridyl-ligated Fe-dichloride species at its linker. X-ray photoelectron spectroscopy (XPS) analysis of bpy-UiO-$FeCl_2$ displayed Fe $2p_{3/2}$ and $2p_{1/2}$ binding energy peaks at 709.8 and 723.6 eV, respectively, signifying the +2 oxidation state of the Fe ion (Figure 6.19b). The presence of the +4 oxidation state of the Zr ion at bpy-UiO-$FeCl_2$ nodes was also confirmed by XPS, which displayed Zr^{IV} binding energies at 182.4 and 184.8 eV (Figure 6.19c). The reaction between bpy-UiO-$FeCl_2$ and $NaEt_3BH$ in THF resulted in the formation of

bpy-UiO-FeH_2 via chloride-hydride exchange at the Fe ion. Subsequently, the treatment of bpy-UiO-FeH_2 with water afforded bpy-UiO-$Fe(OH)_2$, bearing bipyridyl-ligated Fe-dihydroxyl species at its linker. 40% Fe-loading with respect to the bipyridyl linkers was achieved as determined by inductively coupled plasma optical emission spectroscopy (ICP-OES) of the digested bpy-UiO-$Fe(OH)_2$ MOF. The resemblance in the PXRD pattern between bpy-UiO-$FeCl_2$, bpy-UiO-$Fe(OH)_2$, and the pristine bpy-UiO MOF indicated the retention of crystallinity and structure of the bpy-UiO MOFs during postsynthetic treatments (Figure 6.1b) The BET surface area of bpy-UiO-$Fe(OH)_2$ was estimated as 522 m^2/g (Figure 6.1c). The much reduced surface area of bpy-UiO-$Fe(OH)_2$ than that of pristine bpy-UiO (1898 m^2/g) is attributed to the incorporation of the $Fe(OH)_2$ moiety within the pores of the MOF. Scanning electron microscopy (SEM) image displayed bpy-UiO-$Fe(OH)_2$ particles with an average size of 220 nm (Figure 6.1d).

The uniform distribution of Fe and Zr throughout the particles was observed in the SEM-EDX mapping (Figure 6.8). The XPS spectrum of bpy-UiO-$Fe(OH)_2$ confirmed the +2 oxidation state of Fe, which showed binding energies of Fe $2p_{3/2}$ and Fe $2p_{1/2}$ at 710.3 and 723.9 eV, respectively (Figure 6.1e). In the X-ray absorption near-edge structure (XANES), the pre-edge energy of Fe in bpy-UiO-$Fe(OH)_2$ closely matched that of $FeCl_2$ (7112 eV), further indicating the presence of the Fe^{2+} species (Figure 6.2a). Notably, the +4 oxidation state of the Zr ion remained unchanged throughout the transformation of bpy-UiO-$FeCl_2$ to bpy-UiO-$Fe(OH)_2$ as determined by XPS analysis (Figure 6.1f).

The analysis of the Fe K-edge extended X-ray absorption fine structure (EXAFS) of bpy-UiO-$Fe(OH)_2$ revealed that the Fe ion is octahedrally coordinated with two nitrogen atoms of the bipyridine, two hydroxyl groups, and two water molecules (Figure 6.2b). The Fe-N bipyridine distance is 2.03 Å, while the Fe-O_{OH} distance is 1.9 Å, and the Fe-O_{H_2O} distance is 2.09 Å. The EXAFS data of bpy-UiO-$Fe(OH)_2$ were also fitted to its DFT model with 5-80% metallic Fe (Figure 6.17). Significant misfits and higher R-factors indicated the absence of any metallic Fe nanoparticles in the MOF. In addition, the lack of an Fe–Fe scattering feature at 2.2 Å of Fe foil in the phase-corrected k^2-weighted Fe-EXAFS χ(R) of bpy-UiO-$Fe(OH)_2$ further confirmed the absence of Fe nanoparticles in bpy-UiO-$Fe(OH)_2$ (Figure 6.2f). In this spectrum, the lack of Fe-Cl single scattering at 1.6 Å in bpy-UiO-$Fe(OH)_2$ suggests that there is no remaining Fe-Cl bond following postsynthetic modification (Figure 6.2f). The initial scattering peak centered at $\sim$ 1.5 Å is attributed to Fe-O/N single scattering, resembling that of Fe_2O_3, and the secondary weaker scattering at $\sim$ 2.7 Å is attributed to the Fe-$C_{pyridyl}$ scattering (Figure 6.2f). Moreover, the Fe–Fe single scattering feature of Fe_2O_3 at 2.53 Å is absent in the EXAFS image of bpy-UiO-$Fe(OH)_2$, suggesting that bpy-UiO-$Fe(OH)_2$ exclusively contains isolated Fe cations without Fe neighbors. The X-band electron-paramagnetic spectroscopy (EPR) spectrum reveals a broad signal centered at g = 2.055 (Figure 6.1g). The EXAFS and EPR data suggest the exis-

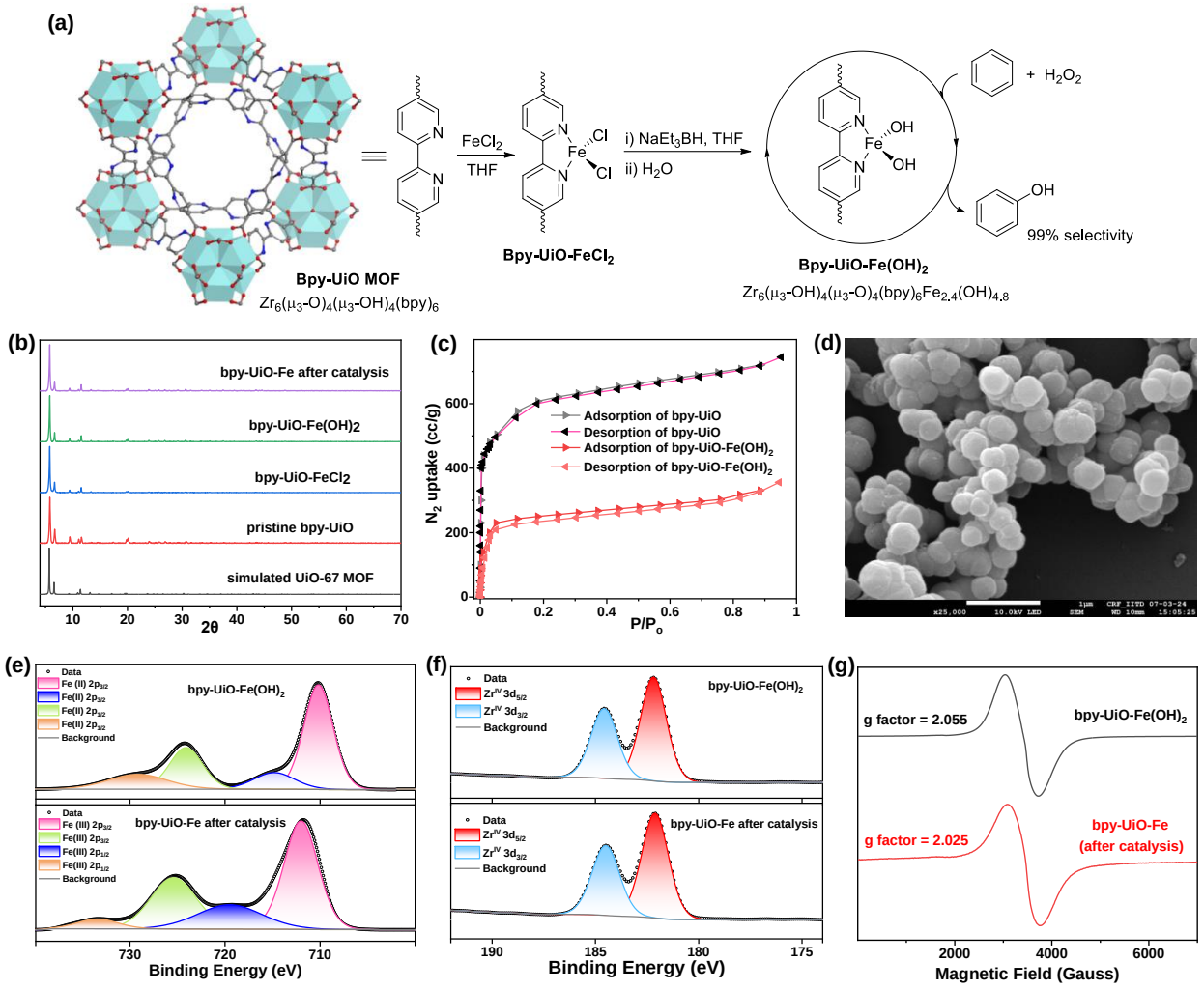


Figure 6.1: (a) Postsynthetic metalation of bpy-UiO to form bpy-UiO-Fe(OH)$_2$ (b) PXRD patterns of the simulated UiO-67 MOF (black), pristine bpy-UiO (red), bpy-UiO-FeCl$_2$ (blue),bpy-Fe(OH)$_2$ (green), and bpy-UiO-Fe recovered after benzene hydroxylation (purple). (c) N$_2$ sorption isotherms of bpy-UiO (gray/black) and bpy-UiO-Fe(OH)$_2$ (red/orange) measured at 77 K. (d) SEM image of bpy-UiO-Fe(OH)$_2$ particles. (e) Fe 2p XPS spectra of bpy-UiO-Fe(OH)$_2$ and bpy-UiO-Fe after catalysis. (f) Zr 3d XPS spectra of bpy-UiO-Fe(OH)$_2$ and bpy-UiO-Fe after catalysis. (g) EPR spectra of solid bpy-UiO-Fe(OH)$_2$ (black) and bpy-UiO-Fe after catalysis (red).

tence of a high spin octahedral (bpy)Fe^{II}(OH)$_2$(OH$_2$)$_2$ species within bpy-UiO-Fe(OH)$_2$.[71;72]

6.2.2 Catalytic Performance for Benzene Hydroxylation

Bpy-UiO-Fe(OH)$_2$ is an active heterogeneous catalyst for the direct hydroxylation of benzene into phenol using H$_2$O$_2$ as the oxidant. The hydroxylation of benzene was optimized by varying solvents, reaction time,

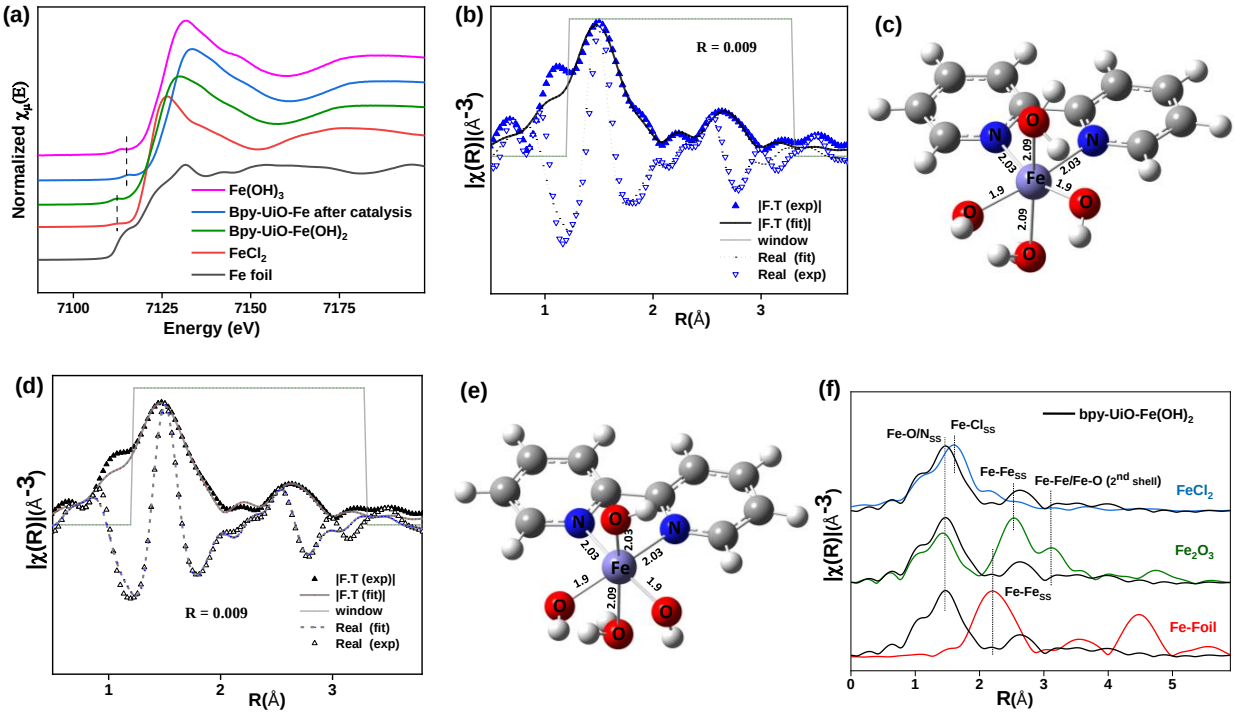


Figure 6.2: (a) XANES spectra of metallic Fe(0) foil (black), bpy-UiO-Fe$(OH)_2$ (green), and bpy-UiO-Fe after catalysis of benzene oxidation to phenol (blue), $Fe(OH)_3$ (magenta), and $FeCl_2$ (red). (b) EXAFS spectra (blue solid and hollow triangles) and fits (black solid and dashed lines) of bpy-UiO-Fe$(OH)_2$ in R space at the Fe K-edge. The fitting range in the R space is 1.2–3.5 Å (c) DFT-optimized structure of the bpy-Fe$(OH)_2(H_2O)_2$ moiety within bpy-UiO-Fe$(OH)_2$ MOFs. The bond distances are given in Å. (d) EXAFS spectra (black solid and hollow triangles) and fits (gray solid and dashed lines) of bpy-UiO-Fe after catalytic benzene hydroxylation to phenol in the R space at the Fe K-edge. The fitting range in the R space is 1.2–3.5 Å. (e) DFT-optimized structure of the bpy-Fe$(OH)_3(H_2O)$ moiety within bpy-UiO-Fe MOFs. The bond distances are in Å. (f) k^2-weighted Fe-EXAFS (R) spectra of bpy-UiO-Fe$(OH)_2$ (black), Fe foil (red), Fe_2O_3 (green), and $FeCl_2$ (blue).

temperature, and the benzene/H_2O_2 molar ratio. In addition, several control experiments were conducted to identify the true catalytic species. First, radical trap experiments were carried out to investigate any role of the $^{\cdot}$OH in bpy-UiO-Fe$(OH)_2$-catalyzed hydroxylation of benzene using H_2O_2. The conversion of benzene to phenol significantly dropped in the presence of Na_2SO_3, *t*-butanol, or isopropyl alcohol as the $^{\cdot}$OH scavenger,[22;73;74] suggesting that the in situ generated $^{\cdot}$OH radical is the key species for benzene hydroxylation (Table 6.1, entries 10-12).

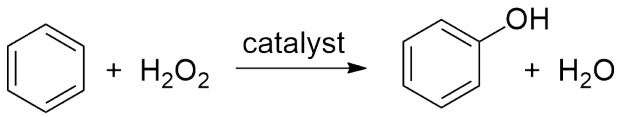
***Effect of Solvents*:**

The effect of different polar solvents was screened for bpy-UiO-Fe$(OH)_2$-catalyzed hydroxylation of benzene to phenol. Among all the solvents screened, a CH_3CN/water mixed solvent [1:1 (v/v)] gave the best performance with 88% conversion of benzene and a remarkable 99% selectivity toward phenol after 4 h reaction, while no conversion was observed when only CH_3CN was used as the solvent. The superior performance in this solvent mixture can be attributed to the fact that acetonitrile being less polar aids the overall dissolution of the reactant benzene, and water being more polar extracts the phenol formed. A similar beneficial effect of a mixed solvent has been observed previously in the benzene hydroxylation with H_2O_2 using other heterogeneous Fe catalysts and homogeneous-complexes.[24;75]

***Effect of Reaction Temperature*:**

To identify the lowest temperature that maximizes benzene conversion to phenol, the impact of the temperature was investigated within the range of 30-70 °C (Figure 6.3a). Analysis of the reaction temperature demonstrated a direct correlation between the conversion of benzene to phenol and temperature, reaching its

Table 6.1: Hydroxylation of Benzene into Phenol Using H_2O_2 as the Oxidant[a]



S. No.	Catalyst	Benzene conversion (%)[b]	Phenol:HQ:BQ
1	Bpy-UiO-Fe$(OH)_2$	88	>99:0:0.5
2	No catalyst	0	–
3[c]	Bpy-UiO-Fe$(OH)_2$	61	>99:0:0.2
4	Bpy-UiO-Fe$(OH)_3$	86	>99:0:0.4
5	Bpy-UiO	0	–
6	Bpy-UiO-$FeCl_2$	0	–
7	Bpy-Fe$(OH)_2$	32	74:16.4:9.6
8	Fe$(OH)_2$	19	57:34:9
9	Fe nanoparticles	0	–
10[d]	Bpy-UiO-Fe$(OH)_2$	24	>99:0:0.1
11[e]	Bpy-UiO-Fe$(OH)_2$	48	>99:0:0.5
12[f]	Bpy-UiO-Fe$(OH)_2$	33	>99:0:0.3

[a]Standard reaction conditions: catalyst (0.31 mol% Fe loading), benzene (3.372 mmol), H_2O_2 (5 equiv), 4 mL CH_3CN:water (1:1), 60 °C, 4 h.
[b]Analyzed by GC-FID using bromobenzene as internal standard.
[c]0.16 mol% Fe loading.
[d]Na_2SO_3 (10 mmol) used as radical scavenger.
[e]*t*-Butanol (10 mmol) used as radical scavenger.
[f]Isopropyl alcohol (10 mmol) used as radical scavenger.

peak at 60 °C. Elevating the reaction temperature allows facile diffusion of the benzene and H_2O_2 molecules through the channels of MOFs, thus boosting the rate of interactions between the Fe catalyst and substrates. However, the yield of phenol decreases above 70 °C, presumably due to the thermal decomposition of H_2O_2 into oxygen and water.

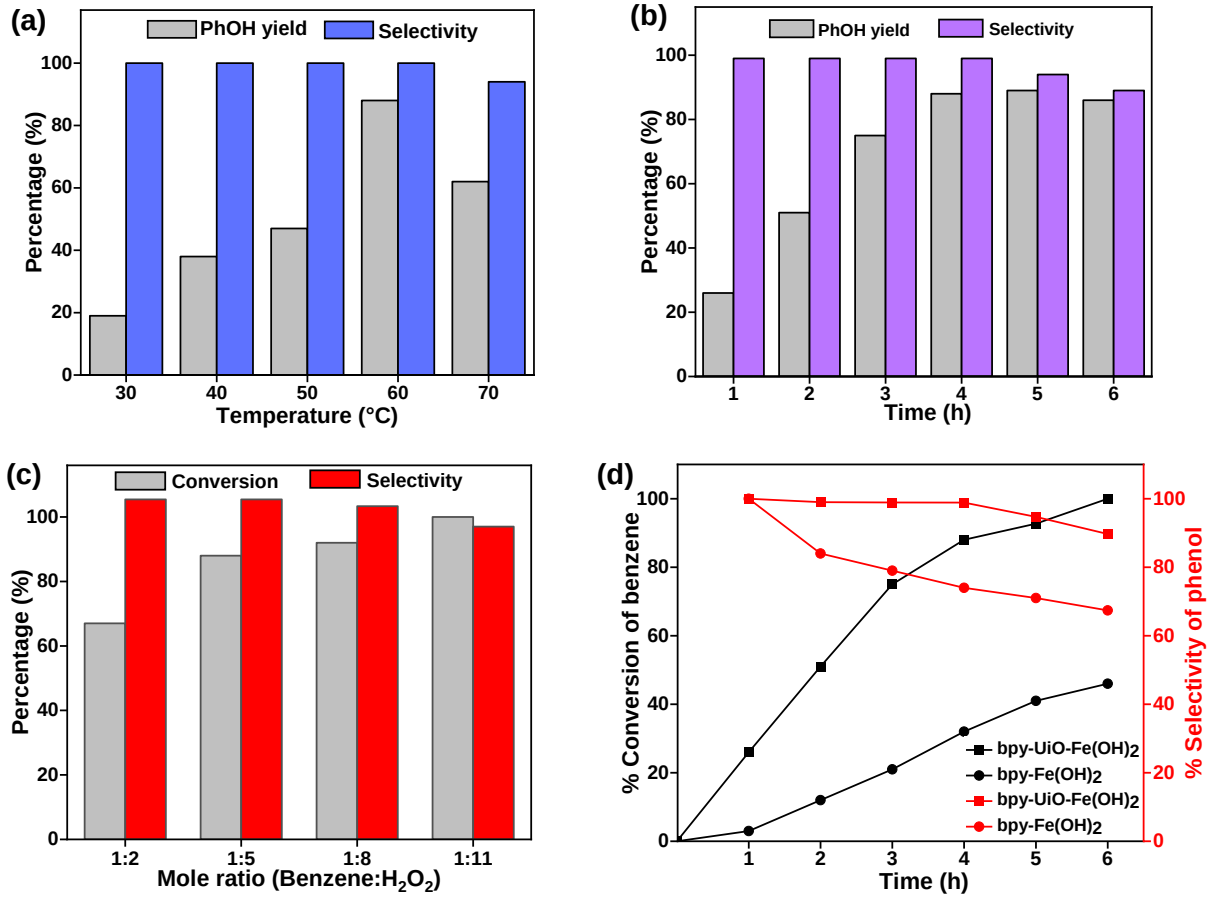


Figure 6.3: (a) Effect of temperature on % GC yield of PhOH and PhOH selectivity for bpy-UiO-Fe(OH)$_2$-catalyzed hydroxylation of benzene. Reaction conditions: benzene (0.3 mL, 3.37 mmol), bpy-UiO-Fe(OH)$_2$ (0.31 mol % Fe), mole ratio of benzene/H_2O_2 (1:5), water/CH_3CN [1:1, v/v, 4 mL], 4 h. (b) % GC yield of phenol and phenol selectivity with time plot for benzene hydroxylation. Reaction conditions: benzene (0.3 mL, 3.37 mmol), bpy-UiO-Fe(OH)$_2$ (0.31 mol %), mole ratio of benzene/H_2O_2 (1:5), water/CH_3CN [1:1, v/v, 4 mL], 60 °C. (c) Dependence of benzene conversion and phenol selectivity on the mole ratio of benzene/H_2O_2 catalyzed by bpy-UiO-Fe(OH)$_2$. Reaction conditions: benzene (0.3 mL, 3.37 mmol), bpy-UiO-Fe(OH)$_2$ (0.31 mol % Fe loading), water/CH_3CN [1:1, v/v, 4 mL], 60 °C, 4 h. (d) Comparison plot for catalytic activity and selectivity of bpy-UiO-Fe(OH)$_2$ and its homogeneous counterpart bpy-Fe(OH)$_2$.

***Effect of Reaction Time*:**

The impact of reaction time is a crucial parameter providing comprehensive insights into the catalytic performance of the catalyst. The influence of reaction time on benzene hydroxylation was assessed within 1-6 h (Figure 6.3b). The data obtained demonstrated a direct proportionality between phenol yield and reaction time. The highest phenol selectivity of 99% with a phenol yield of 88% was achieved after 4 h. Although the maximum phenol yield of 90% occurred after 5 h, phenol selectivity reduced to 94%.Further increasing the reaction time led to a slight decrease in the phenol yield due to the overoxidation of phenol into hydroquinone and benzoquinone as the secondary products.

***Effect of Benzene/H_2O_2 Molar Ratio*:**

To achieve a maximum yield of phenol using UiO-bpy-Fe(OH)$_2$ as a catalyst, we conducted careful adjustments to the benzene to hydrogen peroxide ratio, recognizing that an excessive amount of H_2O_2 could adversely affect the oxidation process. The impact of the benzene to H_2O_2 molar ratio on the hydroxylation of phenol was investigated in the range 1:3 - 1:12, as illustrated in Figure 6.3c. The yield of phenol increased upon increasing the benzene to H_2O_2 molar ratio, reaching its climax at the molar ratio of 1:5 with a H_2O_2 utilization efficiency of 18.6% with phenol selectivity >99%. Beyond this ratio with a higher proportion of H_2O_2, the yield of phenol started declining. When the benzene/H_2O_2 ratio is reduced to 1:3, the H_2O_2 efficiency significantly increases to 33.5% with a relatively lower benzene conversion. The increase in the phenol yield with an elevated benzene/hydrogen peroxide molar ratio is attributed to the presence of a significant amount of H_2O_2 (Figure 6.3c), leading to a greater production of hydroxyl radicals. Employing a molar ratio of 1:8 or higher for benzene to H_2O_2 resulted in the overoxidation of phenol into hydroquinone and benzoquinone. Under the optimized reaction conditions of 10 mg of bpy-UiO-Fe(OH)$_2$ (6.9 μmol of Fe) at 60 °C for 4 h, 2.96 mmol of phenol was afforded in 99% selectivity with a productivity of 1261 $mmol_{PhOH}$ g_{Fe}^{-1} h^{-1} (entry 1, Table 6.1).

6.2.3 Control Experiments

Several control experiments were conducted to elucidate the actual catalytic species in bpy-UiO-Fe(OH)$_2$-catalyzed hydroxylation of benzene to phenol. Reactions (a) without the bpy-UiO-Fe(OH)$_2$ catalyst (entry 2, Table 6.1), (b) with the pristine bpy-UiO MOF (entry 5, Table 6.1), (c) with bpy-UiO-$FeCl_2$ (entry 6, Table 6.1), and (d) Fe nanoparticles (entry 9, Table 6.1) all yielded a negligible quantity of phenol, confirming that bpy-UiO-Fe(OH)$_2$ is the active catalyst for benzene hydroxylation. The hydroxylation of benzene stopped when the solid bpy-UiO-Fe MOF was removed from the reaction mixture, thereby confirming that the active catalytic species was embedded within the MOF solid (Figure 6.9). Bpy-UiO-Fe could be recycled and reused at least three times without any significant loss in its activity

or selectivity for phenol in benzene hydroxylation, demonstrating the robustness and heterogeneity of the MOF catalyst. The percentage of leached Fe or Zr into the supernatant after the first run was 0.03 and 0.8%, respectively, and 0.07 and 1.2%, respectively, after the second run, as analyzed by ICP-OES. Importantly, bpy-UiO-Fe$(OH)_2$ is 2.5 times more active and significantly more selective than its homogeneous counterpart, bipyridine-Fe$(OH)_2$. The time evolution plot of bpy-UiO-Fe$(OH)_2$ (0.31% Fe-loading)-catalyzed benzene hydroxylation showed a linear production of phenol with 99% selectivity with time until the complete conversion of benzene in 4 h. In contrast, under identical reaction conditions and Fe-loading, bipyridine-Fe$(OH)_2$ gave phenol in only 24% yield in 4 h with 74% selectivity (Figure 6.3d). This enhanced catalytic activity of bpy-UiO-Fe$(OH)_2$ over its homogeneous control is attributed to the active site isolation of the bpy-Fe$(OH)_2$ moiety by the solid MOF that prevents intermolecular decomposition. Moreover, the exceptional selectivity of bpy-UiO-Fe$(OH)_2$ in benzene to phenol conversion originated via shape-selective catalysis, where the confined reaction space within the porous MOF prevents the formation of larger overoxidized products such as benzoquinone or hydroquinone, leading to the formation of only the smaller-sized monohydroxylated product, phenol.

6.2.4 Mechanism Exploration of Bpy-UiO-Fe$(OH)_2$-Catalyzed Oxidation of Benzene

We next investigated the mechanism of bpy-UiO-Fe$(OH)_2$-catalyzed benzene hydroxylation by characterizing the catalyst after catalysis, identifying reaction intermediates, and computational studies. The PXRD pattern of the recovered bpy-UiO-Fe MOF after catalysis suggests that the structure and crystallinity of the MOF remained unchanged during catalysis (Figure 6.1b). In addition, the absence of any characteristic peak of metallic iron at a higher 2θ angle in the same PXRD pattern indicates that Fe nanoparticles or metallic Fe particulates did not form during the oxidation reaction (Figure 6.1b). Furthermore, the k^2-weighted wavelet transform of Fe foil exhibited Fe–Fe scattering at a k-value of 7.8 Å^{-1}, which is absent in the wavelet-transformed plots of both bpy-UiO-Fe$(OH)_2$ and recovered bpy-UiO-Fe after catalysis. The only significant scattering of MOFs was observed at ∼4.2 Å^{-1}, which is attributed to single scattering from the Fe-O/N paths. The EXAFS features and wavelet transform plot suggest that Fe nanoparticles and any iron oxides were not formed during catalysis. The pre-edge energy of Fe within the recovered bpy-UiO-Fe at 7116 eV in the XANES spectrum suggests the formation of a Fe^{3+} species after catalysis (Figure 6.2a). The presence of the Fe^{3+} ion in the recovered bpy-UiO-Fe MOF after catalysis is also corroborated by the Fe 2p XPS spectrum, displaying Fe $2p_{3/2}$ and $2p_{1/2}$ binding energy peaks at 711.9 and 725.5 eV, respectively (Figure 6.1e). The X-band EPR spectrum of bpy-UiO-Fe MOF after catalysis reveals a broad signal centered at g = 2.025 (Figure 6.1g), which closely resembles a free electron (g_e = 2.0023), suggesting an octahedral and high-spin Fe^{3+} species with low magnetic anisotropy.[72;76] The analysis of Fe-K edge EXAFS data of the recovered bpy-UiO-Fe after catalysis suggests the existence of (bpy)$Fe^{III}(OH)_3(OH_2)$ species within the

MOF, in which a Fe^{3+} ion octahedrally coordinated with two nitrogens of bipyridine, three OH groups, and one water molecule (Figure 6.2d). Importantly, UiO-MOF-supported (bpy)$Fe^{III}(OH)_3(OH_2)$ [bpy-UiO-$Fe^{III}(OH)_3$] synthesized via postsynthetic metalation of bpy-UiO MOF with a Fe precursor, exhibited similar catalytic activity and selectivity compared to bpy-UiO-$Fe^{II}(OH)_2$ (entry 4, Table 6.1), indicating bpy-UiO-$Fe^{III}(OH)_3$ as the catalytic intermediate as well as the catalyst resting state in benzene hydroxylation. The EPR spectrum of a mixture of bpy-UiO-Fe$(OH)_2$ and H_2O_2 along with 5,5′-dimethyl-1-pyrroline-N-oxide as a radical trapping agent in H_2O at room temperature displayed a $^{\cdot}OH$ radical signal, suggesting bpy-UiO-Fe$(OH)_2$-mediated $^{\cdot}OH$ radical generation from H_2O_2.[24;25;77] $^{\cdot}OH$ signals were also observed in the EPR spectrum of the reaction mixture after catalysis. However, no $^{\cdot}OH$ signals were detected in the reaction mixture without the MOF catalyst, suggesting the involvement of $^{\cdot}OH$ in the benzene hydroxylation (Figure 6.4). During the reaction, in situ X-band EPR spectroscopy was employed on the MOF, showing no discernible Fe(IV) peak with g-values at 8.19 and 4.06, effectively excluding the possibility of Fe(IV) formation as an intermediate species.[78;79]

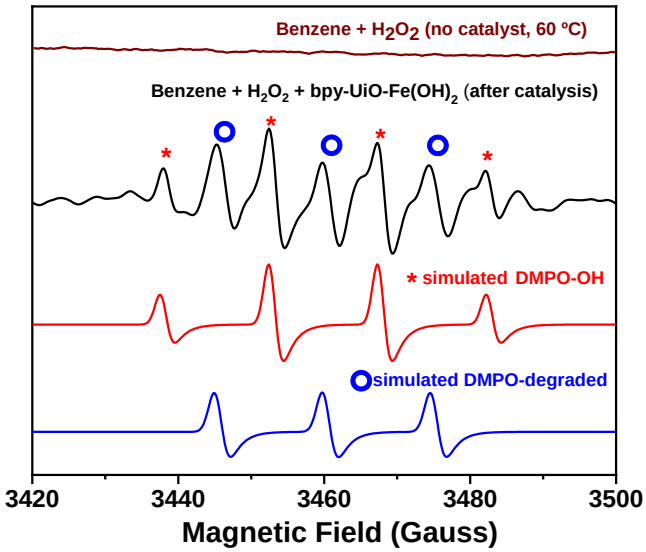


Figure 6.4: X-band (9.85 GHz) EPR spectroscopic spin-trapping experiments. The EPR spectrum from DMPO spin-trapping experiment of uncatalyzed benzene hydroxylation by H_2O_2 at 60 °C (wine), bpy-UiO-Fe$(OH)_2$-catalyzed oxidation of benzene by H_2O_2 at 60 °C for 4 h (black), simulated DMPO-OH (red), and simulated DMPO-degraded adducts during the reaction (blue).

Based on the above spectroscopic data and control experiments, we propose a radical mechanism for bpy-UiO-Fe$(OH)_2$-mediated benzene to phenol conversion.[14;22–25;73;80] The coordination of H_2O_2 to the Fe^{2+} ion of bpy-UiO-Fe$(OH)_2$ forms INT-1, which subsequently transforms into bpy-UiO-$Fe^{III}(OH)_3$ (INT-2) with generation of the $^{\cdot}OH$ radical. Then, the $^{\cdot}OH$ radical reacts with the benzene C-H bond and generates the benzene-OH radical adduct, which further interacts with bpy-UiO-Fe$(OH)_3$ (INT-2) to yield INT-3. INT-2 is

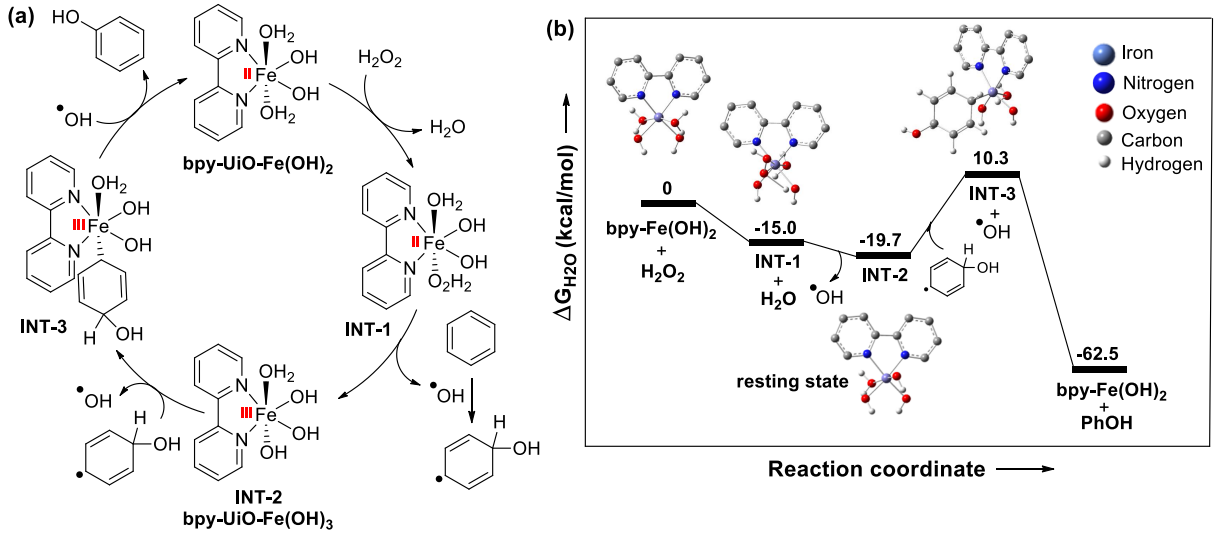


Figure 6.5: (a) Proposed catalytic cycle of bpy-UiO-Fe-catalyzed selective benzene oxidation to phenol. (b) DFT-calculated free energy diagram at 333.15 K for bpy-UiO-Fe-catalyzed benzene to phenol conversion.

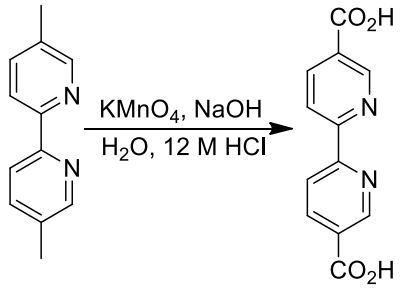
transformed into INT-3 by liberation of a ·OH. The ·OH then abstracts a hydrogen atom of the benzene-OH adduct in INT-3, resulting in the release of H_2O and phenol as products and regenerate the bpy-UiO-Fe$(OH)_2$ catalyst. To gain deeper insights into the reaction pathway, we computed the whole catalytic cycle by DFT using the B3LYP/D3 method and a def2-TZVP basis set on Gaussian 16 software (Figure 6.5). Geometry optimization was completed for all of the considered spin states. DFT-calculated free energy diagram at 333.15 K for bpy-UiO-Fe-catalyzed benzene to phenol conversion revealed that the coordination of H_2O_2 with the bpy-UiO-Fe$(OH)_2$ MOF is energetically favorable by 15.03 kcal/mol.

6.3 Experimental Section

6.3.1 Synthesis and Characterization of Bpy-UiO-Fe MOF

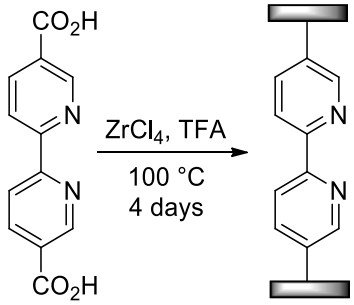
Synthesis of [2,2′-bipyridine]-5,5′-dicarboxylic acid.

[2,2′-bipyridine]-5,5′-dicarboxylic acid was synthesised by a modified reported procedure.[80] 5,5′-Dimethyl-2,2′-bipyridyl (0.500 g, 2.74 mmol), NaOH (0.030 g, 0.75 mmol), and deionized water (12 mL) were placed in a round-bottom flask. The mixture was stirred at 70 °C. Then 1.48 g of NaOH (0.037 mol) was added slowly into the mixture (pH = 12). The resulting



mixture became clear. After 1 hour of stirring, finely powdered $KMnO_4$ (2.140 g, 0.0135 mol) was added into the flask in small portions and was kept overnight at 90 °C. The mixture was cooled at room temperature and filtered. The filtrate was acidified with 12 M HCl. White solid obtained from the resulting mixture after 10 h is analyzed by ^{1}H NMR. ^{1}H NMR (500 MHz, DMSO-d_6): δ 13.52 (s, 2 H), 9.20 (s, 2 H), 8.58 (d, $^3J_{\text{H-H}}$ = 8.8 Hz, 2 H), 8.46 (d, $^3J_{\text{H-H}}$ = 8.4 Hz, 2 H).[81]

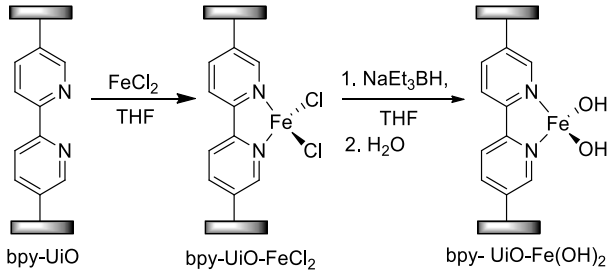
Synthesis of Bpy-UiO.



[2,2′-bipyridine]-5,5′-dicarboxylic acid (0.027 g, 0.111 mmol) and $ZrCl_4$ (0.026 g, 0.112 mmol) were dissolved in 13 mL DMF. After sonication for 30 minutes, TFA (0.040 mL, 0.523 mmol) was added, and the resultant mixture was heated in a sealed 15 mL glass vial at 100 °C for 4 days in an oven.[82] The reaction mixture was allowed to cool at room temperature, and the white crystalline solid was isolated after centrifugation. The MOF was washed with DMF multiple times, followed by THF and stored in THF at room temperature.

Synthesis of Bpy-UiO-Fe(OH)$_2$.

A solution of $FeCl_2$ (0.003 g, 0.024 mmol) in THF was added to bpy-UiO MOF and kept overnight with periodic shaking at room temperature inside the glovebox. The purple solid was centrifuged out of solution and washed 8-10 times with THF to give bpy-UiO-$FeCl_2$



MOF. Bpy-UiO-$FeCl_2$ ($Zr_6C_{72}H_{40}N_{12}O_{32}Fe_{2.4}Cl_{4.8}$) has 40% Fe-loading with respect to bpy moiety as analyzed by ICP-OES.

$NaEt_3BH$ (35 μL, 1 M in toluene) was added dropwise to the vial containing slurry of bpy-UiO-$FeCl_2$ (0.016 g, 0.006 mmol) in 3 mL THF inside the glovebox and was kept at room temperature for 1 h. The resultant dark green solid of bpy-UiO-FeH_2 was separated via centrifugation and washed several times with THF to remove excess $NaEt_3BH$. Bpy-UiO-FeH_2 was taken out of the glovebox and was kept in water for 30 minutes to afford bpy-UiO-$Fe(OH)_2$. The bpy-UiO-$Fe(OH)_2$ has 49% solvent weight analysed by thermogravimetric analysis and 40% iron loading with respect to bpy-moiety as analyzed by ICP-OES, with the formula $Zr_6C_{72}H_{44.8}N_{12}O_{36.8}Fe_{2.4}$.

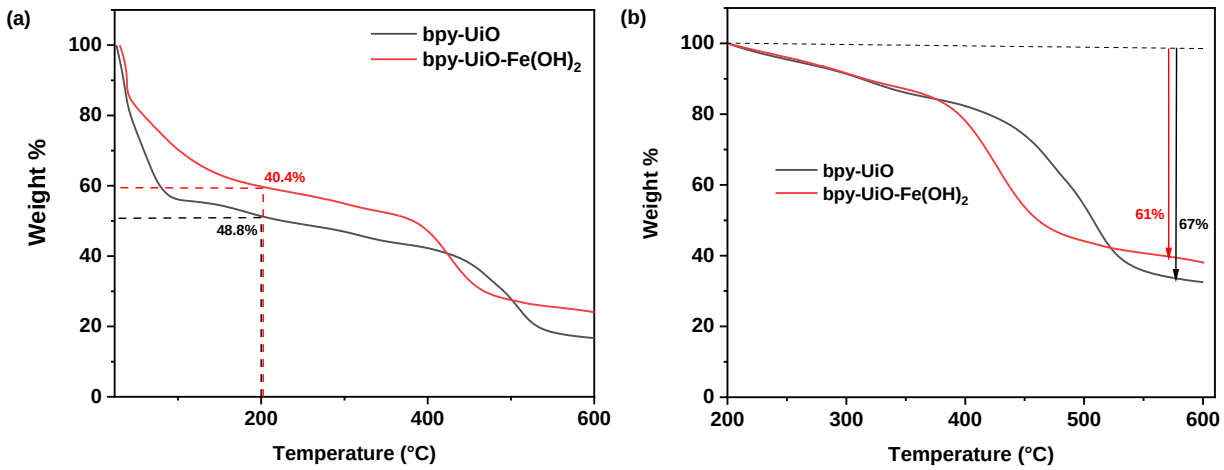


Figure 6.6: (a) TGA curve of freshly prepared bpy-UiO and bpy-UiO-$Fe(OH)_2$. A solvent weight loss, attributed to THF within the pores, of 48.8% in bpy-UiO (black) and 40.4% in bpy-UiO-$Fe(OH)_2$ (red) was observed from 40 °C to 200 °C. (b) TGA curve of freshly prepared bpy-UiO (black) and bpy-UiO-Fe (red) from 200-600 °C. The increased weight of metalated MOF is due to the presence of iron within the MOF.

Table 6.2: Determination of defect sites in bpy-UiO and bpy-UiO-Fe(OH)$_2$ MOF by TGA analysis.

		% Solvnet	**% Linker**	**% Residue**
Bpy-UiO	Calculated	-	68	32
	TGA	49	27	17
	Corrected	-	67	33
Bpy-UiO-Fe(OH)$_2$(40 % Fe-loading)	Calculated	-	62	38
	TGA	40	36	24
	Corrected	-	61	39

Theoretical Calculation

(a) For bpy-UiO with formula [$Zr_6O_4(OH)_4(bpy)_6$]:

$$1 \text{ mole of bpy-UiO} = 6 \text{ moles linker } (C_{12}H_6N_2O_4)$$

$$2132.5 \text{ g of } Zr_6O_4(OH)_4(bpy)_6 = 1453.12 \text{ g linker}$$

$$\% \text{ Linker} = \left(\frac{1453.12}{2132.5}\right) \times 100 = 68\%$$

$$\% \text{ Residue} = 100 - 68 = 32\%$$

(b) For bpy-UiO-Fe(OH)$_2$ with formula [$Zr_6C_{72}H_{44.8}N_{12}O_{36.8}Fe_{2.4}$]:

$$1 \text{ mole of bpy-UiO-Fe(OH)}_2 = 6 \text{ moles linker } (C_{12}H_6N_2O_4)$$

$$2348.2 \text{ g of } Zr_6O_4(OH)_4(bpy)_6 = 1453.12 \text{ g linker}$$

$$\% \text{ Linker} = \left(\frac{1453.12}{2348.2}\right) \times 100 = 62\%$$

$$\% \text{ Residue} = 100 - 62 = 38\%$$

6.3.2 Bpy-UiO-Fe catalyzed hydroxylation of benzene

Typical procedure for Bpy-UiO-Fe catalyzed oxidation of benzene to phneol using H_2O_2.

Solid bpy-UiO-Fe(OH)$_2$ (0.31 mol% Fe) in 4 mL solvent was transferred into a 25 mL Schlenk tube placed in an oil bath at 60 °C and equipped with a water-cooled condenser. Then 30% H_2O_2 (5 eq.) in water along with benzene (300 μL, 3.372 mmol) was added dropwise. After the reaction was completed, the solid MOF was centrifuged out of the suspension, followed by several washing with acetonitrile (CH_3CN) and can be reused. The remaining organic extract were concentrated in vacuo to yield phenol as the pure product

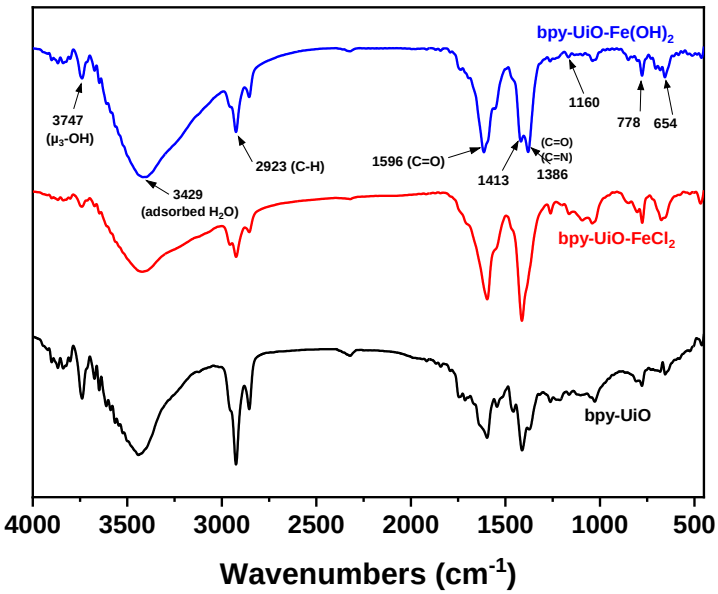


Figure 6.7: IR spectra (KBr) of freshly prepared bpy-UiO (black), bpy-UiO-$FeCl_2$ (red), and bpy-UiO-$Fe(OH)_2$ (blue).

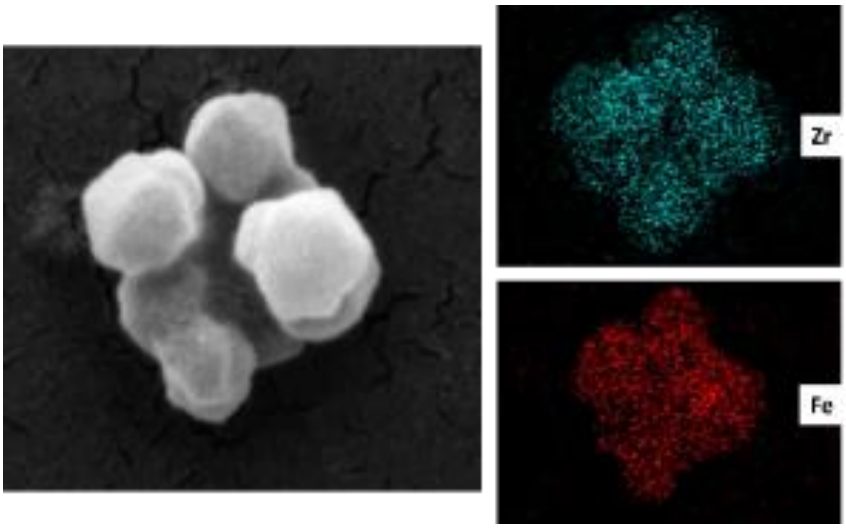
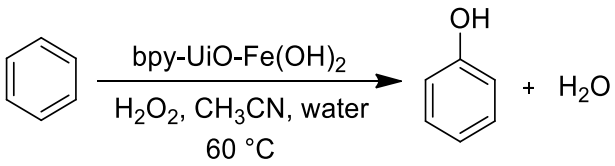


Figure 6.8: SEM image of bpy-UiO-$Fe(OH)_2$ particles, and the SEM-EDX mapping of Fe and Zr of the respective particles. The uniform distribution of Fe and Zr suggests Fe and Zr are homogeneously distributed throughout the MOF.



Effect of mole ratio (benzene:H_2O_2) variation on the % conversion, % phenol selectivity and H_2O_2 efficiency.

~~Solid bpy-UiO-$Fe(OH)_2$ (0.31 mol% Fe) in 4 mL mixture of CH_3CN and water (1:1) was~~ transferred into a 25 mL Schlenk tube placed in an oil bath at 60 °C and equipped with a

water-cooled condenser. Then 30% H_2O_2 in water (2, 5, 8, 11 eq.) along with benzene (300 μL, 3.372 mmol) was added dropwise. After 4 h, the solid MOF was centrifuged out of the suspension, followed by several washing with CH_3CN and can be reused. The remaining organic extract were concentrated in vacuo and analysed by GC-FID. Hydroquinone and benzoquinone were obtained as the side products in case of benzene:H_2O_2 molar ratios of 1:8 and 1:11 resulting in lower phenol selectivity of 98% and 92% respectively.

% conversion with time for benzene hydroxylation to phenol catalyzed by bpy-UiO-Fe(OH)$_2$

Solid bpy-UiO-Fe(OH)$_2$ (0.31 mol% Fe) in a 4 mL mixture of CH_3CN and water (1:1) was transferred into a 25 mL Schlenk tube placed in an oil bath at 60 °C and equipped with a water-cooled condenser. Then, 30% H_2O_2 in water (5 equiv) along with benzene (300 μL, 3.372 mmol) was added dropwise. Reactions were analyzed at different times using GC-FID, and it was observed that the % conversion increased with time, reaching a maximum of 88% after 4 h. Upon further increasing the reaction time, the % conversion remained nearly constant with a slight decrease in selectivity.

Effect of temperature on % conversion and phenol selectivity for bpy-UiO-Fe(OH)$_2$ catalyzed selective hydroxylation of benzene to phenol.

Solid bpy-UiO-Fe(OH)$_2$ (0.31 mol% Fe) in 4 mL mixture of CH_3CN and water (1:1) was transferred into a 25 mL Schlenk tube placed in an oil bath at different temperatures (30, 40, 50, 60 and 70 °C) and equipped with a water-cooled condenser. Then 30% H_2O_2 in water (5 eq.) along with benzene (300 μL, 3.372 mmol) was added dropwise. After 4 h, the solid MOF was centrifuged out of the suspension, followed by several washing with CH_3CN and can be reused. The remaining organic extract were concentrated in vacuo and analysed by GC-FID.

6.3.3 Catalytic testing of Fe nanoparticles.

A 3 mL THF solution of $FeCl_2$. (0.7 mg, 0.31 mol% Fe) was first treated with $NaEt_3BH$ (200 μL, 1 M in toluene) for 1 h. Fe nanoparticles settled down as black solid, was centrifuged

out and washed with THF multiple times, followed by CH_3CN. Fe nanoparticles were then used to setup the reaction. In a Schlenk tube, Fe nanoparticles were added along with 4 mL water and CH_3CN (1:1) and the Schlenk tube was placed in an oil bath at 60 °C and equipped with a water-cooled reflux condenser. Then 300 μL of benzene (3.372 mmol) and 5 eq. of H_2O_2 were added. After 4 h, reaction mixture was filtered to separate the solid nanoparticles and the solution was analysed by GC-FID.

6.3.4 Test for "heterogeneity of bpy-UiO-Fe(OH)$_2$ in benzene hydroxylation to phenol.

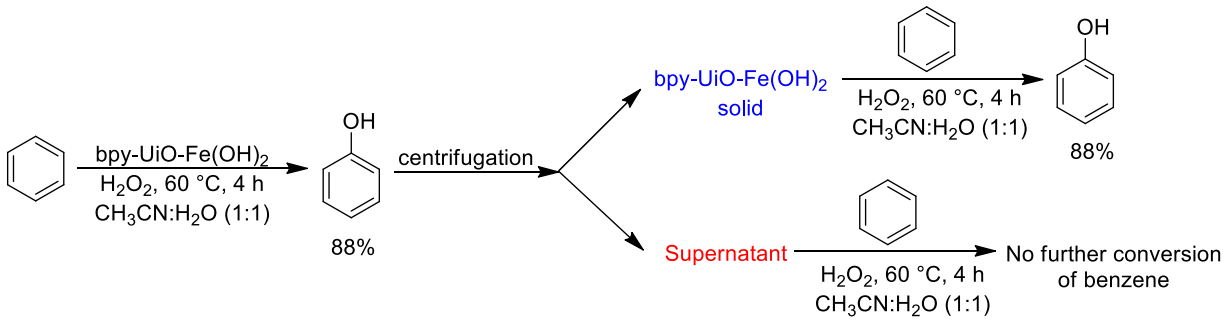


Figure 6.9: Test for "heterogeneity of bpy-UiO-Fe(OH)$_2$ in benzene hydroxylation to phenol. Bpy-UiO-Fe(OH)$_2$ (0.31 mol% Fe) in 4 mL of CH_3CN and water (1:1) was transferred into a 25 mL Schlenk tube. The Schlenk tube was placed in oil bath at temperature of 60 °C and equipped with a water-cooled reflux condenser. To the mixture, benzene (300 μL, 3.37 mmol) was added. Then H_2O_2 (5 eq.) was added dropwise for 4 h. After the reaction was completed, the solid MOF was removed from suspension to separate the solid and the supernatant and washed with CH_3CN multiple times. The conversion analysed by taking aliquots from the supernatant gave 88% phenol.

Two reactions were set up separately in two different Schlenk tubes, one with the solid and the other one with the supernatant recovered from the previous reaction. The extracted solid and supernatant were added into two separate tubes, both the Schlenk tubes were placed in oil bath at temperature of 60 °C and equipped with a water-cooled reflux condenser and benzene (300 μL, 3.37 mmol), 5 eq. H_2O_2, and 4 mL of CH_3CN and water (1:1) were added

to each tube. After 4 h, the reactions were analysed with the GC-FID, which showed that the reaction with the solid MOF gave 88% yield, while the reaction with supernatant gave no further conversion of benzene into phenol. This experiment excludes the potential of any leached Fe-species responsible for catalysis and confirms that solid bpy-UiO-Fe(OH)$_2$ was the actual catalyst for the oxidation of benzene.

6.3.5 Radical Scavenging Experiment.

To investigate the role of any $^{\cdot}$OH in the bpy-UiO-Fe(OH)$_2$ catalysed selective hydroxylation of benzene, catalysis have been performed in the presence of radical scavengers such as Na_2SO_3, *tert*-butyl alcohol (TBA) and isopropyl alcohol (IPA).

Radical scavenging experiment using Na_2SO_3 as the radical scavenger.

Solid bpy-UiO-Fe(OH)$_2$ (0.31 mol% Fe) in 4 mL solvent was transferred into a 25 mL Schlenk tube placed in an oil bath at 60 °C and equipped with a water-cooled condenser. Then, 10 mmol of Na_2SO_3 was added as the radical scavenger, followed by 30% H_2O_2 (5 eq.) in water along with benzene (300 μL, 3.372 mmol). After 4 h, the solid MOF was centrifuged out of the suspension, and the solution was analysed by GC-FID.

Radical scavenging experiment using *tert*-butyl alcohol (TBA) as the radical scavenger.

Solid bpy-UiO-Fe(OH)$_2$ (0.31 mol% Fe) in 4 mL solvent was transferred into a 25 mL Schlenk tube placed in an oil bath at 60 °C and equipped with a water-cooled condenser. Then, 10 mmol of TBA was added as the radical scavenger, followed by 30% H_2O_2 (5 eq.) in water along with benzene (300 μL, 3.372 mmol). After 4 h, the solid MOF was centrifuged out of the suspension, and the solution was analysed by GC-FID.

Radical scavenging experiment using isopropyl alcohol (IPA) as the radical scavenger.

Solid bpy-UiO-Fe(OH)$_2$ (0.31 mol% Fe) in 4 mL solvent was transferred into a 25 mL Schlenk tube placed in an oil bath at 60 °C and equipped with a water-cooled condenser. Then, 10 mmol of IPA was added as the radical scavenger, followed by 30% H_2O_2 (5 eq.) in water along with benzene (300 μL, 3.372 mmol). After 4 h, the solid MOF was centrifuged out of the suspension, and the solution was analysed by GC-FID.

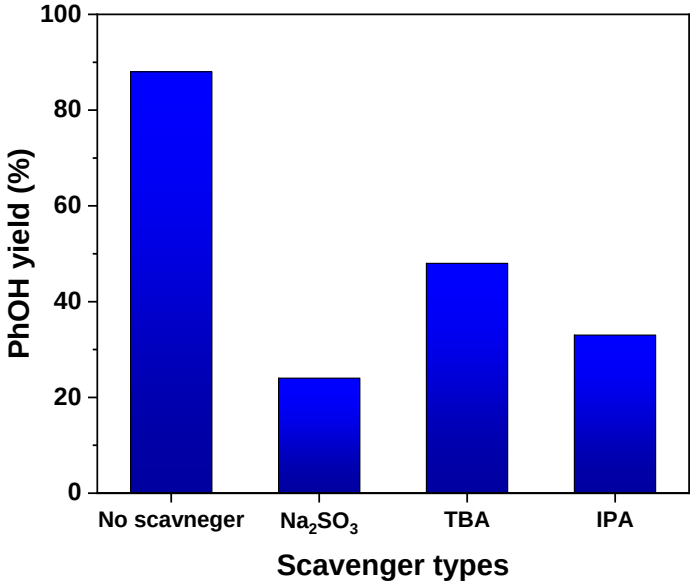


Figure 6.10: Radical scavenger tests. Reaction conditions: bpy-UiO-Fe(OH)$_2$ (0.31 mol% Fe), benzene (3.372 mmol), 60 °C, H_22O_2 (30%) (5 eq.), 4 mL water:CH_3CN (1:1), trapping agent (10 mmol).

Table 6.3: Simulated parameters of EPR spectroscopic spin-trapping experiments for bpy-UiO-Fe(OH)$_2$ catalysed oxidation of benzene.[24;25;83]

Adducts	**g-factor**	**A^{14}N (G)**	**A$^{\alpha}$N (G)**	**lw (mt)[a]**
DMPO-OH	2.001	14.9	14.9	1.6
DMPO$_{\text{degraded}}$	2.001	14.8	-	1.8

[a]The linewidth (lw, in mT) defines the FWHM (full width at half height) of the absorption Gaussian (first number).

We conclude that the presence of the radical scavenger (Na_2SO_3, TBA, IPA) drastically decrease the rate of the oxidation of benzene to phenol catalysed by bpy-UiO-Fe(OH)$_2$, which illustrates that $^{\cdot}$OH radicals plays a vital role in the mechanistic pathway.

6.3.6 DFT Calculations

All quantum chemical calculations were done using the density functional theory (DFT) functional B3LYP-D3/def2-TZVP as implemented in the Gaussian 16 software suite.[84–88] Electronic structure complexes were optimized at the unrestricted level. Dispersion interactions were considered by incorporating the D3 scheme of Grimme.[89] All calculations were performed in the solvated state and at 333.15 K. We used the Polarizable Continuum Model (PCM) using the integral equation formalism variant (IEFPCM) as the default SCRF method by using CH_3CN as the solvent in this DFT calculation. Each structure was first optimized, and then frequency calculation was performed to confirm its geometry and to obtain the thermochemical data. Bpy-UiO-Fe$(OH)_2$ was calculated with zero, one, and two H_2O molecule coordinated to Fe. Internal energies were compared directly after accounting for the difference in the number of coordinated H_2O molecules. To reduce the computational costs, a simplified bipyridyl ligand was used in these calculations.

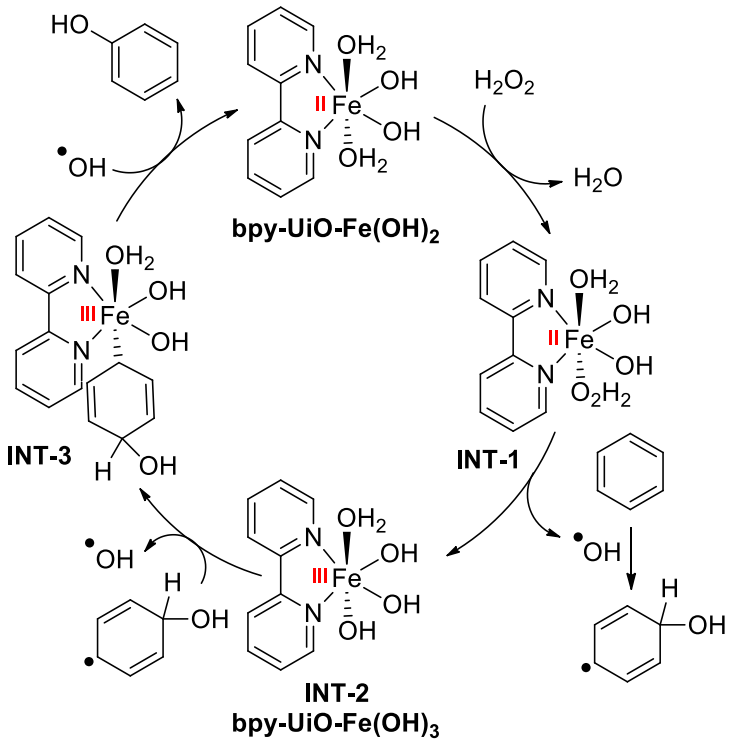


Figure 6.11: Proposed catalytic cycle of bpy-UiO-Fe-catalyzed selective benzene oxidation to phenol.

Table 6.4: Relative energies of the structures in different spin states. All structures are geometry optimized.

		S=0	**S=1/2**	**S=1**	**S=3/2**	**S=2**	**S=5/2**
	O.S.	singlet	doublet	triplet	quartet	quintet	sextet
bpy-Fe(OH)$_2$	Fe (II)	25.32		3.23		0.00	
INT-1	Fe (II)	8.22		-10.73		-15.03	
INT-2	Fe (III)		2.84		-10.92		-19.72
INT-3	Fe (III)		20.95		22.72		10.31

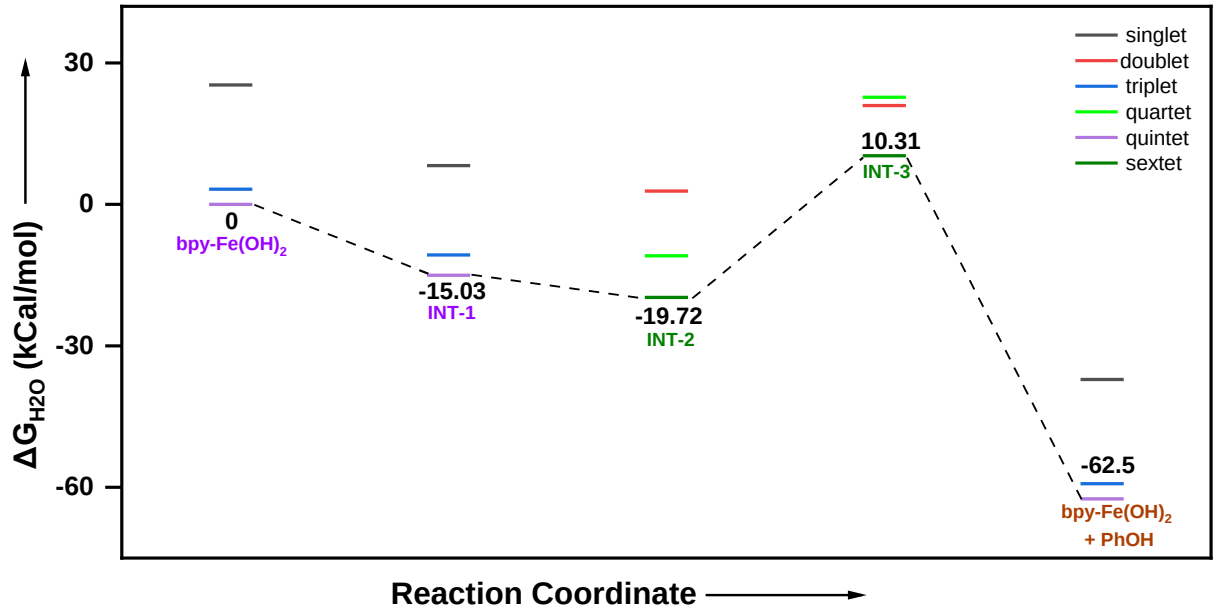
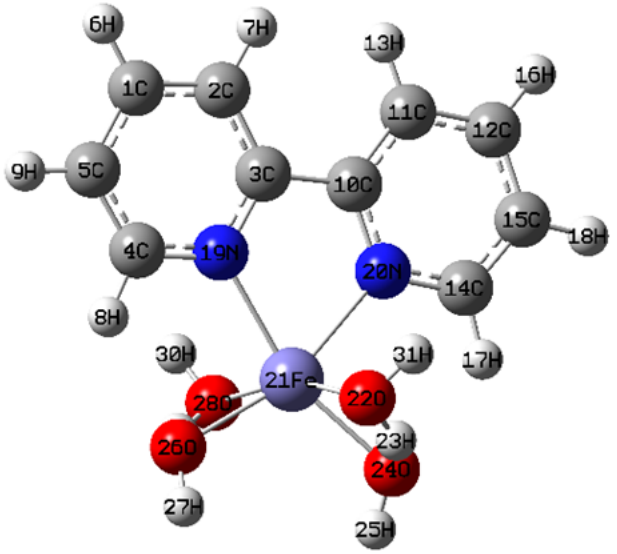
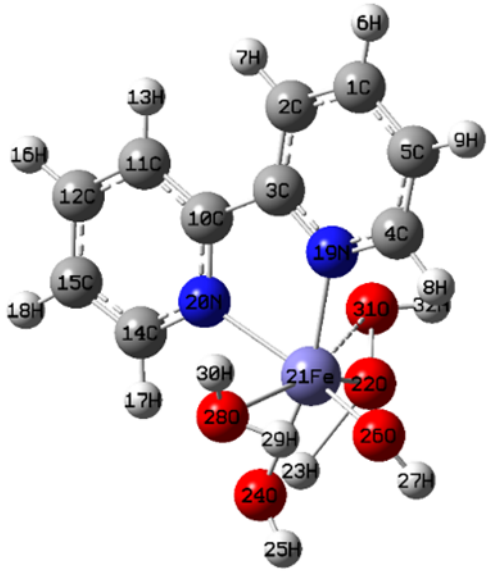


Figure 6.12: DFT-calculated free energy diagram of benzene oxidation to phenol over bpy-UiO-Fe(OH)$_2$ at 333 K.

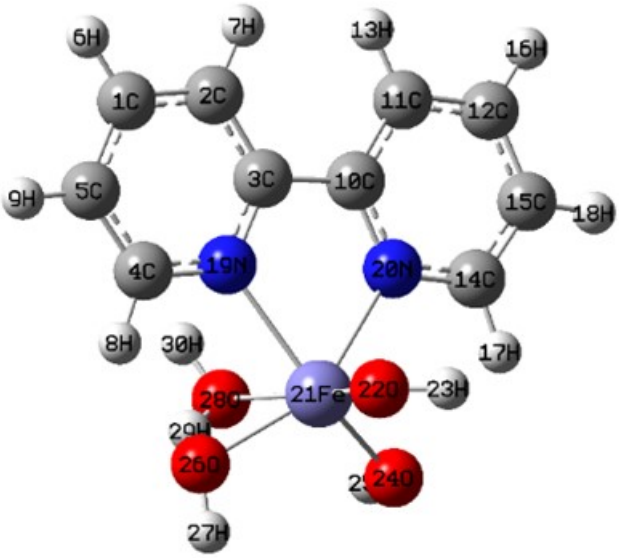
In bpy-Fe(OH)$_2$ and INT-1, according to the DFT calculations, the most stable spin state for Fe(II) is predicted to be quintet (S=2) as indicated in Table 6.4. The singlet spin state for these structures are higher in energy. On the other hand, in INT-2 and INT-3, where Fe is in +3 oxidation state, the sextet is the most stable spin state. To further verify the validity of these spin states for the various intermediates involved in the mechanism, we computed the relative energies for all possible spin states, which are provided in Table 6.4.



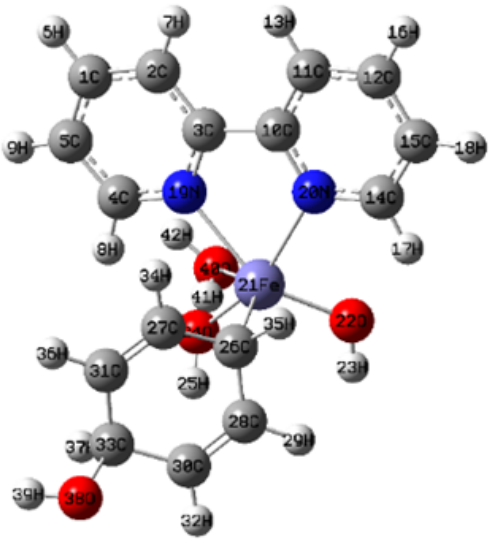
Bpy-UiO-Fe(OH)$_2$



INT-1



Bpy-UiO-Fe(OH)$_3$ (INT-2)



INT-3

Figure 6.13: DFT-optimized structures of intermediates for bpy-UiO-Fe(OH)$_2$ catalyzed oxidation of benzene to phenol.

6.3.7 X-ray absorption spectroscopic analysis (XAS)

X-ray Near-Edge Structure (XANES) and Extended X-ray Absorption Fine Structure (EXAFS) measurements have been carried out at the Energy-Scanning EXAFS beamline (BL-9) at the Indus-2 Synchrotron Source at Raja Ramanna Centre for Advanced Technology (RRCAT), Indore, India.[90] All the measurements were performed at room temperature. This beamline operates in the energy range of 4 keV to 25 keV. The beamline optics consist of a Rh/Pt coated collimating meridional cylindrical mirror and the collimated beam reflected by the mirror is monochromatized by a Si (111) based double crystal monochromator (DCM). The second crystal of the DCM is a sagittal cylindrical crystal which is used for horizontal focusing of the beam while another Rh/Pt coated bendable post mirror facing downward is used for vertical focusing of the beam at the sample position. Two ionization chambers (300 mm length each) have been used for data collection in the transmission mode; one ionization chamber for measuring incident flux, the second one for measuring transmitted flux. For energy calibration, standard metal foils were used. Appropriate gas pressure and gas mixture have been chosen to achieve 10-20% absorption in the first ionization chamber and 70-90% absorption in the second ionization chamber to obtain a better signal-to-noise ratio. Pellets were made from powder samples for recording absorption spectra. Sample powder was mixed homogeneously with cellulose powder in appropriate proportion and pressed (2 Ton) into a 15 mm diameter disc. The amount of the sample was estimated such that to get a reasonable edge jump at a particular absorption edge of the element to be probed. Spectra were collected at the iron K-edge in transmission mode and were calibrated against the reference spectrum of metallic iron (7112 eV). Data were processed using Demeter software.[91] A metallic iron foil standard was used as a reference for energy calibration and was measured simultaneously with experimental samples.

XANES analysis

The oxidation state of Fe within bpy-UiO-Fe(OH)$_2$were determined by comparison of its pre-edge position with that of $FeCl_2$. The position of the pre-edge of bpy-UiO-Fe(OH)$_2$ (7112.4 eV) aligned well with that of $FeCl_2$ (7112 eV) and position of pre-edge of bpy-UiO-Fe after oxidation of benzene aligned well with that of $Fe(OH)_3$ (7114 eV). We, therefore, concluded that Fe ion in bpy-UiO-Fe(OH)$_2$ and bpy-UiO-Fe after oxidation of benzene has +2

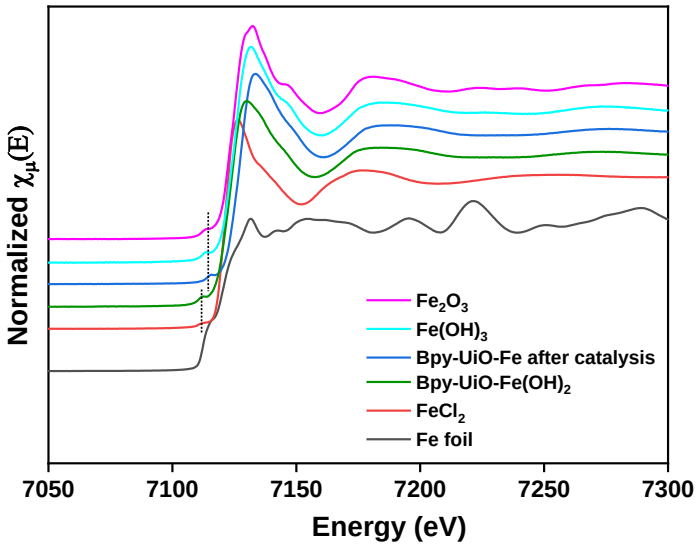
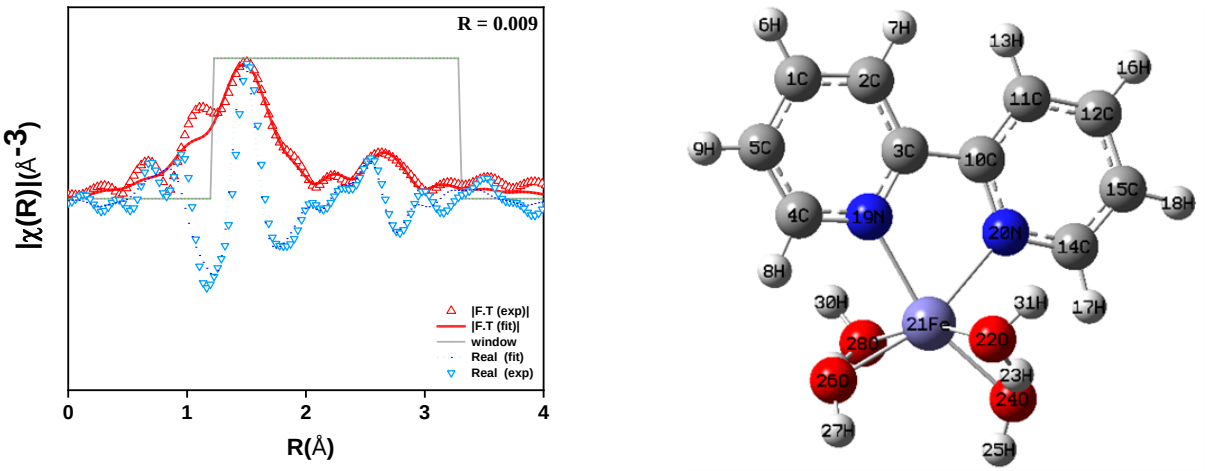


Figure 6.14: μ(E) XAS spectra of metallic Fe(0) foil (black), bpy-UiO-$Fe(OH)_2$ (green), bpy-UiO-Fe after catalysis of benzene oxidation to phenol (dark blue), Fe_2O_3 (magenta), $Fe(OH)_3$ (light blue) and $FeCl_2$ (red).

and +3 oxidation state, respectively. Furthermore, a smaller intensity of pre-edge indicates the presence of octahedral geometry.

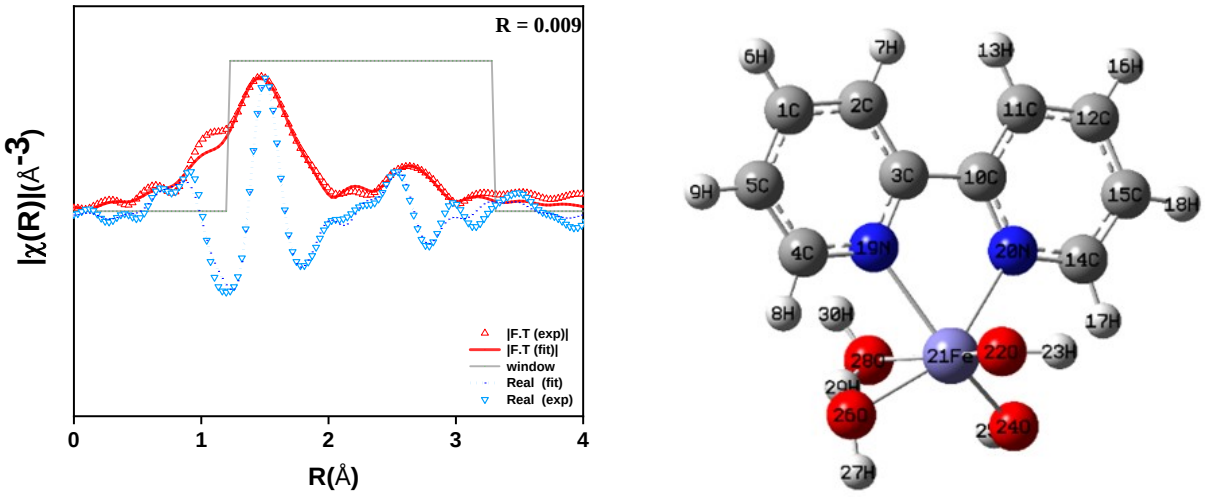
EXAFS fitting using DFT optimized structures.

The spectra were calibrated against the reference spectra and aligned to the first peak in the smoothed first derivative of the absorption spectrum, the background noise was removed, and the spectra were processed to obtain a normalized unit edge step. The fitting parameters of bpy-UiO-$Fe(OH)_2$, bpy-UiO-Fe after oxidation of benzene are summarized in Table 6.5 and Table 6.6, respectively.



(a) (b)

Figure 6.15: (a) EXAFS spectra (red and blue hollow triangles) and fits (red solid and blue dashed line) of bpy-UiO-Fe$(OH)_2(H_2O)_2$ in the R space from 1.2 to 3.5 Å. (b) DFT optimized structure of bpy-UiO-Fe$(OH)_2(H_2O)_2$



(a) (b)

Figure 6.16: (a) EXAFS spectra (green and brown hollow triangles) and fits (green solid and brown dashed line) of bpy-UiO-Fe$(OH)_3(H_2O)$ in the R space from 1.2 to 3.5 Å. (b) DFT optimized structure of bpy-UiO-Fe$(OH)_3(H_2O)$.

Table 6.5: Summary of EXAFS parameters of bpy-UiO-Fe$(OH)_2(H_2O)_2$.

Sample	**Bpy-UiO-Fe$(OH)_2(H_2O)_2$**	**Fitting range**	***k* (3-12.5 Å^{-1}) R (1.2-3.5 Å)**
Independent points	13	**R-factor**	0.01
Variables	8	**S_o^2**	0.74
Reduced chi-square	45.56	ΔE_0 **(eV)**	0.54
R(Fe-O22) (Å)	2.09±0.06	σ^2**(Fe-O22) (Å^2)**	0.001±0.001
R(Fe-O24) (Å)	1.9±0.01	σ^2**(Fe-O24) (Å^2)**	0.001±0.001
R(Fe-O26) (Å)	1.9±0.01	σ^2**(Fe-O26) (Å^2)**	0.002±0.003
R(Fe-O28) (Å)	2.09±0.06	σ^2**(Fe-O28) (Å^2)**	0.002±0.003
R(Fe-N19) (Å)	2.03±0.06	σ^2**(Fe-N19) (Å^2)**	0.001±0.002
R(Fe-N20) (Å)	2.03±0.06	σ^2**(Fe-N20) (Å^2)**	0.001±0.002
R(Fe-C3) (Å)	3.09±0.03	σ^2**(Fe-C3) (Å^2)**	0.002±0.003
R(Fe-C4) (Å)	3.09±0.03	σ^2**(Fe-C4) (Å^2)**	0.002±0.003
R(Fe-C14) (Å)	3.09±0.03	σ^2**(Fe-C14) (Å^2)**	0.002±0.003
R(Fe-C10) (Å)	3.09±0.03	σ^2**(Fe-C10) (Å^2)**	0.002±0.003

Table 6.6: Summary of EXAFS parameters of bpy-UiO-Fe$(OH)_3(H_2O)$.

Sample	**Bpy-UiO-Fe$(OH)_3(H_2O)$**	**Fitting range**	***k* (3-12.5 Å^{-1}) R (1.2-3.5 Å)**
Independent points	13	**R-factor**	0.01
Variables	8	**S_o^2**	0.74
Reduced chi-square	56.226	ΔE_0 **(eV)**	0.54
R(Fe-O26) (Å)	1.9±0.01	σ^2**(Fe-O26) (Å^2)**	0.001±0.001
R(Fe-O24) (Å)	1.9±0.01	σ^2**(Fe-O24)(Å^2)**	0.001±0.001
R(Fe-O22) (Å)	2.03±0.06	σ^2**(Fe-O22) (Å^2)**	0.002±0.003
R(Fe-O28) (Å)	2.09±0.06	σ^2**(Fe-O28) (Å^2)**	0.002±0.003
R(Fe-N19) (Å)	2.03±0.06	σ^2**(Fe-N19) (Å^2)**	0.001±0.002
R(Fe-N20) (Å)	2.03±0.06	σ^2**(Fe-N20) (Å^2)**	0.001±0.002
R(Fe-C3) (Å)	3.09±0.03	σ^2**(Fe-C3) (Å^2)**	0.002±0.003
R(Fe-C4) (Å)	3.09±0.03	σ^2**(Fe-C4) (Å^2)**	0.002±0.003
R(Fe-C14) (Å)	3.09±0.03	σ^2**(Fe-C14) (Å^2)**	0.002±0.003
R(Fe-C10) (Å)	3.09±0.03	$\mathbf{v}^2$**(Fe-C10) (Å^2)**	0.002±0.003

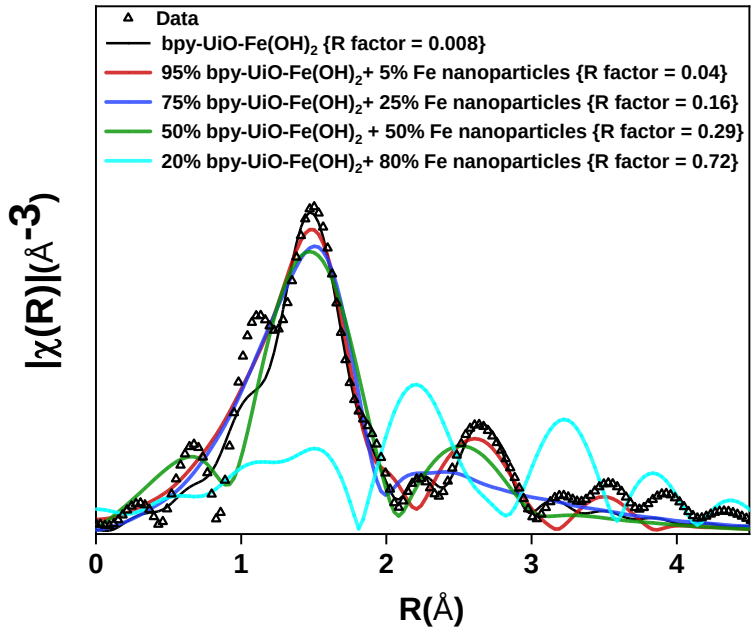


Figure 6.17: EXAFS spectrum of bpy-UiO-Fe(OH)$_2$ fitted with; 5% Fe (0) and 95% bpy-UiO-Fe(OH)$_2$; 25% Fe (0) and 75% bpy-UiO-Fe(OH)$_2$; 50% Fe (0) and 50% bpy-UiO-Fe(OH)$_2$; and 80% Fe(0) and 20% bpy-UiO-Fe(OH)$_2$. The significant misfits indicates that bpy-UiO-Fe(OH)$_2$ does not contain any Fe-nanoparticles.

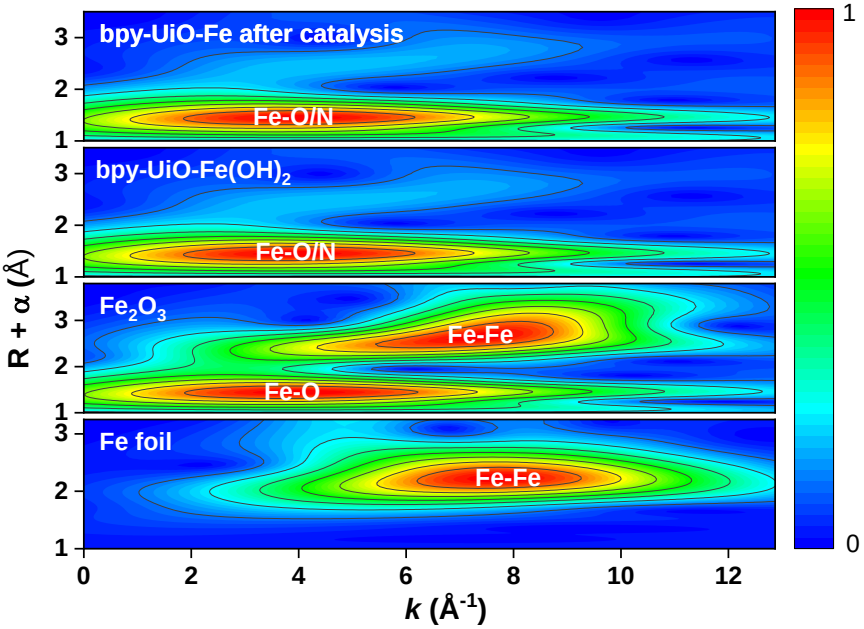


Figure 6.18: Wavelet transform for the k^2-weighted EXAFS signal at the Fe K-edge.

The wavelet transform provides a more detailed analysis of the local structure around the Fe atoms compared to traditional EXAFS. As shown in Figure 6.18, the k^2-weighted wavelet transform of Fe foil exhibits a clear scattering feature at 7.8 Å^{-1}, corresponding to Fe–Fe interactions. However, this Fe–Fe scattering is absent in the wavelet transform of bpy-UiO-Fe(OH)$_2$. The only significant scattering observed in bpy-UiO-Fe(OH)$_2$ occurs at around 4.2 Å^{-1}, which can be attributed to single scattering from Fe-O/N paths. The EXAFS features and wavelet transform plot collectively suggest that the Fe species in the MOF is solely coordinated by O and N atoms, without any Fe neighbors.

6.3.8 XPS analysis of bpy-UiO-FeCl$_2$, bpy-UiO-Fe(OH)$_2$, bpy-UiO-Fe after catalysis.

All the binding energies were corrected with reference to the C1s peak at 284.8 eV. MULTIPAK software was used for peak analysis and de-convolution studies.

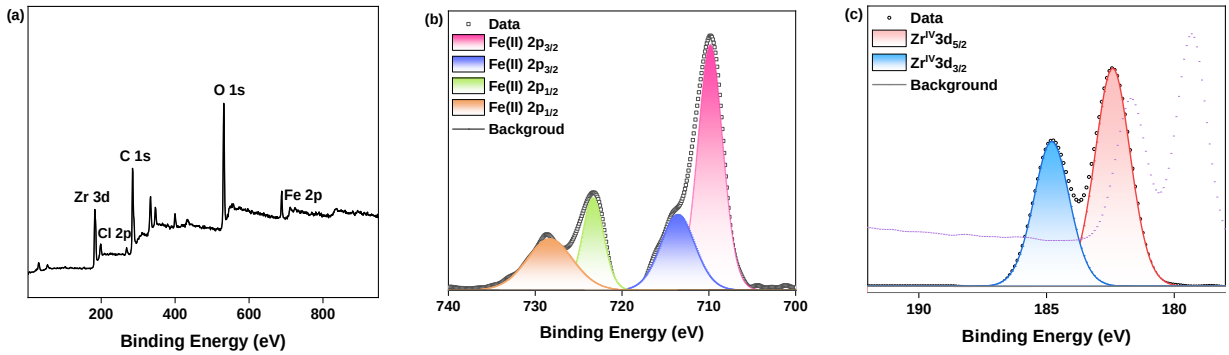


Figure 6.19: (a) Raw XPS data of bpy-UiO-FeCl$_2$. (b) XPS fitting of iron in bpy-UiO-FeCl$_2$. (c) XPS fitting of zirconium in bpy-UiO-FeCl$_2$.

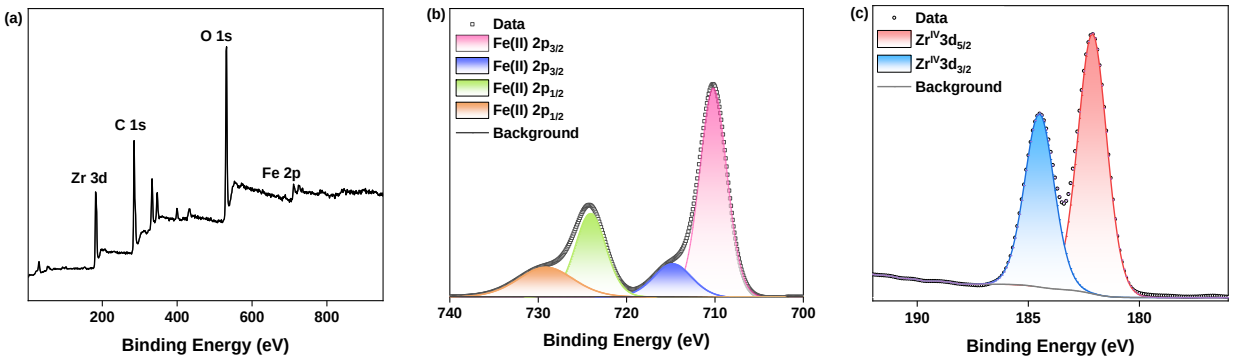


Figure 6.20: (a) Raw XPS data of bpy-UiO-Fe(OH)$_2$. (b) XPS fitting of iron in bpy-UiO-Fe(OH)$_2$. (c) XPS fitting of zirconium in bpy-UiO-Fe(OH)$_2$.

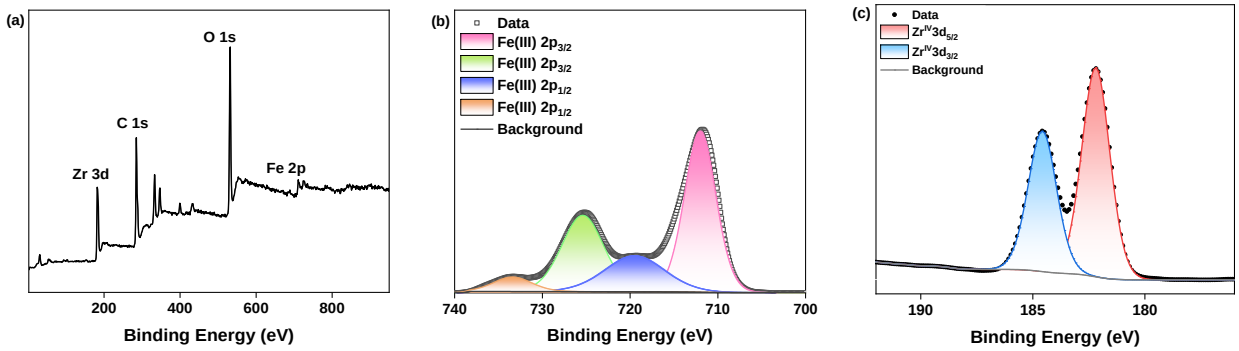


Figure 6.21: (a) Raw XPS data of bpy-UiO-Fe after catalysis. (b) XPS fitting of iron in bpy-UiO-Fe after catalysis (c) XPS fitting of zirconium in bpy-UiO-Fe after catalysis.

6.3.9 GC-FID Spectra

The chromatographic conditions are as follows; Carrier gas: nitrogen, injection volume 1 μL, column oven temperature was initially 4 °C, and then increased up to 70 °C, with the rate of 5 °C/min and then increased to 200 °C, with the rate of 20 °C/min and detector temperature was 250 °C. Products were quantified using a calibration plot of bromobenzene as the internal standard.

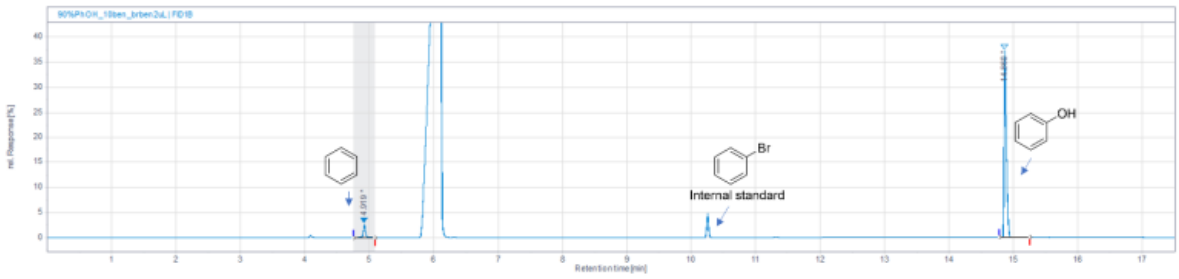


Figure 6.22: Raw GC-FID spectra of bpy-UiO-Fe(OH)$_2$ (0.31 mol% Fe) catalysed hydroxylation of benzene for 4 h at 60 °C. Reaction conditions: benzene (0.3 mL, 3.37 mmol), 30% H_2O_2 (5 eq.), CH_3CN:water [(1:1), 4 mL].

S. No.	**Reference**	**Catalyst**	**Conditions**	**% Yield of Phenol**	**% Selectivity of Phenol**
1	*ACS Catal.* **2015**, *5* (11), 6852-6857.	MIL-100(Fe) and MIL-68(Fe)	Benzene:H_2O_2 (1:2), CH_3CN (4 mL), light irradiation ($\lambda \geq 420$ nm), 8 h.	10.3	>99
2	*ACS Catal.* **2018**, *8*, 10668-10675.	FeOCl	Benzene:H_2O_2 (1:1), acetic acid (1 mL), 60 °C, 4 h	43.5	100
4	*Nat Commun.* **2019**, *10*, 4290.	Fe-N_xC_y	Benzene:H_2O_2 (1:12), CH_3CN, 60 °C, 24 h	78.4	100
5	*Angew. Chem. Int. Ed.* **2021**, *60*, 15248-15253.	SA Fe/C	Benzene:H_2O_2 (1:6), CH_3CN, 60 °C, 24 h	84.8	99
6	*Natl. Sci. Rev.* **2022**, *9* (9), 2095-5138.	Cu_1/GDY	Benzene:H_2O_2(1:20), CH_3CN, 60 °C, 9 h	86	96
7	*Adv. Sci.* **2022**, *9*, 35.	SA Ni-O-C	Benzene:H_2O_2 (1:10), electrolyte: KOH	96.4	100
8	*Appl. Catal. A: Gen.* **2022**, *633*, 118499.	FeCo@C	Benzene:H_2O_2 (1:10), CH_3CN, water, 60 °C, 4 h	26.4	97
9	*Appl. Catal. B: Environ.* **2022**, *304*, 120965	Fe-PHI	Benzene:H_2O_2 (1:15), H_2SO_4, 60 °C, 400 W, 22 h	45.5	98.5
10	*ACS Catal.* **2023**, *13*, 1316-1325.	Cu SACs	Benzene:H_2O_2 (1:1), CH_3CN, 60 °C, 72 h	80	99

S. No.	**Reference**	**Catalyst**	**Conditions**	**% Yield of Phenol**	**% Selectivity of Phenol**
11	*ACS Sustain. Chem. Eng.* **2023**, *11*, 1518-1526.	FeN_x/CCN	Benzene:H_2O_2 (1:3), CH_3CN, water, 60 °C, 4 h, visible light ($\lambda \geq$ 420 nm)	28.1	85
12	*Angew. Chem. Int. Ed.* **2023**, *62*, e202216062.	Fe_x-NOC	Benzene:H_2O_2 (1:12), CH_3CN, 60 °C, 3 h	46.3	94.9
13	**This work**	**Bpy-UiO-Fe(OH)$_2$**	**Benzene:H_2O_2 (1:5), CH_3CN:H_2O (1:1). 60 °C, 4 h**	**88**	**99**

6.4 Conclusions

In summary, we have successfully synthesized a MOF-supported monomeric bipyridine-ligated iron(II) hydroxyl [bpy-UiO-Fe(OH)$_2$] via active-site isolation. Bpy-UiO-Fe(OH)$_2$ is a highly selective and recyclable catalyst for direct hydroxylation of benzene to produce phenol with a productivity of 1261 $mmol_{PhOH}$ g_{Fe}^{-1} h^{-1} with 99% selectivity. The specific pore size of the MOF prevents the formation of larger, overoxidized products like hydroquinone and benzoquinone, contributing to its exceptional selectivity. Additionally, the MOF's shape-selective catalysis ensures the exclusive formation of phenol, distinguishing it from the lower selectivity observed with its homogeneous counterpart. EPR spectroscopic analysis revealed that bpy-UiO-Fe(OH)$_2$ catalyzes the generation of the ·OH radical from H_2O_2, which is the key species for benzene hydroxylation. Theoretical and experimental data complemented each other in identifying the catalytic species and the catalyst's resting state, thereby guiding the proposal of the benzene hydroxylation reaction mechanism. Our work thus highlights the importance of MOFs in developing earth-abundant metal catalysts for economical and environment-friendly production of phenol via direct hydroxylation of

benzene as an alternative to the conventional cumene process.

References

[1] Rappoport, Z. *The chemistry of phenols*; John Wiley & Sons, 2004.

[2] Zeb, A. Concept, mechanism, and applications of phenolic antioxidants in foods. *Journal of Food Biochemistry* **2020**, *44*, e13394.

[3] Kausch, H. Polymers/Properties and Applications. *Polymer fracture* **1987**, *2*.

[4] Weber, M.; Weber, M. Phenols. *Phenolic resins: a century of progress* **2010**, 9–23.

[5] Schmidt, R. J. Industrial catalytic processes—phenol production. *Applied Catalysis A: General* **2005**, *280*, 89–103.

[6] Mortier, J. *Industrial Arene Chemistry: Markets, Technologies, Sustainable Processes and Cases Studies of Aromatic Commodities, 4 Volume Set*; John Wiley & Sons, 2023.

[7] Zhao, Y.; Cao, H.; Tao, L.; Qiao, Z.; Ding, C. Single-atom catalysts for catalytic benzene oxidation to phenol: recent progress and future perspectives. *Dalton Transactions* **2023**, *52*, 5399–5417.

[8] Mancuso, A.; Sacco, O.; Sannino, D.; Venditto, V.; Vaiano, V. One-step catalytic or photocatalytic oxidation of benzene to phenol: possible alternative routes for phenol synthesis? *Catalysts* **2020**, *10*, 1424.

[9] Al Mesfer, M. K.; Danisha, M.; Ahmed, S. Catalytic conversion of benzene to phenol. *Russian Journal of Applied Chemistry* **2016**, *89*, 1869–1878.

[10] Morimoto, Y.; Bunno, S.; Fujieda, N.; Sugimoto, H.; Itoh, S. Direct hydroxylation of benzene to phenol using hydrogen peroxide catalyzed by nickel complexes supported by pyridylalkylamine ligands. *Journal of the American Chemical Society* **2015**, *137*, 5867–5870.

[11] Zhang, X.; Zhang, T.; Li, B.; Zhang, G.; Hai, L.; Ma, X.; Wu, W. Direct synthesis of phenol by novel [FeFe]-hydrogenase model complexes as catalysts of benzene hydroxylation with H 2 O 2. *RSC advances* **2017**, *7*, 2934–2942.

[12] Langeslay, R. R.; Kaphan, D. M.; Marshall, C. L.; Stair, P. C.; Sattelberger, A. P.; Delferro, M. Catalytic applications of vanadium: a mechanistic perspective. *Chemical reviews* **2018**, *119*, 2128–2191.

[13] Capocasa, G.; Olivo, G.; Barbieri, A.; Lanzalunga, O.; Di Stefano, S. Direct hydroxylation of benzene and aromatics with H 2 O 2 catalyzed by a self-assembled iron complex: evidence for a metal-based mechanism. *Catalysis Science & Technology* **2017**, *7*, 5677–5686.

[14] ElMetwally, A. E.; Eshaq, G.; Yehia, F. Z.; Al-Sabagh, A. M.; Kegnæs, S. Iron oxychloride as an efficient catalyst for selective hydroxylation of benzene to phenol. *ACS Catalysis* **2018**, *8*, 10668–10675.

[15] Zhang, T.; Zhang, D.; Han, X.; Dong, T.; Guo, X.; Song, C.; Si, R.; Liu, W.; Liu, Y.; Zhao, Z. Preassembly strategy to fabricate porous hollow carbonitride spheres inlaid with single Cu–N3 sites for selective oxidation of benzene to phenol. *Journal of the American Chemical Society* **2018**, *140*, 16936–16940.

[16] Pan, Y.; Chen, Y.; Wu, K.; Chen, Z.; Liu, S.; Cao, X.; Cheong, W.-C.; Meng, T.; Luo, J.; Zheng, L.; others Regulating the coordination structure of single-atom Fe-N x C y catalytic sites for benzene oxidation. *Nature communications* **2019**, *10*, 4290.

[17] Liu, J.; Cao, C.; Liu, X.; Zheng, L.; Yu, X.; Zhang, Q.; Gu, L.; Qi, R.; Song, W. Direct observation of metal oxide nanoparticles being transformed into metal single atoms with oxygen-coordinated structure and high-loadings. *Angewandte Chemie International Edition* **2021**, *60*, 15248–15253.

[18] Zhang, S.; Jin, M.; Xu, H.; Li, W.; Ye, Y.; Shi, T.; Zhou, H.; Chen, C.; Wang, G.; Zhang, Y.; others Hydrogen peroxide assisted electrooxidation of benzene to phenol over bifunctional Ni–(O–C2) 4 sites. *Advanced Science* **2022**, *9*, 2204043.

[19] Zeng, L.; Liang, H.; An, P.; Yu, D.; Yang, C.; Hou, Y.; Zhang, J. Carbon encapsulated bimetallic FeCo nanoalloys for one-step hydroxylation of benzene to phenol. *Applied Catalysis A: General* **2022**, *633*, 118499.

[20] da Silva, M. A.; Silva, I. F.; Xue, Q.; Lo, B. T.; Tarakina, N. V.; Nunes, B. N.; Adler, P.; Sahoo, S. K.; Bahnemann, D. W.; López-Salas, N.; others Sustainable oxidation catal-

ysis supported by light: Fe-poly (heptazine imide) as a heterogeneous single-atom photocatalyst. *Applied Catalysis B: Environmental* **2022**, *304*, 120965.

[21] Yu, J.; Cao, C.; Jin, H.; Chen, W.; Shen, Q.; Li, P.; Zheng, L.; He, F.; Song, W.; Li, Y. Uniform single atomic Cu1-C4 sites anchored in graphdiyne for hydroxylation of benzene to phenol. *National Science Review* **2022**, *9*, nwac018.

[22] Bu, F.; Chen, C.; Yu, Y.; Hao, W.; Zhao, S.; Hu, Y.; Qin, Y. Boosting Benzene Oxidation with a Spin-State-Controlled Nuclearity Effect on Iron Sub-Nanocatalysts. *Angewandte Chemie* **2023**, *135*, e202216062.

[23] Chen, X.; Cheng, L.; Yang, Y.; Chen, X.; Chen, F.; Lu, W. Construction of high-density Fe clusters embedded in a porous carbon nitride catalyst with effectively selective transformation of benzene. *ACS Sustainable Chemistry & Engineering* **2023**, *11*, 1518–1526.

[24] Wang, D.; Wang, M.; Li, Z. Fe-based metal–organic frameworks for highly selective photocatalytic benzene hydroxylation to phenol. *Acs Catalysis* **2015**, *5*, 6852–6857.

[25] Jin, H.; Cui, P.; Cao, C.; Yu, X.; Zhao, R.; Ma, D.; Song, W. Understanding the density-dependent activity of Cu single-atom catalyst in the benzene hydroxylation reaction. *ACS Catalysis* **2023**, *13*, 1316–1325.

[26] Lee, J.; Farha, O. K.; Roberts, J.; Scheidt, K. A.; Nguyen, S. T.; Hupp, J. T. Metal–organic framework materials as catalysts. *Chemical Society Reviews* **2009**, *38*, 1450–1459.

[27] Zhao, M.; Ou, S.; Wu, C.-D. Porous metal–organic frameworks for heterogeneous biomimetic catalysis. *Accounts of chemical research* **2014**, *47*, 1199–1207.

[28] Xiao, D. J.; Bloch, E. D.; Mason, J. A.; Queen, W. L.; Hudson, M. R.; Planas, N.; Borycz, J.; Dzubak, A. L.; Verma, P.; Lee, K.; others Oxidation of ethane to ethanol by N2O in a metal–organic framework with coordinatively unsaturated iron (II) sites. *Nature chemistry* **2014**, *6*, 590–595.

[29] Burgess, S. A.; Kassie, A.; Baranowski, S. A.; Fritzsching, K. J.; Schmidt-Rohr, K.; Brown, C. M.; Wade, C. R. Improved catalytic activity and stability of a palladium pincer complex by incorporation into a metal–organic framework. *Journal of the American Chemical Society* **2016**, *138*, 1780–1783.

[30] Zhang, T.; Manna, K.; Lin, W. Metal–organic frameworks stabilize solution-inaccessible cobalt catalysts for highly efficient broad-scope organic transformations. *Journal of the American Chemical Society* **2016**, *138*, 3241–3249.

[31] Kutzscher, C.; Nickerl, G.; Senkovska, I.; Bon, V.; Kaskel, S. Proline functionalized UiO-67 and UiO-68 type metal–organic frameworks showing reversed diastereoselectivity in aldol addition reactions. *Chemistry of Materials* **2016**, *28*, 2573–2580.

[32] Manna, K.; Ji, P.; Lin, Z.; Greene, F. X.; Urban, A.; Thacker, N. C.; Lin, W. Chemoselective single-site Earth-abundant metal catalysts at metal–organic framework nodes. *Nature communications* **2016**, *7*, 1–11.

[33] Metzger, E. D.; Comito, R. J.; Hendon, C. H.; Dinca, M. Mechanism of single-site molecule-like catalytic ethylene dimerization in Ni-MFU-4 l. *Journal of the American Chemical Society* **2017**, *139*, 757–762.

[34] Zhang, Y.; Guo, J.; Shi, L.; Zhu, Y.; Hou, K.; Zheng, Y.; Tang, Z. Tunable chiral metal organic frameworks toward visible light–driven asymmetric catalysis. *Science advances* **2017**, *3*, e1701162.

[35] Zhao, X.; Zhang, S.; Yan, J.; Li, L.; Wu, G.; Shi, W.; Yang, G.; Guan, N.; Cheng, P. Polyoxometalate-based metal–organic frameworks as visible-light-induced photocatalysts. *Inorganic chemistry* **2018**, *57*, 5030–5037.

[36] Liu, J.; Ye, J.; Li, Z.; Otake, K.-i.; Liao, Y.; Peters, A. W.; Noh, H.; Truhlar, D. G.; Gagliardi, L.; Cramer, C. J.; others Beyond the active site: tuning the activity and selectivity of a metal–organic framework-supported Ni catalyst for ethylene dimerization. *Journal of the American Chemical Society* **2018**, *140*, 11174–11178.

[37] Baek, J.; Rungtaweevoranit, B.; Pei, X.; Park, M.; Fakra, S. C.; Liu, Y.-S.; Matheu, R.; Alshmimri, S. A.; Alshehri, S.; Trickett, C. A.; others Bioinspired metal–organic framework catalysts for selective methane oxidation to methanol. *Journal of the American Chemical Society* **2018**, *140*, 18208–18216.

[38] Reiner, B. R.; Kassie, A. A.; Wade, C. R. Unveiling reactive metal sites in a Pd pincer MOF: insights into Lewis acid and pore selective catalysis. *Dalton Transactions* **2019**, *48*, 9588–9595.

[39] Feng, X.; Ji, P.; Li, Z.; Drake, T.; Oliveres, P.; Chen, E. Y.; Song, Y.; Wang, C.; Lin, W. Aluminum hydroxide secondary building units in a metal–organic framework support earth-abundant metal catalysts for broad-scope organic transformations. *ACS Catalysis* **2019**, *9*, 3327–3337.

[40] Zheng, J.; Ye, J.; Ortuño, M. A.; Fulton, J. L.; Gutiérrez, O. Y.; Camaioni, D. M.; Motkuri, R. K.; Li, Z.; Webber, T. E.; Mehdi, B. L.; others Selective methane oxidation to methanol on Cu-oxo dimers stabilized by zirconia nodes of an NU-1000 metal–organic framework. *Journal of the American Chemical Society* **2019**, *141*, 9292–9304.

[41] Nguyen, K. D.; Kutzscher, C.; Ehrling, S.; Senkovska, I.; Bon, V.; de Oliveira Jr, M.; Gutmann, T.; Buntkowsky, G.; Kaskel, S. Insights into the role of zirconium in proline functionalized metal-organic frameworks attaining high enantio-and diastereoselectivity. *Journal of Catalysis* **2019**, *377*, 41–50.

[42] Antil, N.; Kumar, A.; Akhtar, N.; Newar, R.; Begum, W.; Manna, K. Metal–Organic Framework-Confined Single-Site Base-Metal Catalyst for Chemoselective Hydrodeoxygenation of Carbonyls and Alcohols. *Inorganic Chemistry* **2021**, *60*, 9029–9039.

[43] Antil, N.; Chauhan, M.; Akhtar, N.; Newar, R.; Begum, W.; Malik, J.; Manna, K. Metal–Organic Framework-Encaged Monomeric Cobalt (III) Hydroperoxides Enable Chemoselective Methane Oxidation to Methanol. *ACS Catalysis* **2022**, *12*, 11159–11168.

[44] Pramanik, B.; Sahoo, R.; Das, M. C. pH-stable MOFs: Design principles and applications. *Coordination Chemistry Reviews* **2023**, *493*, 215301.

[45] Chauhan, M.; Antil, N.; Rana, B.; Akhtar, N.; Thadhani, C.; Begum, W.; Manna, K. Isoreticular Metal–Organic Frameworks Confined Mononuclear Ru-Hydrides Enable Highly Efficient Shape-Selective Hydrogenolysis of Polyolefins. *JACS Au* **2023**, *3*, 3473–3484.

[46] Das, A.; Anbu, N.; SK, M.; Dhakshinamoorthy, A.; Biswas, S. Highly Active Bisamino Functionalized Zr (IV)-UiO-67 Metal-Organic Framework for Cascade Catalysis. *European Journal of Inorganic Chemistry* **2020**, *2020*, 2830–2834.

[47] Furukawa, H.; Cordova, K. E.; O'Keeffe, M.; Yaghi, O. M. The chemistry and applications of metal-organic frameworks. *Science* **2013**, *341*, 1230444.

[48] Chen, Y.; Zhang, X.; Ma, K.; Chen, Z.; Wang, X.; Knapp, J.; Alayoglu, S.; Wang, F.; Xia, Q.; Li, Z.; others Zirconium-based metal–organic framework with 9-connected nodes for ammonia capture. *ACS Applied Nano Materials* **2019**, *2*, 6098–6102.

[49] Antil, N.; Chauhan, M.; Akhtar, N.; Kalita, R.; Manna, K. Selective methane oxidation to acetic acid using molecular oxygen over a mono-copper hydroxyl catalyst. *Journal of the American Chemical Society* **2023**, *145*, 6156–6165.

[50] Cavka, J. H.; Jakobsen, S.; Olsbye, U.; Guillou, N.; Lamberti, C.; Bordiga, S.; Lillerud, K. P. A new zirconium inorganic building brick forming metal organic frameworks with exceptional stability. *Journal of the American Chemical Society* **2008**, *130*, 13850–13851.

[51] Bai, Y.; Dou, Y.; Xie, L.-H.; Rutledge, W.; Li, J.-R.; Zhou, H.-C. Zr-based metal–organic frameworks: design, synthesis, structure, and applications. *Chemical Society Reviews* **2016**, *45*, 2327–2367.

[52] Yuan, S.; Qin, J.-S.; Lollar, C. T.; Zhou, H.-C. Stable metal–organic frameworks with group 4 metals: current status and trends. *ACS central science* **2018**, *4*, 440–450.

[53] Ma, L.; Falkowski, J. M.; Abney, C.; Lin, W. A series of isoreticular chiral metal–organic frameworks as a tunable platform for asymmetric catalysis. *Nature chemistry* **2010**, *2*, 838–846.

[54] Cohen, S. M. Postsynthetic methods for the functionalization of metal–organic frameworks. *Chemical reviews* **2012**, *112*, 970–1000.

[55] Xia, Q.; Li, Z.; Tan, C.; Liu, Y.; Gong, W.; Cui, Y. Multivariate metal–organic frameworks as multifunctional heterogeneous asymmetric catalysts for sequential reactions. *Journal of the American Chemical Society* **2017**, *139*, 8259–8266.

[56] Lin, Z.; Thacker, N. C.; Sawano, T.; Drake, T.; Ji, P.; Lan, G.; Cao, L.; Liu, S.; Wang, C.; Lin, W. Metal–organic layers stabilize earth-abundant metal–terpyridine diradical complexes for catalytic C–H activation. *Chemical science* **2018**, *9*, 143–151.

[57] Zhang, Y.; Li, J.; Yang, X.; Zhang, P.; Pang, J.; Li, B.; Zhou, H.-C. A mesoporous NNN-pincer-based metal–organic framework scaffold for the preparation of noble-metal-free catalysts. *Chemical Communications* **2019**, *55*, 2023–2026.

[58] Kalaj, M.; Cohen, S. M. Postsynthetic modification: an enabling technology for the advancement of metal–organic frameworks. *ACS Central Science* **2020**, *6*, 1046–1057.

[59] Newar, R.; Begum, W.; Antil, N.; Shukla, S.; Kumar, A.; Akhtar, N.; Balendra; Manna, K. Single-Site Cobalt-Catalyst Ligated with Pyridylimine-Functionalized Metal–Organic Frameworks for Arene and Benzylic Borylation. *Inorganic Chemistry* **2020**, *59*, 10473–10481.

[60] Newar, R.; Akhtar, N.; Antil, N.; Kumar, A.; Shukla, S.; Begum, W.; Manna, K. Amino acid-functionalized metal-organic frameworks for asymmetric base–metal catalysis. *Angewandte Chemie International Edition* **2021**, *60*, 10964–10970.

[61] Antil, N.; Akhtar, N.; Newar, R.; Begum, W.; Kumar, A.; Chauhan, M.; Manna, K. Chiral iron (II)-catalysts within valinol-grafted metal–organic frameworks for enantioselective reduction of ketones. *ACS Catalysis* **2021**, *11*, 10450–10459.

[62] Akhtar, N.; Chauhan, M.; Gupta, P.; Antil, N.; Manna, K. A supported pyridylimine–cobalt catalyst for N-formylation of amines using CO 2. *Dalton Transactions* **2023**, *52*, 15384–15393.

[63] Thacker, N. C.; Lin, Z.; Zhang, T.; Gilhula, J. C.; Abney, C. W.; Lin, W. Robust and porous β-diketiminate-functionalized metal–organic frameworks for earth-abundant-metal-catalyzed C–H amination and hydrogenation. *Journal of the American Chemical Society* **2016**, *138*, 3501–3509.

[64] Fei, H.; Shin, J.; Meng, Y. S.; Adelhardt, M.; Sutter, J.; Meyer, K.; Cohen, S. M. Reusable oxidation catalysis using metal-monocatecholato species in a robust metal–organic framework. *Journal of the American Chemical Society* **2014**, *136*, 4965–4973.

[65] Rogge, S. M.; Bavykina, A.; Hajek, J.; Garcia, H.; Olivos-Suarez, A. I.; Sepúlveda-Escribano, A.; Vimont, A.; Clet, G.; Bazin, P.; Kapteijn, F.; others Metal–organic and covalent organic frameworks as single-site catalysts. *Chemical Society Reviews* **2017**, *46*, 3134–3184.

[66] Gascon, J.; Corma, A.; Kapteijn, F.; Llabres i Xamena, F. X. Metal organic framework catalysis: quo vadis? *Acs Catalysis* **2014**, *4*, 361–378.

[67] Genna, D. T.; Wong-Foy, A. G.; Matzger, A. J.; Sanford, M. S. Heterogenization of homogeneous catalysts in metal–organic frameworks via cation exchange. *Journal of the American Chemical Society* **2013**, *135*, 10586–10589.

[68] Rimoldi, M.; Howarth, A. J.; DeStefano, M. R.; Lin, L.; Goswami, S.; Li, P.; Hupp, J. T.; Farha, O. K. Catalytic zirconium/hafnium-based metal–organic frameworks. *Acs Catalysis* **2017**, *7*, 997–1014.

[69] Li, L.; Tang, S.; Wang, C.; Lv, X.; Jiang, M.; Wu, H.; Zhao, X. High gas storage capacities and stepwise adsorption in a UiO type metal–organic framework incorporating Lewis basic bipyridyl sites. *Chemical Communications* **2014**, *50*, 2304–2307.

[70] Schaate, A.; Roy, P.; Godt, A.; Lippke, J.; Waltz, F.; Wiebcke, M.; Behrens, P. Modulated synthesis of Zr-based metal–organic frameworks: from nano to single crystals. *Chemistry–A European Journal* **2011**, *17*, 6643–6651.

[71] Krzystek, J.; Smirnov, D.; Schlegel, C.; Van Slageren, J.; Telser, J.; Ozarowski, A. High-frequency and-field EPR and FDMRS study of the [Fe (H2O) 6] 2+ ion in ferrous fluorosilicate. *Journal of Magnetic Resonance* **2011**, *213*, 158–165.

[72] Krzystek, J.; Ozarowski, A.; Telser, J. Multi-frequency, high-field EPR as a powerful tool to accurately determine zero-field splitting in high-spin transition metal coordination complexes. *Coordination chemistry reviews* **2006**, *250*, 2308–2324.

[73] Li, S.-M.; Wang, J.-L.; Zhou, J.-L.; Xiang, X.-Y.; Yu, Y.-T.; Chen, Q.; Mei, H.; Xu, Y. An iron-containing POM-based hybrid compound as a heterogeneous catalyst for one-step hydroxylation of benzene to phenol. *Dalton Transactions* **2024**, *53*, 1058–1065.

[74] Zhang, L.; Sun, Z.; Lang, J.; Hu, Y. H. Direct conversion of methane to oxygenates catalyzed by iron (III) chloride in water at near ambient temperature. *International Journal of Energy Research* **2021**, *45*, 2581–2592.

[75] Luigi, B.; Daniele, B.; Rossella, B.; others Direct oxidation of benzene to phenol with hydrogen peroxide over a modified titanium silicalite. *Angewandte Chemie International Edition* **2003**, *42*, 4.

[76] Holmberg, R. J.; Burns, T.; Greer, S. M.; Kobera, L.; Stoian, S. A.; Korobkov, I.; Hill, S.; Bryce, D. L.; Woo, T. K.; Murugesu, M. Intercalation of Coordinatively Unsaturated FeIII Ion within Interpenetrated Metal–Organic Framework MOF-5. *Chemistry–A European Journal* **2016**, *22*, 7711–7715.

[77] Fontmorin, J.; Castillo, R. B.; Tang, W.; Sillanpää, M. Stability of 5, 5-dimethyl-1-pyrroline-N-oxide as a spin-trap for quantification of hydroxyl radicals in processes based on Fenton reaction. *Water research* **2016**, *99*, 24–32.

[78] Lacy, D. C.; Gupta, R.; Stone, K. L.; Greaves, J.; Ziller, J. W.; Hendrich, M. P.; Borovik, A. Formation, Structure, and EPR Detection of a High Spin FeIV Oxo Species Derived from Either an FeIII Oxo or FeIII OH Complex. *Journal of the American Chemical Society* **2010**, *132*, 12188–12190.

[79] Kostka, K. L.; Fox, B. G.; Hendrich, M. P.; Collins, T. J.; Rickard, C. E.; Wright, L. J.; Munck, E. High-valent transition metal chemistry. Moessbauer and EPR studies of high-spin (S= 2) iron (IV) and intermediate-spin (S= 3/2) iron (III) complexes with a macrocyclic tetraamido-N ligand. *Journal of the American Chemical Society* **1993**, *115*, 6746–6757.

[80] Zhou, L.-J.; Deng, W.-H.; Wang, Y.-L.; Xu, G.; Yin, S.-G.; Liu, Q.-Y. Lanthanide–Potassium Biphenyl-3, 3-disulfonyl-4, 4-dicarboxylate Frameworks: Gas Sorption, Proton Conductivity, and Luminescent Sensing of Metal Ions. *Inorganic Chemistry* **2016**, *55*, 6271–6277.

[81] Øien, S.; Agostini, G.; Svelle, S.; Borfecchia, E.; Lomachenko, K. A.; Mino, L.; Gallo, E.; Bordiga, S.; Olsbye, U.; Lillerud, K. P.; others Probing reactive platinum sites in UiO-67 zirconium metal–organic frameworks. *Chemistry of Materials* **2015**, *27*, 1042–1056.

[82] Zhao, Y.; Zhang, S.; Wang, M.; Han, J.; Wang, H.; Li, Z.; Liu, X. Engineering iridium-based metal organic frameworks towards electrocatalytic water oxidation. *Dalton Transactions* **2018**, *47*, 4646–4652.

[83] Gorbanev, Y.; O'Connell, D.; Chechik, V. Non-thermal plasma in contact with water: The origin of species. *Chemistry–A European Journal* **2016**, *22*, 3496–3505.

[84] Araujo, M.; Lasorne, B.; Magalhães, A. L.; Worth, G. A.; Bearpark, M. J.; Robb, M. A. The molecular dissociation of formaldehyde at medium photoexcitation energies: A quantum chemistry and direct quantum dynamics study. *The Journal of chemical physics* **2009**, *131*.

[85] Yempally, V.; Kyran, S. J.; Raju, R. K.; Fan, W. Y.; Brothers, E. N.; Darensbourg, D. J.; Bengali, A. A. Thermal and photochemical reactivity of manganese tricarbonyl and tetracarbonyl complexes with a bulky diazabutadiene ligand. *Inorganic Chemistry* **2014**, *53*, 4081–4088.

[86] Ganji, M. D.; Hosseini-Khah, S.; Amini-Tabar, Z. Theoretical insight into hydrogen adsorption onto graphene: a first-principles B3LYP-D3 study. *Physical Chemistry Chemical Physics* **2015**, *17*, 2504–2511.

[87] Impeng, S.; Siwaipram, S.; Bureekaew, S.; Probst, M. Ethane C–H bond activation on the Fe (iv)–oxo species in a Zn-based cluster of metal–organic frameworks: a density functional theory study. *Physical Chemistry Chemical Physics* **2017**, *19*, 3782–3791.

[88] Canneaux, S.; Bohr, F.; Henon, E. KiSThelP: a program to predict thermodynamic properties and rate constants from quantum chemistry results. *Journal of computational chemistry* **2014**, *35*, 82–93.

[89] Grimme, S.; Antony, J.; Ehrlich, S.; Krieg, H. A consistent and accurate ab initio parametrization of density functional dispersion correction (DFT-D) for the 94 elements H-Pu. *The Journal of chemical physics* **2010**, *132*.

[90] Poswal, A.; Agrawal, A.; Yadav, A.; Nayak, C.; Basu, S.; Kane, S.; Garg, C.; Bhattachryya, D.; Jha, S.; Sahoo, N. Commissioning and first results of scanning type EXAFS beamline (BL-09) at INDUS-2 synchrotron source. AIP Conference Proceedings. 2014; pp 649–651.

[91] Ravel, B.; Newville, M. ATHENA, ARTEMIS, HEPHAESTUS: data analysis for X-ray absorption spectroscopy using IFEFFIT. *Journal of synchrotron radiation* **2005**, *12*, 537–541.

Chapter 7

Mononuclear Bipyridyl-Iron(III) Hydroxide in Metal-Organic Framework for Selective Alkene Oxidation

Title of Paper: " Mononuclear Bipyridyl-Iron(III) hydroxide in Metal-Organic Framework for selective Alkene Oxidation"

Citation: Journal of Molecular Chemistry, **2025**, *5* (3), 1225. (doi.org/10.62110/sciencein.jmc.2025.1225)

Author: Poorvi Gupta, Swapnaneel Sarmah, Rahul Kalita, Bharti Rana, and Kuntal Manna*

Abstract

The selective oxidation of styrene to value-added products such as benzaldehyde and benzoic acid is of significant industrial importance. We report the design of a single-site iron catalyst supported on a bipyridine-functionalized metal–organic framework, bpy-UiO-Fe(OH)$_3$, which enables selective oxidation of styrene into benzaldehyde or benzoic acid using H_2O_2 as the oxidant. Systematic optimization of solvent composition, temperature, and reaction time revealed that benzaldehyde can be obtained with 100% selectivity at 80 °C in 8 h, while prolonged reactions furnish benzoic acid in high yields. Control experiments confirmed the heterogeneous, single-site nature of the catalyst, which remained structurally robust and can be recycled at least three times with negligible Fe leaching. Mechanistic studies suggest a non-radical pathway involving epoxide and diol intermediates prior to carbon-carbon bond cleavage. This work demonstrates the potential of MOF-supported abundant-metal catalysts for sustainable oxidation of alkenes under environmentally benign conditions.

7.1 Introduction

The selective oxidation of styrene is an important industrial process, as its products—benzaldehyde, benzoic acid, and styrene oxide—are key intermediates in the production of perfumes, pharmaceuticals, dyes, agrochemicals, and polymer additives.[1;2] Traditional production methods, such as toluene oxidation or benzyl chloride hydrolysis, often require harsh conditions, lead to poor selectivity, and generate environmentally harmful chloride waste.[3;4] Catalytic oxidation of styrene has emerged as a more attractive alternative, allowing for the direct conversion to benzaldehyde and benzoic acid under relatively mild conditions. However, conventional oxidants such as peroxyacids,[5;6] manganese dioxide,[7] osmium tetroxide,[8;9] selenium dioxide,[10] and ozone,[11] often generate harmful byproducts, which limits their practical use. In contrast, environmentally benign oxidants such as O_2 and H_2O_2 offer sustainable options, though the challenge remains to achieve both high activity and controllable selectivity between benzaldehyde and benzoic acid using these oxidants.

A wide range of catalytic systems have been explored for the oxidation of styrene, including photocatalysts,[12–14] heteropolyacids,[15] transition-metal complexes with Schiff bases,[16–18]

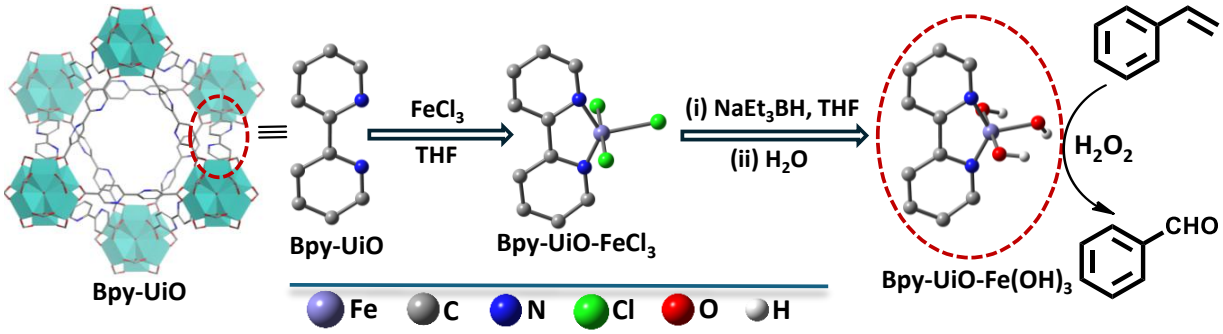


Figure 7.1: Postsynthetic metalation of bpy-UiO to form porous Zr-MOF-confined Fe(III) hydroxyl species for selective oxidation of styrene to benzaldehyde.

and porphyrins.[19;20] Most of these homogeneous systems employ oxidants such as H_2O_2, TBHP, or O_2.[16–18;21;22] These catalysts typically produce styrene oxide and phenylacetaldehyde, with the latter resulting from the isomerization of the epoxide, along with benzaldehyde and benzoic acid. Although homogeneous catalysts provide well-defined active sites, they often suffer from low selectivity, difficult recovery, and limited reusability. To address these issues, significant efforts have been made to develop heterogeneous systems, including metal oxides,[23–25] polyoxometalates (POMs),[26–28] and metal nanoparticles supported on silica, zeolites, or carbon materials.[12;29–32] However, many of these catalysts still exhibit limited selectivity toward benzaldehyde, underscoring the continuing need for efficient, recyclable, and sustainable catalytic alternatives.

Metal–organic frameworks (MOFs) have emerged as versatile platforms for designing robust, single-site heterogeneous catalysts based on earth-abundant metals.[33–42] Their intrinsic high porosity, crystallinity, and structural tunability provide unique opportunities for post-synthetic functionalization. Among them, UiO-type MOFs stand out due to the remarkable thermal and chemical stability imparted by $Zr_6(\mu_3\text{-O})_4(\mu_3\text{-OH})_4$ secondary building units (SBUs) interconnected by linear dicarboxylate linkers.[43–45] The post-synthetic modifications allow precise tailoring of MOF linkers, enabling the incorporation of metals to generate single-site base-metal catalysts. The rigid, porous environment of the framework stabilizes coordinatively unsaturated single-site metal catalytic species and suppresses undesired multinuclear aggregation via active-site isolation.[46;47] As a result, MOF-supported catalysts exhibit uniform active sites along with the robustness and recyclability typical of heterogeneous solids. Building on this foundation, the present work features the devel-

opment of single-site iron(III) hydroxyl species coordinated by the bipyridine linkers of a bpy-UiO MOF. The resulting MOF-supported mononuclear bipyridyl-iron(III) hydroxide demonstrates excellent activity and recyclability, enabling selective conversion of styrene to benzaldehyde and benzoic acid using H_2O_2 as the oxidant.

7.2 Results and Discussion

7.2.1 Synthesis and Characterization of bpy-UiO-Fe(OH)$_3$

A three-step postsynthetic modification was employed to transform pristine bpy-UiO MOF into the catalytically active bpy-UiO-Fe(OH)$_3$. Heating a mixture of $ZrCl_4$, [2,2]-bipyridine-5,5-dicarboxylic acid, and CF_3CO_2H in DMF at 100 °C for 4 days yielded bpy-UiO MOF in ∼69% yield.[48] The bpy-UiO framework, composed of $Zr_6O_4(OH)_4$ nodes bridged by 2,2-bipyridine-5,5-dicarboxylate linkers, was post-synthetically metalated by adding a THF solution of $FeCl_3$ to yield bpy-UiO-$FeCl_3$. Reaction between bpy-UiO-$FeCl_3$ and $NaEt_3BH$ (3.5 eq. with respect to Fe) in THF generated the putative bpy-UiO-FeH_3 intermediate, which was then treated with water at room temperature to afford bpy-UiO-Fe(OH)$_3$. Powder X-ray diffraction (PXRD) analysis confirmed that the crystallinity and structure of bpy-UiO were retained throughout the postsynthetic modification (Figure 7.2a). Inductively coupled plasma optical emission spectroscopy (ICP-OES) analysis of the digested bpy-UiO-Fe(OH)$_3$ MOF confirmed Fe incorporation corresponding to 72% of the available bipyridyl sites. Thermogravimetric analysis (TGA) showed ∼42% and ∼39% solvent loss between 40–200 °C for bpy-UiO and bpy-UiO-Fe(OH)$_3$, respectively, and both MOFs were thermally robust up to ∼550 °C (Figure 7.7). Nitrogen sorption isotherm analysis gave a BET surface area of 501 $m^2\ g^{-1}$ for bpy-UiO-Fe(OH)$_3$, substantially lower than that of pristine bpy-UiO (1898 $m^2\ g^{-1}$),[49] indicating the incorporation of Fe(OH)$_3$ within the MOF pores (Figure 7.2b). Scanning electron microscopy (SEM) images of bpy-UiO-Fe(OH)$_3$ showed well-defined particles with an average size of ∼225 nm, and energy-dispersive X-ray spectroscopy (EDX) elemental mapping demonstrated a homogeneous distribution of Fe and Zr throughout the MOF particles (Figure 7.2c). X-ray photoelectron spectroscopy (XPS) showed Fe $2p_{3/2}$ and $2p_{1/2}$ binding energies at 710.12 and 723.43 eV, respectively, corresponding to Fe^{3+} oxidation state (Figure 7.2d). XPS analysis also confirmed Zr^{4+} in the

MOF nodes, with binding energies at 182.1 and 184.5 eV (Figure 7.2e).

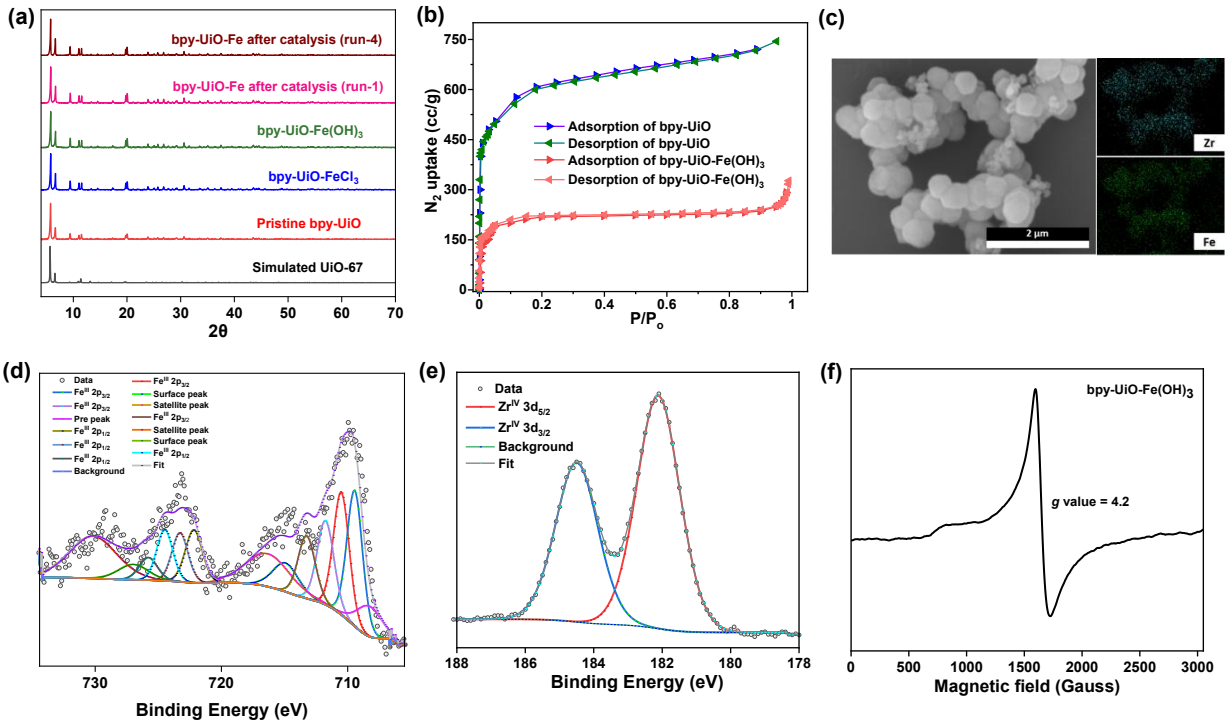


Figure 7.2: (a) PXRD patterns of simulated UiO-67 (black), pristine bpy-UiO (red), bpy-UiO-$FeCl_3$ (blue), bpy-UiO-$Fe(OH)_3$ (green), and bpy-UiO-Fe recovered after run-1 (pink) and run-4 (wine) of styrene oxidation. (b) N_2 sorption isotherms of bpy-UiO (blue/green) and bpy-UiO-$Fe(OH)_3$ (red/orange) measured at 77 K. (c) SEM-EDX mapping of bpy-UiO-$Fe(OH)_3$ particles. (d) Fe 2p XPS spectra of bpy-UiO-$Fe(OH)_3$. (e) Zr 3d XPS spectra of bpy-UiO-$Fe(OH)_3$. (f) EPR spectra of solid bpy-UiO-$Fe(OH)_3$.

The X-ray absorption near edge structure (XANES) spectrum of bpy-UiO-$Fe(OH)_3$ exhibits a pre-edge feature at 7116 eV, consistent with the presence of Fe^{3+} species.[49] The X-band electron paramagnetic resonance (EPR) spectrum of the Fe^{3+} centers shows a signal at g $\sim$ 4.2, characteristic of high-spin Fe^{3+} in a distorted octahedral environment (Figure 7.2f).[50–52] Extended X-ray absorption fine structure (EXAFS) analysis confirms the existence of (bpy)$Fe^{III}(OH)_3(H_2O)$, where the Fe^{3+} ion adopts an octahedral geometry comprising two bipyridyl nitrogens (2.03 Å, 2.03 Å), three hydroxyl ligands (1.9 Å, 1.9 Å, 2.03 Å), and one aqua ligand (2.09 Å).[49]

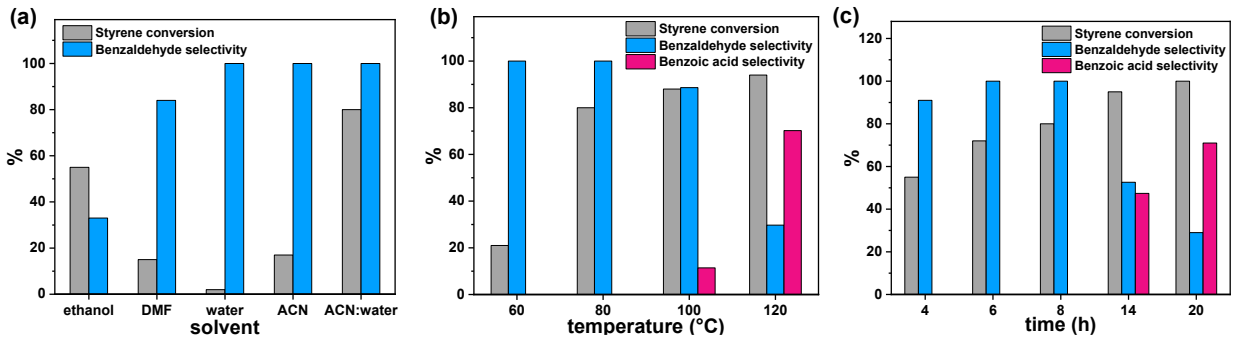


Figure 7.3: (a) Effect of solvent on the conversion of styrene and benzaldehyde selectivity for bpy-UiO-Fe(OH)$_3$-catalyzed oxidation of styrene. Reaction conditions: bpy-UiO-Fe(OH)$_3$ (0.4 mol% Fe), styrene (1.5 mmol), H_2O_2 (30% w/v, 2.5 eq.), 80 °C, 8 h. (b) Effect of temperature on the conversion of styrene and benzaldehyde selectivity for bpy-UiO-Fe(OH)$_3$-catalyzed oxidation of styrene. Reaction conditions: bpy-UiO-Fe(OH)$_3$ (0.4 mol% Fe), styrene (1.5 mmol), H_2O_2 (30% w/v, 2.5 eq.), H_2O/CH_3CN (1:1, 4 mL), 8 h. (c) Effect of reaction time on styrene conversion and benzaldehyde selectivity for bpy-UiO-Fe(OH)$_3$-catalyzed oxidation of styrene. Reaction conditions: bpy-UiO-Fe(OH)$_3$ (0.4 mol% Fe), styrene (1.5 mmol), H_2O_2 (30% w/v, 2.5 eq.), H_2O/CH_3CN (1:1, 4 mL), 80 °C. Reaction products were analyzed by GC–MS.

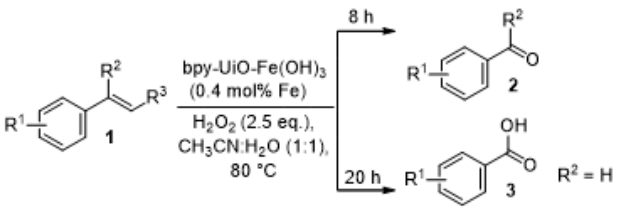
7.2.2 Bpy-UiO-Fe(OH)$_3$ Catalyzed Oxidation of Styrene Derivatives.

The selective oxidation of styrene derivatives to carbonyl compounds has significant industrial importance, as these compounds are essential intermediates in the production of pharmaceuticals, dyes, fragrances, and fine chemicals.[1;21;53] Styrene was first employed as a model substrate to investigate the catalytic activity of bpy-UiO-Fe(OH)$_3$. Optimization studies were conducted at 80 °C using hydrogen peroxide (H_2O_2) at a 2.5 equivalent ratio as the oxidant, with different solvent conditions tested (Figure 7.3a). The reactions conducted in ethanol and DMF resulted in moderate conversions of styrene, at 55% and 15%, respectively, but exhibited poor selectivity for benzaldehyde, with selectivities of 33% and 84%, respectively. In acetonitrile, while the conversion of styrene was low at 17%, the selectivity for benzaldehyde reached 100%. However, reactions in water faced challenges due to the low solubility of styrene, leading to negligible yields of benzaldehyde. A mixed solvent system of acetonitrile and water (1:1) afforded 80% conversion with 100% benzaldehyde selectivity in 8 h. Consequently, this mixed solvent system, along with H_2O_2 (30% w/v, 2.5 eq.), was utilized to optimize the reaction temperature. Increasing the temperature to 100 °C decreased

selectivity, likely due to benzaldehyde overoxidation to benzoic acid, whereas lowering the temperature to 60 °C reduced the styrene conversion (Figure 7.3b). The optimal reaction temperature for the oxidation of styrene to benzaldehyde was determined to be 80 °C, as it provides a good balance between activity and selectivity. Notably, at a higher temperature of 120 °C, the selectivity for benzoic acid increased significantly to 70%, accompanied by a styrene conversion rate of 94% (Figure 7.3b). The effect of reaction time on styrene oxidation was systematically studied at 80 °C within a range of 4 to 20 h. When the reaction time was extended from 4 to 8 h, the conversion of styrene increased, reaching approximately 80% with the exclusive production of benzaldehyde at 8 h (Figure 7.3c). However, extending the reaction time beyond 8 h led to decreased selectivity for benzaldehyde due to its overoxidation to benzoic acid. After 20 h, benzoic acid became the predominant product, exhibiting a maximum selectivity of 71% with complete conversion of styrene (Figure 7.3c).

The catalytic system was tested further with various styrene derivatives under the optimized reaction conditions for 8 h and 20 h (Figure 7.4). Both electron-donating and electron-withdrawing substituents were well tolerated, affording the corresponding aromatic aldehydes and acids in 8 h and 20 h, respectively, in high yield and selectivity. For example, *p*-chlorostyrene (**1g**) and *m*-chlorostyrene (**1h**) were converted to the respective aldehydes (**2g-2h**) in 99% and 87% yields after 8 h, while *o*- and *p*-methoxystyrene (**1e-1f**) afforded 70-75% carbonyl (**2e-2f**) yields with selectivities of 96% and 94%, respectively. Similarly, *p*- and *o*-methylstyrene (**1b-1c**) gave 82% and 83% yields, whereas the bulkier *p*-*tert*-butylstyrene (**1d**) underwent smooth oxidation to the aldehyde (**2d**) with 71% conversion and 82% selectivity. Electron-deficient substrates, such as *m*-nitrostyrene (**1l**), reacted efficiently, achieving 86% conversion to aldehyde (2l) with 100% selectivity in 8 h. More sterically demanding substrates, including trans-β-methylstyrene (**1k**) and trans-β-phenylstyrene (**1l**), were also well accommodated, producing aldehydes (**2k-2l**) in 70% and 71% yields, respectively. All the aldehyde products were purified by silica gel column chromatography. Importantly, upon extending the reaction time to 20 h, all substrates underwent further oxidation to their corresponding carboxylic acids. Both electron-donating and electron-withdrawing styrene derivatives displayed comparable reactivity, with most substrates affording 65-75% selectivity toward the acids (Figure 7.4).

Figure 7.4: Bpy-UiO-Fe(OH)$_3$ catalyzed oxidation of styrene derivatives.[a]



Entry	Substrate	% Conversion (% yield of 2) [b]	% Conversion (% yield of 3)[c]
1	1a	2a 80 (79)	3a 100 (71)
2	1b	2b 84 (82)	3b 100 (72)
3	1c	2c 85 (83)	3c 100 (69)
4	1d	2d 71 (58)	3d 91 (56)
5	1e	2e 75 (70)	3e 99 (57)
6	1f	2f 78 (75)	3f 99 (60)
7	1g	2g 100 (99)	3g 100 (78)
8	1h	2h 89 (87)	3h 100 (69)
9	1i	2i 86 (84)	3i 100 (73)
10	1j	2j 100 (99)	
11	1k	2k 100 (70)	3k 100 (69)
12	1l	2l 95 (71)	3l 100 (73)

[a] Reaction conditions: bpy-UiO-Fe(OH)$_3$ (0.4 mol% Fe), substrate (1.5 mmol), H_2O_2 (30% w/v, 2.5 eq.), 4 mL CH_3CN:H_2O (1:1), 80 °C.
[b] Reaction time was 8 h.
[c] Reaction time was 20 h.

7.2.3 Control Experiments.

Control experiments were performed to confirm the single-site nature of bpy-UiO-Fe(OH)$_3$ in the oxidation of styrene. Reactions using pristine bpy-UiO, Fe_2O_3, Fe nanoparticles, or Fe(0) nanoparticles encapsulated within the UiO-67 MOF (Fe@UiO-67) under similar reaction conditions (0.4 mol% Fe, styrene (1.5 mmol), 30% w/v H_2O_2 (2.5 eq.), 80 °C, 8 h) showed low conversion rates of styrene to benzaldehyde, ranging from 24% to 79% (Figure 7.5a). In contrast, bpy-UiO-$FeCl_3$ achieved 100% conversion of styrene but exhibited poor selectivity for benzaldehyde at only 14% (Figure 7.5a). This indicates that bpy-UiO-Fe(OH)$_3$ is the active catalyst for the oxidation of styrene to benzaldehyde.

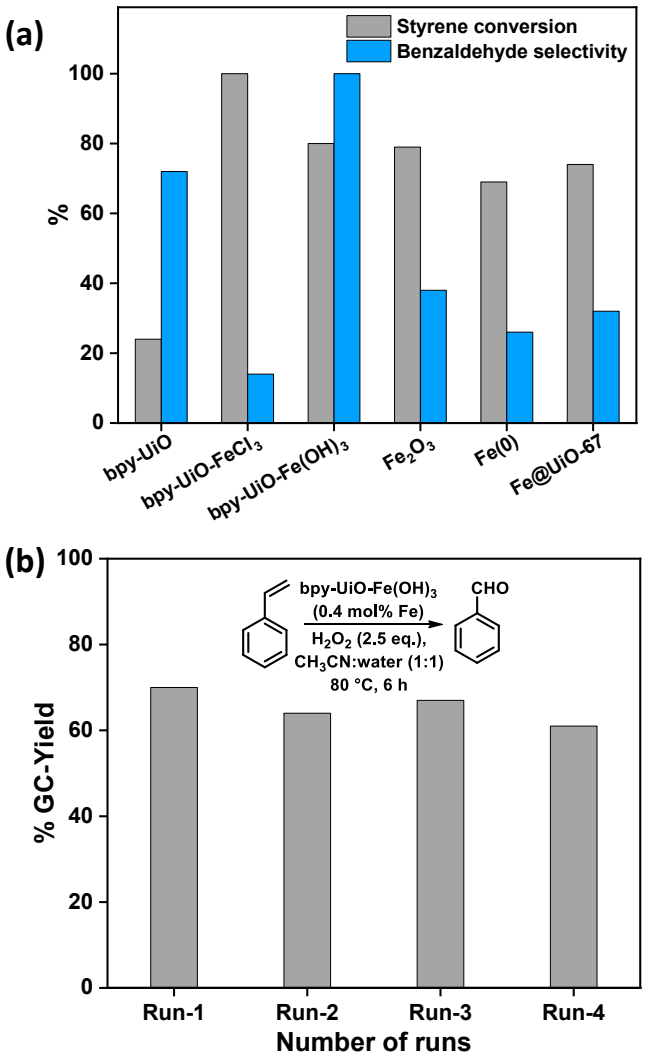


Figure 7.5: (a) Comparison of catalytic activity of bpy-UiO-Fe(OH)$_3$ with other catalysts at 80 °C (8 h). (b) Recycling test for bpy-UiO-Fe(OH)$_3$-catalyzed styrene oxidation to benzaldehyde under optimized reaction conditions in 6 h.

Furthermore, after removal of bpy-UiO-Fe(OH)$_3$ via hot filtration, negligible conversion of styrene to benzaldehyde was observed (Figure 7.9), confirming that the active sites responsible for catalysis reside within the bpy-UiO-Fe(OH)$_3$ framework. Moreover, the bpy-UiO-Fe(OH)$_3$ catalyst retained its activity and could be reused for at least four consecutive cycles in the oxidation of styrene, giving a cumulative TON of 563 (Figure 7.5b). ICP analysis revealed minimal leaching of Fe and Zr, with values of 0.07% and 0.8% after the first run, and 0.05% and 1.1% after the fourth run, respectively (Table 7.3). PXRD analysis of bpy-UiO-Fe after run-1 and run-4 of styrene oxidation confirmed that the MOF maintained its structural integrity under the reaction conditions (Figure 7.2a).

The homogeneous control of bpy-UiO-Fe(OH)$_3$, prepared from a 1:1 molar ratio of bipyri-

dine and $Fe(OH)_3$, afforded only 20% styrene conversion with 72% selectivity for benzaldehyde. In contrast, bpy-UiO-$Fe(OH)_3$ achieved 80% conversion with 100% selectivity under identical reaction conditions and Fe loading. These experiments suggest that bpy-UiO-$Fe(OH)_3$ is at least fourfold more active and significantly more selective than its homogeneous analogue, likely due to stabilization of the monomeric Fe(III) hydroxyl species within the MOF pores via active site isolation.

7.2.4 Mechanistic Insights into bpy-UiO-$Fe(OH)_3$-Catalyzed Oxidation of Styrene.

To probe possible intermediates, the reaction mixture was analyzed under partial conversion by GC–MS. Oxidation of styrene with H_2O_2 at 80 °C for 4 h using 0.4 mol% bpy-UiO-$Fe(OH)_3$ yielded mainly benzaldehyde (50%), along with small amounts of styrene oxide (3%) and 1-phenylethane-1,2-diol (2%), at an overall 55% conversion. These findings suggest that styrene may first undergo epoxidation, followed by hydrolysis to form the diol, which could then be further oxidized to benzaldehyde.

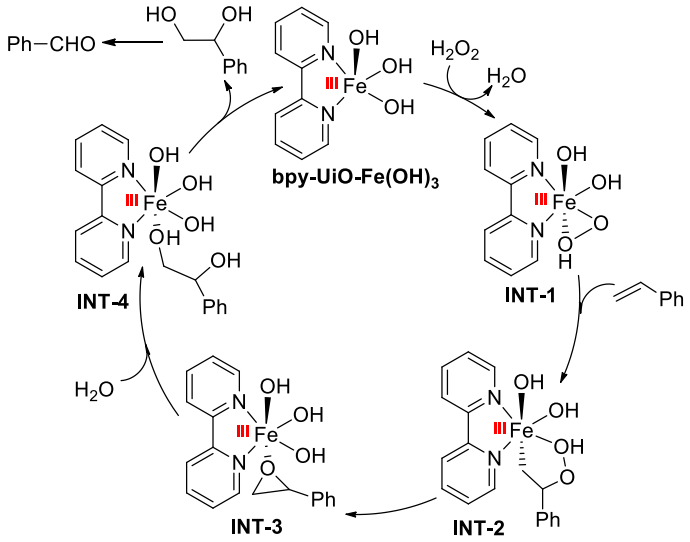


Figure 7.6: Plausible reaction pathway illustrating the bpy-UiO-$Fe(OH)_3$ catalyzed styrene oxidation to benzaldehyde.

The high selectivity toward benzaldehyde suggests a non-radical pathway, involving initial epoxidation, subsequent diol formation, and oxidative C-C cleavage, rather than a Fenton-type radical pathway, which typically produces a mixture of products. To assess the possibility of a radical pathway, a control reaction was performed using Na_2SO_3 as a radical scavenger; however, the rate of styrene oxidation was largely unaffected, indicating

a non-radical pathway in bpy-UiO-Fe(OH)$_3$-catalyzed styrene oxidation to benzaldehyde.

We propose that bpy-UiO-Fe(OH)$_3$ interacts with H_2O_2 to generate an iron(III)- hydroperoxo intermediate (INT-1). Subsequent insertion of the alkene into the Fe-O bond of INT-1 affords INT-2, which undergoes structural rearrangement to yield INT-3. Hydrolysis of the coordinated epoxide in INT-3, initiated by nucleophilic attack of water at the more substituted carbon, produces INT-4. INT-4 then regenerates the bpy-UiO-Fe(OH)$_3$ catalyst while releasing the corresponding 1,2-diol. The aromatic 1,2-diol subsequently undergoes oxidative C-C bond cleavage, yielding benzaldehyde, a pathway favored by resonance stabilization of the benzylic carbocation intermediate.

Further evidence for the epoxide–diol route was obtained from control experiments. Under identical reaction conditions, styrene epoxide (1 mmol) afforded 70% conversion to benzaldehyde within 5 h in the presence of bpy-UiO-Fe(OH)$_3$, compared to only 40% in the absence of the catalyst. This enhanced reactivity likely arises from activation of the epoxide at the electrophilic Fe center within the MOF, which facilitates nucleophilic attack of water at the more hindered carbon atom, thereby accelerating diol formation and subsequent oxidation to benzaldehyde.

7.3 Experimental Section

7.3.1 Synthesis and Characterization of bpy-UiO-Fe(OH)$_3$.

Synthesis of bpy-UiO.[48]

[2,2′-Bipyridine]-5,5′-dicarboxylic acid (H_2bpydc) was synthesized following a reported procedure.[49] A mixture of [2,2′-bipyridine]-5,5′-dicarboxylic acid (0.027 g, 0.111 mmol) and $ZrCl_4$ (0.026 g, 0.112 mmol) was dissolved in 13 mL of DMF and sonicated for 30 min. Trifluoroacetic acid (0.040 mL, 0.523 mmol) was then added to the mixture. The solution was heated in a sealed 15 mL glass vial at 100 °C for four days in an oven. After cooling to room temperature, the resulting white crystals were isolated by centrifugation, washed several times with DMF and THF, and stored in THF at room temperature.

Synthesis of bpy-UiO-Fe(OH)$_3$.

A solution of $FeCl_3$ (0.04 g, 0.024 mmol) in THF was added to bpy-UiO MOF (0.008 g), and the mixture was stirred overnight at room temperature inside a glovebox. The resulting yellowish-brown solid was collected by centrifugation and washed several times with THF to afford bpy-UiO-$FeCl_3$. Next, $NaEt_3BH$ (3.5 equiv. w.r.t. Fe) was slowly added to a slurry of bpy-UiO-$FeCl_3$ in 3 mL THF inside the glovebox and stirred at room temperature for 1 h. The black solid bpy-UiO-FeH_3 was isolated by centrifugation and washed multiple times with THF to remove excess reducing agent. Bpy-UiO-FeH_3 was then taken out of the glovebox and suspended in water for 30 min, resulting in bpy-UiO-Fe(OH)$_3$. Thermogravimetric analysis (TGA) indicated that bpy-UiO-Fe(OH)$_3$ contains 39% solvent by weight, and ICP-OES confirmed 72% iron loading relative to bpy moieties, with the overall formula $Zr_6O_4(OH)_4(bpy)_6Fe_{4.32}(OH)_{12.96}$.

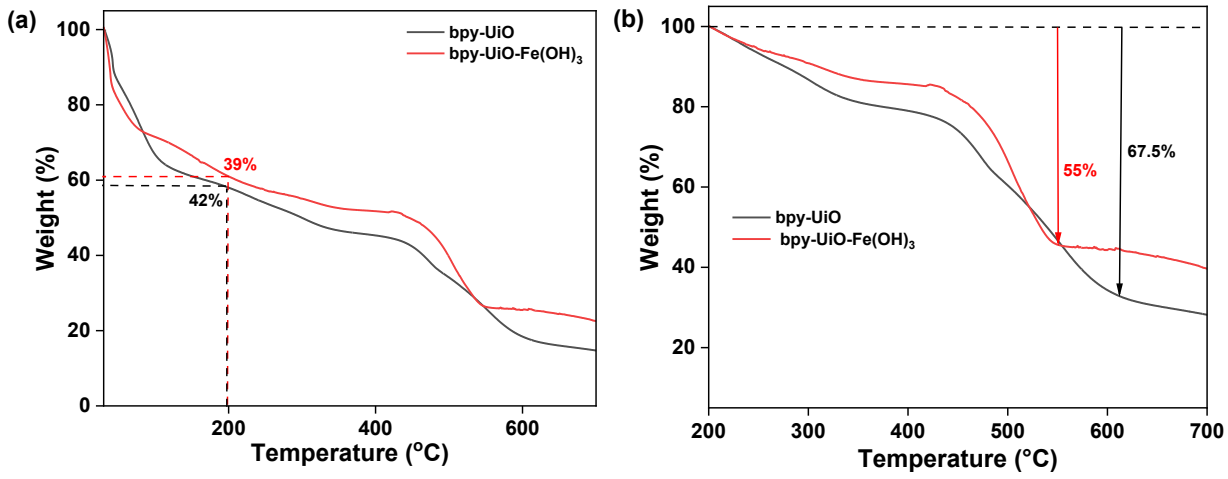


Figure 7.7: (a) TGA curves of freshly prepared bpy-UiO and bpy-UiO-Fe(OH)$_3$. A solvent weight loss of 42% in bpy-UiO (black) and 39% in bpy-UiO-Fe(OH)$_3$ (red) was observed from 40 °C to 200 °C. (b) TGA curves of freshly prepared bpy-UiO (black) and bpy-UiO-Fe(OH)$_3$ (red) from 200–700 °C. The increased weight of the metalated MOF is due to the presence of iron within the framework.

Theoretical calculation:

(a) For bpy-UiO:

1 mole of $Zr_6O_4(OH)_4(bpy)_6$ = 6 moles of linker ($C_{12}H_6N_2O_4$)

2132.5 g of $Zr_6O_4(OH)_4(bpy)_6$ = 1453.12 g of linker

Table 7.1: Determination of defects in bpy-UiO and bpy-UiO-Fe(OH)$_3$ by TGA analysis.

Sample	Condition	% Solvent	% Ligand	% Residue
	Calculated	–	68	32
bpy-UiO	TGA	42	40	18
	Corrected	–	67.5	32.5
	Calculated	–	56	44
bpy-UiO-Fe(OH)$_3$	TGA	39	35	26
	Corrected	–	55	45

$\%\ \text{Linker} = \frac{1453.12}{2132.5} \times 100 = 68\%$

$\%\ \text{Residue} = 100 - 68 = 32\%$

(b) For bpy-UiO-Fe(OH)$_3$:

1 mole of $Zr_6O_4Fe_{4.32}(OH)_{12.96}(C_{12}H_6N_2O_4)_6(OH)_4$ = 6 moles of linker ($C_{12}H_6N_2O_4$)

2594.1 g of $Zr_6O_4Fe_{4.32}(OH)_{12.96}(C_{12}H_6N_2O_4)_6(OH)_4$ = 1453.12 g of linker

$\%\ \text{Linker} = \frac{1453.12}{2594.1} \times 100 = 56\%$

$\%\ \text{Residue} = 100 - 56 = 44\%$

The wt% ligand calculated theoretically matches closely with the wt% ligand observed experimentally for bpy-UiO and bpy-UiO-Fe(OH)$_3$. This indicates the absence of any missing-linker defects within bpy-UiO and bpy-UiO-Fe(OH)$_3$.

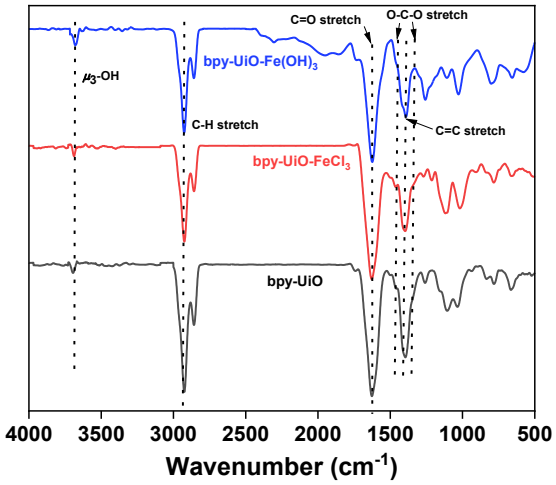
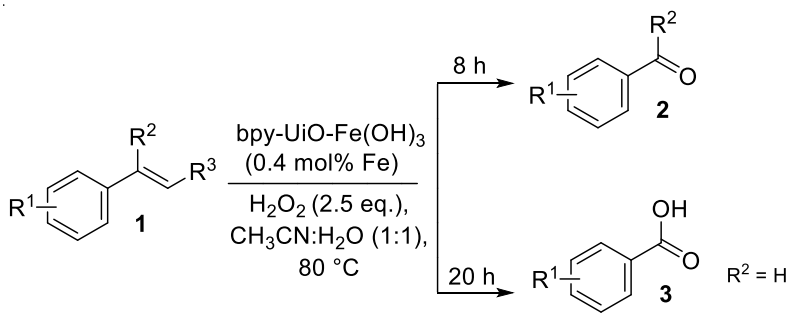


Figure 7.8: FT-IR (KBr) spectrum of freshly prepared bpy-UiO (black), bpy-UiO-FeCl$_3$ (red) and bpy-UiO-Fe(OH)$_3$ (blue).

7.3.2 Bpy-UiO-Fe(OH)$_3$ catalyzed oxidation of styrene substrates.

General procedure for bpy-UiO-Fe(OH)$_3$ catalyzed oxidation of styrene and styrene derivatives.



Solid MOF bpy-UiO-Fe(OH)$_3$ (0.4 mol% Fe) in 4 mL CH_3CN:H_2O (1:1) was introduced into a 25 mL Schlenk tube equipped with a water-cooled condenser and placed in an oil bath at 80 °C. Styrene (1.5 mmol) was then added, followed by the dropwise addition of 30% w/v H_2O_2 (2.5 equiv). The reactions were performed for 8 h and 20 h. After the completion of the reaction, the solid MOF was centrifuged out of the suspension. An aliquot of the supernatant was analyzed by GC-MS.

Isolation of products:

(a) *Aldehyde (reaction time: 8 h):*

The organic layer of the reaction mixture was separated and extracted with ethyl acetate (3 × 10 mL). The combined organic extracts were dried over anhydrous Na_2SO_4, filtered, and concentrated under reduced pressure. The crude residue was purified by silica gel column chromatography using hexane/ethyl acetate (5:1) as the eluent to afford the pure aldehyde products.

(b) *Carboxylic acid (reaction time: 20 h):*

The crude mixture was first extracted with aqueous NaOH solution (1–2 M, 3 × 10 mL) to convert the carboxylic acid products into their corresponding sodium salts. The aqueous phase was separated, acidified to pH ∼ 1 with dilute HCl, and subsequently extracted with chloroform (3 × 10 mL). The combined chloroform extracts were dried over anhydrous Na_2SO_4, filtered, and concentrated under reduced pressure to yield the pure carboxylic acid

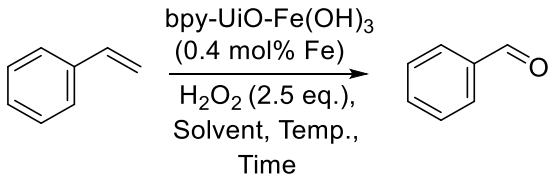
products.

Analysis of products by GC-MS.

The conversion and selectivity of the products were determined using GC-MS analysis. Using the area percentage method, the peak areas of the remaining reactants, products, and by-products were determined.

GC-MS conditions: The column used was the Agilent DB-WAX column with 30 m length, 0.320 mm internal diameter, and 0.25 μm film. The chromatographic conditions were: flow rate of helium at 1 mL min^{-1}, injection volume: 1 μL, column oven temperature was initially 40 °C and then increased up to 230 °C with the rate of 5 °C min^{-1}, and detector temperature was 250 °C.

Table 7.2: Optimization of reaction conditions for the oxidation of styrene.[a].



S. No.	Catalyst	Temp. (°C)	Time (h)	Solvent	Conversion (%)[b]	Selectivity (%)[b]
1	bpy-UiO-Fe(OH)$_3$	80	4	CH_3CN:H_2O (1:1)	55	100
2	bpy-UiO-Fe(OH)$_3$	80	6	CH_3CN:H_2O (1:1)	72	100
3	bpy-UiO-Fe(OH)$_3$	80	8	CH_3CN:H_2O (1:1)	80	100
4	bpy-UiO-Fe(OH)$_3$	80	14	CH_3CN:H_2O (1:1)	95	52.6
5[c]	bpy-UiO-Fe(OH)$_3$	80	20	CH_3CN:H_2O (1:1)	100	29
6	bpy-UiO-Fe(OH)$_3$	60	8	CH_3CN:H_2O (1:1)	21	100
7	bpy-UiO-Fe(OH)$_3$	100	8	CH_3CN:H_2O (1:1)	88	88.6
8[d]	bpy-UiO-Fe(OH)$_3$	120	8	CH_3CN:H_2O (1:1)	94	29.7
9	bpy-UiO-Fe(OH)$_3$	80	8	CH_3CN	17	100
10	bpy-UiO-Fe(OH)$_3$	80	8	H_2O	2	100
11	bpy-UiO-Fe(OH)$_3$	80	8	EtOH	55	33
12	bpy-UiO-Fe(OH)$_3$	80	8	DMF	15	84

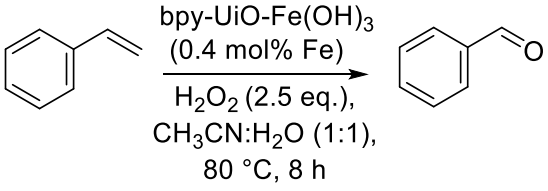
[a] Styrene (1.5 mmol), solvent used was 4 mL.

[b] Reaction was analyzed by GC-MS.

[c] Benzoic acid was formed as the major product with selectivity of ∼71%.

[d] Benzoic acid was formed as the major product with selectivity of ∼70%.

Typical procedure for bpy-UiO-Fe(OH)$_3$ catalysed oxidation of styrene to benzaldehyde.



Solid MOF bpy-UiO-Fe(OH)$_3$ (0.4 mol%) in 4 mL CH_3CN:H_2O (1:1) was introduced into a 25 mL Schlenk tube equipped with a water-cooled condenser and placed in an oil bath at 80 °C, and styrene (1.5 mmol) was added. Subsequently, 30% w/v H_2O_2 (2.5 eq.) was added dropwise to the reaction mixture. After 8 h, the reaction was cooled to room temperature and the solid MOF was centrifuged out of the suspension. The remaining solution was extracted with ethyl acetate (3 × 10 mL); the combined organic layers were dried (Na_2SO_4), filtered, and concentrated *in vacuo* to afford the crude products. The residue was purified by silica gel column chromatography (hexane/ethyl acetate, 5:1) to yield the aldehyde products, which were characterized by ^{1}H and ^{13}C NMR and confirmed by GC-MS.

Effect of time on conversion (%) and selectivity (%) for styrene oxidation to benzaldehyde catalyzed by bpy-UiO-Fe(OH)$_3$.

Solid MOF bpy-UiO-Fe(OH)$_3$ (0.4 mol% Fe) in 4 mL CH_3CN:H_2O (1:1) was introduced into a 25 mL Schlenk tube, equipped with a water-cooled condenser, and placed in an oil bath at 80 °C, and styrene (1.5 mmol) was added. Subsequently, 30% w/v H_2O_2 (2.5 eq.) was added dropwise to the above reaction mixture. The progression of the reaction was monitored using GC-MS analysis at various times (4, 6, 8, 14, and 20 h). With increasing reaction time, product conversion gradually increased, reaching 100% at 20 h. The selectivity toward benzaldehyde increased initially, attaining 80% at 8 h. Beyond 8 h, overoxidation of benzaldehyde led to a rise in benzoic acid formation, reaching 71% selectivity toward benzoic acid at 20 h.

Effect of temperature on conversion (%) and selectivity (%) for styrene oxidation to benzaldehyde catalyzed by bpy-UiO-Fe(OH)$_3$.

Solid MOF bpy-UiO-Fe(OH)$_3$ (0.4 mol% Fe) in 4 mL CH_3CN:H_2O (1:1) was introduced into four different 25 mL Schlenk tubes, each equipped with a water-cooled condenser and placed in oil baths at different temperatures (60, 80, 100, and 120 °C), and styrene (1.5 mmol) was added. Subsequently, 30% w/v H_2O_2 (2.5 eq.) was added dropwise to all the tubes. After 8 h of reaction time, the solid MOF was centrifuged out of the suspension. The conversion and selectivity of the products were then analyzed using GC–MS. It was observed that with increasing temperature, the conversion of styrene increased. However, at temperatures

above 80 °C, the selectivity toward benzaldehyde decreased due to its overoxidation, leading to the formation of benzoic acid.

Control reactions for styrene oxidation reaction.

(a) Styrene oxidation with Fe@UiO-67.[54] UiO-67 MOF was prepared according to the reported literature.[44] It is isostructural to bpy-UiO MOF but contains biphenyl (bpdc) linkers instead of bipyridyl (bpydc) linkers. In a 5 mL round-bottom flask, a solution of $FeCl_3 \cdot 6H_2O$ (50 mg, 0.18 mmol) in ethyl acetate (2 mL) was prepared, followed by the addition of UiO-67 (100 mg). The mixture was heated for 8 h at a temperature of 50 °C. Then, it was allowed to cool down, and the solid was collected by centrifugation, washed thoroughly, and dried to give UiO-67-$FeCl_3$.

Next, a solution of $NaBH_4$ was prepared (10 mg) in 6 mL of deionized water in a round-bottom flask, and 80 mg of UiO-67-$FeCl_3$ was added to this solution. The pH was controlled in the range of 6-8 throughout the addition of $NaBH_4$. The resultant solution was stirred for 30 min, and then it was filtered out to get the solid product. The collected solid was washed thoroughly with deionized water to give a black powder of Fe@UiO-67. Finally, the Fe@UiO-67 was activated at 150 °C for 12 h under high vacuum.

For the catalytic oxidation reaction, Fe@UiO-67 (0.4 mol% Fe) in 4 mL CH_3CN:H_2O (1:1) was introduced into a 25 mL Schlenk tube, equipped with a water-cooled condenser and placed in an oil bath at 80 °C, and styrene (1.5 mmol) was added. Subsequently, 30% w/v H_2O_2 (2.5 eq.) was added dropwise to the reaction mixture. After 8 h of the reaction, the solid catalyst was centrifuged out of the suspension and washed several times with CH_3CN. The conversion and selectivity of the products were then analyzed using GC-MS.

(b) Styrene oxidation with Fe nanoparticles.[55] An aqueous solution of 1.6 M $NaBH_4$ was added slowly into a 1.0 M aqueous solution of $FeCl_3 \cdot 3H_2O$ with constant stirring at room temperature to obtain black-colored Fe(0) nanoparticles. The black solid was then washed several times with THF and dried.

Fe nanoparticles (0.4 mol% Fe) were added into a 25 mL Schlenk tube equipped with a

water-cooled condenser, along with 4 mL CH_3CN:H_2O (1:1), and placed in an oil bath at 80 °C. Styrene (1.5 mmol) was then added, followed by the dropwise addition of 30% w/v H_2O_2 (2.5 eq.). The reactions were performed for a period of 8 h. After the completion of the reaction, the solid was centrifuged out of the suspension. An aliquot of the supernatant was analyzed by GC-MS. The remaining solution was extracted with ethyl acetate (3 × 10 mL); the combined organic layers were dried (Na_2SO_4), filtered, and concentrated *in vacuo* to afford the crude products. The residue was further concentrated *in vacuo* to yield the corresponding products.

Test for "heterogeneity of bpy-UiO-Fe(OH)$_3$" in styrene oxidation.

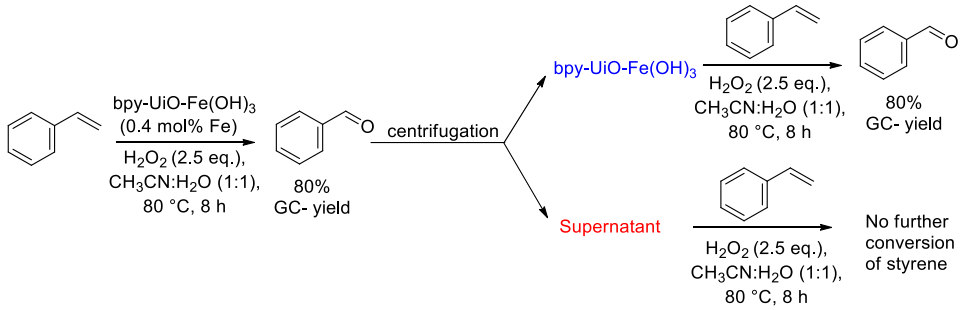


Figure 7.9: Hot filtration test of bpy-UiO-Fe(OH)$_3$ catalyzed styrene oxidation.

General procedure mentioned in Section 7.3.2 was followed. After 8 h of reaction, the solid MOF catalyst was removed from the hot reaction mixture by filtration and thoroughly washed with water. Two separate reactions were set up in two different Schlenk tubes, one with the solid MOF and the other with the supernatant. The extracted solid and supernatant were added into two separate Schlenk tubes, each equipped with a water-cooled reflux condenser, and both tubes were placed in oil baths set at a temperature of 80 °C. Then, styrene (1.5 mmol) and 30% w/v H_2O_2 (2.5 eq.) were added dropwise to each of the tubes. After 8 h, the reactions were analyzed with GC-MS, which revealed that the reaction with the solid MOF gave 80% yield of benzaldehyde, while the reaction with the supernatant showed no conversion of styrene to benzaldehyde. This experiment rules out the potential of any leached Fe species responsible for catalysis and confirms that solid bpy-UiO-Fe(OH)$_3$ is the sole catalyst for the oxidation of styrene.

Recycling of bpy-UiO-Fe(OH)$_3$ for the oxidation of styrene.

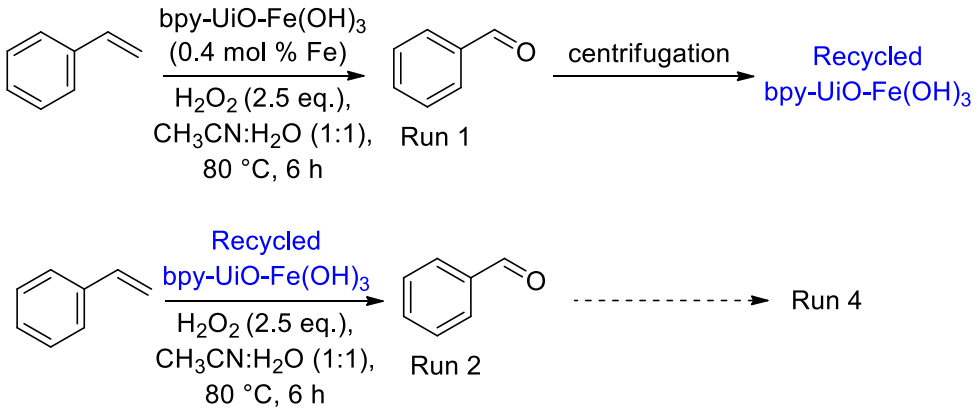


Figure 7.10: Recyclability and reusability of bpy-UiO-Fe(OH)$_3$ for styrene oxidation.

The recycle and reuse experiment was conducted to check the stability of the MOF catalyst. The general procedure mentioned in Section 7.3.2 was followed, except that the recovered MOF catalyst was washed several times with CH_3CN. For the recycling experiments, the recovered catalyst was introduced into a 25 mL Schlenk tube, equipped with a water-cooled condenser, and placed in an oil bath at 80 °C; styrene (1.5 mmol) was then added. Subsequently, 30% w/v H_2O_2 (2.5 eq.) was added dropwise to the reaction mixture. After 6 h of the reaction, the solid MOF was centrifuged out of the suspension, washed several times with CH_3CN, and the product was analyzed using GC-MS. The procedure was repeated three times with very minimal leaching (<1%) of Fe and Zr (Table 7.3). The MOF retained its crystallinity and structural stability, as confirmed by the PXRD patterns of the recycling experiments (Figure 7.2a). The catalyst could be recycled and reused at least three times without any loss of activity, giving a cumulative TON of 563.

Table 7.3: % GC yield of benzaldehyde and the leaching of Fe and Zr in various runs of the recycling of bpy-UiO-Fe(OH)$_3$ for the oxidation of styrene.

No. of Run	**Time (h)**	**% GC Yield of Benzaldehyde**	**% Leaching (Fe, Zr)**
Run-1	6	70	0.07, 0.8
Run-2	6	66	0.06, 0.9
Run-3	6	67	0.03, 0.7
Run-4	6	61	0.05, 1.1

Radical scavenging test with Na_2SO_3 as the radical scavenger.

To investigate any role of ·OH in bpy-UiO-Fe(OH)$_3$ catalyzed oxidation of styrene, we performed the catalysis in the presence of a known ·OH radical scavenger, Na_2SO_3, and the catalytic activity and selectivity were compared to those of reactions carried out in the absence of ·OH radical scavengers. Reaction conditions: bpy-UiO-Fe(OH)$_3$ (0.4 mol% Fe), styrene (1.5 mmol), Na_2SO_3 (10 mmol), H_2O_2 (2.5 eq.), CH_3CN:H_2O (1:1, 4 mL), 8 h. The general procedure mentioned in Section 7.3.2 was followed, with Na_2SO_3 (10 mmol) added to study its effect on the catalytic reaction. It was observed that the yield of benzaldehyde was similar for the reaction with Na_2SO_3 (80% GC yield) to that without Na_2SO_3. This experiment confirms that there is no role of the radical scavenger Na_2SO_3 and rules out the participation of ·OH radicals in the reaction mechanism.

7.3.3 XPS analysis of bpy-UiO-Fe(OH)$_3$.

All the binding energies were corrected with reference to the C1s peak at 284.8 eV. CasaXPS software was used for peak analysis and de-convolution studies.

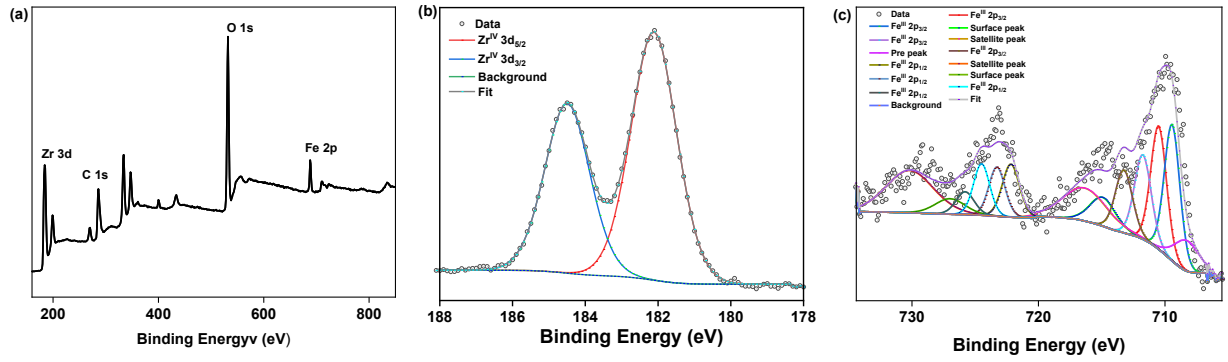


Figure 7.11: (a) Raw XPS data of bpy-UiO-Fe(OH)$_3$. (b) XPS fitting of Zr 3d in bpy-UiO-Fe(OH)$_3$. (c) XPS fitting of Fe 2p in bpy-UiO-Fe(OH)$_3$.

Table 7.4: Fe 2p XPS fitting parameters for bpy-UiO-Fe(OH)$_3$.

Component	**Position (eV)**	**FWHM (eV)**	**Area%**	**Line shape**
Fe(III) $2p_{3/2}$	708.30	2.3	5.39	GL(30)
Fe(III) $2p_{3/2}$	709.44	1.4	15.09	GL(30)
Fe(III) $2p_{3/2}$	710.50	1.4	13.88	GL(30)
Fe(III) $2p_{3/2}$	711.75	1.6	10.13	GL(30)
Fe(III) $2p_{3/2}$	713.25	1.6	7.70	GL(30)
Fe(III) $2p_{3/2}$	714.93	2.4	5.28	GL(30)
Fe(III) $2p_{3/2}$	717.24	4.1	10.54	GL(30)
Fe(III) $2p_{1/2}$	722.09	1.6	6.19	GL(30)
Fe(III) $2p_{1/2}$	723.19	1.5	5.38	GL(30)
Fe(III) $2p_{1/2}$	724.40	1.5	5.63	GL(30)
Fe(III) $2p_{1/2}$	725.70	1.7	2.81	GL(30)
Fe(III) $2p_{1/2}$	726.90	2.8	3.15	GL(30)
Fe(III) $2p_{1/2}$	730.10	3.6	8.82	GL(30)

7.3.4 Characterization of the products.

Benzaldehyde (2a).[56] Benzaldehyde was synthesized with 79% yield according to the general procedure for the oxidation of styrene derivatives using bpy-UiO-Fe(OH)$_3$ (0.4 mol% Fe), styrene (1.5 mmol), and H_2O_2 (2.5 eq.) at 80 °C for 8 h. After 8 h, the combined organic extracts were concentrated *in vacuo* followed by column chromatography using hexane and ethyl acetate (5:1) as an eluent to yield benzaldehyde. ^{1}H NMR (400 MHz, $CDCl_3$, ppm): δ 10.01 (s, 1H), 7.90 (s, 2H), 7.69 (d, J = 4.8 Hz, 1H), 7.58 (d, J = 5.5 Hz, 2H). ^{13}C NMR (151 MHz, DMSO-d_6): 193.0, 136.2, 134.5, 129.4, 129.1.

4-Methyl benzaldehyde (2b).[56] 4-Methyl benzaldehyde was synthesized with 82% yield according to the general procedure for the oxidation of styrene derivatives using bpy-UiO-Fe(OH)$_3$ (0.4 mol% Fe), 4-methyl styrene (1.5 mmol), and H_2O_2 (2.5 eq.) at 80 °C for 8 h. After 8 h, the combined organic extracts were concentrated *in vacuo* followed by column chromatography using hexane and ethyl acetate (5:1) as an eluent to yield 4-methyl benzaldehyde. ^{1}H NMR (400 MHz, DMSO-d_6, ppm): δ 9.95 (s, 1H), 7.80 (d, J = 7.9 Hz, 2H), 7.40 (d, J = 7.8 Hz, 2H), 2.39 (s, 3H). ^{13}C NMR (101 MHz, DMSO-d_6, ppm): 192.6, 145.2, 134.0, 129.7, 129.6, 21.4.

2-Methyl benzaldehyde (2c).[57] 2-Methyl benzaldehyde was synthesized with 83% yield according to the general procedure for the oxidation of styrene derivatives using bpy-UiO-Fe(OH)$_3$ (0.4 mol% Fe), 2-methyl styrene (1.5 mmol), and H_2O_2 (2.5 eq.) at 80 °C for 8 h. After 8 h, the combined organic extracts were concentrated *in vacuo* followed by column chromatography using hexane and ethyl acetate (5:1) as an eluent to yield 2-methyl benzaldehyde. ^{1}H NMR (400 MHz, $CDCl_3$, ppm): δ 10.26 (s, 1H), 7.79 (dd, J = 7.6, 1.5 Hz, 1H), 7.47 (td, J = 7.5, 1.6 Hz, 1H), 7.36 (td, $^3J_{H-H}$ = 7.5, 1.2 Hz, 1H), 7.28–7.22 (m, 1H), 2.67 (s, 3H). ^{13}C NMR (101 MHz, $CDCl_3$, ppm): δ 192.73, 140.53, 134.07, 133.58, 131.98, 131.70, 126.25, 19.52.

4-*tert*-Butylbenzaldehyde (2d).[56]

4-*tert*-Butylbenzaldehyde was synthesized with 58% yield according to the general procedure for the oxidation of styrene derivatives using bpy-UiO-Fe(OH)$_3$ (0.4 mol% Fe), 4-*tert*-butylstyrene (1.5 mmol), and H_2O_2 (2.5 eq.) at 80 °C for 8 h. After 8 h, the combined organic extracts were concentrated *in vacuo* followed by column chromatography using hex-

ane and ethyl acetate (5:1) as eluent to yield 4-*tert*-butylbenzaldehyde. ^{1}H NMR (400 MHz, $CDCl_3$, ppm): δ 9.98 (s, 1H), 7.82 (d, J = 8.5 Hz, 2H), 7.55 (d, J = 8.3 Hz, 2H), 1.36 (s, 9H). ^{13}C NMR (101 MHz, $CDCl_3$, ppm): δ 192.0, 158.4, 134.1, 129.7, 126.0, 35.4, 31.1.

4-Methoxybenzaldehyde (2e).[56]

4-Methoxybenzaldehyde was synthesized with 70% yield according to the general procedure for the oxidation of styrene derivatives using bpy-UiO-Fe(OH)$_3$ (0.4 mol% Fe), 4-methoxystyrene (1.5 mmol), and H_2O_2 (2.5 eq.) at 80 °C for 8 h. After 8 h, the combined organic extracts were concentrated *in vacuo* followed by column chromatography using hexane and ethyl acetate (5:1) as eluent to yield 4-methoxybenzaldehyde. ^{1}H NMR (400 MHz, DMSO-d_6, ppm): δ 9.87 (s, 1H), 7.87 (d, J = 8.6 Hz, 2H), 7.12 (d, J = 8.6 Hz, 2H), 3.86 (s, 3H). ^{13}C NMR (101 MHz, DMSO-d_6, ppm): δ 191.3, 164.2, 131.8, 129.7, 114.5, 55.7.

2-Methoxy benzaldehyde (2f).[57]

2-Methoxy benzaldehyde was synthesized with 75% yield according to the general procedure for the oxidation of styrene derivatives using bpy-UiO-Fe(OH)$_3$ (0.4 mol% Fe), 2-methoxy styrene (1.5 mmol), H_2O_2 (2.5 eq.) at 80 °C for 8 h. After 8 h, the combined organic extracts were concentrated *in vacuo* followed by column chromatography using hexane and ethyl acetate (5:1) as an eluent to yield 2-methoxy benzaldehyde product. ^{1}H NMR (400 MHz, $CDCl_3$, ppm): δ 10.45 (s, 1H), 7.80 (dd, J = 7.7, 1.8 Hz, 1H), 7.52 (ddd, J = 8.2, 7.4, 1.8 Hz, 1H), 7.08–6.90 (m, 2H), 3.90 (s, 3H); ^{13}C NMR (101 MHz, $CDCl_3$, ppm): δ 189.62, 161.75, 135.83, 128.38, 124.80, 120.55, 111.58, 55.53.

4-Chloro benzaldehyde (2g).[58]

4-Chloro benzaldehyde was synthesized with 99% yield according to the general procedure for the oxidation of styrene derivatives using bpy-UiO-Fe(OH)$_3$ (0.4 mol% Fe), 4-chloro styrene (1.5 mmol), H_2O_2 (2.5 eq.) at 80 °C for 8 h. After 8 h, the combined organic extracts were concentrated *in vacuo* followed by flash chromatography using hexane and ethyl acetate (7:3) as an eluent to yield 4-chloro benzaldehyde product. ^{1}H NMR (300 MHz, $CDCl_3$, ppm): δ 10.13 (s, 2H), 8.05 (s, 4H); ^{13}C NMR (75 MHz, $CDCl_3$, ppm): δ 191.63, 140.13, 130.27.

3-Chloro benzaldehyde (2h).[57]

3-Chloro benzaldehyde was synthesized with 87% yield according to the general procedure for the oxidation of styrene derivatives using bpy-UiO-Fe(OH)$_3$ (0.4 mol% Fe), 3-chloro

styrene (1.5 mmol), H_2O_2 (2.5 eq.) at 80 °C for 8 h. After 8 h, the combined organic extracts were concentrated *in vacuo* followed by column chromatography using hexane and ethyl acetate (5:1) as an eluent to yield 3-chloro benzaldehyde product. ^{1}H NMR (400 MHz, $CDCl_3$, ppm): δ 9.94 (s, 1H), 7.81 (dd, J = 2.1, 1.5 Hz, 1H), 7.73 (dt, J = 7.5, 1.4 Hz, 1H), 7.56 (ddd, J = 8.0, 2.1, 1.2 Hz, 1H), 7.45 (t, J = 7.8 Hz, 1H); ^{13}C NMR (101 MHz, $CDCl_3$, ppm): δ 190.81, 137.78, 135.40, 134.35, 130.38, 129.22, 127.98.

3-Nitro benzaldehyde (2i).[59]

3-Nitro benzaldehyde was synthesized with 84% yield according to the general procedure for the oxidation of styrene derivatives using bpy-UiO-Fe(OH)$_3$ (0.4 mol% Fe), 3-nitro styrene (1.5 mmol), H_2O_2 (2.5 eq.) at 80 °C for 8 h. After 8 h, the combined organic extracts were concentrated *in vacuo* followed by column chromatography using hexane and ethyl acetate (5:1) as an eluent to yield 3-nitro benzaldehyde product. ^{1}H NMR (500 MHz, $CDCl_3$, ppm): δ 10.13 (s, 1H), 8.72–8.70 (m, 1H), 8.49 (d, J = 8.2 Hz, 1H), 8.24 (d, J = 7.6 Hz, 1H), 7.78 (t, J = 7.9 Hz, 1H); ^{13}C NMR (126 MHz, $CDCl_3$, ppm): δ 189.82, 148.92, 137.53, 134.76, 130.50, 128.66, 124.50.

Acetophenone (2j).[55]

Acetophenone was synthesized with 99% yield according to the general procedure for the oxidation of styrene derivatives using bpy-UiO-Fe(OH)$_3$ (0.4 mol% Fe), α-methylstyrene (1.5 mmol), H_2O_2 (2.5 eq.) at 80 °C for 8 h. After 8 h, the combined organic extracts were concentrated *in vacuo* followed by flash chromatography using hexane and ethyl acetate (5:1) as an eluent to yield acetophenone product. ^{1}H NMR (600 MHz, $CDCl_3$, ppm): δ 7.95 (d, J = 8.1 Hz, 2H), 7.56 (t, J = 7.8 Hz, 1H), 7.46 (t, J = 7.7 Hz, 2H), 2.60 (s, 3H); ^{13}C NMR (151 MHz, $CDCl_3$, ppm): δ 198.3, 137.3, 133.3, 128.7, 128.5, 26.8.

Benzoic acid (3a).[60]

Benzoic acid was synthesized with 71% yield according to the general procedure for the oxidation of styrene derivatives using bpy-UiO-Fe(OH)$_3$ (0.4 mol% Fe), styrene (1.5 mmol), H_2O_2 (2.5 eq.) at 80 °C for 20 h. Upon completion, the catalyst was removed by centrifugation, and the reaction mixture was treated with 1–2 M aqueous NaOH to convert the acids to their sodium salts. The organic phase was removed with $CHCl_3$ (3 × 10 mL). The aqueous layer was then acidified to pH ∼1 with dilute HCl and extracted with $CHCl_3$ (3 × 10 mL). The combined organic extracts were dried over Na_2SO_4, filtered, and

concentrated under reduced pressure to afford benzoic acid (71% yield) as a white solid. ^{1}H NMR (400 MHz, $CDCl_3$, ppm): δ 11.67 (s, 1H), 8.20 (d, J = 7.2 Hz, 2H), 7.68 (t, J = 7.4 Hz, 1H), 7.68 (t, J = 7.9 Hz, 2H); ^{13}C NMR (100 MHz, $CDCl_3$, ppm): δ 172.60, 133.89, 130.28, 129.39, 128.55.

4-Methyl benzoic acid (3b).[60]

4-Methyl benzoic acid was synthesized with 72% yield according to the general procedure for the oxidation of styrene derivatives using bpy-UiO-Fe(OH)$_3$ (0.4 mol% Fe), 4-methyl styrene (1.5 mmol), H_2O_2 (2.5 eq.) at 80 °C for 20 h. Upon completion, the catalyst was removed by centrifugation, and the reaction mixture was treated with 1–2 M aqueous NaOH to convert the acids to their sodium salts. The organic phase was removed with $CHCl_3$ (3 × 10 mL). The aqueous layer was then acidified to pH ∼1 with dilute HCl and extracted with $CHCl_3$ (3 × 10 mL). The combined organic extracts were dried over Na_2SO_4, filtered, and concentrated under reduced pressure to yield 4-methyl benzoic acid product. ^{1}H NMR (400 MHz, DMSO-d_6, ppm): δ 12.80 (s, 1H), 7.84 (d, J = 6.48 Hz, 2H), 7.29 (d, J = 7.88 Hz, 2H), 2.36 (s, 3H); ^{13}C NMR (100 MHz, DMSO-d_6, ppm): δ 167.80, 143.46, 129.80, 129.55, 128.52, 21.55, 126.75.

2-Methyl benzoic acid (3c).[61]

2-Methyl benzoic acid was synthesized with 69% yield according to the general procedure for the oxidation of styrene derivatives using bpy-UiO-Fe(OH)$_3$ (0.4 mol% Fe), 2-methyl styrene (1.5 mmol), H_2O_2 (2.5 eq.) at 80 °C for 20 h. Upon completion, the catalyst was removed by centrifugation, and the reaction mixture was treated with 1–2 M aqueous NaOH to convert the acids to their sodium salts. The organic phase was removed with $CHCl_3$ (3 × 10 mL). The aqueous layer was then acidified to pH ∼1 with dilute HCl and extracted with $CHCl_3$ (3 × 10 mL). The combined organic extracts were dried over Na_2SO_4, filtered, and concentrated under reduced pressure to afford 2-methyl benzoic acid product. ^{1}H NMR (400 MHz, $CDCl_3$, ppm): δ 12.58 (s, 1H), 8.09 (dd, J = 7.3, 1.8 Hz, 1H), 7.47 (t, J = 7.8 Hz, 1H), 7.28–7.32 (m, 2H), 2.68 (s, 3H); ^{13}C NMR (101 MHz, $CDCl_3$, ppm): δ 173.79, 141.54, 133.12, 132.08, 131.76, 128.47, 126.01, 22.29.

4-*tert*-Butylbenzoic acid (3d).[61]

4-*tert*-Butylbenzoic acid was synthesized with 56% yield according to the general procedure for the oxidation of styrene derivatives using bpy-UiO-Fe(OH)$_3$ (0.4 mol% Fe), 4-*tert*-

butylstyrene (1.5 mmol), H_2O_2 (2.5 eq.) at 80 °C for 20 h. Upon completion, the catalyst was removed by centrifugation, and the reaction mixture was treated with 1–2 M aqueous NaOH to convert the acids to their sodium salts. The organic phase was removed with $CHCl_3$ (3 × 10 mL). The aqueous layer was then acidified to pH ∼1 with dilute HCl and extracted with $CHCl_3$ (3 × 10 mL). The combined organic extracts were dried over Na_2SO_4, filtered, and concentrated under reduced pressure to yield 4-*tert*-butylbenzoic acid product. ^{1}H NMR (400 MHz, $CDCl_3$, ppm): δ 12.67 (s, 1H), 8.07 (d, J = 8.3 Hz, 2H), 7.51 (d, J = 8.3 Hz, 2H), 1.37 (s, 9H); ^{13}C NMR (101 MHz, $CDCl_3$, ppm): δ 172.80, 157.75, 130.29, 126.75, 125.62, 35.33, 31.23.

4-Methoxy benzoic acid (3e).[61]

4-Methoxybenzoic acid was synthesized with 57% yield according to the general procedure for the oxidation of styrene derivatives using bpy-UiO-Fe(OH)$_3$ (0.4 mol% Fe), 4-methoxy styrene (1.5 mmol), H_2O_2 (2.5 eq.) at 80 °C for 20 h. Upon completion, the catalyst was removed by centrifugation, and the reaction mixture was treated with 1–2 M aqueous NaOH to convert the acids to their sodium salts. The organic phase was removed with $CHCl_3$ (3 × 10 mL). The aqueous layer was then acidified to pH ∼1 with dilute HCl and extracted with $CHCl_3$ (3 × 10 mL). The combined organic extracts were dried over Na_2SO_4, filtered, and concentrated under reduced pressure to afford 4-methoxy benzoic acid product. ^{1}H NMR (400 MHz, $CDCl_3$, ppm): δ 12.13 (s, 1H), 8.08 (d, J = 8.3 Hz, 2H), 6.95 (d, J = 9.2 Hz, 2H), 3.88 (s, 3H); ^{13}C NMR (101 MHz, $CDCl_3$, ppm): δ 171.70, 164.19, 132.51, 121.75, 113.90, 55.64.

2-Methoxy benzoic acid (3f).[61]

2-Methoxybenzoic acid was synthesized with 60% yield according to the general procedure for the oxidation of styrene derivatives using bpy-UiO-Fe(OH)$_3$ (0.4 mol% Fe), 2-methoxy styrene (1.5 mmol), H_2O_2 (2.5 eq.) at 80 °C for 20 h. Upon completion, the catalyst was removed by centrifugation, and the reaction mixture was treated with 1–2 M aqueous NaOH to convert the acids to their sodium salts. The organic phase was removed with $CHCl_3$ (3 × 10 mL). The aqueous layer was then acidified to pH ∼1 with dilute HCl and extracted with $CHCl_3$ (3 × 10 mL). The combined organic extracts were dried over Na_2SO_4, filtered, and concentrated under reduced pressure to afford 2-methoxy benzoic acid product. ^{1}H NMR (400 MHz, $CDCl_3$, ppm): δ 10.82 (s, 1H), 8.18 (dd, J = 8.3, 1.8 Hz, 1H), 7.58 (ddd, J = 8.3, 7.3, 1.8 Hz, 1H), 7.14 (t, J = 7.8 Hz, 1H), 7.06 (d, J = 8.3 Hz, 1H),

4.08 (s, 3H); ^{13}C NMR (101 MHz, $CDCl_3$, ppm): δ 165.66, 158.18, 135.22, 133.86, 122.27, 117.66, 111.77, 56.78.

4-Chloro benzoic acid (3g).[62]

4-Chlorobenzoic acid was synthesized with 78% yield according to the general procedure for the oxidation of styrene derivatives using bpy-UiO-Fe(OH)$_3$ (0.4 mol% Fe), 4-chloro styrene (1.5 mmol), H_2O_2 (2.5 eq.) at 80 °C for 20 h. Upon completion, the catalyst was removed by centrifugation, and the reaction mixture was treated with 1–2 M aqueous NaOH to convert the acids to their sodium salts. The organic phase was removed with $CHCl_3$ (3 × 10 mL). The aqueous layer was then acidified to pH ∼1 with dilute HCl and extracted with $CHCl_3$ (3 × 10 mL). The combined organic extracts were dried over Na_2SO_4, filtered, and concentrated under reduced pressure to yield 4-chloro benzoic acid product. ^{1}H NMR (400 MHz, DMSO-d_6, ppm): δ 13.16 (br s, 1H), 7.93 (d, J = 8.0 Hz, 2H), 7.54 (d, J = 8.0 Hz, 2H); ^{13}C NMR (100 MHz, DMSO-d_6, ppm): δ 166.5, 137.8, 131.2, 129.7, 128.8.

3-Chloro benzoic acid (3h).[61]

3-Chlorobenzoic acid was synthesized with 69% yield according to the general procedure for the oxidation of styrene derivatives using bpy-UiO-Fe(OH)$_3$ (0.4 mol% Fe), 3-chloro styrene (1.5 mmol), H_2O_2 (2.5 eq.) at 80 °C for 20 h. Upon completion, the catalyst was removed by centrifugation, and the reaction mixture was treated with 1–2 M aqueous NaOH to convert the acids to their sodium salts. The organic phase was removed with $CHCl_3$ (3 × 10 mL). The aqueous layer was then acidified to pH ∼1 with dilute HCl and extracted with $CHCl_3$ (3 × 10 mL). The combined organic extracts were dried over Na_2SO_4, filtered, and concentrated under reduced pressure to yield 3-chloro benzoic acid product. ^{1}H NMR (400 MHz, $CDCl_3$, ppm): δ 11.57 (s, 1H), 8.10 (s, 1H), 8.01 (d, J = 8.3 Hz, 1H), 7.60 (d, J = 7.3 Hz, 1H), 7.43 (t, J = 7.8 Hz, 1H); ^{13}C NMR (101 MHz, $CDCl_3$, ppm): δ 171.23, 134.87, 134.08, 131.09, 130.42, 130.00, 128.48.

3-Nitro benzoic acid (3i).[62]

3-Nitrobenzoic acid was synthesized with 73% yield according to the general procedure for the oxidation of styrene derivatives using bpy-UiO-Fe(OH)$_3$ (0.4 mol% Fe), 3-nitro styrene (1.5 mmol), H_2O_2 (2.5 eq.) at 80 °C for 20 h. Upon completion, the catalyst was removed by centrifugation, and the reaction mixture was treated with 1–2 M aqueous NaOH to convert the acids to their sodium salts. The organic phase was removed with $CHCl_3$

(3 × 10 mL). The aqueous layer was then acidified to pH ∼1 with dilute HCl and extracted with $CHCl_3$ (3 × 10 mL). The combined organic extracts were dried over Na_2SO_4, filtered, and concentrated under reduced pressure to yield 3-nitro benzoic acid product. ^{1}H NMR (400 MHz, DMSO-d_6, ppm): δ 13.66 (br s, 1H), 8.61 (s, 1H), 8.46 (d, J = 8.0 Hz, 1H), 8.34 (d, J = 8.0 Hz, 1H), 8.34 (d, J = 8.0 Hz, 1H), 7.81 (t, J = 8.0 Hz, 36 1H). ^{13}C NMR (100 MHz, DMSO-d_6, ppm) δ 165.5, 147.9, 135.4, 132.5, 130.5, 127.3, 123.7.

Conclusion

In summary, we have developed a robust single-site Fe(III) catalyst supported on a bipyridine-functionalized UiO framework (bpy-UiO-Fe$(OH)_3$) for the chemoselective oxidation of styrene using H_2O_2 as an environmentally benign oxidant. The catalyst enables tunable selectivity between benzaldehyde and benzoic acid by adjusting reaction conditions, delivering up to 100% selectivity for benzaldehyde at 80 °C in 8 h and favoring benzoic acid upon extended reaction times. Control studies confirmed the heterogeneous, single-site nature of the MOF catalyst, while recycling experiments demonstrated high stability with negligible metal leaching. Mechanistic investigations suggest a non-radical pathway involving epoxide and diol intermediates prior to oxidative C–C bond cleavage. These findings highlight the potential of MOF-supported single-site iron catalysts as sustainable platforms for selective alkene oxidation and offer new opportunities for designing environmentally friendly catalytic systems for fine chemical synthesis.

References

[1] Mu, M.; Wang, Y.; Qin, Y.; Yan, X.; Li, Y.; Chen, L. Two-Dimensional Imine-Linked Covalent Organic Frameworks as a Platform for Selective Oxidation of Olefins. *ACS Applied Materials & Interfaces* **2017**, *9*, 22856–22863.

[2] Opgrande, J. L.; Dobratz, C. J.; Brown, E.; Liang, J.; Conn, G. S.; Shelton, F. J.; With, J. *Kirk-Othmer Encyclopedia of Chemical Technology*; John Wiley & Sons, Ltd, 2000.

[3] Satrio, J. A. B.; Doraiswamy, L. K. Production of Benzaldehyde: A Case Study in

a Possible Industrial Application of Phase-Transfer Catalysis. *Chemical Engineering Journal* **2001**, *82*, 43–56.

[4] Daniel, C. (54) PROCESS FOR CONVERSION OFTOLUENE TO BENZAALDEHYDE.

[5] Singh, F. V.; Milagre, H. M. S.; Eberlin, M. N.; Stefani, H. A. Synthesis of Benzophenones from Geminal Biaryl Ethenes Using M-Chloroperbenzoic Acid. *Tetrahedron Letters* **2009**, *50*, 2312–2316.

[6] Bai, X.; Zhu, M.; Liu, Y.; Xing, M.; Ji, X.; Zhang, A.; Yang, Y.; Lu, Y.; Liu, S. Effective Oxygen Activation on Polyoxometalate-Based Hybrids for Epoxidation of Alkenes. *Dalton Transactions* **2024**, *53*, 6875–6880.

[7] Arian, M.; Mollabagher, H.; Taheri, S.; Zamanian, A.; Mousavi, S. A. H. S. Preparation and Characterization of Nano MnO-CaLs as a Green Catalyst for Oxidation of Styrene. *Turkish Journal of Chemistry* **2021**, *45*, 1882–1894.

[8] Roy, M. *Trends in Chemical and Biological Research*; Lincoln University College, Malaysia, 2023; pp 10–24.

[9] Pappo, R.; Allen, D.; Lemieux, R.; Johnson, W. Notes - Osmium Tetroxide-Catalyzed Periodate Oxidation of Olefinic Bonds. *The Journal of Organic Chemistry* **1956**, *21*, 478–479.

[10] Nguyen, T. M.; Lee, D. A Novel Reactivity of SeO2 with 1,3-Dienes: Formation of Syn 1,2- and 1,4-Diols via a Facile C-Se Bond Oxidation. *Organic Letters* **2001**, *3*, 3161–3163.

[11] Criegee, R. Mechanism of Ozonolysis. *Angewandte Chemie International Edition in English* **1975**, *14*, 745–752.

[12] Hu, Y.; Song, Z.; Zheng, P.; Zhang, Q.; Liu, J. Selective Oxidation of Styrene to Valuable C7 or C8 Aromatics via Green Photocatalysis with TiO2-based Catalysts. *Molecular Catalysis* **2024**, *569*, 114585.

[13] Peng, Z.; Chen, R.; Li, H. Heterogeneous Photocatalytic Oxidative Cleavage of Polystyrene to Aromatics at Room Temperature. *ACS Sustainable Chemistry & Engineering* **2023**, *11*, 10688–10697.

[14] Cheng, C.; Zhu, B.; Cheng, B.; Macyk, W.; Wang, L.; Yu, J. Catalytic Conversion of Styrene to Benzaldehyde over S-Scheme Photocatalysts by Singlet Oxygen. *ACS Catalysis* **2023**, *13*, 459–468.

[15] Rodikova, Y. A.; Zhizhina, E. G. Homogeneous Redox Catalysts Based on Heteropoly Acid Solutions: 5. Developing a Two-Stage Process for Propylene Oxidation to Acetone: A Review. *Kinetics and Catalysis* **2023**, *64*, 687–699.

[16] McCaffrey, V. P.; Conover, O. Q.; Bernard, M. A.; Yarranton, J. T.; Lessnau, N. R.; Hempfling, J. P. Substituent Effects in Dioxovanadium(V) Schiff-Base Complexes: Tuning the Outcomes of Oxidation Reactions. *Polyhedron* **2021**, *205*, 115268.

[17] Lawal, N. S.; Ibrahim, H.; Bala, M. D. Oxidation of Styrene to Benzaldehyde Catalyzed by Schiff Base Functionalized Triazolylidene Ni(II) Complexes. *Molecules* **2022**, *27*, 4941.

[18] Lashanizadegan, M.; Asna Ashari, H.; Sarkheil, M.; Anafcheh, M.; Jahangiry, S. New Cu(II), Co(II) and Ni(II) Azo-Schiff Base Complexes: Synthesis, Characterization, Catalytic Oxidation of Alkenes and DFT Study. *Polyhedron* **2021**, *200*, 115148.

[19] Liu, J.-Y.; Li, X.-F.; Li, Y.-Z.; Chang, W.-B.; Huang, A.-J. Oxidation of Styrene by Various Oxidants with Different Kinds of Metalloporphyrins. *Journal of Molecular Catalysis A: Chemical* **2002**, *187*, 163–167.

[20] De Paula, R.; Simões, M. M. Q.; Neves, M. G. P. M. S.; Cavaleiro, J. A. S. Oxidation of Styrene and of Some Derivatives with H2O2 Catalyzed by Novel Imidazolium-Containing Manganese Porphyrins: A Mechanistic and Thermodynamic Interpretation. *Journal of Molecular Catalysis A: Chemical* **2011**, *345*, 1–11.

[21] Gonzalez-de Castro, A.; Xiao, J. Green and Efficient: Iron-Catalyzed Selective Oxidation of Olefins to Carbonyls with O_2. *Journal of the American Chemical Society* **2015**, *137*, 8206–8218.

[22] Duarte, T. A. G.; Estrada, A. C.; Simões, M. M. Q.; Santos, I. C. M. S.; Cavaleiro, A. M. V.; Neves, M. G. P. M. S.; Cavaleiro, J. A. S. Homogeneous Catalytic Oxidation of Styrene and Styrene Derivatives with Hydrogen Peroxide in the Presence of Transition Metal-Substituted Polyoxotungstates. *Catalysis Science & Technology* **2014**, *5*, 351–363.

[23] Li, X.; Wang, Q.; Lyu, J.; Li, X. Recent Investigation on Epoxidation of Styrene with Hydrogen Peroxide by Heterogeneous Catalysis. *ChemistrySelect* **2021**, *6*, 9735–9768.

[24] Manimaran, S.; Subramanian, K.; Tschentscher, R.; Pandurangan, A. Epoxidation of Alkene Using Bi-Functional Metal Oxide Supported SBA-16 Catalyst. *Journal of Porous Materials* **2022**, *29*, 357–369.

[25] Kumar Sharma, R.; Bandichhor, R.; Mishra, V.; Sharma, S.; Yadav, S.; Mehta, S.; Arora, B.; Rana, P.; Dutta, S.; Solanki, K. Advanced Metal Oxide-Based Nanocatalysts for the Oxidative Synthesis of Fine Chemicals. *Materials Advances* **2023**, *4*, 1795–1830.

[26] Amanchi, S. R.; Patel, A.; Das, S. K. Polyoxometalate Coordinated Transition Metal Complexes as Catalysts: Oxidation of Styrene to Benzaldehyde/Benzoic Acid. *Journal of Chemical Sciences* **2014**, *126*, 1641–1645.

[27] Pathan, S.; Patel, A. Keggin Type Transition Metal Substituted Phosphomolybdates: Heterogeneous Catalysts for Selective Aerobic Oxidation of Alcohols and Alkenes under Solvent Free Condition. *Catalysis Science & Technology* **2014**, *4*, 648–656.

[28] Maksimchuk, N. V.; Kholdeeva, O. A. H2O2-Based Selective Oxidations Catalyzed by Supported Polyoxometalates: Recent Advances. *Catalysts* **2023**, *13*, 360.

[29] Guan, X.; Duan, C.; Wang, H.; Lu, B.; Zhao, J.; Cai, Q. Tuneable Oxidation of Styrene to Benzaldehyde and Benzoic Acid over Co/ZSM-5. *New Journal of Chemistry* **2021**, *45*, 18192–18201.

[30] Andrade, M. A.; Martins, L. M. D. R. S. Selective Styrene Oxidation to Benzaldehyde over Recently Developed Heterogeneous Catalysts. *Molecules* **2021**, *26*, 1680.

[31] Wang, Y.; Liu, H.; Cai, D.; Zhou, J.; Wu, M.; Zheng, H.; Xie, D. Ru@C as a Safety-Release RuO3@C Catalyst Precursor for Selective Oxidative Cleavage of Alkenes to

Aldehydes or Ketones and Alkynes to 1, 2-Diketones. *Applied Organometallic Chemistry* **2022**, *36*, e6831.

[32] Lashanizadegan, M.; Habibi, N.; Mirzazadeh, H.; Ghiasi, M. Immobilized Magnetic Copper Hydrazone Complexes for Oxidation of Styrene to Benzaldehyde by Tert-Butylhydroxyperoxide: An Experimental and Theoretical Approach. *Reaction Kinetics, Mechanisms and Catalysis* **2022**, *135*, 3223–3242.

[33] Furukawa, H.; Cordova, K. E.; O'Keeffe, M.; Yaghi, O. M. The Chemistry and Applications of Metal-Organic Frameworks. *Science* **2013**, *341*, 1230444.

[34] Ikuno, T. et al. Methane Oxidation to Methanol Catalyzed by Cu-Oxo Clusters Stabilized in NU-1000 Metal–Organic Framework. *Journal of the American Chemical Society* **2017**, *139*, 10294–10301.

[35] Lin, Z.; Thacker, N. C.; Sawano, T.; Drake, T.; Ji, P.; Lan, G.; Cao, L.; Liu, S.; Wang, C.; Lin, W. Metal–Organic Layers Stabilize Earth-Abundant Metal–Terpyridine Diradical Complexes for Catalytic C–H Activation. *Chemical Science* **2017**, *9*, 143–151.

[36] Newar, R.; Begum, W.; Akhtar, N.; Antil, N.; Chauhan, M.; Kumar, A.; Gupta, P.; Malik, J.; Balendra; Manna, K. Mono-Phosphine Metal-Organic Framework-Supported Cobalt Catalyst for Efficient Borylation Reactions. *European Journal of Inorganic Chemistry* **2022**, *2022*.

[37] Seo, J. S.; Whang, D.; Lee, H.; Jun, S. I.; Oh, J.; Jeon, Y. J.; Kim, K. A Homochiral Metal–Organic Porous Material for Enantioselective Separation and Catalysis. *Nature* **2000**, *404*, 982–986.

[38] Mohanty, B.; Kumari, S.; Yadav, P.; Kanoo, P.; Chakraborty, A. Metal-Organic Frameworks (MOFs) and MOF Composites Based Biosensors. *Coordination Chemistry Reviews* **2024**, *519*, 216102.

[39] Begum, W.; Chauhan, M.; Kalita, R.; Gupta, P.; Akhtar, N.; Antil, N.; Newar, R.; Manna, K. Synergetic Ni–Ce Active Sites in Mixed Cerium/Zirconium Metal–Organic Framework Nodes for Selective Methane Oxidation into Ethanol. *ACS Catalysis* **2024**, *14*, 10427–10436.

[40] Simons, M. C.; Prinslow, S. D.; Babucci, M.; Hoffman, A. S.; Hong, J.; Vitillo, J. G.; Bare, S. R.; Gates, B. C.; Lu, C. C.; Gagliardi, L.; Bhan, A. Beyond Radical Rebound: Methane Oxidation to Methanol Catalyzed by Iron Species in Metal–Organic Framework Nodes. *Journal of the American Chemical Society* **2021**, *143*, 12165–12174.

[41] Chauhan, M.; Rana, B.; Gupta, P.; Kalita, R.; Thadhani, C.; Manna, K. Tailored Pore-Confined Single-Site Iron(III) Catalyst for Selective CH4 Oxidation to CH3OH or CH3CO2H Using O2. *Nature Communications* **2024**, *15*, 9798.

[42] Gupta, P.; Chauhan, M.; Rana, B.; Kalita, R.; Maurya, R.; Manna, K. Engineering Mono- vs Dinuclear Iron(II)-Active Sites to Steer Liquid Oxygenate Selectivity in Methane Oxidation Pathways Using O2. *Journal of the American Chemical Society* **2025**, *147*, 25372–25384.

[43] Bai, Y.; Dou, Y.; Xie, L.-H.; Rutledge, W.; Li, J.-R.; Zhou, H.-C. Zr-Based Metal–Organic Frameworks: Design, Synthesis, Structure, and Applications. *Chemical Society Reviews* **2016**, *45*, 2327–2367.

[44] Cavka, J. H.; Jakobsen, S.; Olsbye, U.; Guillou, N.; Lamberti, C.; Bordiga, S.; Lillerud, K. P. A New Zirconium Inorganic Building Brick Forming Metal Organic Frameworks with Exceptional Stability. *Journal of the American Chemical Society* **2008**, *130*, 13850–13851.

[45] Biswas, S.; Van Der Voort, P. A General Strategy for the Synthesis of Functionalised UiO-66 Frameworks: Characterisation, Stability and CO2 Adsorption Properties. *European Journal of Inorganic Chemistry* **2013**, *2013*, 2154–2160.

[46] Zhang, T.; Manna, K.; Lin, W. Metal–Organic Frameworks Stabilize Solution-Inaccessible Cobalt Catalysts for Highly Efficient Broad-Scope Organic Transformations. *Journal of the American Chemical Society* **2016**, *138*, 3241–3249.

[47] Manna, K.; Zhang, T.; Carboni, M.; Abney, C. W.; Lin, W. Salicylaldimine-Based Metal–Organic Framework Enabling Highly Active Olefin Hydrogenation with Iron and Cobalt Catalysts. *Journal of the American Chemical Society* **2014**, *136*, 13182–13185.

[48] Zhao, Y.; Zhang, S.; Wang, M.; Han, J.; Wang, H.; Li, Z.; Liu, X. Engineering Iridium-

Based Metal Organic Frameworks towards Electrocatalytic Water Oxidation. *Dalton Transactions* **2018**, *47*, 4646–4652.

[49] Gupta, P.; Akhtar, N.; Begum, W.; Rana, B.; Kalita, R.; Chauhan, M.; Thadhani, C.; Manna, K. Metal–Organic Framework-Supported Mono Bipyridyl–Iron Hydroxyl Catalyst for Selective Benzene Hydroxylation into Phenol. *Inorganic Chemistry* **2024**, *63*, 11907–11916.

[50] Hagen, W. R. EPR Spectroscopy as a Probe of Metal Centres in Biological Systems. *Dalton Transactions* **2006**, 4415–4434.

[51] An, B. et al. Direct Photo-Oxidation of Methane to Methanol over a Mono-Iron Hydroxyl Site. *Nature Materials* **2022**, *21*, 932–938.

[52] Bou-Abdallah, F.; Chasteen, N. D. Spin Concentration Measurements of High-Spin (G = 4.3) Rhombic Iron(III) Ions in Biological Samples: Theory and Application. *JBIC Journal of Biological Inorganic Chemistry* **2008**, *13*, 15–24.

[53] G. Duarte, T. A.; C. Estrada, A.; Q. Simões, M. M.; S. Santos, I. C. M.; V. Cavaleiro, A. M.; S. Neves, M. G. P. M.; S. Cavaleiro, J. A. Homogeneous Catalytic Oxidation of Styrene and Styrene Derivatives with Hydrogen Peroxide in the Presence of Transition Metal-Substituted Polyoxotungstates. *Catalysis Science & Technology* **2015**, *5*, 351–363.

[54] Yang, Q.; Zhang, H.-Y.; Wang, L.; Zhang, Y.; Zhao, J. Ru/UiO-66 Catalyst for the Reduction of Nitroarenes and Tandem Reaction of Alcohol Oxidation/Knoevenagel Condensation. *ACS Omega* **2018**,

[55] Ma, X.; He, D.; Jones, A. M.; Collins, R. N.; Waite, T. D. Reductive Reactivity of Borohydride- and Dithionite-Synthesized Iron-Based Nanoparticles: A Comparative Study. *Journal of Hazardous Materials* **2016**, *303*, 101–110.

[56] Guo, B.; Xue, J.-Y.; Li, H.-X.; Tan, D.-W.; Lang, J.-P. Design of recyclable TEMPO derivatives bearing an ionic liquid moiety and N, N-bidentate group for highly efficient Cu (I)-catalyzed conversion of alcohols into aldehydes and imines. *RSC Advances* **2016**, *6*, 51687–51693.

[57] Liu, Z.; Wang, P.; Yan, Z.; Chen, S.; Yu, D.; Zhao, X.; Mu, T. Rhodium-catalyzed reductive carbonylation of aryl iodides to arylaldehydes with syngas. *Beilstein Journal of Organic Chemistry* **2020**, *16*, 645–656.

[58] Jiang, X.; Wang, J.-M.; Zhang, Y.; Chen, Z.; Zhu, Y.-M.; Ji, S.-J. Palladium-catalyzed formylation of aryl halides with tert-butyl isocyanide. *Organic Letters* **2014**, *16*, 3492–3495.

[59] Kalita, R.; Begum, W.; Gupta, P.; Chauhan, M.; Akhtar, N.; Newar, R.; Manna, K. Chemoselective Oxidation of Alkenes by Metal-Organic Framework-Supported Copper Catalyst. *European Journal of Inorganic Chemistry* **2023**, *26*, e202300215.

[60] Zhang, Y.; Cheng, Y.; Cai, H.; He, S.; Shan, Q.; Zhao, H.; Chen, Y.; Wang, B. Catalyst-free aerobic oxidation of aldehydes into acids in water under mild conditions. *Green Chemistry* **2017**, *19*, 5708–5713.

[61] Hu, D.; Jiang, X. Stepwise benzylic oxygenation via uranyl-photocatalysis. *Green Chemistry* **2022**, *24*, 124–129.

[62] Salem, M. S.; Dubois, C.; Takamura, Y.; Kitajima, A.; Kawai, T.; Takizawa, S.; Kirihara, M. Light-induced autoxidation of aldehydes to peracids and carboxylic acids. *Green Chemistry* **2024**, *26*, 375–383.

Author's Profile

Name: Poorvi Gupta

Date of Birth: 27th June, 1998

Nationality: Indian

Email: poorvigupta2706@gmail.com



Educational Qualifications

- **Indian Institute of Technology Delhi, India, 2021–2026**
  PhD. Thesis titled: Engineering Earth-Abundant Metal Catalysts using Metal-Organic Frameworks (MOFs) for Selective Oxidation of Methane and other Hydrocarbons.
- **Indian Institute of Technology Madras, India, 2019–2021**
  Masters in Chemistry; Score: 8.74 CGPA
- **Ramjas College, Delhi University, India, 2016–2019**
  Graduation in Chemistry (Honours); Score: 7.851 CGPA
- **Queen Mary's School, Delhi, India**
  Class 12th **2015–2016**; CBSE-Board; Score: 94%
  Class 10th **2013–2014**; CBSE-Board; Score: 93.1%

Awards and Honors

- **Research Excellence Travel Award (RETA)**, a financial travel grant for attending 17th International conference on materials chemistry (MC17), Edinburgh, Scotland **July 2025**
- **Research Scholar Travel Award (RSTA)**, a financial travel grant for attending IUPAC|CHAINS 2023 in The Hague, The Netherlands. **August 2023**
- **CSIR-Junior and Senior Research Fellowship, IIT Delhi August 2021 - April 2026**

List of publications

1. Gupta, P.; Chauhan, M.; Rana, B.; Kalita, R.; Maurya, R. Manna, K. Engineering Mono- Vs Dinuclear Iron(II)-Active Sites to steer Liquid Oxygenate Selectivity in Methane Oxidation Pathways using O_2. *J. Am. Chem. Soc.* **2025**, *147*, 25372. (link)

2. Gupta, P.; Rana, B.; Maurya, R.; Kalita, R.; Chauhan, M.; Manna, K. Copper Catalyzed Selective Methane Oxidation into Acetic Acid using O_2. *Chem. Sci.* **2025**, *16*, 2785. (link)

3. Gupta, P.; Akhtar, N.; Begum, W.; Rana, B.; Kalita, R.; Chauhan, M.; Thadhani, M.; Manna, K. Metal-Organic Framework supported Mono Bipyridyl-Iron Hydroxyl Catalyst for Selective Benzene Hydroxylation into Phenol. *Inorg. Chem.* **2024**, *63*, 11907. (link)

4. Gupta, P.; Sarmah, S.; Kalita, R.; Rana, B. Manna, K. Mononuclear Bipyridyl-Iron(III) hydroxide in Metal-Organic Framework for Selective Alkene Oxidation. *J. Mol. Chem.* **2025**, *5*(3), 1225. (link)

5. Gupta, P.; Yadav, P.; Rana, B. Biplab, G.; Dhaka, R. S.; Manna, K. Ni_2MnAl Heusler Alloy Nanoparticles for Chemoselective Hydrogenation of Nitro Compounds. *Eur. J. Inorg. Ch.* **2024**, *27*, e202400157. (link)

6. Kumar, A.; Kalita, R.; Gupta, P.; Rana, B.; Chauhan, M.; Manna, K. Regioselective Hydroboration of Alkenes by Metal-Organic Framework Confined Mononuclear Bipyridyl–Iron Hydride Catalyst. *Inorg. Chim. Acta.* **2026**, *594*, 123082. (link)

7. Kalita, R.; Chauhan, M.; Gupta, P.; Begum, W.; Manna, K. Selective Monoborylation of Methane by a Mono Bipyridyl-Nickel(II) Hydride Catalyst. *Angew. Chem., Int. Ed.*, **2025**, e202413402. (link)

8. Chauhan, M.; Rana, B.;Gupta, P.; Choudhary, A.; Kalita, R.; Manna, K. Architecting Molecularly Dispersed Cu(I)-Active Sites at UiO-MOF Nodes for Thermocatalytic

Oxidation of Methane to Ethanol Using O_2. *Appl. Catal., B. Environ.*, **2025**, *377*, 125474. (link)

9. Thadhani, C.; Kalita, R.; Rana, B.; Akhtar, N.; Chauhan, M.; Gupta, P.; Biplab, G.; Manna, K. Cobalt Catalyzed Selective Monoborylation of Methane. *ACS Catal.* **2025**, *15*, 13958. (link)

10. Thadhani, C.; Kalita, R.; Rana, B.; Gupta, P.; Sarmah, S.; Manna, K. Selective borylation of methane by an iron(iii) dihydride catalyst. *Chem. Commun.* **2025**, *61*, 15818. (link)

11. Sharma, R.; Sihag, N.; Gupta, P.; Manna, K.; Yadav, M. R. Photoinduced Ni-Catalyzed Carbohalogenation of mono-Fluoro, gem-Difluoro, and Trifluoromethyl Tethered Alkenes. *Chem. Commun.*, **2025**, 61, 7273. (link)

12. Kalita, R.; Kumar, A.; Gupta, P.; Rana, B.; Sardar, B.; Chauhan, M.; Ghosh, B.; Monga, Y.; Manna, K. Regioselective Oxidative Bromination of Arenes by Metal-Organic Framework Confined Mono-Bipyridyl Iron(III) Catalyst. *Dalton Trans.*, **2025**, *54*, 6812. (link)

13. Chauhan, M.; Rana, B.; Gupta, P.; Kalita, R.; Thadhani, R.; Manna, K. Tailored Pore-Confined Single-Site Iron(III) Catalyst for Selective Methane Oxidation to Methanol or Acetic Acid Using O_2. *Nat. Commun*, **2024**, *15*, 9798. (link)

14. Begum, W.; Chuahan, M.; Kalita, P.; Gupta, P.; Akhtar, N.; Antil, N.; Newar, R.; Manna, K. Synergetic Ni-Ce Active Sites in Mixed Cerium/Zirconium Metal–Organic Framework Nodes for Selective Methane Oxidation into Ethanol. *ACS Catal.*, **2024**, *14*, 10427. (link)

15. Chauhan, M.; Thadhani, C.; Rana, B.; Gupta, P.; Ghosh, B.; Manna, K. Hydrogenolysis of Polyethylene by Metal-Organic Framework Confined Single-Site Ruthenium Catalysts. *Chem. Mater.*, **2024**, *36*, 10670. (link)

16. Kalita, R.; Chauhan, M.; Gupta, P.; Thadhani, C.; Begum, W.; Ghosh, B.; Balendra; Bisht, H.; Manna, K. Selective Monoborylation of Methane over Pore Confined Mononuclear Pyridylimine-Iridium(I)-Hydride. *Chem. Commun.*, **2024**, *60*, 6504. (link)

17. Akhtar, N.; Chuahan, M.; Gupta, P.; Antil, N.; Manna, K. Supported Pyridylimine-Cobalt Catalyst for N-Formylation of Amines Utilizing CO_2. *Eur. J. Inorg. Chem.*, **2023**, *52*, 15384. (link)

18. Kalita, R.; Begum, W.; Gupta, P.; Chuahan, M.; Akhtar, N.; Newar, R.; Manna, K. Chemoselective Oxidation of Alkenes by Metal-Organic Framework-Supported Copper Catalyst. *Eur. J. Inorg. Chem.*, **2023**, e202300. (link)

19. Newar, R.; Begum, W.; Akhtar, N.; Antil, N.; Chauhan, M.; Kumar, A.; Gupta, P.; Jaideep, M.; Balendra, Manna, K. Mono-Phosphine Metal-Organic Framework-Supported Cobalt Catalyst for Efficient Borylation Reactions. *Eur. J. Inorg. Chem.*, **2022**, e202101019. (link)

Research Presentations:

1. Poster Presentation at the 22nd International Conference on Modern Trends in Inorganic Chemistry (MTIC-XXII) held at the Department of Chemistry, University of Delhi, New Delhi, India, on the topic "Engineering Mono- vs Dinuclear Iron(II) Active Sites to Steer Liquid Oxygenate Selectivity in Methane Oxidation Pathways Using O_2." **2025**.

2. Oral presentation in In-House Symposium conducted at IIT Delhi. **2025**

3. Poster Presentation at 17th International conference on materials chemistry (MC17) conducted in Edinburgh, UK on the topic "Copper Catalyzed Selective Methane Oxidation into Acetic Acid using O_2." **2025**

4. Poster Presentation in Indo-Japan Scientific Meeting on Organometallic Chemistry organized by American Chemical Society (ACS) in collaboration with Indian National Science Academy and IIT Delhi on the topic "Metal-Organic Framework-Supported Mono Bipyridyl-Iron Hydroxyl Catalyst for Selective Benzene Hydroxylation into Phenol." **2024**

5. Oral Presentation at Graduate Student Seminar (GSS) at IIT Delhi on the topic entitled "Metal-Organic Framework confined Abundant Metal Catalysts for Chemoselective C-H Oxidation." **2024**

6. Oral Presentation at IUPAC|CHAINS2023 International Conference held at The World Forum The Hague, The Netherlands on the topic "Supported Pyridylimine-Cobalt Catalyst for *N*-Formylation Utilizing Carbon-Dioxide." **2023**.

7. Poster presentation in the 32nd CRSI National Symposium in Chemistry (CRSI-NSC-32) on the topic "Ni_2MnAl Heusler Alloy Nanoparticles for Chemoselective Hydrogenation of Nitro Compounds." **2024**

8. Poster presentation in In-House Symposium conducted at IIT Delhi. **2024**